Transactions of the ASME

Journal of Engineering for Power (ISSN 0022-0825) is edited and published quarterly at the offices of The American Society of Mechanical Engineers, United Engineering Center, 345 E. 47th St., New York, N. Y. 10017. ASME-TWX No. 710-581-5267, New York. Second Class postage paid at New York, N.Y., and at additional mailing offices.

CHANGES OF ADDRESS must be received at Society headquarters seven weeks before they are to be effective. Please send old label and new address.

PRICES: To members, $30.00, annually; to nonmembers, $60.00. Single copies, $20.00 each. Add $1.50 for postage to countries outside the United States and Canada.

INDEXED by the Engineering Index, Inc.

Journal of Engineering for Power

Published Quarterly by The American Society of Mechanical Engineers
VOLUME 102 • NUMBER 4 • OCTOBER 1980

(*Continued on page 769*)

D. J. Salamone
Project Engineer,
Compressor Division,
Allis-Chalmers Corporation,
Milwaukee, Wisc.
Assoc. Mem. ASME

E. J. Gunter
Professor,
Dept. of Mechanical and Aerospace Engineering,
University of Virginia,
Charlottesville, Va.
Mem. ASME

Synchronous Unbalance Response of an Overhung Rotor with Disk Skew

This paper deals with the influence of disk skew on the synchronous unbalance response of flexible rotors in damped bearings. A simple overhung rotor is treated to illustrate the effects of various combinations of unbalance and disk skew on the amplitude and phase angle response at the disk and bearings. The paper shows that it is impossible to balance the rotor at all speeds by single plane balancing even if three correction planes are employed. The presence of disk skew may be best detected by monitoring the far bearing for a rapid phase angle decrease after passing through the first critical speed.

Introduction

Within the past ten years, the technology for the design of high-speed turbo-rotors has become very sophisticated. These advanced design capabilities have supported the continuing emphasis in industry to build rotating machinery with larger capacities. Larger capacity designs often require longer, more flexible rotors capable of operating above several critical speeds. In order to safely operate through these critical speeds, a good balance is necessary to control rotor amplitudes and bearing forces.

Many extensive multi-plane balancing techniques, based on the influence coefficient method, have been developed in this country. These techniques have assumed that (1) the transverse axes of the rotor disks are perpendicular to the elastic centerline of the shaft, and (2) the shaft is not distorted. With these assumptions, the synchronous rotor excitation is due only to asymmetric radial mass distributions or disk eccentricities. However, in an actual rotor the shaft centerline may be bowed and the disks can be skewed, which induces effective external forces and moments on the shaft. A rotor might appear to be well balanced at a particular design speed when balanced with a technique that considers only the radial unbalance forcing function. However, the rotor may be considerably out of balance at other operating speeds as a result of the shaft bow and disk skew effects. These influences can induce large amplitudes of motion on the rotor when it is operating in the vicinity of critical speeds. Ultimately, these large amplitudes can lead to extensive rotor and bearing damage.

Extensive publications are available on the dynamic unbalance response of complex flexible rotor systems by such authors as Lund and Orcutt [1], Kawamo, et al. [2], Kirk and Gunter [3], Wolfe and Wong [4], Barrett, et al. [5], and Koenig [6]. However, their investigations have focused primarily on rotor response due to the action of radial unbalance forces, but do not include shaft bow and disk skew. Kikuchi [7] made a significant contribution toward developing the matrix transfer equations for a multimass rotor with shaft bow and disk skew. However, his formulation has several discrepancies which are pointed out in [8]. Nicholas, et al. [9] presented a very complete treatment of the influence of shaft bow on the single mass rotor in rigid bearings.

The incorporation of disk skew is considerably more complicated than the treatment of the radial unbalance alone. In order to examine the influence of disk skew, two additional equations of motion must be considered to represent the disk angular motion and gyroscopic moments. When the general Euler rotation angles are implemented to develop the dynamic equations of motion for a general precessing, nutating gyroscope, these equations are highly nonlinear. Consequently, only limited solutions can be obtained analytically. For example, Lund's [10] original synchronous unbalance response equations include the non-linear gyroscopic terms for a disk (however, permanent disk skew is not considered). This treatment requires an iterative procedure to include these nonlinear effects. Yamamoto [11] presented the general equations of motion for a skewed disk, transformed into linearized stationary coordinates. The Yamamoto approach employed the transformation of the Eulerian equations to a fixed coordinate system. Then, the governing dynamic equations of motion are obtained by applying a disk kinetic energy expression to Lagrange's equations of motion. The resulting equations are then linearized for small displacements and rotations. In the treatment of rotating machinery, the disk angular displacements and the shaft slopes are small in comparison to the characteristic length of the rotor. Therefore, the Yamamoto formulation may be used to describe the disk linear dynamic equations of motion.

The case of a single, overhung skewed disk on a uniform elastic shaft was treated by Benson [12] at the University of Virginia. Benson demonstrated that permanent disk skew can have a pronounced effect on the dynamics of the rotor shaft and that the single plane balancing procedure is not adequate to balance the overhung skewed disk at all speeds. This analytical formulation is of considerable value as it provides insight into the dynamic behavior of an overhung rotor system. However, this procedure is not readily adaptable to the evaluation of a multimass stepped rotor with skewed disks.

Salamone and Gunter [13] presented the governing transfer matrix equations to include the effects of disk skew and shaft bow, in addition to unbalance, for a general multimass rotor in fluid film bearings. The importance of these two additional effects was illustrated in an analysis of a multimass water pump. It was reported that bow and

Contributed by the Gas Turbine Division of The American Society of Mechanical Engineers and presented at the Gas Turbine Conference and Exhibit and Solar Energy Conference, San Diego, California, March 12–15, 1979. Manuscript received at ASME Headquarters December 26, 1978. Paper No. 79-GT-135.

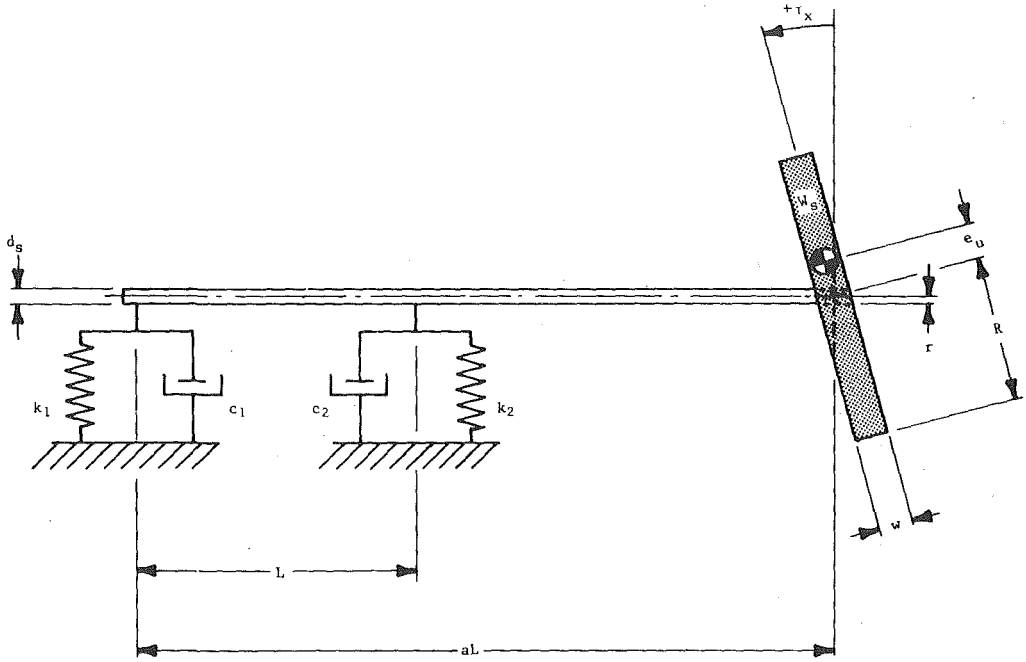

Fig. 1 Single mass unbalanced rotor with overhung skewed disk on flexible damped bearings

Table 1 Rotor Model Parameters*

L = 255.25 cm (100.49 in.)	R = 50.8 cm (20.0 in.)	I_p = 4.082 × 10^6 N-cm^2 (1.4224 × 10^5 lbf-in^2)
aL = 340.33 cm (133.99 in.)	r = 5.08 cm (2.0 in.)	I_t = 2.039 × 10^6 N-cm^2 (7.106 × 10^4 lbf-in^2)
d_s = 10.16 cm (4.0 in.)	$\dot{w}$ = 5.08 cm (2.0 in.)	$k_1 = k_2$ = 13171.11 N/cm (7520.9 lbf/in.)
W_s = 3132.04 N (704.14 lbf)	e_u = 0.025 cm (10 mils)	$c_1 = c_2$ = 51.28 N-s/cm (29.28 lbf-s/in.)
τ_x = 0.0684°	U_x = 8114.53 gm-cm (112.66 oz-in)	

* Refer to Fig. 1

skew can significantly alter the rotor response due to unbalance; particularly at the critical speeds.

Another formulation which has been successfully used to express the dynamical equations of motion of a complex rotor bearing system is the modal representation of Childs [14]. In the Childs derivation, the products of inertia have also been included, although the effects of disk skew and products of inertia were not explored.

In the treatment of disk skew in this paper, the angle of the disk skew τ is considered to be very small. Under these circumstances, it can be shown that the product of interia term is proportional to the product of the difference between the polar and transverse moments of inertia and the skew angle. An effect equivalent to disk skew can be generated by two radial out of phase unbalance components, which are separated by a finite axial distance on the disk. The resulting system is mathematically identical to a small disk skew, and the resulting unbalance components produce a bending moment about the disk center.

The results of [13] have inspired further study of disk skew effects to better understand the fundamental rotor behavior and the impact on balancing. Because of the complexity of the multimass rotor behavior with shaft bow and disk skew, it is desirable to first examine a single mass overhung rotor on flexible damped bearings with a skewed disk. The cases presented herein illustrate the potential impact of disk skew in comparison to, and in combination with, the commonly treated unbalance excitation.

Dynamic Motion of the Overhung Thin Disk Rotor

Description of the Rotor System. The single-mass overhung rotor model, as shown in Fig. 1, is a dimensionalized version of the model analyzed by Benson [12]. This model was used for verification of the general multimass matrix transfer equations in [8] and [13]. It should be noted that this is strictly an arbitrary rotor configuration which has been selected to illustrate the effects of disk skew on the synchronous rotor response. The dimensional characteristics of the thin disk rotor system are given in Table 1. Note that the bearing coefficients are assumed constant with rotor speed. The values of stiffness and damping were calculated from the nondimensional expressions in [12]. Bearing cross-coupling and shaft weight are neglected.

Nomenclature

A = amplitude ratio, δ/e_u
e_u = radial unbalance mass eccentricity, L
f = frequency ratio, ω/ω_{cr}
I_p = polar mass moment of inertia of disk, FLT^2
I_t = transverse mass moment of inertia of disk, FLT^2
$j = \sqrt{-1}$
K = constant
K_{ij} = stiffness, FL^{-1}
m = disk mass, FT^2L^{-1}
m_j = mass at station j, FT^2L^{-1}
t = time, T
U = complex unbalance, $U_x + jU_y$, FL
w = disk thickness, L
z = complex rotor displacement, L
α_j = angular location of unbalance at station j, RAD
β_j = angular location of disk skew at station j, RAD
δ = rotor displacement, L
θ = complex rotor slope, RAD
τ = complex disk skew angle, $\tau_x + j\tau_y$, RAD
ω = angular rotor shaft rotational speed, T^{-1}
ω_{cr} = angular rotor critical speed, T^{-1}

For a "thin" disk, the polar moment of inertia I_p is greater than the transverse moment of inertia I_t. In this analysis, it is assumed that the polar is twice the transverse. Note that this system will have only one synchronous critical speed of forward precession. The Benson analysis also considered the thick disk configuration in which the transverse moment of inertia I_t is greater than the polar moment of inertia I_p. In that case, there are two critical speeds of forward synchronous precession.

Rotor Equations of Motion. The general transfer matrix equations used in this analysis have previously been derived and presented in [8] and [13], respectively. These multimass matrix equations become greatly simplified for the single mass overhung rotor illustrated in Fig. 1. Benson [12] expressed eight equations of motion that specifically apply to this rotor system, with isotropic bearings and a massless shaft. These eight equations were expressed as the following four complex equations:

$$e^{j\omega t}\begin{Bmatrix} me_u\omega^2 e^{j\alpha} \\ \tau\omega^2(I_p - I_t)e^{j\beta} \\ 0 \\ 0 \end{Bmatrix} = \begin{bmatrix} m & 0 & 0 & 0 \\ 0 & I_t & 0 & 0 \\ 0 & 0 & 0 & 0 \\ 0 & 0 & 0 & 0 \end{bmatrix}\begin{Bmatrix} \ddot{Z} \\ \ddot{\theta} \\ \ddot{Z}_1 \\ \ddot{Z}_2 \end{Bmatrix} + \begin{bmatrix} C & 0 & 0 & 0 \\ 0 & -j\omega I_p & 0 & 0 \\ 0 & 0 & C_1 & 0 \\ 0 & 0 & 0 & C_2 \end{bmatrix}\begin{Bmatrix} \dot{Z} \\ \dot{\theta} \\ \dot{Z}_1 \\ \dot{Z}_2 \end{Bmatrix} + \begin{bmatrix} K_{zz} & K_{z\theta} & K_{z1} & K_{z2} \\ & K_{\theta\theta} & K_{\theta_1} & K_{\theta_2} \\ (\text{SYM}) & & K_{11} & K_{12} \\ & & & K_{22} \end{bmatrix}\begin{Bmatrix} Z \\ \theta \\ Z_1 \\ Z_2 \end{Bmatrix} \quad (1)$$

Examination of these equations of motion illustrate several important features. First, it is observed that there are two forcing functions acting on the disk deflection equation Z and slope equation θ which are generated by radial unbalance and disk skew. The second feature, observed from the moment forcing term, is that the sign of the term is dependent upon whether the polar moment of inertia is larger than the transverse moment of inertia. In the case of a thick disk, where the transverse is larger than the polar, the skew gyroscopic moment would be opposite in sign compared to the moment for a thin disk. Therefore, considerably different dynamic effects are observed with disk skews on thick disks as compared to thin disks. This feature will be discussed in detail in a future paper.

Synchronous Response of the Overhung Thin Disk Rotor. The rotor response results for five computer cases are illustrated in Figs. 2–7. These are plots of the dimensionless amplitude and phase angle versus frequency ratio for the three rotor locations corresponding to the near bearing (closest to disk), the far bearing and the disk. The amplitude of motion δ is made dimensionless by dividing by the unbalance eccentricity e_u. The speed ω is made dimensionless by dividing by the rotor critical speed on rigid supports ω_{cr}. The rotor synchronous response was calculated for various combinations of unbalance and disk skew. Note that for this rotor system, there is only one critical speed which is approximately 60 percent of the rigid support value. This reduction from the rigid value is due to the flexibility of the bearings. In Cases 1–5, the values of unbalance and disk skew correspond to those originally used by Benson. This was done in order to verify the accuracy of the matrix transfer procedure.

Fig. 2 illustrates the disk amplitude versus speed for various cases of disk unbalance and skew. With unbalance only, it is seen that the disk peak amplitude is 9.5. When the rotor is operating well above the critical speed, the dimensionless amplitude is 1. Therefore, the rotor has an amplification factor of 9.5 at the critical speed.

Fig. 3 represents the disk phase angle change versus speed for the various cases of disk skew and unbalance. For the case of unbalance alone, the rotor experiences a 90 deg phase shift at the critical speed. Above the critical, this phase angle increases to 180 deg and then remains constant for speed ratios in excess of $f = 1$. This phase angle behavior corresponds to the phase angle response of the single mass Jeffcott model.

In Cases 2 and 3, positive and negative disk skew only are considered. For the amount of disk skew assumed, Fig. 2 shows that the amplitude at the critical speed is approximately 2. Above the critical speed, the amplitude will decrease with increasing speed. This physically corresponds to the situation in which the disk is straightening out and is attempting to rotate about its principal inertia axis. For the case of radial unbalance only, at super critical speeds, the disk will rotate about its mass center. This will cause a circular orbit or radius e_u, which represents the displacement of the mass center from the shaft elastic axis.

For the case of disk skew only, Fig. 3 shows that the disk phase angle will change through 90 deg at the critical speed and on to approximately 180 deg for $f = 1.0$. For the case of negative disk skew, the phase angle change observed at the disk is almost identical to the response observed with radial unbalance. For positive disk skew, the phase angle changes are 180 deg out of phase with the negative disk skew phase angles and vary from 180 deg to approximately 360 deg. One slight variation in the phase angle behavior, in comparison to the response with pure unbalance, is the phase behavior at supercritical speeds in which $f > 1$. Here it is seen that the Case 2 phase angle reduces slightly from 180 to 150 deg for f varying from 1 to 5. It will be seen later that the observation of the phase change on the rotor at supercritical speeds is an indicator that disk skew is present in the system.

In Case 4, a combination of unbalance and negative disk skew is assumed. In this situation, the unbalance moment acts in conjunction with the radial unbalance to increase the rotor shaft motion at the disk location. The response of Case 4 is equivalent to a linear vector superposition of Cases 1 and 2. Since Fig. 3 shows that the phase angle change for radial unbalance and negative disk skew is similar, the vector combination of positive unbalance and negative disk skew will always result in an increase in rotor response. This can be observed in Fig. 2, Case 4, where the amplitude at the critical is 11.5. For Case 5, unbalance and a positive disk skew are assumed. In this situation, the maximum amplitude at the critical speed has reduced to 7.5. Note that by shifting the disk skew by 180 deg, the rotor amplitude has been decreased from 11.5 to 7.5.

In the analytic equations of motion developed by Benson or in the matrix transfer equations of motion, the system is assumed to be linear. Therefore, the principle of linear superposition of loads may be applied. It will be shown later, that if the unbalance in this case were reduced by a factor of 4.75, then the combination of unbalance and positive disk skew would result in zero amplitude at the critical speed. This observation was not originally made in the Benson analysis.

If one were to observe the amplitude of an overhung disk with a combination of unbalance and disk skew, Fig. 2 shows that the unbalance response looks very similar to the standard response as obtained for the single mass Jeffcott rotor. That is, the amplitude reaches a peak and then reduces to a constant value. Fig. 3 shows that the phase angle changes observed at the disk for various combinations of both unbalance and disk skew are also very similar in appearance to the standard single mass Jeffcott model without gyroscopic effects. Hence, it is not readily apparent from the observation of the disk unbalance response and phase angle that there may be disk skew present in the system. For the speed range from 1 to 5, there is a slight reduction in the phase angle for the case of disk skew alone. Since this phase angle change in quite small, it would be difficult to determine the amount of disk skew present in the system by observation of the phase angle change at the disk end. The best way to determine if a system has disk skew is to observe the motion at locations other than the disk. Next, it will be shown that the amplitude of motion and the phase change at the near and the far bearing locations, can be used to indicate disk skew effects. These amplitude and phase characteristics are not observed in the overhung rotor system with conventional radial unbalance only.

Fig. 4 represents the amplitude of motion for the various cases of radial unbalance and disk skew as observed at the near bearing. For

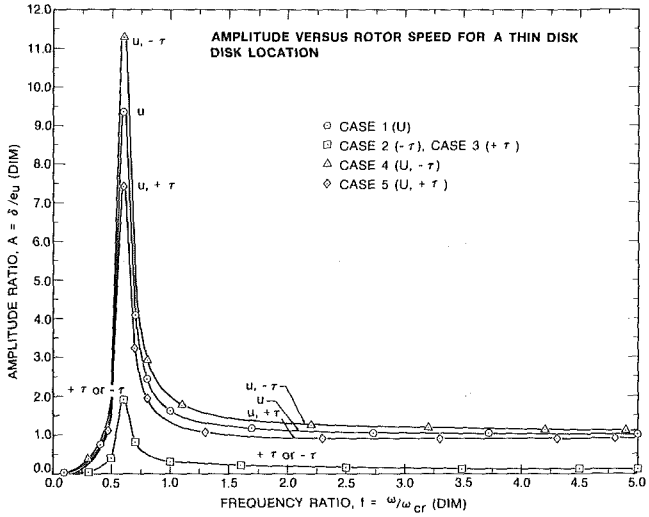

Fig. 2 Dimensionless disk amplitude versus rotor speed for a thin disk

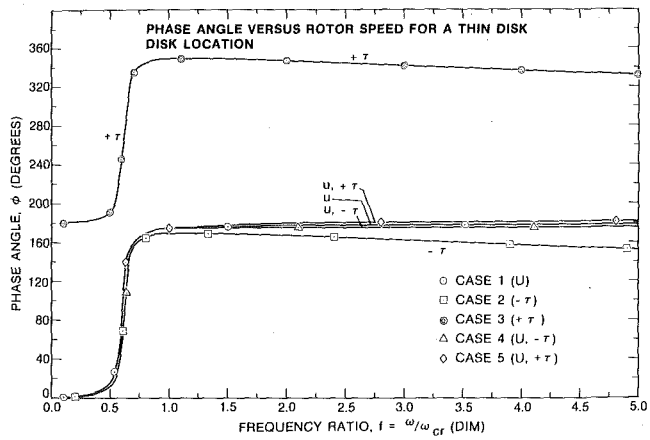

Fig. 3 Disk phase angle versus rotor speed for a thin disk

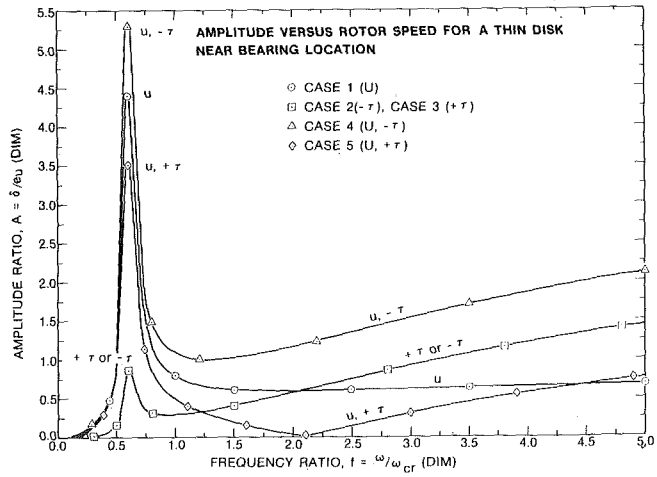

Fig. 4 Dimensionless near bearing amplitude versus rotor speed for a thin disk

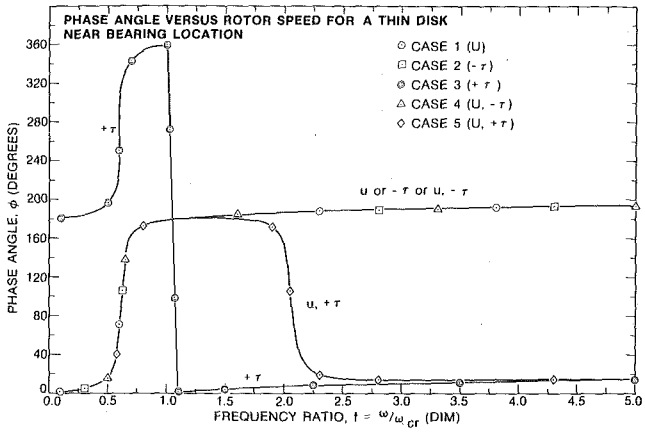

Fig. 5 Near bearing phase angle versus rotor speed for a thin disk

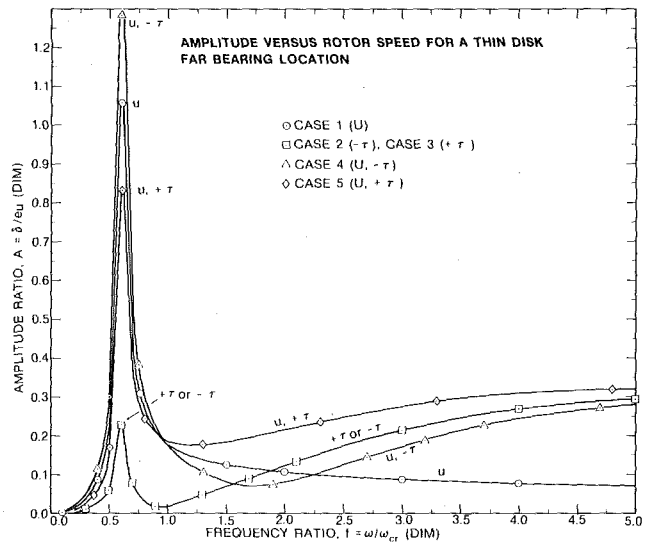

Fig. 6 Dimensionless far bearing amplitude versus rotor speed for a thin disk

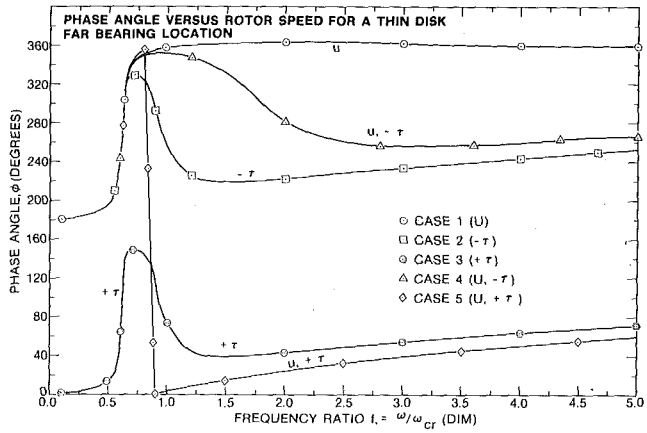

Fig. 7 Far bearing phase angle versus rotor speed for a thin disk

the case of radial unbalance only, the maximum amplitude at the near bearing is approximately one-half of the amplitude at the disk location. Upon passing through the critical speed, the dimensionless unbalance response is approximately 0.7 and remains constant with speed. The shape of the curve with unbalance at the near bearing is similar to the observed amplitude at the disk location. For the case of disk skew only, the maximum amplitude at the near bearing is 1, which again is approximately one-half of the amplitude at the disk location. Above the critical, the amplitude reduces and reaches a minimum at approximately $f = .9$. However, as the rotor speed is increased above $f = 1.0$, the rotor amplitude increases with speed.

The associated phase angle changes for the near bearing are shown in Fig. 5. The important characteristic to observe is that disk skew causes an increase in amplitude with little increase in phase angle. At first one would suspect that the rotor amplitude of motion is slowly building up due to the approach of a second critical speed. However, for this system there is no second critical speed of forward synchronous precession. The buildup in rotor amplitude is due to the skewed disk attempting to straighten out and rotate about its principal inertia axis.

Fig. 4 illustrates that the worst combination is radial unbalance and negative disk skew. This case causes a maximum amplitude of 5.3 to

occur at the near end. The minimum response at the near bearing occurs at a speed ratio of $f = 1.2$. Above this speed, the rotor amplitude continues to increase in value. However, from the phase relationship for the combination of unbalance and negative disk skew a conventional 0–180 deg phase shift is again observed.

If a positive disk skew is incorporated with the radial unbalance, there is a reduction in the amplitude of motion at the near bearing. The amplitude of motion continues to reduce and actually goes to zero at a frequency ratio of $f = 2.1$. At this speed, the near bearing is perfectly balanced. Associated with the reduction to zero amplitude is a reversal in the phase angle from 180 deg to a value approaching 15 deg. This phase angle reversal has also been observed in rotors with flexible foundations [3] and radial unbalance only. From the large phase angle shift, one might improperly conclude that the rotor is going through a housing or support resonance. However, the overhung rotor in this analysis does not have a flexible foundation. Therefore, it is disk skew that causes this unusual behavior.

Figs. 6 and 7 represent the amplitude and phase angle changes for the various conditions of unbalance and disk skew at the far end bearing. For the case of unbalance only, (Case 1), the maximum amplitude is 1.05 at the critical speed. At speeds well above the critical, the amplitude reduces to an asymptotic value of 0.07. Thus we see that for this model, radial unbalance at the disk causes a maximum displacement of 9.5 at the disk, 4.5 at the near bearing and only 1.06 at the far end bearing. The phase angle for Case 1, at the far end, varies from 180 to 360 deg with a shape that is similar to the Case 1 phase angle change observed at the disk and the near bearing. However, the far end bearing phase angle is 180 deg out of phase to the disk or near end bearing. Therefore, with unbalance alone, the amplitude response at the far bearing is only approximately 10–15 percent of the response observed at the disk and is out of phase with it.

If we examine Fig. 6 for the far end bearing with disk skew alone, the maximum amplitude is 0.22 at the critical speed, which again is only 10 percent of the value observed at the disk. However, the interesting phenomena observed in this case is that upon passing through the critical speed, the amplitude reduces and reaches a minimum at $f = .9$ and then continues to increase with speed. The examination of Fig. 7 for the phase angle change due to disk skew is even more revealing. The phase angle change through the critical is only 150 deg instead of 180 deg. After passing through the critical speed, the phase angle reduces over 100 deg from its maximum value at $f = 9.7$. Above $f = 1.5$, the phase angle gradually begins to increase.

From the data examined, it can be concluded that a rapid phase angle reversal at the far bearing, after passing through the critical speed, is indicative of a significant disk skew in the overhung rotor system. This reversal of phase angle has an important effect on the far bearing response when both unbalance and disk skew are present. At all of the rotor stations, the phase angles due to positive unbalance and negative disk skew are in-phase when passing through the critical speed. This implies that the vector addition of the two effects will result in an increase in amplitude at all stations along the rotor at the critical speed. After passing through the critical speed region, the far end phase angle with negative skew deviates from the phase angle due to unbalance alone. This then causes a reduction in amplitude at the far bearing. Another important characteristic to observe at the far end bearing is that at $f = 0.9$, the amplitudes due to unbalance alone, and in combination with disk skew, all cross over. Therefore, while the Case 5 amplitude is less than the unbalance amplitude at the critical speed, it has the highest amplitudes of all five cases at speeds above $f = 0.9$.

In all cases where disk skew is present, the far end shaft amplitude increases with speed above $f \approx 1.5$. This type of behavior is not observed at the disk. Therefore, in order to detect a possible condition of the disk skew in an overhung wheel, it is desirable to monitor the amplitude and phase angle behavior at both the near and the far end bearing positions. For example, with unbalance and disk skew, the near bearing amplitude of motion may increase at speeds above the critical speed without any associated phase angle change as in Case 4. At the far bearing location, the amplitude may increase at super-critical speeds with increasing or decreasing phase angles. The behavior, as shown by Figs. 6 and 7, has been observed numerous times in industry, not only with overhung rotors, but also with conventional rotors with inboard disks. The increase in amplitude above the critical speed with and without a change in phase angle has often been perplexing to investigators, particularly in the case when the operation is far removed from a second critical speed. Figs. 4–7, for the behavior of the near and the far bearings, show that disk skew can cause phase angle shifts which cannot be generated by radial unbalance alone. The reversal of phase angle change at the far bearing after passing through the first critical speed, and the increase in amplitude, is an indication of a skewed disk or a moment unbalance distribution acting at the opposite end of the machine. Notice that this phase reversal is not observed at the disk, itself.

Balancing the Overhung Thin Disk Rotor

From the behavior of the single mass overhung rotor with unbalance and disk skew, it is observed that the characteristic bearing amplitudes and phase angles significantly differ from those of the conventional single mass Jeffcott model. It is then desirable to consider various techniques to balance the overhung rotor configuration with a skewed disk. The previously discussed case of positive disk skew only ($\tau = +0.0684$ deg) was selected as the rotor excitation to be balanced out. No radial unbalance is assumed. Figs. 8–10 are the balancing plots of amplitude versus rotor speed for the far bearing, near bearing, and disk, respectively, for the various balancing cases considered.

Balance No. 1—Single Plane Disk Correction at the Critical Speed. Fig. 2, for the disk motion with various combinations of disk skew and radial unbalance, showed that the combination of positive disk skew with positive radial unbalance caused a net reduction in amplitude over the case with only unbalance. It is therefore logical to assume that if disk skew is initially present in the wheel without radial unbalance, that a radial unbalance correction weight could be placed on the wheel to cancel, or balance-out, the disk motion while passing through critical speed.

The first balance was intended to balance out the amplitude due to disk skew ($\tau = +0.0684$) using a single plane correction on the overhung disk by taking amplitude and phase measurements at the far bearing location. The balancing speed is the first critical speed ($f = 0.6$). The disk correction is determined by linear superposition using the amplitude and phase readings from the far bearing probe (Figs. 6, 7) due to the assumed unbalance from Case 1 and positive disk skew from Case 3. The dimensionless amplitude responses at the far bearing due to unbalance and disk skew are: A_F = total far bearing amplitude; A_{Fu} = far beairng amplitude due to unbalance at the disk = 1.059 ∟ 270 deg; $A_{F\tau}$ = far bearing amplitude due to positive disk skew = 0.225 ∟ 90 deg; U = Case 1 unbalance at disk = 8114.53 ∟ 0 deg gm-cm (112.66 ∟ 0 deg oz-in) and; U_B = unbalance correction at disk.

The amplitude of motion at the far end bearing is a linear superposition of the influences of disk skew and unbalance as follows:

$$A_F = \left(\frac{A_{Fu}}{U} * U_B\right) + A_{F\tau} = \frac{1.059 \text{ ∟ } 270 \text{ deg}}{8114.53 \text{ ∟ } 0 \text{ deg}} * U_B + 0.225 \text{ ∟ } 90 \text{ deg} \quad (2)$$

Specifying that the unbalance correction weight U_B will cause the total amplitude A_F at the far end bearing to be zero. The required amount of balance correction weight is given by

$$U_B = -\frac{0.225 \text{ ∟ } 90 \text{ deg}}{0.00013 \text{ ∟ } 270 \text{ deg}} = \begin{matrix} 1724.03 \text{ ∟ } 0 \text{ deg gm-in} \\ (23.93 \text{ ∟ } 0 \text{ deg oz-in}) \end{matrix}$$

With the correction, Fig. 8 indicates that the resulting far bearing amplitude at the first critical is reduced to 0.025 from the initial amplitude of 0.225. The near bearing amplitude (Fig. 9) is reduced from 0.88 to 0.05, and the disk amplitude (Fig. 10) is reduced from 1.93 to 0.11. After this balance, the rotor can safely pass through this critical without danger of excessive amplitudes at the bearings and the disk. Fig. 10 shows that by taking influence coefficients at the far bearing, when operating through the first critical speed, the disk may

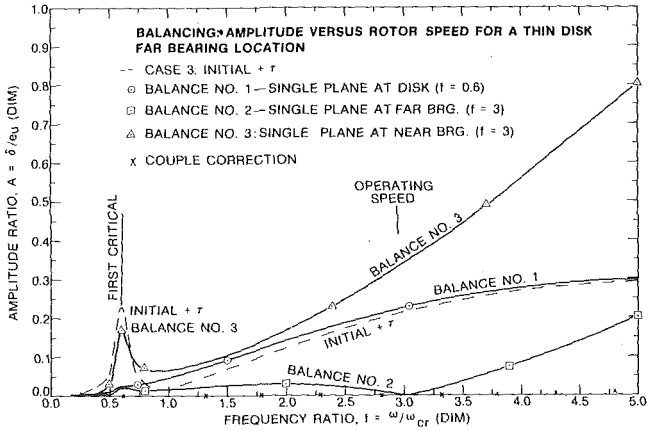

Fig. 8 Amplitude at the far bearing versus speed for various balancing cases

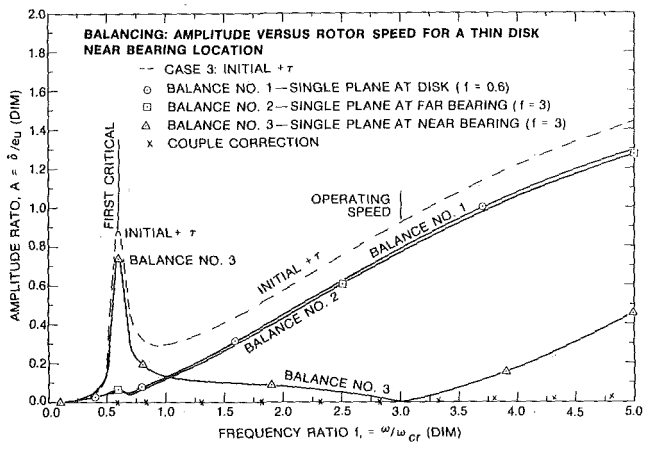

Fig. 9 Amplitude at the near bearing versus speed for various balancing cases

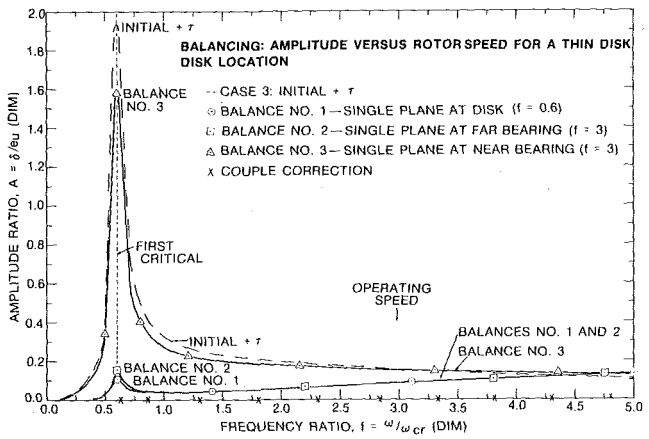

Fig. 10 Amplitude at the disk versus speed for various balancing cases

be successfully balanced. The disk amplitude then remains well behaved with low level motion throughout the entire speed range. However, Figs. 8 and 9 show that beyond the first critical speed, the amplitudes of motion at both bearings increase, with the largest amplitude occurring at the near bearing.

Balancing No. 2—Far End Correction above the Critical Speed. The second balancing correction is intended to balance out the far bearing amplitude at a post-critical speed value of $f = 3.0$ with a single plane correction at the far bearing. It will be assumed that $f = 3.0$ is the operating speed. The correction from balance No. 1 is to remain on the disk.

The balance correction is determined by the method of influence coefficients with the following equation

$$\vec{U}_u = \vec{U}_t * \frac{\vec{Z}_1}{\vec{Z}_2 - \vec{Z}_1} \tag{3}$$

where $\vec{Z}_1$ = rotor amplitude vector before the trial weight at the balancing speed = $Z_1 e^{-j\phi_1}$; $\vec{Z}_2$ = rotor amplitude vector after the trial weight at the balancing speed = $Z_2 e^{-j\phi_2}$; $\vec{U}_t$ = unbalance trial weight vector = $U_t e^{-j\phi_1}$; $\vec{U}_u$ = rotor unbalance vector = $U_u e^{-j\phi_u}$. Then the magnitude of the balance correction is

$$|U_c| = |U_u| \tag{4}$$

and the correction phase angle is then 180 deg out of phase with the unbalance. Thus

$$\phi_c = \phi_u + 180 \text{ deg} \tag{5}$$

For balance No. 2 at the far bearing for $f = 3.0$ the balancing information is: $\vec{Z}_1 = 0.2264\, e^{-j50.35\text{deg}}$ dim; $\vec{U}_t = 720.27\, e^{-j129.65\text{deg}}$ gm-cm ($10\, e^{-j129.65\text{deg}}$ oz-in); $\vec{Z}_2 = 0.53868\, e^{-j142.53\text{deg}}$ dim.

The resultant balance correction is $\vec{U}_c = 275.37\, e^{-j195.0118\text{deg}}$ gm-cm ($3.8232\, e^{-j195.0118\text{deg}}$ oz-in). Balance No. 2 was successful in reducing the far bearing amplitude (Fig. 8) from 0.2264 to 0.0 at $f = 3.0$, without disturbing the first balance at $f = 0.6$. The near bearing and disk amplitude remained unchanged as indicated in Figs. 9 and 10, respectively.

Balance No. 3—Near Bearing Correction above the Critical Speed. The third balance is intended to reduce the near bearing amplitude (Fig. 9) at operating speed ($f = 3.0$) without disturbing the previous two balance improvements. The balancing information is: $\vec{Z}_1 = 0.7716\, e^{-j9.507\text{deg}}$ dim; $\vec{U}_t = 720.27\, e^{-j190\text{deg}}$ gm-cm ($10\, e^{-j190\text{deg}}$ oz-in.); and $\vec{Z}_2$ 0.59723 $e^{-j5.806\text{deg}}$ dim.

The resultant correction is then $\vec{U}_c = 3091.15\, e^{-j177.6197\text{deg}}$ gm-cm ($42.9167\, e^{-j177.6197\text{deg}}$ oz-in.).

Balance No. 3 was successful in reducing the near bearing amplitude (Fig. 9) from 0.7716 to 0.0 at $f = 3.0$. However, the amplitude at the first critical ($f = 0.6$) significantly increased from 0.06 to 0.735. The other two rotor locations also show detrimental results. At the far bearing (Fig. 8) the amplitude increased from 0.02 to 0.17 at the first critical, and from 0.0 to 0.34 at the operating speed. In fact, at speeds above the first critical, the far bearing amplitudes are worse than the original response caused by the skewed disk (Case 3) before balancing. The amplitudes at the disk (Fig. 10) indicate an increase from 0.14 to 1.58 at the first critical. At operating speed, the amplitudes are the same as for the initial rotor before balancing.

From these three balancing runs, it is evident that while the single plane balancing technique is sufficient for balancing out the amplitudes for a specific rotor location and speed, it is not successful in balancing the overall overhung rotor over the operating speed range. It is then desirable to try balancing with a couple correction.

Balancing with a Couple Correction

A couple correction consists of two correction weights separated by the thickness of the disk and 180 deg out of phase with each other. This produces an equivalent balance moment vector, whereas the single plane corrections produce equivalent balance force vectors.

Starting with the original rotor with positive disk skew only (Case 3), a trial couple is applied to the disk to balance the rotor at the first critical ($f = 0.6$). Then the influence coefficient technique (equation (3)), as previously described for single plane balancing, is used. However, the trial weight vector becomes a trial couple vector. The balancing information is: $\vec{Z}_1 = 1.9312\, e^{-j245.66\text{deg}}$ dim; $\vec{U}_t = 720.27\, e^{-j0\text{deg}}$ gm-cm ($10\, e^{-j0\text{deg}}$ oz-in couple); and $\vec{Z}_2 = 1.9028\, e^{-j245.66\text{deg}}$ dim.

The resulting couple balance correction vector is then

$$\vec{U}_c = 48978.15 e^{-j0\text{deg}} \text{ gm-cm } (680\, e^{-j0\text{deg}} \text{ oz-in. couple})$$

With this correction, Figs. 8–10 indicate essentially zero amplitudes for all three rotor locations throughout the speed range.

There are numerous rules of thumb for estimating reasonable amounts of residual unbalance for analytical rotor response analyses. However, it is often difficult for a designer to physically arrive at

reasonable values of the disk skew angle. For small disk skew angles, it can be shown that two balance correction weights placed on a disk 180 deg out of phase and separated by distance w is equivalent to a uniform disk skewed an angle τ from the vertical.

The transformation angle to principal directions for a disk with a couple unbalance is given by

$$\tan 2\theta_p = \frac{2I_{12}}{I_{11} - I_{22}} \tag{6}$$

The product of inertia term is given by

$$I_{12} = \int_v \rho x Z dm = \frac{Uw}{\mathrm{Kg}} \tag{7}$$

For small disk angles

$$\theta_p = \tau = \frac{Uw}{K(I_p - I_t)} \tag{8}$$

Where τ = disk skew angle (radians); U = equivalent unbalance couple, gm-cm (oz-in); w = disk thickness, cm (in.); I_p = disk polar weight moment of inertia, N-cm^2 (lb-in.^{2}); I_t = disk transverse weight moment of inertia, N-cm^2 (lb-in^2); and K = constant = 102 gm/N (= 16 oz/lb).

As an example, the equation (8) was applied to the overhung rotor discussed in this paper. The known parameters are $I_p = 4.082 \times 10^6$ N-cm^2 (1.422×10^5 lb-in^2); $I_t = 2.039 \times 10^6$ N-cm^2 (7.106×10^4 lb-in^2); $w = 5.08$ cm (2.0 in.); and $\tau = 1.194 \times 10^{-3}$ rad (0.0684 deg).

The equivalent unbalance couple can then be calculated from equation (8)

$$U = \tau K(I_p - I_t)/w = 4.8979 \times 10^4 \text{ gm-cm (679.9 oz-in.)}$$

This is the same answer as was found by the influence coefficient method with the trial couple.

Summary

The sample problem of the overhung rotor with disk skew illustrates the influence of disk skew on unbalance response and phase angle changes. It produces an effect which cannot be obtained with the usual unbalance distribution on a flexible rotor. This effect is the occurrence of a rapid reduction in phase angle at the far bearing upon passing through the critical speed. The sample problem also shows that it is impossible to balance the rotor at all speeds with single plane radial unbalance corrections in the presence of a skewed disk. The equations of motion to include disk skew or shaft bow may be expressed in matrix transformation form or by a modal formulation as has been done by Childs [14] or Gunter and Choy [15]. A condition for modal balancing a particular critical speed can be obtained from [15] by setting the modal forcing function P_{xi} for the i-th mode equal to zero. This results in the condition

$$\phi_{ij}{}^t m_j e_{uj}[\omega^2 \cos(\omega t + \alpha_j) + \dot{\omega} \sin(\omega t + \alpha_j)] + \phi_{ij}{}'^t \tau_j (I_p - I_t)_j [\omega^2 \cos(\omega t + \beta_j) + \dot{\omega} \sin(\omega t + \beta_j)] = 0 \tag{9}$$

Where ϕ_i = i-th mode shape and ϕ_i' = i-th mode shape slope. From the above condition, it is apparent that if the unbalance is selected to balance out one critical speed due to the presence of disk skew, the system will not be balanced at high critical speeds.

Conclusions—Thin Disk Overhung Rotor

1 A skewed disk will excite the first critical speed of an overhung rotor.

2 A radial disk correction can always be selected to balance out the effect of disk skew at the first critical speed.

3 Although the rotor balance may be acceptable at the first critical speed, the bearing forces and rotor amplitudes may be unacceptable at higher speeds. This system cannot be adequately balanced by single plane procedures.

4 Amplitudes and phase angles monitored at the overhung disk appear to be similar to the behavior of the elementary Jeffcott rotor model. Hence disk skew effects cannot be distinguished from unbalance by monitoring the motion only at the disk location.

5 The response characteristics at the bearings of the overhung rotor can differ considerably from Jeffcott behavior when disk skew is introduced. The amplitude is not constant above the first critical-instead, it increases with speed.

6 At the far bearing, a rapid decrease in phase angle above the first critical speed is an indication of significant disk skew. Hence, a probe at the far bearing end can indicate disk skew.

7 Two unbalance weights placed on a disk 180 deg out of phase and separated by an axial distance w can create an equivalent disk skew in the rotor. Hence, any grinding of impeller wheels in which the correction planes on the front and back are 180 deg out of phase can create equivalent disk skew effects.

References

1 Lund, J. W. and Orcutt, F. K., "Calculations and Experiments on the Unbalance Response of a Flexible Rotor," *Journal Engineering for Industry*, Nov. 1967.

2 Kawamo, K., Matsukura, Y., and Inoue, T., "Analysis of Lateral Vibration Characteristics of Rotating Shafts with Flexible and Axi-Asymmetric Bearings," 1975, Joint JSME-ASME Applied Mechanics Western Conference, 1975.

3 Kirk, R. G. and Gunter, E. J., "The Effect of Support Flexibility and Damping on the Synchronous Response of a Single-Mass Flexible Rotor," ASME *Journal of Engineering for Industry*, Vol. 94, No. 1, Feb. 1972, pp. 221–232.

4 Wolfe, W. A. and Wong, P. Y., "On the Transfer Matrix for Rotor Dynamics," Manuscript No. 72-CSME-37, EIC Accession No. 1320, July 3, 1974.

5 Barrett, L. E., Gunter, E. J., Allaire, P. E., "Optimum Bearing and Support Damping for Unbalance Response and Stability of Rotating Machinery," ASME JOURNAL ENGINEERING FOR POWER, Dec. 1976.

6 Koenig, E. C., "Analysis for Calculating Lateral Vibration Characteristics of Rotating Systems with Any Number of Flexible Supports, Part 1—The Method of Analysis," *Journal Appl. Math.*, Dec. 1961.

7 Kikuchi, K., "Analysis of Unbalance Vibration of Rotating Shaft System with Many Bearings and Disks," *JSME Bulletin*, June 16, 1969.

8 Salamone, D. J., *Synchronous Unbalance Response of a Multimass Flexible Rotor Considering Shaft Warp and Disk Skew*, M.S. Thesis, University of Virginia, May 1977.

9 Nicholas, J. C., Gunter, E. J., and Allaire, P. E., "Effect of Residual Shaft Bow on Unbalance Response and Balancing of a Single Mass Flexible Rotor," Parts I and II. ASME JOURNAL OF ENGINEERING FOR POWER, Vol. 98, Series A, No. 2, April 1976, pp. 171–189.

10 Lund, J. W., "Rotor-Bearing Dynamics Design Technology, Part V: Computer Program Manual for Rotor Response and Stability," Air Force Technical Report AFAPL-TR-65-45, Part V, May 1965.

11 Yamamoto, T., "On the Critical Speeds of a Shaft," *Memoirs of the Faculty of Engineering*, Nagoya University, Japan, Nov. 1954.

12 Benson, R. C., *Dynamic Response of an Overhung, Unbalance Skewed Rotor in Fluid Film Bearings*, M.S. Thesis, University of Virginia, Aug. 17, 1974.

13 Salamone, D. J. and Gunter, E. J., "Effects of Shaft Warp and Disk Skew on the Synchronous Unbalance Response of a Multimass Rotor in Fluid Film Bearings," *Topics in Fluid Film Bearing and Rotor Bearing System Design and Optimization*, ASME Book No. 100118, pp. 79–107, April 1978.

14 Childs, D. W., "Two Jeffcott-Based Modal Simulation Models for Flexible Rotating Equipment," ASME *Journal Engineering for Industry*, Aug. 1975.

15 Gunter, E. J., Choy, K. C., and Allaire, P. E., "Modal Analysis of Turborotors Using Planar Modes—Theory," *Journal of the Franklin Institute*, Vol. 305, No. 4, pp. 221–243, April 1978.

D. M. Berchowitz
Junior Lecturer,
Mechanical Engineering,
University of the Witwatersrand,
Johannesburg, South Africa
Assoc. Mem. ASME

I. Urieli
Development Engineer,
Ormat Turbines Ltd.,
Yavne, Israel
Mem. ASME

C. J. Rallis
Professor,
Mechanical Engineering,
University of the Witwatersrand,
Johannesburg, South Africa
Mem. ASME

A Numerical Model for Stirling Cycle Machines

The further development of a model to accurately simulate the performance and detailed behavior of Stirling cycle machines is described. The transport equation set (which describe the working gas) is derived in both the so-called integral and differential forms. Only the integral equation set is solved for the simulation. The differential equation set is used to investigate the structure of individual terms in the integral equation set. This procedure allows these terms to be more accurately understood and, hence, modeled. The energy equation includes kinetic energy and dissipation terms while the momentum equation includes the effects of working gas acceleration and viscous friction. Heat leakage and longitudinal conduction in the machine walls are accounted for and due regard is taken of the working gas instantaneous properties. The Reynolds analogy is used to calculate the local heat transfer coefficients.

Introduction

This paper presents the continuing efforts by the authors to develop and justify an accurate computer simulation of Stirling cycle machines. Various stages of the development of the simulation model have been previously presented in the literature [1] and at conferences [2, 3]. A unique approach has evolved which utilizes the integral (or macroscopic) formulation of the transport equation set. The system (i.e., the machine) is subdivided into a finite number of discrete cells which are interconnected by mass, momentum and energy fluxes which cross the boundaries (or nodes) of the cells. The working gas properties are assumed to be spatially constant over each cell at their mean spatial values. The three transport equations (continuity, momentum and energy) plus the equation of state are applied to each individual cell. The resulting set of first order differential equations are solved simultaneously by explicit methods for the entire system.

It is the purpose of this paper to justify this approach.

The Cellular Model

Fig. 1 indicates how the machine is subdivided into a finite number of thermodynamic entities (or cells).

The most general i'th elemental cell (Fig. 2) consists of a void space V_i containing working gas of temperature T_i, pressure p_i and specific volume v_i (or density ρ_i). The working gas in this void space is in intimate open communication with the porous cell matrix. The matrix presents a wetted area Amg_i to the working gas, allowing heat Q_i to be transferred by convention from the matrix to the working gas. The cell axial length is Δx_i and is bounded by node i being the interface to adjacent cell $i+1$. Mass flux density g_i flows across node i through the free flow area A_i. The various working gas properties are defined as being constant throughout the cell and discontinuous at the nodes. Thus the node temperature Tn_i are conditional variables, taking on their respective adjacent upstream cell values, conditional on the direction of mass flux density g_i. The definition of conditional nodal temperatures was introduced by Finkelstein [4].

The cell matrix is defined in terms of the matrix overall volume (being the void volume V_i plus the volume occupied by the matrix material Vm_i), porosity ψ_i, temperature Tm_i and specific volume vm_i. Heat transfer by conduction between adjacent cell matrices Qm_i takes place at node i through matrix effective cross sectional area Am_i. Heat transfer by conduction Qwm_i takes place between the matrix and containing wall through the effective area of contact Awm_i. The

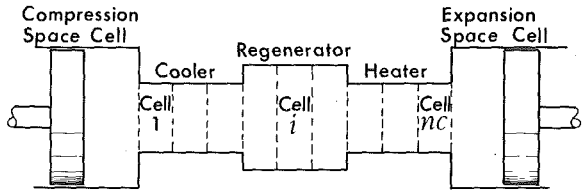

Fig. 1 Cellular model [8]

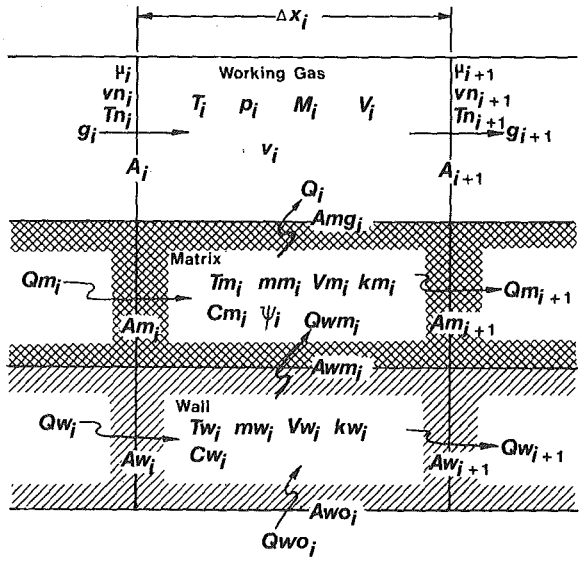

Fig. 2 Generalized i'th elemental cell [8]

Contributed by the Gas Turbine Division of THE AMERICAN SOCIETY OF MECHANICAL ENGINEERS and presented at The 1979 Israel Joint Gas Turbine Congress, Haifa, Israel, July 9–11, 1979. Manuscript received at ASME Headquarters May 7, 1979. Paper No. 79-GT/Isr-16.

containing wall associated with the i'th cell is defined in terms of its volume Vw_i, specific volume vw_i and temperature Tw_i. Heat conduction between adjacent walls Qw_i occurs at node i through the wall cross sectional area Aw_i. Heat transfer with the external environment adjacent to the wall of the i'th cell, Qwo_i, takes place through the external wall area Awo_i. For the regenerator cell it can generally be assumed that the regenerator is externally adiabatic (i.e., $Qwo_i = 0$). In the special case where there is no regenerator matrix i.e., that the wall acts as the regenerator or if the cell is part of the heater or cooler, the heat transfer to the working gas Q_i takes place between the working gas and the cell wall.

The boundary conditions for the series connected heat exchanger cells are the compression and expansion spaces respectively.

The effective cylinder wall temperature (Twc for the compression space) cannot be accurately determined analytically and depends *inter alia* upon the nature of the environment, the cylinder configuration, the mechanical friction heat generated by the piston seals and the heat transfer to the working fluid. It is usually assumed that the cylinder wall is adiabatic (for machines with separate heat exchangers). In this work it is further assumed that the gas momentum in the working spaces is negligible. Mechanical work is done on the external environment by virtue of a change in volume (pdV/dt).

The Transport Equation Set

The derivation of the transport equation set is directly pertinent to the simulation technique; for this reason it is included here.

The lumped parameter approach is used in the integral equation set to account for viscous effects (friction and dissipation) and heat transfer by means of friction factors and heat transfer coefficients. The integral equations are thus a pseudo three-dimensional system with only two independent variables; time (t) and axial position in the machine (x). These equations are then applied to the cellular model.

Consider a completely arbitrary control volume V within the flowing working gas (Fig. 4).

The control volume, which is located in an Eulerian framework is represented by its specific volume v (or density ρ), pressure p, temperature T and momentum per unit volume $\boldsymbol{g}$. The momentum per unit volume $\boldsymbol{g}$ assumes the role of a mass flux density while crossing the control surface A transporting matter, energy and momentum into and out of the control volume. Heat Q crosses the control surface and mechanical work W is done by the control volume on the environment.

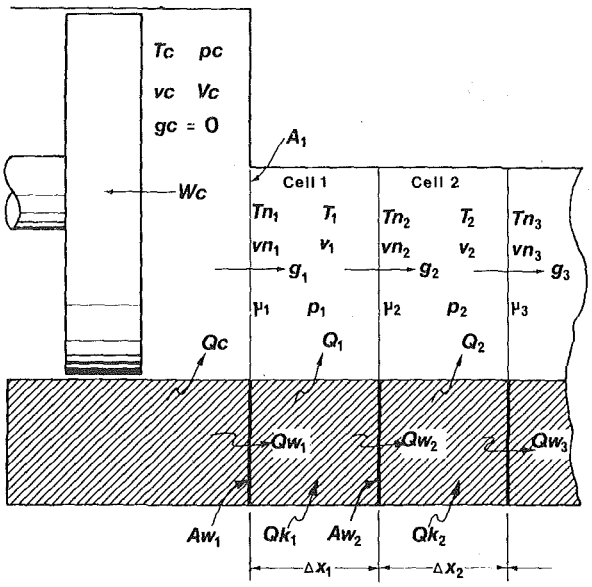

Fig. 3 Generalized compression space

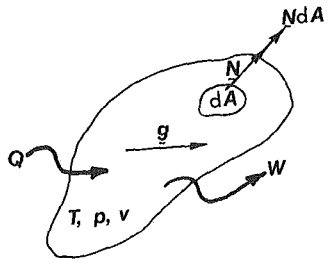

Fig. 4 Generalized control volume

1 **Continuity (Conservation of Mass).** This equation is developed by writing a mass balance over a stationary volume element V through which fluid is flowing.

Rate of increase of mass in the control volume	=	net mass flux convected inwards through the control surface

Nomenclature

A = free flow area
Am = effective area for conduction in matrix
Aw = effective area for conduction in wall
Amg = wetted area of matrix
Awm = effective area of contact between wall and matrix
Awo = effective area of contact between wall and environment
Cm = heat capacity of matrix
Cw = heat capacity of wall
d = hydraulic diameter
e = specific total energy
E = rate of viscous dissipation
F = force of fluid on solid surfaces; viscous forces
Ff = Fanning friction factor
Fr = Reynolds friction factor
g = mass flux density or momentum per unit volume (note that gv is velocity)
$\boldsymbol{g}$ = mass flux density vector
h = specific enthalpy; heat transfer coefficient
k = thermal conductivity
$\boldsymbol{N}$ = unit normal vector
p = pressure
$\boldsymbol{q}$ = heat flux vector
Q = convective heat transfer
$\dot{Q}$ = rate of convective heat transfer
Qm = conductive heat transfer in matrix
Qw = conductive heat transfer in wall
Qwm = conductive heat transfer between wall and matrix
Qwo = conductive heat transfer between wall and environment
R = gas constant
Re = Reynolds number
t = time
T = temperature of working gas
Tn = node temperature (working gas)
Tm = temperature of matrix
Tw = temperature of wall
Twc = compression cyclinder wall temperature
u = specific internal energy
U = internal energy
v = specific volume of working gas
vm = specific volume of matrix
vn = node specific volume (working gas)
vw = specific volume of wall
V = void volume
Vm = matrix volume
Vw = wall volume
W = work
x = axial position
γ = ratio of specific heats (working gas)
Δ = small increment
ψ = porosity
ρ = density
μ = dynamic viscosity
σ = stress tensor

Subscripts

i = inlet conditions; location at cell i
e = exit conditions

$$\frac{d}{dt}\int_V \rho dV = \oint_A \rho(\boldsymbol{g}v)\cdot(-\boldsymbol{N})dA \quad (1)$$

$$\frac{d}{dt}\int_V \rho dV = -\int_A \boldsymbol{g}\cdot\boldsymbol{N}dA \quad (2)$$

Equation (2) is integrated for the integral form of the continuity equation:

$$\frac{dm}{dt} = (gA)_i - (gA)_e \quad (3)$$

where i refers to the surface through which fluid flows into the cell and e refers to the surface through which fluid exits the cell. It is important to note that the integral result automatically assumes the area average value of the local flux parameter.

If the system is considered continuous in both time and space, it is possible to derive the differential continuity equation; applying Gauss' theorem to (2):

$$\frac{d}{dt}\int_V \rho dV = -\int_V \nabla\cdot\boldsymbol{g}dV \quad (4)$$

By the Leibnitz rule for differentiating a volume integral:

$$\int_V \left(\frac{\partial\rho}{\partial t} + \nabla\cdot\boldsymbol{g}\right)dV = 0 \quad (5)$$

Since the control volume is entirely arbitrary and the integrand is continuous, the integrand must itself be zero:

$$\frac{\partial\rho}{\partial t} + \nabla\cdot\boldsymbol{g} = 0 \quad (6)$$

This is the differential equation of continuity for non-steady compressible flow.

2 Momentum (Equation of Motion). A momentum balance for the control volume is:

rate of change of momentum within the control volume = net momentum flux convected inwards through the control surface + net forces acting on the fluid in the control volume

$$\frac{d}{dt}\int_V \boldsymbol{g}dV = \oint_A \boldsymbol{g}(\boldsymbol{g}v)\cdot(-\boldsymbol{N})dA + \oint_A p(-\boldsymbol{N})dA + \oint_A \sigma(-\boldsymbol{N})dA \quad (7)$$

where: $\boldsymbol{g}v$ is the velocity; σ is the viscous stress tensor

In equation (7) only the surface forces are considered. Body forces such as gravitational, centripital, magnetic and electrical have been neglected as irrelevant to the class of problems treated here.

Equation (7) is integrated to give the integral form of the momentum equation.

$$\frac{d}{dt}(gV) = (g^2vA)_i - (g^2vA)_e + (pA)_i - (pA)_e - F \quad (8)$$

Note that F is the force of the fluid on the solid surfaces and is made up of the sum of all viscous and pressure forces experienced on these surfaces (viscous forces are empirically determined). The differential form of the momentum equation is derived in a manner similar to that used for the continuity equation, the result is:

$$\frac{\partial\boldsymbol{g}}{\partial t} + [\nabla\cdot(\boldsymbol{g}\boldsymbol{g}v)] + \nabla p + [\nabla\cdot\sigma] = 0 \quad (9)$$

Note that this equation has three components, one for each spatial direction.

3 The Mechanical Energy Equation. By forming the scalar product of the local velocity with equation (9) and using the differential continuity equation (6) it is possible to derive the following result [5]

$$\frac{\partial}{\partial t}(\boldsymbol{g}v)^2/2 = -\boldsymbol{g}v\cdot\nabla(\boldsymbol{g}v)^2/2 - v(\nabla\cdot\boldsymbol{g}vp) - v(\nabla\cdot[\sigma\cdot\boldsymbol{g}v]) - vp(-\nabla\cdot\boldsymbol{g}v) - v(-\sigma:\nabla\boldsymbol{g}v) \quad (10)$$

Equation (10) is important for understanding the inter conversions of mechanical energy; the word statement is as follows:

rate of increase in specific kinetic energy = net input of specific kinetic energy by virtue of convection through control surface

− rate of specific work done by pressure of the surroundings on control volume − rate of specific work done by viscous forces on control volume

− rate of reversible conversion to specific internal energy by compression − rate of irreversible conversion to specific internal energy due to dissipation

Bird, Stewart and Lightfoot [6] indicate that the term $(-\sigma:\nabla\boldsymbol{g}v)$ is always positive and is generally referred to as the dissipation function. It can thus be expected that in all flow systems this term represents the degradation of mechanical energy into thermal energy and that therefore no real processes are reversible. If this term is ignored then all forms of energy in (10) would be freely interconvertible.

Furthermore, Bird, Stewart and Lightfoot point out that the $p(\nabla\cdot\boldsymbol{g}v)$ term causes appreciable temperature effects for gas undergoing sudden expansion or compression. The $(\sigma:\boldsymbol{g}v)$ term on the other hand causes measurable temperature changes in flow systems where the velocity gradients are large. Both these conditions are likely to be found in Stirling cycle machines.

Note that (10) is not a new equation; it is simply a different form of the momentum equation.

4 The Energy Equation. The word statement for this equation is as follows:

rate of increase in total energy (including kinetic, internal and potential) in the control volume = rate of total energy flux convected inwards through the control surface

+ rate of internal heat generation e.g., electrical and chemical

− rate at which the fluid does work on its surroundings by virtue of pressure and viscous stresses (normal and shear) + rate of energy input by conduction through the control surface

It is assumed that potential energy and internal heat generation by chemical or electrical means can be ignored as being irrelevant to the class of systems treated in this work. It should be noted, however, that internal heat absorption and release would be important in Stirling cycles operating with a dissociating gas [7].

Mathematically the verbal statement becomes:

$$\frac{d}{dt}\int_V \rho e dV = \oint_A \rho e(\boldsymbol{g}v)\cdot(-\boldsymbol{N})dA - \oint_A p(\boldsymbol{g}v)\cdot\boldsymbol{N}dA - \oint_A [\sigma\cdot\boldsymbol{g}v]\cdot\boldsymbol{N}dA + \oint_A \boldsymbol{q}\cdot(-\boldsymbol{N})dA \quad (11)$$

where $e = (\boldsymbol{g}v)^2/2 + u$

It is possible to derive an integral form of the energy equation directly from (11). However, a more convenient integral form can be derived from the simplified differential energy equation. Therefore the differential energy equation is derived first.

Using Gauss' theorem and the continuity equation (6), equation (11) can be manipulated to give [5]:

$$\frac{1}{v}\frac{\partial}{\partial t}(\boldsymbol{g}v)^2/2 + \boldsymbol{g}\cdot\nabla(\boldsymbol{g}v)^2/2 + \nabla\cdot\boldsymbol{g}vp + (\nabla\cdot[\sigma\cdot\boldsymbol{g}v])$$

$$+\frac{1}{v}\frac{\partial u}{\partial t} + \boldsymbol{g}\cdot\nabla u + \nabla\cdot\boldsymbol{g} = 0 \quad (12)$$

which is the differential form of the energy equation.

Comparing equations (12) and (10) it is noted that the first four terms in the differential energy equation are repeated in the differential mechanical energy equation. Therefore subtracting (10) from (12):

$$\frac{1}{v}\left(\frac{\partial u}{\partial t} + \boldsymbol{g}v\cdot\nabla u\right) = p(-\nabla\cdot\boldsymbol{g}v) + (-\sigma{:}\nabla\boldsymbol{g}v) - \nabla\cdot\boldsymbol{g} \quad (13)$$

which is sometimes referred to as the equation of thermal energy. The word statement is as follows:

rate of gain of internal energy per unit volume both locally and by convention = rate of reversible internal energy increase per unit volume by compression

+ rate of irreversible internal energy increase per unit volume by viscous dissipation + rate of internal energy input by conduction per unit volume.

If the equations of mechanical and thermal energy are compared (10) and (13), the only terms that are common to both equations are $p(\nabla\cdot\boldsymbol{g}v)$ and $(-\sigma{:}\nabla\boldsymbol{g}v)$. Thus these equations are coupled through these terms and they must therefore describe the interconversion of mechanical and thermal energy. The term $p(\nabla\cdot\boldsymbol{g}v)$ can either be positive or negative, depending on whether the working gas is expanding or contracting, hence it represents a reversible mode of interchange. On the other hand, the term $(-\sigma{:}\nabla\boldsymbol{g}v)$ is always positive as previously noted and therefore represents an irreversible degradation of mechanical energy into thermal energy.

Defining specific enthalpy:

$$h = u + pv \quad (14)$$

substituting (14) into (13) and after manipulation:

$$\frac{\partial}{\partial t}\left(\frac{u}{v}\right) + \nabla\cdot h\boldsymbol{g} - \nabla\cdot[p\boldsymbol{g}v] = p(-\nabla\cdot\boldsymbol{g}v) + (-\sigma{:}\nabla\boldsymbol{g}v) - \nabla\cdot\boldsymbol{q} \quad (15)$$

Since pressures are assumed to be spatially constant over each cell and discontinuous at the nodes, it is possible to derive the integral form of equation (15) by integrating directly using Gauss' theorem and Liebnitz's rule:

$$\frac{d}{dt}\int_V \rho u dV + \oint_A h\boldsymbol{g}\cdot\boldsymbol{N}dA - \oint_A p(\boldsymbol{g}v)\cdot\boldsymbol{N}dA$$

$$= -p\oint_A (\boldsymbol{g}v)\cdot\boldsymbol{N}dA + \int_V(-\sigma{:}\nabla\boldsymbol{g}v)dV - \oint_A \boldsymbol{g}\cdot\boldsymbol{N}dA \quad (16)$$

Evaluating:

$$\frac{dU}{dt} + (hgA)_e - (hgA)_i - (pAgv)_e + (pAgv)_i = -p[(Agv)_e$$

$$-(Agv)_i] + \int_V(-\sigma{:}\nabla\boldsymbol{g}v)dV + (qA)_i - (qA)_e \quad (17)$$

Note that the areas may be different for each group, for example the area for heat flux is generally different to the area for enthalpy flux.

No further manipulation can be performed on the dissipation work integral, this term is evaluated from empirical considerations, and is denoted by E.

In accordance with the assumptions made by Urieli [2, 8], heat conduction along the gas is neglected. The only heat transfer accounted for is that due to convection, which is evaluated from empirical considerations. The heat flow terms are thus replaced by $\dot{Q}$. Substituting for the perfect gas definitions of internal energy and enthalpy, (17) finally becomes:

$$\dot{Q} = \frac{R}{\gamma-1}\frac{d}{dt}(mT) - \frac{\gamma R}{\gamma-1}[(TgA)_i - (TgA)_e]$$

$$+ [(pAgv)_i - (pAgv)_e] - p[(Agv)_i - (Agv)_e] - E \quad (18)$$

This is the final form of the energy equation as used in this work.

Empirical Factors

There are three parameters which have to be evaluated empirically, they are:

(a) F: The total force of the working gas on the solid surfaces. This includes pressure and viscous forces.

(b) E: The dissipation of mechanical energy over the cell volume, also known as lost work.

(c) Q: The heat transferred between the solid surfaces and the gas.

At the cellular level it can be shown [5] that by replacing the pressure terms $(pA)_i - (pA)_e$ in the momentum equation by $A(p_i - p_e)$ where A is the smallest area of flow, it becomes a reasonable approximation to assume that F is only the viscous force on the control volume. This simplification allows the momentum equation to be more easily modelled. Another potential difficulty is the fact that friction factors only account for the shear stresses. Fortunately, it is a simple matter to include the normal stresses which are evaluated from the differential momentum equation by making the relevant Newtonian assumptions. Writing the shear stresses in terms of the so-called Reynolds friction factor as suggested by Urieli [2, 8], and evaluating the normal stresses from the differential momentum equation, the final form of F is:

$$F = \frac{4}{3}\mu\left\{\left[\left[A\frac{\partial}{\partial x}(gv)\right]_i - \left[A\frac{\partial}{\partial x}(gv)\right]_e\right\} + 2Fr\mu gVv/d^2 \quad (19)$$

where

$$Fr \triangleq Ff\mathrm{Re} \quad (20)$$

$$\mathrm{Re} \triangleq |gd/\mu| \quad (21)$$

There is a certain degree of uncertainty associated with the Fanning friction factor Ff as applied to reversing flow. The Fanning friction factor is usually experimentally determined for steady, incompressible and isothermal flow. In this work the quasi-steady selection of friction factors coupled with the inclusion of the normal stresses help to limit the effects of the steady and incompressible requirements, whilst the general turbulent nature of the working gas flow in Stirling-type machines help to reduce the requirement for isothermality [5].

Dissipation can generally be divided into two main parts. Firstly, the viscous work done by standing eddies forming in the abrupt expansions and contractions, or in any other fittings that interrupt the smooth flow of the fluid; and secondly, the viscous work done in parallel flow. This distinction is purely empirical, since on an elemental level, both forms of dissipation are the result of the same mechanism, i.e., the irreversible work done against the local normal and shear stresses acting on the fluid element.

In Stirling machines the dissipation due to the standing eddies forming in the abrupt expansion or contraction to or from the working spaces is important and must be included in any analysis such as this. Generally in steady flow work, a pressure loss term is included to account for this dissipation. This term is either added to or subtracted from the pressure for expansion or contraction as the case may be. This approach was used by Urieli [2, 8] and Schock [9]. Unfortunately this approach is not valid for non-steady or reversing flow situations since it is not meaningful to add or subtract a loss term to or from the pressure at every differential time increment. A better approach is to relate the pressure loss term to the rate of dissipation since this is in fact what it is derived from [6]. This is done by working "backwards" from the empirical result for Δp to evaluate the rate of dissipation which then features in the thermal energy equation as part of E. From these arguments the following result can be derived [5]:

$$E = |g^3| A v^2 K/2 \tag{22}$$

where K is the expansion or contraction loss coefficient as defined by Kays and London [10]. This result is valid for both expansions and contractions.

It is important to note that the derivation of (22) assumes that for an instantaneous Reynolds number and geometry, the rate of dissipation for unsteady conditions is approximately the same as that for steady conditions.

Bird, et al. [6] show that for steady, incompressible isothermal flow there is a relationship for E in terms of the steady-state friction factor Ff:

$$E = [2(gv)^2 \Delta x Ff/d] gA \quad \begin{matrix}(\text{parallel flow} - \text{shear} \\ \text{stress terms only})\end{matrix} \tag{23}$$

If (23) can be considered to replace only those terms due to shear work (in accordance with the previous assumptions on the friction factor), then (23) may be modified to include the effects of the normal stresses which are again easily evaluated from the differential energy equation (again making the relevant Newtonian assumptions). The final result for parallel flow dissipation is then [5]:

$$E = V\mu \left\{ 2(gv)^2 Fr/d^2 + \frac{4}{3}\left[\frac{\partial}{\partial x}(gv)\right]^2 \right\} \quad \text{(parallel flow)} \tag{24}$$

Note that (24) is always positive as would be expected.

A heat transfer coefficient is defined to evaluate the $\dot{Q}$. Again the quasi-steady assumption is used by assuming that the local heat transfer coefficient is solely dependent on the flow geometry and the local Reynolds number. In this work the Reynolds simple analogy [11] has been found to be satisfactory since Prandtl numbers are in the region of unity. The local heat transfer coefficient is given as follows:

$$h = kFr/(2d) \tag{25}$$

Transport properties are either evaluated from ideal gas results (specific heats at constant pressure or volume and gas conductivity) or empirical formulas (viscosity using the Sutherland formula). This approach has been found to work well, but it is quite possible to use empirical formulas for all the transport properties if additional accuracy is required.

Method of Solution

To complete the equation set, an equation of state must be specified. For this work the ideal gas equation was found to be adequate:

$$pV = mRT \tag{26}$$

Conduction in the machine's solid parts is included by writing the energy equation for each solid section within each cell [2, 8]. This procedure is standard and is not repeated here.

The complete set of equations for the working gas and the solid portions of the machine are applied simultaneously to each elemental cell as indicated in Fig. 5. The energy and continuity equations are applied to each consecutive cell whilst the momentum fluxes are not defined within the cells but only at the nodes. The momentum equation is however stepped along the machine by one cell length at a time. This arrangement staggers the application of the momentum equation so that the momentum fluxes can be determined at each node.

The resulting set of first order differential equations (in time) is solved simultaneously by using explicit techniques such as Runge Kutta [2, 5, 8]. This process has a warm up period which requires that the equations are cycled through a number of times until cyclic steady state has been reached. This would be equivalent to the thermal equilibrium state of a real machine. A technique has been devised to force the system to cyclic steady state at a much faster rate. This is done by altering the regenerator matrix temperatures in a weighted fashion until no net heat is transferred to the regenerator over a cycle [2, 8].

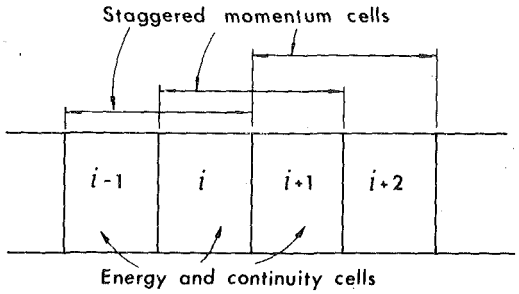

Fig. 5 Application of the continuity, energy and momentum equations

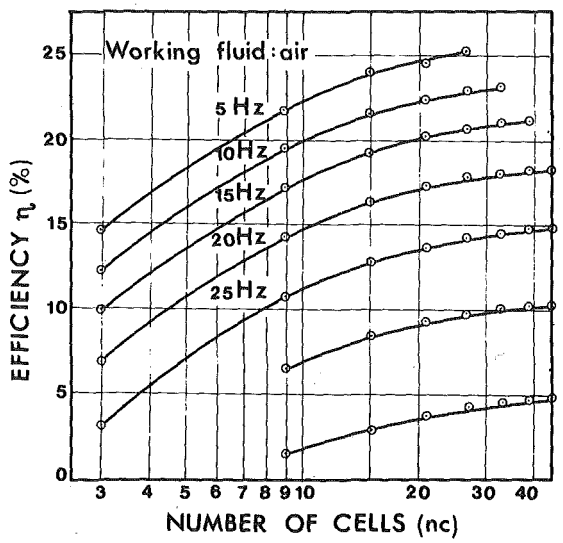

Fig. 6 Efficiency versus number of cells [2]

Results

1 **Numerical Behavior.** Fig. 6 shows thermal efficiency plotted against the number of cells, using air as a working fluid and at different operating frequencies. These curves were derived for a hypothetical engine previously described by Urieli, et al. [2].

It can be seen that the model is extremely well behaved. The difference in thermal efficiency for 39 cells and 45 cells is only 0.1.

2 **Experimental Verification.** A preliminary program to experimentally verify this approach has just been completed at the University of the Witwatersrand and has been presented in the literature [3]. Figs. 7 and 8 show an example comparison between experimental and simulation pressure-theta diagrams. Fig. 9 shows a similar comparison for the temperature distribution along the machine.

The discrepancy between the experimental and simulation expansion space pressure profiles is not fully understood. It is believed that this is probably due to not taking sufficient account of gas momentum in the working spaces [3, 5].

Table 1 gives a comparison between experimental and simulation values for a heat balance over the entire machine. There is an experimental error of approximately ± 7 percent.

A comparison with ideal analyses was also investigated which showed no inconsistancies in the simulation results [3, 5].

3 **Performance of a Hypothetical Engine.** Urieli [2, 8] has shown that it is possible to use this approach to generate performance curves for any hypothetical Stirling engine. A set of such curves is given in Fig. 10. These curves have been shown to be in agreement with the general trend of performance curves of real Stirling machines [2].

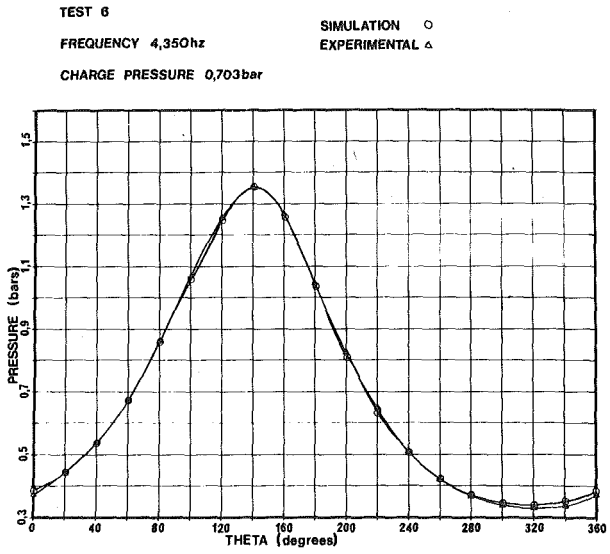

Fig. 7 Compression space pressure profiles [3]

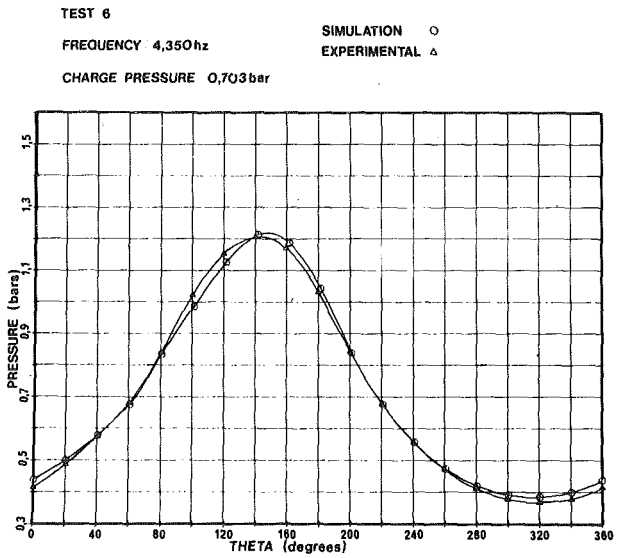

Fig. 8 Expansion space pressure profiles [3]

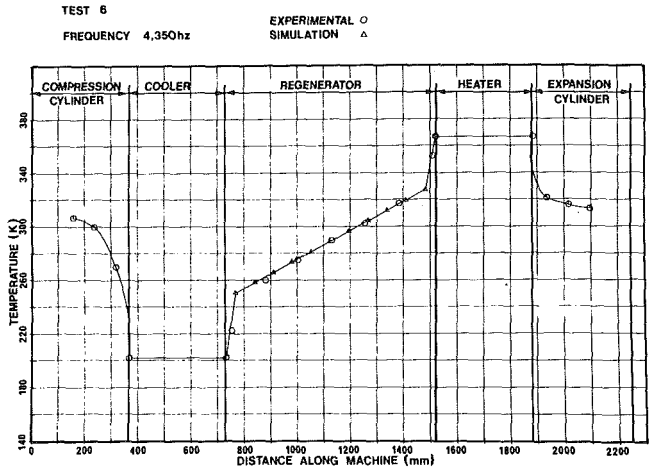

Fig. 9 Temperature distribution along machine [3]

Table 1 Overall energy balances

	Speed [Hz]	Q_k [J] Cooler	Q_h [J] Heater	W [J] Work	Energy Balance Error	Efficiency
Simulation	2,50	-46,628	49,047	2,886	-0,95%	5,88%
	3,35	-46,384	46,219	1,261	-3,09%	2,73%
	4,35	-44,690	42,288	-1,172	-2,91%	-2,77%
Exprmt.	2,50	-53,655	56,516	4,127	-2,24%	7,30%
	3,35	-53,895	51,387	2,592	-9,92%	5,04%
	4,35	-51,227	41,156	-0,860	-22,38%[1]	-2,09%

[1]This discrepancy has since been established as being due to a seal failure.

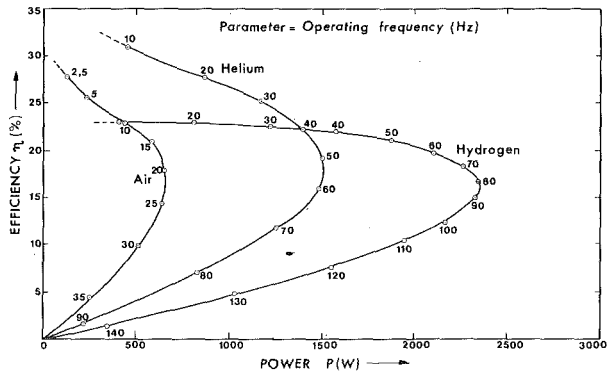

Fig. 10 Thermal efficiency versus power output

Conclusions

A more rigorous analysis has been presented to rationalise the approach first presented by Urieli, et al. [2]. The modelling of viscous dissipation and the inclusion of the normal stress terms have further improved the accuracy of the model.

Preliminary experimental comparisons are favourable and it would appear that the model can predict the performance of a real Stirling machine with an acceptable degree of accuracy.

References

1 Urieli, I., Rallis, C. J., "A New Regenerator Model for Stirling Cycle Machines," Report 67, School of Mechanical Engineering, University of the Witwatersrand, May 1976.

2 Urieli, I., Rallis, C. J., Berchowitz, D. M., "Computer Simulation of Stirling Cycle Machines," *Proceedings of the 12th IECEC*, Paper 779252, pp 1512–1521, 1977.

3 Berchowitz, D. M., Rallis, C. J., "A Computer and Experimental Simulation of Stirling Cycle Machines," *Proceedings of the 13th IECEC*, Paper 789111, 1978.

4 Finkelstein, T., "Generalized Thermodynamic Analysis of Stirling Engines," SAE paper 118B, Jan. 1960.

5 Berchowitz, D. M., *"A Computer and Experimental Simulation of Stirling Cycle Machines,"* Dissertation MSc(Eng), University of the Witwatersrand, 1978.

6 Bird, R. B., Stewart, W. E., Lightfoot, E. N., *Transport Phenomena*, New York, John Wiley and Sons, 1960.

7 Kovtum, I. M., Nanmov, A. N., Nesterenko, V. B., "The Stirling Cycle in a Dissociating Gas," *International Chemical Engineering*, Vol. 7, No. 4, 1967.

8 Urieli, I., *"A Computer Simulation of Stirling Cycle Machines,"* Thesis PhD, University of the Witwatersrand, 1977.

9 Schock, A., Private communication with C. J. Rallis concerning equations used for Stirling machine simulation, 1977.

10 Kays, W. M., London, A. L., *Compact Heat Exchangers* 2nd Ed. McGraw-Hill, 1964.

11 Knudsen, J. G., Katz, D. L., *Fluid Dynamics and Heat Transfer*, Tokyo, McGraw-Hill, 1958.

B. F. J. Cossar
Assistant Professor.

W. C. Moffatt[1]
Professor.
Mechanical Engineering Dept.,
Royal Military College of Canada,
Kingston, Ontario, Canada

R. E. Peacock
Senior Lecturer,
The School of Mechanical Engineering,
Cranfield, Bedford, U.K.

Compressor Rotating Stall in Uniform and Nonuniform Flow

Rotating stall in axial compressors consists of regions or cells of retarded flow moving around the annulus relative to the blades. Planar symmetry is destroyed, resulting in stalled blades in part of the annulus and unstalled blades in the remainder. The stall cell moves in the direction opposite to the rotor, relative to the blades, but since the relative speed of propagation is usually less than the rotor speed, the cell is seen to move in the same direction as the rotor from an absolute reference frame. The presence of the stall cells results in a deterioration of compressor performance since the maximum pressure ratio is not achieved in regions of retarded flow. Furthermore, since this self-induced distortion is periodic, the forced frequencies generated may coincide with the natural harmonics of the blading, tending to cause structural damage. This paper describes a series of experiments in which a single-stage, lightly loaded compressor operated under stall-free conditions and with rotating stall, both with uniform inlet flow and with distortions generated by an upstream screen of uniform porosity. Not only was the overall compressor performance determined in the traditional manner, but the distribution of static pressure over the rotor suction and pressure surfaces was measured with high response instrumentation. The rotor pressure profiles measured in both undistorted and distorted flow are presented for operation before and after the onset of rotating stall and the latter are compared with the steady flow results. It is observed that two distinctly different types of rotating stall exist depending upon whether or not an inlet flow distortion is present. These cells differ not only in macroscopic properties—rotational speed, circumferential extent, mass-averaged flow conditions, etc.—but also in detailed flow characteristics as evidenced by the rotor blade static pressure distributions. It is further observed that not all inlet distortion geometries lead to the development of rotating stall.

Introduction

The existence of large-scale nonuniformities in the inlet flow of axial compressors has recently received widespread attention. The mathematical difficulties in handling other than linearised models of such flows have however limited theoretical developments: furthermore, the complexities of data acquisition and presentation and even the development of suitable parameters by which to describe these unsteady phenomena have severely hampered the experimentalist. Nevertheless, continued improvement to axial compressor performance, particularly in surgemargin and operating range, must include an improved understanding of unsteady effects.

For compressors operating near the surge line, the development of rotating stall cells appear to be a common or maybe universal [1, 2], precursor to complete breakdown of performance. This phenomenon consists of regions or cells of retarded flow moving around the annulus relative to the blades. Axial symmetry is destroyed, resulting in stalled blades in parts of the annulus and unstalled blades in the remainder. The stall cell moves in the direction against that of the rotor relative to the blades, but since the relative speed of propagation is usually less than the rotor speed, the cell is seen to move in the same direction as the rotor in an absolute frame of reference.

The presence of the stall cells results in a deterioration of compressor performance since the maximum pressure ratio is not achieved in regions of retarded flow. Furthermore, since this self-induced distortion is periodic, the forced frequencies generated may coincide with the natural harmonics of the blading, tending to cause structural damage.

The effects of nonuniform inlet conditions and the development of rotating stall are clearly not unrelated; one results from an external influence upstream of the stage, the other can be generated within the blade row, but both result in non-axisymmetric and therefore unsteady flow conditions with rotor rows. The distortions may be from one to many blade passages in circumferential extent and therefore have associated frequencies of the order of the rotor rotating speed. These are of course, much lower than the blade passage frequencies encountered when considering blade wake effects.

This Paper describes a series of experiments in which a fully instrumented axial compressor was tested over a wide range of operating conditions. Not only was the compressor overall performance obtained, but the distribution of static pressure along the rotor blade surfaces was measured with high response instrumentation. Data were obtained both for undistorted and distorted inlet flows, the latter being generated by uniform porosity screens of various circumferential extent mounted at the compressor inlet.

Of particular interest was the development of rotating stall cells when the compressor operated near the stability limit line. The on-rotor pressure measurements showed very clearly the formation of

[1] Presently Visiting Professor, von Karman Institute for Fluid Dynamics, Rhode-St-Genese, Belgium.

Contributed by the Gas Turbine Division of The American Society of Mechanical Engineers and presented at the 1979 Israel Joint Gas Turbine Congress, Haifa, Israel, July 9–11, 1979. Manuscript received at ASME Headquarters May 11, 1979. Paper No. 79-GT/Isr-18.

these cells, whose development, circumferential extent and speed of rotation were found to be significantly affected by the nature of the upstream flow.

The Experimental Facility

The test rig (Fig. 1) was a lightly-loaded, single stage axial compressor, having constant annulus cross-section measuring 25.4 cm dia at the hub and 50.8 cm at the tip. All blades were built up from C4 sections. A variable-speed, 5hp motor drove the compressor at speeds up to a maximum of 1500 rpm. The mass flow was controlled by a throttle-valve situated at the tailpipe exit.

The rig was fitted with the usual instrumentation required to evaluate overall compressor performance. Inner and outer wall static tappings were positioned ahead of and behind every blade row, and the downstream stagnation pressures were measured by four rakes disposed orthogonally, each having nine shrouded pitot heads. All pressure readings were taken from inclined multiple manometer banks. Hot wire anemometer measurements were taken with the probe situated in the compressor inlet, providing both mean and turbulence velocities for a selected number of operating conditions.

The compressor pressure ratio was calculated from the total pressure measured downstream of the stage by the 36 stagnation pressure probes. Using the averaged value of static pressure from the inner and outer wall tappings downstream of the stage, together with the 36 stagnation pressure readings, the velocity distribution was obtained radially. Area weighted integration of this distribution yielded the compressor mass flow.

The rotor speed was measured by mounting a 60 tooth gear wheel on the drive shaft. An inductive pick-up sensed the passage of each tooth and the number counted over a period of one second was displayed on a frequency meter (yielding speed in rev/min directly).

Two rotor blades were instrumented at blade mid-height (bmh), one with eight static pressure tappings on the pressure surface, and the other with eight tappings on the suction surface. A high-frequency response transducer (70 kHZ) was mounted at bmh for each tapping. The pressure was fed from the blade surface to the transducer volume within the blade via a 0.038 cm dia transfer tube (maximum length of 0.152 cm). The transducers had a miniature silicon diaphragm (0.318 cm) on which a full Wheatstone bridge network was diffused. The electrical output wires were routed down through the blade root to a remotely-controlled switching circuit mounted on the rotor disc. The signals were then taken from the rotating rig via a precision slipring assembly (noise $< 5\mu$V/ma) to an external switch control device and finally to amplification/recording equipment.

The system was designed so that any eight transducers could be recorded simultaneously. This was wired for four channels (combinations) of eight transducers. Selection of channel A connected the eight pressure surface transducers to eight galvanometers in an ultraviolet recorder. The other three channels were: (B) 8 suction; (C) 4 leading edge (LE) suction and 4 LE pressure; (D) 4 trailing edge (TE) suction and 4 TE pressure tappings. Channels C and D were included to permit time-matching of suction and pressure surface measurements (taken from different blades) during unsteady flow.

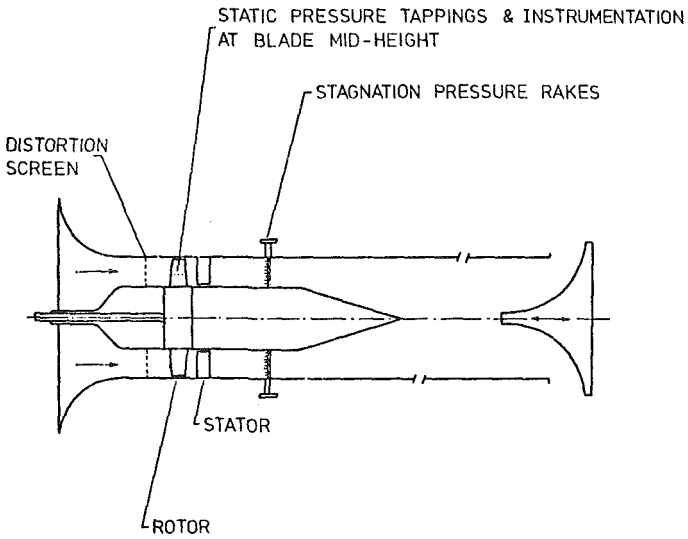

Fig. 1 The single stage compressor rig

The entire pick-up and recording system had a frequency response in excess of 1000 Hz, sufficiently high to handle all frequencies encountered.

A Yawmeter was located one-half chord upstream of the rotor, permitting calculation of the upstream static pressure and inlet relative velocity.

The blade surface pressure distribution data were evaluated in the usual pressure coefficient (C_p) form, where

$$C_p = \frac{p - p_1}{\frac{1}{2}\rho W_1^2}$$

In the case of the unsteady experiments, where only time averaged values of p_1 and V_1 were known, a new pressure coefficient C^* was utilized, where

$$C^* = \frac{p - p_\theta}{\frac{1}{2}\rho W_1^2}$$

p_θ is the static pressure measured at the same blade tapping at the same flow conditions in steady flow and the denominator represents the time-averaged dynamic pressure as seen by the rotor. Thus C^*

Nomenclature

$a, b \ldots j$ = compressor operating points on characteristic in undistorted flow

$q, r \ldots v$ = compressor operating points on characteristic in distorted flow

C_p = blade surface coefficient of pressure $= \dfrac{p - p_1}{\frac{1}{2}\rho_1 W_1^2}$

C^* = dimensionless blade surface pressure change due to stall or distortion $= \dfrac{p - p_\theta}{\frac{1}{2}\rho W_1^2}$

$C.P.R.$ = compressor stagnation pressure ratio

$C_{\Delta T}$ = stagnation pressure coefficient $= \dfrac{P - P_1}{\frac{1}{2}\rho_0 V_0^2}$

C_S = static pressure coefficient $= \dfrac{p - p_1}{\frac{1}{2}\rho V_0^2}$

M = Mass flow rate

N = Rotor rotational speed

P = Stagnation pressure

p = static pressure

P_θ = blade surface static pressure in distorted flow rotating stall

Δp = blade surface static pressure relative to atmospheric pressure $= p_\infty - p$

R_b = Reynolds' Number based upon blade chord

T = absolute temperature

V = gas velocity in absolute frame of reference

W = gas velocity relative to the rotor

x/c = dimensionless chordal distance

θ = circumferential position with respect to a fixed reference

θ_D = circumferential extent of distortion

θ' = circumferential position of stall cell with respect to a reference fixed to the rotor

U = rotor blade speed

i = flow incidence to blade

ρ = fluid density

τ = angular extent of rotating stall cell period, expressed in absolute degrees of rotor rotation

Subscripts

0 = upstream of distortion screen

1 = upstream of rotor

∞ = ambient

Superscripts

= mass averaged quantity

represents the change in the blade surface static pressure distribution resulting from the presence of the rotating stall and/or inlet flow distortion.

Experimental Results in Undistorted Inlet Flow

Unstalled Flow. The experimental compressor performance map is shown in Fig. 2. Data are shown for ten operating points at a constant rotational speed of 1250 rev/min. Measured rotor blade surface pressure distributions are plotted in Fig. 3 for the nine stalled operating conditions ($a - i$) of Fig. 2.

While at the higher and lower incidences these data show unexpected excursions, they are in good agreement with other data near the design incidence. Fig. 4 shows a comparison between the present results and those reported in [3] and [4] for similar blades operating at similar incidences and Reynolds' numbers for rotor and cascade respectively. Fig. 5 shows a comparison between the present and experimental data and those calculated by the analytical method of Martensen [5]. In all cases the agreement is good. It may be observed that the ripple in the convex surface measured by Rhoden [4] and followed by the data reported here, was ascribed to the presence of a laminar separation bubble, a phenomenon which, in any case, could not be predicted by the inviscid model of Martensen [5].

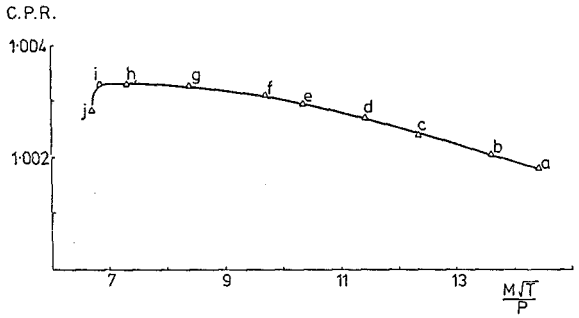

Fig. 2 Undisturbed compressor characteristic — 1250 rev/min

Rotating Stall. Further reduction of the compressor mass flow from point i of Fig. 2 to point j led to the inception of rotating stall in the rotor. Fig. 6 shows the variation of rotor blade pressure surface static pressure as a function of circumferential location at a constant flow condition indicated by point j (Fig. 2). Data are given for seven chordal locations, with tapping 1 being nearest the leading edge. Rotor movement was in the direction of increasing θ.

Examination of Fig. 6 reveals that at a given tapping, the pressure pattern repeated itself approximately every 540 deg of absolute rotor rotation and thus the stall pattern moved in the same direction as the rotor at one-third its rotational speed when viewed in the absolute frame of reference. Relative to the rotor however, the stall pattern moved in the opposite direction at roughly two-thirds the rotor rotational speed.

It may also be seen from Fig. 6 that the rotating stall cell first appeared at the rearmost portion of the rotor blade and moved upstream requiring about 20 deg of relative rotation (i.e., three blade passages) to reach the leading edge and become fully established. The cell occupied roughly 20 percent of the circumferential extent to the annulus.

The data of Fig. 6 are replotted in the form of pressure coefficient and chordal dimension in Figs. 7 and 8. Fig. 7 shows a comparison of the results obtained in the unstalled flow ($i = 11.9$ deg) with those for flow with rotating stall at a point circumferentially remote from the stall cell ($\theta = 660$ deg). The incidence at the latter condition was approximately 14 deg. Given the modest difference in incidence, the two results are in excellent agreement, showing that the flow had adequate opportunity to re-establish its steady-state flow pattern between successive passages of the stall (a key assumption in the parallel compressor model of the rotating stall flow). Fig. 8 shows the measured rotor pressure coefficient for a number of azimuthal positions (the reference position for θ and θ' are shown in Fig. 6). It is clear that at $\theta = 180$ deg a significant pressure distribution change had been experienced by the suction surface and the leading edge region of the pressure surface. By the time the rotor had moved to $\theta = 225$ deg both

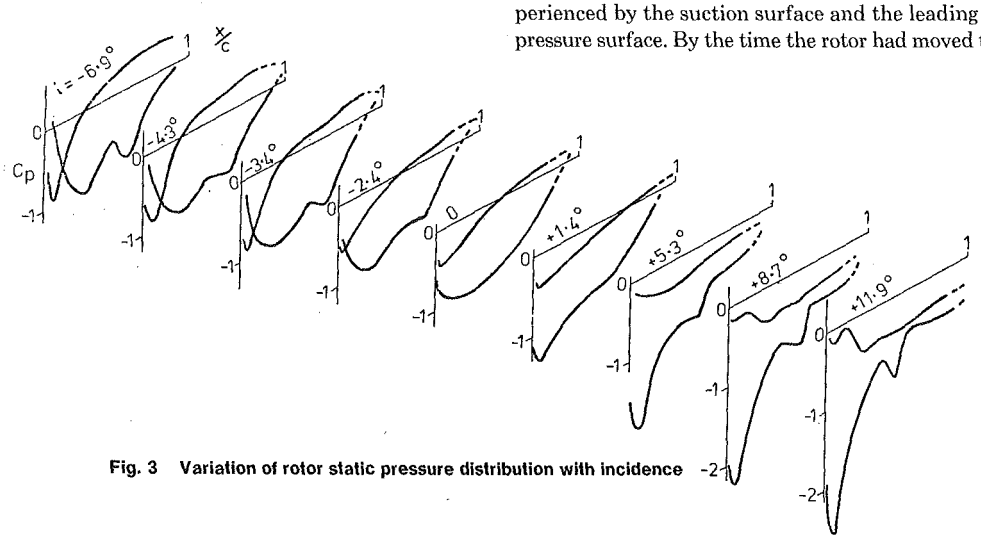

Fig. 3 Variation of rotor static pressure distribution with incidence

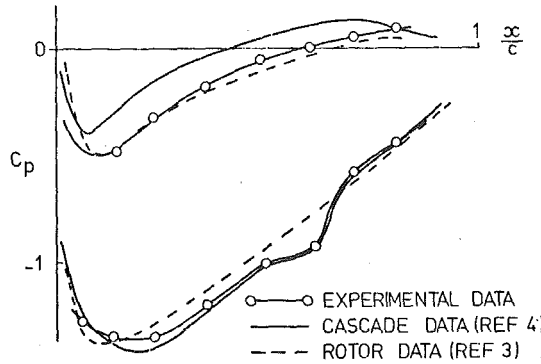

Fig. 4 Comparison of data with other experiments

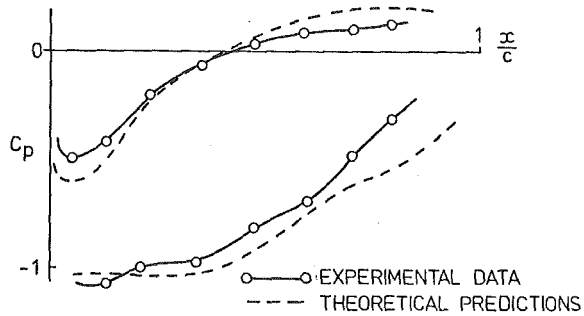

Fig. 5 Comparison of data with theory

surfaces experienced gross changes in pressure distribution. Not until the rotor had rotated nearly a full revolution (to $\theta = 540$ deg) was the flow fully reestablished.

To illustrate more clearly the effect of the rotating stall cell on blade element performance Fig. 9 shows a plot of C^*v chord. The reference state for p_θ and hence C^* was the pressure distribution obtained at $\theta = 45$ deg, a condition sufficiently removed from the stall cell that 'clear flow' prevailed. Absolute values of C^* are not particularly meaningful in view of the averaging required in computing the denominator, but shifts from the zero reference are a qualitative measure of change in blade surface pressure distribution as a result of the pressure of rotating stall. As was observed by Day [6], the rotating cell is a highly active region of flow; and this is supported by these data; the rapid changes of surface pressure in the region of $\theta = 405$ deg are evidence that reversed flow existed in the blade passage.

Experimental Results in Distorted Flow

Unstalled Flow. To assess the effects of inlet distortion on the blade pressure distributions a 90 deg squarewave distortion was generated by positioning a uniform low porosity wire-mesh screen one-half diameter upstream of the stage. The resulting overall compressor characteristic is shown in Fig. 10 superimposed for comparison upon the undistorted flow characteristic. The movement of the stability line, yielding a surge-margin reduction for an operational compressor, is evident.

The associated variation of stagnation and static pressure upstream of the stage is indicated in Fig. 11 for the operating points $q - v$ on the characteristic (Fig. 10). A discussion of the seemingly anomolous

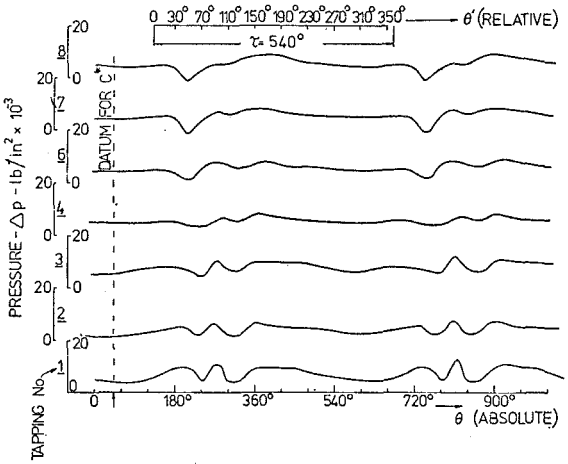

Fig. 6 Rotor pressure surface unsteady pressure measurements undisturbed inlet flow, rotating stall present

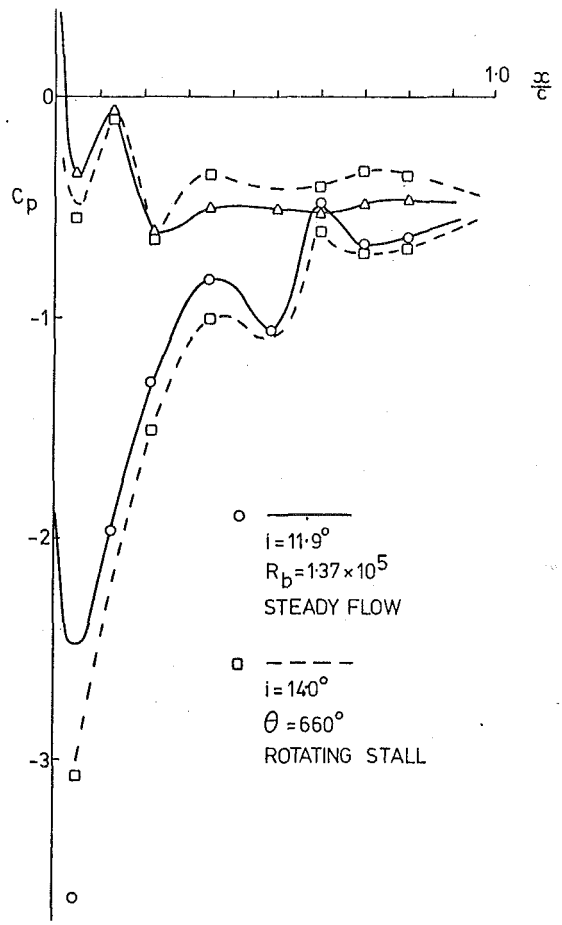

Fig. 7 Comparison of data measured under steady flow conditions and in rotating stall but remote from the stall cell

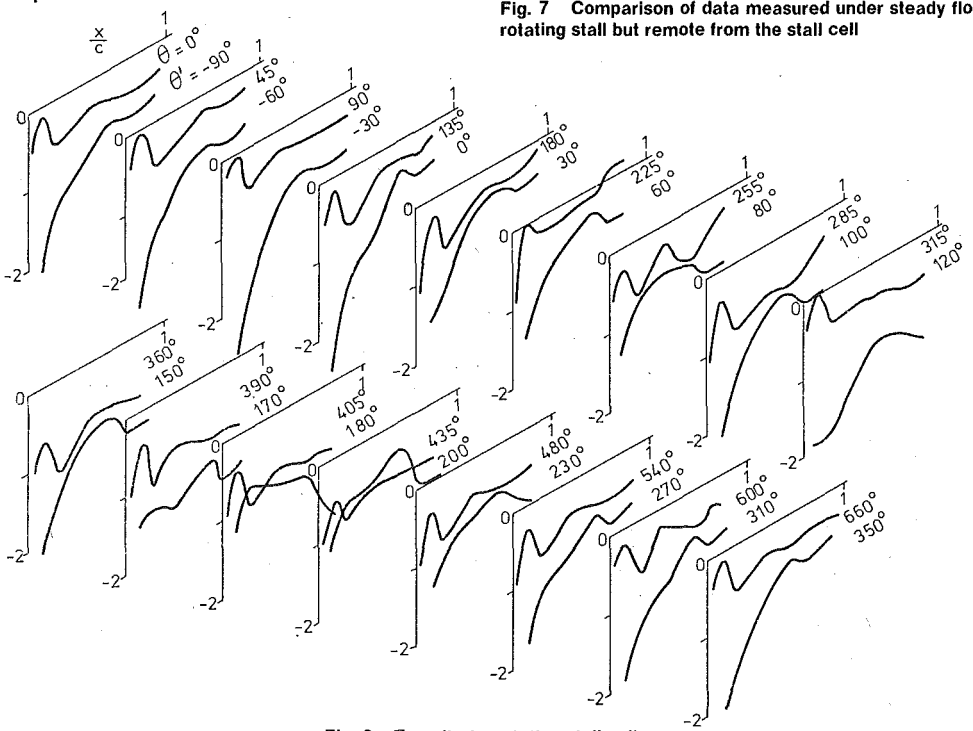

Fig. 8 Transit of a rotating stall cell

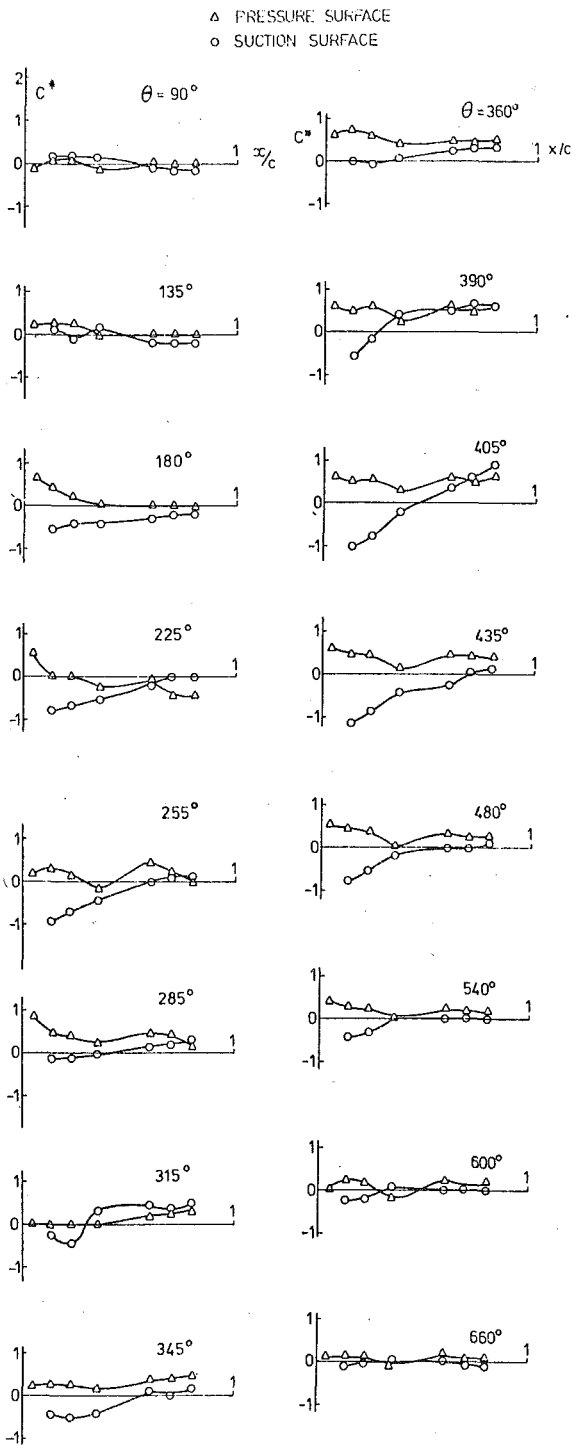

Fig. 9 Effect of rotating stall on the unsteady pressure coefficient C^*

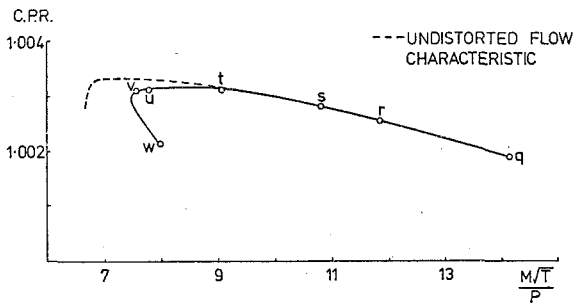

Fig. 10 Distorted flow compressor characteristic — 1250 rev/min $\theta = 90$ deg

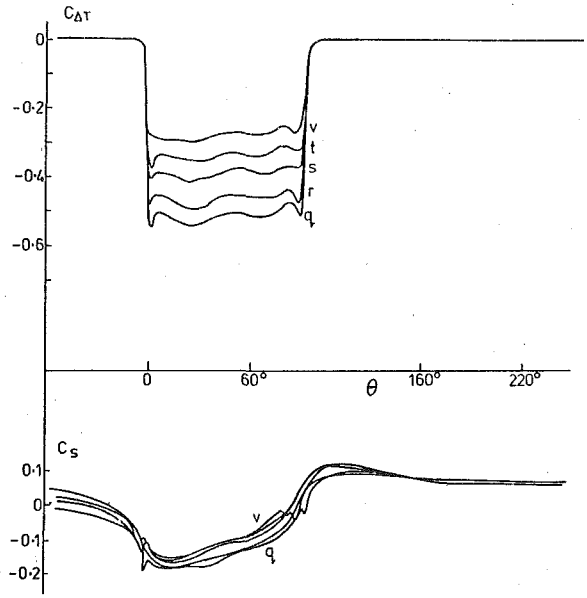

Fig. 11 Effect of compressor operating point upon distortion profile — 1250 rev/min $\theta_D = 90$ deg

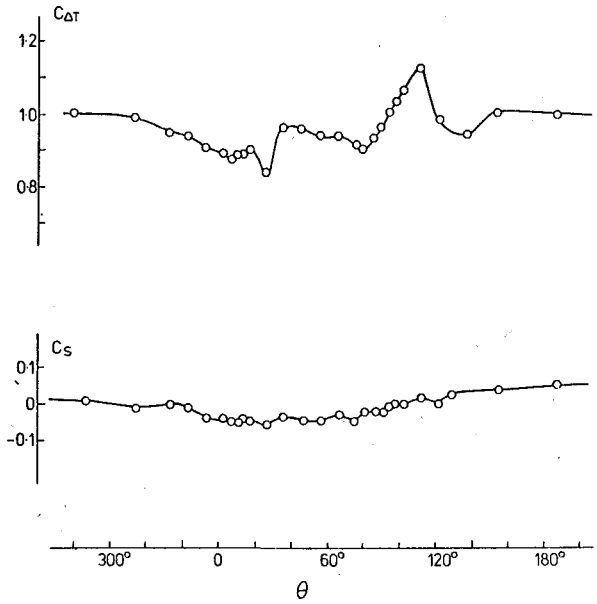

Fig. 12 Circumferential pressure variation downstream of compressor — 1250 rev/min, POINT 'v', $\theta_D = 90$ deg

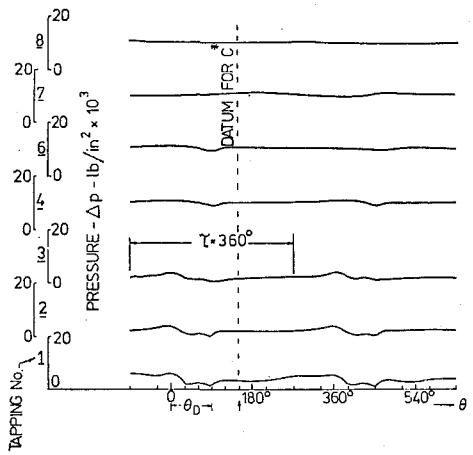

Fig. 13 Rotor pressure surface unsteady pressure measurements $\theta_D = 90$ deg, unstalled flow

rise in static pressure upstream of the rotor as it emerged from the distortion region is given in [3]. The corresponding circumferentially varying stagnation and static pressures downstream of the stage are presented in Fig. 12 for an operating point, v, close to the stability limit.

An example of a typical rotor blade concave surface pressure distribution at the same operating condition is shown in Fig. 13. The blade clearly experienced a significant pressure disturbance every revolution, but the effect was generally limited to the forward portion of the passage. The effect of the distortion screen may be seen more clearly in Fig. 14 in which C^* is plotted as a function of blade chord for a number of tangential locations. In this instance $C_\theta{}^*$ is a measure of the difference in static pressure between that at a given and that prevailing at a reference value of θ for comparatively undisturbed flow—in this case at $\theta = 150$ deg. If the undistorted flow pressure distribution is taken to correspond roughly to that shown for $\theta = -90$ deg, it is clear that major pressure changes began to take place some 30 deg before the rotor entered the shadow of the screen and persisted for at least 60 deg after it emerged from behind the screen. This observation is consistent with the spread in upstream static pressure (Fig. 11) and the corresponding downstream stagnation pressure distribution (Fig. 12).

Rotating Stall. Closure of the throttle to move the compressor operating point from v to w on Fig. 10 led into what, from instrument observation, may be described as a classic rotating stall mode. For example, Fig. 15 shows rotor blade concave surface pressure distributions as a function of θ. While superficially similar to those data found in the rotating stall case without inlet distortion screens (Fig. 6) several important differences may be observed. The period of the rotating stall cell cycle lengthened from 540 to 720 deg of rotor rotation, meaning that the cell was rotating at one-half the rotor speed relative to a stationary observer (cf. one-third rotor speed in the case of undistorted inlet flow). Thus the cell was moving at $U/2$ relative to the rotor, compared with $2U/3$ for flow without a distortion screen. It is also clear that the pressure perturbation propagated from the leading to the trailing edge of the blade, unlike the distorted flow case (Fig. 6) in which the reverse was true. Furthermore, on alternate revolution, when the instrumented blade passed through the screen shadow but the stall cell was diametrically opposite in the compressor annulus, only a minor perturbation in static pressure was experienced at the forward three measuring stations. The remainder were unaffected.

The rotor blade surface pressure distributions were plotted in the form of C^*vx/c in Fig. 16 where the reference condition for C^* was taken at $\theta = 225$ deg (see Fig. 15). In the region 0 deg $\leqslant \theta <$ 75 deg, following the transit of the stall cell the flow was being reestablished in the blade passage. For the range 75 deg $< \theta \leqslant$ 150 deg the flow was apparently stabilized, the apparently unusual pressure distribution being a consequence of selecting $\theta = 225$ deg as the reference condition for C^*. For 150 deg $\leqslant \theta \leqslant$ 330 deg the blade experienced modest pressure fluctuations as a result of passing through the distorted inlet flow, but major pressure excursions did not commence until $\theta = 630$ deg. In the range 630 deg $\leqslant \theta \leqslant$ 780 deg the rotor blade clearly experienced rapid changes in loading, characteristic of the transit of a rotating stall cell. Finally ($\theta \geqslant 810$ deg) the flow was restored to the state which prevailed 720 deg earlier.

Other distortion screens of different circumferential coverage (15 to 120 deg) and varying porosity were investigated, but in no other instance was rotating stall observed. For example, a 15 deg screen of the same (low) porosity as that described above did not produce rotating stall.

Discussion and Conclusions

It would be inappropriate to draw general conclusions from the limited data presented in this Paper. Our purpose, rather, is to present detailed blade element information for a lightly loaded compressor operating in two distinctly different regimes of rotating stall in the hope that current models of cell structure and behaviour may be reinforced by this addition to the body of experimental data.

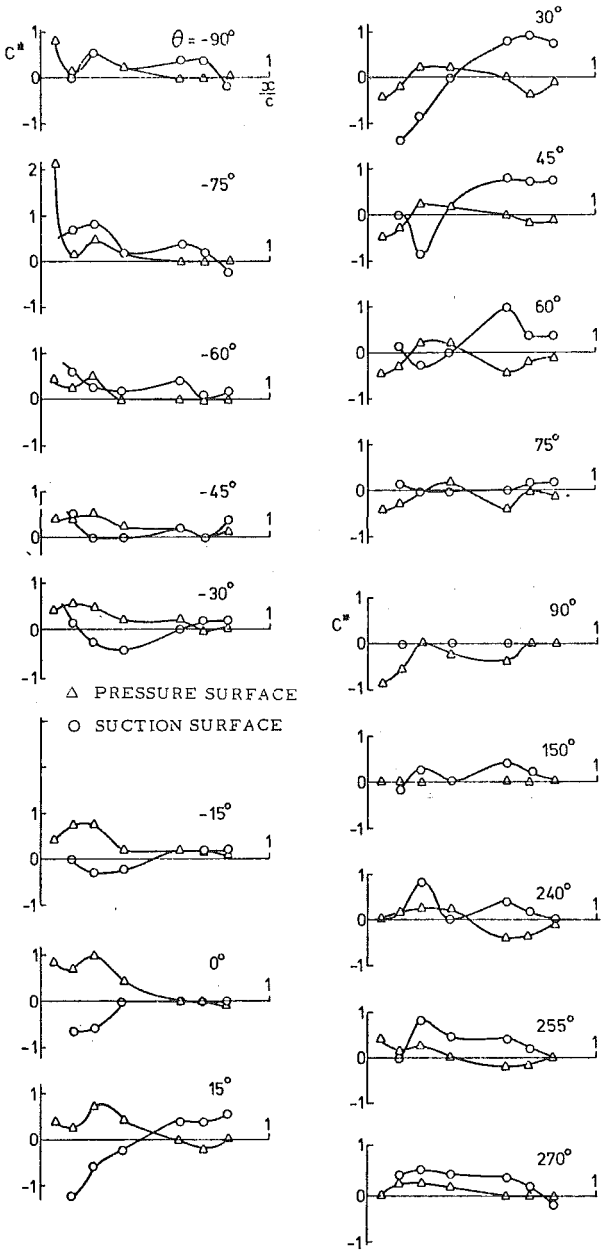

Fig. 14 Effect of distortion on the unsteady pressure coefficient C^*

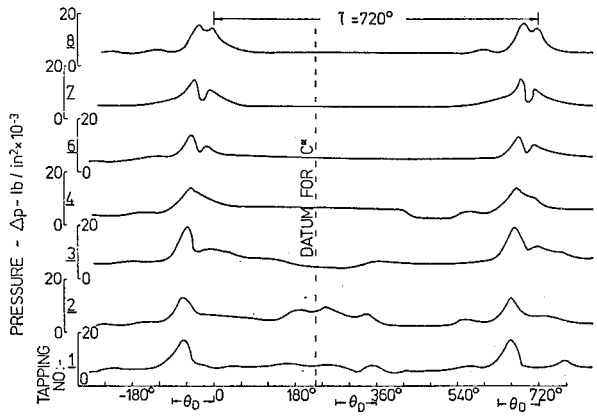

Fig. 15 Rotor pressure surface unsteady pressure measurements $\theta_D = 90$ deg, with rotating stall

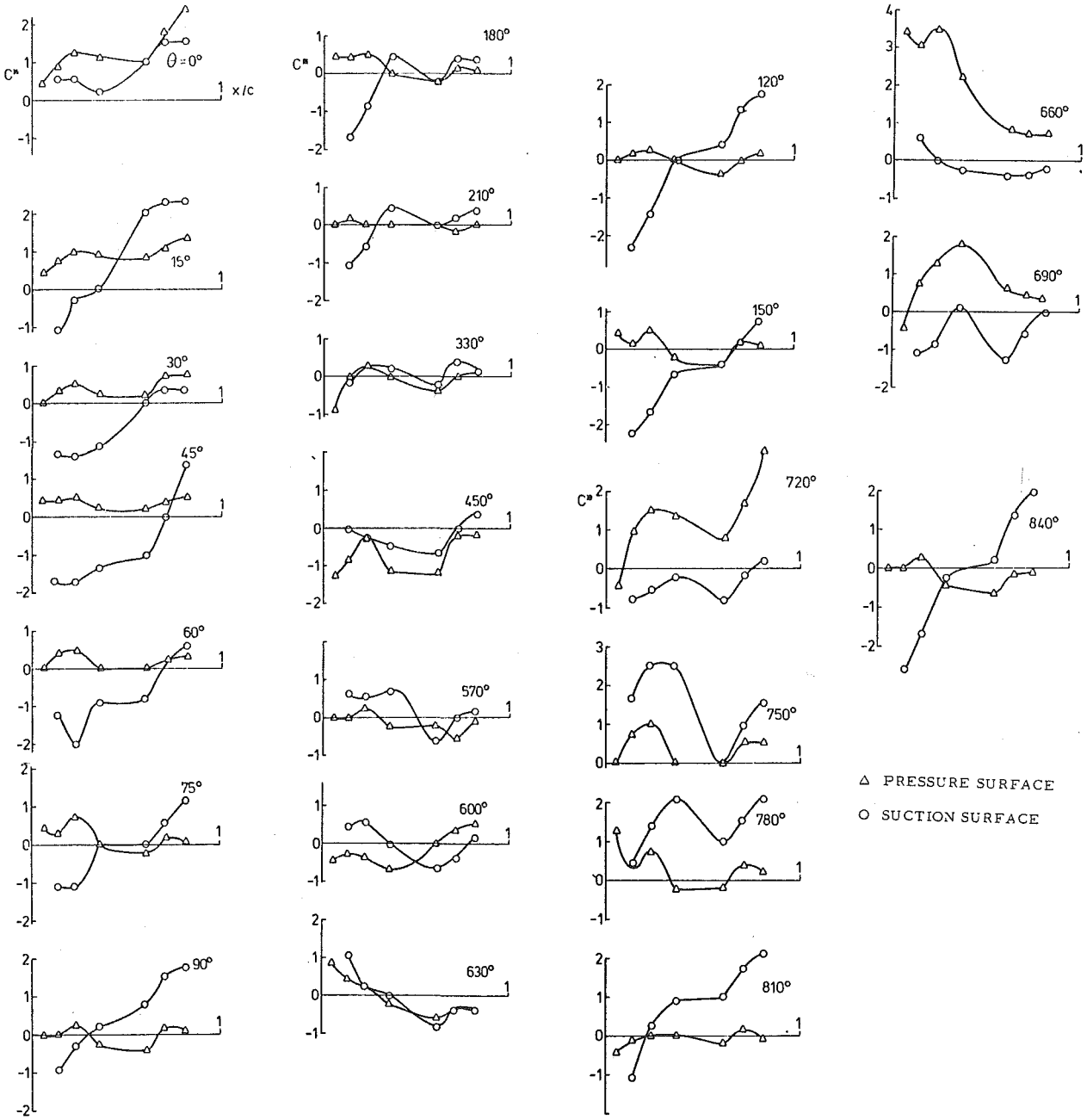

Fig. 16 Effect of distortion and rotating stall upon the unsteady pressure coefficient C^*

The existence of two different stall regimes suggests that two different mechanisms of rotating stall initiation on the rotor are possible. In the undistorted flow case, the rotor blade surface pressure distributions indicate a disturbance moving forward in the blade row. This is not inconsistent with the observations of others (e.g., [6]), who, on the basis of observations made upstream and downstream of the blade row, concluded that reverse flow is possible. It further suggests the rotating stall cell has its origins in the stator and that the rotor is responding to a rotating downstream blockage. To check this, further experiments would be needed.

In the case of the distorted inlet flow, the stall cell is clearly rotor initiated. The perturbation resulting from passage of the stall cell is much greater than that caused solely by the distortion screen and in fact, once rotating stall is established, the unstalled portion of the annulus is virtually unaffected by the distortion. This latter observation lends support to the stall model of [7] in which it is suggested that the unstalled portion of the flow is operating well below the stall line on the operating curve; it is therefore comparatively immune to upstream perturbations. This flow, combined with the small mass flow rate passing through the stall cell, results in the mass-averaged performance given by the point w in Fig. 10.

The inception of rotating stall and the flow pattern within a stall cell and the mechanism controlling the flow pattern within the stall cell are not currently well understood. This presentation, with the detailed information on flow within the rotating blade row may have some value in improving knowledge in this complex flow situation, which is still a limitation in axial compressor performance.

Acknowledgments

The experimental phase of this work was carried out in the U.K. under the United States Air Force Research Grant AFOSR-77-3305. Analysis in Canada was supported by the Defence Research Board of Canada under grant number 3610-147. These sources of sponsorship are gratefully acknowledged.

References

1 Greitzer, E. M., "Surge and Rotating Stall in Axial Flow Compressors, Part 1: Theoretical Compression System Model," ASME JOURNAL OF ENGINEERING FOR POWER, Apr. 1976 Vol. 98, pp. 190–198.

2 Greitzer, E. M., "Surge and Rotating Stall in Axial Flow Compressors, Part II: Experimental Results and Comparison with Theory," ASME JOURNAL OF ENGINEERING FOR POWER, Apr. 1976 Vol. 98, pp. 199–211.

3 Peacock, R. E., "Dynamic Internal Flows in Compressors with Pressure Maldistributed inlet Conditions," AGARD-CP-177 46th P.E.P. Conference of AGARD Monterey, CA., Sept. 1975.

4 Rhoden, H. G., "Effects of Reynolds Number on the Flow of Air through Cascades of Compressor Blades," A.R.C. R & M No. 2919, 1952.

5 Martensen, E., "The Calculation of the Pressure Distribution of Thick Aerofoils by Means of Fredholm Integral Equations of the Second Kind," N.A.S.A. TTF-702 July 1971.

6 Day, I. J., "Detailed Flow Measurement During Deep Stall in Axial Flow Compressors," AGARD-CP-177 46th P.E.P. Conference of AGARD, Monterey, CA, Sept. 1975.

7 Day, I. J., Greitzer, E. M., Cumpsty, N. A., "Prediction of Compressor Performance in Rotating Stall," ASME JOURNAL OF ENGINEERING FOR POWER, Jan. 1978 Vol 100, pp. 1–12

S. C. Singhal
R. J. Bratton
Westinghouse Research and Development Center
Pittsburgh, PA 15235

Stability of a $ZrO_2(Y_2O_3)$ Thermal Barrier Coating in Turbine Fuel with Contaminants

Corrosion behavior of recently developed plasma sprayed duplex thermal barrier coating systems, consisting of Udimet-500 alloy metal substrate, MCrAlY (M = Ni or Ni/Co) bond coat and ZrO_2 stabilized with 12 wt percent Y_2O_3 overcoat, has been evaluated in environments now used or anticipated in utility turbines burning liquid fuels. The base fuel, GT-2, was doped with desired concentrations of sodium, vanadium and sulfur, and burned in a gas turbine simulator which contained the coated, air-cooled specimens. The coatings were found to behave well when exposed to combustion gases obtained by burning clean GT-2 fuel oil and that containing 1 ppm Na. However in the presence of vanadium in the fuel, the ZrO_2-12 wt percent Y_2O_3 oxide coating showed severe cracking, chipping and spalling. Possible causes for such oxide coating degradation are discussed. This work shows that the thermal barrier coating concept is feasible for utility turbines; but further coating development, specifically for utility turbines burning residual fuels, is required.

Introduction

There is considerable incentive to increase gas inlet temperature in power generation gas turbines to improve thermal efficiency and increase power output for a given engine size. Because of the difficulty in achieving major improvements in temperature capabilities of metallic alloy systems and the significant losses in turbine efficiency in using airfoil cooling, serious consideration is being given to coating the metal components with a thermally insulating ceramic material for maintaining metal components at much lower temperatures than the hot combustion gases [1]. Potential benefits from the use of such thermal barrier coatings are quite large and include reduction of metal temperature by about 100–250°C or reduction in cooling air requirements. Moreover, significant performance improvements and reductions in cost of electricity can be achieved in very near term by increasing the turbine inlet temperature in today's combined cycle power plants. Thus, these thermal barrier coatings may well provide the transition between metallic systems and the apparent ultimate solution of bulk ceramic airfoils.

A two-layer thermal barrier coating consisting of yttria-stabilized zirconia over a NiCrAlY bond coat, shown schematically in Fig. 1, has recently been investigated [1] at the NASA-Lewis Research Center. Their research program identified yttria-stabilized zirconia as being most promising for aircraft turbine engines on the basis of adherence to the NiCrAlY bond coat, thermal shock resistance, and resistance to cracking. The tests in an aircraft type gas turbine engine showed that the NiCrAlY/$ZrO_2(Y_2O_3)$ coating successfully withstood 35 start-stop thermal cycles (total testing time of 150 hr) at turbine inlet temperatures as high as 1375°C and 500 2 min cycles from 1375°C to flame-out with no signs of deterioration. In addition, thermal measurements made on coated and uncoated blades during the engine tests corroborated the theoretically predicted insulating effect of the coating. Also, the coating system exhibited good adherence to blade and vane metals when cycled in a static burner rig 40 times between 1100 and 27°C. However, preliminary hot corrosion tests with sea salt injected into the flame at gas temperature of 900°C indicated coating adherence problems after 40 1 hr cycles.

Duplex thermal barrier coatings have also been investigated by Tucker, et al. [2], at the Linde Division of the Union Carbide Corporation. In their duplex thermal barrier coatings, both pre-alloyed and Met-sealed[1] MCrAlY (M = Ni, Ni/Co) bond coats were used which were applied by plasma spraying using a proprietary inert gas shroud surrounding the plasma spraying effluent. This inert gas shroud effectively eliminates any oxidation of the alloy as it is sprayed. The oxides used in their work were yttria-stabilized zirconia and magnesia-zirconia. The coatings were tested in isothermal and cyclic oxidation tests in air. From these tests, they concluded that in these duplex coatings, the bond coat must be effectively sealed to prevent any significant oxidation of the substrate or internal oxidation of the bond coat itself; the surface of the bond coat be rough enough to provide an adherent surface for the oxide overcoat; and the oxide density be controlled (to 88 percent of theoretical density) for optimum thermal shock resistance.

In order to be used commercially, these thermal barrier coatings

[1] Met-sealed is a proprietary Union Carbide process.

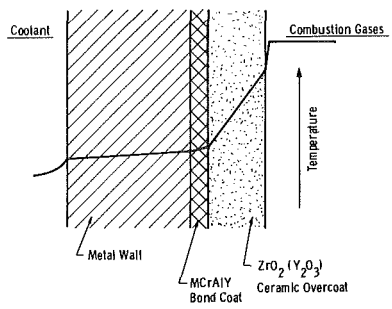

Fig. 1 Schematic representation of the thermal barrier coating system

Contributed by the Gas Turbine Division and presented orally at the Gas Turbine Conference and Exhibit and Solar Energy Conference, San Diego, California, March 12–15, 1979. Manuscript received at ASME Headquarters June 4, 1979.

will have to successfully withstand, among other things, the corrosive environments of industrial gas turbines. In this paper, the effect of several fuel contaminants on the behavior of duplex thermal barrier coating systems, consisting of a MCrAlY (M = Ni or Ni/Co) bond coat and Y_2O_3-stabilized ZrO_2 overcoat, under simulated industrial gas turbine conditions is discussed and analyzed.

Experimental

The Experimental Equipment. The behavior of duplex thermal barrier coating systems has been studied in a pressurized turbine test passage which simulates the operational environment of a stationary gas turbine. Fig. 2 shows a schematic diagram of this test facility. In this facility, air compressed to about 7 atm is preheated in an indirectly fired air heater to ~315°C and fed into a Hastelloy-X combustor. Fuel is injected into the primary combustion zone through a bayonet-mounted fuel nozzle in the dome-shaped front portion of the combustor and burned with the compressed air. Combustion gases are then mixed with secondary cooling air, the amount of which is adjusted to attain the desired gas temperature. At the combustor exit, an array of 16 thermocouples measures the temperature of the combustion gases.

Downstream of the thermocouple array, a transition section reduces the flow area and increases the gas velocity to ~150 $m \cdot s^{-1}$. At this location, the coated specimens are exposed to the high velocity hot combustion gases. A test section holds a set of two air-cooled cylindrical sleeves 2.5 cm dia and 5 cm long. These cylindrical sleeves have 12 holes drilled lengthwise to various depths to accommodate thermocouples which measure the metal surface temperature. Cooling air is passed through the inside of the sleeves to achieve the desired metal temperature. At the other end of the test section, a water-cooled barrier plate acts as a damper valve and maintains a pressure of 4 atm in the passage. The exhaust gases are cooled by a water spray and vented into the atmosphere through an extensive muffler system.

The basic fuel used for the experiments described in this paper was No. GT-2 fuel oil.[2] A typical chemical analysis of this fuel is shown in Table 1. The levels of sulfur, sodium and vanadium in the fuel were increased to desired levels by mixing in appropriate amounts of following compounds in the fuel oil:

Sulfur: Ditertiary butyl disulfide
Sodium: Sodium napthenate
Vanadium: Vanadium carboxylate

In a typical test run, the temperature of the combustion gases was gradually increased in ~1 h to the desired gas temperature. During this heat-up, the specimens were kept away from the combustion gases and experienced temperature of 250–310°C. After the combustion gases reached the desired temperature, the specimens were lowered in the gas stream (within ~1 min) and exposed isothermally to the combustion gases. After 8 to 10 hr, the specimens were retracted away from the gas stream (within ~1 min) and then the fuel cut-off gradually to complete shut down in ~5 min. The specimens cooled down to the room temperature in ~30 min. In this fashion, the testing was continued from day to day to accumulate the desired exposure time on the specimens. Thus, even though no thermal cycling of the specimens was intended, the specimens did experience one heat-up and cool-down for every 8–10 hr of exposure time.

Following exposure to combustion gases in the pressurized turbine test passage, the specimens were weighed, measured and examined visually and optically. The specimens were then analyzed in detail by metallography, x-ray diffraction and electron microprobe analyses. However, even though all the specimens were weighed and measured before and after exposure to combustion gases, these measurements were not found to be of much value because of uneven attack (spalling, chipping, etc.) and formation of deposits on the surface of the specimens from the combustion gases. The data on weight and dimensional changes, therefore, are not reported here. The most valuable information was obtained by metallographic, x-ray diffraction and electron microprobe analyses.

[2] Exxon Corporation, No. 260.

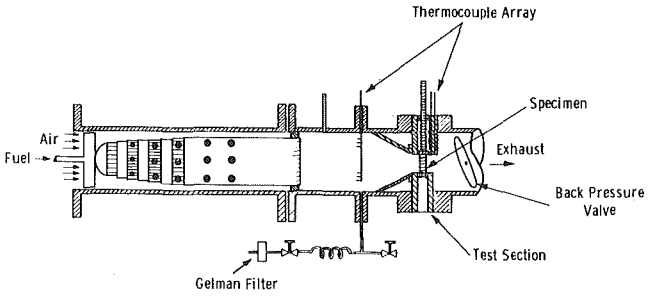

Fig. 2 High temperature pressurized turbine test passage

Table 1 Typical chemical analysis of No. GT-2 fuel oil (Exxon 260)

Element	Concentration (ppm)
Fe	2.0
Cu	0.8
Si	0.8
Mn	0.6
Pb	0.5
Al	0.3
Mg	0.3
Na and K	0.3
P	0.3
Ca	0.2
Cr	0.2
V	0.07
S	0.242 (wt percent)

The Coating Systems. The duplex coatings consisting of a MCrAlY (M = Ni or Ni/Co) bond coat and the Y_2O_3-stabilized ZrO_2 overcoat on Udimet-500 specimens were obtained from two sources: (1) NASA-Lewis Research Center (2) Union Carbide Corporation—Linde Division.

Both the bond coat and the oxide overcoat in each of the coating systems were deposited by plasma spraying. The Linde coating was deposited using an inert gas shroud surrounding the plasma spray effluent in order to eliminate any oxidation of the bond coat alloy powder as it was sprayed. No such protective shield was used by NASA in depositing the coatings.

The NiCrAlY/$ZrO_2(Y_2O_3)$ Coating from NASA. The bond coat in the NASA coating had a nominal composition of 16 wt percent Cr, 5 wt percent Al, 0.6 wt percent Y and the balance Ni, while the overcoat was ZrO_2-stabilized with nominally 12 wt percent Y_2O_3. Detailed chemical analysis of the oxide overcoat is shown in Table 2. Metallographic cross-section of a typical NASA coating is shown in Fig. 3. The bond coat in these coatings was found to vary from ~12 to 100 μm in thickness around the circumference of the specimen, and at a few points, there was practically no bond coat present. The $ZrO_2(Y_2O_3)$ oxide overcoat was relatively uniform in thickness, ~355 μm. The surface roughness of this oxide overcoat averaged ~10 μm, rms.

The oxide overcoat was found by x-ray diffraction analysis to contain only the cubic $ZrO_2(Y_2O_3)$ phase with lattice parameter a equal to 5.1367 Å. The electron microprobe scans revealed the presence of large inclusions of alumina in the NiCrAlY bond coat; these inclusions appear as dark regions in the metallographic cross-section shown in Fig. 3. The electron microprobe scans also revealed the presence of a minor second phase in the $ZrO_2(Y_2O_3)$ overcoat. This phase consisted mainly of yttrium and silicon, possibly yttrium silicide.

The NiCoCrAlY/$ZrO_2(Y_2O_3)$ Coating from Linde Division. The bond coat in the Linde coating consisted of a cobalt-base alloy with 32 wt percent Ni, 21 wt percent Cr, 7.5 wt percent Al and 0.5 wt percent Y, while the overcoat was again ZrO_2 stabilized with nominally 12 wt percent Y_2O_3. Detailed chemical analysis of the oxide overcoat is shown in Table 2. The metallographic cross-section of a typical

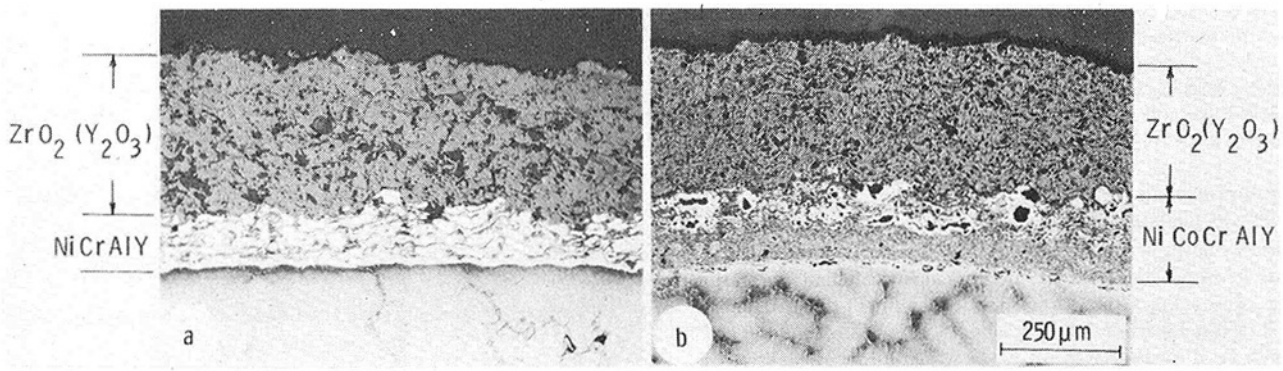

Fig. 3 Metallographic cross sections of the duplex thermal barrier coatings: (*a*) from the NASA-Lewis Research Center (*b*) from the Linde Division—Union Carbide Corporation

Linde coating is also shown in Fig. 3. Both the bond coat and the oxide overcoat in the Linde coatings were found to be fairly uniform in thickness; the bond coat being ~165 μm and the oxide overcoat ~305 μm in thickness.

X-ray diffraction analysis revealed the oxide overcoat to be predominantly a tetragonal $ZrO_2(Y_2O_3)$ phase with the following lattice parameters:

$$a = 5.1232 \text{ Å}$$

$$c = 5.1528 \text{ Å}$$

The oxide overcoat possibly also contained the cubic $ZrO_2(Y_2O_3)$ phase; its determination was made difficult and rather uncertain because the lattice parameters of the tetragonal and cubic phases differ only very slightly. Also, in contrast to the NASA coating, the electron microprobe scans indicated the absence of any alumina inclusions in the bond coat or any yttrium silicide in the oxide overcoat.

Results

In order to separate the effects of various fuel contaminants on the oxide coating behavior, a series of six parametric tests were conducted in the pressurized turbine test passage using GT-2 fuel oil as the basic fuel to which different contaminants were added. These tests were conducted at 1100°C gas temperature, keeping the maximum metal surface temperature at ~800°C. This meant an average metal surface temperature of ~675°C.

The different fuel conditions under which this series of tests were conducted, the test duration, and the condition of the coating after test are summarized in Table 3. One NASA-coated and one Linde-coated specimen was exposed in each of these tests. Coatings from both the NASA-Lewis Research Center and the Linde Division performed similarly under the environments employed in this investigation. The physical appearance of the exposed specimens from each test is illustrated in Fig. 4. A typical metallographic cross-section from the exposed specimens from each test is shown in Fig. 5. The detailed observations from each test are described below.

Test No. 1 (Clean Fuel with No Dopants). In this test, the coating remained intact and free of any macrocracking or spalling in 98 hr of exposure to combustion gases. This is apparent in the photograph of the surface of the exposed specimen shown in Fig. 4. The surface did pick up small amounts of deposits from the combustion gases. The electron microprobe scans from the exposed coated specimens showed appreciable amounts of Fe, Ni, Co and Cr on the surface of the $ZrO_2(Y_2O_3)$ oxide coating. These elements are from the surface deposits of α-Fe_2O_3 and spinel, which come from the metallic structural parts of the pressurized turbine test passage. A trace amount of phosphorous at the oxide surface was also evident in these scans. Phosphorous is present in the basic clean fuel as shown in Table 1. X-ray diffraction analysis identified predominantly $ZrO_2(Y_2O_3)$ (tetragonal/cubic) in the surface oxide; however, minor amounts of spinel and α-Fe_2O_3, and trace amounts of ZrO_2 (monoclinic), YPO_4 and $NaZr_2(PO_4)_3$ were also detected.

Table 2 Chemical analysis of the oxide overcoat in NASA and Linde thermal barrier coating

Element	Concentration, wt percent NASA	Linde
ZrO_2	85.78 (± 0.5)	87.30 (±0.5)
Y_2O_3	13.30 (±0.5)	11.45 (±0.5)
Si	0.2	0.02
Al	0.02	0.2
Fe	0.1	0.1
Mg	0.03	0.008
Ni	0.02	0.03
Ti	0.06	0.03
V	0.01	0.01
Cr	0.01	0.02
Hf	>1.0	not detectable
Yb	detectable[1]	detectable

[1] Yb about 10 times greater in the NASA coating than in the Linde coating.

Table 3 Summary of parametric tests with cooled specimens

Test No.	Fuel Dopant[1]	Total Test Time	Coating Condition after Test
1	None	98 hr	Intact
2	1 ppm Na	131 hr	Intact
3	10 ppm V	42 hr	Chipped and spalled
4	10 ppm V KI-16 Mg additive[2]	52 hr	Chipped and spalled
5	1 ppm Na, 10 ppm V, 0.5 wt percent S Cr-Mg-Si additive[3]	59 hr	Chipped and spalled
6	10 ppm V Cr-Mg-Si additive[3]	41 hr	Chipped and spalled

[1] Basic Fuel: GT-2 fuel oil (Exxon 260).
[2] Manufactured by Tretolite Division, Petrolite Corporation, St. Louis, MO.
[3] Westinghouse proprietary additive.

Test No. 2 (with 1 ppm Na in the Fuel). In this test also, the coating remained intact and free of any macrocracking or spalling even after 131 hr of exposure to combustion gases. This is clear from the photograph of the surface of the exposed specimen shown in Fig. 4. However, the micrographs of the exposed specimens indicated considerable longitudinal cracking in the oxide overcoat, both for the NASA and the Linde-coated specimens. Long-term exposure is required to assess the effect of this cracking on coating integrity.

The electron microprobe scans from the exposed specimens again showed considerable amounts of Fe, Ni, Co and Cr-containing deposits on the oxide surface. X-ray diffraction analysis identified $ZrO_2(Y_2O_3)$ (tetragonal/cubic) as the major phase in the oxide surface with minor amounts of spinel, α-Fe_2O_3 and ZrO_2 (monoclinic), and traces of YPO_4.

Test No. 3 (with 10 ppm V in the Fuel). In this test, the oxide coating chipped and spalled after only 42 hr exposure to combustion gases. The most chipping and spalling occurred on the front sides of

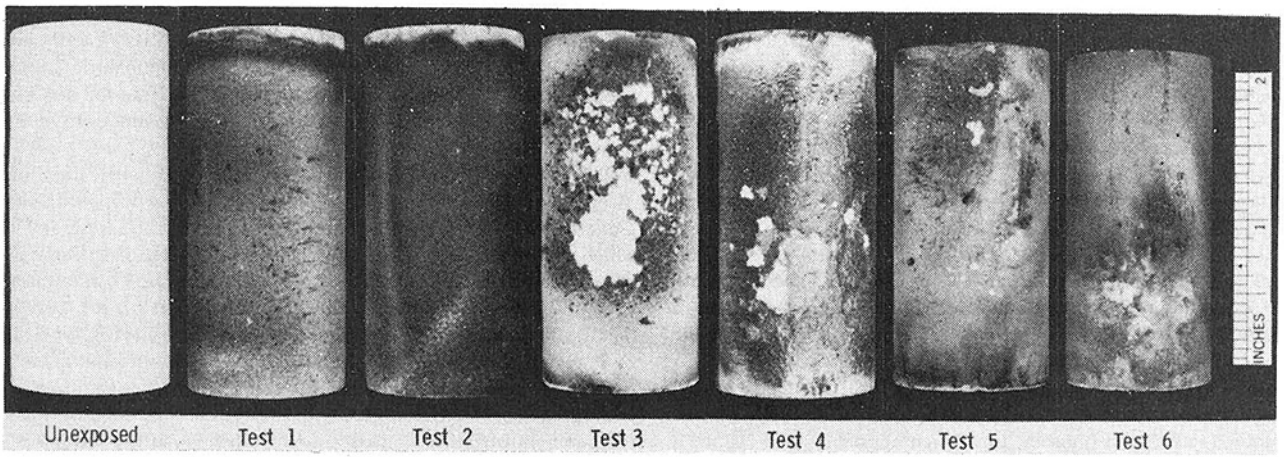

Fig. 4 Surface appearance of thermal barrier coated specimens after exposure in different tests

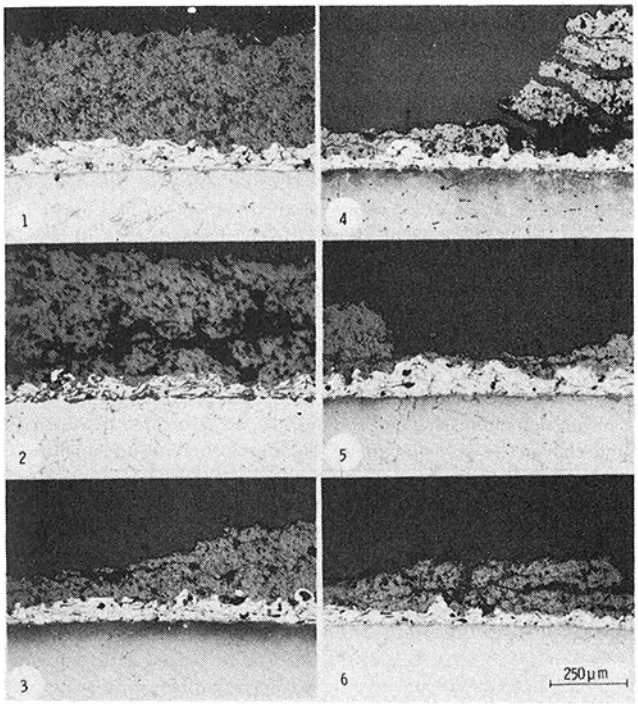

Fig. 5 Typical metallographic cross sections from the coated specimens after exposure in different tests (test number indicated)

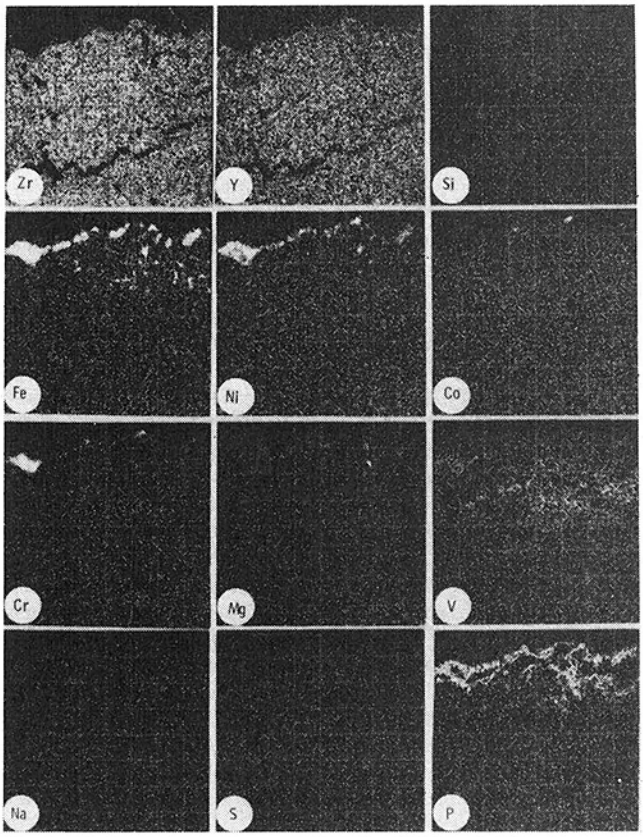

Fig. 6 Electron microprobe scans from the NASA-coated specimen after 42 hr of exposure with 10 ppm V in the fuel. Scans were taken from typical reaction zone at the front specimen face

the specimens which faced the gas flow. This is evident from the photograph of the exposed specimen, Fig. 4. The micrographs from the exposed specimen indicated that the oxide coating cracks and spalls off from within its own thickness rather than at the MCrAlY/oxide interface.

The electron microprobe scans from the exposed NASA-coated specimen are shown in Fig. 6. These scans reveal that significant amounts of vanadium and phosphorous penetrate inside the oxide coating during exposure to the combustion gases. Aso evident in the microprobe scans are surface deposits rich in Fe, Co, Ni and Cr which were found in all the experiments. X-ray diffraction analysis identified $ZrO_2(Y_2O_3)$ (tetragonal/cubic) as the predominant phase in the oxide coating with minor amounts of ZrO_2 (monoclinic), spinel, α-Fe_2O_3, YPO_4 and $NaZr_2(PO_4)_3$.

Test No. 4 (with 10 ppm V and Mg-Additive). In this test, a magnesium-based additive,[3] which is frequently used to prevent vanadium attack on metals, was added to the fuel in a quantity necessary to give Mg/V ratio equal to 3. However, this additive did not prove very successful, and the oxide coating again chipped and spalled off after as early as 26 hr of exposure to combustion gases. The most attack occurred on the front of the specimens facing the gas flow. The micrographs of the exposed specimens indicated considerable cracking, chipping and spalling of the oxide coating.

The electron microprobe scans from the exposed coated specimens indicated large concentrations of Mg, V and P on the surface of the oxide coating. Also apparent from these scans were Fe, Co and Cr-rich surface deposits. X-ray diffraction analysis detected $ZrO_2(Y_2O_3)$ (tetragonal/cubic), $Mg_3(PO_4)_2$, $Mg_3(VO_4)_2$, MgO, $MgSO_4$, $MgSO_4 \cdot 6H_2O$ and spinel in the surface coating. Thus, magnesium in the additive reacts with V and P in the fuel to form massive $Mg_3(VO_4)_2$ and $Mg_3(PO_4)_2$ deposits. However, the coating still cracks and spalls.

Test No. 5 (with 1 ppm Na, 10 ppm V, 0.5 wt percent S and a Cr-Mg-Si Additive). In this test, an additive[4] containing Cr, Mg

[3] KI-16, Tretolite Division, Petrolite Corporation, St. Louis, MO.

[4] Westinghouse Electric Corporation, Proprietary composition.

and Si, was added to the fuel with the objective of preventing corrosion by Na and V. However, even in the presence of this additive, the coating showed cracking and chipping in 59 hr of exposure to combustion gases. This is clear from the photograph of the exposed specimen shown in Fig. 4. The cracking and chipping of the oxide coating is also evident in the micrograph of the exposed specimen shown in Fig. 5.

X-ray diffraction analysis identified mainly $ZrO_2(Y_2O_3)$ (tetragonal/cubic), SiO_2 (quartz), SiO_2 (cristobalite), $Mg_3(PO_4)_2$, α-Fe_2O_3 and spinel in the surface coating. However, trace amounts of ZrO_2 (monoclinic) and $NaZr_2(PO_4)_3$ were also detected. Silica is apparently formed by oxidation of Si in the additive. Surprisingly, no magnesium vanadate or any other vanadium compound was detected in the surface after exposure to the combustion gases even though the additive was used in quantity sufficient to give a Mg/V ratio equal to 3, same as in Test No. 4. Apparently, either all the magnesium in the additive combined with phosphorous in the combustion gases to form $Mg_3(PO_4)_2$; or alternatively, if present, was not detected by X-ray diffraction analysis because the strongest diffraction line for $Mg_3(VO_4)_2$ coincides with the strongest diffraction line for $ZrO_2(Y_2O_3)$.

Test No. 6 (with 10 ppm V and a Cr-Mg-Si Additive). In this test also, the oxide coating showed signs of chipping and spalling after as early as 41 hr of exposure to combustion gases. X-ray diffraction analysis identified predominantly $ZrO_2(Y_2O_3)$ (tetragonal/cubic), SiO_2 (quartz), SiO_2 (cristobalite), $Mg_3(PO_4)_2$ and α-Fe_2O_3 in the surface deposits. Silica is formed by the oxidation of Si in the additive, and $Mg_3(PO_4)_2$ is formed by the reaction of Mg in the additive with P in the combustion gases. Again, no vanadium compound was detected in the surface coating after exposure to combustion gases.

Discussion

It is evident from the results presented in the previous section that the clean fuel or that containing 1 ppm Na is not detrimental to the ZrO_2-12 wt percent Y_2O_3 coating, at least for the short exposure times of 100–150 hr employed in this investigation. However phosphorous and vanadium in the fuel cause severe cracking and progressive spalling of the oxide coating. Furthermore, as mentioned earlier, coatings from both the NASA-Lewis Research Center and the Linde Division perform similarly under the environments employed in this investigation.

Phosphorous is present in the clean fuel at a level of 0.3 ppm as shown in Table 1. It is also possible that additional phosphorous gets introduced in the combustion gases either through air or through organic additives used to increase the contaminants (particularly sulfur) level in the fuel. The phosphorous oxidizes to P_2O_5 in the combustion chamber and enters the turbine in the gaseous form.[5] This P_2O_5 (g) apparently reacts with Y_2O_3 in the coating to form YPO_4, and in conjunction with sodium-containing compounds in the combustion gases forms $NaZr_2(PO_4)_3$ according to the following reactions:

$$ZrO_2 \cdot Y_2O_3 + P_2O_5\ (g) \rightarrow 2YPO_4 + ZrO_2$$
(tetragonal/cubic) (*monoclinic*)

$$8ZrO_2 + 4Na + O_2 + 6P_2O_5\ (g) \rightarrow 4NaZr_2(PO_4)_3$$

$$8ZrO_2 \cdot Y_2O_3 + 4Na + O_2 + 14P_2O_5\ (g) \rightarrow 4NaZr_2(PO_4)_3 + 16YPO_4$$

The thermodynamic properties of the reaction products, YPO_4 and $NaZr_2(PO_4)_3$, are not available in the literature to determine either the feasibility or the extent of the above reactions, and to estimate the minimum amounts of Na and P in the combustion gases required for the above reactions to proceed. Nonetheless, even though phosphorous is present in the fuel at a low level, it was evident from the x-ray diffraction and the electron microprobe analysis results that it greatly gets concentrated on the surface of the exposed specimens and forms compounds like YPO_4 and $NaZr_2(PO_4)_3$. Reaction between Y_2O_3 in the coating and P_2O_5 (g) to form YPO_4 decreases the Y_2O_3 concentration in the originally cubic/tetragonal $ZrO_2(Y_2O_3)$ solid solution and thereby results in the formation of monoclinic ZrO_2 in the oxide coating. This was evident in the x-ray diffraction analyses of the exposed specimens which showed varying amounts of the monoclinic phase.

The ZrO_2-Y_2O_3 system has been the subject of many investigations [3–6], but there is no general agreement between the proposed phase diagram. The lower Y_2O_3 limit for the cubic $ZrO_2(Y_2O_3)$ phase field, which is of particular interest in the present study, has been variously determined to be 10 mol percent $YO_{1.5}$ by Hund [7], 13 by Duwez, et al. [3], and Srivastava, et al. [5], 15 by Dixon, et al. [8], 16.5 by Schusterius and Padurow (9) and Strickler and Carlson [10] and <14.0 by Forestier, et al [11]. Scott [5] determined this lower limit of cubic solid solution more precisely and showed that it varies significantly with temperature between 1400 and 2000°C. He concluded from this temperature variation that cubic solid solutions in the lower Y_2O_3 range can be prepared at temperatures from above 2200 to 1700°C, which if cooled rapidly will be tetragonal at room temperature. The phase diagram of the ZrO_2-rich region proposed by Scott is reproduced in Fig. 7. It is clear from this diagram that the Y_2O_3 concentrations in the NASA- and the Linde-thermal barrier coatings[6] actually fall in the two-phase (monoclinic + cubic) field. The fact that the coatings consisted of tetragonal/cubic phases even at these lower Y_2O_3 concentrations indicates that the coatings were cooled rapidly from the high-temperature phase. Under these circumstances, appearance of the monoclinic phase in the coatings after extended isothermal exposure to combustion gases is not entirely unexpected. This may explain why the monoclinic phase appeared, although only in trace quantities, even in specimens exposed to clean fuel combustion gases. Furthermore, any reduction in Y_2O_3 concentration in the coating by chemical reactions can easily cause formation of the monoclinic phase. This explains the presence of greater amounts of monoclinic ZrO_2 phase in the coating after exposure to the combustion gases with increased contaminants. Monoclinic ZrO_2 phase undergoes phase transformation on heating and cooling with an associated disruptive volume change (~4 volume percent) leading to cracking and spalling. Formation of other secondary phases such as $NaZr_2(PO_4)_3$ also causes volumetric changes that lead to cracking and spalling.

Vanadium in the fuel also gets oxidized to V_2O_5 and enters the turbine in the gaseous form. The ZrO_2-V_2O_5 and Y_2O_3-V_2O_5 phase

[5] P_2O_5 sublimes at ~300°C.

[6] Linde Coating: 11.45 wt percent Y_2O_3 ≡ 13.2 mole percent $YO_{1.5}$. NASA Coating: 13.30 wt percent Y_2O_3 ≡ 15.44 mole percent $YO_{1.5}$.

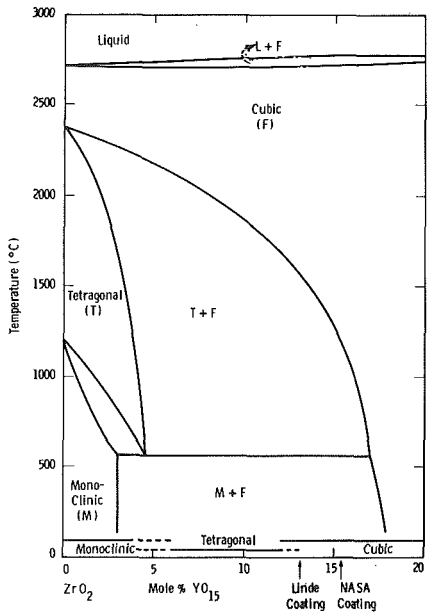

Fig. 7 Phase diagram for the zirconia-rich region of the ZrO_2-Y_2O_3 system, after Scott [5]

diagrams [12] indicate that this V_2O_5 could react with ZrO_2 in the coating to form ZrV_2O_7, and/or with Y_2O_3 to form Y_5VO_{10}, $Y_8V_2O_{17}$ or YVO_4. Contrary to expectations, no such vanadium compounds were detected in the oxide coating after exposure to combustion gases even with fuel containing as much as 10 ppm V, even though the electron microprobe analysis indicated that vanadium appreciably penetrated the oxide coating. Vanadium and phosphorous usually form isomorphic (structurally similar) compounds, e.g., YVO_4 and YPO_4; and it is possible that these two compounds formed a solid solution in the exposed oxide coating explaining the absence of YVO_4 lines in the x-ray diffraction patterns. Detailed x-ray diffraction work through use of premixed YVO_4-YPO_4 standards is required to conclusively identify such solid solutions in the coating after exposure to the combustion bases. Also V_2O_5 is known [13, 14] to form glasses with P_2O_5 and many other oxides such as Fe_2O_3, NiO, SiO_2, Na_2O, MgO, etc., which were all present on the surface of the $ZrO_2(Y_2O_3)$ coating after exposure to combustion gases. Thus, V_2O_5 could have easily formed such glasses in the pores of the oxide coating, making their detection by x-ray diffraction impossible. Furthermore, solidification of such glasses from the liquid state in the pores would result in volume shrinkage and the resultant strains could be responsible for crack initiation in the coating. In any case, it is apparent that vanadium in the fuel causes severe degradation of the oxide coating through cracking and progressive spalling.

The magnesium-based additives, commonly employed to inhibit the vanadium-corrosion of superalloys and MCrAlY coatings, were found to be ineffective in preventing degradation of the $ZrO_2(Y_2O_3)$ coating. It appears that elements like P and V are more reactive toward Y_2O_3 in the coating than with magnesium in the additives. Thus, other additives more reactive toward P and V than Y_2O_3 will have to be found if the ZrO_2·12 wt percent Y_2O_3 is to be used successfully as a thermal barrier coating in contaminated fuels.

It has also been found (15) that the plasma sprayed $ZrO_2(Y_2O_3)$ undergoes considerable densification (sintering) during heating to 1200°C. Such sintering of the oxide coating could also lead to spalling due to reduced thermal shock resistance. This indicates the need for careful preheat treatment of the oxide coating prior to use in order to minimize stresses arising from the volumetric changes due to sintering.

It should also be noted that there is a large difference between the thermal expansion coefficients of the $ZrO_2(Y_2O_3)$ oxide overcoat and the MCrAlY bond coat. The stresses resulting from this thermal expansion mismatch could spall off the oxide coating from the MCrAlY bond coat. In the present investigation there appeared to be no separation of the oxide at the $ZrO_2(Y_2O_3)$/MCrAlY interface; all the cracking and spalling occurred within the thickness of the oxide coating. Thus, under the thermal conditions employed in the present study, chemical reactions rather than thermal expansion mismatch seem to have caused the coating degradation. However, under severe thermal cycling conditions, the stresses caused by the thermal expansion mismatch must be carefully considered in evaluating the expected performance of duplex thermal barrier coatings under conditions encountered in stationary combustion turbines at different stages of operation.

Conclusions

1 The ZrO_2·12 wt percent Y_2O_3 coating performs satisfactorily in clean fuel and that containing 1 ppm Na, at least for 100–150 h.

2 Vanadium and/or phosphorous in the fuel are detrimental to the stability of the ZrO_2·12 wt percent Y_2O_3 thermal barrier composition.

3 The principal cause of failures of the ZrO_2·12 wt percent Y_2O_3 coating in the presence of vanadium is localized destabilization of the original tetragonal/cubic $ZrO_2(Y_2O_3)$ solid solution. The formation of other reaction products and localized sintering (densification) are also likely contributing factors.

4 Magnesium-based fuel additives are ineffective in inhibiting the corrosion of the oxide coating by phosphorous and for vanadium.

5 The duplex thermal barrier coating concept seems feasible for utility turbines in that the bond coat alloy protects the base alloy when alloy temperatures are limited to ≤900°C. Improved oxide coatings will need to be developed specifically for utility turbines burning dirty fuels.

Acknowledgments

This work was conducted as part of the Electric Power Research Institute Contract No. RP 421-1. The authors thank S. R. Levine, NASA-Lewis Research Center, for supplying the coatings, and acknowledge invaluable contributions of S. Y. Lee, C. J. Spengler, R. C. Kuznicki and R. W. Palmquist in the performance of this investigation. Technical assistance of T. A. Manion, J. J. Haugh, G. A. Blann and J. A. Fraino is also gratefully acknowledged.

References

1 Stecura, S., "Two-Layer Thermal Barrier Coating for High Temperature Components," *Am. Ceram. Soc. Bull.*, No. 12, 1977, pp. 1082–1089.

2 Tucker, Jr., R. C., Taylor T. A., and Weatherly, M. H., "Plasma Deposited MCrAlY Airfoil and Zirconia/MCrAlY Thermal Barrier Coatings," *Proc. Third Conference on Gas Turbine Materials in the Marine Environment*, University of Bath, England, Sept. 1976.

3 Duwez, P., Brown, Jr., F. H. and Odell, F., "Zirconia-Yttria-System," *J. Electrochem. Soc.*, Vol. 98, No. 9, 1951, pp. 356–62.

4 Srivastava, K. K., Patil, R. N., Choudhary, C. B., Gokhale K. V. G. K., and Subbarao, E. C., "Revised Phase Diagram of the System ZrO_2-$YO_{1.5}$," *Trans. J. Brit. Ceram. Soc.*, Vol. 73, No. 3, 1974, pp. 85–91.

5 Scott, H. G., "Phase Relationship in the Zirconia-Yttria System," *J. Mater. Sci.*, Vol. 10, No. 9, 1975, pp. 1527–1535.

6 Stubican, V. S., Hink, R. C., and Ray, S. P., "Phase Equilibria and Ordering in the System ZrO_2-Y_2O_3," *J. Amer. Ceram. Soc.*, Vol. 61, No. 1–2, 1978, pp. 17–21.

7 Hund, F., "Anomalous Solid Solutions in the System Zirconia-Yttria; Crystal Structure of Nernst Glowers," *Z. Electrochem.*, Vol. 55, 1951, pp. 363–366.

8 Dixon, J. M., LaGrange, L. D., Merten, U., Miller, C. F., and Porter, II, J. T, "Electrical Resistivity of Stabilized ZrO_2 at Elevated Temperatures," *J. Electrochem. Soc.*, Vol. 110, No. 4, 1963, pp. 276–280.

9 Schusterius, C., and Padurow, N. N., "Isomorphism in the System Indium Oxide-Yttria-Zirconia," *Ber. Dtsch. Keram: Ges.*, Vol. 30, 1953, pp. 235–239.

10 Strickler, D. W., and Carlson, W. G., "Ionic Conductivity of Cubic Solid Solutions in the System CaO-Y_2O_3-ZrO_2", *J. Amer. Ceram. Soc.*, Vol. 47, No. 3, 1964, pp. 122–127.

11 Forestier, M., Robert, G., Caillet, M., and Deportes, C., "Domain of Existence and Crystallographic Parameter of the Fluoritic Phase in the Zirconium Oxide-Cerium (IV) Oxide-Yttrium (III) Oxide System," *Mat. Res. Bull.*, Vol. 4, No. 10, 1969, pp. 727–740.

12 Levin, E. M., Robbins, C. R., and McMurdie, H. F., *Phase Diagrams for Ceramists*, Edited by M. K. Reser, American Ceramic Society, Columbus, Ohio, 1969.

13 Rawson, H., *Inorganic Glass Forming Systems*, Academic Press, New York, 1967.

14 Grechanik, L. A., Petrovykh, N. V., and Karpchenko, V. G., "Preparation and Properties of Glassy Oxide Semiconductors of the $VO_{2.5}$–$PO_{2.5}$-RO_x," *Soviet Phys. Solid St.*, Vol. 2, 1961, pp. 1908–1915.

15 Singhal, S. C., Bratton, R. J., and Valentich, J., to be published.

S. K. Chaturvedi
Assistant Professor,
Old Dominion University,
Norfolk, VA
Mem. ASME

R. W. Porter
Associate Professor of Mechanical Engineering,
Illinois Institute of Technology,
Chicago, IL 60616
Mem. ASME

Thermal Performance of Spray-Canal Cooling Systems

Spray canals are alternatives to cooling ponds and towers for steam-electric power plants. The literature of thermal modeling is reviewed. A rational analysis supported by field experiments at two large central power stations has led to correlation of local spray cooling performance in terms of two dimensionless groups, one of which is dependent mainly on the type of spray module, and the other is d heating-humidification interference-allowance parameter which depends on wind speed and direction and the type and placement of modules. The analysis is incorporated into a systems performance model for arbitrary canal layout. Examples presented are the circular, race-track and straight double-back canals. Implications for design are discussed.

Introduction

Atmospheric spray cooling systems are attractive because the direct-contact heat exchange of droplets requires less land area than cooling ponds, and they may be more environmentally acceptable and less costly than evaporative cooling towers [1]. Floating spray modules are employed in the presently discussed spray-canal configuration for steam-condenser applications [2].

In a typical spray-canal system, several hundred 50-Kw spray modules might be moored in four rows across a 60 m wide canal, several kilometers long, in order to provide closed-cycle cooling for generating capacity in the 1000-Mw(e) range (Fig. 1). In each pass of four modules proceeding along the canal, only several per cent of the total flow is sprayed and mixed with the remaining canal flow which results in its very gradual approach towards the ambient wet-bulb temperature. The modules usually are designed to spray about 40,000 liters/min, but various manufacturers distribute the spray quite differently. In one widely used module [2], there are four 12 m diam sprays, 5.5 m high, generated by using small cone-impact nozzles which results in a relatively fine spray. Another manufacturer [2] uses large single slot nozzles, resulting in a 16 m dia spray of 5 m height. Mean diameters of water globules are in the centimeter range which permits a relatively high flow rate to be achieved with low drift loss. The spray-canal geometry has evolved from the spray-pond design [3] for apparently two reasons. First, the use of individual floating spray modules in an open channel saves the expense of extensive manifolding. Second, a large pond may be subject to intense local heating and humidification in its interior which reduces its effectiveness.

The objective of the present work was to produce a practical technique for the analysis and design of spray-canal systems in terms of the theoretical or experimental performance of a single module by accounting for module placement, canal layout and meteorological conditions through simplified but rational fluid-dynamic and heat-transfer modeling.

Literature Survey. The cooling range of a spray or spray module may be predicted by integrating the governing heat, mass and momentum differential equations for an average droplet along the spray trajectory, usually by numerical analysis. Earlier work of Elgawhary and Rowe [4] utilized droplet correlations such as those of Ranz and Marshall [5]. Unfortunately, these correlations are limited in applicability in terms of steady velocity and relatively low Reynolds number. More recent work left the thermal parameters combined into a dimensionless group Number of Transfer Units (NTU) to be determined directly from observed performance. Kelley [6] and Porter and Chen [2] present numerical analyses using this approach to analyze both the local spray-module cooling and the subsequent overall canal performance by treating the mixing of spray and canal flows pass by pass. The local heating-humidification effect was incorporated by Porter and Chen [2] through a dimensionless interference-allowance parameter which was determined experimentally. Arndt and Barry [7] computed the interference effect theoretically by treating each spray as a point source of heat and humidity using results from air-pollution dispersion studies. Frediani and Smith [8] computed both the droplet parameters using the Ranz-Marshall correlations [5] and the interference effect by using an energy and moisture balance on

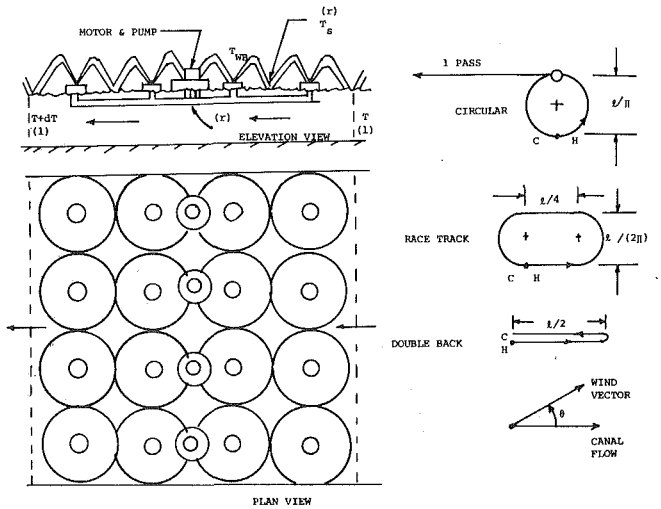

Fig. 1 Typical spray-canal layouts with 4-spray modules arranged in four rows

Contributed by the Utility Operations Committee for publication in the JOURNAL OF ENGINEERING FOR POWER. Manuscript received at ASME Headquarters August 13, 1979.

the air-vapor flow, assuming an unperturbed wind. Berger and Taylor [9] based the transport rates on the air-vapor outlet flow conditions which produces a conservative analysis for the nuclear ultimate-heat-sink spray-pond application.

While the above computer-oriented numerical analyses are useful for studying complex systems, they sometimes tend to obscure the underlying physics and make correlation of data and preliminary design both difficult and tedious. For this reason, a simplified analytical model was introduced [10] which considers the spray system as a continuum. The analytical and numerical predictions are virtually identical when applied to a large system using the same parameters. Soo [11] has used a similar analytical approach to suggest optimal drop size by defining the NTU parameter through a droplet heat transfer correlation. Chen and Trezek [12, 13] use the same basic approach for a spray pond but denote their principal dimensionless group as SER (Spray Energy Release). They consider the interference effect by analyzing the heating and humidification of air and vapor as it proceeds downwind through the spray field [14]. Porter, Yang and Yanik [15] have analyzed rigorously the assumptions in the simplified NTU analysis [10] by including various neglected effects such as solar and atmospheric radiation, non-unit psychrometric ratio, evaporative mass losses, etc., and conclude that the simpler case is adequate for practical applications. The basic NTU thermal model has now been used to design or analyze several existing spray canals at large central stations.

By measuring both local cooling ranges and local wet-bulb temperatures in field experiments at Commonwealth Edison Company's Dresden and Quad-Cities Nuclear Stations (Illinois), both the dropwise parameter (NTU) and the interference-allowance parameter were implied by using the simplified theory of Porter of reference [10], [16]. It was concluded that the dropwise parameter NTU is dominated by the high-speed drop trajectory and is essentially independent of prevailing wind conditions and module placement and depends only on the type of module. On the other hand, the local interference parameter was found both spatially variable, depending on module type and placement, and sensitive to prevailing conditions including wind speed and direction. Wilber [17] has also used the simplified analysis of Porter [10] to correlate performance data of Richards modules at Pacific Gas and Electric Company's Pittsburg (California) plant. The air-vapor dynamics were recently analyzed in detail by Chaturvedi and Porter [18] including coupled heat and mass transfer between the spray and the air-vapor mixture. It was found from a numerical analysis that the aerodynamic blockage of sprays, which tends to attenuate the wind and increase heating and humidification, nearly balances atmospheric turbulent diffusion, which relieves the effect. The net result, employed in the present paper, is a relatively simple expression for the interference-allowance parameter, based on unperturbed wind gaining heat and humidity and depending on the distance windward into the spray field, NTU, and other observable spray and meteorological parameters.

It is now possible to apply the thermal model to arbitrary spray-canal systems with the principal requirement that the spray-module NTU is known. It should be emphasized that this approach is "empirical" only in the sense that NTU is usually determined from experiments. In any case, the computed results will only be as good as the input data. Uncertainties due to the scatter in the NTU data (typically ±15 percent), the tolerance of various power-plant parameters such as lift-pump flow rates (typically ±10 percent), and the wide variation of prevailing meteorological conditions that can be encountered all suggest that a conservative deisgn is prudent. Further, site-specific effects such as abnormally high bank heights, irregular terrain, etc. may degrade performance [19].

Present Work. In the next section, Thermal Model, we first summarize the simplified heat-exchanger model [10] for both a spray module and a spray canal which is at the foundation of the present approach. This section also includes summaries of the technique for prediction of the interference-allowance parameter as well as the experimental data base of the current authors. In the section on System Performance, we analyze first an arbitrary canal configuration and then elements including straight, 45 and 90 deg turns from which many practical layouts may be segmented in series. Complete systems are also analyzed including circular, race-track and straight double-back canals. The full range of 0–360 deg of wind direction is considered in each case. Environmental effects are reported in another article [20].

Thermal Model

Module Performance. The equations of mass and energy transfer from a spray of flow rate $\dot{m}_s$, elemental interfacial area dA_s, specific enthalpy i_s, temperature T', mass-transfer coefficient K based on humidity potential ω, and sensible heat-transfer coefficient H are [15]

$$-d\dot{m}_s = K(\omega_S(T') - \omega_a)dA_s \tag{1}$$

$$-d(\dot{m}_s i_s) = [H(T' - T_a) + Ki_g(\omega_S(T') - \omega_a)]dA_s \tag{2}$$

where S denotes saturated air and vapor, g represents saturated vapor and "a" denotes local air-vapor conditions. In the "simplified" analysis the following additional assumptions are employed [15]: (1) ideal-caloric liquid water, (2) constant latent heat, and (3) unit psychrometric ratio ($H/(c_s K)$, where c_s is specific heat of air and vapor per unit mass of dry air). Thus, equations (1) and (2) combine to [1, 2, 6, 10–17]

$$-c_w\dot{m}_s dT' = K(h(T') - h_a)dA_s \tag{3}$$

where c_w is liquid water specific heat and h is total heat. Quantity $h \equiv i - wi_f = h(T_{wB})$ where i is specific enthalpy of air and vapor per unit mass of dry air, and f denotes saturated liquid water and WB wet-bulb.

Equation (3) may be conveniently integrated in closed form from

Nomenclature

A_s = spray-air interfacial area
$b = dh/dT_{WB}$
c_w = specific heat of liquid water
f = dimensionless interference allowance = $(T_{WB_a} - T_{WB_\infty})/(T - T_{WB_\infty})$
i = specific enthalpy (per mass of dry air for air and vapor)
H = sensible heat-transfer coefficient
h = total heat = $i_a - \omega_a i_f(T_{WB_a})$
k = attenuation factor
K = mass-transfer coefficient
ℓ = length of canal
m = number of modules across canal
$\dot{m}_s$ = spray mass flow rate
n = number of modules along canal
N = number of modules
NTU = number of transfer units = $\overline{K/\dot{m}_s}A_s$
r = ratio of module and canal flow rates
s = distance along canal
T = temperature (canal if unsubscripted)
$\overline{V}_s$ = wind speed averaged over z_s
x = normal distance across canal
z_s = spray height
w = normal width of canal spray region
η = system effectiveness = $(T_H - T_C)/(T_H - T_{WB_\infty})$
ρ_a = dry air density
$\sigma = k_c w$
θ = angle of wind vector to canal flow vector
ω = specific humidity

Subscripts

a = air
c = cross flow of wind
C = cold water
f = saturated-liquid water, film temperature for b evaluation
g = saturated-vapor water
s = spray
S = saturated
WB = wet-bulb
∞ = ambient atmosphere
w = downwind ($x = w$)

Superscripts

$''$ = per unit area
$\bar{}$ = average across canal
$\hat{}$ = average for system

an initial temperature T to a final spray temperature T_s by assuming $dh/dT_{WB} = b_f$ evaluated at a mean wet-bulb temperature T_f (Table 1). Thus

$$(T_s - T_{WB_a})/(T - T_{WB_a}) = \exp(-\text{NTU}\ b_f/c_w) \quad (4)$$

where NTU $\equiv \overline{K/\dot{m}_s} A_s$ is Number of Transfer Units (NTU) and T_{WB_a} is the average local wet-bulb temperature. Quantity NTU may be calculated in principle by integrating a correlation for the mass-transfer coefficient of droplets over the spray trajectory, or, as in the present work, NTU may be implied from field experiments wherein temperatures are measured. For application to individual modules, we suggest $T_f = (T + T_{WB_a})/2$ be used for property evaluation.

Interface Allowance. Thermodynamic considerations suggest T_{WB_∞} is bounded between the ambient wet-bulb temperature T_{Wb_∞} (limit for liquid-to-gas ratio $L/G = 0$) and the local canal temperature (limit for $L/G = \infty$). Thus

$$f \equiv (T_{WB_a} - T_{WB_\infty})/(T - T_{WB_\infty}) \quad (5)$$

represents a dimensionless interference allowance which is bounded between 0 and 1. Quantity f has been shown to be governed in general by a convective-diffusion equation [18]. However as noted before, numerical results [18] suggested it is reasonable to assume an unperturbed wind velocity through the frontal area of the sprays. Averaging over the spray height and spaces between sprays, the result of an energy balance on the air and vapor is

$$f(x) = 1 - \exp(-kx) \quad (6)$$

where x is the normal distance into the spray field, and the attenuation factor is

$$k(\theta) = k_c/|\sin\theta| \quad (7)$$

where θ is the local wind angle measured from the canal flow vector to the wind vector. Quantity k_c is the value for normal cross flow of the wind ($\theta = \pm 90$ deg)

$$k_c = [1 - \exp(-\text{NTU}\ b_f/c_w)]\dot{m}_s'' c_w/(b_f \rho_a \overline{V}_s z_s) \quad (8)$$

where $\dot{m}_s''$ is spray mass flow rate per unit collecting surface area averaged over the spray region, ρ_a is approach-flow dry air density, and $\overline{V}_s$ is wind speed averaged over the spray height z_s. One may approximate $\overline{V}_s$ as the wind speed at the arithmetic-average spray height. The above equations produce an interference allowance effectively averaged over the spray height, and over any spaces between sprays. The relationships are valid so long as there is an appreciable component of wind cross flow to the canal ($\theta \neq 0$). The case of wind blowing along the canal requires special treatment as discussed later.

Table 1 Derivative of total heat b_f/c_w

$\downarrow T_f$(C)	0	10	20	30	40
0	0.395	0.545	0.785	1.18	1.84
2	0.415	0.584	0.850	1.29	2.03
4	0.430	0.627	0.924	1.41	2.24
6	0.485	0.677	1.00	1.54	2.46
8	0.510	0.726	1.09	1.66	2.72

Canal Performance. Simple mixing considerations for canal flow mixing with spray flow (Fig. 1) yield for row i across the canal

$$dT_i/dn = -mr(T_i - T_{s_i}) \quad (9)$$

where n is the number of passes along the canal and m is the number of modules across the canal. Quantity r is the ratio of spray-module flow to canal flow. The evaporation per pass has been neglected, an approximation based on more exact integrations [15]. Using the thermal model of equation (4) and the interference allowance of equation (6), and averaging equation (9) across the canal in order to determine the average temperature T at a section

$$dT/dN = -r(1 - \bar{f})[1 - \exp(-\text{NTU}\ b_f/c_w)](T - T_{WB_\infty}) \quad (10)$$

where $N = \int m dn$ is the number of modules passed and

$$\bar{f}(\theta) = w^{-1}\int_0^w f dx = 1 - [1 - \exp(-k_c/|\sin\theta|)]\ |\sin\theta|/k_c \quad (11)$$

where w is the width of the spray field measured normal across the canal. Because $\bar{f}$ depends on the wind angle to the canal, which varies along the path N in general, equation (10) requires further consideration for curved canals. However, for a straight segment it can be integrated directly from the hot end at T_H to the cold end at T_C. Thus, for constant $\bar{f}$

$$(T_C - T_{WB_\infty})/(T_H - T_{WB_\infty}) = \exp[-rN(1 - \bar{f}) \times [1 - \exp(-\text{NTU}\ b_f/c_w)]] \quad (12)$$

This expression is particularly useful for assessing the performance of a straight segment of modules for NTU by observing temperatures T_H, T_C and T_{WB_∞}, although $\bar{f}$ must be predicted. For application to a canal system we suggest using $T_f = (T_H + T_{WB_\infty})/2$ as a mean value for evaluating b_f/c_w.

Field Experiments. The systems analyzed are described qualitatively in the Introduction. Additional detail is provided elsewhere [15, 16, 18] and a point-by-point listing of data is given in [16]. Nominal prevailing conditions are listed in Table 2. The buoyancy parameter of Table 2, Δ/ρ, corresponds to the fractional density increment of air and vapor due to heat and humidity in the limit of equilibrium with the liquid. Quantity z_B is bank height over water level.

In experiments $3b$, $5a-1$, $5a-2$ and $5b$ (Ceramic modules) and $4a$ and $4b$ (Richards modules), a psychromater assembly was mounted over module motors, 2m over the water level, at various positions proceeding down-wind across the Quad-Cities spray canal. The local and ambient wet-bulb temperatures and canal temperature T produce experimental local f values. Data are correlated in Fig. 2 with the product kx as suggested by equations (6). The experimental error of the present investigators is estimated to contribute less than ±15 percent, as bracketed in Fig. 2.

Quantity NTU for Ceramic modules was determined simultaneously in experiment $3a$ and $5b$ at Quad-Cities by collecting spray water at 4 90 deg separated but radially integrated positions in each spray and using the measured temperatures including local wet-bulb

Table 2 Nominal field experimental conditions

Symbol	Exp.	Station	Modules	Rows	WS (m/s)	WD* (0)	HWT (C)	WBT (C)	DBT (C)	$-\Delta\rho/\rho$	z_B (m)	r	$\bar{f}$
△	$1a$	Dresden	26 Ceramic	2	2.7	47	40	24	26	0.061	2.1	0.020	0.22
▷	$1b$	Dresden	26 Ceramic	2	3.2	80	40	25	31	0.048	2.1	0.020	0.13
▽	$1c$	Dresden	35 Ceramic	2	3.0	86	25	−3	2	0.088	2.4	0.030	0.16
◁	$1d$	Dresden	34 Ceramic	2	5.5	68	24	11	18	0.027	2.2	0.027	0.17
⊖	2	Dresden	Ceramic	2	4.6	10	34	14	22	0.065	2.4	—	0.21
○	$3a$	Quad-Cities	Ceramic	4	4.6	19	30	16	21	0.043	2.0	—	—
○	$3b$	Quad-Cities	Ceramic	4	2.0	52	32	15	23	0.035	2.0	—	—
□	$5a-1$	Quad-Cities	Ceramic	4	1.3	30	36	22	26	0.043	2.0	—	—
○	$5a-2$	Quad-Cities	Ceramic	4	1.8	61	39	18	22	0.041	2.0	—	—
◇	$5b$	Quad-Cities	Ceramic	4	2.4	81	26	14	18	0.038	2.0	—	—
●	$4a$	Quad-Cities	Richards	4	2.2	97	36	22	26	0.045	1.2	—	—
■	$4b$	Quad-Cities	Richards	4	2.1	118	39	19	22	0.078	2.7	—	—

* 90 deg is ⊥.

temperature in equation (4). There was no apparent significant dependency of NTU on row position. Similar data were also obtained at Dresden (experimental 2) and were reduced using computed interference allowances. Computed f were also used to reduce data of experiment 1a, 1b, 1c and 1d for Dresden wherein the performance of an entire canal segment was analyzed, and NTU were implied using equation (10). Experimental values for all experiments are correlated with wind speed in Fig. 3. The average of 38 Ceramic-module data points gives NTU = 0.149 with a standard deviation of about 15 percent which is also the estimated maximum experimental error. More limited analysis of Richards modules suggests NTU $\approx$ 0.06. We caution against simply comparing these NTU with each other because of the other widely varying parameters which ultimately govern cost-effective performance.

System Performance

In general, the values of r, NTU and $\bar{f}$ may vary along the canal. Because the cold water temperature of one run of modules is the hot water temperature of the next run, equation (12) may be replaced with

$$(T_C - T_{WB_\infty})/(T_H - T_{WB_\infty}) = \exp\left[\prod_{i=1}^{M} r_i N_i (1 - \bar{f}_i)[1 - \exp(-\mathrm{NTU}_i b_f/c_w)]\right] \quad (13)$$

for the case of M runs. One may approximate a curved canal with a sereis of straight segments. However, for uniform curvilinear canals, an integration can be performed. For simplicity we assume constant r and NTU and neglect any interference due to upwind elements of the canal, which is valid if the separation distance is greater than several hundred meters [20]. The case of close proximity of a return leg is treated later.

For a curvilinear canal or canal segment, variation of $\bar{f}(\theta)$ from equation (11) results in the integrated average and effective value of $\bar{f}$ along the canal being

$$\hat{f}_i = N_i^{-1} \int_0^{N_i} [1 - [1 - \exp(-k_c w/|\sin\theta|)]|\sin\theta|/(k_c w)]dN_i \quad (14)$$

which replaces $\bar{f}_i$ in the previous expressions. Equation (14) has been integrated numerically using a standard Runge-Kutta subroutine for a 45 deg turn and integer multiples of 90 deg turns, assuming uniform placement of modules along the turn ($dN/\Delta N = d\theta/\Delta\theta$). Results are plotted in Fig. 4. It is interesting to note that $\hat{f}_i$ is independent of wind angle for any integer product of 90 deg turns.

Another case of interest is wind in parallel ($\theta = 0$) or counter (θ = 180 deg) flow to a canal segment. An energy balance is applied as in the case of cooling towers and other heat exchangers. That is, the energy lost by the water is considered gained by the air and vapor. Assuming straight canal segments along a distance s [21]

$$dT/ds = -A(T - T_{WB}) \quad (15)$$

$$dT_{WB}/ds = \pm B(T - T_{WB}) \quad (16)$$

for parallel and counter flow, respectively, where

$$A = N' r[1 - \exp(-\mathrm{NTU}\ b_f/c_w)] \quad (17)$$

$$B = [\dot{m}_s'' c_w/(\rho_a \overline{V}_s z_s b_f)][1 - \exp(-\mathrm{NTU}\ b_f/c_w)] = k_c \quad (18)$$

where N' is the number of modules per unit length s. We neglect dispersion of heat and humidity both laterally in the horizontal plane and vertically, which tends to be conservative.

For the parallel-flow case we find the solution by integrating (15) and (16) simultaneously from $s = 0 (T = T_H, T_{WB} = T_{WB_\infty})$ to $s = \ell$ $(T = T_C, N = N'\ell)$. The resulting "effectiveness" is

$$\eta \equiv (T_H - T_c)/(T_H - T_{WB_\infty}) = [1 - \exp[-(A + B)]]A/(A + B) \quad (19)$$

while for counter flow [21]

$$\eta = 1/[(A - B)/[A(\exp(A - B) - 1)] + 1] \quad (20)$$

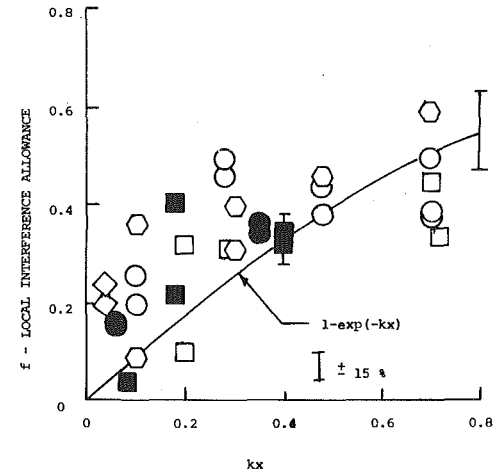

Fig. 2 Local interference allowance

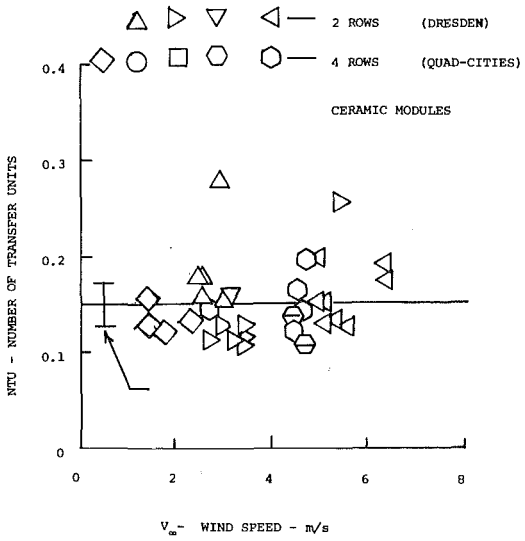

Fig. 3 Correlation of NTU with ambient wind speed at 2 m height

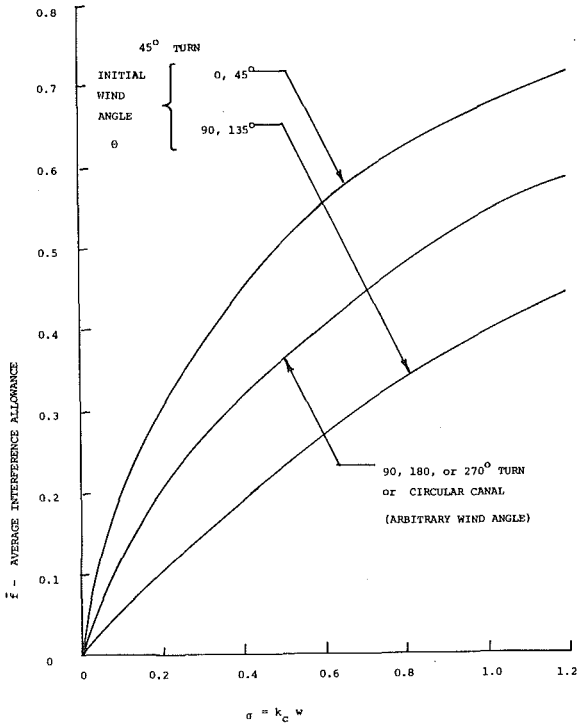

Fig. 4 Effective average interference allowance for uniform circular turns

It is now possible to analyze canals made up of a series of elements of straight-line segments ($\bar{f}$ constant) and uniform turns ($\bar{f}$ given in Fig. 4). For example, the resulting system effectiveness $(T_H - T_C)/(T_H - T_{WB_\infty})$ is illustrated in Fig. 5 for a uniform circular canal and a particular uniform "race-track" configuration, with parameters as shown. The parameters assumed are hypotehtical but typical and correspond to moderately low-wind speeds of about 2 m/s. Additional data for existing-system parameters are given in [18]. It should be noted that buoyancy may become important at lower wind speeds. It is interesting to note that the circular canal is independent of wind direction due to its symmetry. The race-track shape might be used due to land constraints, or to take advantage of prevailing winds. However, even if one can predict the prevailing wind direction, the example race-track geometry can increase effectiveness by only up to about 10 percent for the case shown. Conversely, the most adverse wind direction for the race-track shape produces an effectiveness about 40 percent below the circular case. This occurs when the wind blows along the straight segments.

The case of a double-back canal with counter-flowing elements in close proximity is also of possible interest in practice where land area is extremely limited. In this circumstance, the upwind leg interferes with the downwind one by producing an elevated f in the incident wind of the latter. The situation is identical to that of a heat exchanger with two passes of one fluid (the canal). The second fluid (air and vapor) may be at an arbitrary angle including the cases of wind blowing along the system, the most adverse case. The system is analyzed by taking the cold water temperature of the upstream canal leg as the hot water temperature of the downstream leg, the respective leg interference factors f being independent to the present approximation. The above results for parallel and counter flow are used to construct the net system effectiveness. The case of a nonzero component of cross-flow wind is analyzed by computing the factor f downwind of the upwind leg of the canal. Denoting the width of the canal w, equation (6) yields the required quantity $f_w \equiv f(w)$. For the case of the hot leg upwind, the result for the system effectiveness is [21]

$$\eta = (1 - f_w/2)[1 - exp\ (-A'\ell)] \tag{21}$$

where $A' = A\ (1 - \bar{f})$ with $\bar{f}$ averaged across a single leg, and ℓ is the total length of the canal. Similarly, for the case of the hot leg being downwind [21]

$$\eta = (1 - f_w/2)[1 - \exp\ (-A'\ell)]/[1 - (f_w/2)(1 - \exp\ (-\mathrm{A}'\ell))] \tag{22}$$

The several complete configurations are compared in Fig. 5. It is apparent that the two-pass double-back system with a return leg in close proximity is subject to severe loss of cooling effectiveness in the worst cases of wind along the canal. The double-back canal is inferior to the circular one except for a 30 deg range of near cross flow from the cold side. Interference is greater with wind blowing from the hot side because of the corresponding greater temperature difference between the water and wet-bulb temperatures.

Summary and Conclusions

The simplified thermal model can be conveniently applied to an individual spray module. Assuming that the local average wet-bulb temperature is known, dimensionless cooling depends only on a dimensionless group NTU. Quantity NTU may be predicted using droplet theory or implied from field experiments. The dimensionless cooling of a system of modules depends on both NTU and the interference effect of the collection of modules on each other depending on their placement, spray parameters and wind conditions. The dimensionless interference allowance is a convenient representation.

In the present paper, the interference effect was determined by assuming an unperturbed wind blowing through the spray field. Downwind spray modules in proximity were then subject to an increased local wet-bulb temperature depending on the heat and humidity released.

Performance was analyzed for several canal segments including straight runs and 45 and 90 deg turns. From these results, circular, race-track and two-pass double-back canals were compared for typical parameters of a hypothetical large 400 module system. The circular canal seems to offer the best compromise in terms of wind direction and is independent of it. Only a 10 percent improvement was determined for the race-track case in the most favorable winds, with a 40 percent degraded performance in the most adverse case. The two-pass canal with a return leg in close proximity appears very unfavorable when the wind blows along the canal. The 2-pass cross-flow case appears inferior to the circular canal as well except in a narrow range of wind directions from the cold side.

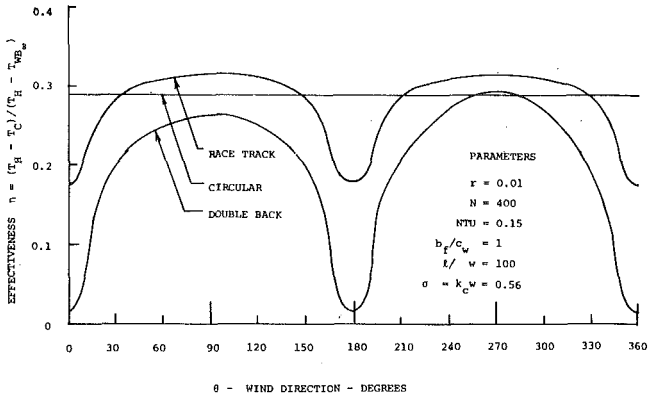

Fig. 5 System effectiveness for several configurations (Fig. 1)

In conclusion, the designer may wish to reduce the uncertainty of performance with very little penalty by utilizing a circular or near-circular spray canal. Where siting prohibits this approach due to space limitations, alternate layouts may be analyzed and compared for various anticipated wind directions. It is also possible to vary the density of placement of the sprays ($\dot{m}_s''$) and width of the canal (w) in order to reduce interference at the expense of surface area.

Acknowledgments

This work was supported by the U. S. Department of Energy under contract ERDA EC-77-S-02-4531. The cooperation of Commonwealth Edison Company and the comments and suggestions of our project technical committee including representatives of the equipment manufacturers are also gratefully acknowledged.

References

1 Hoffman, D. P., "Spray Cooling for Power Plants," *Proceedings of the American Power Conference*, Vol. 35, 1973, p. 702.

2 Porter, R. W. and Chen, K., "Heat and Mass Transfer of Spray Canals," ASME *Journal of Heat Transfer*, Vol. 96, No. 3, 1974, pp. 286–291.

3 Schrock, V. E., Trezek, G. J. and Keilman, L. R., "Performance of a Spray Pond for Nuclear Power Plant Ultimate Heat Sink," ASME JOURNAL OF ENGINEERING FOR POWER, Vol. 98, No. 4, 1977, pp. 650–656.

4 Elgawhary, A. M. and Rowe, A. M., "Spray Pond Mathematical Model for Cooling Fresh Water and Brine," *Environmental and Geophysical Heat Transfer*, ASME HT, Vol. 4, 1971.

5 Ranz, W. E. and Marshall, W. R. Jr., "Evaporation from Drops," *Chemical Engineering Progress*, Vol. 48, 1952, pp. 141–146 and 173–180.

6 Kelley, R., "Large Scale Water Cooling Via Floating Spray Devices," *Energy Production and Thermal Effects*, Ann Arbor Science Publishers, Jan. 1974, p. 92.

7 Arndt, C. R. and Barry, R. E., "Simulation of Spray Canal Cooling for Power Plants-Performance and Environmental Effects," ASME Paper No. 76-WA/HT-28, Dec. 1976.

8 Frediani, H. A., Jr. and Smith, N., "Mathematical Model for Spray Cooling Systems," ASME JOURNAL OF ENGINEERING FOR POWER, Vol. 98, No. 2, 1977, pp. 279–283.

9 Berger, M. H. and Taylor, R. E., "An Atmospheric Spray Cooling Model," *Environmental Effects of Atmospheric Heat/Moisture Releases*, ASME, May 1978, pp. 59–64.

10 Porter, R. W., "Analytical Solution for Spray Canal Heat and Mass Transfer," Joint ASME Paper No. 74-HT-58, AIAA Paper No. 74-764, July 1974.

11 Soo, S. L., "Power Spray Cooling-Unit and System Performance," ASME Paper No. 75-WA/Pwr-8, Nov. 1975.

12 Chen, K. H. and Trezek, G. J., "Thermal Performance Models and Drift Loss Predictions for a Spray Cooling System," ASME *Journal of Heat Transfer*, Vol. 99, No. 2, 1977.

13 Chen, K. H. and Trezek, G. J., "The Effect of Heat Transfer Coefficient, Local Wet Bulb Temperature and Drop Size Distribution Function on the Thermal Performance of Sprays," ASME *Journal of Heat Transfer*, Vol. 99, No. 3, 1977.

14 Chen, K. H. and Trezek, G. J., "Spray Energy Release (SER) Approach to Analyzing Spray System Performance," *Proceedings of the American Power Conference*, Vol. 38, 1976, p. 1435.

15 Porter, R. W., Yang, U. M. and Yanik, A., "Thermal Performance of Spray Cooling Systems," *Proceedings of the American Power Conference*, Vol. 38, 1976, p. 1458.

16 Porter, R. W. and Chaturvedi, S. K., "Atmospheric Spray-Canal Cooling Systems for Large Electric Power Plants," *Proceedings of the Waste Heat Management and Utilization Conference*, Vol. 2, University of Miami, Coral Gables, May 1977, p. IV-C-121.

17 Wilber, K. R., "Examination of the Sensitivity of Spray Cooling to Wind Speed and Direction," presented at Cooling Tower Institute Annual Meeting, Jan. 1978.

18 Chaturvedi, S. and Porter, R. W., "Air-Vapor Dynamics in Large-Scale Atmospheric Spray Cooling Systems," ASME *Journal of Fluids Engineering*, Vol. 100, No. 1, March 1978, pp. 65–72.

19 Wang, W. and Porter, R. W., "Bank Aerodynamics of Atmospheric Spray Cooling Systems," ITT Waste Energy Management Technical Report TR-77-3, IIT, Chicago, Dec. 1977.

20 Chaturvedi, S. and Porter, R. W., "Environmental Effects of Heat and Moisture Release from Atmospheric Spray Cooling Systems," *Environmental Effects of Atmospheric Heat/Moisture Releases*, ASME, May 1978 pp. 65–74.

21 Chaturvedi, S. and Porter, R. W., "Systems Performance Relations for Spray Canals," IIT Waste Energy Management Technical Memoradum TM-79-1, IIT, Chicago, June 1979.

S. S. Rao
Professor,
Department of Mechanical Engineering,
Indian Institute of Technology,
Kanpur-208016, India

R. S. Gupta
Assistant Professor,
Department of Mechanical Engineering,
Punjab Engineering College,
Chandigarh-160012, India

Optimum Design of Axial Flow Gas Turbine Stage

Part I: Formulation and Analysis of Optimization Problem

The problem of stage design of axial flow gas turbines has been formulated as a nonlinear mathematical programming problem with the objective of minimizing aerodynamic losses and mass of the stage. The aerodynamic as well as mechanical constraints are considered in the problem formulation. A method of evaluating the objective function and constraints of the problem is presented in Part I of this paper. The optimization problem is solved by using the interior penalty function method in which the Davidon-Fletcher-Powell variable metric unconstrained minimization technique with cubic interpolation method of one-dimensional minimization is employed. Problems involving the optimization of efficiency and/or mass of the stage have been solved numerically in Part II of the paper. The results of a sensitivity analysis conducted about the optimum point have also been reported.

Introduction

Besides conventional power generating units, gas turbines are being used successfully in space, aviation, marine, nuclear, rail-road, vehicular, cryogenic and petro-chemical applications. The analytical procedures used in designing such turbomachines have now undergone a major revision. The empirical relations used in the design process are being replaced by more sophisticated methods of analysis. These methods provide detailed information regarding static and dynamic loads as well as machine response in the form of stresses and deflections. In recent years turbines of considerable size and capacity have been produced with many stages. Along with the demand for larger gas turbines, factors like efficiency and component weight have become major design considerations.

The conventional aerodynamic design of gas turbines has been discussed by Emmert [1], Horlock [2] and Cohen, et al. [3]. The three-dimensional modifications in gas turbine design have been discussed by Wu and Wolfenstein [4], Hawthorne and Ringrose [5], Carter, et al. [6] and Davis and Millar [7]. A good collection of papers on the design of gas turbines has been edited in [8 to 11].

Very little work has been reported on the application of optimization techniques in the design of turbomachines. George [12] reported about the optimization of a rocket engine turbine using a differential calculus approach. Balje [13] applied optimization techniques in the design of axial turbines using Wood's method of pattern search. He maximized the efficiency by selecting six design variables and considering only the aerodynamic aspects of design according to a two dimensional approach. Swift [14] published a flow chart for optimizing pump-turbine designs using computers. Kar and Reddy [15] found the optimum shape of the impeller of a pump using a differential calculus approach. Gupta [16] optimized the radial impeller of a pump by using the graphical procedures. Saravanamuttoo and MacIsaac [17] published about the use of hybrid computer simulations of single-spool turbojet engines for optimizing thrust response. Yadav and Gupta [18] optimized the losses of a centrigugal compressor. Blaho

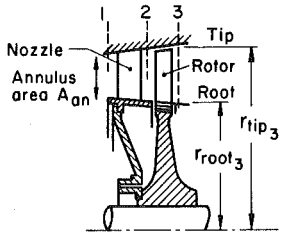

Fig. 1 (*a*) Turbine stage

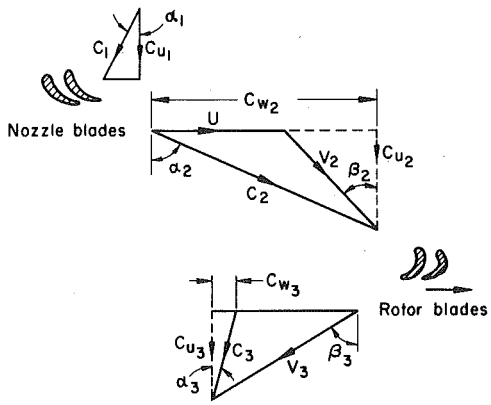

Fig. 1 (*b*) Velocity triangle

Fig. 1 Axial flow turbine stage

Contributed by the Aircraft Committee for publication in the JOURNAL OF ENGINEERING FOR POWER. Manuscript received at ASME Headquarters August 20, 1979.

[19] discussed the optimum design of axial flow fans from the view point of losses using experimental curves. Paranjpe and Murthy [20] discussed the optimization and standardization of steam turbine blade profiles.

In the present work an attempt has been made to optimize the efficiency and/or the weight of an axial flow gas turbine stage by considering deflection, stress and vibration aspects along with the aerodynamic requirements.

Formulation of the Optimum Design Problem

Any optimization problem involves the identification of design variables, objective function and constraints of the problem.

Design Variables. These are preselected variables which can take independent values in the design process. The other data of the problem is either given at the beginning of the design process or can be expressed in terms of the design variables. For the design of a gas turbine stage, the following parameters are taken as the design variables: X_1 = mean diameter of the rotor (d); X_2 = ratio of the chord of rotor blade to mean diameter, (c_R/d); X_3 = ratio of the chord of nozzle blade to mean diameter, (c_N/d); X_4 = ratio of spacing to diameter at mean radius of the nozzle blades (s_N/d); X_5 = ratio of spacing to diameter at mean radius of the rotor blades (s_R/d); X_6 = relative angle of the velocity triangle at the inlet of the rotor blade at mean radius (β_2); X_7 = relative angle of the velocity triangle at the exit of the rotor blade at mean radius (β_3); X_8 = axial velocity of flow across the stage (C_a). Thus the vector of design variables $\vec{X}$ becomes

$$\vec{X} = \begin{Bmatrix} X_1 \\ X_2 \\ X_3 \\ X_4 \\ X_5 \\ X_6 \\ X_7 \\ X_8 \end{Bmatrix} \equiv \begin{Bmatrix} d \\ c_R/d \\ c_N/d \\ s_N/d \\ s_R/d \\ \beta_2 \\ \beta_3 \\ C_a \end{Bmatrix} \quad (1)$$

In the design vector $\vec{X}$, X_1 to X_7 are physical variables and X_8, namely, the axial velocity is related to the physical variables as

$$C_a = \frac{\pi d N}{\tan \alpha_2 - \tan \beta_2} \quad (2)$$

Objective Function. A design problem usually has several solutions which may satisfy the specified functional requirements adequately. The objective function in a general optimization problem represents a basis for the choice between alternate acceptable designs. In most of the practical design problems the minimization of weight, cost, volume or losses, or maximization of profit, rigidity or efficiency is taken as the objective. In the case of gas turbines used in aerospace applications the minimization of weight is one of the most important criteria while in the case of gas turbines used in stationary power

Nomenclature

A_1, A_2, A_3 = area of flow at stations 1, 2, 3
A_N, A_R = area of nozzle and rotor blade section
A_{root} = area of cross section of blade at root
b_{eq} = equivalent breadth of rectantular section
B = constant for clearance space
c_N, c_R = chord of the nozzle and rotor blade
c_p = specific heat at constant pressure
C_1, C_2, C_3 = absolute velocity at stations 1, 2 and 3
C_a = axial velocity
C_L = lift coefficient
C_{w2}, C_{w3} = whirl component of velocity
d = mean diameter of the turbine
$f(\vec{X})$ = function of vector $\vec{X}$ and objective function
$g_j(\vec{X})$ = jth constraint
h_1, h_2, h_3 = blade height at stations 1, 2 and 3
h_N, h_R = height of nozzle and rotor blades
$[H_i]$ = a positive definite symmetric matrix
I_{xx}, I_{yy}, I_{xy} = moment of inertia about xx, yy and xy axes
$I_{\overline{xx}}, I_{\overline{yy}}, I_{\overline{xy}}$ = moment of inertia about $\overline{xx}$, $\overline{yy}$ and $\overline{xy}$ axes
K_1, K_2 = weightage to the losses and mass in mixed objective function
m = mass rate of flow of gases
M_{C_2}, M_{C_3} = Mach number corresponding to C_2 and C_3
$\overline{k}$ = clearance
n_N, n_R = number of nozzle and rotor blades
N = revolutions per second
p_{01}, p_{02}, p_{03} = stagnation pressure at stations 1, 2 and 3
p_1, p_2, p_3 = static pressure at stations 1, 2 and 3
$p_{02\text{rel}}, p_{03\text{rel}}$ = stagnation pressure for relative velocities
p_c = critical pressure
r_k = response factor for sequential minimization
$r_{\text{root}}, r_{\text{tip}}$ = radius of root and tip
R, R_{root} = degree of reaction at mean radius and root
$\overline{R}$ = gas constant
$(\text{R}_\text{e})_N, (\text{R}_\text{e})_R$ = Reynolds number for nozzle and rotor
s_N, s_R = spacing of nozzle and rotor blades
S = entropy
$\vec{S}_i$ = ith direction vector
t_e = trailing edge thickness
t_{eq} = equivalent thickness
T = temperature
T_{01}, T_{02}, T_{03} = stagnation temperature at stations 1, 2 and 3
T_1, T_2, T_3 = temperature at stations 1, 2 and 3
T_2', T_3', T_3'' = temperatures as shown in T-S diagram
U = peripheral velocity
V_2, V_3 = relative velocity at stations 2 and 3
x, y, z = coordinate axes
x_1, x_2, x_m = value of x at 1, 2 and point m
$\overline{x}, \overline{y}$ = coordinates of centroid of airfoil
x', y' = axes inclined from x, y
x_c, y_c = camber line coordinates
$\vec{X}$ = n-dimensional design vector
$\vec{X}_i$ = ith vector of design variables
$\vec{X}_0$ = starting design vector
$y(x)$ = a dependent variable of x
Y, Y_N, Y_R = loss coefficients defined from pressure drop
Y_k, Y_p, Y_s = clearance, profile and secondary loss coefficients
α = depth taper ratio = (depth at root/depth at tip)
$\alpha_1, \alpha_2, \alpha_3$ = angles of absolute velocity at 1, 2 and 3
α_c = included angle of divergence of walls of annulus
α_m = mean angle
α_s = stagger angle
β = breadth taper ratio = (breadth at root/breadth at tip)
β_2, β_3 = rotor blade angle at inlet and outlet
β_m = mean blade angle
γ = ratio of specific heats
Δ_t = tip clearance of the rotor blades
ΔT_{0s} = stagnation temperature drop
ϵ = small quantity
η_s = stage efficiency
Θ = twist of equivalent rectangular section
$\lambda, \lambda_N, \lambda_R$ = blade loss coefficient defined from temperature drop
$\lambda_{cN}, \lambda_{cR}$ = parameters for nozzle and rotor
$\overline{\mu}$ = viscosity of gases
ρ_1, ρ_2, ρ_3 = gas density at stations 1, 2 and 3
ρ_m = centrifugal tensile strength
$\sigma_{\max}$ = maximum stress at root
τ^* = the minimizing step length in the direction $\vec{S}_i$
ϕ = flow coefficient
$\phi(\vec{X}, r_k)$ = penalty function
ψ = stage temperature drop coefficient
$\omega^{(1)}$ = natural frequency of vibration (cycles/s)
σ_{cr} = centrifugal tensile strength

Subscripts

1, 2, 3 = station number
N = nozzle
r = radius r
root = value at root of blade
R = rotor
tip = value at the tip of the blade

Superscripts

u = upper limit of variables
ℓ = lower limit of variables

plants, the maximization of efficiency represents a more useful criterion. In some cases a mixed objective function representing a linear combination of weight and efficiency will be a more appropriate objective. In this work the mixed objective function is used so that the optimum design of aerospace turbines or industrial turbines can be found using the same computer program by giving suitable weightages to the weight and efficiency in the objective function.

Evaluation of Objection Function

Fig. 1 shows a typical axial flow gas turbine stage with its associated velocity triangles. The temperature-entropy diagram for the stage is indicated in Fig. 2. The enlarged view of the flared turbine annulus with the nozzle and rotor blades is shown in Fig. 3. As the objective function comprises two distinct quantities, namely, losses and mass of the stage, each one will be considered separately.

1 Evaluation of Losses of the Stage. In the design of an axial flow gas turbine stage it is assumed that the stagnation pressure at inlet to the stage (p_{01}), stagnation temperature at inlet to the stage (T_{01}), mass flow rate across the stage (m), and the speed of the rotor (N) are preassigned parameters. Further it is assumed that the properties of air like specific heat at constant pressure (c_p), gas constant ($\bar{R}$), viscosity of gas ($\bar{\mu}$) and the ratio of specific heats (γ) are known or can be calculated from suitable formulae. The values of design variables are assumed to be known at the beginning of the analysis and will be modified during the design-analysis iterative process.

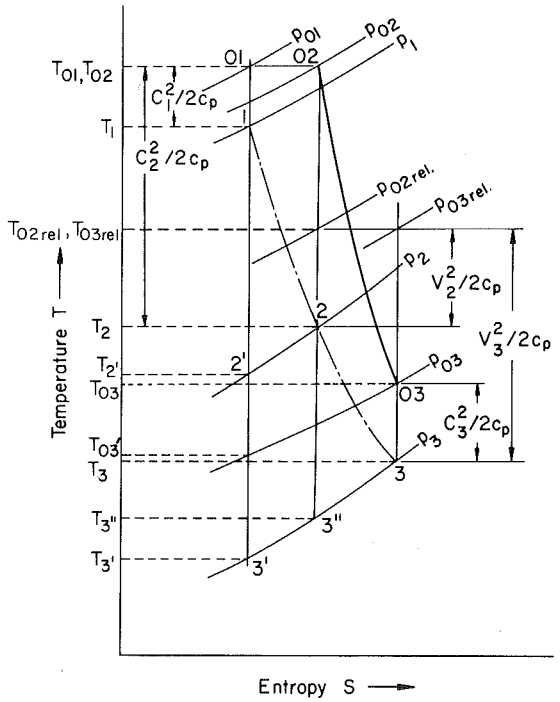

Fig. 2 Temperature-entropy diagram for a reaction stage

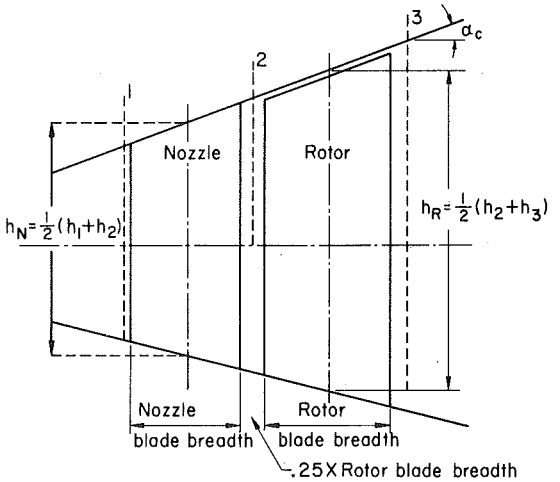

Fig. 3 Flared turbine annulus

2 Evaluation of Mass of the Stage. The mass of the stage is assumed to be the sum of rotor blade, stator blade and rotor disc masses.

The necessary equations for evaluating the isentropic stage efficiency are stated sequentially in this section. This involves assuming a trial value of efficiency η_s to calculate a more accurate value η_{si}. Thus the process is iterative and has to be continued until the values of stage efficiency in two consecutive iterations are sufficiently close to each other. The free vortex assumption is employed for three dimensional design consideration and for calculating the degree of reaction at the root. The computation of profile losses is made with the help of Fig. 4 due to Ainley and Mathieson [21]. In calculating the efficiency, the profile loss, leakage loss and secondary flow losses are accounted for as stated by Ainley and Mathieson [21] with the suggested modification of Dunham and Came [22]. The losses in the stage are taken as one minus the stage efficiency. The Reynolds number correction has also been made with the help of equation (A 68) of Appendix A. The computation of stage efficiency is represented as a flow chart in Fig. 5, using the aerodynamic relationships presented in Appendix A.

The nature of convergence of the iterative procedure for computing the isentropic efficiency was studied by using different trial values of efficiency in the range 0.60 to 1.05, and convergence criteria [24]. It has been found that the efficiency converged essentially to the same value with all trial values of efficiencies; however, lesser number of iterations were required when the trial efficiency was taken as 0.9. In all the cases, the convergence has been achieved in less than four iterations [24].

Specification of profile and geometrical properties of blades:

In order to avoid storing of a large number of airfoil sections for different combinations of inlet and outlet angles in the computer, it is proposed to obtain the profile of the mean line by satisfying certain desired conditions and then superimposing the thickness distribution of a standard airfoil. In Fig. 6, line 1-2 and curve 1-m-2 represent the chord and camber lines of the blade respectively. The maximum camber with respect to chord occurs at the point m. The angle between the chord line (x-axis) and the axial direction (X-axis) is given by the stagger angle α_s. It is assumed that the location of the point m depends on the type of blading (reaction or impulse) and hence the coordinates of m (x_m and y_m) are known. Thus the following conditions are to be satisfied by the camber line of Fig. 6:

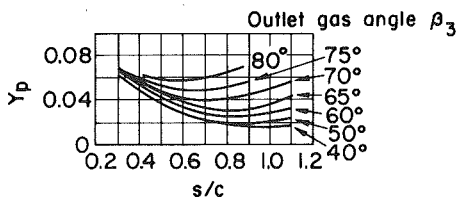

Fig. 4 (*a*) Profile loss coefficient for nozzle blades, $\beta_2 = 0 (t/c = 0.2)$

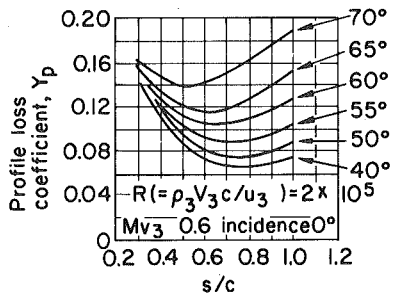

Fig. 4 (*b*) Profile loss coefficient for impulse blades, $\beta_2 = \beta_3 (t/c = 0.20)$

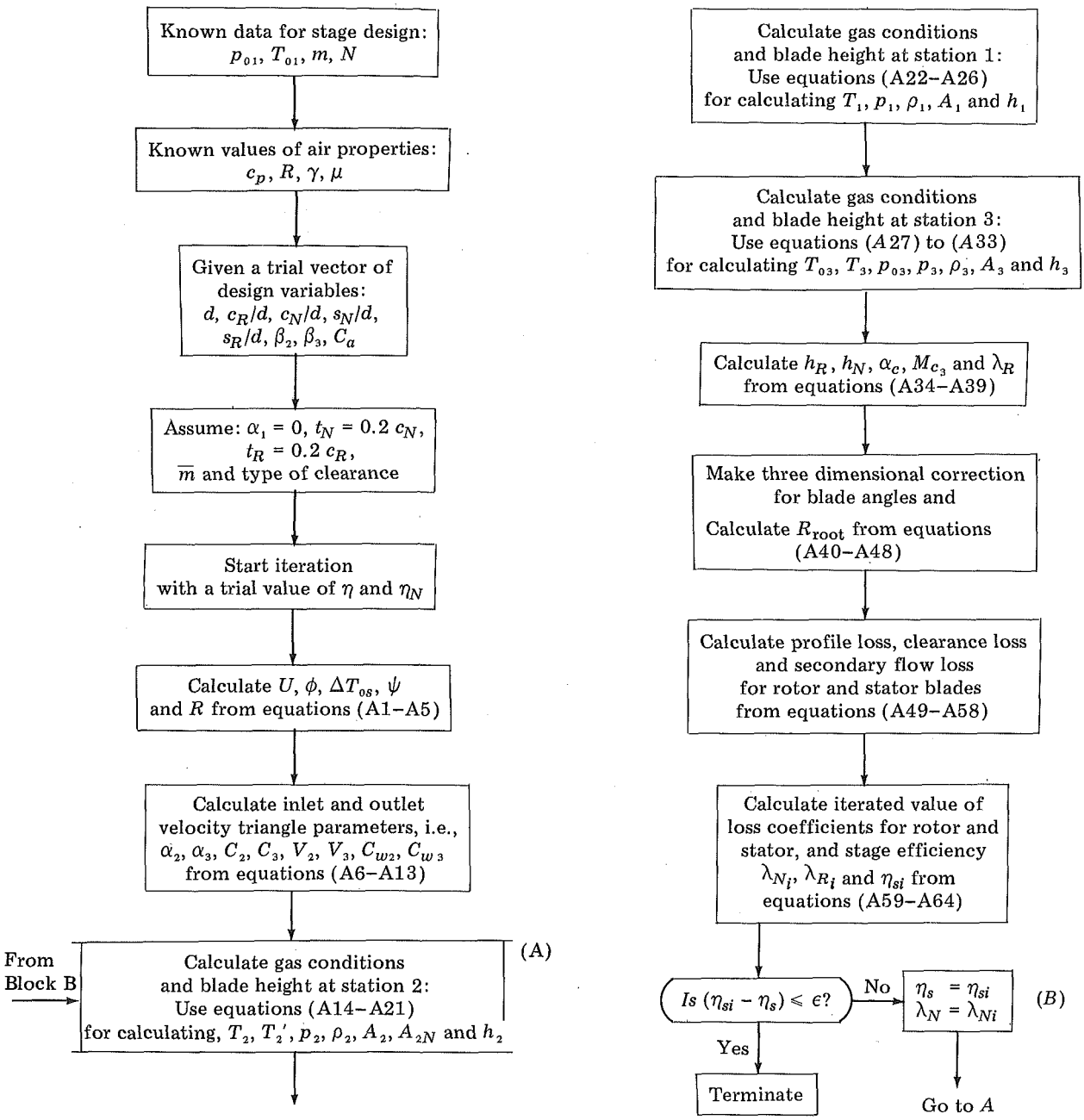

Fig. 5 Flow chart for the calculation of efficiency

$$\text{At } x = x_1 = x^{(\ell)}, \quad y = y_1 \text{ and } \frac{dy}{dx} = \tan \alpha_1$$

$$x = x_2 = x^{(u)}, \quad y = y_2 \text{ and } \frac{dy}{dx} = -\tan \alpha_2 \qquad (3)$$

$$x = x_m, \quad y = y_m \text{ and } \frac{dy}{dx} = 0$$

Thus there are six conditions to be met by the camber line and hence a polynomial of degree five can be fitted exactly. Once the equation of the mean line is obtained, the thickness distribution of a standard profile (A_3K_7 in this case) can be superimposed. The upper and lower boundaries of the airfoil section are expressed as $y^{(u)}(x)$ and $y^{(\ell)}(x)$ by using a curve fitting technique. The geometrical properties of the airfoil section are thus given by:

area of cross-section = A

$$= \int_{x^{(\ell)}}^{x^{(u)}} \int_{y^{(\ell)}(x)}^{y^{(u)}(x)} dx\,dy$$

$$= \int_{x^{(\ell)}}^{x^{(u)}} \{y^{(u)}(x) - y^{(\ell)}(x)\}dx \qquad (4)$$

x-coordinate of the centroid

$$= \overline{x} = \frac{1}{A} \int_{x^{(\ell)}}^{x^{(u)}} x\{y^{(u)}(x) - y^{(\ell)}(x)\}dx \qquad (5)$$

y-coordinate of the centroid

$$= \overline{y} = \frac{1}{2A} \int_{x^{(\ell)}}^{x^{(u)}} \{y^{(u)2}(x) - y^{(\ell)2}(x)\}dx \qquad (6)$$

moment of inertia about x-axis = I_{xx}

$$= \frac{1}{3} \int_{x^{(\ell)}}^{x^{(u)}} \{y^{(u)3}(x) - y^{(\ell)3}(x)\}dx \qquad (7)$$

moment of inertia about y-axis = I_{yy}

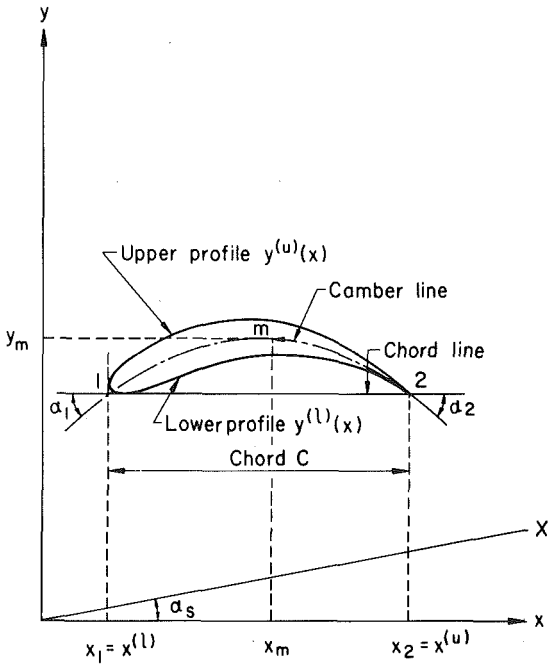

Fig. 6 Camber line and profile shape of a blade section

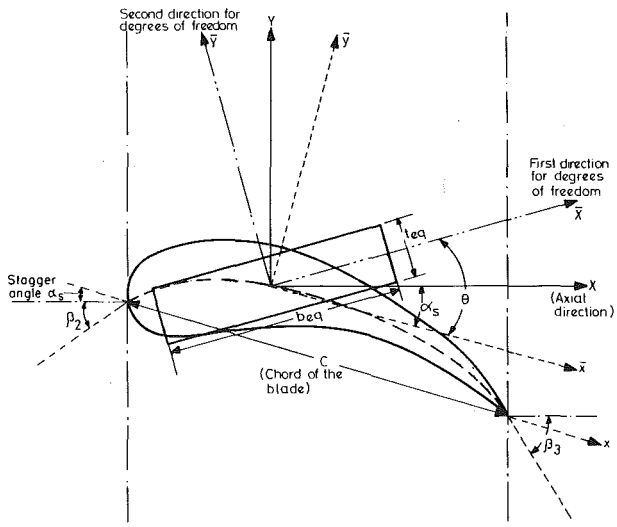

Fig. 7 Equivalent rectangular section of an airfoil

$$= \int_{x^{(\ell)}}^{x^{(u)}} x^2\{y^{(u)}(x) - y^{(\ell)}(x)\}dx \quad (8)$$

product of inertia = I_{xy}

$$= \tfrac{1}{2} \int_{x^{(\ell)}}^{x^{(u)}} x\{y^{(u)2}(x) - y^{(\ell)2}(x)\}dx \quad (9)$$

The areas of cross-section of the rotor and nozzle blades can be computed with the help of equation (4). If the density of the blade material is known, the mass of the rotor and stator blades can be computed.The rotor disk is assumed to have a constant thickness equal to the chord length at the root of the rotor blade. The material of blades and rotor disk is assumed to be the same.

Design Constraints. In a gas turbine design generally the following requirements are to be met from aerodynamic, vibrational and strength considerations:

1 The rotational velocity of the rotor should be within some upper and lower bounds.

2 The aspect ratio (height/chord) of rotor and nozzle blades should be within some specified upper and lower bounds.

3 The pitch-chord ratio of the rotor and nozzle blades should lie within certain limits.

4 The relative gas velocity angles at inlet and outlet of rotor blades (β_2 and β_3) should be within the specified bounds.

5 The axial velocity of flow should lie within some upper and lower bounds.

6 The actual pressure ratio across the nozzle blades should be below the critical pressure ratio.

7 The Mach number at the exit from the stage should be less than a specified value.

8 The included angle of divergence of the turbine annulus walls should not exceed the specified upper limit.

9 The flow coefficient (ϕ) and the stage temperature drop coefficient (ψ) should lie within some upper and lower bounds.

10 The degree of reaction at mean radius should be within some upper and lower bounds while the degree of reaction at the root of rotor blades should be a non-negative quantity.

11 The fundamental natural frequency of the blades should be away from the forcing frequency of the blade in order to avoid resonance.

12 The stresses developed at the root of the rotor blade should be less than the permissible value.

13 The tip deflection of the rotor blade should be less than some specific value.

Evaluation of Design Constraints. The constraints other than those involving stress, deflection and vibration can be specified with the help of the relations given in Appendix A. For the purpose of stress, deflection and vibration analysis, the tapered twisted and rotating blade is idealized as a rectangular cantilever beam having linear taper in depth, breadth and twist from root to tip and subjected to rotational, pressure and gas bending stresses.

Equivalent Cantilever Beam of a Rotor Blade. From the known values of area A and moments of inertia I_{xx}, I_{yy} and I_{xy}, the moments of inertia $I_{\bar{x}\bar{x}}$ and $I_{\bar{y}\bar{y}}$ with respect to $\bar{x}$ and $\bar{y}$ axes (Fig. 7) passing through the centroid of the airfoil section can be computed as

$$I_{\bar{x}\bar{x}} = I_{xx} - A\bar{y}^2 \quad (10)$$

$$I_{\bar{y}\bar{y}} = I_{yy} - A\bar{x}^2 \quad (11)$$

A rectangular section having twist Θ, breadth b_{eq} and height t_{eq} is then considered to be equivalent to the given airfoil section by equating their areas, and moments of inertia about $\bar{x}$ and $\bar{y}$ axes as

$$A = b_{eq} \cdot t_{eq} \quad (12)$$

$$I_{\bar{x}\bar{x}} = \frac{1}{12} b_{eq} t_{eq}^3 \cos^2\Theta + \frac{1}{12} t_{eq} b_{eq}^3 \sin^2\Theta \quad (13)$$

$$I_{\bar{y}\bar{y}} = \frac{1}{12} t_{eq} b_{eq}^3 \cos^2\Theta + \frac{1}{12} b_{eq} t_{eq}^3 \sin^2\Theta \quad (14)$$

The three unknowns t_{eq}, b_{eq} and Θ can be solved with the help of equations (12–14) to obtain

$$t_{eq} = \left[\frac{6}{A}(I_{\bar{x}\bar{x}} + I_{\bar{y}\bar{y}} \pm \left\{\frac{9}{A^2}(I_{\bar{x}\bar{x}} + I_{\bar{y}\bar{y}})^2 - A^2\right\}^{0.5}\right]^{0.5} \quad (15)$$

$$b_{eq} = \frac{A}{t_{eq}} \quad (16)$$

$$\tan\Theta = \{(12I_{\bar{y}\bar{y}} - b_{eq}{}^2A)/(12I_{\bar{x}\bar{x}} - b_{eq}{}^2A)\}^{0.5} \quad (17)$$

Equations (15) and (16) will give two equivalent rectangular sections whose orientations are perpendicular to each other. Out of these the one having a larger value of b_{eq} compared to t_{eq} is selected as the desired equivalent section.

The chord at the root and tip can be determined from the assumed value of the breadth taper ratio β as

$$(c_R)_{root} = \frac{2\beta c_R}{(1+\beta)} \quad (18)$$

$$(c_R)_{tip} = (c_R)_{root}/\beta \quad (19)$$

The blade angles β_{2root} and β_{3root} at the root and β_{2tip} and β_{3tip} at the tip are already available from the free vortex analysis. Once the values of $(c_R)_{root}$, β_{2root} and β_{3root} are known, one can get the equivalent rectangular section of dimensions $(b_{eq})_{root}$, $(t_{eq})_{root}$ and twist Θ_{root} at the root from equations (3–17). Similarly using the values $(c_R)_{tip}$, β_{2tip} and β_{3tip}, one can obtain an equivalent rectangular section of dimensions $(b_{eq})_{tip}$, $(t_{eq})_{tip}$ and twist Θ_{tip} at the tip. Hence the pretwist of equivalent blade will be

$$\Theta = \Theta_{tip} - \Theta_{root} \tag{20}$$

Thus the actual rotor blade is idealized as a doubly tapered cantilever beam of length h_R and pretwist Θ whose dimensions are $(b_{eq})_{root}$ and $(t_{eq})_{root}$ at the root and $(b_{eq})_{tip}$ and $(t_{eq})_{tip}$ at the tip. If the airfoil blade itself has an original pretwist of Θ_0, the total pretwist of the blade would be $(\Theta + \Theta_0)$.

Rotor Blade Stresses. Among the various types of stresses induced in the rotor blades of axial flow gas turbines, only the centrifugal stress, gas bending stress and stress due to pressure force have larger magnitudes and hence are included in the present analysis. Although the stress varies from the root to the tip of the blade, its maximum value generally occurs near the root of the blade.

The maximum value of the centrifugal tensile stress (which occurs at the root and is perpendicular to the XY plane), is given by

$$(\sigma_{ct})_{max} = \frac{\rho_m \Omega^2}{A_{root}} \int_{r_{root}}^{r_{tip}} A_r . r . dr \tag{21}$$

where ρ_m is the mass density of the blade material, Ω is the angular velocity of the blade (rad/s), A_r is the cross sectional area of the blade at any radius r and A_{root} is the cross-sectional area of the blade at the root.

The pressure force F_p per blade acting in the X-direction (which occurs due to differences of pressure at inlet and outlet to the rotor blade of the axial flow turbine), can be expressed as

$$F_p = (p_2 - p_3) \frac{\pi d h_R}{n_R} \tag{22}$$

The force F_b due to the gas bending per blade in the Y direction is due to the change of the whirl component at inlet and outlet of rotor blade and is expressed as

$$F_b = (c_{w_2} + c_{w_3}) \frac{m}{n_R} \tag{23}$$

The finite element method has been used for finding the stresses and deflections under the stated loading and the natural frequency of the doubly tapered and twisted rectangular beam. The details of the generation of the stiffness and mass matrices of the element and other computational aspects have been given in [23] and [24].

Statement of the Optimization Problem

The optimization problem can now be stated in the format of a nonlinear programming problem as follows:

Find $\vec{X}$ which minimizes

$$f(\vec{X}) = K_1(1 - \eta_s) + K_2 \rho_m \left\{ \frac{\pi \beta c_R (d - h_R)^2}{2(1 + \beta)} + n_R h_R A_R + n_N h_N A_N \right\} \tag{24}$$

subject to the constraints

$$g_1 = \frac{U^{(\ell)}}{U} - 1.0 \le 0 \tag{25}$$

$$g_2 = \frac{U}{U^{(u)}} - 1.0 \le 0 \tag{26}$$

$$g_3 = \left(\frac{c_R}{d}\right)^{(\ell)} - \left(\frac{c_R}{d}\right) \le 0 \tag{27}$$

$$g_4 = \left(\frac{c_R}{d}\right) - \left(\frac{c_R}{d}\right)^{(u)} \le 0 \tag{28}$$

$$g_5 = \left(\frac{c_N}{d}\right)^{(\ell)} - \left(\frac{c_N}{d}\right) \le 0 \tag{29}$$

$$g_6 = \left(\frac{c_N}{d}\right) - \left(\frac{c_N}{d}\right)^{(u)} \le 0 \tag{30}$$

$$g_7 = \left(\frac{s_N}{c_N}\right)^{(\ell)} - \left(\frac{s_N}{c_N}\right) \le 0 \tag{31}$$

$$g_8 = \left(\frac{s_N}{c_N}\right) - \left(\frac{s_N}{c_N}\right)^{(u)} \le 0 \tag{32}$$

$$g_9 = \left(\frac{s_R}{c_R}\right)^{(\ell)} - \left(\frac{s_R}{c_R}\right) \le 0 \tag{33}$$

$$g_{10} = \left(\frac{s_R}{c_R}\right) - \left(\frac{s_R}{c_R}\right)^{(u)} \le 0 \tag{34}$$

$$g_{11} = \beta_2^{(\ell)} - \beta_2 \le 0 \tag{35}$$

$$g_{12} = \beta_2 - \beta_2^{(u)} \le 0 \tag{36}$$

$$g_{13} = \beta_3^{(\ell)} - \beta_3 \le 0 \tag{37}$$

$$g_{14} = \beta_3 - \beta_3^{(u)} \le 0 \tag{38}$$

$$g_{15} = \frac{c_a^{(\ell)}}{C_a} - 1.0 \le 0 \tag{39}$$

$$g_{16} = \frac{C_a}{C_a^{(u)}} - 1.0 \le 0 \tag{40}$$

$$g_{17} = \frac{p_{01}}{p_2} - \frac{p_{01}}{p_c} \le 0 \tag{41}$$

$$g_{18} = M_{c_3} - M_{c_3}^{(u)} \le 0 \tag{42}$$

$$g_{19} = \alpha_c - \alpha_c^{(u)} \le 0 \tag{43}$$

$$g_{20} = \phi^{(\ell)} - \phi \le 0 \tag{44}$$

$$g_{21} = \phi - \phi^{(u)} \le 0 \tag{45}$$

$$g_{22} = \psi^{(\ell)} - \psi \le 0 \tag{46}$$

$$g_{23} = \psi - \psi^{(u)} \le 0 \tag{47}$$

$$g_{24} = R^{(\ell)} - R \le 0 \tag{48}$$

$$g_{25} = R - R^{(u)} \le 0 \tag{49}$$

$$g_{26} = \alpha_2^{(\ell)} - \alpha_2 \le 0 \tag{50}$$

$$g_{27} = R_{root}^{(\ell)} - R_{root} \le 0 \tag{51}$$

$$g_{28} = \frac{N}{\omega^{(1)}} - 1.0 \le 0 \tag{52}$$

$$g_{29} = \sigma_{max} - \sigma^{(u)} \le 0 \tag{53}$$

$$g_{30} = \frac{\Delta_t}{\Delta_t^{(u)}} - 1.0 \le 0 \tag{54}$$

Equations (25–40) represent the geometrical or side constraints which impose limits on the size of design variables. The quantities p_2, p_c, M_{c_3}, α_3, ϕ, R, α_2, R_{root}, Δ_t and the stresses are dependent on the design variables X_i and hence the constraint equations (41–54) denote the behavior constraints. The relation between the behavior quantities and the design variables cannot be expressed directly in closed form. However, for any given design vector $\vec{X}$, the behavior quantities can be evaluated numerically upto any desired accuracy. It can be seen that the objective function of equation (24) is a nonlinear function of the design variables, and the side constraints of equations (25–40) are linear while the behavior constraints are nonlinear. Hence the optimization problem is a nonlinear programming problem.

Conclusions

1 The problem of optimum design of axial flow gas turbine stages has been formulated. A method of computing the objective function and constraints of the problem has been presented. The present ap-

proach unifies the design methodology and can be used in preliminary design studies.

2 The convergence of the iterative method for the calculation of stage efficiency has been found to be very good. The method converged in three to four iterations irrespective of the initial trial value given for reasonable convergence criteria [24].

4 A procedure has been stated for converting a turbine blade airfoil section into an equivalent doubly tapered and twisted rectangular cantilever beam.

5 The analysis of stress, deflection and natural frequencies of vibration of doubly tapered and twisted cantilever beams has been performed by finite element methods. The element developed has been found to give good results even with four elements in a blade [23].

References

1 Emmert, H. D., "Current Design Practices for Gas Turbine Power Elements," *Trans. ASME*, Vol. 72, 1950, p. 189.

2 Horlock, J. H., *Axial Flow Turbines*, Butterworths, London, 1966.

3 Cohen, H., Rogers, G. F. C. and Saravanamuttoo, H. I. H., *Gas Turbine Theory*, Longman, London, 1972.

4 Wu, C. H. and Wolfenstein, L., "Application of Radial Equilibrium Conditions to Axial Flow Compressor and Turbine Design," NACA Rep. 955, 1955.

5 Hawthorne, W. R. and Ringrose, J., "Actuator Disc Theory of Compressible Flow in Free-Vortex Turbomachinery," *Proc. Instn. Mech. Engrs.*, Vol. 178, Part 3, 1963-64, p. 1.

6 Carter, A. F., Platt, M. and Lenherr, F. K., "Analysis of Geometry and Design Point Performance of Axial Flow Turbines, Part I, Development of the Analysis Method and Loss Coefficient Correlation," NASA CR-1181, Sept. 1968; "Part II, Computer Programme," NASA, CR-1187, Oct. 1968.

7 Davis, W. R. and Millar, D. A. J., "A Comparison of Matrix and Streamline Curvature Methods of Axial Flow Turbomachine Analysis, From a User's Point of View," ASME JOURNAL OF ENGINEERING FOR POWER, Vol. 97, 1975, p. 549.

8 Sawyer, J. W. (ed.), *Gas Turbine Engineering Handbook*, Gas Turbine Publication, 1966.

9 "Technical Advances in Gas Turbine Design," Instn. of Mech. Engrs. Symposium, 1969.

10 Laxminarayana, B., Britsch, W. R. and Gearhart, W. S. (eds.), "Fluid Mechanics, Acoustics, and Design of Turbomachinery," Parts I and II, NASA, SP-304, 1974.

11 A. J. Glassman (Ed.), "Turbine Design and Application," 3 Volumes, NASA, SP-290, 1975.

12 George, B. B., "Rocket Engine Turbine Optimization," Aerojet-General Corporation, TM 4901; 66-401, April 1966.

13 Balje, O. E., "Axial Turbine Performance Evaluation: Part A--Loss Geometry Relationship, Part B- Optimization with and without Constraints," ASME JOURNAL OF ENGINEERING FOR POWER, 1968, pp. 341-360.

14 Swift, W. L., "Optimizing Turbine and Pump-Turbine Design by Use of Computers," *Water Power*, Sept. 1971.

15 Kar, S. and Reddy, Y. R., "Optimum Vane Number and Angle of Centrifugal Pumps with Logarithmic Vanes," ASME *Journal of Basic Engineering*, Vol. 93, 1971, p. 411.

16 Gupta, R. S., "Optimum Design of Radial Impeller Having Logarithmic Vanes," All India Symposium on System Engineering, H.B.T.I. Kanpur, Aug. 1973.

17 Saravanamuttoo, H. I. H., and MacIsaac, B. D., "The Use of Hybrid Computer in the Optimization of Gas Turbine Control Parameters," ASME JOURNAL OF ENGINEERING FOR POWER, Vol. 95, 1973, p. 257.

18 Yadav, R. and Gupta, B. K., "Analytical Method of Optimizing Number of Blades and Blade Angles of Centrifugal Compressor Impellers," *Journal of Instn. of Engineers*, (India), Mech. Engg. Div., Vol. 55, No. ME 3, 1975, pp. 103-107.

19 Blaho, M., "Optimum Design of Axial Flow Fans with Cambered Blades of Constant Thickness," *Periodica Polytechnica*, Mechanical Engineering, Mashinostoenie, Vol. 19, 1975, pp. 79-89.

20 Paranjpe, P. A. and Murthy, M. V. A., "Optimization and Standardization of Steam Turbine Blade Profiles," Symposium on Blade Design and Development, BHEL Hyderabad, Sept. 1975.

21 Ainley, D. G. and Mathieson, G. C. R., "A Method of Performance Estimation for Axial-Flow Turbines," H.M.S.O., A.R.C., R & M 2974, 1957.

22 Dunham, J. and Came, P. M., "Improvements to the Ainley-Mathieson Method of Turbine Performance Prediction," ASME Paper No. 70-GT-2, 1970.

23 Gupta, R. S. and Rao, S. S., "Finite Element Eigenvalue Analysis of Tapered and Twisted Timoshenko Beams," *Journal of Sound and Vibration*, Vol. 56, 1978, pp. 187-200.

24 Gupta, R. S., "Automated Optimum Design of Axial Flow Gas Turbine Stage," Ph.D. Thesis, Indian Institute of Technology, Kanpur, Aug., 1977.

APPENDIX A

Aerodynamic Relations for the Design of Axial Flow Turbine Stage

$$U = \pi d N \tag{A1}$$

$$\phi = C_a/U \tag{A2}$$

$$R = \frac{\phi}{2}(\tan\beta_3 - \tan\beta_2) \tag{A3}$$

$$\Delta T_{0s} = [UC_a(\tan\beta_2 + \tan\beta_3)]/c_p \tag{A4}$$

$$\psi = (2c_p \Delta T_{0s})/U^2 \tag{A5}$$

$$\tan\alpha_2 = \tan\beta_2 + \frac{1}{\phi} \tag{A6}$$

$$\tan\alpha_3 = \tan\beta_3 - \frac{1}{\phi} \tag{A7}$$

$$C_2 = C_a/\cos\alpha_2 \tag{A8}$$

$$C_3 = C_a/\cos\alpha_3 \tag{A9}$$

$$V_2 = C_a/\cos\beta_2 \tag{A10}$$

$$V_3 = C_a/\cos\beta_3 \tag{A11}$$

$$C_{w_2} = C_2 \sin\alpha_2 \tag{A12}$$

$$C_{w_3} = C_3 \sin\alpha_3 \tag{A13}$$

$$T_2 = T_{01} - (C_2^2/2c_p) \tag{A14}$$

$$T_{2'} = T_2 - (\lambda_N C_2^2/2c_p) \tag{A15}$$

$$p_2 = p_{01}\Big/\left(\frac{T_{01}}{T_{2'}}\right)^{\gamma/(\gamma-1)} \tag{A16}$$

$$\frac{p_{01}}{p_c} = \left(\frac{\gamma+1}{2}\right)^{\gamma/(\gamma-1)} \tag{A17}$$

$$\rho_2 = p_2/(\bar{R}T_2) \tag{A18}$$

$$A_2 = \frac{m}{\rho_2 C_a} \tag{A19}$$

$$A_{2N} = \frac{m}{\rho_2 C_2} \tag{A20}$$

$$h_2 = \frac{A_2 N}{U} \tag{A21}$$

$$T_1 = T_{01} - (C_1^2/2c_p) \tag{A22}$$

$$p_1 = p_{01}(T_1/T_{01})^{\gamma/(\gamma-1)} \tag{A23}$$

$$\rho_1 = \frac{p_1}{(\bar{R}T_1)} \tag{A24}$$

$$A_1 = m/(\rho_1 C_a) \tag{A25}$$

$$h_1 = (A_1 N/U) \tag{A26}$$

$$T_{03} = T_{01} - \Delta T_{0s} \tag{A27}$$

$$T_3 = T_{03} - (C_3^2/2c_p) \tag{A28}$$

$$p_{03} = p_{01}\left(1 - \frac{\Delta T_{0s}}{\eta_s T_{01}}\right)^{\gamma/(\gamma-1)} \tag{A29}$$

$$p_3 = p_{03}\left(\frac{T_3}{T_{03}}\right)^{\gamma/(\gamma-1)} \tag{A30}$$

$$\rho_3 = p_3/(\bar{R}T_3) \tag{A31}$$

$$A_3 = m/(\rho_3 C_a) \tag{A32}$$

$$h_3 = A_3 N/U \tag{A33}$$

$$h_R = (h_2 + h_3)/2 \tag{A34}$$

$$h_N = (h_1 + h_2)/2 \tag{A35}$$

$$\tan \alpha_c = \frac{(h_3 - h_1)}{2} \cdot \frac{1}{d\left\{\left(\frac{C_N}{d}\right) + 1.25\left(\frac{c_R}{d}\right)\right\}} \tag{A36}$$

$$M_{c_3} = \frac{C_3}{(\gamma \bar{R} T_3)^{0.5}} \tag{A37}$$

$$T_3'' = T_2 \Big/ \left(\frac{p_2}{p_3}\right)^{(\gamma-1)/\gamma} \tag{A38}$$

$$\lambda_R = \frac{(T_3 - T_3'')}{(V_3^2/2c_p)} \tag{A39}$$

$$\tan \alpha_{2\text{root}} = \left(\frac{d}{d - h_2}\right) \tan \alpha_2 \tag{A40}$$

$$\tan \alpha_{3\text{root}} = \left(\frac{d}{d - h_3}\right) \tan \alpha_3 \tag{A41}$$

$$\tan \beta_{2\text{root}} = \left(\frac{d}{d - h_2}\right) \tan \alpha_2 - \left(\frac{d - h_2}{d}\right) \frac{U}{C_a} \tag{A42}$$

$$\tan \beta_{3\text{root}} = \left(\frac{d}{d - h_3}\right) \tan \alpha_3 + \left(\frac{d - h_3}{d}\right) \frac{U}{C_a} \tag{A43}$$

$$\tan \alpha_{2\text{tip}} = \left(\frac{d}{d + h_2}\right) \tan \alpha_2 \tag{A44}$$

$$\tan \alpha_{3\text{tip}} = \left(\frac{d}{d + h_3}\right) \tan \alpha_3 \tag{A45}$$

$$\tan \beta_{2\text{tip}} = \left(\frac{d}{d + h_2}\right) \tan \alpha_2 - \left(\frac{d + h_2}{d}\right) \frac{U}{C_a} \tag{A46}$$

$$\tan \beta_{3\text{tip}} = \left(\frac{d}{d + h_3}\right) \tan \alpha_3 + \left(\frac{d + h_3}{d}\right) \frac{U}{C_a} \tag{A47}$$

$$R_{\text{root}} = \frac{C_a\, d}{2U(d - h_R)} \{\tan \beta_{3\text{root}} - \tan \beta_{2\text{root}}\} \tag{A48}$$

$$(Y_p)_R = \left[Y_p(\beta_2 = 0) + \left(\frac{\beta_2}{\beta_3}\right)^2 \{Y_p(\beta_2 = \beta_3) - Y_p(\beta_2 = 0)\}\right] \times \left(\frac{t_R/c_R}{0.2}\right)^{\beta_2/\beta_3} \tag{A49}$$

$$(Y_p)_N = \left[Y_p(\alpha_1 = 0) + \left(\frac{\alpha_1}{\alpha_2}\right)^2 \{Y_p(\alpha_1 = \alpha_2) - Y_p(\alpha_1 = 0)\}\right] \times \left(\frac{t_N/c_N}{0.2}\right)^{\alpha_1/\alpha_2} \tag{A50}$$

$$\tan \alpha_m = \frac{(\tan \alpha_2 - \tan \alpha_1)}{2} \tag{A51}$$

$$\tan \beta_m = \frac{(\tan \beta_3 - \tan \beta_2)}{2} \tag{A52}$$

$$(C_L)_N = 2\left(\frac{s_N}{c_N}\right) (\tan \alpha_1 + \tan \alpha_2) \cos \alpha_m \tag{A53}$$

$$(C_L)_R = 2\left(\frac{s_R}{c_R}\right) (\tan \beta_2 + \tan \beta_3) \cos \beta_m \tag{A54}$$

$$\lambda_{cN} = 0.0334 \left(\frac{c_N}{h_N}\right)\left(\frac{\cos \alpha_2}{\cos \alpha_1}\right) \tag{A55}$$

$$\lambda_{cR} = 0.0334 \left(\frac{c_R}{h_R}\right)\left(\frac{\cos \beta_3}{\cos \beta_2}\right) \tag{A56}$$

$$(Y_s + Y_k)_R = \left\{\lambda_{cR} + B\left(\frac{c_R}{h_R}\right)\left(\frac{\bar{k}}{c}\right)^{0.78}\right\} \times \left\{\frac{(C_L)_R{}^2}{(s_R/c_R)}\right\}\left(\frac{\cos^2 \beta_3}{\cos^3 \beta_m}\right) \tag{A57}$$

$$(Y_s + Y_k)_N = \lambda_{cN}\left\{\frac{(C_L)_N{}^2}{(s_N/c_N)}\right\}\left(\frac{\cos^2 \alpha_2}{\cos^3 \alpha_m}\right) \tag{A58}$$

$$Y_N = (Y_p)_N + (Y_s + Y_k)_N \tag{A59}$$

$$Y_R = (Y_p)_R + (Y_s + Y_k)_R \tag{A60}$$

$$\lambda_{N_i} = \frac{Y_N T_2'}{T_{01}} \tag{A61}$$

$$T_{03\text{rel}} = T_3 + \left(\frac{V_3^2}{2c_p}\right) \tag{A62}$$

$$\lambda_{R_i} = \frac{Y_R T_3''}{T_{03\text{rel}}} \tag{A63}$$

$$\eta_{s_i} = \frac{1}{1 + \left[\left\{\lambda_{R_i}\left(\frac{V_3^2}{2c_p}\right) + \left(\frac{T_3}{T_2}\right)\lambda_{N_i}\left(\frac{c_2^2}{2c_p}\right)\right\} \Big/ (T_{01} - T_{03})\right]} \tag{A64}$$

$$n_N = \frac{\pi d}{s_N} \tag{A65}$$

$$n_R = \frac{\pi d}{s_R} \tag{A66}$$

$$\mathrm{R_e} = \frac{\rho_2 C_2 c_N + \rho_3 V_3 c_R}{2\bar{\mu}} \tag{A67}$$

$$(\eta_s)_{\mathrm{R_e}} = 1 - (1 - \eta_s)\left(\frac{2 \times 10^5}{\mathrm{R_e}}\right)^{0.2} \tag{A68}$$

S. S. Rao
Professor,
Department of Mechanical Engineering,
Indian Institute of Technology,
Kanpur-208016, India

R. S. Gupta
Assistant Professor,
Department of Mechanical Engineering,
Punjab Engineering College,
Chandigarh, 160012, India

Optimum Design of Axial Flow Gas Turbine Stage

Part II: Solution of the Optimization Problem and Numerical Results

The problem of stage design of axial flow gas turbines has been formulated as a nonlinear mathematical programming problem with the objective of minimizing aerodynamic losses and mass of the stage. The aerodynamic as well as mechanical constraints are considered in the problem formulation. A method of evaluating the objective function and constraints of the problem is presented in Part I of this paper. The optimization problem is solved by using the interior penalty function method in which the Davidon-Fletcher-Powell variable metric unconstrained minimization technique with cubic interpolation method of one dimensional minimization is employed. Problems involving the optimization of efficiency and/or mass of the stage have been solved numerically in Part II of the paper. The results of sensitivity analysis conducted about the optimum point have also been reported.

Introduction

The problem of optimum design of a gas turbine stage has been formulated and a method of computing the objective function and constraints has been developed in Part I of this paper. The problem formulated is in the form of a nonlinear mathematical programming problem and can be stated in the standard form:

$$\text{Find } \vec{X} = \begin{Bmatrix} X_1 \\ X_2 \\ \vdots \\ X_n \end{Bmatrix} \text{ which minimizes } f(\vec{X})$$

and satisfies the constraints

$$g_j(\vec{X}) \leq 0, j = 1, 2, \ldots, \ldots, m \tag{1}$$

There are two general classes of widely used nonlinear programming methods, namely, the methods of feasible directions, and the penalty function methods, available for solving the problem stated in equation (1). The feasible direction method of Zoutendijk [1] is based on the generation of usable feasible directions at constraint boundaries. Although this method works in a direct manner in solving the problem, the analyses during optimization have to be done accurately as they influence the rate of convergence and accuracy. The penalty function methods are quite reliable and their sequential nature allows a gradual approach to criticality of constraints. In the present work, the penalty function method of Fiacco and McCormick [2] is used as it has been found to be quite reliable. The generality and effectiveness of the computer program developed for the optimum design of a gas turbine stage has been demonstrated by solving several numerical design examples. The sensitivity of an optimum design with respect to the various design parameters has also been found.

Contributed by the Aircraft Committee for publication in the JOURNAL OF ENGINEERING FOR POWER. Manuscript received at ASME Headquarters August 20, 1979.

Solution Procedure

In the Fiacco-McCormick interior penalty function method, the objective function is augmented with a penalty term consisting of the constraints:

$$\phi(\vec{X}, r_k) = f(\vec{X}) - r_k \sum_{j=1}^{m} \frac{1}{g_j(\vec{X})} \tag{2}$$

where $\phi(\vec{X}, r_k)$ is called the penalty function. The minimization of $\phi(\vec{X}, r_k)$ is performed for a decreasing sequence of r_k so that

$$r_{k+1} < r_k \tag{3}$$

Equation (2) requires a feasible starting point and, in the present work, it is found by a process of trial and error. Since each of the designs generated during the optimization process lies inside the acceptable design space, the method is classified as an interior penalty function formulation.

The sequence of unconstrained minimizations of $\phi(\vec{X}, r_k)$ is done according to the iteration:

$$\vec{X}_{i+1} = \vec{X}_i + \tau^* \vec{S}_i \tag{4}$$

where $\vec{X}_{i+1}$ is the design vector corresponding to the minimum value of ϕ along the current search direction $\vec{S}_i$, $\vec{X}_i$ is the starting design vector, and τ^* is the minimizing step length in the direction $\vec{S}_i$.

Out of the several methods available for finding the search direction $\vec{S}_i$, the Davidon-Fletcher-Powell variable metric method [3] is a powerful general method for finding a local unconstrained minimum of a function of many variables [4]. In this method, the ith search direction $\vec{S}_i$ is computed as follows:

$$\vec{S}_i = -[H_i]\nabla\phi(\vec{X}_i) \tag{5}$$

where $\nabla\phi(\vec{X}_i)$ denotes the gradient of the ϕ-function at $\vec{X}_i$ and $[H_i]$ is a positive definite symmetric matrix. The matrix $[H_i]$ is updated according to the following rule:

$$[H_{i+1}] = [H_i] + [A_i] + [B_i] \tag{6}$$

where

$$[A_i] = \frac{\tau^* \vec{S}_i \vec{S}_i{}^T}{\vec{S}_i{}^T \vec{V}_i}$$

$$[B_i] = \frac{[H_i]\vec{V}_i \vec{V}_i{}^T [H_i]^T}{\vec{V}_i{}^T [H_i] \vec{V}_i}, \text{ and}$$

$$\vec{V}_i = \nabla\phi(\vec{X}_{i+1}) - \nabla\phi(\vec{X}_i)$$

The updating of $[H_i]$ preserves the symmetric positive definiteness of $[H_{i+1}]$ which ensures the stability of the procedure. The positive definiteness of $[H_{i+1}]$ is influenced only by the accuracy with which τ^* is determined. To start with $[H_0]$ is taken as the identity matrix in the present work. The cubic interpolation method is used to find the optimal step length τ^*. In this method the values of $\phi(\tau)$ and $d\phi/d\tau(\tau)$ at the points $\tau = A = 0$ and $\tau = B$ where B is the first value among 1, 2, 4, 8, . . . , at which $d\phi/d\tau$ is non-negative, are evaluated. By assuming a cubic variation for ϕ in the interval $A \leq \tau \leq B$, $\phi(\tau)$ is expressed as

$$\phi(\tau) \approx a + b\tau + c\tau^2 + d\tau^3 \tag{7}$$

where a, b, c and d are constants. The values of these four constants are determined by using the conditions:

$$\left.\begin{aligned} \phi_A = \phi(\tau = A);\ \phi_A{}' = \frac{d\phi}{d\tau}(\tau = A); \\ \phi_B = \phi(\tau = B);\ \phi_B{}' = \frac{d\phi}{d\tau}(\tau = B) \end{aligned}\right\} \tag{8}$$

The minimum of the cubic polynomial of equation (7) is given by

$$\bar{\tau}^* = A + \left(\frac{\phi_A{}' + Z + Q}{\phi_A{}' + \phi_B{}' + 2Z}\right)(B - A) \tag{9}$$

where

$$Z = \frac{3(\phi_A - \phi_B)}{(B - A)} + \phi_A{}' + \phi_B{}',$$

and

$$Q = (Z^2 - \phi_A{}'\phi_B{}')^{1/2}$$

If the value of $\bar{\tau}^*$ given by equation (9) is not accurate enough, a new cubic equation is fitted between the best two points out of A, τ^* and B. This refitting scheme is continued until the correct value $\tau^* = \bar{\tau}^*$, which satisfies the stated convergence criterion, is found [4].

This algorithm is reapplied until the cosine of the angle between the vectors $\vec{S}_i$ and $\nabla\phi_{i+1}$ at the minimizing step length τ^* is sufficiently small (ϵ), i.e.,

$$\cos\bar{\theta} = \frac{\vec{S}_i{}^T \nabla\phi_{i+1}}{|\vec{S}_i| \cdot |\nabla\phi_{i+1}|} < \epsilon \tag{10}$$

This ensures that $\vec{X}_{i+1}$ is the minimum along the direction $\vec{S}_i$.

Numerical Examples

The program for evaluating the objective function and constraints discussed in Part I is coupled with the optimization program. To demonstrate the effectiveness and flexibility of the program, a few numerical examples were considered [5]. These problems are solved with different objective functions under different constraint sets. The data pertinent to the design of the stage along with the material properties of the blades and gas properties are given in Table 1. The side and behaviour constraints considered are given by g_1 to g_{16} and g_{17} to g_{30}, respectively, in Appendix A.

Example 1: Maximization of Isentropic Stage Efficiency. The maximization of isentropic stage efficiency (or minimization of losses) is considered as the objective in the first example. The starting point, upper and lower bounds, and the optimum values of the design variables are shown in Table 2. The bounds on the behaviour constraints and the values of the response quantities at the starting and optimum designs are shown in Table 3. The progress of the optimization path showing the cumulative number of one-dimensional minimization steps versus the objective function is shown in Fig. 1. In this figure, the variations of the penalty function and the mass of the stage have also been represented. The results of optimization show that there is a 30.5 percent reduction in the objective function. The optimum point corresponds to an increase in the efficiency of the stage by 2.48

Table 1 Data for optimization problems

Number of design variables, $n = 8$
Number of constraints = 30
Number of finite elements in a blade = 4
Number of eigen values computed = 2
Number of degrees of freedom of an element = 8 (since shear deformation effect is neglected)
Maximum number of cubic interpolations used in one dimensional minimization = 3
Maximum number of unconstrained minimization steps for any value of penalty parameter = 5
Gas constant, $\bar{R}$ = 287 N-m/Kg-K
Viscosity, $\bar{\mu} = 4.0 \times 10^{-5}$ Kg/m-s
Ratio of specific heats of the gas, $\gamma = 1.333$
Density of the blade material, $\rho_m = 800$ Kg/m^3
Young's modulus of the material, $E = 2.0 \times 10^{11}$ N/m^2
Shear modulus, G = E/2.6
Stagnation pressure of entering gas in the stage,

$$p_{01} = 4.0 \times 10^5 \text{ N/m}^2$$

Stagnation temperature of entering gas in the stage,

$$T_{01} = 1100 \text{ K}$$

Mass flow of the gases across the stage = 20 Kg/s
Rotational speed of the turbine, N = 250 rps
Radial clearance of the blades, $\bar{k}$ = .000154 m
Breadth taper ratio, $\beta = 2.0$
Depth taper ratio, $\alpha = 1.5$
Shear coefficient, $\mu = .833$

Table 2 Initial and optimum design variables for examples 1 and 2

			Maximization of efficiency (Example 1)						
			First starting point					Minimization of weight (Example 2)	
Design variable	Bounds		Initial point	Optimum point with $3\,r_k$	Optimum point with $6\,r_k$	Second starting point			
	Lower	Upper				Initial point	Optimum point	Initial point	Optimum point
X_1	0.064	0.512	0.432	0.3378	0.3370	0.276	0.3254	0.432	0.2764
X_2	0.020	0.080	0.046	0.0611	0.0609	0.056	0.0656	0.046	0.0559
X_3	0.016	0.080	0.040	0.0473	0.0462	0.068	0.0438	0.040	0.0683
X_4	0.008	0.080	0.035	0.0335	0.0322	0.059	0.0309	0.035	0.0595
X_5	0.010	0.080	0.044	0.0428	0.0425	0.028	0.0474	0.044	0.0284
X_6	0.600°	57.0°	20.5°	15.4°	15.2°	18.6°	11.9°	20.5°	18.7°
X_7	40.000°	80.0°	54.57°	59.5°	58.9°	52.5°	58.8°	54.57°	52.8°
X_8	50.000	400.00	272.0	191.4	188.2	252.7	187.0	272.0	252.7
Objective function	—	—	0.0813	0.0565	0.0557	0.122	0.0543	29.939	4.223

Table 3 Response quantities at initial and optimum points for Examples 1 and 2

Response quantities	Bounds		Maximization of efficiency (Example 1)					Minimization of weight (Example 2)	
			First starting point			Second starting point			
	Lower	Upper	Initial point	Optimum point with 3 r_k	Optimum point with 6 r_k	Initial point	Optimum point	Initial point	Optimum point
Pressure ratio, p_{01}/p_{02}	—	1.853	1.602	1.262	1.266	1.303	1.128	1.602	1.303
Mach number, M_{C_3}	—	1.000	0.465	0.322	0.315	0.453	0.317	0.465	0.453
Annulus angle, α_c	—	22.5°	15.0°	18.9°	16.92°	18.87°	16.5°	15.0°	20.4°
Flow coefficient	0.25	2.0	0.802	0.721	0.71	1.16	0.732	0.802	1.164
Temperature drop coefficient	0.50	6.0	2.89	2.805	2.76	3.854	2.77	2.89	3.854
Reaction at mean radius	0.30	0.70	0.422	0.502	0.4962	0.569	0.538	0.422	0.569
Angle α_2	40.0°	—	58.2°	58.2°	58.92°	50.1°	57.3°	58.2°	49.9°
Root reaction	0.01	—	0.202	0.04	0.0130	0.088	0.052	0.202	0.088
$\omega(1)$ in rps	250.00	—	975.0	542.0	530.0	455.0	515.0	975.0	455.0
Root stress, N/m^2	—	$.3 \times 10^9$	$.281 \times 10^9$	$.297 \times 10^9$	$.299 \times 10^9$	$.295 \times 10^9$	$.299 \times 10^9$	$.281 \times 10^9$	0.296×10^9
Tip deflection, m	—	3.5×10^{-3}	$.304 \times 10^{-3}$	$.439 \times 10^{-3}$	$.443 \times 10^{-3}$	$.843 \times 10^{-3}$	$.457 \times 10^{-3}$	$.304 \times 10^{-3}$	$.843 \times 10^{-3}$
OBJ 1	—	—	0.0813	0.0565	0.0557	0.122	0.0543	0.813	0.122
OBJ 2	—	—	21.94	9.80	9.585	4.22	8.818	21.94	4.223

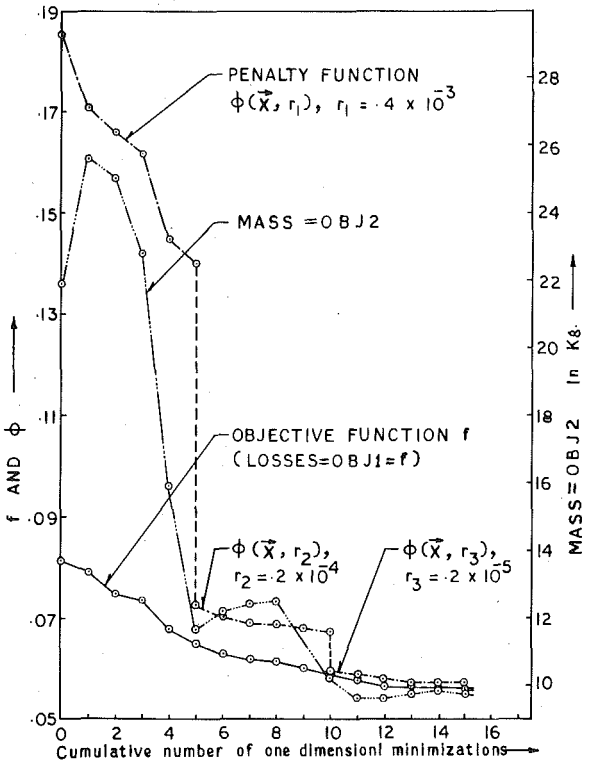

Fig. 1 Progress of efficiency optimization path for example 1

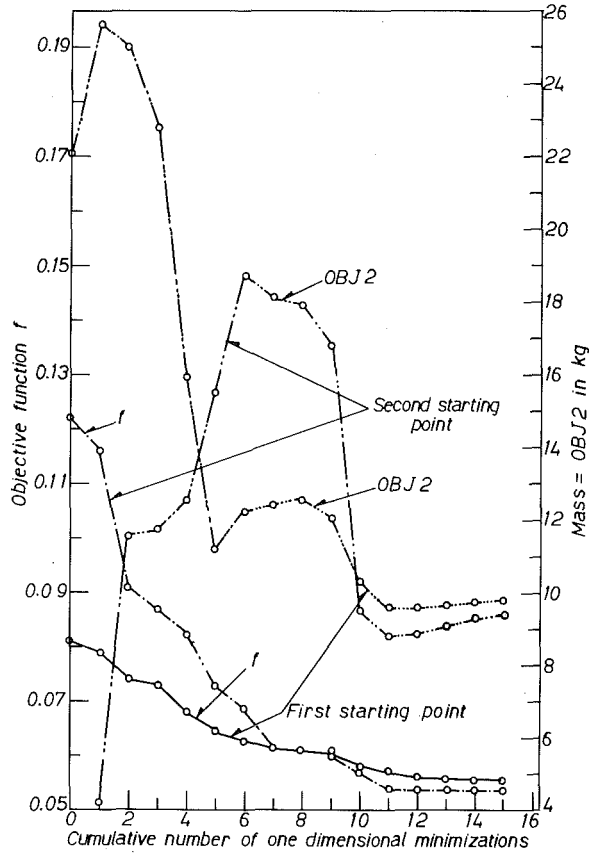

Fig. 2 Progress of optimization path for efficiency (second starting point) and comparison with first starting point

percent and a reduction in weight of the stage by 55.3 percent compared to the starting design vector. None of the side constraints is active at the optimum point. The constraints on stress and degree of reaction at root have become active (out of the behaviour constraints) at the optimum point. It can be observed that X_3, X_4 and X_5 have not changed much from the starting point while the other variables show appreciable change from the initial starting point. The optimum point has been found with three values of r_k in 15 one-dimensional minimization steps which required about 61 min of computer time on an IBM 7044 computer.

Although the point obtained at the end of 15 one-dimensional steps (with three values of r_k) can be taken as the optimum (evident from Fig. 1), the minimization is carried for three more values of r_k which required an additional computational time of 70 min. The results obtained with six values of r_k are compared with those obtained with three values of r_k in Tables 2 and 3. It can be seen that while the first three values of r_k reduced the objective function (one minus the efficiency) from 0.0813 to 0.0565, the additional three values of r_k could reduce it to 0.0557 only. Thus no significant reduction in the objective could be achieved by proceeding beyond three values of r_k. Since this behavior is characteristic of the interior penalty function method, all the subsequent examples are solved by using three values of r_k only.

In order to test whether the optimum point found corresponds to a local minimum or the absolute minimum in the design space, the same example has been solved with a second starting design vector. The progress of the optimization path is shown in Fig. 2. This plot is similar to Fig. 1 and the optimum point obtained ($f = 0.0543$) also compares well with that of the previous case ($f = 0.0557$). The starting and optimum designs of the two cases are compared in Tables 2 and 3. The optimum design variables are also in good agreement with each other. Apart from a small difference that might have occurred due to numerical instability, the two optimum points appear to be same. On the basis of the two trial starting designs, it is hard to say whether the

minimum obtained is the absolute minimum over the design space. However, finding a similar optimum design by starting from two different initial designs is at least a pointer in that direction.

Example 2: Minimization of Mass. In the second example, the optimization of weight (mass) of the axial flow gas turbine stage is considered. The constraints, design variables and their bounds are same as in the case of the first example (first starting point).

The optimization results are shown in Tables 2 and 3. The progress of the optimization path, showing the cumulative number of one dimensional minimization steps versus the objective function is shown in Fig. 3. The optimization results show that there is 80.5 percent reduction in the objective function (mass). Out of all the side and behavior constraints, only the degree of reaction at root and the stress at root of the rotor blade have become active at the optimum point. Comparatively X_6, X_7 and X_8 have not changed much from their initial starting values. From Fig. 3, it can be observed that the losses decreased by small amount first and then increased at a faster rate. This indicates that the reduction in weight can be obtained only at the cost of efficiency. For this example, the computer time required is 60 minutes on an IBM 7044 computer for 15 one-dimensional minimization steps.

Example 3: Optimization of Weighted Combination of Efficiency and Mass. The minimization of a weighted sum of efficiency and mass (weight) of the gas turbine stage is considered in the third example. The constraints, design variables and their bounds are the same as in example 2. The magnitude of losses and mass (weight) of the stage are normalized such that their contributions will be equal at the starting design point. The progress of the optimization path is shown in Fig. 4, where the variations of penalty function, losses and mass of the stage with the number of one dimensional minimizations are shown. It is observed that there is a 45 percent reduction in the objective function while the efficiency increased by 1.65 percent and the weight reduced by 69.5 percent. The variables X_4, X_6 and X_7 have not changed much from the starting point. The constraints on the degree of reaction at the root and the stress have become active at the optimum point. It can be seen that the reduction in losses or mass of the stages is less in this case compared to the case where the individual objective function is considered for optimization. Thus the present results indicate a compromise between efficiency and mass of the stage. Here 15 one-dimensional minimization steps required about 62 min of computer time on an IBM 7044 computer.

Example 4: Optimization of Weighted Combination of Efficiency and Mass by Considering only the Side Constraints. In the fourth problem, a linear combination of the mass and the losses of the stage has been minimized with equal contribution of losses and mass at the starting design point. Only the side constraints (g_1 to g_{16} of Appendix A) are considered with no constraints on the behaviour (response) quantities in the problem formulation and solution.

The optimization results are shown in Tables 4 and 5. The progress of the optimization path showing the cumulative number of one dimensional minimizations versus the values of objective function, losses and mass is shown in Fig. 5. It is found that the objective function was reduced by 47.6 percent while there is an increase of 2.1 percent in efficiency and a reduction of 69.3 percent in mass of the stage. It is observed that although the objective function (losses as well as mass of the stage) has been reduced by a larger amount, the behaviour quantities like stress, degree of reaction at root and tip deflection have become larger than the permissible values. This clearly demonstrates the necessity of putting bounds on these response quantities. The program required only about 20 min of computer time on IBM 7044 computer for 15 one-dimensional minimization steps in this case.

Sensitivity Analysis

In practice a designer would be interested in knowing how the response quantities vary with a change in the design variables. This type of sensitivity analysis will help the designer in manipulating the design variables to suit some specific requirements. Further, in some cases, the results obtained from the optimization procedure may have to be rounded-off to the nearest practical values of the design variables. Hence a sensitivity analysis of response quantities, namely, the objective function, losses, mass, stress, degree of reaction at root and mean radius, first natural frequency, flow coefficient, stage temperature drop coefficient and angle of nozzle blade at outlet, with respect to the various design variables is conducted. In this analysis, the reference design is taken as the optimum point of example three. The design variables are varied on the negative and positive sides of the reference (optimum) values and the magnitudes of the response quantities are plotted against the percentage changes of the design variables in Fig. 6–14.

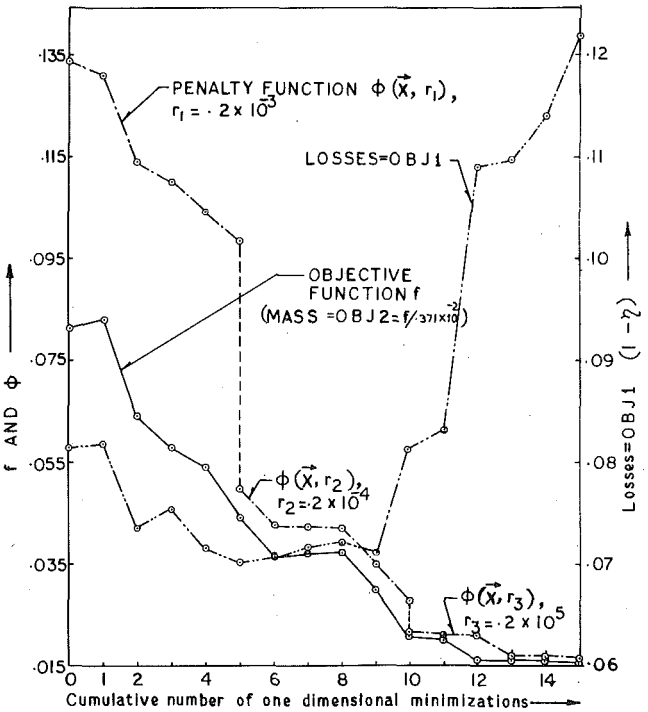

Fig. 3 Progress of weight optimization path for example 2

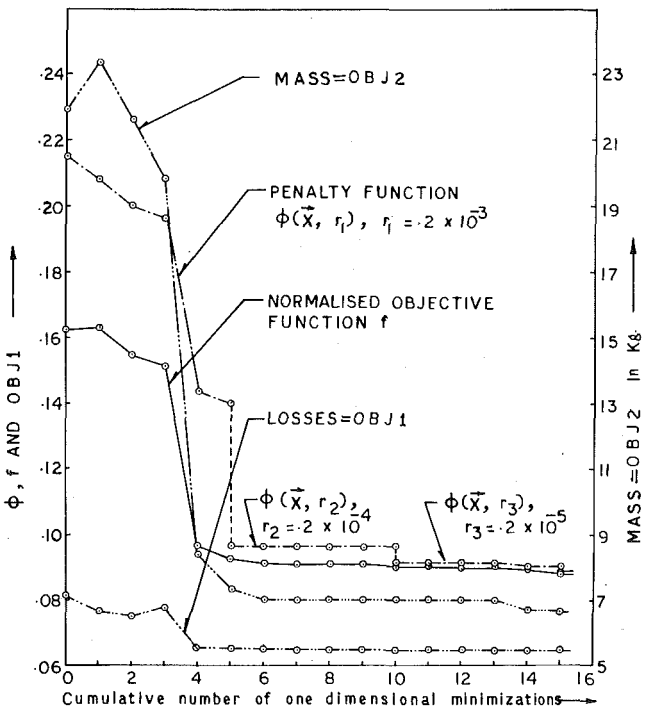

Fig. 4 Progress of optimization path (equal weightage to losses and mass) for example 3

Table 4 Initial and optimum design variables for minimization of weighted combination of losses and mass

Design variables	Bounds		Initial point	Optimum points	
	Lower	Upper		Example 3	Example 4 (with side constraints only)
X_1	0.064	0.512	0.432	0.3055	0.285
X_2	0.020	0.080	0.046	0.0579	0.0464
X_3	0.016	0.080	0.040	0.0475	0.0457
X_4	0.008	0.080	0.035	0.0338	0.0321
X_5	0.010	0.080	0.044	0.390	0.0327
X_6	0.600°	57.0°	20.5°	19.8°	19.5°
X_7	40.0°	80.0°	54.57°	54.8°	54.8°
X_8	50.0	400.0	272.0	232.9	218.2
Objective function	—	—	0.162	0.0895	0.0853

Table 5 Initial and optimal response quantities for minimization of weighted combination of losses and mass

Response quantities	Bounds		Initial point	Optimum points	
	Lower	Upper		Example 3	Example 4 (with side constraints only)
Pressure ratio, p_{01}/p_2	—	1.853	1.602	1.309	1.076
Mach number, M_{C_3}	—	1.0	0.465	0.407	0.395
Annulus angle, α_c	—	22.5°	15.0°	20.3°	21.0°
Flow coefficient	0.25	2.0	0.802	0.971	0.954
Temperature drop coefficient	0.50	6.0	2.89	3.458	3.399
Reaction of mean radius, R	0.30	0.70	0.422	0.515	0.5194
Angle, α_2	40.0°	—	58.2°	54.1°	54.4°
Root reaction, R_{root}	0.01	—	0.202	0.0517	−0.099
First natural frequency in rps	250.0	—	975.0	527.0	392.0
Root stress in N/m^2	—	0.3×10^9	0.281×10^9	0.298×10^9	2.298×10^9
Tip deflection in m	—	3.5×10^{-3}	0.304×10^{-3}	0.683×10^{-3}	16.20×10^{-3}
OBJ1	—	—	0.813	0.0648	0.0603
OBJ2 in Kg	—	—	21.94	6.65	6.75

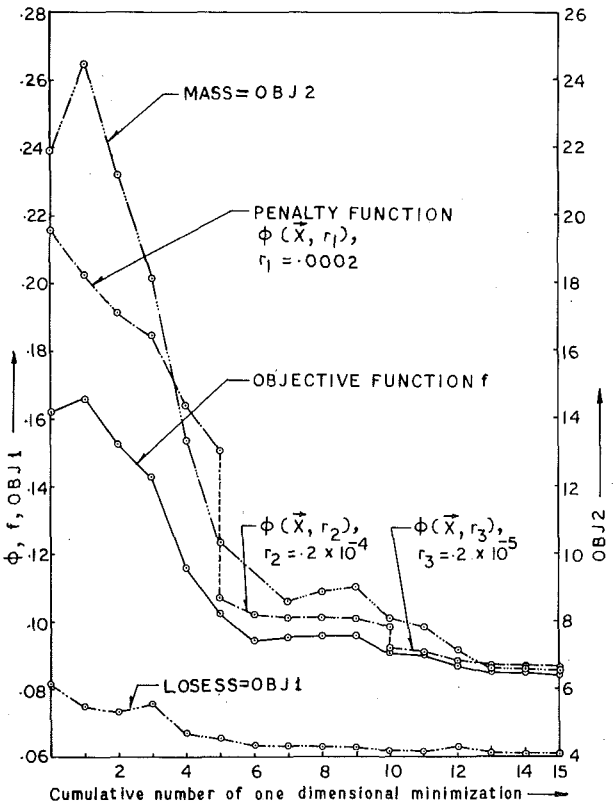

Fig. 5 Optimization path for example 4 (side constraints only)

From Fig. 6 it is observed that the objective function (weighted combination of losses and mass) is quite sensitive to variations in X_1, X_2, X_4 and X_5. The sensitivity of the two components of the objective function is shown in Figs. 7 and 8. Fig. 7 shows that the losses are more sensitive to the variables X_2, X_3, X_4 and X_5 compared to the other four variables. Similarly figure 8 indicates that the mass of the stage is more sensitive to the diameter of the turbine compared to the variables X_2, X_7 and X_8. The mass is almost independent of the variables X_3, X_4, X_5 and X_6.

The sensitivity of the mechanical response quantities, namely, stress, deflection and fundamental natural frequency with respect to the various design parameters is shown in Figs. 9–11. It can be observed that all these quantities are most sensitive to the variables X_1 to X_7 and less sensitive to the other variables.

Figs. 12–14 represent the variation of the aerodynamic response quantities, namely, degree of reaction at root, flow coefficient, stage temperature drop coefficient, stator blade angle at outlet, and degree of reaction at mean radius with a percentage change in design variables. It can be seen (Fig. 12) that the degree of reaction at root is more sensitive to the variables X_7 and X_8 compared to the other variables. The stage temperature drop coefficient is found (Fig. 13) to be quite sensitive to X_1, X_6, X_7 and X_8, and independent of the variables X_2, X_3, X_4 and X_5. The flow coefficient is found to increase with increasing values of X_8, and decrease with increasing values of X_1, while it is independent of the remaining six variables. Fig. 14 represents the sensitivity analysis of degree of reaction at mean radius and gas outlet angle of stator blades. It is seen that the degree of reaction is most sensitive to the variable X_7, less sensitive to X_1, X_6 and X_8, and insensitive to the variables X_2, X_3, X_4 and X_5. Similarly the stator blade outlet angle (α_2) is found to be more sensitive to X_1, X_6 and X_8 and insensitive to changes in the remaining variables.

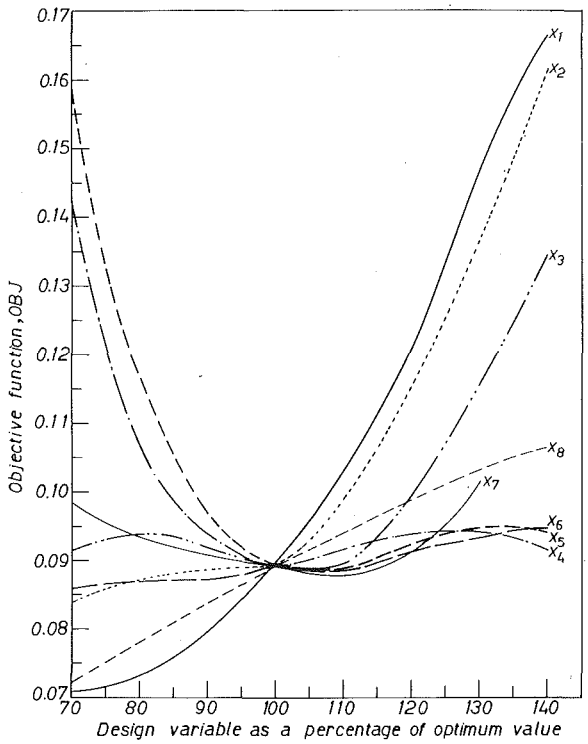

Fig. 6 Sensitivity analysis of objective function

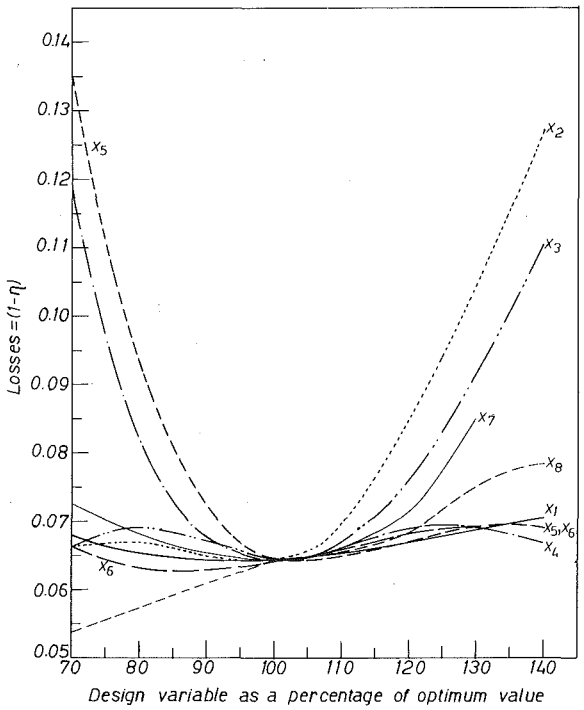

Fig. 7 Sensitivity analysis of losses

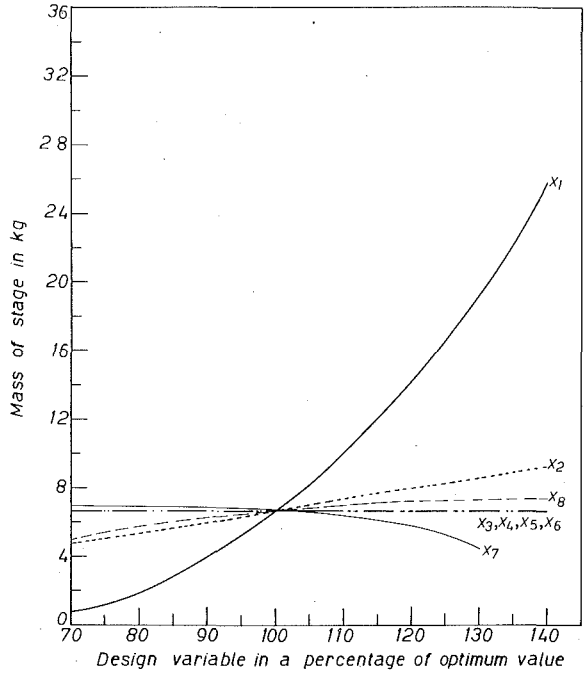

Fig. 8 Sensitivity analysis of mass

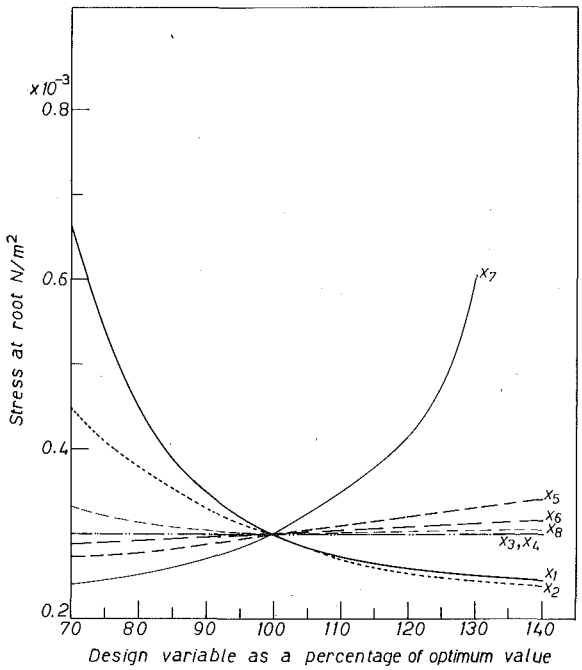

Fig. 9 Sensitivity analysis of stress at root

Discussion and Conclusion

For the solution of the problem of designing an axial flow gas turbine stage, the interior penalty function approach with Davidon-Fletcher-Powell method of unconstrained optimization and cubic interpolation technique of one dimensional minimization has been found to be quite satisfactory and gave the optimum results in about 15 one dimensional steps.

An increase of 2.48 percent efficiency has been obtained with the first starting point while it was 6.70 percent with the second starting point in the first example. Along with the increase in efficiency, there has been an appreciable decrease in the mass of the stage. In the case of example 2, it has been found that there is a drastic decrease in the mass of the stage (about 80 percent) at the optimum point. Mostly this decrease is due to the decrease in the mean diameter of turbine stage. When the mean diameter is reduced the blade size reduces, and since this smaller blade has to carry all the gas bending force, the gas bending stresses become larger and reach criticality at the optimum point. It has been observed that efficiency also increases along with the decrease of weight. However, the optimum results indicate that more reduction in weight can be obtained only at the cost of efficiency. When equal weightage is given to the loss and the mass of the stage, the optimum results indicate a compromise between maximization of efficiency and minimization of mass. It has been observed that in all the cases the weight reduction is mostly due to the decrease in the mean diameter. In all the optimization problems, the constraints on the degree of reaction at the root and the stresses in the blade have been found to be critical at the optimum.

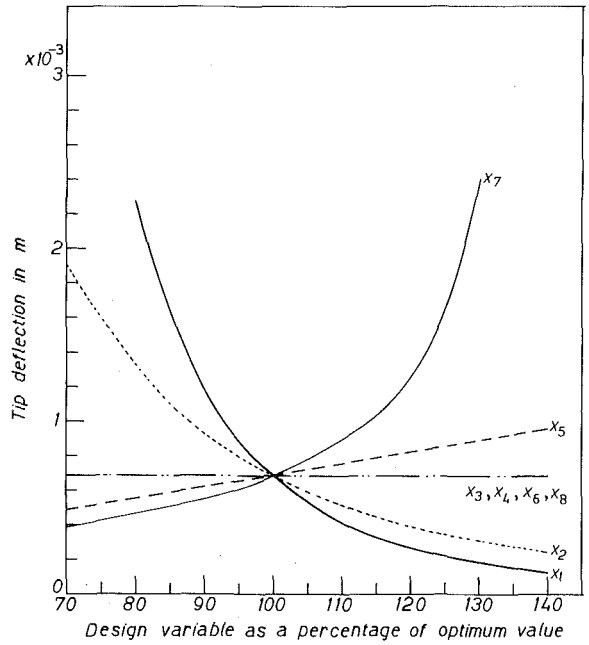

Fig. 10 Sensitivity analysis of tip deflection

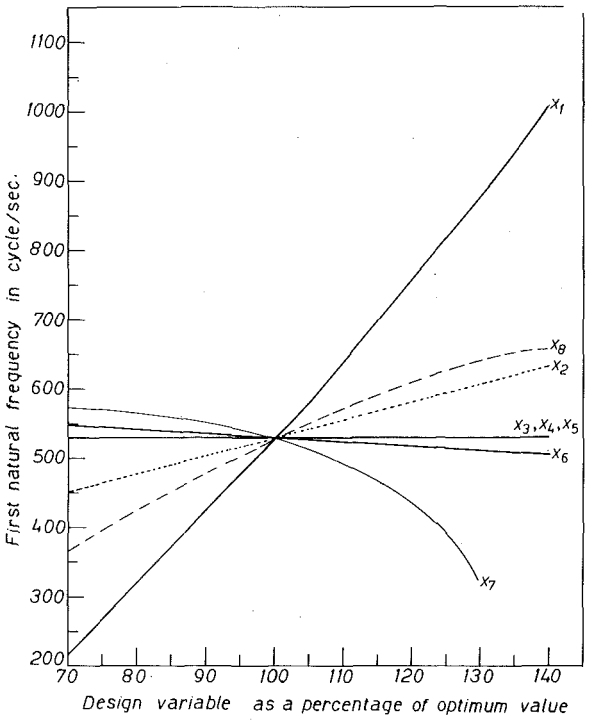

Fig. 11 Sensitivity analysis of first natural frequency

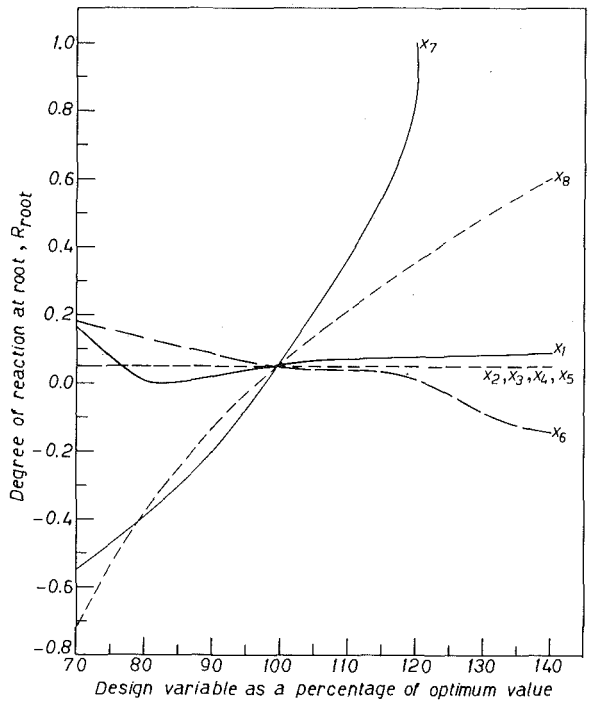

Fig. 12 Sensitivity analysis of degree of reaction at root

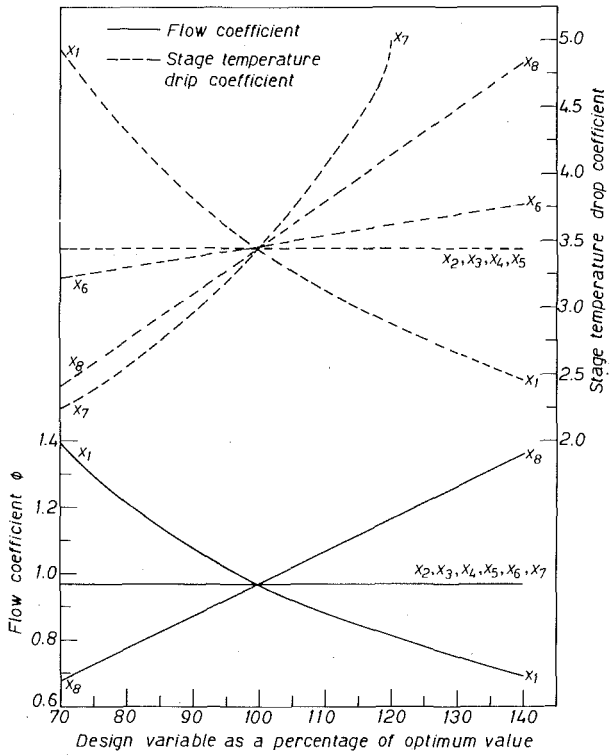

Fig. 13 Sensitivity analysis of flow coefficient and stage temperature drop coefficient

It has been observed that the losses are more sensitive to the chord and spacing of the rotor blades while the mass of the stage is most sensitive to the mean diameter of the rotor. The mechanical response parameters, namely the deflection, stress and fundamental natural frequency of vibration of the blade, have been found to be most sensitive to variations in the mean diameter of the rotor and the exit angle of the rotor blade (β_3). The degree of reaction at root was found to be most sensitive with respect to β_3 and axial velocity of flow.

The present study demonstrates that the computer program developed can be used for the unified design of axial flow gas turbine stage. The method can also be used for the optimization of multistage turbines without much difficulty.

References

1 Zoutendijk, G., *Methods of Feasible Directions*, Elsevier, Amsterdam, 1960.

2 Fiacco, A. and McCormick, G. P., "The Sequential Unconstrained Minimization Technique for Nonlinear Programming, A Primal-Dual Method," *Journal of Management Science*, Vol. 10, No. 2, Jan. 1964.

3 Box, M. J., "A Comparison of Several Current Optimization Methods and the Use of Transformations in Constrained Problems," *Computer Journal* (British), Vol. 9, 1966.

4 Rao, S. S., *Optimization: Theory and Applications*, Wiley Eastern Ltd., New Delhi, 1978.

5 Gupta, R. S., "Automated Optimum Design of Axial Flow Gas Turbine Stage," Ph.D. Thesis, Indian Institute of Technology, Kanpur, Aug., 1977.

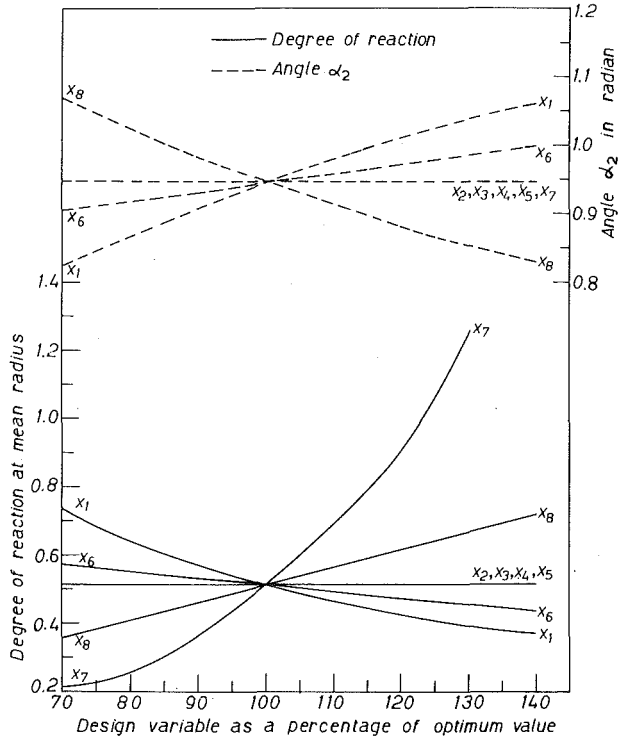

Fig. 14 Sensitivity analysis for degree of reaction and angle α_2.

APPENDIX A

Constraints of the Numerical Problem

$$g_1 = \frac{50}{U} - 1.0 \le 0$$

$$g_2 = \frac{U}{400} - 1.0 \le 0$$

$$g_3 = \frac{h_R}{8d} - X_2 \le 0$$

$$g_4 = X_2 - \frac{h_R}{2d} \le 0$$

$$g_5 = \frac{h_N}{10d} - X_3 \le 0$$

$$g_6 = X_3 - \frac{h_N}{2d} \le 0$$

$$g_7 = 0.5 - \frac{X_4}{X_3} \le 0$$

$$g_8 = \frac{X_4}{X_3} - 1.0 \le 0$$

$$g_9 = 0.5 - \frac{X_5}{X_2} \le 0$$

$$g_{10} = \frac{X_5}{X_2} - 1.0 \le 0$$

$$g_{11} = 0.01 - X_6 \le 0$$

$$g_{12} = X_6 - 1.0 \le 0$$

$$g_{13} = \frac{40}{57} - X_7 \le 0$$

$$g_{14} = X_7 - 1.4 \le 0$$

$$g_{15} = \frac{50.0}{X_8} - 1.0 \le 0$$

$$g_{16} = \frac{X_8}{400} - 1.0 \le 0$$

$$g_{17} = \frac{p_{01}}{p_2} - \frac{p_{01}}{p_c} \le 0$$

$$g_{18} = M_{C_3} - 1.0 \le 0$$

$$g_{19} = \frac{12\alpha_c}{\pi} - 1.5 \le 0$$

$$g_{20} = 0.25 - \phi \le 0$$

$$g_{21} = \phi - 2.0 \le 0$$

$$g_{22} = 0.5 - \psi \le 0$$

$$g_{23} = \psi - 6.0 \le 0$$

$$g_{24} = 0.3 - R \le 0$$

$$g_{25} = R - 0.7 \le 0$$

$$g_{26} = \frac{40}{57} - \alpha_2 \le 0$$

$$g_{27} = 0.01 - R_{\text{root}} \le 0$$

$$g_{28} = \frac{N}{\omega^{(1)}} - 1.0 \le 0$$

$$g_{29} = \frac{\alpha}{0.30 \times 10^9} - 1.0 \le 0$$

$$g_{30} = \frac{\Delta_t}{0.05\, h_R} - 1.0 \le 0$$

W. D. Bachalo

C. F. Hess

C. A. Hartwell

Spectron Development Laboratories, Inc., Costa Mesa, Calif.

An Instrument for Spray Droplet Size and Velocity Measurements

Laser light scattering techniques that measure the size of single droplets at a time have experienced difficulties when applied to high number density sprays. This problem has been alleviated by developing the particle sizing interferometric method for the off-axis detection of scattered light. The method has the advantages of being insensitive to the absolute intensity of the light scattered and light absorbed by the droplet and measures the droplet size and velocity simultaneously. A theoretical description of the technique is given along with experimental verifications of the results. The experiments showed that the method can produce accurate in situ measurements of typical nozzle sprays when large off-axis light collection angles are used.

Introduction

Accurate size and velocity measurements of liquid sprays are important for a broad range of applications. General areas of application include fuel nozzle spray characterization, evaluation of scrubbers, aircraft icing studies and measurements of industrial and agricultural sprays. The fuel spray applications are of contemporary interest in combustion research because of the need to improve the combustion efficiency and reduce harmful emissions. Research into fuel atomization and fuel-air preparation dynamics requires the measurement of fuel droplet size, size-velocity correlations, air and fuel velocity and turbulence intensity. Several laser light scattering techniques have been developed that satisfy some of the measurement requirements.

The light scattering detection techniques can be separated into two categories, those that make size measurements of single droplets and systems that measure the light scattered by a collection of particles in the collimated laser beam. Multiple scatter detection systems can typically make size measurements in particle or droplet fields having a higher number density than the available single particle counters can handle. Unfortunately, the method does not provide a good spatial resolution and it does not measure the velocity of the droplets which limits its application in spray nozzle measurements. In addition, the method assumes an *a priori* particle size distribution which it fits mathematically. Measurements in the presence of facility windows have also been reported to have created errors in the measurements. The single particle detection techniques have relatively good spatial resolution and signal-to-noise characteristics but have been limited to sprays with low to moderate number densities.

In the present paper, an instrument based on an interferometric technique has been developed for measuring the size and velocity of individual droplets at rates to 10^4/s in sprays with relatively high number densities. Particle sizing interferometry has been described in the literature [1–4]. Recently, the general concept has been extended by Bachalo [5] to utilize off-axis scatter detection which is effective in reducing the size of the measurement volume and the background noise produced by particles crossing the laser beams outside of the crossover region. In the size range (3 μm to 5 mm) over which this technique can be used, the scattered light fields can be defined with geometrical optics laws. For sufficiently large off-axis collection angles, as defined in the analysis, the scattered light is primarily due to refraction and reflection with the diffractive component remaining concentrated in the near-forward direction. It is the refracted and reflected light that is used to measure the droplet size. With this analysis, the measurement capability of the interferometric method has been extended to a much greater size range and can operate in sprays with at least an order of magnitude greater number densities than the on-axis single particle counters.

The off-axis detection method will be described briefly and the relevant parameters identified. Several detection angles, including 90 deg, have been tested and these results will be presented to help demonstrate the flexibility of the measurement concept. As in all scatter detection instruments, the measurement cross-section is a function of the particle size and the collection optics. An analysis of this functional relationship is given. The complete optical package and electronic processing systems required for the convenient operation of this instrument have been developed. Descriptions of the hardware and software required for the implementation of this technique are given.

Contributed by the Gas Turbine Division of THE AMERICAN SOCIETY OF MECHANICAL ENGINEERS and presented at the Winter Annual Meeting, New York, N.Y., December 2–7, 1979. Manuscript received at ASME Headquarters August 22, 1979. Paper No. 79-WA/GT-13.

Droplet Sizing Interferometry

Theoretical Description. Light scattered by spherical droplets with diameters much larger than the wavelength of the incident light can be described by the simplified geometrical optics theory. Van de Hulst [6] has shown that for $\alpha > 10$ (where $\alpha = \pi d/\lambda$), the scattered electromagnetic radiation can be described using the simplified theories of diffraction, refraction and reflection. One half of the scattered light is due to diffraction which is concentrated in the forward direction about the laser beams. The other half is due to refraction and reflection which are scattered in all directions about the spherical droplet. With the appropriate selection of off-axis angles for the size and index of refraction of the droplets to be measured, the diffracted light can be removed from consideration.

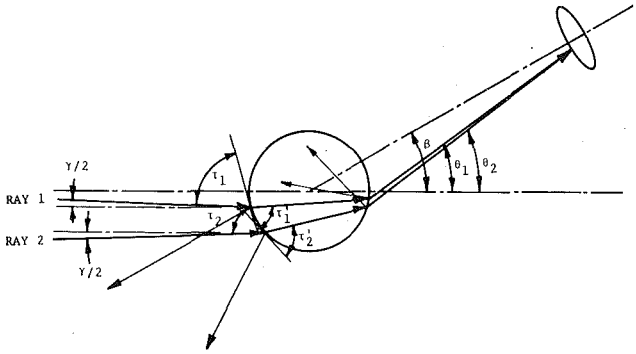

Fig. 1 Ray trace diagram showing the angles used in the light scattering analysis

The present technique for sizing spherical droplets is based on the measurement of the relative phase shift that occurs when two light waves pass through the droplets on different paths. Figure 1 shows a sketch of two rays (which are normal to the waves) that pass through the droplet and arrive at a common point on the plane of detection. It remains to measure the interference pattern of the scattered light and relate it to the droplet size. To accomplish this, a method was adopted which has been used for particle sizing interferometry [1]. The schematic diagram of the optical arrangement required for the implementation of the technique and the coordinate system used in the analysis are given in Fig. 2. By measuring the visibility or amplitude modulation of the interference pattern formed by the scattered

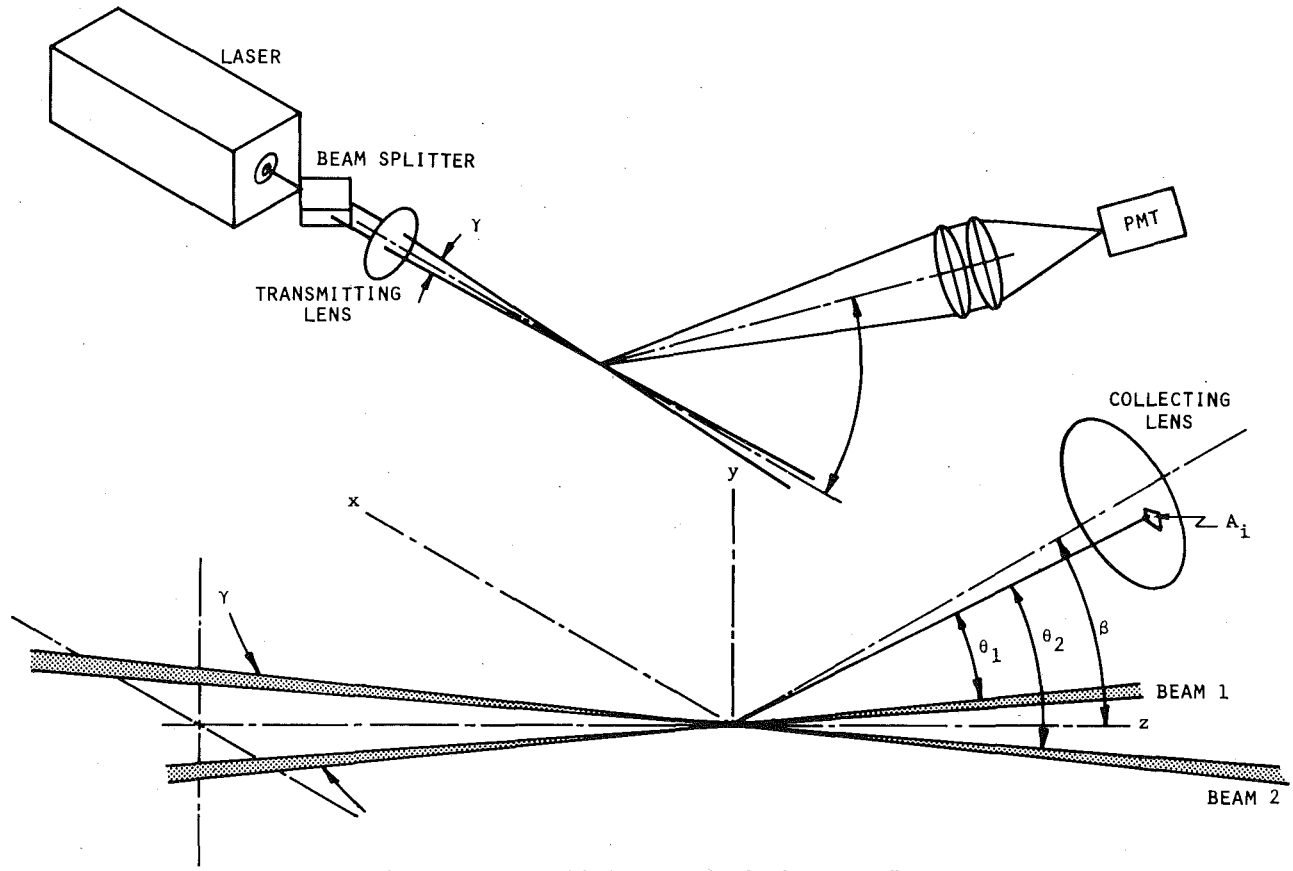

Fig. 2 Schematic diagram of the interferometer showing the coordinate system

Nomenclature

A = area of the lens aperture
d = particle diameter
E_{s1}, E_{s2} = complex electromagnetic field functions
I = scattered light intensity
I_D = Doppler component of the Doppler burst signal
$I_{max}(I_{min})$ = total energy received by the collecting lens when a bright (dark) fringe is centered on the lens
m = droplet index of refraction
n = light wave impedance
P = pedestal component of the Doppler burst signal
V = measured signal visibility
x = coordinate normal to the bisector and in the plane of the two beams
y = coordinate normal to the bisector and the plane of the two beams
Z = coordinate along the bisector of the two beams
$\alpha = \pi d/\lambda$ = dimensionless size parameter
β = angle measured from the bisector of the laser beams to the center of the collecting lens
γ = beam intersection angle
$\delta = \lambda/2\mathrm{Sin}\gamma/2$ = interference fringe spacing in the probe volume
θ_1, θ_2 = scattering angles from beams 1 and 2
λ = laser light wavelength
σ = phase angle between scattered fields E_{s1} and E_{s2}
τ_1, τ_2 = ray incident angles measured from the droplet surface tangent for beams 1 and 2
τ_1', τ_2' = refracted ray angles for beams 1 and 2

light and collected over a finite collecting aperture, adequate information to size the droplets can be obtained.

The intensity of the light scattered by a droplet located at the intersection of two laser beams can be written as

$$I = \frac{1}{n}\{|E_{s1}|^2 + |E_{s2}|^2 + 2|E_{s1}|\,|E_{s2}|\cos\sigma\} \tag{1}$$

where $|E_s|$ is the magnitude of the complex field function, σ is the phase angle between the scattered fields E_{s1} and E_{s2}, and n is the wave impedance. The visibility which is the ratio of the a.c. or Doppler component of the signal to the d.c. or pedestal component (Fig. 3) can be defined as

$$V = 2\left|\frac{\int A_{\text{lens}} \int |E_{s1}|\,|E_{s2}|\cos\sigma\, dA}{\int A_{\text{lens}} \int \{|E_{s1}|^2 + |E_{s2}|^2\}\, dA}\right| \tag{2}$$

The scattered light amplitude functions are described using the theory outlined in Van de Hulst [6] and the details of the analysis are given in reference [5]. Information on the size of the droplet is contained in the phase shift of the light waves passing through the spherical droplet. Two plane waves incident on the droplet, one from each beam, pass through the droplet at angles that differ by the beam intersection angle. The waves scattered from each beam arrive at the detection plane with a phase difference which forms the interface pattern. Relationships describing the phase shift of the light waves passing through the droplet (or reflected from it) assume that the particles are spherical. However, for most applications, this assumption is good as has been demonstrated by holographic and flash photography imaging of the spray droplets. In general, detecting reflected light is not as sensitive as refracted light for sizing droplets, but can be advantageous in some special applications. For example, when sizing opaque fuel droplets, there is no choice but to collect reflected light. The use of a small f/No. will increase the area of the droplet from which scattered light is detected and will thus provide adequate sensitivity to the droplet size.

There are angles at which the light reflected and refracted by the droplet are of the same order of magnitude but will be out of phase. Light collection at these angles should be avoided in order to prevent ambiguity in the measurements. In some special cases, the visibility from the reflected component can be very close to that measured from the refracted light. Fortunately, the expressions are simple enough such that the visibility curves for any number of collection angles, collection f/Nos. and indices of refraction can be calculated easily with a computer.

Figure 4 shows the theoretical curves relating the visibility to the particle size to fringe spacing ratio (d/δ), for three off-axis collection angles. By choosing the appropriate value of δ any size range of 10:1 can be measured within the total range of 3 μm to 5 mm. The 10:1 size range is limited by the loss of sensitivity of the visibility to droplet size at the high visibility end and the secondary increase in visibility at the low end where more than one particle size could produce the same visibility.

Parameters affecting the measured visibility include the fringe spacing, the collection aperture (shape and size), the collection angle, and the droplet index of refraction. The fringe spacing, or more appropriately, the beam intersection angle determines the phase difference of the two waves passing on different paths through the droplet and arriving at the same point in the detection plane. A unique relationship exists between the projected fringe spacing and the incident beam intersection angle, droplet index of refraction and diameter. The projected fringe pattern, Fig. 5, collected over a finite lens aperture produces a visibility that will depend on the size and shape of the collection aperture. In the detection plane, the scattered fringe

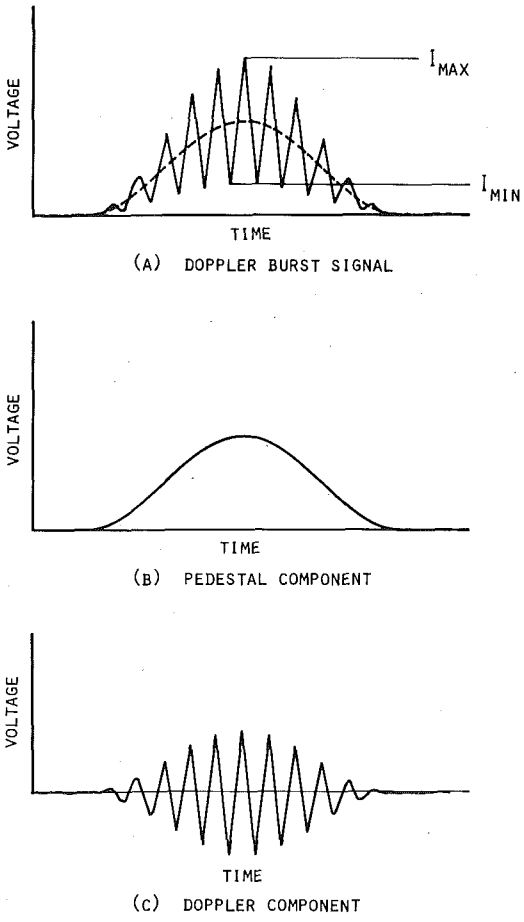

Fig. 3 Doppler burst signal showing the doppler and pedestal components

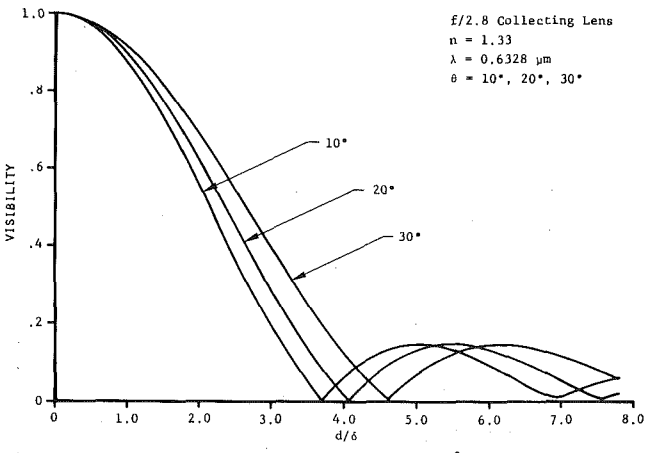

Fig. 4 Theoretical curves relating the visibility to d/δ with different off-axis angles

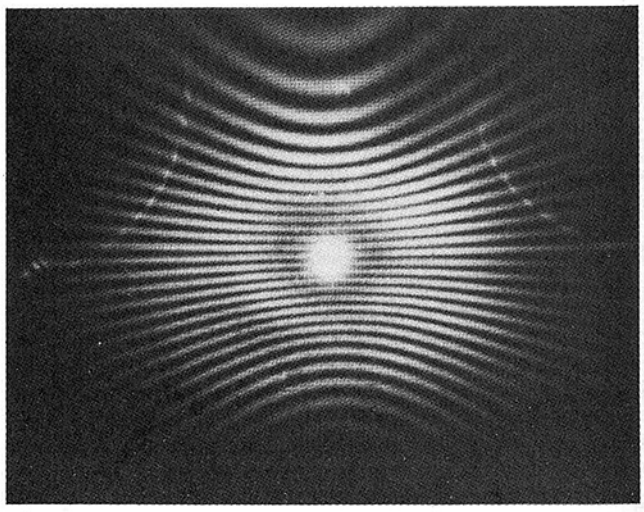

Fig. 5 Photograph of the far field scatter distribution

pattern forms hyperbolic curves centered on the transmitted beams. Larger off-axis angles increase the visibility detected because the spacing of the fringes produced by the scattered light increases with distance from the beam axis.

The droplet index of refraction influences the phase shift produced as the waves pass through the droplet; that is, when refracted light is collected. The visibility produced by reflected light is independent of the index of refraction which makes it a useful alternative when refracting index is unknown. Figure 6 demonstrates the relative effect of the index of refraction on the visibility produced by refracted light at 30 deg. A rather extreme difference in refractive index of 1.33 (characteristic of water droplets) and 1.45 (for some organic compounds) would cause a measurement uncertainty of $\sim \pm 6$ percent if the index was assumed to be 1.4. The change of index of refraction of liquids with temperature is very small. For example, water changes $m_0 - m_{100} \cong 0.014$ over 100°C change in temperature. If larger changes of index of refraction are expected (for instance, in pressurized combustors), reflected light should be collected since its visibility is independent of m.

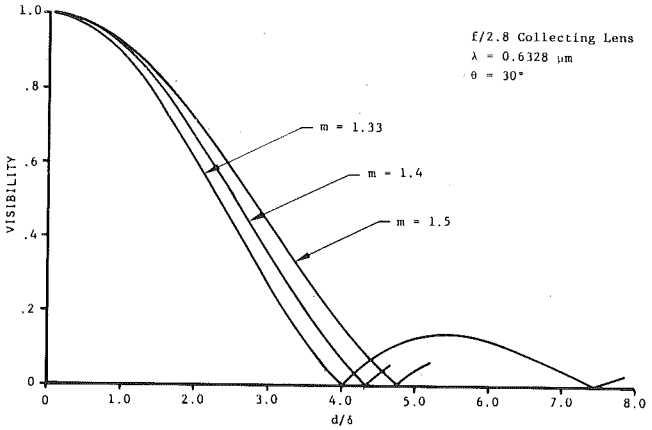

Fig. 6 Effects of refractive index on the visibility curve

Experimental Verification

Extensive droplet measurements were made of known-sized droplets throughout the size range of the instrument and with various optical configurations. In the intermediate size range (30 μm to 500 μm), the Berglund-Liu [7] vibrating orifice monodisperse particle generator was used to produce known-sized primary droplets. Figure 7 shows an example of one such mono-disperse stream of droplets 46 μm in diameter produced by the device. The small sizes (3 to 30 μm) required the use of the dilution technique which entailed mixing alcohol and oil together in a known concentration and to form primary droplets from the solution. Then the alcohol, being more volatile, evaporated to leave small secondary droplets of oil of known size.

Producing large droplets (2 − 3 mm) was accomplished with a hypodermic needle and a constant flow-rate syringe drive used to form a steady stream of drops. Knowing the drop formation rate and liquid flowrate, the droplet size was accurately determined. Photographs of these droplets were also made to verify their size.

The instrument was used to measure the monodisperse droplet streams and the results were stored in histogram form on the video display unit. Figure 8 is an oscilloscope trace of a string of Doppler burst signals produced by the instrument while measuring the droplet stream shown in Fig. 7. A histogram of the measured 46 μm droplets is given in Fig. 9. With 64 bins or size increments per decade of size range, most often only one bin would fill even after several repeated measurements. Broadening in the data distribution was inevitably traced to the monodisperse generator. Although the droplet generator provided exceptionally uniform droplet sizes when it is working properly, its use requires a great deal of patience and careful operating practices to maintain optimum conditions.

Figure 10 shows the comparison of the measured visibility related to droplet size and the theoretically computed curves. These examples are typical of the results obtained for different collection angles and optical parameters. It was determined that the large droplets could be measured with the interferometer to ±2 percent of the actual size determined by direct measurement. Similar accuracies were observed in the intermediate size range (30 to 500 μm). In the size range of 3 to 30 μm, it was much more difficult to control the droplet formation due to difficulties with the monodisperse generator. Nonetheless, the achievable accuracy was determined to be within ±5 percent of the expected droplet size.

Measurements in sprays were also performed to evaluate the technique when used in high density polydisperse sprays. By comparison to the on-axis mode of operation, the signals at a 30 deg off-axis angle, for example, showed significant improvement in the signal-to-noise ratio because the aperture on the photo-multiplier rejects the light scattered from all particles passing through the beams except those that pass through the beam overlap region. This also serves to reduce the error in the measurement resulting from droplets being detected that did not cross the beams where they completely overlap. The reduction in the measurement cross-section served to signifi-

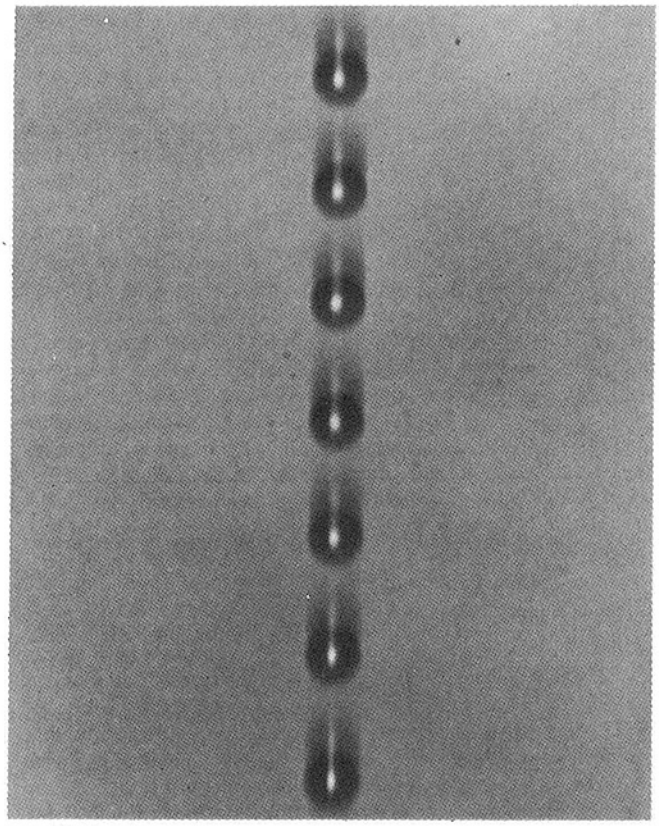

Fig. 7 Monodisperse stream of water droplets 46 μm in diameter

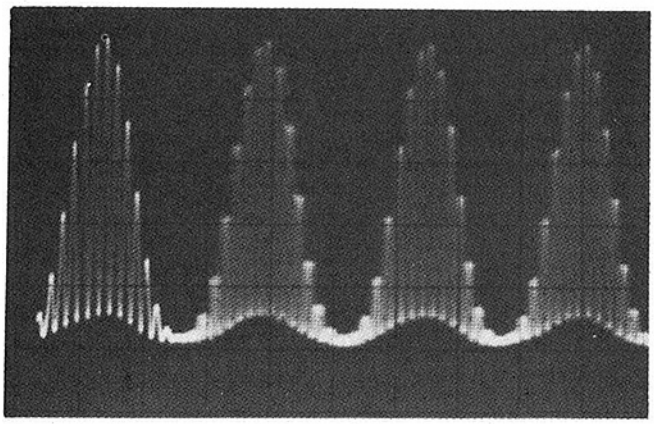

Fig. 8 Oscilloscope trace of doppler burst signals produced by the monodisperse droplet stream

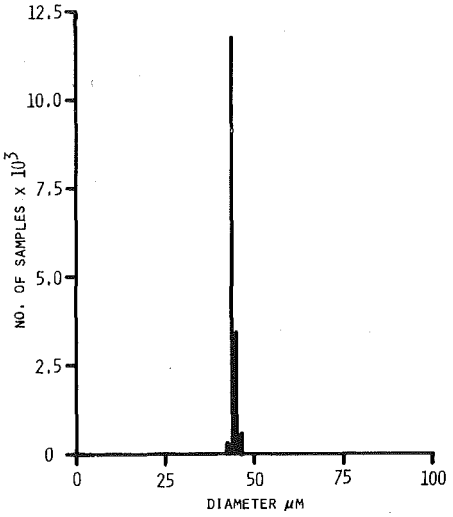

Fig. 9 Histogram of the measured 46 μm droplets

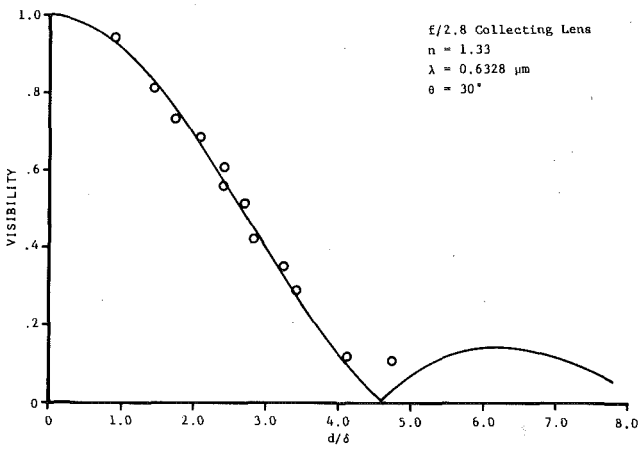

Fig. 10 Comparison of the theoretically computed curves to the measured results

cantly reduce the probability of more than one droplet being detected in the probe volume at one time. A qualitative estimate of the spray number densities that can be handled with the system was obtained by observing the separation between signal bursts on the oscilloscope trace. Sprays with at least an order of magnitude higher number density than was measurable with the on-axis technique could be measured with the off-axis scatter detection method.

In very dense sprays or as a result of facility constraints, 90 deg scatter detection can be used. The light scattered by the droplet is, in this case, dominated by reflection. Figure 11(a) shows the schematic of the measurement region for this case. It is not difficult to see how the 90 deg cone of light collection intersecting the focused laser beams forms an extremely small measurement volume. The focused beam diameters can be as small as 50 μm in the standard system and the aperture on the photomultiplier is set to admit the image of the beam ($\sim$ 50 μm diameter for 1:1 magnification). The theoretical curve for the 90 deg scatter detection angle is shown in Figure 11(b) along with experimentally obtained data points that verify the predictions. Good agreement demonstrates the accuracy of the theoretical predictions and serves to demonstrate the versatility of the method.

Defining the Measurement Cross-Sectional Area

As discussed above, one of the most important characteristics of the off-axis particle sizing interferometer method is its ability to restrict the measurements to a very small cross sectional area. This reduces the probability of multiple particles in the proble volume and thus allows the application of the method in the presence of high particle densities. Particles crossing the probe volume will scatter light

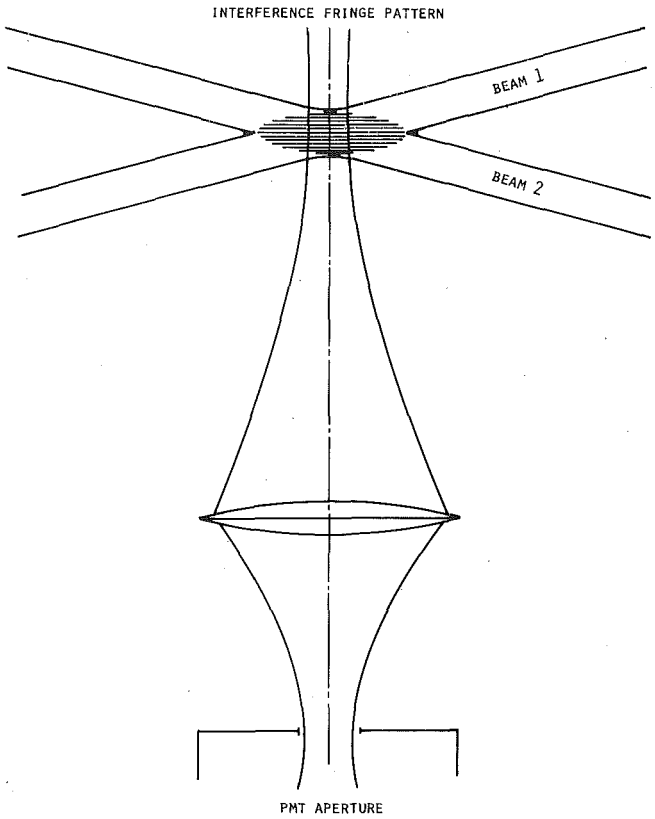

Fig. 11(a) Schematic of the 90 deg light scatter detection showing the effective reduction in the measurement cross section

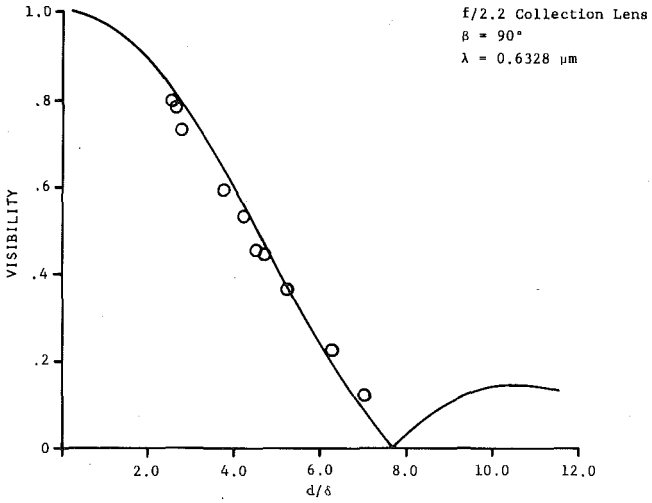

Fig. 11(b) Visibility curve for the 90 deg light scatter detection with measured data

in proportion to their size [6]. However, Fig. 4 shows that in the range of interest (no ambiguity) the larger particles will also have a smaller visibility. That is, the pedestal component of the signal will grow with the size of the particle but the Doppler modulation will grow as the product of the pedestal and the visibility. This product is zero when the diameter is very small, reaches a maximum for intermediate size particles and decreases to zero again for larger particles. Figure 12 illustrates this effect.

The magnitude of the pedestal and the Doppler component will then determine the size of the sampling volume. Particles with a large magnitude of the Doppler component will be detected over a larger volume than those with a smaller modulated signal.

The instrument described will count the number of particles in each size range. Because the probability of detecting particles that produce a small modulated signal (have a small sampling volume) is smaller

than the probability of detecting particles with a large modulated signal, the instrument will display a biased histogram of particle size versus the number of particles. In order to correct for this biasing effect, the detectable cross sectional area of each particle size must be known. The number of particles detected at a given size range will then be divided by the normalized cross sectional area to obtain the correct distribution. Notice that this correction is necessary in any optical method presently used.

Some of the details to obtain this detectable cross sectional area will now be presented.

For any configuration the visibility can be expressed as:

$$V = \frac{I_{\max} - I_{\min}}{I_{\max} + I_{\min}} \tag{3}$$

where $I_{\max}$ ($I_{\min}$) is the total energy received by the collecting lens when a bright (dark) fringe is centered over the lens. This definition is equivalent to equation (2).

The pedestal component is given by (see Fig. 3):

$$P = \frac{I_{\max} + I_{\min}}{2} \tag{4}$$

and the peak to peak Doppler component by:

$$I_D = I_{\max} - I_{\min} \tag{5}$$

Detectable particles are those that produce signals with a Doppler intensity component exceeding the minimum threshold level (I_T) imposed by the electronics but do not saturate the amplifiers.

In order to limit the size of the detectable cross sectional area and at the same time obtain an accurate measurement of the visibility, it is required that a minimum number of fringes be processed by the visibility processor. Typical number of fringes range between 8 and 20. Hence, it is only of interest to detect particles that exceed the threshold when crossing that many fringes.

If the gain of the photodetector, the amplification level of the processor, or the intensity of the laser were increased, there would be particles whose scattered light would saturate the amplifiers and would not be detected due to the overload protection system. This feature is used to obtain very broad particle size distributions, since the dynamic range is constrained by about a factor of 10. That is, of particles in the range 10 to 600 μm are to be measured, two ranges would be used to measure this broad distribution: 10 to 90 μm and 80 to 640 μm. It is important that the gain of the detector be set properly such that all particles in the decade size range are detectable. For this purpose, an electronics level detection logic circuit has been developed to automatically set the photomultiplier gain.

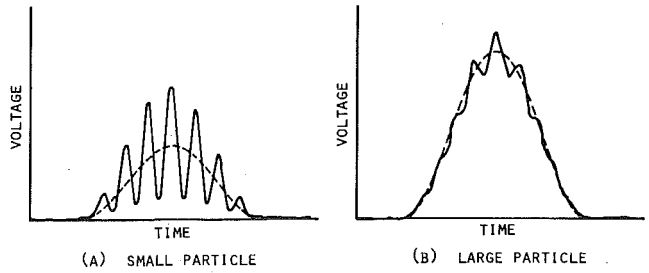

Fig. 12 The effect of particle size on the signal visibility and amplitude

Figure 13 illustrates a particle in the probe volume. The image of this particle will be collected through an aperture by the photomultiplier tube. If the scattered light collected by the PM tube exceeds the threshold when crossing the minimum number of fringes established without overloading the amplifiers, its signal will be accepted and stored in the memory of the processor.

Notice that if an aperture did not limit the measuring area, particles far from the center of the probe volume would be detected. The visibility of such particles is different [8] than particles of similar size crossing through the center of the probe volume. To minimize this error, the measuring area is kept as small as possible using a small aperture on the photomultiplier tube. The off-axis light scattering detection technique is especially effective in minimizing this error source. Since the measuring cross sectional area can be used to determine the sample volume of different size particles, and the particle velocity is measured, the number density of the particle or droplet field can be determined.

Instrument Design

Optical Configuration. The optical system must have sufficient flexibility to accommodate the wide range of size measurements, various off-axis scattered light detection angles, and flow directions. Figure 14 is a schematic drawing of the optical system which consists of separate transmitting and collecting packages. Separation of the two packages is convenient for off-axis forward scattering applications wherein the optics must be located on both sides of the test facility. Where this is not the case, the packages can be fixed together on a common base.

A 15 mW helium-neon laser provides the required coherent light source. Several optical configurations are required to provide the probe diameters and interference fringe spacings appropriate to the size ranges to be measured. With the combination of the collimating beam expander and transmitting lens that can be easily inserted or removed from the optical path, the complete range of probe diameters can be achieved. A path-matched beamsplitter and rotator assembly has been designed to make the setting of the beam spacing and flow direction sensitivity accurate and easy. To establish the correct optical arrangement for the droplet size range to be measured, the estimated

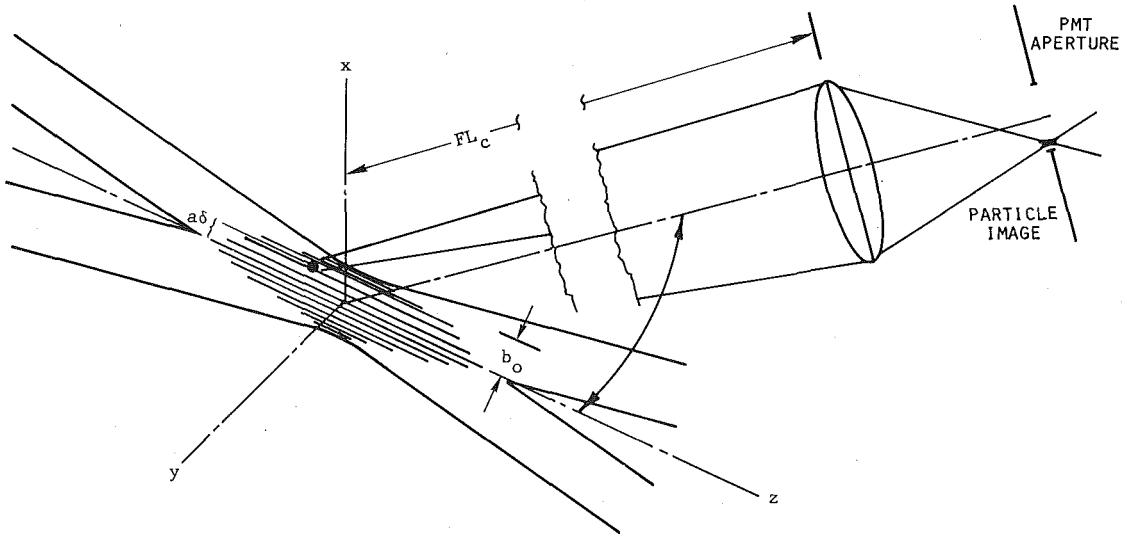

Fig. 13 Schematic showing the constraints on the measurement cross section

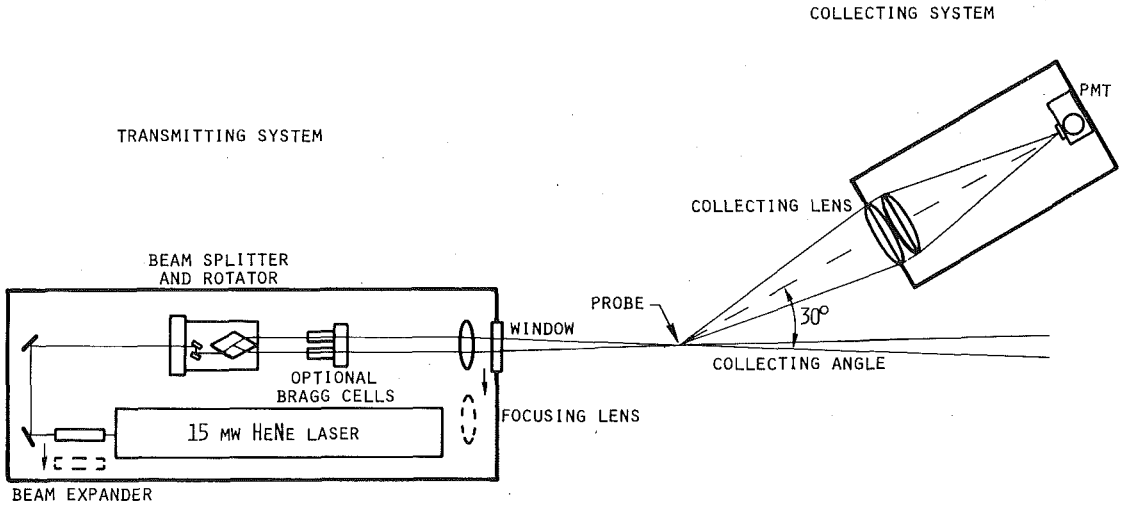

Fig. 14 Optical configuration of the instrument

mean size is input to the system's microcomputer and the required optical setup is displayed on the video monitor. In the standard system, the beam crossover that forms the measurement volume is 75 cm from the exit window. This distance can be changed from a few centimeters to several meters if necessary.

The transmitting system can be fitted with Bragg cell frequency shifting to control the relative frequency bandwidth and to resolve any flow direction ambiguity. An example of such an application is in the measurement of the mass flow of water droplets impinging on a nuclear reactor fuel rod and the amount of droplet rebound that occurs. With the present system, the size and velocity of each droplet incident and rebounding can be measured. Frequency shifting allows the separation of the incident droplets from those rebounding.

Scattered light is collected in the standard system with a 125 mm diameter, f/5 lens. In the collecting optics package, the collected light is focused by a second lens onto an aperture on the photomultiplier tube. The size of the aperture is variable to accommodate the particular probe diameter being used and still remain small enough to block light scattered from outside of the probe volume.

Electronics for Data Processing. A visibility processor has been developed to rapidly and accurately measure the signal visibility and Doppler period. The system has several innovations that ensure accuracy in the signal processing and simplify the operation of the instrument. A TMS 9900 16-bit microprocessor is used in the system to control the processing functions and data outputs.

Signals from the photomultiplier are separated into the ac and pedestal components with built-in filters. The a-c signal is tested with a three-level detector that rejects signals that do not cross the positive threshold voltage level, the zero level, and then the negative threshold on each cycle of the burst. This circuit is very effective in rejecting spurious noise that may have been generated electronically or optically. In addition, a periodicity check is made on the burst signal to ensure that the period of the Doppler frequency remained constant over the burst duration to within a preset percentage. The Doppler period is measured over 5, 8 or 16 cycles. A 62.5 MHz clock oscillator is used to load counters that are turned on by the first valid cycle and turned off at the end of 5, 8 or 16 cycles. The microprocessor determines the Doppler period averaged over the number of cycles, routes the data to the front panel display and multiplexes the period and visibility to the output port. Visibility can be measured over a signal frequency range from 2 KHz to 5 MHz and the Doppler period from 2 KHz to 10 MHz.

Signal visibility is determined by performing an analog integration of the rectified a.c. and d.c. components of the signal and dividing the result. The result is displayed on the front panel LCDs and also output as a 10-bit number. Data rates as high as 10^4/s are possible with this system.

In an effort to remove the subjective judgment from the setup of the system, the instrument functions have been automated wherever possible. Setting the correct photomultiplier voltage is handled by the microprocessor which automatically raises the gain so that the largest particles will not saturate the amplifiers but the smallest particles in the range will be detected. A circuit has been introduced to automatically null any d-c background that may occur. The signal detection level or threshold can be set automatically or manually.

Data Management. A microcomputer utilizing a 6502 microprocessor is used for the data handling and reduction. The system produces histograms of the droplet size and velocity on a video display unit as the data is accumulated. Sample time and the number of samples recorded are also displayed. When a preset number of samples have been measured, the tabulated results can be printed or stored on floppy disks. Two 100 kilobyte floppy disk units are provided, one for software storage and the other for data.

Software is used to reduce the data and to calculate the various mean particle sizes, e.g., Sauter, linear, surface and volume mean diameters. With the measured velocity and the probe cross section, the mass flux and concentration can be evaluated. Mean velocity, turbulence intensity and droplet size-velocity correlations are also available from the measured quantities.

Preliminary Experimental Data

In fuel spray combustion, it is known that the spray density, and the fuel-air mixing can significantly increase the amount of unburned hydrocarbons and formation of NO_x in the flow. The present method will be invaluable in evaluating the affects of droplet size and velocity, and the air-fuel mixing on the combustion processes. A measurements program is currently in progress to characterize the spray from a Sonicore atomizer operating with Number 2 fuel oil. Measurement of the atomizer spray distributions were made with the droplet sizing interferometer and will also be made with the holographic imaging system. These measurements will allow the comparison of the measured size distributions and a determination of the morphology of the spray.

Figure 15 shows the Sonicore atomizing nozzle mounted in the spray rig. It is evident from the scattered light intensity seen in the photograph that the spray droplet number densities are high. Nonetheless, single droplet measurements were obtained without difficulty. Measurements were possible at locations within a few centimeters of the nozzle exit. The spray size and velocity distributions were measured at various axial and radial locations. For each droplet measured, the size and velocity was determined and stored in the data management system memory. These data could then be used to evaluate the size and velocity distributions, turbulent fluctuations, and the size velocity correlations.

A sample size distribution is shown in Fig. 16. This sample was obtained 5 cm below the nozzle exit on the centerline of the spray. The nozzle air pressure was 6.89 kPa. At this station, the Sauter mean droplet diameter and the size standard deviation were measured to

Fig. 15 Photograph showing the Sonicore spray nozzle, the spray plume, and the laser beams forming the measurement cross section

be d_{32} = 48.6 μm and s = 7.58 μm, respectively. The mean size was found to increase slightly with radial distance from the spray centerline. This was due to the fact that the droplets left the nozzle with a radial component of velocity. The larger droplets had a greater momentum, and hence traveled further outward from the centerline of the spray.

In Fig. 17, the droplet velocity has been plotted for increments of size taken at the same location as the size distribution of Fig. 16. The smaller droplets can be seen to have decelerated more rapidly than the larger ones. This effect produces differences in the size distributions determined by systems that measure over a collection of particles in a collimated laser beam and those that measure single particles. Since the droplet flux given by

$$F = N(d)\, v(d)\, A \tag{6}$$

is constant (assuming no impaction or evaporation), a change in velocity, $v(d)$, of the small droplets may result in a proportionate change in the number density, $(N(d))$. Thus, an instrument that measures the particle size distribution over a volume will measure more of the slower particles than the single particle counter instruments. The droplet sizing interferometer responds to the particle flux and local number densities can be obtained since velocities are also measured. These local values can be integrated throughout a cross section to obtain the average size provided by the first instrument or can be used as such when the size distribution is needed.

The ability to measure the size distribution at essentially point locations in the spray proved to be important. Because of the nozzle construction, the spray field was not axisymmetric. Furthermore, the small droplets at the outer edge of the spray were seen to recirculate even with a 0.4m/s screen airflow around the nozzle. A path integration measurement of the spray would have been biased toward the smaller droplets depending on the amount of recirculation that occurred.

The complete nozzle characterization data and analysis will be published at a later date.

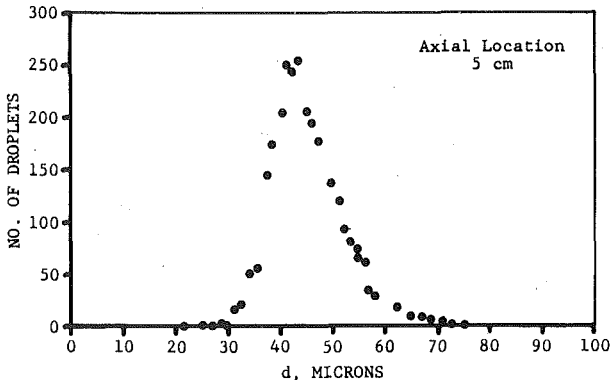

Fig. 16 Sample droplet size distribution of the Sonicore atomizer

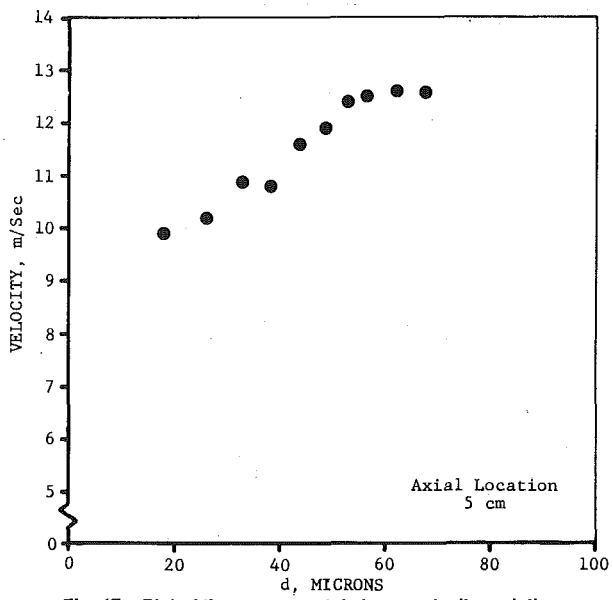

Fig. 17 Plot of the spray droplet size — velocity variations

Conclusions

An instrument for measuring droplet size and velocity in sprays has been developed. Although the method is conceptually similar to particle sizing interferometry, the interference pattern measured is produced by a different light scattering mechanism. Utilizing off-axis light scattering detection made possible with this analysis, has proven to be a significant advantage when measuring in high density sprays. By the measurement of known-sized droplets, the theoretical description of the visibility variation with droplet size has been verified for both refracted and reflected light.

Measurement difficulties using refracted light may be experienced if the droplet index of refraction is not known or varies because of thermal effects. This effect is, in general, very small (Fig. 11) and reflected scattered light could be used when large changes are expected in the index of refraction. Droplet asphericity may also affect the measurements. But, if the droplets are randomly oscillating, measurement over 10,000 or more should produce an accurate measurement of the equivalent sphere. When the droplet is deformed in some preferred direction, for example, because of the aerodynamic pressure distribution, the fringe pattern can be rotated to measure the droplet diameter in two or more directions. A shape factor of the droplet can then be determined.

The most significant contributions realized with the present technique are the ability to make measurements over a very large size range (3 μm to 5 mm). The system can be used either as an on-axis particle sizing interferometer for particles in the size range of 2 to 200 μm or in the off-axis forward, 90 deg, or backscatter mode when sizing liquid droplets. It is conceivable that more than one light scattering mode would be used for simultaneous particle and droplet measurements or to cover more than one decade of droplet size at one time.

Acknowledgment

The Sonicore atomizer measurements were conducted in a spray facility provided by the Energy and Environmental Research Corporation, El Toro, Calif. and funded under the Fundamental Combustion Research Program project manager, Mr. Steve Lanier.

References

1 Farmer, W. M., "The Interferometric Observation of Dynamic Particle Size, Velocity and Number Density," Ph.D. Thesis, University of Tennessee, 1973.

2 Robinson, D. M., and Chu, W. P., "Diffraction Analysis of Doppler Signal Characteristics for a Cross-Beam Laser Doppler Velocimeter," *Applied Optics*, Vol. 14, No. 9, Sept. 1975.

3 Roberds, D. W., "Particle Sizing Using Laser Interferometry," *Applied Optics*, Vol. 16, No. 7, July 1977.

4 Adrien, R. J., and Orloff, K. L., "Laser Anemometer Signals: Visibility Characteristics and Application to Particle Sizing," *Applied Optics*, Vol. 16, No. 3, 1977.

5 Bachalo, W. D., "A Method for Measuring the Size and Velocity of Spheres by Dual Beam Scatter Interferometry," submitted to *Applied Optics*.

6 van de Hulst, H., *Light Scattering by Small Particles*, John Wiley & Sons, New York, 1957.

7 Berglund, R. N., and Liu, B. Y. H., "Generation of Monodisperse Aerosol Standards," *Environmental Science and Technology*," Vol. 7, Feb. 1973.

8 Roberds, D. W., Brasier, C. W., and Bonar, B. W., "Use of a Particle Sizing Interferometer to Study Water Droplet Size Distribution," *Optical Engineering*, Vol. 18, No. 3, May–June 1979.

Ali Montakhab[1]

Mechanical Engineering Department,
Stanford University, Stanford, CA
Mem. ASME

Analysis of Heat Transfer Surface Geometries for Dry Cooling Tower Applications

An analysis of heat exchanger surface geometries for the purpose of reducing dry cooling tower cost is presented. Two sets of results are derived. The first set can be used to evaluate heat transfer surface geometries in an attempt to select those most suitable for dry cooling tower applications. The second set of results can be used to direct research and development efforts toward developing better geometries for dry cooling tower applications. The first set of results is general and is applicable to all heat exchanger surface geometries. The second set is valid only for helical round or continuous fins having smooth, serrated, or cut fins and for staggered and in-line tube arrangements. The methods developed in this paper are not restricted to dry cooling towers per se, but are valid for other applications of fin tube heat exchangers as well.

Introduction

There is growing acceptance of the future necessity for dry and wet/dry cooling tower systems for large power station. This is in spite of their economic penalty compared with once-through cooling, cooling ponds, and evaporative cooling towers. If technological improvements succeed in reducing the current costs of dry cooling towers, their future applications will be accelerated.

The cost of the heat exchanger surface is a large fraction of the total dry cooling tower cost, and the tower structure, which is indirectly affected by the heat exchanger system, is also a major cost factor. In a mechanical-draft dry cooling tower, a major operating cost is the fan power requirements, which is dependent on the pressure drop and flow rate of the air through the heat exchanger. The hot-fluid pumping power in the indirect system is also another operating cost factor. In the direct air-cooled condenser system, this pumping power is not applicable but the pressure drop of the steam in the condenser has to be paid for in terms of a higher turbine backpressure, which results in lower plant efficiency and specific power.

A method was developed in [1] for the design, analysis, and prediction of dry cooling tower performance. In [1] tower size, pumping power requirement and heat exchanger surface geometry is related to the flow conditions, heat exchanger surface geometry and other key design variables. The present paper uses the results obtained in [1] as a basis for the analysis of finned tube surface geometries in order to establish methods of reducing heat exchanger surface area, tower size, and pumping power requirements.

Influence Coefficients

Four criteria are used in studying the effect of heat transfer surface geometry on dry cooling tower design: (1) the draft height or pumping power requirement on the air side Z_E, (2) heat transfer surface area requirement $\overline{A}$, (3) pumping power requirement on the water side $\dot{W}k_p$, and (4) heat exchanger frontal area A_1. The expressions for these quantities are derived in [1] and is summarized in the table of influence coefficients (Table 1) given in this reference:

draft height:[1]

$$Z_E = \frac{1}{\sigma^2} \cdot \frac{f\lambda}{\mathrm{St}} \frac{V_1^2}{2g} \cdot \theta\theta_m \frac{N_{tu}}{\epsilon\delta} \tag{1}$$

heat transfer surface area:

$$\overline{A}/\dot{q} = \frac{1}{\rho_1 c_p T_1} \cdot \sigma \cdot \frac{\lambda}{\mathrm{St}\, V_1} \cdot \frac{N_{tu}}{\epsilon\delta} \tag{2}$$

water-side pumping power requirement:

$$\frac{\eta_p \dot{W}k_p/\dot{q}}{f_w V_w{}^3} = \frac{1}{\rho_1 c_1 T_1} \cdot \frac{\rho_w}{2g_c} \cdot \frac{\sigma\sigma_w}{\alpha D_i} k_\ell \cdot \frac{\lambda}{\mathrm{St}\, V_1} \cdot \frac{N_{tu}}{\epsilon\delta} \tag{3}$$

heat exchanger frontal area:

$$A_1/\dot{q} = \frac{1}{\rho_1 c_p T_1} \cdot \frac{1}{V_1} \cdot \frac{1}{\theta - 1} \tag{4}$$

The influence coefficients for equations (1–4) are given in Table 1.

It is assumed that the water flow rate, water inlet and outlet temperature, and ambient conditions are specified. Then, using the approach described in [2], the air temperature rise or air flow rate can be made to result in optimum design conditions exclusive of heat transfer surface geometry selection. If optimum air temperature rise or air flow rate are found, then property-dependent and capacity-rate-dependent influence coefficient of Table 1 can be established. Then to find the conditions for the most suitable heat exchanger surface geometry, it is necessary to study the geometry-dependent and Reynolds-number-dependent influence coefficients of Table 1.

For fixed values of property-dependent and capacity-rate-dependent influence coefficients and for given values of η_p and k_ℓ, the following expressions can be written from Table 1:

[1] Because the geometry of the heat exchanger surface affects only the Z_E component of the draft height, it is not necessary to include other draft height component in this analysis.

[1] Present address: Teheran University of Technology, P.O. Box 3406, Teheran, Iran

Contributed by the Utility Operations Committee for publication in the JOURNAL OF ENGINEERING FOR POWER. Manuscript received at ASME Headquarters September 14, 1979.

Table 1 Influence coefficients for the draft height, heat transfer surface area, water pumping power, and heat exchanger frontal area

Design Parameter	Property-Dependent Coefficients: Air	Property-Dependent Coefficients: Water	Geometry-Dependent Coefficient	Reynolds-Number-Dependent Coefficient	Capacity-Rate Dependent Coefficient
Z_E	1	1	$\frac{1}{\sigma^2}$	$\frac{f\lambda}{\mathrm{St}}\frac{V_1^2}{2g}$	$\theta\theta_m\frac{N_{tu}}{\epsilon\delta}$ [a]
$\frac{\overline{A}}{\dot{q}}$	$\frac{1}{\rho_1 c_p T_1}$	1	σ	$\frac{\lambda}{\mathrm{St}\,V_1}$	$\frac{N_{tu}}{\epsilon\delta}$
$\frac{\eta_p \dot{W}k_p/\dot{q}}{f_w V_w{}^3}$	$\frac{1}{\rho_1 c_p T_1}$	$\frac{\rho_w}{2g_c}$	$\frac{\sigma\sigma_w}{\alpha D_i}k_\ell$	$\frac{\lambda}{\mathrm{St}\,V_1}$	$\frac{N_{tu}}{\epsilon\delta}$
$A_1/\dot{q}$	$\frac{1}{\rho_1 c_p T_1}$	1	1	$\frac{1}{V_1}$	$\frac{1}{\theta-1}$

[a] Notice that $N_{tu}/\epsilon\delta = 1/F\Delta T_{\ell m}/T_1$.

$$Z_E \propto \frac{f\lambda}{\mathrm{St}\,\sigma^2}\frac{V_1^2}{2g}, \tag{5}$$

$$\frac{\overline{A}}{\dot{q}} \propto \frac{\lambda\sigma}{\mathrm{St}\,V_1}, \tag{6}$$

$$\frac{\dot{W}k_p}{\dot{q}} \propto f_w V_w{}^3 \cdot \frac{\sigma\sigma_w}{\alpha D_i}\cdot\frac{\lambda}{\mathrm{St}\,V_1}, \tag{7}$$

$$\frac{A_1}{\dot{q}} \propto \frac{1}{V_1} \tag{8}$$

It can be shown for circular tubes that the quantity $\sigma_w/\alpha D_i$ in equation (7) is proportional to $D_i{}^*/A_r$, where $D_i{}^* \equiv D_i/D_0$. Introducing this condition into equation (7) enables water pumping power to be represented by $\sigma D_i{}^*\lambda f_w V_w{}^3/\mathrm{St}\,A_r V_1$. Multiplication of the functions for draft height, heat transfer surface area, and water pumping power by the inlet approach velocity V_1 yields groupings that are useful in establishing draft height (X_Z), heat transfer surface area ($X_{\overline{A}}$), and water pumping power ($X_{\dot{W}k}$) for a given heat exchanger frontal area. These groupings are as follows:

$$X_Z \equiv Z_E/A_1 \propto \frac{f}{\mathrm{St}}\frac{\lambda}{\sigma^2}V_1{}^3, \tag{9}$$

$$X_{\overline{A}} \equiv \overline{A}/A_1 \propto \frac{\lambda\sigma}{\mathrm{St}}, \tag{10}$$

$$X_{\dot{W}k} \equiv \dot{W}k_p/A_1 \propto \frac{D_i{}^*}{A_r} f_w V_w{}^3 X_{\overline{A}}. \tag{11}$$

Considering that Z_E, $\overline{A}$, and $\dot{W}k_p$ strongly affect the overall cost of dry cooling tower, these functions may be used as a measure to: (1) evaluate heat transfer surface geometries in an attempt to select suitable surfaces for dry cooling tower applications, and (2) to direct research and development efforts toward the manufacture of new, improved circular finned tube heat exchanger surfaces for the dry cooling tower applications.

Heat Transfer and Flow Friction Data

Reference [3] provides a comprehensive compilation of heat transfer and flow friction design data for finned tube heat exchanger surfaces. These data have been analyzed, and generalized correlations[2] have been proposed in the form of f and j versus Reynolds number [4]. For

[2] By generalized correlations it is meant that the correlation is sufficiently general to apply to a class of geometries, not all geometrically similar, and not just a single geometry and its class of geometrically similar surfaces.

Nomenclature

A_r = ratio of total air-side area/bare tube area
A_1 = heat exchanger frontal area
$\overline{A}$ = heat transfer surface area
c_p = specific heat at constant pressure, air side
D_h = hydraulic diameter, air-side hydraulic diameter
D_i = tube inside diameter
D_o = tube outside diameter
$D_h{}^* \equiv D_h/D_o$
$D_i{}^* \equiv D_i/D_o$
f = friction factor, air-side friction factor
g = acceleration due to gravity
g_c = proportionality constant in Newton's Second Law
H = heat exchanger height
h = convective heat transfer coefficient, air-side convective coefficient
$h^* \equiv h/h_w$
$j \equiv \mathrm{St} \times \mathrm{Pr}^{2/3}$
k = thermal conductivity, air-side thermal conductivity
$k_\ell \equiv L_w/nH$
L_w = water flow length
ℓ_f = fin length
ℓ_p = longitudinal tube spacing
$\ell_p{}^* \equiv l_p/D_o$
m = defined by equation (17)
n = number of passes
N_{tu} = number of heat transfer units
Nu = Nusselt number
Pr = Prandtl number, air-side Prandtl number
$\dot{q}$ = heat transfer rate
Re = Reynolds number, air-side Reynolds number
St = Stanton number, air-side Stanton number
T = temperature, absolute scale*
U = overall heat transfer coefficient
V = velocity, air velocity
V_w = water velocity in heat exchanger tube passages
$\dot{W}k$ = shaft power
X = defined by equations (9–11)
Z_E = draft height due to heat exchanger drag
α = surface area density (transfer area per total volume), air-side surface area density
$\delta \equiv T_{w1}/T_1 - 1$
δ^+ = defined by equation (20)
δ_f = fin thickness
δ_{wall} = tube wall thickness
ϵ = heat transfer effectiveness
η_f = fin efficiency
η_0 = surface effectiveness
$\theta \equiv T_2/T_1$
$\theta_m \equiv (\theta + 1)/2$
$\lambda \equiv h/U$
μ = viscosity, air-side viscosity
ρ = density
σ = ratio of free-flow area/frontal area, ratio of air-side free-flow area/frontal area
∇ = defined by equation (27)

Subscripts

E = heat exchanger
f = fin
p = pump
w = water
1 = heat exchanger inlet

* Absolute temperature scale is used throughout this paper to avoid ambiguity. The reader, however, can use a relative temperature scale wherever appropriate.

a staggered tube arrangement, the heat transfer correlation proposed by [4] for helical, round, smooth fins predicts 80 percent of the data presented in [3] to within ±10 percent and 95 percent of the data to within ±18 percent. For serrated or cut fins, the proposed heat transfer correlation matches 80 percent of the data to within ±15 and 95 percent of the data to within ±20 percent. This correlation is valid for a Reynolds number range of 1000 to 10,000 and an extended area ratio A_r range of 4 to 25. The heat transfer correlation for the continuous-plate finned tubes predicts 80 percent of the data in [3] to within ±12 percent. Fig. 1 compares the deviation of the correlated Stanton number of [4] with the experimental results of Kays and London [5] for circular fins.

The data presented for in-line tube arrangements [3] is somewhat less extensive. The error for heat transfer correlations for in-line flow arrangements is estimated to be ±20 percent. Reference [4] does not discuss the uncertainty of the flow friction design data, however the present study found that the correlations in [4] were in close agreement with data from other sources (e.g., [5]). Fig. 2 compares the deviation of the correlated friction factor of [4] with the experimental results of [5] for circular fins.

The correlations for heat transfer and flow friction proposed by [4] are as follows for the staggered and in-line tube geometries:

$$f = \alpha_1 \left(\frac{D_h^*}{\mathrm{Re}}\right)^{\alpha_D} \left(\frac{1}{A_r}\right)^{\alpha_A} \tag{12}$$

$$j = \left(\frac{\beta_0}{\mathrm{Re}} + \frac{\beta_1}{\mathrm{Re}^{\beta}}\right)\left(\frac{D_h^*}{\ell_p^*}\right)^{\beta_D} \tag{13}$$

Table 2 presents the coefficients and exponents for different fin types for staggered and in-line tube arrangements.

Fundamental Relations

It can be shown that the air/water area density ratio (α/α_w) is equal to A_r/D_i^*, where A_r is the air-side surface area per unit bare tube surface area. For the case of negligible wall resistance and zero fouling resistance, this relation, introduced in equation (13) of [1]:

$$\lambda \equiv \frac{h}{U} = \frac{1}{\eta_0} + \frac{\alpha}{\alpha_w}\frac{h}{h_w},$$

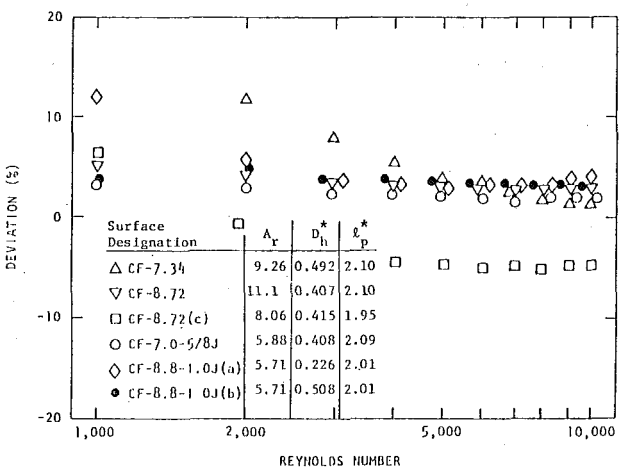

Fig. 1 Correlated Stanton number data [4] compared with experimental data of Kays and London [5]. Deviation ≡ (correlation—experiment)/experiment

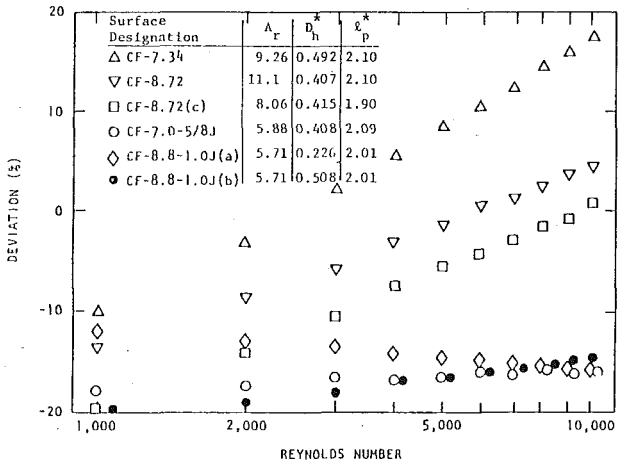

Fig. 2 Correlated friction factor data of [4] compared with experimental data of Kays and London [5]. Deviation ≡ (correlation—experiment)/experiment

Table 2 Coefficients for generalized heat transfer and flow friction correlations[a,b]

Fin Type	a_1[c]	a_D	a_λ	Restriction	β_0	β_1	β	β_D
Helical, round, smooth fins	0.29 (0.145)	0.367 (0.367)	0.170 (0.170)	$\ell_p/D_h \le 4$	0 (0)	3.4 (2.04)	0.30 (0.30)	1.42 (1.42)
				$\ell_p/D_h > 4$	37.5 (22.5)	0.45 (0.27)	0.20 (0.20)	0.65 (0.65)
Helical, round, serrated or cut fins	0.195 (0.0975)	0.300 (0.300)	0.170 (0.170)	$\ell_p/D_h \le 4$	0 (0)	4.76 (2.86)	0.30 (0.30)	1.42 (1.42)
				$\ell_p/D_h \ge 4$	52.5 (31.5)	0.63 (0.378)	0.20 (0.20)	0.65 (0.65)
Continuous-plate fins	0.130 (0.065)	0.330 (0.330)	0 (0)	None	27.5 (16.5)	0.3375 (0.2025)	0.20 (0.20)	0.65 (0.65)

[a] From [4].
[b] The coefficient a_R is defined as

$$a_R \equiv 1 - a_D.$$

The coefficient β_R is given by

$$\beta_R \equiv \frac{1 + \frac{\beta_1}{\beta_0}\beta \mathrm{Re}^{1-\beta}}{1 + \frac{\beta_1}{\beta_0}\mathrm{Re}^{-\beta}}.$$

These coefficients α_R and β_R are used in equations (26) and (29), respectively.
[c] Numbers without parentheses are for staggered tube arrangements; numbers in parentheses are for in-line flow arrangements.

yields the following equation:

$$\lambda = \frac{1}{\eta_0} + \frac{A_r}{D_i^*} h^*, \tag{14}$$

where

$$\eta_0 = \frac{1}{A_r} + \eta_f \left(1 - \frac{1}{A_r}\right). \tag{15}$$

A useful approximate equation for fin efficiency is [5]

$$\eta_f = \frac{\tanh(m\ell_f)}{m\ell_f}, \tag{16}$$

where

$$m \equiv \sqrt{\frac{2h}{k_f \delta_f}}. \tag{17}$$

Equation (16) is derived for a straight fin with a constant conduction cross section. It provides a less accurate approximation for circular and plate-finned tubes.[3]

The convective heat transfer coefficient on the air side, written in terms of $j \equiv \mathrm{St} \times \mathrm{Pr}^{2/3}$ can be introduced in equation (17) to yield

$$m\ell_f = \left(2\mathrm{Pr}^{1/3} \frac{k}{k_f} \frac{\mathrm{Re}\, j}{D_h^* \delta^+}\right)^{1/2} \tag{18}$$

where

$$D_h^* \equiv D_h/D_o, \tag{19}$$

$$\delta^+ \equiv D_o \delta_f / \ell_f^2. \tag{20}$$

If the convective heat transfer coefficient on the air side is written in terms of j and normalized by dividing by the heat transfer coefficient on the liquid side (found from the Nusselt number definition), then

$$h^* = \frac{j\, \mathrm{Pr}^{1/3} \mathrm{Re}}{\mathrm{Nu}_w} \frac{k}{k_w} \frac{D_i^*}{D_h^*}. \tag{21}$$

The Nusselt number for water and light liquids ($1 < \mathrm{Pr} < 20$) in a turbulent flow regime through smooth tubes is given by the following correlation [6]:

$$\mathrm{Nu}_w = 0.0155 \mathrm{Pr}_w^{0.5} \mathrm{Re}_w^{0.83}; \qquad \mathrm{Re} > 10{,}000 \tag{22}$$

The Reynolds numbers on the air and liquid sides can be written as follows:

$$\mathrm{Re} = \frac{\rho_1 V_1}{\mu\sigma} D_h, \tag{23}$$

$$\mathrm{Re}_w = \frac{\rho_w}{\mu_w} V_w D_i. \tag{24}$$

Sensitivity Coefficients

Equations (15–22) provide an implicit relationship for λ in equation (14) in terms of a set of seven independent variables. These independent variables, symbolized for convenience as x_i, are A_r, D_i, D_o, σ, δ^+, V_1, and V_w. Two other independent variables which appear in the analysis are D_h^* and ℓ_p^*. The following equation for $d\lambda/\lambda$ can be derived by combining differentials of equations (12–24). The derivation of this equation is lengthy and beyond the scope of this paper. The reader can find the derivation in [2].

$$\frac{d\lambda}{\lambda} = \sum_i Q_{xi} \frac{dx_i}{x_i} = Q_{A_r} \frac{dA_r}{A_r} + Q_{Di} \frac{dD_i^*}{D_i^*} + Q_{D_0} \frac{dD_o}{D_o} + Q_\sigma \frac{d\sigma}{\sigma} + Q_\delta \frac{d\delta^+}{\delta^+} + Q_{V_1} \frac{dV_1}{V_1} + Q_{V_w} \frac{dV_w}{V_w}, \tag{25}$$

where the expressions for Q_{x_i} are

$$\left.\begin{aligned} Q_{A_r} &\equiv (1 - \alpha_A)\nabla_h - \alpha_A \nabla_m + \nabla_f, \\ Q_{D_i} &\equiv -\alpha_w \nabla_h, \\ Q_{D_o} &\equiv \alpha_R(\nabla_h + \nabla_m) - \alpha_w \nabla_h, \\ Q_{D_\sigma} &\equiv \alpha_R(\nabla_h + \nabla_m), \\ Q_\delta &\equiv -\nabla_m, \\ Q_{V_1} &\equiv \alpha_R(\nabla_h + \nabla_m), \\ Q_{V_w} &\equiv -\alpha_w \nabla_h. \end{aligned}\right\} \tag{26}$$

The variables ∇_h, ∇_m, and ∇_f are defined as follows:

$$\left.\begin{aligned} \nabla_h &\equiv \frac{h^* A_r}{\lambda D_i^*}, \\ \nabla_m &\equiv \frac{u}{2\lambda\eta_0^2}\left(1 - \frac{1}{A_r}\right), \\ \nabla_f &\equiv \frac{1 - \eta_f}{\lambda \eta_0^2 A_r}, \end{aligned}\right\} \tag{27}$$

$$u \equiv (m\ell_f)^2 \eta_f^2 + \eta_f - 1. \tag{28}$$

There are two properties of the coefficients Q_{xi} which enable certain conclusions regarding the function λ to be drawn: (1) the coefficients Q_{x_i} represent change in λ for a 1 percent change in the independent variables x_i; (2) if Q_{x_i} is positive, λ is an increasing function of x_i, and if Q_{x_i} is negative, λ is a decreasing function of x_i. Since ∇_h, ∇_m, ∇_f, and the coefficients α_w and α_R are positive, Q_{D_i}, Q_σ, Q_δ, and Q_{V_w} are always negative. Therefore, λ is generally a decreasing function of D_i^*, σ, δ^+, and V_w regardless of the heat transfer surface geometry and flow conditions on the air and water sides. Since Q_{V_1} is always positive, λ is generally an increasing function of V_1, and since Q_{D_h} and Q_{ℓ_p} are zero, λ is independent of D_h^* and ℓ_p^*.

Equation (25) is an intermediate step in the analysis of the effect of heat exchanger surface geometry on draft height, heat exchanger surface area, and water pumping power. Reference [2] employs equations (9–11) in conjunction with equation (25) to derive the following differentials for draft height, heat exchanger surface area, and water pumping power.

$$\frac{dX_Z}{X_Z} = \sum_i Z_{x_i} \frac{dx_i}{x_i} = (Q_{A_r} + \alpha_A) \frac{dA_r}{A_r} + Q_{D_i} \frac{dD_i^*}{D_i^*} + (Q_{D_o} + \alpha_D - \beta_R) \frac{dD_o}{D_o} + (Q_{V_1} + \alpha_D - \beta_R + 3) \frac{dV_1}{V_1} + (Q_\sigma + \beta_R - \alpha_D - 2) \frac{d\sigma}{\sigma} + Q_{V_w} \frac{dV_w}{V_w} + Q_\delta \frac{d\delta^+}{\delta^+} + (\beta_D - \beta_R) \frac{dD_h^*}{D_h^*} + (-\beta_D) \frac{d\ell_p^*}{\ell_p^*} \tag{29}$$

The same approach enables the following results to be derived:

$$\frac{dX_{\overline{A}}}{X_{\overline{A}}} = \sum_i \overline{A}_{x_i} \frac{dx_i}{x_i} = (Q_{A_r} + \alpha_A) \frac{dA_r}{A_r} + Q_{D_i} \frac{dD_i^*}{D_i^*} + (Q_{D_o} + \alpha_D) \frac{dD_o}{D_o} + (Q_{V_1} + \alpha_D) \frac{dV_1}{V_1} + (Q_\sigma + 1 - \alpha_D) \frac{d\sigma}{\sigma} + Q_{V_w} \frac{dV_w}{V_w} + Q_\delta \frac{d\delta^+}{\delta^+}, \tag{30}$$

$$\frac{dX_{\dot{W}k}}{X_{\dot{W}k}} = \sum_i \dot{W}_{x_i} \frac{dx_i}{x_i} = (Q_{A_r} + \alpha_A - 1) \frac{dA_r}{A_r} + (Q_{D_i} + 1) \frac{dD_i^*}{D_i^*} + (Q_{D_o} + \alpha_D) \frac{dD_o}{D_o} + (Q_{V_1} + \alpha_D) \frac{dV_1}{V_1} + (Q_\sigma + 1 - \alpha_D) \frac{d\sigma}{\sigma} + (Q_{V_w} + 3) \frac{dV_w}{V_w} + Q_\delta \frac{d\delta^+}{\delta^+} \tag{31}$$

Equations (29–31) can be used to draw some practical conclusions regarding the geometry of finned tube heat exchanger surfaces in dry cooling towers. The sensitivity coefficients for the draft height, heat

[3] Equation (16) overestimates the fin efficiency of circular finned tubes by a maximum value of about 10 percent in the range $D_f/D_o \leq 2$ and $\eta_f \geq 0.75$. The error associated with surface temperature effectiveness η_0 is slightly lower.

exchanger surface area, and water pumping power requirement are listed in Table 3.

Sign of the Sensitivity Coefficients

The sensitivity coefficients summarized in Table 3 are used to draw some conclusions about the geometry of finned-tube heat exchanger surfaces for dry cooling towers. The analysis is performed in two steps. First (preliminary analysis), the range of variation of the sensitivity coefficients is found in a crude but conservative manner. In a large number of cases, the sensitivity coefficients are either positive or negative in the domain enclosed by the constraints on the independent variables. This leads to the conclusion that the dependent variables are either an increasing or a decreasing function of the independent variable in question. Second, a more extensive analysis of areas for which the preliminary analysis do not provide definitive conclusions is undertaken.

The recommended tube thickness requirements were studied considering erosion, corrosion, and stresses. A D_i^* range of 0.80 for small diameter tubes to values close to unity for large-diameter tubes was obtained. Therefore,

$$1 > D_i^* \geq 0.80.$$

The air-side convective heat transfer coefficient can be as high as 50 Btu/hr-ft^2-°F and as low as zero for zero air approach velocity. The water-side convective heat transfer coefficient ranges from 50 to 2000 Btu/hr-ft^2-°F. Hence,

$$1 > h^* > 0.$$

A fin efficiency range of variation of 0.70 to 1 is considered; the surface effectiveness has the same range of variation:

$$0.7 \leq \eta_f < \eta_0 < 1.$$

The variable u in equation (28) has a lower bound of zero and an upper bound of 0.426:

$$0.426 \geq u > 0.$$

To evaluate the upper and lower bounds for β_R for $\ell/D_h > 4$, a Reynolds number range of 1000 to 10,000 is considered, and the above constraints are introduced into equations (29–31) to find a crude but conservative estimation of the upper and lower bounds for the sensitivity coefficients. Because of the approximations used in establishing the upper and lower bounds of the dependent variables, the results for Z_{D_o}, $\overline{A}_{D_o}$, $\overline{A}_\sigma$, W_{A_r}, W_{D_i}, W_{D_o}, and W_σ are not conclusive. Then, a rigorous analysis of these functions is undertaken [2] and definitive conclusions are reached. The final result is given in Table 4.

Summary and Conclusions

The effects of heat transfer surface geometry on draft height Z_E, heat transfer surface area $\overline{A}$, and water pumping power $\dot{W}k_p$ are investigated using the geometry- and Reynolds number-dependent influence coefficients given in Table 1. The X-factors given in equations (9–11) may be used as a measure to evaluate heat transfer surface geometries in an attempt to select suitable surfaces for dry cooling tower applications. The effects of finned circular tube geometry on Z_E, $\overline{A}$, and $\dot{W}k_p$ has been investigated using equations (9–11) and heat transfer and flow friction correlations given in Table 2. The results are valid for helical round and continuous fins having smooth, serrated or cut fins and for staggered and in-line tube arrangements. These results are useful in directing research and development efforts toward manufacture of new, improved circular-finned tube heat exchanger surfaces for dry cooling tower applications. At the present time there are no generalized heat transfer and flow friction correlations for heat transfer surface geometries other than the finned circular tubes considered in this paper. However, the method of analysis is adaptable to other surface geometries when basic design data resulting in generalized correlations are available.

Each set of X-factors in Table 3 is a function of nine independent variables relating to the basic geometry of the finned-tube surface. The sensitivity coefficients listed in Table 3 have two properties which enable certain conclusions regarding the X-factors to be drawn: (1) the sensitivity coefficients represent the percentage change in the X-factor for a 1 percent change in the independent variable; (2) if a sensitivity coefficient is positive, the corresponding X-factor is an increasing function of the independent variable, and if the sensitivity coefficient is negative, the corresponding X-factor is a decreasing function of the independent variable. Table 4 summarizes the sign of the sensitivity coefficients for a wide range of variations of the nine independent variables listed in Table 3.

Table 3 Sensitivity coefficients

Independent Variable	Dependent Variable X_Z	Dependent Variable $X_{\overline{A}}$	Dependent Variable $X_{\dot{W}k}$
D_o	$Q_{D_o} + \alpha_D - \beta_R$	$Q_{D_o} + \alpha_D$	$Q_{D_o} + \alpha_D$
A_r	$Q_{A_r} + \alpha_A$	$Q_{A_r} + \alpha_A$	$Q_{A_r} + \alpha_A - 1$
D_i^*	Q_{D_i}	Q_{D_i}	$Q_{D_i} + 1$
σ	$Q_\sigma + \beta_R - \alpha_D - 2$	$Q_\sigma + 1 - \alpha_D$	$Q_\sigma + 1 - \alpha_D$
δ^+	Q_δ	Q_δ	Q_δ
D_h^*	$\beta_D - \beta_R$	0	0
ℓ_p^*	$-\beta_D$	0	0
V_1	$Q_{V_1} + \alpha_D - \beta_R + 3$	$Q_{V_1} + \alpha_D$	$Q_{V_1} + \alpha_D$
V_w	Q_{V_w}	Q_{V_w}	$Q_{V_w} + 3$

Table 4 Signs of the sensitivity coefficients[a]

Independent Variable	Dependent Variable[b] Z_E/A_1	Dependent Variable[b] $\overline{A}/A_1$	Dependent Variable[b] $\dot{W}k_p/A_1$
D_o	(c)	+	+
A_r	+	+	−
D_i^*	−	−	+
σ	−	+	+
δ^+	−	−	−
D_h^*	+	0	0
ℓ_p^*	−	0	0
V_1	+	+	+
V_w	−	−	+

[a] The results are valid for $0.8 < D_i^* < 1$; $0 < h^* < 1$; $\mathrm{Re} > 1000$; $\mathrm{Re}_w > 10{,}000$; and $0.7 \leq \eta_f < \eta_0 < 1$.

[b] A plus (minus) sign indicates that the dependent variable is an increasing (decreasing) function of the independent variable. A zero indicates no dependence.

[c] See Summary and Conclusions.

Several general conclusions, listed below, can be drawn from the analysis performed in this paper. These conclusions are applicable to the finned tube types described in Table 2 and consequently are limited by the Reynolds number range of validity of the heat transfer and flow friction correlations given in [4]. A certain amount of extrapolation of the correlated data given in [4] is acceptable, but an extreme departure from the basic geometry of the tested surfaces is not advisable.

1 The draft height per unit heat exchanger frontal area is an increasing function of A_r, D_h^*, and V_1 and a decreasing function of D_i^*, σ, δ^+, ℓ_p^*, and V_w.

2 The heat transfer surface area per unit heat exchanger frontal area is an increasing function of D_o, A_r, σ, and V_1; a decreasing function of D_i^*, δ^+, V_w; and independent of D_h^* and l_p^*.

3 The water pumping power per unit heat exchanger frontal area is an increasing function of D_o, D_i^*, σ, V_1, and V_w; a decreasing function of A_r and δ^+; and independent of D_h^* and ℓ_p^*.

Analysis of the function Z_{D_o} is quite involved and is beyond the scope of this paper. This analysis which is presented in [2] concludes that although draft height per unit frontal area is an increasing function of D_o for a wide range of conditions, there are conditions for which draft height could be a decreasing function of D_o, i.e., in the range of low air-side Reynolds numbers ($\mathrm{Re} < 2000$), large A_r ($A_r > 20$), and high h^* ($h > 0.01$). Serrated or cut fins are more susceptible

to these conditions, particularly for $\ell_p/D_h > 4$, high fin effectiveness, and low air-side Reynolds number.

Acknowledgment

The encouragement and technical guidance of Professor A. L. London of Stanford University is gratefully acknowledged.

References

1 Montakhab, A., "Waste Heat Disposal to Air with Mechanical and Natural Draft-Some Analytical Considerations." ASME JOURNAL OF ENGINEERING FOR POWER, Vol. 102, No. 3, 1980, pp. 719–727.

2 Montakhab, A., "Waste Heat Disposal to Air with Mechanical and Natural Draft-Some Analytical Design Considerations," Ph.D. Disertation, Stanford University, May 1978.

3 "Heat Transfer and Pressure Drop Characteristics of Dry Tower Extended Surfaces, Part I: Heat Transfer and Pressure Drop Data," PFR Engineering Systems, March 1976.

4 "Heat Transfer and Pressure Drop Characteristics of Dry Tower Extended Surfaces, Part II: Data Analysis and Correlation," PFR Engineering Systems, June 1976.

5 Kays, W. M. and London, A. L., *Compact Heat Exchangers,* 2nd ed., McGraw-Hill, New York, 1964.

6 Kays, W. M., *Convective Heat and Mass Transfer,* McGraw-Hill, New York, 1966.

Fuel Treatment Chemical Additives Progress Report

A. E. Bischof

Manager, Technical Services,
Mogul Division,
Dexter Corporation,
Chagrin Falls, OH

A detailed discussion of fuel quality as related to associated fuel use problems is presented. The generic chemical solution to the problems is covered with emphasis on the correction of system mechanical and instrumental malfunctions. Three case histories concerning high temperature corrosion, combustion efficiency and deposit accumulation are explored.

Introduction

The efficient use of fuels is an essential part of all industrial steam generator operations. This is particularly true today with the increasing cost of fuels, their tight supply, and the widely varying quality from shipment to shipment. In an effort to squeeze as much economy as possible from a unit of fuel, operators are paying more and more attention to details of fuel use that were overlooked in the past. This includes the beneficial application of fuel additives.

Making sense out of all the technical information available and the supplier product information and claims can be made a lot easier once specific fuel related problems have been identified and understood.

Fuel Quality

Fuel quality, as might be expected, must be watched closely to ensure proper firing and to minimize operating difficulties. For instance, a high capacity oil fired boiler with a close space tube arrangement could not stay clean using a low grade fuel oil with high ash; tube bridging could occur. Also, a coal fired, slag tap boiler could not burn a coal that has a high melting point ash.

Boiler design is based to a great extent on specific fuel quality. When a specific boiler was designed and placed in operation, the design fuel may have been plentiful at a reasonable cost. Ten or 15 years later a fuel of the design quality may not be available at an affordable cost and lower quality fuels have to be used. A note to the wise operator: stay in touch with your purchasing agent and make him aware of your needs. More than once a purchasing agent has saved a few dollars by buying lower quality fuel, at the expense of plant maintenance department. Tables 1, 2, and 3 indicate the wide variation in fuel quality and characteristics that can be encountered in liquid and solid fuels [1–3].

Problem Identification

The proper identification of a fuel problem requires consideration of all aspects of the fuel program. It is the total system that must be considered. A problem eliminated via treatment in the preburner system could cause another adverse situation in the boiler furnace. One of the case histories describes this kind of situation.

In all cases, you should ensure that the mechanical and instrumental control systems are in good working order and that the boiler design is suitable for the type, grade and quality of fuel being fired. Once the operator has identified and rectified the mechanical and control sources of fuel handling and firing problems, chemical fuel additives can then be considered and properly evaluated.

Fuel Problems

For the industrial boiler operator, the difficulties usually start with fuel storage and ends with stack emissions and ash handling. Many fuel problems are directly related to the mode of transportation used to deliver the fuel. For instance, water and sodium in fuel oils can be traced to improper ballast tank cleaning when the fuel is transported by sea going vessels.

Table 4 relates general fuel use problem areas to the generic types of fuel additives used to correct the problem. The chemical class for fuel additives and a brief comment concerning problem cause are also included [4].

Fuel and Fuel Ash Chemistry

To date, most boiler operators view fuel and fuel additive chemistry as a black art. The situation exists that there are very complex reactions taking place in the combustion flame zone and the gas passages of the boiler, in particular, the fuel ash constituents and the combustion product refuse. Tables 2 and 3 list fuel ash constituents. It is not very difficult to surmise the complex mixture that actually exists as refuse.

Table 5 lists some of the many minerals, known to exist in coal [5], that combine in various ways and ratios creating a very complex compound matrix. These minerals may have a small heating value in the combustion process, but for the most part they contribute only to the corrosion, erosion, deposit and particulate problems associated with coal firing.

These same types of chemical complexes exist in fuel oil ash, particularly in the lower grade oils such as No. 5 and No. 6 oil. Table 2 lists typical compositions of residual oil and oil ash. As with coal, the fuel oil ash after leaving the flame envelope combines in complex oxide states. Table 6 [7] lists many of the oil ash compounds formed.

Fuel Additive Chemistry

Realizing that fuel quality can change from one shipment to the next is significant in understanding fuel additive application. As in most chemical reactions there is an optimum treatment range; too little treatment will not be effective and too much treatment can lead to other problems.

Column I of Table 4 lists the fuel problems of most general importance to the user. Following is a brief discussion of the chemistry of additives used to control these problems.

Contributed by The Power Division for publication in the JOURNAL OF ENGINEERING FOR POWER. Manuscript received at ASME Headquarters September 24, 1979.

Deicers. Deicers are used to keep coal from freezing in the transporting vehicle and in storage. Deicers include polymers, and desiccating agents, salts and oils. They are usually applied to the coal as the transporting vehicle is being loaded. Polymers are reported by researchers to interact with the ice crystals as the crystal forms, creating a very weak crystal structure lattice that is easily fractured [8]. Desiccating agents in the accepted way absorb moisture. Salts such as calcium and sodium chloride lower the freezing point of water. Oils form a water immiscible layer on the coal surface. The treatment rates for each deicer will vary with the amount of moisture on the coal. To date, polymers show the most promise.

Table 1 Typical heating values [1]

Fuel	Typical Heating Values
Anthracite coal	13,900 Btu/lb
Bituminous coal	14,000 Btu/lb
Sub-Bituminous coal	12,600 Btu/lb
Lignite coal	11,000 Btu/lb
Kerosene	134,000 Btu/gal
No 2 Burner Fuel Oil	140,000 Btu/gal
No 4 Heavy Fuel Oil	144,000 Btu/gal
No 5 Heavy Fuel Oil	150,000 Btu/gal
No 6 Heavy Fuel Oil 2.9% Sulfur	152,000 Btu/gal
No 6 Heavy Fuel Oil 0.7% Sulfur	147,500 Btu/gal
No 6 Heavy Fuel Oil 0.3% Sulfur	143,800 Btu/gal

Dust Suppressants/Sealers. Dust and windage loss of coal in transportation and storage are controlled through a physical coating system using light oils, surfactants and polymers. This is a wetting type of chemistry, and we suspect that a surface charge neutralization phenomenon is also at work.

Microbiocides. Refining operations usually preclude microbiological growth in fuels before the fuel leaves the refinery. It has been our experience that microbiological problems usually are the result of water contamination of the fuel during shipment or water intrusion of storage facilities at either the supplier's terminal or the user's plant.

Microbial growth takes place in the water phase of the oil-water mixture, and it usually occurs at the water oil interface where significant concentrations of water exist (>1 percent). These microbes cause sludge and corrosion. The biocides used to control microbial growth include quaternary ammonium salts, organo tins and borinanes. Chemical treatment rates depend on the severity of the problem.

Water Emulsifiers/Water Demulsifiers. Water and fuel oil do not mix, and for the most part, water present in concentrations exceeding 2 percent of the fuel by volume is undesirable. The presence of water in the fuel can cause loss of storage capacity, preburner and system corrosion, organic and biological sludge and poor atomization. When water is present in concentrations greater than 2 percent by volume, we recommend that the water be mechanically removed from the storage facilities. Pretreatment of the oil in the storage tank with

Table 2 Typical composition of residual oil and oil ash

Constituent	Parts per Million Residual Oil	Percent by Weight in ash [2]					
		Constituent	California	Midcontinent	Texas	Pennsylvania	Iran
SiO_2	6–86	SiO_2	38.8	31.7	1.6	0.8	12.1
Fe_2O_3	0.9–57	Fe_2O_3					
Al_2O_3	3–76	Al_2O_3	17.3	31.8	8.9	97.5	18.1
TiO		TiO_2					
CaO	1.4–10	CaO	8.7	12.6	5.3	0.7	12.7
MgO	1–1.7	MgO	1.8	4.2	2.5	0.2	0.2
MnO		MnO	0.3	0.4	0.3	0.2	Trace
V_2O_5	14–740	V_2O_5	5.1	Trace	1.4	—	38.5
NiO	1.3–25	NiO	4.4	0.5	1.5	—	10.7
Na_2O	5–35	Na_2O	9.5	6.9	30.8	0.1	
K_2O	0.2–1.2	K_2O	—	—	1.0	—	—
SO_3	0.1–3.0	SO_3	15.0	10.8	42.1	0.9	7.0
Chloride		Chloride	—	—	4.6	—	

Table 3 Ash content and ash fusion temperatures of some US coals and lignite [3]

Rank:	Low Volatile Bituminous	High Volatile Bituminous				Sub-bituminous	Lignite
Seam	Pocahontas No 3	No 9	Pittsburg	No 6			
Location		Ohio	West Virginia	Illinois	Utah	Wyoming	Texas
Ash, dry basis, %	12.3	14.10	10.87	17.36	6.6	6.6	12.8
Sulfur, dry basis, %	0.7	3.30	3.53	4.17	0.5	1.0	1.1
Analysis of ash, % by wt							
SiO_2	60.0	47.27	37.64	47.52	48.0	24.0	41.8
Al_2O_3	30.0	22.96	20.11	17.87	11.5	20.0	13.6
TiO_2	1.6	1.00	0.81	0.78	0.6	0.7	1.5
Fe_2O_3	4.0	22.81	29.28	20.13	7.0	11.0	6.6
CaO	0.6	1.30	4.25	5.75	25.0	26.0	17.6
MgO	0.6	0.85	1.25	1.02	4.0	4.0	2.5
Na_2O	0.5	0.28	0.80	0.36	1.2	0.2	0.6
K_2O	1.5	1.97	1.60	1.77	0.2	0.5	0.1
Total	98.8	98.44	95.74	95.20	97.5	86.4	84.3
Ash fusibility							
Initial deformation temperature, °F							
Reducing	2900+	2030	2030	2000	2060	1990	1975
Oxidating	2900+	2420	2265	2300	2120	2190	2070
Softening temperature, °F							
Reducing		2450	2175	2160		2180	2130
Oxidizing		2605	2385	2430		2220	2190
Hemispherical temperature, °F							
Reducing		2480	2225	2180	2140	2250	2150
Oxidizing		2620	2450	2450	2220	2240	2210
Fluid temperature, °F							
Reducing		2620	2370	2320	2250	2290	2240
Oxidizing		2670	2540	2610	2460	2300	2290

Table 4 Fuel problems and chemical additives [4]

GENERIC ADDITIVES FOR FUEL PROBLEMS	TYPE OF FUEL COAL	OIL	PROBLEM AREAS	CHEMICAL CLASS FOR FUEL ADDITIVES	COMMENTS
Deicers	X		Transportation and Outside Storage	Polymers, Desiccating agents	Ice can prevent coal from being unloaded from rail or truck transport. Can hinder transfer within plant. Can be the cause of excess moisture getting into furnace.
Dust Suppressants	X		Transportation and Storage	Light Oils, Surfactants	Dust is housekeeping problem as well as a health hazard.
Sealers	X		Transportation and Outside Storage	Polymers, Light Oils	Use of sealers can prevent up to 2-3% loss of coal during rail transportation period. Also can act as dust suppressant and deicer.
Microbiocides		X	Transportation, Storage Tank, Pipe Lines, Pumps and Filters, Burners	Quats, Organo Tins, Borinanes	Microbial growths can be the cause of sludge formation, corrosion and burner problems.
Water Emulsifiers		X	Transportation, Storage Tank, Pipe Lines, Pumps and Filters, Burners, Combustion Process	Surfactants, Organic Esters, Alcohols	Water can be the cause of sludge, corrosion, burner problems, and can also effect the combustion process.
Water Demulsifiers		X	Transportation, Storage Tank, Pipe Lines, Pumps and Filters, Burners, Combustion	Surfactants, Organic Solvents	Water can be handled either by emulsifying it with the oil and having it pass through the system with it, or by separating it from the oil and them removing it from the storage tanks. Type of treatment will usually depend on amount of water present. Presence of sea water with high sodium content may also be reason to use demulsifiers.
Sludge Dispersants		X	Storage Tank, Pipe Lines, Pumps and Filters, Burners, Combustion Process	Surfactants, Organic Esters, Imidazolines	Sludge deposits can be due wholly or partially to many different reasons, ie, oil contaminants, water in oil, microbiological growths, aging of oil.
Pour Point Depressants		X	Pipe Lines, Pumps and Filters, Burners, Combustion Process	Polymers, Natural Waxes	Pour Point depressants prevent viscosity of oil to increase when temperatures decrease. Problem is usually found only with distillate (No 1,2,3 oil) fuels. Residual (No 4,5,6 and Bunker C) fuels use external heating to keep viscosity low under all weather conditions.
Burner Atomization Improvers		X	Burner, Combustion Process	Polymers, Surfactants, Organic Amines	
Combustion Catalysts	X	X	All areas from furnace through stack.	Transition and alkali metals in both inorganic and organic form. Halogenated organic compounds.	Problems related to smoke and particulates are very often caused by not having the proper combustion of fuels.
Slag Modifiers	X	X	Furnace and Generating Sections	Transition and alkalai metals including boron and lithium compounds	Slag modifiers can also help to prevent smoke and particulate problems.
Corrosion Inhibitors	X	X	All areas from furnace to stack	Alkaline earth compounds	Lack of good corrosion inhibition can be the major factor for equipment failure from the furnace on through the stack.
Conductivity Control Agents	X		Electrostatic Precipitator	Ammonium salts, SO_2 gas	Conductivity of fly ash can effect the operation

a demulsifier is recommended. Under 2 percent water by volume in the oil can usually be handled by emulsifying the water to produce a uniform homogenized suspension.

Table 4 lists surfactants, esters, alcohols and solvents as effective chemical classes of emulsifiers/demulsifiers. McCutcheony's "Detergents and Emulsifiers" lists in excess of 2500 such chemicals.

The chemical activity of a demulsifier is that it is selectively soluble in either the oil or the water phase, creating a surface tension condition in that phase not compatible with other phase. Conversely, the chemical activity of an emulsifier is that it is partially soluble in both oil and water phases.

Sludge Dispersants. Sludge can be defined as a mixture of water, oil, dirt, polymerized organics and bioactive masses. Although separated from water as a subject, the treatment additives are of the same classes of chemicals. In the majority of cases treating with organic solvents or dispersants for a sludge problem will minimize the water condition.

Dosage is again dependent on the severity of the condition, and a tank profile should be made, followed by laboratory product selection tests. Sludge will cause preburner and burner system fouling. Note: Organic sludge (polymerized hydrocarbon) can be caused by overheating the oil.

Pour Point Depressants. Pour point is defined as that temperature 5 °F above which the oil will not flow when the test vessel is held in a horizontal position for 5 s. Pour point depressants are most applicable in fuels refined from high paraffinic crudes. Chemically, they react with wax crystals modifying their shape and size. In essence, the additive helps to keep the oil fluid at temperatures 20–30 °F below the fuel's normal pour point, depending on treatment dosage and the paraffinic content of the oil.

Cloud Point Depressants. The cloud point is defined as that temperature at which a general haze appears in the oil. The haze is caused by wax crystal formation. Many companies are working to develop effective cloud point depressants In general, the most effective pour point depressant, a vinyl acetate ethylene copolymer [9], while reducing the pour point by 20–30 °F, will reduce the cloud point temperature by only 5 to 10 °F.

Burner Atomization Improvers. Proper atomization of fuel oils is critical to the combustion process to achieve maximum efficiency and to eliminate carbon deposits in the boiler and objectionable black stack emissions. Chemical additives include polymers and surfactants. These materials change the surface tension of the oil and/or condition the burner nozzle to promote a consistent fine droplet size and thereby maximize fuel surface area in the flame envelope.

Note: No chemical additive can take the place of proper preheat temperatures, line pressures or burner nozzle selection.

Combustion Catalysts. Combustion catalysts include transition and alkaline earth metals in both organic and inorganic form. Man-

Table 5 Minerals in coal [5]

Mineral	Formula
Shale group	$(K,Na,H_3O_3,Ca)_2(Al,Mg,Fe,Ti)_4(Al,Si)_8O_{20}(OH,F)_4$
Clay group (Kaolinite)	$x(K,Na)_2O{\cdot}yAl_2O_3{\cdot}zSiO_2{\cdot}tH_2O$
Sulfur group	$FeS_2, FeSO_4, Na_2SO_4$
Carbonate group	$CaCO_3, CaCO_3{\cdot}MgCO_3$
Associated Minerals	
Quartz	SiO_2
Feldspar	$(K,Na)_2O{\cdot}Al_2O_3{\cdot}6SiO_2$
Garnet	$3CaO{\cdot}Al_2O_3{\cdot}3SiO_2$
Hornblende	$CaO{\cdot}3FeO{\cdot}4SiO_2$
Gypsum	$CaSO_4{\cdot}2H_2O$
Apatite	$9CaO{\cdot}3P_2O_5{\cdot}CaF_2$
Zircon	$ZrSiO_4$
Epidote	$4CaO{\cdot}3Al_2O_3{\cdot}6SiO_2{\cdot}H_2O$
Biotite	$K_2O{\cdot}MgO{\cdot}Al_2O_3{\cdot}3SiO_2{\cdot}H_2O$
Qugite	$CaO{\cdot}MgO{\cdot}2SiO_2$
Prochlorite	$2FeO{\cdot}2MgO{\cdot}Al_2O_3{\cdot}2SiO_2{\cdot}2H_2O$
Diaspore	$Al_2O_3{\cdot}H_2O$
Lepidocrocite	$Fe_2O_3{\cdot}H_2O$
Magnetite	Fe_3O_4
Kyanite	$Al_2O_3{\cdot}SiO_2$
Staurolite	$2FeO{\cdot}5Al_2O_3{\cdot}4SiO_2{\cdot}H_2O$
Topaz	$(Al,F)_2SiO_4$
Tourmaline	$MgAl_3(BOH)_2Si_4O_{19}$
Hematite	Fe_2O_3
Penninite	$5MgO{\cdot}Al_2O_3{\cdot}3SiO_2{\cdot}2H_2O$

ganese is the most widely used combusion catalyst. Lead and others have been phased out for environmental reasons. Table 7 [10] lists the relative toxicity of some common metal catalysts.

A number of mechanisms have been suggested for the combustion catalysts reactions:

1 Flame dissociation and ionization which appear to be directly related to the carbon reduction properties

2 Direct surface catalysis of the combustion reactions

3 Atomic oxygen scavenging properties

Use rates for catalysts vary from 5 to 50 ppm. Table 8 [10] lists various metallic additives and their effective use rate vs. percent carbon reduction (last column). Combustion catalysts can be applied in various ways. The most effective way is to mix the catalyst completely with the fuel prior to ignition. For oil or liquid fuels this presents a minimal problem; however, with coal or other solid fuels the additive application is very difficult. Case History 2 covers combustion catalyst application in oil.

Slag Modifiers. The primary result of using slag modifiers is to change the ash melting temperature. Usually, the additive increases the melting point of the ash to a temperature above the hottest heat transfer temperature encountered in the boiler fireside system. Occasionally additives are used to lower the melting point of ash. This occurs primarily in coal fired slag tap and wet bottom furnaces and cyclone burners. The fuel ash constituents and the additives combine in the area of the flame envelope, or just beyond, forming complex compound mixtures. These mixtures, have melting temperatures very much different than the individual compounds. This combined melting point is the eutectic temperature of the mixture.

Slag modifiers also are usually transition and alkaline earth metal compounds, i.e., MgO, CaO, Al_2O_3 and SiO_2. Oil ash modification is better understood as compared with coal ash modification and the additive technology is further advanced. Referring to Table 6, the melting points of various oil ash constituents are listed. Note the wide range encountered. Magnesium compounds are the most widely used oil ash modifiers, and vanadium is the most widely encountered cause of slag from fuel oil. As can be seen in Table 6, vanadium has many oxidation states with varying melting temperatures. Pure vanadium in its highest oxidation state (V_2O_5) has a melting temperature 1243°F. If significant amounts of sodium are present (sea water contamination), the melting point decreases, and, in the right ratio of Na_2O to V_2O_5, eutectic temperatures as low as 995°F can exist. Since flame envelope temperatures approach 3000°F, the ash leaving the flame envelope is molten, and the ash will adhere when impinging on cooler boiler metal and refractory surfaces.

Fuel additives increase the melting point significantly to prevent extensive slag buildup. The melting point modification additive produces a powder type of ash which is easily removed by soot blowers and/or water washing during periodic shut downs.

Fig. 1 shows the effects of Na_2O on the melting point of V_2O_5.

Fig. 2 shows the effect of MgO on the melting point of a 1:3 molar ratio of Na_2O to V_2O_5.

Figs. 1 and 2 were developed from original laboratory work conducted by the author using sea water recovered magnesium. Since this work, advances in magnesium oxide production and product manufacturing have shifted this curve in Fig. 2 significantly to the left. The new methods have produced a more reactive and finer magnesium which is more effective at lower MgO to V_2O_5 ratios. Other oil ash impurities of significance include iron, sulfur and nickel.

Table 6 Ash constituents formed during combustion of fuel oil and their melting points [6]

Compound		Melting Point, °F
Aluminum oxide	Al_2O_3	3720
Aluminus sulfate	$Al_2(SO_4)_3$	Decomposes at 1418 to Al_2O_3
Calcium oxide	CaO	4662
Calcium sulfate	$CaSO_4$	2642
Ferric oxide	Fe_2O_3	2849
Ferric sulfate	$Fe_2(SO_4)_3$	Decomposes at 896 to Fe_2O_3
Magnesium oxide	MgO	4532
Magnesium sulfate	$MgSO_4$	Decomposes at 2055 to MgO
Michel oxide	NiO	3794
Nickel sulfate	$NiSO_4$	Decomposes at 1544 to NiO
Silicon dioxide	SiO_2	3128
Sodium sulfate	Na_2SO_4	1616
Sodium bisulfate	$NaHSO_4$	482
Sodium pyrosulfate	$Na_2S_2O_7$	752
Sodium ferric sulfate	$Na_2Fe(SO_4)_3$	1000
Vanadium trioxide	V_2O_3	3580
Vanadium tetroxide	V_2O_4	3580
Vanadium pentoxide	V_2O_5	1243
Zinc oxide	ZnO	3270
Zinc sulfate	$ZnSO_4$	Decomposes at 1364 to ZnO
Sodium metavanadate	$Na_2O\text{-}V_2O_5$	1166
Sodium pyrovanadate	$2Na_2O\text{-}V_2O_5$ ($NaVO_3$)	1184
Sodium orthovanadate	$3Na_2O\text{-}V_2O_5$	1562
Nickel pyrovanadate	$2NiO\text{-}V_2O_5$	>1650
Nickel orthovanadate	$3NiO\text{-}V_2O_5$	>1650
Ferric metavanadate	$Fe_2O_3\text{-}V_2O_5$	1580
Ferric vanadate	$Fe_2O_3\text{-}2V_2O_5$	1571
Sodium vanadic vanadates	$Na_2O\text{-}V_2O_4\ 5V_2O_5$	1157
	$5Na_2O\text{-}V_2O_4\text{-}11V_2O_5$	995

Table 7 Relative Toxicity of Selected Metals [10]

ELEMENT	TLV* mg/m³	RELATIVE TOXICITY (to Lead—Pb)
Cu	0.1	2
Ba	0.002	100
Co	0.1	2
Mn	5.0	1/25
Fe	1.0	1/5
Mg	15.0	1/75
Ni	1.0	1/5
Pb	0.2	1
Zn	5.0	1/25

* Atmospheric concentration for selected toxic elements (abridged)
TLV—threshold limiting values for natural inspiration by individuals, safe limiting levels of exposure for eight hours in any one day.

Table 8 Combustion catalysts comparisons

Compound	Conc. ppmw Metal	Total Partic. W Addit.	% Reduc. from Arith. Avg.[1]	% Reduc. per ppmw Metal[2]	Carbon Loadings W Addit.[3]	% Reduc. Carbon W Addit.	% Reduc. per ppmw Metal[2]
Zn Naphth.	27	106	−1.0	0	56	+2	0
Co "	27	74	29.5	1.09	24	56.3	2.09
Fe "	27	80	23.7	0.88	30	45.4	1.68
Fe "	11	71	32.3	2.94	21	61.7	5.61
Mn "	27	77	26.6	0.99	27	50.8	1.88
Ca "	27	62	40.9	1.51	12	78.1	2.89
Ba "	51	48	54.2	1.06	−2	103.6	2.03
Ba "	51	50	52.3	1.03	0	100.0	1.96
Ba "	26	75	28.5	1.10	25	54.5	2.1
Ba "	10	89	15.2	1.52	39	29.0	2.9
Ba 2-Ethyl Hexano.	40	55	47.6	1.19	5	90.9	2.3
Ba Sulph.	20	83	20.9	1.05	33	39.9	2.0
Fe 5-Carb.	27	78	25.6	0.95	28	49.0	1.8
Mn MMT[4]	21	97	7.5	0.36	47	14.4	0.7
Mn MC[5]	6	86	18.0	3.0	36	34.4	5.7

[1] Total particulate collected, including oxides from the additives, milligrams per standard cubic meter (mg/sm^3), arithmetic mean base-line level for all groups = 104.9 mg/sm^3.
[2] Percent reduction from the average base-line level, per part per million of the additive metal on a weight basis.
[3] Arithmetic mean carbon level for all groups—54.9 mg/sm^3.
[4] MT—Methyl-cyclopentadienyl-manganese-tricarbonyl.
[5] MC—Manganese carboxylate complex.
[6] All tests conducted using residual fuel oil in a 680 kg/hr. boiler at steady load and conditions.

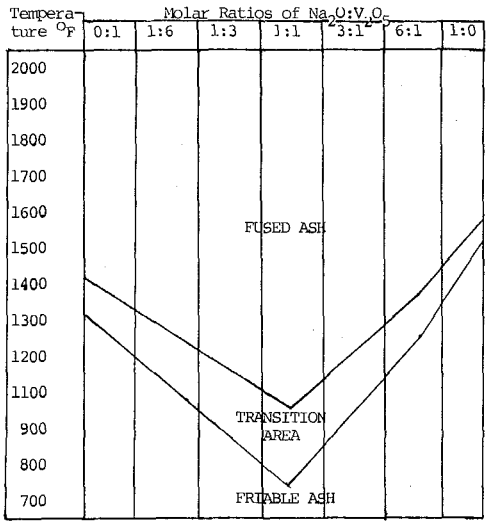

Fig. 1 Temperature effects on synthetic fuel oil ash

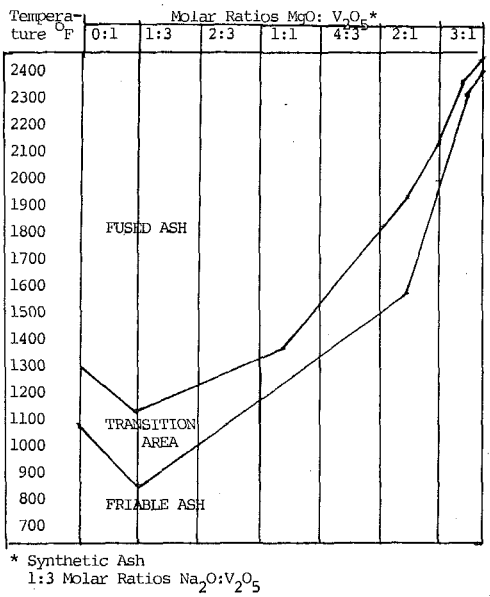

Fig. 2 MgO effect on Vanadium slag formation

Coal ash modification is achieved through the same type of chemical reactions. However, it is much more complicated in actual practice. This is apparent when reviewing the literature on the subject. For instance, Babcock and Wilcox in their book *Steam, Its Generation and Use,* Chapter 15, indicates four different methods for calculating and predicting coal ash melting temperatures. Many investigators are hard at work on coal ash problems, and significant technological advances are expected in the foreseeable future.

Corrosion Inhibitors. Discounting the corrosion problems in the preburner part of the system, there are two main types of corrosion: high temperature and low temperature. High temperature corrosion is usually encountered in those areas of the furnace where temperatures of the combustion gases and metal surfaces are in excess of 1000°F. However, keep in mind the eutectic temperature condition discussed previously.

Case History 1 is an example of high temperature superheater corrosion as the result of high sodium, where the sodium in the fuel exceeded the vanadium and combined with sulfur to produce sodium pyrosulfate ($Na_2S_2O_7$) with an eutectic temperature around 752°F. Sodium pyrosulfate in a molten state like sodium vanadates is very corrosive.

Low temperature corrosion, usually referred to as cold end corrosion, (economizers, airheaters, etc.) is directly attributable to acid formation. Sulfuric acid (H_2SO_4), the oxidation product of the sulfur in the fuels and in some cases hydrochloric acid (HCl), a product of chloride in the fuel, condense at temperatures below their dew points and corrode metal surfaces.

Typically, both high and low temperature corrosion are minimized by treating with alkaline earth metal compounds. Calcium, aluminum and magnesium compounds are the most widely used, with the latter being the most popular. In the case of cold end corrosion, the alkali metals combine with the acid to form a neutral salt which is noncorrosive. In the case of high temperature corrosion, the metals combine with the ash constituents producing a compound with a melting temperature higher than the boiler metal temperatures.

The chemicals are fed with the fuel and/or at other locations such as ahead of the economizer or air preheater, depending on system configuration and economics.

Conductivity Control Agents. To function properly, electrostatic precipitators require a specific resistivity range for the fly ash particles being collected. This surface resistivity (electrical capacity) is largely dependent on the sulfur concentration in the fuel and the temperatures of the system. If the temperatures in the system are low and alkali metals are used to control end corrosion, the fly ash resistivity will be increased due to the neutralization of the SO_2 and SO_3.

Also, if the sulfur in the fuel is low in relation to the amount of ash, an excessively high resistivity fly ash will exist.

On the other hand, if the temperatures are too high, SO_2 and SO_3 will not condense on the ash particles, also causing a high resistivity. If the sulfur is high, the fly ash resistivity would be too low (a high charge condition) resulting in fouling of the precipitator electrodes.

Various treatments are being utilized to improve the operation of electrostatic precipitators due to high ash resistivity. Sulfur dioxide gas can be generated on-site and fed to the flue gas upstream of the precipitator. Also, urea and ammonia salts are used and fed in a similar location.

Conversely, low ash resistivity is corrected by using alkali metals to neutralize the high electrical capacity.

Before discussing some case histories, a final word on chemical fuel additives and their applications. If there are mechanical and/or instrumentation fuel flow and combustion control problems they should be corrected. Once corrected, the beneficial effects of fuel additives can be fairly evaluated. Chemical additives can help minimize some problems, but chemical additives should not be used as a replacement for good mechanical and/or instrumentation operation.

Case History 1

Industry: Pulp and Paper Mill
Location: Northeastern State
Fuel Type: No. 6 Oil
Boiler Type: Erie City D Type
Boiler Design: Steam Rate 60,000 #/hr.
Pressure 285 psig
Superheat 600°F

Statement of Conditions. Superheater tube failures forced the boiler out of service. 100 of 350 tubes had to be replaced; others were damaged but serviceable. An examination of the failed tubes revealed heavy fireside deposits and underdeposit corrosion. Analysis of the deposit identified a high percentage of sodium, sulfur and iron, and a low concentration of vanadium. A sample of fuel oil was obtained from the storage tank and a Bacon Bomb profile was conducted of the storage tank. The oil sample had a low vanadium to sodium ratio and the tank samples were high in chloride and water. This is indicative of salt water contamination.

Fuel Treatment Approach. All the evidence for the fireside tube failures pointed to high temperature corrosion. A look at the fuel oil and deposit analyses confirm this. When the sodium concentration in the fuel is greater than the vanadium (>1:1), the sodium through reaction Kinetics will combine with sulfur to form sodium pyrosulfate ($Na_2S_2O_7$). Sodium pyrosulfate has a eutectic melting temperature of 752°F which is near the skin temperature in the superheater zone. Sodium pyrosulfate in the molten state is very corrosive. The high iron in the fireside deposit was the result of the corrosivity of sodium pyrosulfate.

The plant was using a water and sludge emulsifier to prevent sludge and water buildup. The emulsifier treatment aggravated the sodium condition by emulsifying the high chloride (+ sodium) water in the oil. Since the sodium-vanadium ratios in the fuel promoted the formation of sodium pyrosulfate, the correct fuel treatment approach is to minimize the sodium. In order to accomplish this objective, the following recommendations were made:

1 Stop the use of the emulsifier and use a demulsifier
2 Mechanically clean the oil storage tank
3 Prepare a fuel quality specification from bids setting the maximum metals, sulfur and water concentration as well as the sodium to vanadium ratio
4 Add a light dosage of magnesium dispersion (1:10,000) to the oil going to the burners to combine with the low level metals creating a high melting point ash minimizing deposit

Results of Recommendations. After 30 days, the storage tank was cleaned. The fuel specification is currently out for long-term supply bids.

The boiler furnace and the superheater were inspected after 45 days treatment with magnesia. The boiler tubes had a light coat of magnesia but no hard deposit buildup or any signs of corrosion. Refractory deterioration has also been brought under control. This case history is an example of where the generalized approach of emulsifying water and sludge caused extensive corrosion damage. Your fuel additive supplier must make a thorough examination of your boiler operation as related to fuel quality. Fuel quality specifications need to be established so that immediate and long-term treatment objectives can be achieved. You may not be able to purchase the quality of fuel you specify. If this is so, and you have a fuel treatment program, have the fuel analyzed periodically to ensure the program's success.

Case History 2

Industry: Basic Chemical Manufacturer
Location: North Central State
Fuel Type: No. 5 Oil
Boiler Type: Combustion Engineering A Type
Boiler Design: Steam Rate 60,000 #/hr.
Pressure 150 psig

Statement of Conditions. A carbon buildup on all furnace wall tubes was observed. The flame pattern (steam atomized fuel) was a wide angle (≃120°) impinging on the sidewall tubes. Severe black stack emissions were evident during increased load change. To eliminate the smoke, the boiler is operated at 3.5 to 4.0 percent, excess oxygen at low loads and 2.9 to 3.2 percent excess oxygen at high loads. These oxygen levels are excessive and uneconomical. The plant however, being located in a residential area was image conscious.

Fuel Treatment Approach. The basic problem, which was recognized by plant supervision, is the air to fuel ratio cam-following control system. Air flow increase on load change lagged fuel resulting in incomplete combustion. Replacing a relatively new combustion control system was an unacceptable monetary alternative. We recommended evaluation of a manganese combustion catalyst. Two manganese organics were selected for evaluation. The pertinent test data is below along with a typical fuel analysis:

Test Data

Product	Base Line	Manganese Napthanate	Manganese Carboxylate
Active Concentration mg/l	0	6	2
Steam Load #/hour	21,000	20,000	21,000
% Excess Oxygen (O_2)	3.0–3.8	3.0–3.3	1.5–2.5
% Smoke Point (O_2)	2.4–2.6	2.4–2.6	0.9–1.2
% Carbon Dioxide (CO_2)	12.1	12.2	12.8
% Carbon in Stack Particulate	65	61	27
Acid Dew Point °F	265	260	255
Mg/l SO_3	5.0	2.5	1.8
Stack Temperatures Corrected °F	356	347	325

The quality of the fuel oil remained constant for the three month evaluation period.

Fuel Oil Analysis

Parameter	Concentration	Parameter	Concentration
Ash	<0.02%	Sodium	27 mg/kg
Sulfur	0.89%	Vanadium	1.0 mg/kg
Water	1.70%	Iron	15.3 mg/kg

Results of Recommendations. The test data above tells the story. By using the manganese carboxylate the average oxygen (O_2) level to reach the smoke point was drastically reduced from 2.5 to 1.0 percent. A side benefit was the reduction in the acid dew point and stack gas temperature, the latter reducing the corrosivity of the stack gases to heat recovery equipment and the former a direct fuel savings calculated as 1.3 percent on a 24 hour average.

Physically, using the manganese carboxylate, the flame color changed from a yellow/orange to a yellow/white, the carbon buildup on the walls of the furnace slowly cleaned up and the amount of carbon in the fly ash was significantly reduced. The manganese naphthanate did not exhibit this much improvement in performance.

Operating experience, using the manganese carboxylate, since February of this year, has permitted boiler operation under extreme swing load conditions without objectionable smoke generation. Although economy of treatment vs. fuel cost was of secondary interest, a 0.4 percent fuel savings over fuel treatment cost is 3.06 dollars per 1000 gallons of oil which is less than 0.9 percent of fuel costs. Other cost savings, not factored into this figure include reduced maintenance, longer burner tip life and obviously no law suits or court actions.

This case history is an instance where a fuel additive can be used economically as a viable solution to a combustion control problem. Keep in mind, however, that chemical additives are an alternative but not a permanent solution to mechanical problems. A burner nozzle with a narrower angle should also be evaluated.

Case History 3

Industry: Textile Printing and Finishing
Location: Southeastern State
Fuel Type: No. 6 Oil
Boiler: Combustion Engineering A Type
Boiler Design: Steam Rate 150,000 #/hr.
Pressure 265 psig

Statement of Conditions. This particular boiler had been fired for seven years using a high sulfur (2.0 percent) and vanadium (300 ppm) residual fuel. The boiler was shut down each weekend due to production schedules. The Lungstrom airheater baskets showed signs of acid corrosion and the furnace, in particularly the first pass, had significant deposit accumulations.

The major cause of the deposits is the vanadium in the fuel. The vanadium deposits had accumulated to 15 to 18 in. deep on top of the two bottom drums for the entire length of the first pass. These deposits and other accumulations in the furnace caused a loss of 12 percent in boiler generating capacity.

Fuel Treatment Approach. The mechanism for deposit accumulations is a direct function of the melting temperatures of the metals in the fuel oil. When the first layer of metal oxide deposits forms on the tube, an insulating film results. The surface temperature of this deposit approaches the temperature of the combustion gases and remains in a molten state due to the insulating condition. A tacky surface is then available for additional deposits to adhere to. The fuel treatment approach called for an additive that would combine with the metals in the molten state and increase the melting temperature of the deposit. A concentrated magnesium oxide dispersion product was selected. The product was proportionally fed directly to the fuel going to the burner at a feed rate of 1 to 8000 gallons of fuel.

The alkali magnesium oxide was also the product of choice to neutralize cold end acid corrosion resulting from the sulfur in the fuel.

Results of Recommendations. After 30 days of treatment, a boiler inspection was conducted. The crystalline insoluble vanadium deposit was modified to a noncrystalline, water soluble form. The furnace deposits were noticeably less indicating that an on-line cleaning was taking place.

The Lungstrom heater, which was usually wet on weekend shutdowns, was dry indicating adequate treatment levels for acid neutralization.

By using a highly reactive concentrated magnesium oxide product, an economical solution to two fuel related problems was found. Prior treatment efforts by others, using magnesium type products, failed. Failed to the point that one company paid for a mechanical cleaning.

Why did these other products fail when this one was successful? We believe that the difference was due to product reactivity which is related to the surface area and processing of the magnesium product.

The cost of treatment at 1 gallon to 8,000 gallons of oil was 2.75 dollars per 1000 gallons. A small price to pay to ensure full boiler capacity.

References

1 Lube Text D250, "Industrial Fuel Conservation Through Energy Management," Exxon Corp., Houston, TX 1974, p. 8.

2 Reid, W. T., "Mineral Matter in Fuels," *External Corrosion and Deposits, Boilers and Gas Turbines,* American Elsevier, New York, 1971, pp. 69–70.

3 "Fuel Ash Effects on Boiler Design and Operation," *Steam Its Generation and Use,* 38th Ed., Babcock and Wilcox, 1972, chapter 15, p. 15-2.

4 Weidner, R. F., "Fuel Additives—Types and Used," The Mogul Corporation, Cleveland, Ohio 1978, Chart No. 2.

5 Reid, W. T., "Mineral Matter in Fuels," *External Corrosion and Deposits, Boilers and Gas Turbines,* American Elsevier, New York, 1971, p. 53.

6 Reid, W. T., "Mineral Matter in Fuels," *External Corrosion and Deposits, Boilers and Gas Turbines,* American Elsevier, New York, 1971, p. 71.

7 Gaff, G. M., "Industry Warms Up to Coal De-Icers," *Research, Chemical Week,* McGraw-Hill, New York, Feb. 8, 1978, p. 39.

8 Specialty Chemicals Product Bulletin, ICI U.S. Inc., 1977.

9 "TLV Values and Relative Toxicity of Selected Metals," *American Laboratory,* Aug. 1971, p. 9.

10 Giammer, R. D., Krause, H. H., Locklin, D. W., "The Effect of Additives in Reducing Particulate Emissions from Residual Oil Combustion," ASME Paper No. 75-WA/CD-7, 1975.

G. Fabris[1]
Mem. ASME

J. C. F. Chow[2]
P. F. Dunn

Engineering Division,
Argonne National Laboratory,
Argonne, IL 60439

On Formation of a Homogeneous Two-Phase Foam Flow[3]

This paper presents the results of a series of experiments conducted to evaluate the fluid mechanical performance of various two-phase LMMHD mixer designs. The results from both flow visualization studies of the local two-phase flows downstream from various mixer-element configurations and local measurements performed to characterize these flows are presented. A conceptual LMMHD mixer design is described that insures the generation of small bubbles, prevents the formation of gas slugs and separated regions, and favors the stabilization of a homogeneous foam flow.

Introduction

Although a mixer of gaseous and liquid phases is an important component in many current chemical and mechanical engineering systems, surprisingly little attention has been directed toward its proper design from a fluid-mechanical point of view. Some applications require a mixer to create a fine spray of liquid droplets in a gaseous medium, while others, as in the case of a LMMHD (liquid-metal magnetohydrodynamics) mixer, require a uniform dispersion of gaseous bubbles in a liquid medium.

Certain requirements for LMMHD mixer design result from the mixer's relation to the LMMHD energy conversion system. A schematic representation of the two-phase LMMHD system is shown in Fig. 1 and the typical LMMHD mixer-generator arrangement in Fig. 2. Refer to Fabris and Hantman [1] for a recent review on the specifics of the system. The heat-to-mechanical-to-electrical energy conversion characteristics of this LMMHD system require that the mixture's void fraction in the generator be high (on the order of 0.8 or greater) for maximum cycle efficiency (assuming generator isentropic efficiency is not significantly lowered with increasing void fraction.) This is achieved through the creation of a stable two-phase homogeneous foam flow of high void fraction by the mixer. Prediction codes developed at ANL have shown that if such a flow is maintained in the generator the isentropic efficiency of the LMMHD generator remains high provided the two-phase mixture behaves as a no-slip[4] homogeneous fluid.

It was proposed by Fabris, et al. [2] to use surface-active additives for liquid metals in order to prevent bubble coalescence, thereby creating a high-void-fraction foam flow with essentially zero slip. Such a foam flow behaves as a single-phase fluid with expansion properties very similar to that of a gas (important for heat-to-mechanical energy conversion). Literature on the formation of such a bubbly two-phase high-void fraction mixture is non-existent. However, some studies relevant to this problem have been made. Kling [3] experimentally investigated the injection of a gas through a single orifice into a stagnant liquid column at various pressure differentials and found a limiting bubble production rate. Wallis [4] showed that a surface-active liquid is a "necessary but not sufficient condition" for the creation of a homogeneous foam flow. These results indicate that increased surface activity delays the transition to slug flow with increasing void fraction, provided the air injection velocity remains below a critical superficial air velocity (Fig. 3). Further, if small superficial air injection velocities (<0.05 m/s) are maintained, high-void-fraction bubbly flows can be readily achieved. Staub [5] also pointed out that the manner of gas injection can have a detrimental influence on the resulting two-phase flow pattern and velocity slip between the gas and liquid phase when the liquid component is surface-active. Fujii-e, et al. [6] have noted that the increased turbulence intensity of the liquid at the entrance of a two-phase flow mixer strongly influences the resulting two-phase flow pattern and increases slip. Prins [7] made an attempt to derive a theoretical formulation on how velocity fluctuations in already generated foam flows could destroy it for some surface-active systems. More recently, Adler [1], testing two different air injection devices, revealed that the resulting non-surface-active high-void-fraction two-phase flow in both cases manifested practically the same flow characteristics.

All of the above clearly point out the importance of the proper design of a two-phase flow mixer which would create a homogeneous and stable foam of high void fraction at the entrance to a LMMHD generator. These considerations led to the initiation of the experiments described below.

Experimental Facility

A schematic of the ANL (Argonne National Laboratory) two-phase air-water test facility and its mixer design-evaluation test section is shown in Fig. 4. The 0.1 m × 0.1 m × 2.0 m vertically-aligned plexiglas test section utilizes a perforated plate at its domestic water supply inlet to create a uniform high level of downstream turbulence and a uniform velocity profile. A honeycomb made of packed straws then reduces the turbulence level perpendicular to the flow and provides a further uniform large obstruction, thereby producing a relatively-high pressure drop which reduces the streamwise component of turbulence. The flow downstream of the honeycomb is uniform with a low turbulence level. Further, the wall boundary layers are thin since

---

[1] Present affiliation: Senior Scientist, Combustion Dynamics and Propulsion Technology Division, Science Applications Inc., 21133 Victory Blvd., Canoga Park, CA. 91303.

[2] On sabbatical leave from the University of Illinois at Chicago Circle.

[3] Work prepared under the auspices of the U.S.D.O.E. and supported in part by the Office of Naval Research.

[4] Slip refers to the positive difference between the gas and liquid velocities at a particular cross section. It depends on the effectiveness of coupling between the liquid and gas phases and is inversely related to bubble coalescence.

Contributed by the Facilities Design Committee for publication in the JOURNAL OF ENGINEERING FOR POWER. Manuscript received at ASME Headquarters October 9, 1979.

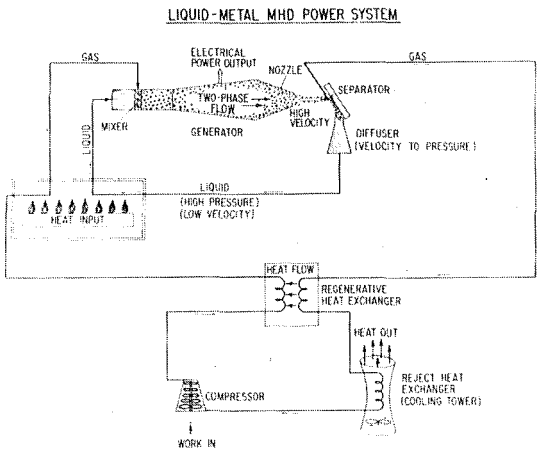

Fig. 1 Schematic of the LMMHD energy conversion system

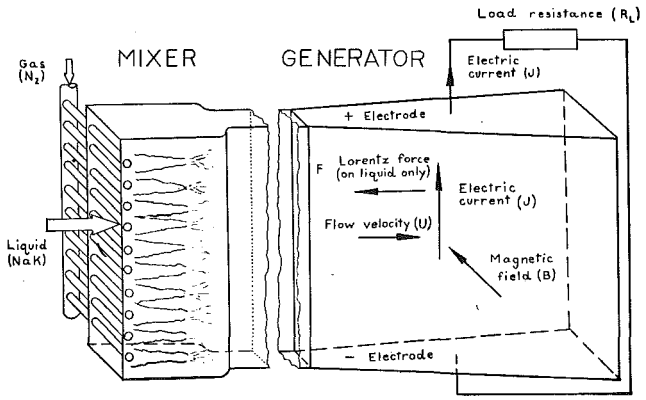

Fig. 2 Typical LMMHD mixer-generator configuration

they originate downstream of the honeycomb. Series of pressure taps and ports for the insertion of resistivity and hot-film probes are located along the test section length.

Compressed laboratory air is supplied via a manifold to the mixer elements. Both air and water flow meters are used to determine the inlet two-phase mixture quality. Various means of slow- and high-speed photography (Polaroid, 35mm, and Fastax cameras) are employed in conjunction with different ambient and stroboscopic lighting techniques to visualize the local two-phase flow.

The two-phase flow's local void fraction is measured via fine resistivity probes used in conjunction with resistivity probe and discriminator circuits developed for these experiments (Fig. 5). A gamma-ray attenuation system employing thullium sources is also present to obtain average void fraction profiles and these are compared with those obtained using the resistivity-probe method. Fig. 6 represents comparison of the average void fractions obtained by the resistivity probe and the γ-ray system. Agreement was reasonable even when a surfactive soap solution was used.

Plexiglas plates of different dimensions are inserted in the test section for each of the four mixer elements tested (single-tube, nine-tubes, nine-tubes with downstream contraction, and airfoil configurations). All tubes are 0.25 in. (0.6 cm) dia stainless steel tubing, with 0.076 in. (0.2 cm) size holes positioned 0.19 in. (0.5 cm) apart, staggered in two rows each 45 deg directed into the flow. The typical channel cross-sectional area of 1×4 in. (2.5×10 cm) is reduced to 0.5×4 in. (1×10 cm) at 2 in. (5 cm) downstream from the mixer elements for the case of the nine tubes with an abrupt downstream contraction.

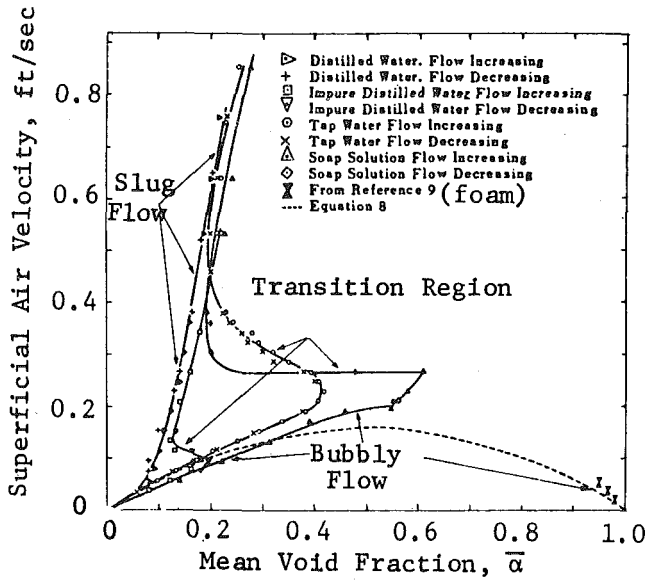

Fig. 3 Influence of surface activity on superficial air velocity in a bubbling column (Wallis, [4])

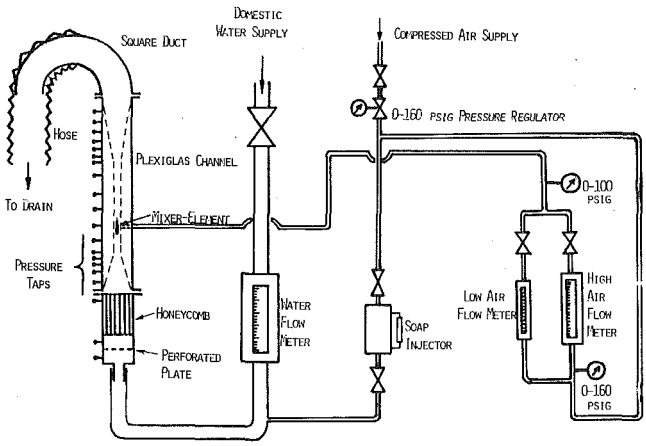

Fig. 4 Schematic of the air-water test facility

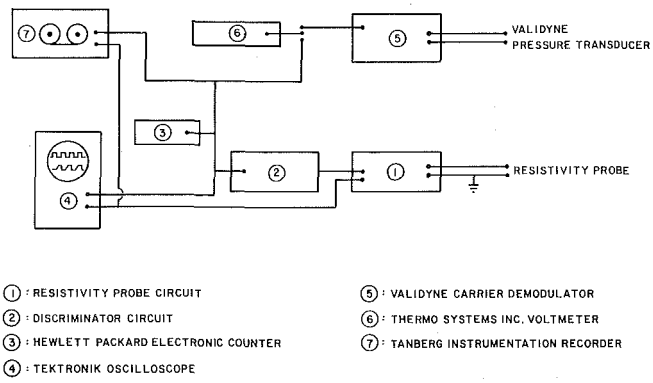

Fig. 5 Schematic of the data acquisition arrangement

Nomenclature

$\dot{V}_G$ = volumetric gas flow rate
$\dot{V}_L$ = volumetric liquid flow rate
U = axial velocity
α = local void fraction
$\bar{\alpha}$ = average void fraction of the cross-sectional area
$\beta = \dot{V}_G/(\dot{V}_G + \dot{V}_L)$

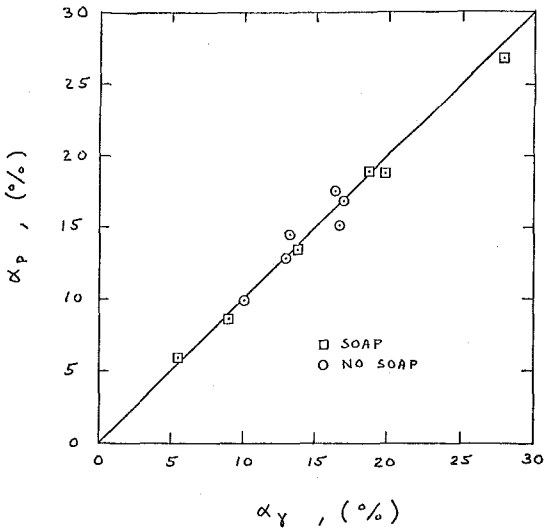

Fig. 6 Comparison of average void fractions obtained by the resistivity probe and a γ-ray system

Experimental Procedure

Each test run consisted of three different air flow rates at a predetermined constant water flow rate. For a given air flow, static pressures along the channel were measured in addition to local void fractions and bubble frequencies. Local void fractions were obtained approximately 12 in. (30 cm) downstream of the mixer element in both cross-sectional directions at a minimum of five cross-channel points. The bubble frequencies were recorded three times at each probe location for a duration of 10 s.

For flow visualization, 35 mm and Fastax cameras were used. The probe responses were observed on an oscilloscope and photographed using a Polaroid camera. In some selective runs, the probe responses were recorded on tape for further analysis. For a single-tube mixer, the void fractions were taken only along the narrow portion of the channel, but at two locations along the channel instead of one. In some instances, a soap solution (surfactant) was injected into the inlet water to determine the effect of increased surface activity.

Experimental Results

The typical operating parameter ranges included volumetric flow rates of water from 0.06 to 0.4 × 10^{-2} m^3/s and air from zero to 2.19 × 10^{-2} m^3/s, and local and averaged void fractions from zero to 0.8 and zero to 0.43, respectively. The results of tests for the various mixer designs are summarized in the following.

Single-Tube Mixer in a Straight Channel. The local void fraction and the bubble frequency were measured approximately 3 in. (8 cm) and 12 in. (30 cm) downstream of the mixer element to study the development of the mixing process in the channel. Measurements showed that near the mixer element the air was concentrated in the center portion of the channel, and further downstream the void-fraction distribution assumed a parabolic shape (see Fig. 7).

Experiments with soap solution injected upstream exhibited almost no noticeable change in void fraction profile shape and magnitude and in measured bubbling frequency. The slow injection of air in stagnant water produced bubbles of widely different sizes and shapes, as is evident in Fig. 8. Turbulent vortices created by the movement of large gas bubbles had the tendency to break the bubbles into smaller ones. Note that this "favorable effect" of turbulence exists only at low average void fractions (~0.1).

The high injection of air into stagnant water created churn turbulent slugs with water splashing up and down making observation in the region of gas injection difficult. When a lower water flow rate was applied, water would sweep exiting gas bubbles around the tube (due to the high momentum of the water with respect to the air) as shown in Fig. 9. A separated air-filled region was formed at the trailing edge of the mixer injection tube. The separated region broke up into bubbles of widely different sizes and shapes. This irregularity in shapes

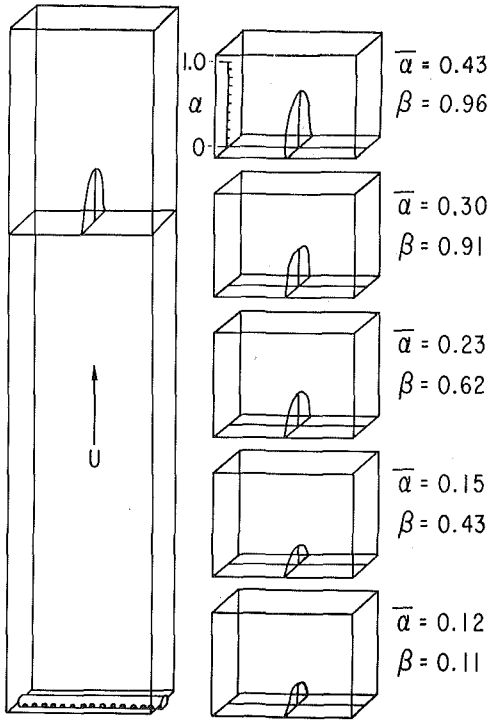

Fig. 7 Single-tube mixer in a straight channel: local void fraction profiles V_L = 0.06(*a*), 0.2(*b*), 0.06(*c*), 0.06(*d*), 0.4(*e*) × 10^{-2} m^3/s

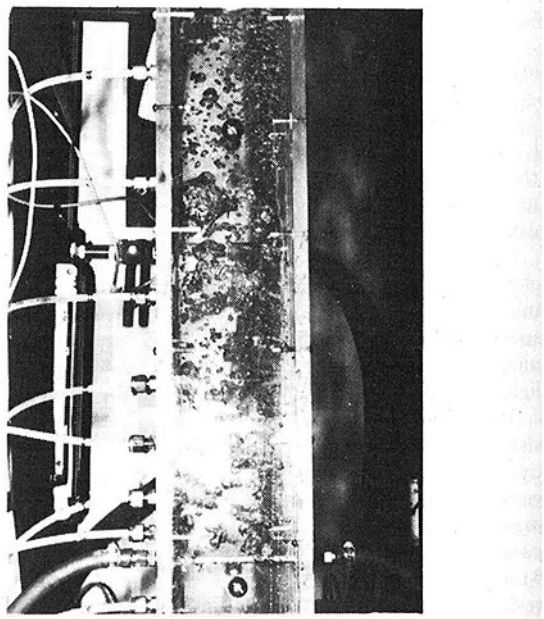

Fig. 8 Two-phase flow pattern for a single-tube mixer in a straight channel: zero water flow rate and low air flow rate

was attributed to the influence of vortices and, to some degree, to coalescence. Increasing the velocity of the water resulted in more than a proportional increase in the length of the separated region. At high velocities the air-water interface appeared relatively flat with many small-scale waves.

Nine-Tube Mixer in a Straight Channel. The measurements were taken approximately 12 in. (30 cm) downstream from the tubes. (This distance is roughly the same as the length from the mixer to the generator entrance in the present ambient-temperature LMMHD generator experiment at ANL.) Two-phase flow patterns obtained are illustrated in Fig. 10. Distinct separated regions were found to form downstream of each tube. These individual separated regions persisted for several tube diameters downstream, and their length in-

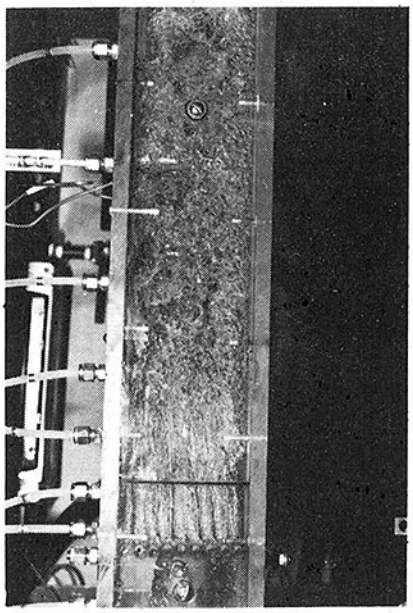

Fig. 9 Two-phase flow pattern for a single-tube mixer in a straight channel: medium water and medium air flow rates

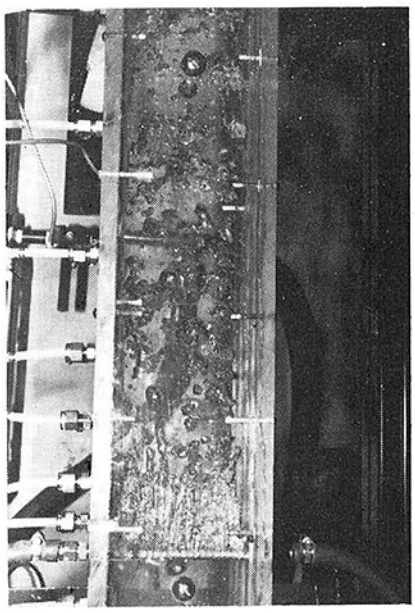

Fig. 10 Two-phase flow pattern for a nine-tube mixer in a straight channel: medium water and medium air flow rates

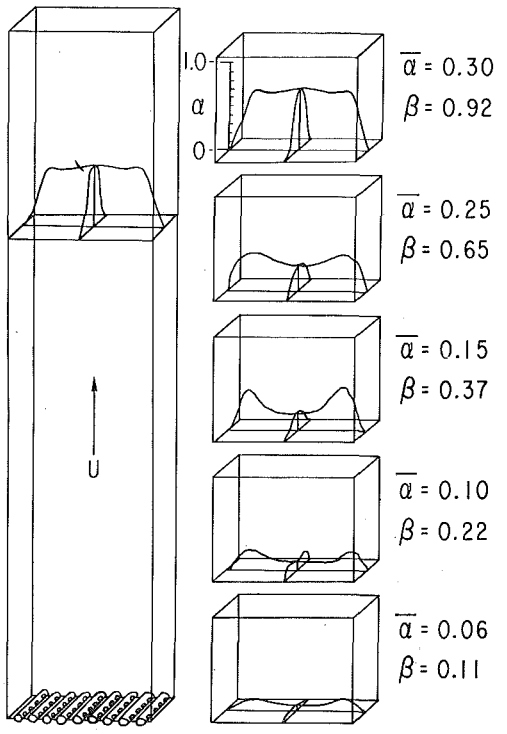

Fig. 11 Nine-tube mixer in a straight channel: local void fraction profiles V_L = 0.02(*a*), 0.06(*b*), 0.2(*c*), 0.2(*d*), 0.4(*e*) × 10^{-2} m^3/s

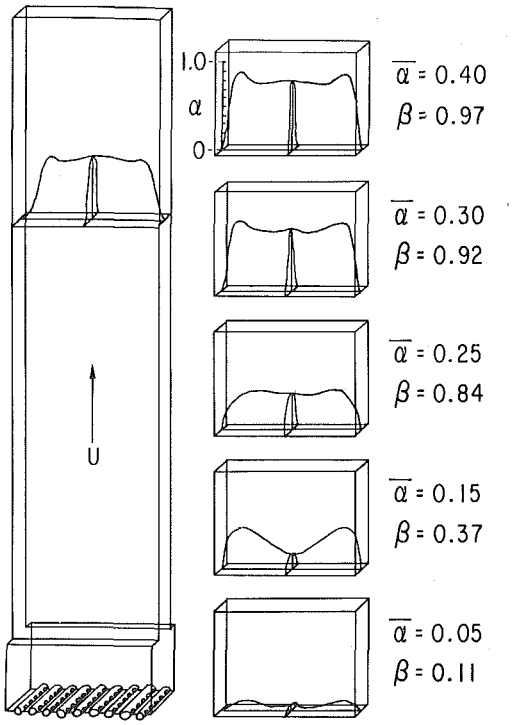

Fig. 12 Nine-tube mixer in a straight channel with an abrupt contraction: local void fraction profiles V_L = 0.06(*a*), 0.2(*b*), 0.4(*c*), 0.2(*d*), 0.4(*e*) × 10^{-2} m^3/s

creased with increasing water flow rate. Details of the mechanism of break-up of the separated regions were difficult to observe. Observations made along the narrower side of the channel revealed that a continuous air-water interface existed on the narrow side of the channel. Measurements showed that for a given water flow rate, the lateral void fraction distribution changed from a parabolic-like to a Gaussian-shaped distribution as the air flow rate increased. This was likely caused by a rapid migration of the bubbles toward the center of the channel due to bubble coalescence brought about by increased agitation. The void-fraction measurement made near the tubes showed a more-parabolic-like distribution. The depression of the void-fraction distribution in the central portion of the channel (see Fig. 11) across the wide cross-sectional area was probably caused by the higher stagnation pressure of the faster-moving water in the central portion. This induced a lower air flow rate for the perforated cylindrical tubes located in the center portion of the channel. Also, in this case stable separated regions filled with air were formed downstream of the tubes, and the length of these regions increased with increasing velocity.

Nine-Tube Mixer with Abrupt Contraction. The void-fraction distribution observed was found to closely resemble that noted for the straight channel, except that the air was more-evenly distributed

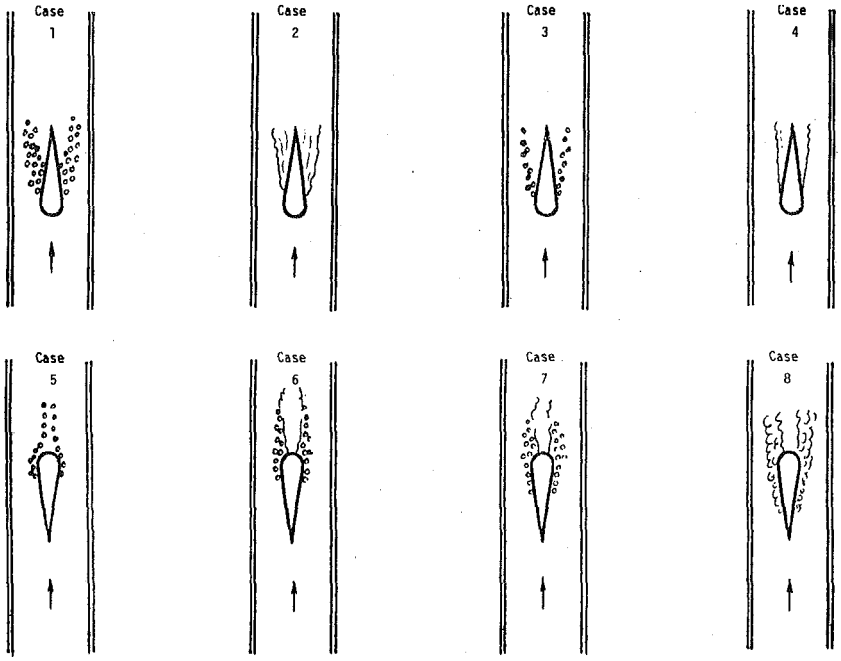

Fig. 13 Airfoil-shaped element in upward flow (Case 1 (low water and air flow): bubbles (~3–5 mm dia) emanate from trailing holes. Case 2 (low water and high air flow): a slug is generated at the surface (resembling film boiling) with a very turbulent interface. Case 3 (high water and low air flow): bubbles (~1 mm dia) emanate from leading holes. Case 4 (high water and medium air flow): separation occurs with a finely structured smooth interface. Case 5 (low water and air flow): bubbles (~3 mm dia) emanate from trailing holes with no separation. Case 6 (low water and medium air flow): bubbles (~3–5 mm dia) emanate and mix with separated region. Case 7 (medium water and low air flow): pattern similar to Case 6 but bubbles ~1–3 mm dia. Case 8 (low or medium water and high air flow): structure resembles film boiling with a very turbulent interface.) Flow rates at ambient pressure and temperature—Air: low: up to 0.0007 m^3/s, medium: from 0.0007 to 0.0018 m^3/s, high: above 0.0018 m^3/s. Water: low: up to 0.002 m^3/s, medium: from 0.002 to 0.007 m^3/s, high: above 0.007 m^3/s

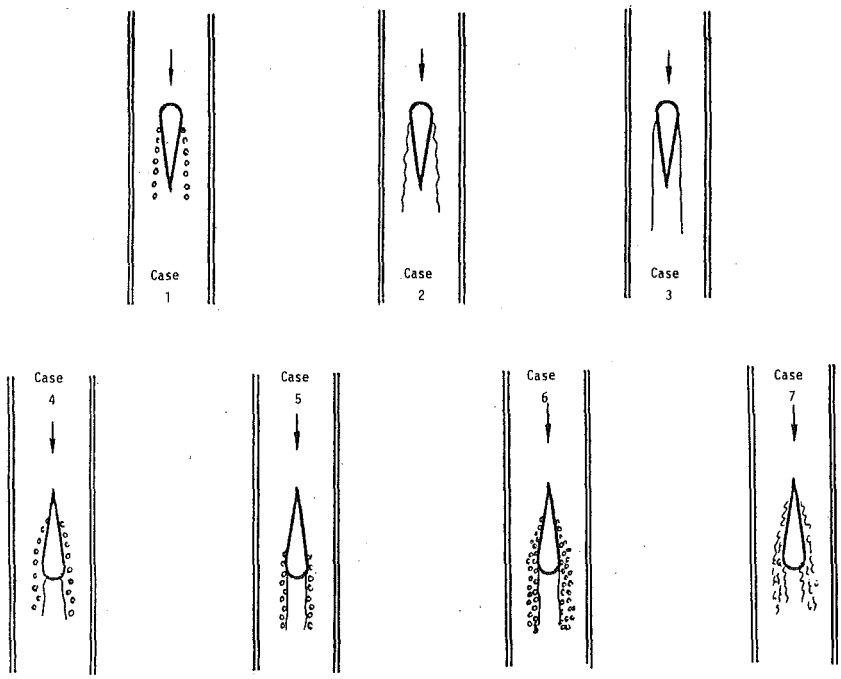

Fig. 14 Airfoil-shaped element in downward flow (Case 1 (low water and air flow): bubbles (~3–4 mm dia) emanate from leading holes only. Case 2 (low water and medium air flow): separation occurs with relatively smooth interface. Case 3 (medium or high water and low air flow): separation occurs with straight and smooth interface. Case 4 (low water and air flow): bubbles (~3–5 mm dia) emanate from leading holes only and then coalesce with separated region. Case 5 (high water and low air flow): bubbles (~1 mm dia) emanate from trailing holes and then coalesce with separated region. Case 6 (high water and medium air flow): bubbles (~1 mm dia) emanate from most of the holes and some coalesce with separated region. Case 7 (medium or high water and high air flow): structure resembles film boiling with a very turbulent interface and turbulent separated region.) Flow rates at ambient pressure and temperature—Air: low: up to 0.0007 m^3/s, medium: from 0.0007 to 0.0018 m^3/s, high: above 0.0018 m^3/s. Water: low: up to 0.002 m^3/s, medium: from 0.002 to 0.007 m^3/s, high: above 0.007 m^3/s

across the wide cross-sectional area (see Fig. 12). This was attributed to the forced turbulent mixing caused by the abrupt contraction. This was especially true at high water flow rates.

When the soap solution was injected for this configuration, a number of very small bubbles produced by the two-phase turbulence were observed. However, measurements displayed no appreciable change in void fraction distributions and only a slight increase in bubbling frequencies.

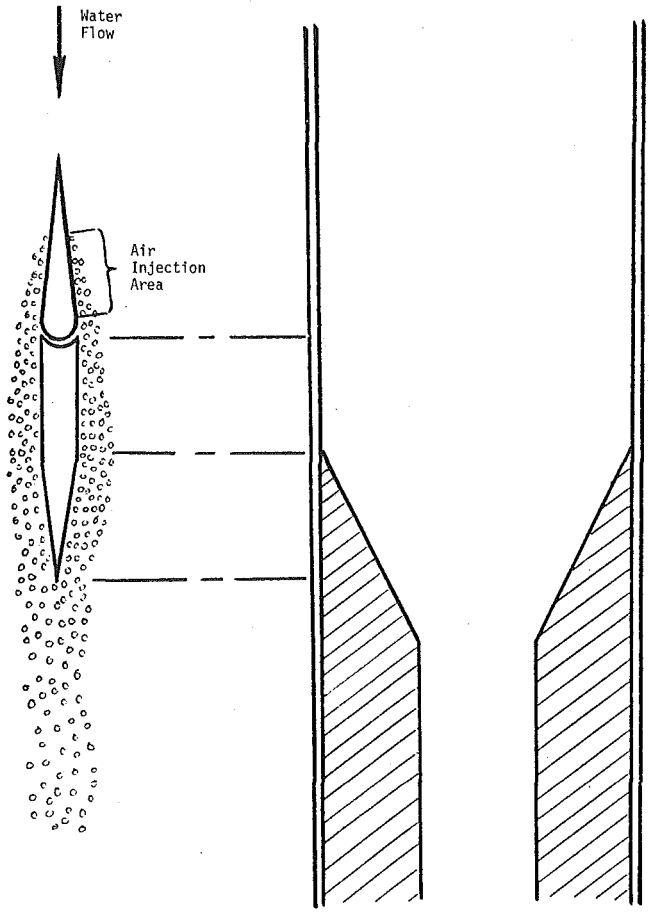

Fig. 15 Extended perforated-plate airfoil element with contraction

Perforated-Plate Airfoil Mixer. In addition to the above element tests, a series of semi-quantitative tests were run to initially investigate the flow structure produced by an airfoil-shaped mixer element. In this case two 3.8 cm-thick plexiglas plates were inserted, reducing the cross-sectional area to 4×1 in. (10×2.5 cm), as indicated by the dashed lines in Fig. 4. The element was installed in the center of this reduced channel and constructed from a perforated aluminum plate with 0.05-in. (0.13-cm) dia holes, constituting 23 percent open-surface area. The element is 3 in. (7.62 cm) long and 0.63 in. (1.6 cm) thick. Figs. 13 and 14 contain summary sketches of the flow regimes for various flow configurations. It was readily demonstrated from these experiments that the geometry of the mixer and the local pressure distribution decisively influenced the structure of the generated two-phase flow. The results from the various configurations are briefly summarized as follows:

Configuration 1 (*upward flow with aligned element, Cases 1–4, Fig. 13*). The lowest pressure region in the water flow adjacent to the mixer element was found to occur at the downstream holes of the element where the first air bubbles appeared. For high water velocities this region moved to the chord of the element. However, for high air injection rates the water flow was found to separate from the entire element area.

Configuration 2 (*upward flow with reversed element, Cases 5–8, Fig. 13*). As the water velocity increased along the element, resulting in a negative pressure gradient along the flow, the ejected bubbles were driven along the flow, and this tended to minimize their coalescence and postpone separation. Still, a separated region downstream of the bluff trailing edge formed. With high air flow, separation characterized by a very turbulent interface occurred at the element.

Configuration 3 (*downward flow with aligned element, Cases 1–3, Fig. 14*). Here the hydrostatic weight of the water increased the pressure gradient along the mixer element and this was found to enhance the onset of the type of flow separation observed for Configuration 1.

Configuration 4 (*downward flow with reverse element, Cases 4–7, Fig. 14*). In this configuration the type of separation analogous to that found for Configuration 2 was observed.

Based on these results another series of element tests were conducted to eliminate the separated region that occurred downstream of the bluff trailing edge for Configuration 3. The basic design of the

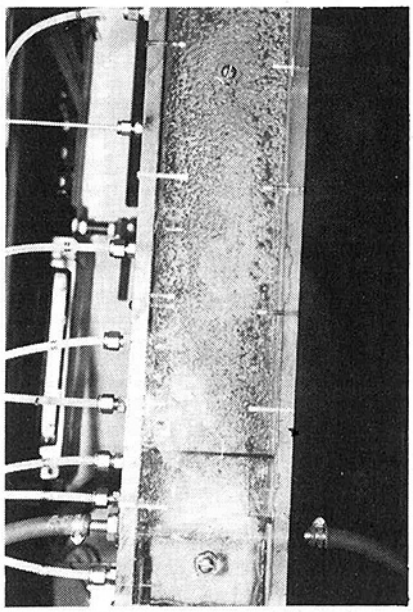

Fig. 16 Two-phase flow pattern obtained in tap water for a single porous airfoil mixer in a straight channel: low water and medium air flow rates

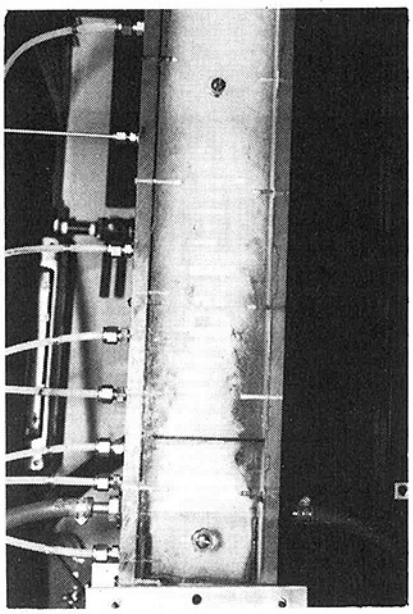

Fig. 17 Two-phase flow pattern obtained in soap-water solution for a single porous airfoil mixer in a straight channel: low water and medium air flow rates

extended element for these tests (Fig. 15) consisted of a gradually-tapered trailing edge with the surrounding channel walls contracting perpendicular to the tapered edge, but at a larger angle. This constriction forced the velocity to increase and the pressure to decrease along the flow, thereby eliminating flow separation at the trailing edge over a very wide range of gas injection rates.

Porous Airfoil Mixer. It was noticed in a number of the experiments with the perforated-plate mixer element that air was exiting from only two or three adjacent rows of holes. This occurred where the pressure in the water (or two-phase flow) was the lowest, since gas will exit where the highest positive pressure differential is available. To insure the generation of bubbles over the whole element, it is necessary to increase the pressure difference across the injection plate so that it exceeded the pressure difference in the water channel along the length of the element. For this reason, it was decided to make an airfoil shaped mixer element out of sintered porous metal with 10 μm dia pores. The element was placed with the narrower edge facing a flow that was vertically upwards. The air and water flow patterns for low flow rates are given in Fig. 16. Bubbles about 3 mm in diameter were obtained. Higher water velocities yielded smaller bubbles while higher air flow rates eventually caused transition to slug flow and hydrodynamic instability.

The effect of the addition of a surfactant (soap solution) is illustrated in Fig. 17. The air and water flow rates are the same as for Fig. 16. It is striking to see that the diameter of the bubbles was decreased by a factor of five to ten, hence their volume decreased by a factor of a hundred to a thousand. The relative slip velocity (or rise velocity) of these tiny bubbles appeared to be lower. (This can easily be observed when bubbling through stagnant water.) When the air injection rate was high, the two-phase flow at the element resembled that found in film boiling. Large gas slugs were present in the downstream flow, but they were more difficult to observe due to presence of many tiny bubbles with the soap surfactant.

Conclusions and Summary

Results from these experiments indicate that element and contraction-geometry designs are the most critical factors in mixer development. Two-phase flow turbulence is not effective itself in the creation of a homogeneous two-phase flow at high void fractions even in strongly surface-active systems. This is somewhat contrary to the behavior at low void fractions where turbulence breaks large bubbles into smaller ones. It seems that in some mixers churn turbulent slug flow is established in the mixer and is maintained further downstream regardless of the level of surface activity of the system. (One explanation of how agitation may act to destroy foam is given by Prins [9].)

A favorable (decreasing) pressure gradient in and downstream from the injection region tends to drive bubbles along the flow and postpone their possible coalescence and hence the creation of separated regions. The latter themselves could be sources of large bubbles or slugs. The most effective way of insuring the existence of a favorable pressure gradient was found in the experiments to be through the use of various contraction geometries. Such contractions can have other beneficial effects, such as decreased frictional and two-phase mixing losses upstream of an LMMHD generator. Further, since high velocities are desired in LMMHD generators (perhaps as high as 50 m/s), high pressure drops across the contraction will exist. This is advantageous since the actual two-phase mixing is accomplished at higher pressures and lower void fractions where it is easier to create a homogeneous bubbly flow. Expansion of the bubbly flow through the contraction represents a favorable condition for the stabilization of the foam flow since no additional flow disturbances are introduced, and leads to the higher void fractions desired at the generator entrance.

The literature and the above experiments show that the injection of gas through porous surfaces should be done at low superficial velocities (volumetric gas flow rate/total porous area), i.e., below the critical velocity at which hydrodynamic instability creates gas slugs at the injection surface. A low injection velocity, however, requires a relatively-large injection surface, which can be best achieved through the use of several long airfoil-shaped elements.

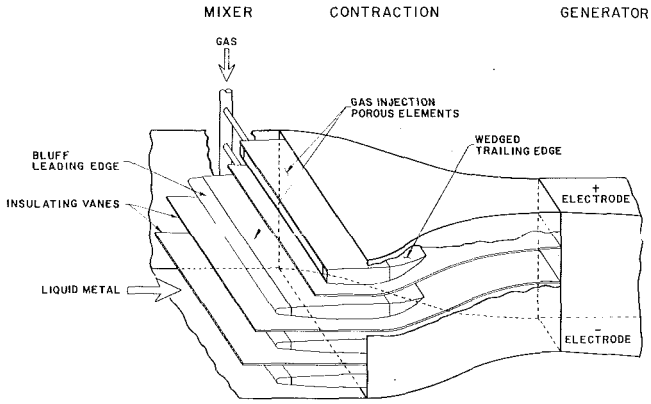

Fig. 18 Conceptual design of mixer-generator inlet assembly

The findings of this research have led to the conceptual design of a two-phase LMMHD mixer shown in Fig. 18. By placing a contraction and several long porous mixer elements upstream of the generator, a large-enough area is provided for the injection of the gas, thus ensuring a below-critical injection velocity and the creation of a multitude of small bubbles. The wedged-element trailing edges are placed in the two-dimensional contraction to provide for smooth transition in the flow, thereby preventing separation. (In this design, a continuous-accelerating region actually exists all the way from the leading edge of the porous elements to the beginning of the LMMHD generator.) The resulting favorable pressure gradient ensures that the wall boundary layers are thin and laminar. In this way, losses in the mixer are minimized.

Acknowledgment

The authors wish to acknowledge Dr. E. S. Pierson for his comments and support during the course of this research, and Mr. Robert Kolp for his technical assistance.

References

1 Fabris, G., and Hantman, R. G., "Fluid Dynamic Aspects of Liquid-Metal Gas Two-Phase Magnetohydrodynamic Power Generators," *Proceedings of the 1976 Heat Transfer and Fluid Mechanics Institute,* Davis, CA, Stanford University Press, 1976, pp. 92–113.

2 Fabris, G., Cole, R., and Hantman, R. G., "Fluid Dynamic Studies of Two-Phase Liquid Metal Flow in an MHD Generator," *Proceedings of the 6th International Conference on MHD Electrical Power Generation,* Vol. 3, Washington, D. C., 1975, pp. 363–376.

3 Kling, G., "Über die Dynamik der Blasenbildung beim Begasen von Flüssigkeiten unter Druck," *International Journal of Heat and Mass Transfer,* Vol. 5, 1962, pp. 211–223.

4 Wallis, G. B., "Some Hydrodynamic Aspects of Two-Phase Flow and Boiling," *International Development in Heat Transfer,* ASME Paper 38, Vol. 2, 1961, pp. 319–340.

5 Staub, F. W., "Flow Regimes and Mixture Densities in Froth-Foam Columns," *Proceedings of the Meeting of American Institute of Chemical Engineers,* Boston, Sept. 1975.

6 Fujii-e, Y., Miyazaki, K., Inoue, S., Saito, M., and Suita, F., "Experimental Study on Two-Phase Induction Power Generation using NaK-N_2 Mixture," *Proceedings of the 6th International Conference on MHD Electrical Power Generation,* Vol. 3, Washington, D. C., 1975, pp. 247–263.

7 Prins, A., "Dynamic Surface Properties and Foaming Behavior of Aqueous Surfactant Solutions," *Foams,* R. J. Akers, ed., Pergamon Press, 1976, pp. 51–60.

8 Adler, P. M., "Formation of an Air-Water Two-Phase Flow," *AIChE Journal,* Vol. 23, 1977, pp. 185–191.

T. Azuma
Manager

Y. Tokunaga
Diesel Engine Research Department,
Kawasaki Heavy Industries, Ltd.,
14, Higashi Kawasaki-cho, 2-chome
Ikuta-ku, Kobe,
Japan

T. Yura
Lecturer,
Osaka Institute of Technology,
16, Ohmiya-cho, 5-chome, Asahi-Ku,
Osaka,
Japan

Characteristics of Exhaust Gas Pulsation of Constant Pressure Turbo-Charged Diesel Engines

The constant pressure turbo-charge system has now been increasingly adopted for marine diesel engines because of its higher thermal efficiency in the range of higher mean effective pressure. However, it seems that there has been no paper published on the exhaust gas pulsation of this sytem. In this study, a gas flow model of the constant pressure turbo-charged diesel engines was assumed as a basic and fundamental one, and an investigation was made of it. As a result, some characteristics of the exhaust gas pulsation of this system have been clarified and a mathematical simulation system has been established. It must be emphasized that the filling and emptying method which neglects wave propagation cannot simulate the pulsation, although it can simulate the average exhaust gas pressure and temperature of this system.

Introduction

Nowadays, engines of higher thermal efficiency are more urgently required and investigated than ever in order to save energy.

Under such circumstances, the constant pressure turbo-charge system has been increasingly adopted for marine diesel engines because of its higher thermal efficiency in the range of higher mean effective pressure.

However, it seems that there has been no paper published on the exhaust gas pulsation of this system.

The purpose of this study is to clarify the characteristics of the exhaust gas pulsation of the constant pressure turbo-charged diesel engines and then to establish a mathematical simulation system for it.

As a result of the study, some of the characteristics of the mentioned exhaust system have been clarified and a mathematical simulation system has been established.

Steps in this Study

To begin with, a basic and fundamental model is assumed as a gas flow system of the constant pressure turbo-charged diesel engines. At a glance, the flow in the system seems to be very complicated, i.e., three-dimensional. However, it is desirable that it can be simulated by a one-dimensional system. With this in mind, the study was made in three stages.

In the first stage, an experimental unit was made, which used air for working fluid and whose pipe system was 53 mm in diameter and 8300 mm in length. Theoretical analysis by one-dimensional theory and experiments were made.

Air was also used in the second stage as a working fluid. The flow system of the experiment unit was a model for that of a two-cycle engine. Using this equipment, some measurements were made which were very difficult, or impossible, to make in actual engines; also, a study was done on the possibility of applying the one-dimensional theory to the exhaust system of actual engines.

In the final stage, a study was made of the exhaust pulsation of some engines.

The pressure drop δP by friction loss in the exhaust pipe and the exhaust temperature drop δT along the pipe were studied using the following formulas for steady flow:

$$\delta P = \frac{4f}{D} \cdot \frac{1}{2} \rho u^2 \cdot L \tag{1}$$

$$\frac{\delta T}{T_0 - T_E} \cdot \frac{D}{4L} \cdot \mathrm{Pr}^{2/3} \left[\frac{\mu}{\mu_0}\right]^{-0.14} \doteqdot \frac{f}{2} \tag{2}$$

where T_0 = wall temperature of exhaust pipe
Pr = Prandtle number = 0.73
μ_0 = viscosity at the temperature T_0

As a result, the temperature drop was neglected not only in the pipe system of the two experiment units but also in those of actual engines. The pressure drop was taken into consideration in the pipe system with a diameter of 53 mm but neglected in the other systems.

Theory

Basic Gas Flow Model. A model of the gas flow system of the constant pressure turbo-charged diesel engines is shown in Fig. 1. Thus, the system is assumed to be constructed of a scavenge air duct, ports, cylinders, connecting ducts, an exhaust pipe, exhaust gas turbines and outlet pipes which connect the exhaust gas pipes with the turbines.

In the model, the volume of the scavenge air manifold is infinitely large, the scavenge air pressure Ps and the scavenge temperature Ts are constant. The scavenge ports, the exhaust ports and the turbines are substituted by nozzles at pipe ends. The exhaust pipe, the connecting ducts and the outlet pipes are regarded as straight pipes.

Thus, the basic gas flow model is assumed to be constructed of four kinds of hydrodynamic elements, namely: volumes, nozzles, straight

Contributed by the Diesel and Gas Engine Division and presented at the Energy Technology Conference and Exhibition, February 3–7, 1980, New Orleans, La., of THE AMERICAN SOCIETY OF MECHANICAL ENGINEERS. Revised manuscript received at ASME Headquarters October 15, 1979. Paper No. 80-DPG-5. This paper was originally presented at the CIMAC Conference, Vienna, Austria, May 7–10, 1979.

pipes and branches (Fig. 1) while it is assumed to be constructed of seven kinds of structural elements.

The straight pipes are not necessarily those of constant diameter or of constant cross-sectional area along their longitudinal axis.

Fig. 2 shows a sketch of an exhaust system used in some engines as an improved exhaust system which can also be constructed using the hydrodynamic elements mentioned above.

In this study, the system shown in Fig. 1 is to be mainly studied. However, in order to prepare for the later analysis, orifices inserted in the exhaust pipe is taken into consideration in the analysis. They are assumed to be of infinitely small thickness.

Mathematical Model. The exhaust pipe system is to be regarded as one-dimensional, and the gas to be a perfect gas. The heat loss from the exhaust system is neglected, and the system is to be regarded as a non-isoentropic adiabatic system. The mathematical model is necessary for each one of the five hydrodynamic elements mentioned, i.e., flow in straight pipe, branch flow, flow at nozzle, flowless volume and throttled flow (flow at orifice).

Unsteady Flow in Straight Pipe. One-dimensional unsteady flow is represented by the following formulas.

Equation of motion
$$\frac{\partial u}{\partial t} + u\frac{\partial u}{\partial x} + \frac{1}{\rho}\cdot\frac{\partial P}{\partial x} = X \tag{3}$$

Continuity equation
$$\frac{\partial \rho}{\partial t} + u\frac{\partial \rho}{\partial x} + \rho\frac{\partial u}{\partial x} = Y \tag{4}$$

Entropy equation
$$\frac{\partial s}{\partial t} + u\frac{\partial s}{\partial x} = Z \tag{5}$$

X is an external force by pipe friction and is represented as follows:

$$X = -\frac{4f}{2D}u^2\left\{\frac{u}{|u|}\right\} \tag{6}$$

where f = friction coefficient. Y is an influence by the change of sectional area and is represented as follows:

$$Y = -\frac{\rho u}{F}\cdot\frac{\partial F}{\partial x} \tag{7}$$

Z shows change of entropy due to friction loss and is given by the following formula.

$$Z = -\frac{dq}{T} = -\frac{A(uX)}{T} \tag{8}$$

where uX = friction work/s.

Mathematical Model at the Branch. The exhaust pipe of the engines is such that the branch pipe intersects the exhaust pipe at a right angle. At first, the simplest constant pressure theory is applied as a mathematical model of branch.

By the constant pressure theory of branch, the static pressure is assumed to be equal at the junction-end of all pipes of the branch. Therefore, the following formula is given to the three-way branch, shown in Fig. 3.

$$P_1 = P_2 = P_3 \tag{9}$$

In the branch of the exhaust system of the engines, the most complicated branch has four ways. Therefore, the formulas are so constructed that the four-way branch can be calculated.

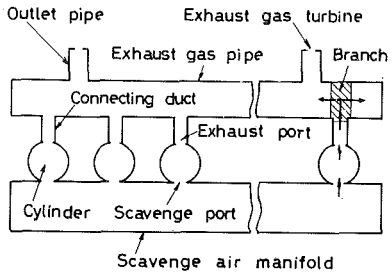

Fig. 1 A basic and fundamental model for engine gas flow systems

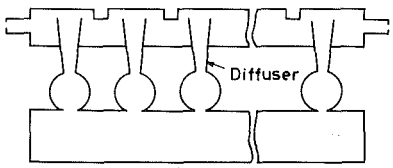

Fig. 2 An example of improved gas flow system

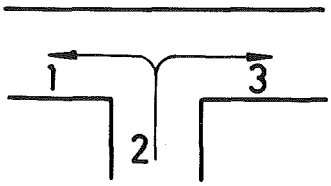

Fig. 3 Flow model of branch

As the so-called momentum theory is now thought to be the most accurate one for the branch of one-dimensional flow, it is to be studied afterwards.

Flow at Nozzle. Because the formulas for the flow at nozzle are fundamentally the same as those for throttled flow, to be described later, they are omitted here.

Mathematical Model for Volume. Suppose the gas dG_{in} with the temperature of T_{in} flows into the gas with volume V, pressure P, temperature T and weight G during a time increment dt. Suppose also that the air dG_{out} flows out and the air volume has changed by dV during dt. Then, the change of P, T and G in dt can be given by the following formulas:

Energy equation
$$dQ = CvGdT + APdV \tag{10}$$

Mass conservation
$$dG = \Sigma dGi \ (i = 1, 2, 3..) \tag{11}$$

State equation
$$PV = GRT \tag{12}$$

here
$$\left.\begin{aligned} dQ &= h_{in}dG_{in} - h_{out}dG_{out} \\ h_{in} &= c_pT_{in}, \quad h_{out} = c_pT \end{aligned}\right\} \tag{13}$$

Using the relations between (11, 12) and (13), equation (10) can be given as follows:

$$dT = (\kappa T_{in} - T)\frac{dG_{in}}{G} - (\kappa - 1)T\frac{dG_{out}}{G} - (\kappa - 1)T\frac{dV}{V} \tag{14}$$

Nomenclature

a = speed of sound
A = thermal equivalent of mechanical work
c_p = specific heat under constant pressure
c_v = specific heat under constant volume
d = diameter of nozzle or orifice
D = diameter of exhaust pipe
f = coefficient of friction loss of pipe
F = cross-sectional area
g = gravity
G = gas weight
h = specific enthalpy
L = length of exhaust pipe
n = rotational speed of engine or rotary valve
P = absolute pressure
Q = heat
R = gas constant
s = specific entropy
T = absolute temperature
u = gas velocity
v = specific volume
γ = specific weight
θ = crank angle
K = specific heat ratio
μ = viscosity
ρ = density

Subscripts

DC = delivery close
DO = delivery open
EC = exhaust close
EO = exhaust open
E = exhaust system
s = scavenge air manifold

Then, P, T and G after dt can be obtained from (11, 12) and (14).

Mathematical Model of Throttled Flow. Now, consider the flow model in Fig. 4 where u, T and P are uniformly distributed at upper flow side, throttled part and lower flow side with the throttle of sectional area F_2 as a boundary. Formulas for the flow model are as follows.

Continuity equation $$\rho_1 u_1 F_1 = \rho_2 u_2 F_2 = \rho_3 u_3 F_3 \tag{15}$$

Energy equation $$\frac{1}{2}u_1^2 + \frac{\kappa}{\kappa-1}\frac{P_1}{\rho_1} = \frac{1}{2}u_2^2 + \frac{\kappa}{\kappa-1}\frac{P_2}{\rho_2} = \frac{1}{2}u_3^2 + \frac{\kappa}{\kappa-1}\frac{P_3}{\rho_3} \tag{16}$$

Isoentropic change $$\frac{P_1}{\rho_1^{\kappa}} = \frac{P_2}{\rho_2^{\kappa}} \tag{17}$$

Momentum conservation $$P_3 = P_2 + \rho_3 u_3 (u_2 - u_3) \tag{18}$$

However, $$u_2 = a_2 \tag{19}$$

is substituted for (18) where the flow at the throttle is choked.

Numerical Analysis by the Method of Characteristics. Equations (3–5) are solved by the method of characteristics on the basis of numerical analysis. At first, entropy s is given in terms of ρ and P to change the original equation so that the numerical integration may be easy.

$$ds = Cv\left(-\kappa\frac{d\rho}{\rho} + \frac{dP}{P}\right) \tag{20}$$

Then, introduce the following variables.

$$\sigma = P^{\kappa - 1/2\kappa} \tag{21}$$

$$\psi = \frac{2}{\kappa-1}\cdot\frac{a}{\sigma} \tag{22}$$

$$a = \sqrt{\frac{\kappa P}{\rho}} \tag{23}$$

ψ is an increasing function of entropy s and a is the speed of sound. With the above relation, the original equations are changed as follows:

$$\frac{\partial u}{\partial t} + u\frac{\partial u}{\partial x} + a\psi\frac{\partial \sigma}{\partial x} - X = 0 \tag{24}$$

$$\psi\frac{\partial \sigma}{\partial t} + \psi u\frac{\partial \sigma}{\partial x} + a\frac{\partial u}{\partial x} - a\left(\frac{Y}{\rho} + \frac{Z}{C_{v\kappa}}\right) = 0 \tag{25}$$

$$\frac{\partial \psi}{\partial t} + u\frac{\partial \psi}{\partial x} - \frac{Z}{2C_{v\kappa}}\psi = 0 \tag{26}$$

The equations to obtain the numerical analysis of (24, 25) and (26) by the method of characteristics are as follows:

$$\begin{cases} \dfrac{dx}{dt} = u + a & \text{Propagation direction of pressure} \end{cases} \tag{27}$$

$$du + \psi d\sigma = bdt \tag{28}$$

$$\begin{cases} \dfrac{dx}{dt} = u - a & \text{Propagation direction of pressure} \end{cases} \tag{29}$$

$$du - \psi d\sigma = e \cdot dt \tag{30}$$

$$\begin{cases} \dfrac{dx}{dt} = u & \text{Flow direction} \end{cases} \tag{31}$$

$$d\psi = h \cdot dt \tag{32}$$

where $$b = X + a\left(\frac{Y}{\rho} + \frac{Z}{C_{v\kappa}}\right) \tag{33}$$

$$e = X - a\left(\frac{Y}{\rho} + \frac{Z}{C_{v\kappa}}\right) \tag{34}$$

$$h = \frac{Z}{2C_{v\kappa}}\psi \tag{35}$$

A method which substitutes (27) and (29) with the following formula is referred to as a linear calculation.

$$\frac{dx}{dt} = u \pm a = \pm\bar{a} \tag{36}$$

where $\bar{a}$ is the mean speed of sound.

Experiment and Simulation

A study of air models and some engines has proved that exhaust pulsation can be simulated with satisfactory accuracy by the method of characteristics, regarding the exhaust pipe system as one-dimensional.

One-dimensional Air Model. *Experiment Unit.* As illustrated in Fig. 5, the gas flow system of the experiment unit is constructed of rotary valves, straight pipes, orifices and pipe-end nozzles. The equipment was so designed that it could simulate the gas flow in the engines as similarly as possible. In other words, the surge tank is so designed that the pressure can be maintained at a constant, and the volume of rotary valve, time area of exhaust port and the diameter of exhaust pipe are so designed that the flow rate, amplitude and shape of the pulsation can approximate those of the engines. The air flows in and out once each time the valve rotates. The opening period of the exhaust port is about $\pi/2$. The volume of the rotary valve is 7.13 liters. A photograph of the unit is shown in Fig. 6.

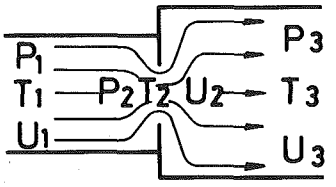

Fig. 4 Flow model of orifice

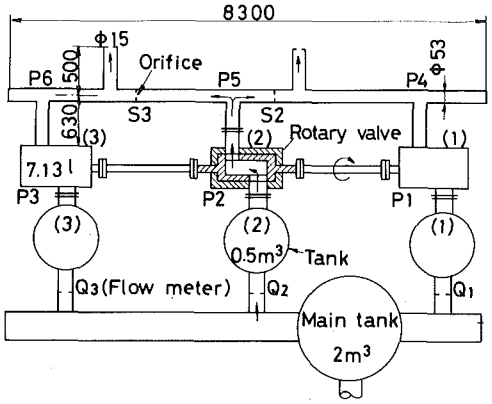

Fig. 5 Sketch of one-dimensional air model

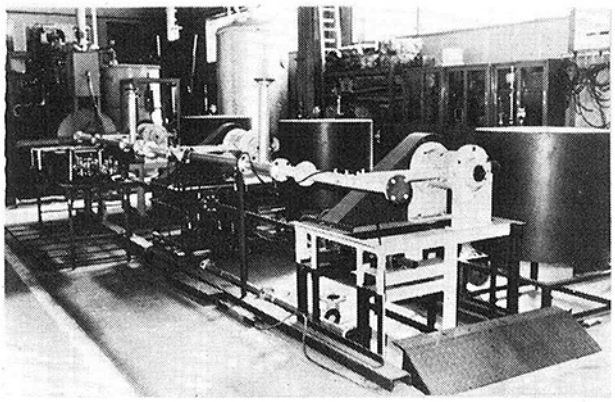

Fig. 6 One-dimensional air model

The air, after being fed out of the main surge tank, is led to sub-surge tanks (1, 2) and (3) through the orifices for flow rate measurement, from where the air is stored in each rotary valve. The compressed air stored in the rotary valve is blown down from the exhaust port to generate the pulsation. The pressure in the rotary valve P_1, P_2 and P_3 vary as shown in Figs. 7 and 8.

In the experiment, the pressure measurement was made at all the points from P_1–P_6 shown in Fig. 5 using pick-ups of strain-gauge type. The flow rate was measured at Q_1, Q_2 and Q_3.

Experiment and Simulation. A study of the influence of friction coefficient on the simulation has proved that $f = 0.009$ is proper.

Figs. 7 and 8 show a comparison of the experiment with the simulation. The conditions for the experiment and the simulation are shown in Figs. 5, 7 and 8; n = 134 rpm, tank pressure P_T = 0.13 MN/m^2 (gauge pressure), and nozzle diameter of pipe end d = 15 mm. Fig. 7 shows the case where no orifices are installed in the pipe, and Fig. 8 shows the case where the orifices with a hole diameter of 26 mm are provided at S_2 and S_3.

In the simulation, three methods were used: the method of characteristics, the linear calculation and the volume theory. Although the results obtained by the method of characteristics best matches that measured, the difference from that obtained by the linear calculation may be neglected. When orifices with small area ratio $(d/D)^2$ are provided at rather short intervals, the simulation by the volume theory approximates the actual pulsation, if roughly viewed, as shown in Fig. 8. However, the simulation by the volume theory differs greatly from the actual pulsation when wave propagation cannot be neglected as shown in Fig. 7.

The above results have proved that the pulsation of the air model which has the branch as shown in Fig. 5 and is provided with orifices can be precisely simulated by the theory described in the previous chapter.

Air Model of a Diesel Engine. *Experiment Unit.* Fig. 9 shows a model of a two-cycle engine, which is constructed like the gas flow system of the engine. The cylinder is an aluminium casting. A photograph of the equipment is shown in Fig. 10.

In the actual engines, the exhaust pipe is constructed of the exhaust pipe segment for each cylinder, and each segment is connected by the connecting piece (expander). The exhaust pipe of the model is constructed of ten segments; in other words, the model is supposed to simulate the exhaust pipe of an engine with ten cylinders.

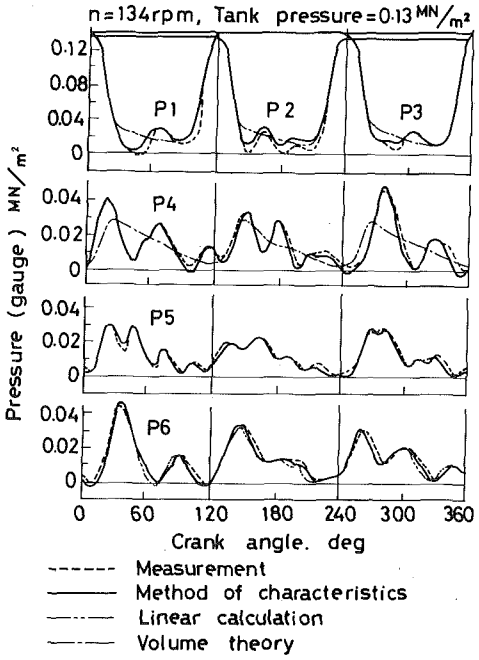

Fig. 7 Pulsation in one-dimensional air model without orifices in exhaust pipe

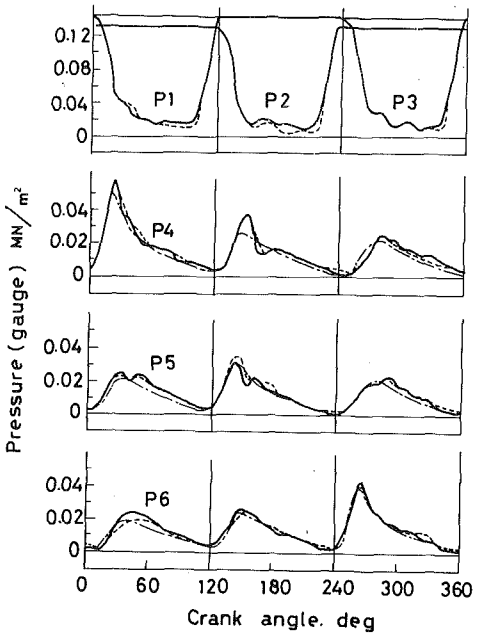

Fig. 8 Pulsation in one-dimensional model with the orifices (S_2 and S_3 in Fig. 5)

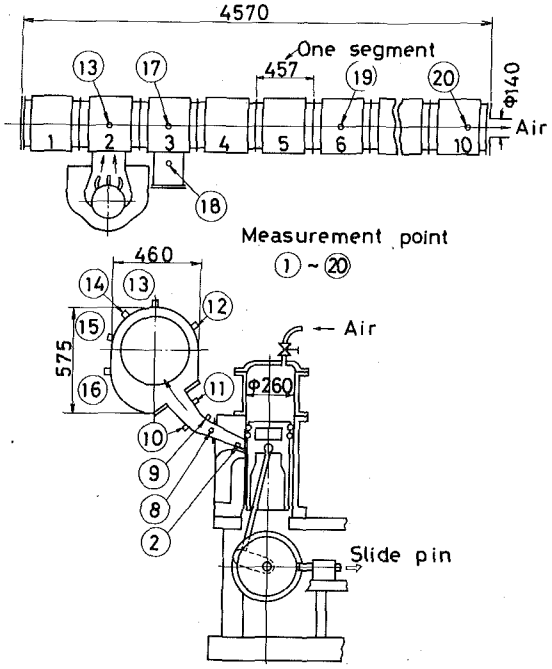

Fig. 9 Half scale air model of a two-cycle engine

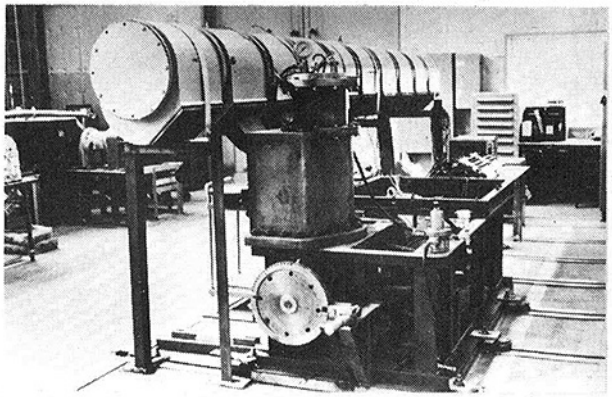

Fig. 10 View of the model for a two-cycle engine

As shown in the drawing, the piston is fixed by fixing the fly-wheel with a slide pin. In the experiment, the piston is fixed where the second piston ring is several centimeters above the exhaust ports. In the cylinder, compressed air of about 0.5 MN/m^2 (gauge pressure) is accumulated. When the pin is removed, the piston is moved by the air pressure inside the cylinder, and the air is blown down from the cylinder into the exhaust pipe through the connecting duct.

The pick-ups installed near the exhaust port are mini-size pressure sensors of strain-gauge type of 2 mm thickness and 6 mm dia.

Experiment and Simulation. Fig. 11 show a comparison of the measurement with the simulation made on the air model of the two-cycle engine mentioned.

The result shows that they agree very well in the main pipe and in the neighboring connecting duct, namely, at the points 13, 17, 18, 19 and 20.

Because the blow-down process is a very complicated event and the actual flow during the blow-down is three-dimensional near the ports and in the connecting duct (Fig. 12), there exists a considerable difference between the measurement and the simulation at the local points of 2 and 9.

However, it is believed that the one-dimensional theory as a whole simulates the events near the ports and in the connecting duct during the blow-down, because it is otherwise impossible to simulate the event in the main pipe and the neighboring duct as precisely as shown in Fig. 11.

The slight difference between the simulation and the measurement at No. 2 segment of the exhaust pipe is due to the dynamic pressure picked up here. Although the simulation shows static pressure, the pressure pick-up at No. 2 segment where the blow-down gas hits the pipe wall possibly measures dynamic pressure besides the static pressure.

In short, the gas flow in the model of Fig. 9 can be regarded as one-dimensional in practice, which possibly shows that the flow system of the engines can also be regarded as one-dimensional from the view point of the practical simulation for exhaust pulsation.

Exhaust Pulsation of Engines. Figs. 13 and 14 show the comparison of pulsation measurements on a two-cycle and a four-cycle engine with the simulations. Table 1 shows the data used for the calculation.

In the simulation for the exhaust pulsation of actual engines, such data as the pressure P_{EO} and the temperature T_{EO}, etc. in the cylinders at the time of exhaust open (EO) are given as input data for the calculation system. They are obtained or estimated from the measurement on the engines concerned. Because the combustion process in the cylinder is not calculated and P_{EO}, T_{EO}, etc. are given as input data, the simulated cylinder pressure, for example, jumps at the exhaust open as shown in Fig. 13 (a) and Fig. 14 (a).

As for the measurement of the two-cycle engine, the result was that the pulsations were larger in amplitude at both ends of the exhaust pipe than those near the longitudinal center. In Fig. 13 each one at the pipe end and near the center is shown. This means that the exhaust pulsation has the fundamental vibration mode of an air column in the pipe with both ends closed. It is to be noticed that the frequency of the pulsation is ten cycles per one revolution of the engine, although seven cylinders are connected with the exhaust pipe. The dynamic pressure is picked up at No. 1 segment of the exhaust pipe during the blow-down from No. 1 cylinder and, therefore, the measurement is slightly larger than that calculated.

In the four-cycle engine, the frequency of the pulsation is eight cycles per two revolutions before the turbo-charger, as shown in Fig. 14 (b). Although the data are not given, the pulsation amplitude near the center is smaller as in the case of the two-cycle engine.

In the four-cycle engine, an experiment was made in which an orifice was inserted between the No. 5 and the No. 6 cylinder. The orifice

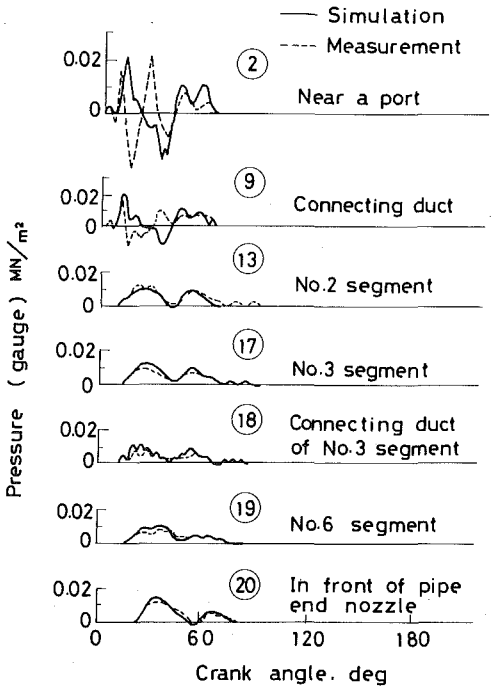

Fig. 11 Experiment and simulation of model for a two-cycle engine

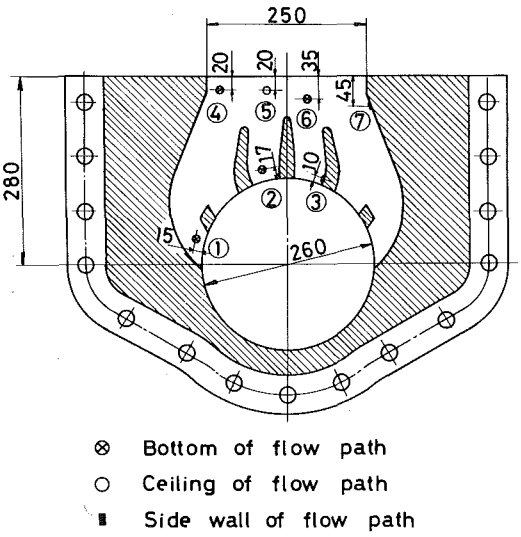

Fig. 12(a) Detailed cross-sectional view of the air model and measurement points

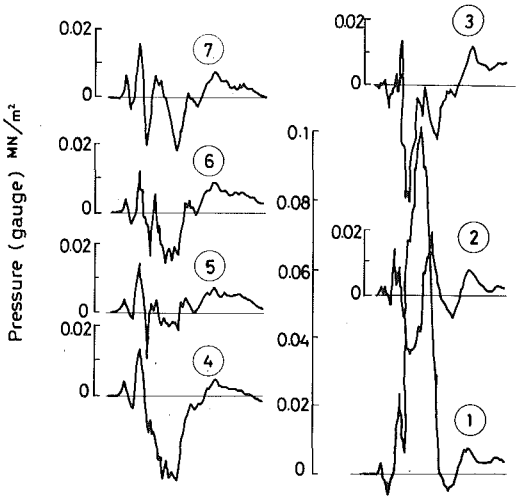

(b) Fig. 12(b) Measurement at points ①-⑦ P_{EO} = 0.5 MN/m^2 (gauge pressure)

Fig. 12 Pressure fluctuation during blow-down (air model of a two-cycle engine)

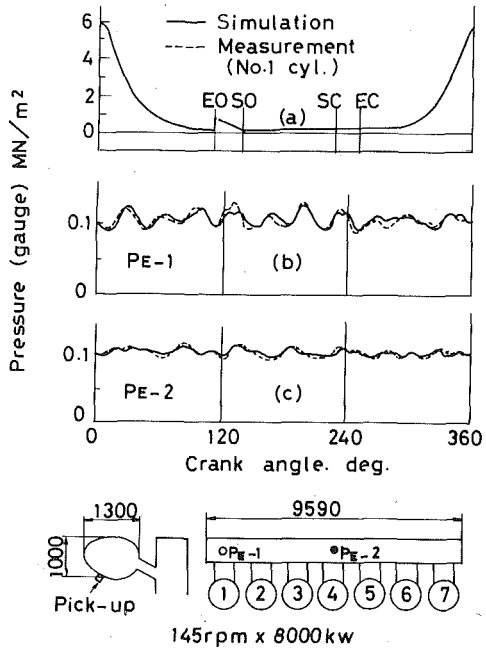

Fig. 13 Experiment and simulation of exhaust pulsation for a two-cycle engine

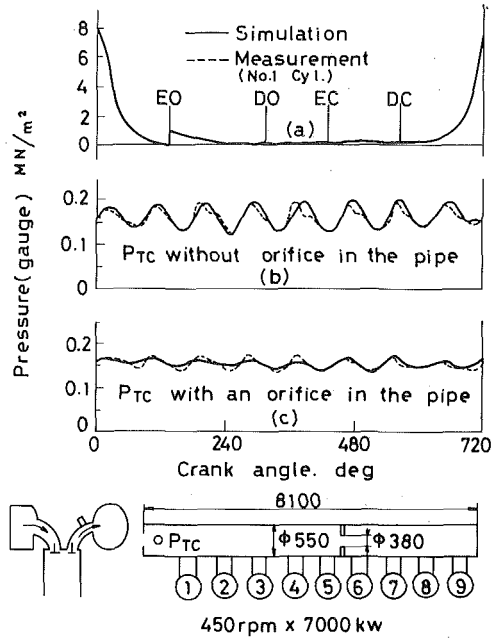

Fig. 14 Experiment and simulation of exhaust pulsation for a four-cycle engine

Table 1 Data for calculation

Engine type		two-cycle	four-cycle
Revolutional speed	n rpm	145	450
Scavenge air pressure (gauge)	Ps MN/m²	0.117	0.190
Scavenge air temperature	Ts K	313	313
Cylinder pressure at EO	P_{EO} MN/m²	0.65	1.05
Cylinder temperature at EO	T_{EO} K	1005	1023
Diameter of cylinder	D mm	700	520
Stroke	s mm	1200	550
Number of cylinders	z	7	9
Firing order		1725436	135798642

was 380 nm in diameter. As shown in Fig. 14 (c), the pressure fluctuation was attenuated by the orifice, and the simulation and the measurement agreed very well.

The results in Figs. 13 and 14 prove that, although the gas flow system of the constant pressure turbo-charged diesel engines can be regarded as a very simple one, the exhaust pulsation, which is formed by the pulses of blow-down and the reflected waves, is very complicated. It is also proved that the one-dimensional theory can correctly simulate the exhaust pulsation by using the method of characteristics.

Characteristics of Pulsation

It has been proven that the one-dimensional theory can simulate the unsteady flow in the exhaust system of constant pressure turbo-charged engines.

Based on the results of the study, characteristics of the pulsation in the exhaust system corresponding to the basic model shown in Fig. 1 are to be studied in this chapter.

The two-cycle and the four-cycle engine to be referred to in this chapter are those mentioned in the previous chapter.

General Features. First, it should be emphasized as one of the characteristics that the unsteady flow in the exhaust system can be simulated by one-dimensional theory although the flow in the system seems very complicated at first sight.

Second, it should be emphasized that the pulsation of the constant pressure system is a complicated one, and it can never be simulated by the filling and emptying method (volume theory) which neglects wave propagation.

It is widely misunderstood that the exhaust pulsation of this system can be simulated by the volume theory because the volume is very large and the pressure fluctuation is relatively small in the exhaust pipe of this system. However, when the problem concerned is the influence of the pulsation on gas exchange in cylinders, it is quite impossible to simulate the pulsation by the volume theory. Fig. 15 shows that the simulation by the volume theory is drastically different from that actually measured in the two-cycle engine, while the simulation by the method of characteristics agrees well with the measurement shown in Fig. 13.

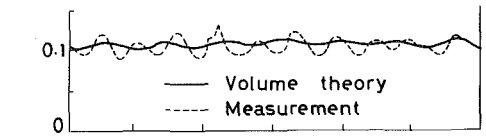

Fig. 15 Simulation by volume theory

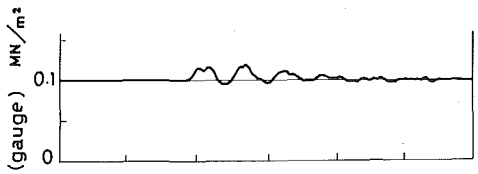

Fig. 16 Simulated pulsation by one pulse (pulsation by blow-down of No. 1 cylinder)

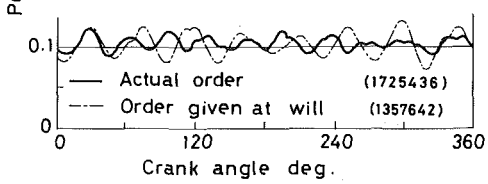

Fig. 17 Simulation for influence of firing order on exhaust pulsation (two-cycle engine)

Fig. 16 shows the case where the pulsation caused by a single pulse of cylinder No. 1 is simulated in the two-cycle engine. As shown, the reflections to the third are rather strong. Each pulsation caused by each cylinder in a cycle interacts to form a complicated pulsation that cannot be simulated by the volume theory.

Third, the strong influence of the firing order on the pulsation is one of the characteristics as shown in Fig. 17. One of the two simulations uses the firing order that is actually used in the two-cycle engine, and the other uses a firing order that is given at random.

It is well known that gas exchange is badly interfered with by the pulsation in the pulse turbo-charged system if the firing order is not

properly determined. On the other hand, it is assumed in general that the firing order is not restricted by the exhaust pulsation in the constant pressure system, and this is even believed to be one of the main merits of this system. However, the results of the study show that the firing order is not necessarily free of the exhaust pulsation.

Fourth, it is to be mentioned that the pulsations near both ends of the exhaust pipe are larger in amplitude than those near the longitudinal center, which means that the pulsation has the fundamental vibration mode of a gas column in the pipe with the both ends closed. Figs. 13 and 14 are examples.

Linearity of the Pulsation. The calculation method which uses equation (36) instead of equations (27) and (29) is referred to as a linear calculation, as was already mentioned.

In the pulsation of the two-cycle engine, no significant difference was recognized when comparing the simulation by the linear calculation with that by the original method of characteristics. This means that when the pulsation caused by each single blow-down, σ_i, is known, the resultant pressure pulsation in the exhaust pipe, σ, can be obtained by linear summation of each pulsation, as shown in the following equation (refer to Appendix).

$$\sigma = \sigma_c + (\sigma_1 + \sigma_2 + \sigma_3 + \ldots\ldots) \tag{37}$$

where the variable σ is a function of pressure defined by the equation (21) and σ_c is an integration constant.

It is one of the characteristics of the constant exhaust pulsation that it can be obtained by linear summation of each pulsation caused by each cylinder.

However, this does not mean that the pulsation can be easily obtained. It is generally impossible to analyze the pulsation of the constant pressure system by any simple method, and there is no other suitable method than using the computer simulation.

Flow at Branch. Benson[1] offers correction factors for momentum theory for the flow at the branch. The factors were experimentally obtained, and he proved that the analysis of the blow-down process of the pulse turbo-charge system was improved by using the factors.

By using Benson's factor, pressure drop at the branch (Fig. 18) is described as follows:

$$P_1 - P_2 = C_4(\rho_2 u_2^2 - \rho_1 u_1^2) \tag{38}$$

$$P_3 - P_2 = C_5(\rho_2 u_2^2 - \rho_1 u_1^2) \tag{39}$$

where C_4 and C_5 are Benson's factors.

A simulation using the constant pressure theory of branch was compared with that using the momentum theory in which Benson's factors were applied. The result showed little difference between them.

One of the remarkable features of the constant pressure system is that the characteristics of the branch are described by the constant pressure theory which assumes no pressure drop at the branch, because mixing of the high-speed blow-down gas in the connecting ducts and the gas in the main pipe may cause some pressure drop at the branch.

However, Benson's momentum theory very clearly explains why the branch characteristic is described by the constant pressure theory. Applying Benson's theory, it follows that it is the flow speed in the main pipe but not the speed in the connecting duct that contributes to the pressure drop at the branch. However, the flow speed in the main pipe is too small due to its large diameter to generate any pressure drop at branch.

Pulsation in Connecting Duct. In general, the cross-sectional area of the main pipe is much larger than that of the connecting duct in the constant pressure turbo-charge system. Furthermore, the pressure fluctuation in the main pipe is supposed to be very small in this system.

This means that the main pipe is an open end for the connecting ducts. Therefore, the event in a connecting duct is equivalent to gas column vibration in a pipe with one end closed and the other end open, while the exhaust ports are closed. On the other hand, it is equivalent to gas column vibration in a pipe with one end connected with a volume (cylinder) and the other end open, while the exhaust ports are closed.

If there is no pressure fluctuation at all in the main pipe, the events will be the same in all the connecting ducts.

However, pressure pulsation actually exists in the exhaust pipe and the event is different in each connecting duct (Fig. 19).

Control of Pulsation. As explained, it is preferable to control and attenuate the pressure fluctuation in the main exhaust pipe which leads to more uniform events in each connecting duct.

In the exhaust system, corresponding to the basic model shown in Fig. 1, the length of the exhaust pipe L, the engine rotational speed n, the exhaust gas temperature T_E, the volume of the exhaust pipe V_E and the firing order are the main factors affecting pulsation.

However, L, n, T_E and the firing order are strongly restricted by the engine specifications and V_E is the single factor which can be changed, especially when the engine has already been constructed.

However, while a simulation shown in Fig. 20 shows that the enlargement of the volume is effective in attenuating the pulsation, another simulation shown in Fig. 21 proves that it is not always effective, which may be attributed to the complexity of the pulsation of this system. Furthermore, the extremely large volume is restricted not only due to structural reasons but also due to worse response to load change of engines.

There are some other ways to attenuate the pressure fluctuation among which inserting orifices in the exhaust pipe is a very simple one; an example of an experiment using an orifice was described in the previous section.

However, care should be taken that energy loss may not be increased by applying these methods to attenuate the pulsation.

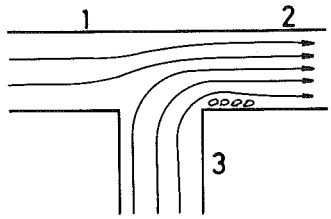

Fig. 18 An example of branch flow

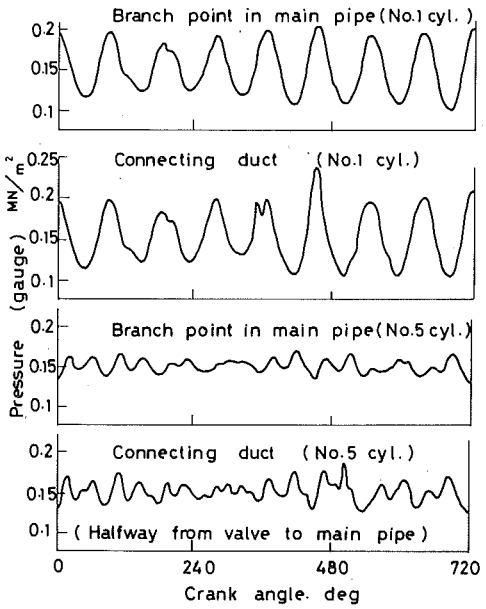

Fig. 19 Pressure fluctuation in main exhaust pipe and connecting duct (a four-cycle engine)

[1] R. S. Benson, D. Woollatt, and W. A. Woods "Unsteady Flow in Simple Branch Systems," *Proceedings of the Institute of Mechanical Engineers*, Vol. 178, 3I(iii), 1963–64.

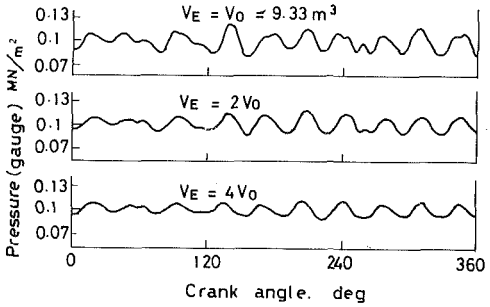

Fig. 20 Influence of exhaust pipe volume on pulsation. (a two-cycle engine)

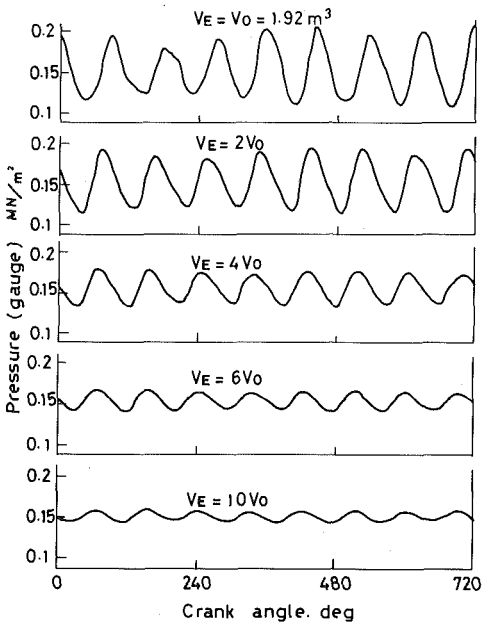

Fig. 21 Influence of exhaust pipe volume on pulsation (a four-cycle engine)

Inserting orifices will probably increase the resistance to gas flow. However, in the case shown in Fig. 14, no increase of the fuel consumption was recognized in the four-cycle engine.

Possibility of Utilizing Pulsation. The gas column in the connecting duct is a vibration system for which the main exhaust pipe is supposed to be an open end. Therefore, it is possible to utilize the vibration in the duct by designing the relevant parameters so that they may improve the interaction between the cylinders and the events in the ducts. This is possible, however, only when the pressure fluctuation in the main exhaust pipe is very small because the pulsation in the main pipe leads to different gas column vibrations in the connecting ducts (Fig. 19).

As far as we know, it is very difficult to positively generate a stronger pulsation in the main pipe and to utilize it for the improvement of engine performance. This is because the pulsation in the main pipe is far too complicated to be consciously generated in a form that enables it to have a stronger, better and more uniform vibration in every connecting duct.

On the contrary, care should be taken so that pressure fluctuation in the main exhaust pipe is minimized for better engine performance.

Flow Velocity. It is now clear that one of the main features of the constant pressure system is supposed to have been realized when the pressure fluctuation in the main exhaust pipe is very small even if the cross-sectional area, or the volume of the exhaust pipe, is small. However, an extremely small area of cross section leads to a remarkable loss of kinetic energy.

When exhaust systems are planned, the average gas speed, $\overline{w}$, through a cross-section concerned is usually estimated by the following equation:

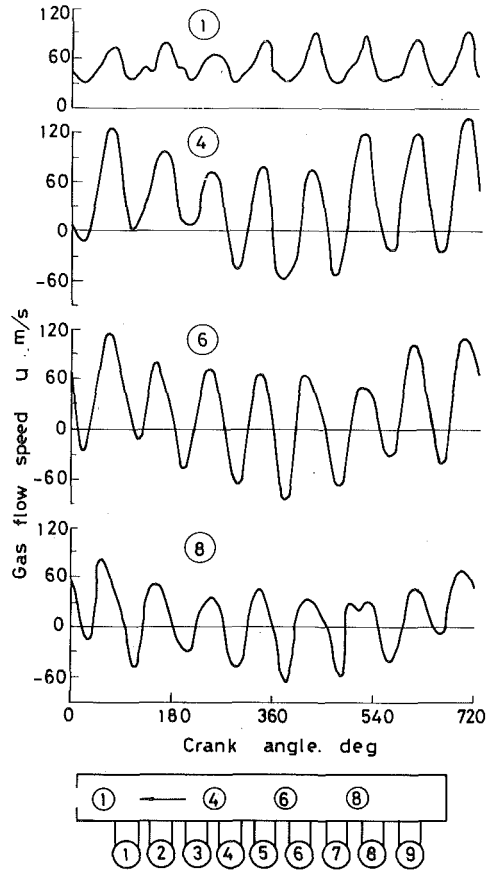

Fig. 22 A simulation of gas flow speed in the exhaust pipe

Table 2 Gas speed and kinetic energy

	$\overline{u}$ (m/s)	$\overline{w}$ (m/s)	$\overline{u^2}$ (m^2/s^2)	$(\overline{w})^2$ (m^2/s^2)	$\frac{\overline{u}}{\overline{w}}$	$\frac{\overline{u^2}}{(\overline{w})^2}$
1	51.5	54.0	2950	2930	0.96	1.01
4	34.7	36.0	4020	1290	0.96	3.12
6	23.0	24.0	3313	532	0.96	6.22
8	11.4	12.0	1392	144	0.95	9.65

$$\overline{w} = \frac{1}{F_E}\left(\frac{\dot{G}_E R T_E}{P_E}\right) \tag{40}$$

where F_E = cross-sectional area concerned

$\dot{G}_E$ = gas-flow rate through F_E

However, the actual gas speed fluctuates because the flow in the exhaust system is unsteady. A simulation shown in Fig. 22 shows the fluctuation of the gas speed u at points 1, 4, 6 and 8 in the four-cycle engine.

Table 2 compares $\overline{u}$ and $\overline{u^2}$ with $\overline{w}$ and $(\overline{w})^2$, respectively, where $\overline{u}$ is the time mean value of the calculated unsteady speed u and $\overline{u^2}$ is that of u^2, while $\overline{w}$ was calculated by equation (40), based on the measured data of mean value.

The square of the speed is a measure of the loss of kinetic energy.

Although the unsteady gas speed u fluctuates over the whole range of the engine cycle (Fig. 22), it is a matter of course that $\overline{u}$ is nearly equal to $\overline{w}$ at all the points as shown in Table 2 because the simulation of the unsteady flow and the resulting time mean values agree well with the measurement.

On the other hand, Table 2 shows that the estimation of the square of the gas speed based on unsteady flow is much greater than that based on the average gas speed by equation (40), except for that in front of the gas turbine, namely at the point 1.

This means that the actual energy loss is greater than that estimated in the usual way, because of the strong fluctuation of the gas speed back and forth.

Conclusion

As a result of this study, some of the characteristics of the exhaust gas pulsation of the constant pressure turbo-charge system have been clarified, and a simulation system for it has been established.

Above all, it must be emphasized that the exhaust pulsation of this system can never be simulated by the filling and emptying method which neglects wave propagation.

It is also to be noticed that the unsteady flow in this system can be described by the one-dimensional theory, although the gas flow in the system seems to be far more complicated at a glance.

The simulation system is now being improved not only in the calculation method of the pulsation but also in the whole simulation system to make a new one, which will be able to analyze also the interaction between the whole process in cylinders and the pulsation in the exhaust and scavenge system.

The new system will be, in other words, a combination of two simulations; the simulation of the pulsation in exhaust and scavenge system and the so-called engine performance simulation.

Acknowledgments

We should like to express our heartiest thanks to Professor Dr. N. Mizumachi of Tokyo University, Professor Dr. S. Ohigashi of Kyoto University and Professor Dr. S. Ohmi of Osaka University for their useful advice.

Also, the Ship Building Research Association of Japan is gratefully acknowledged for its financial aid.

APPENDIX

Linear Calculation. As already explained, the calculation method which assumes equation (36) instead of equations (27) and (29) as the characteristic lines of the pressure propagation is referred to as a linear calculation.

Equation (36) assumes that the gas flow speed is negligibly small compared with the speed of sound and that the speed of sound can be regarded as constant in the system concerned.

Solving the linear calculation means solving equations (28, 30) and (32), where the characteristic lines of pressure propagation are represented by equation (36) and that of fluid elements by equation (31).

Accordingly, equations (28) and (30) are represented in the following form:

$$\frac{\partial u}{\partial t} + \bar{a}\frac{\partial u}{\partial x} + \psi\left(\frac{\partial \sigma}{\partial t} + \bar{a}\frac{\partial \sigma}{\partial x}\right) = X + a\left(\frac{Y}{\rho} + \frac{Z}{C_{VK}}\right) \tag{41}$$

$$\frac{\partial u}{\partial t} - \bar{a}\frac{\partial u}{\partial x} - \psi\left(\frac{\partial \sigma}{\partial t} - \bar{a}\frac{\partial \sigma}{\partial x}\right) = X - a\left(\frac{Y}{\rho} + \frac{Z}{C_{VK}}\right) \tag{42}$$

The following equations are obtained by (4, 42), and (31) and (32).

$$\frac{\partial u}{\partial t} + \psi\bar{a}\frac{\partial \sigma}{\partial x} = X \tag{43}$$

$$\bar{a}\frac{\partial u}{\partial x} + \psi\frac{\partial \sigma}{\partial t} = a\left(\frac{Y}{\rho} + \frac{Z}{C_{VK}}\right) \tag{44}$$

$$\frac{\partial \psi}{\partial t} + u\frac{\partial \psi}{\partial x} = \frac{Z}{2C_{VK}}\psi \tag{45}$$

However, the equations obtained above are not linear in a precise sense.

If, in the system concerned, the entropy change Z due to friction work can be neglected and the events at boundaries are isoentropic, namely, $Z = 0$ and $\psi = \bar{\psi}$, the above equations are changed as follows:

$$\frac{\partial u}{\partial t} + \bar{\psi}\bar{a}\frac{\partial \sigma}{\partial x} = X \tag{46}$$

$$\bar{a}\frac{\partial u}{\partial x} + \bar{\psi}\frac{\partial \sigma}{\partial t} = a\frac{Y}{\rho} \tag{47}$$

Moreover, if the external force X and the change of cross-sectional area Y can be neglected, the following linear equations are obtained.

$$\frac{\partial^2 u}{\partial t^2} - \bar{a}^2\frac{\partial^2 u}{\partial x^2} = 0 \tag{48}$$

$$\frac{\partial^2 \sigma}{\partial t^2} - \bar{a}^2\frac{\partial^2 \sigma}{\partial x^2} = 0 \tag{49}$$

This means that the pulsation is linear in the exhaust system, which can be regarded as isoentropic at the boundaries, and where the external force due to friction, heat generation, heat transfer, and change of sectional area can be neglected in practice.

A result similar to the one described by equations (48) and (49) can be obtained for the system where the characteristic lines of the pressure propagation are represented by the following equation:

$$\frac{dx}{dt} = \bar{u} \pm \bar{a} \tag{50}$$

The system which follows equation (50) is the one where the mean speed of gas flow cannot be neglected.

P. C. Vorum
Consulting Engineer,
Tipp City, Ohio
Assoc. Mem. ASME

Short Pipe Manifold Design for Four-Stroke Engines: Part II

Continued study has gone on examining a discrete modal model of intake and exhaust breathing of four-stroke engines. By matching a Helmholtz defined pressure excursion to specific average flow velocities, maximum ram supercharge on intake and scavenging on exhaust are possible. Inclusion of all engine parameters allows for a quick, accurate design of an intake/exhaust pair. Trends are noted easily and errors can be corrected quickly. The intake and exhaust systems can be designed to compliment the additional power possible when a turbocharger, Roots blower, or some other supercharger system is added to the engine. Improved performance, economy, and emissions characteristics are possible with the careful matching of the manifolds to the operating conditions.

Introduction

A two mode model of intake and exhaust breathing in four-stroke engines has been studied under Dr. Helmuth W. Engelman at the University of Wisconsin and the Ohio State University. This model splits each intake or exhaust sequence into two discrete elements. The dominant opened valve period is examined as a Helmholtz resonator matched to specific flow velocities in the primary (cylinder runner) and secondary (runner to the atmosphere) pipes. In a short pipe (much less than a wavelength of pipe), the closed valve period does contain a standing wave oscillation of minor consequence, but may be dismissed as *the* tuning model.

Ram supercharge on intake and scavenging on exhaust perform over a broad speed range. Just as a sine wave is positive for one half of its cycle (a 2-to-1 time ratio), the torque improvement is available for a 2-to-1 engine speed range. A single cylinder or group of five or more cylinders breathing off of a common supply (the popular V-8 single plane manifold) acts as a one degree of freedom system with a single torque peak defined by the resonances present. A group of two, three, or four cylinders breathing through a common runner that is opened to the atmosphere is a two degree of freedom system with two torque peaks. The goal is to improve performance, economy, and emissions characteristics by using the dynamics of the manifold rather than depending entirely on the chemical energy released when fuel is burned, for power.

Publications that consider the two mode model are presented in [1–14] at the end of this paper. Recent reconfirmation of Engelman's assumptions, velocity data, and details of a resonance factor are examined here.

Background

Popular design theory used today is derived from assumptions expressed by Taylor of MIT's Sloan Research Lab [15–19]. Morse, et al. studied the pipe as though flow is steady state, with an interruption begun on valve closure, which would set up a standing wave in the intake pipe, which could be timed to the engine as a quarter wave organ pipe oscillation. The model describes a 200 in. "long" pipe fairly well, but Taylor commented that transients seemed to govern a more reasonable pipe length (20–40 in.). One conclusion of their multicylinder work was that a pipe as short as possible should be used to connect all cylinders [17] p. 9). Perhaps the common log-runner manifold developed because of their anonymous influence. A complete set of performance coefficients is necessary for each design speed with this technique. The required tests can become a time consuming process which may ultimately get a reasonable design, but usually only after a great deal of hack-saw dynamometer testing. A more likely result is that acceptance is given to the first manifold that meets some minimum criteria or at the end of the boss's budget or patience.

Recently, finite difference techniques have been applied to the theory that continuously traveling positive and negative waves coexist in the pipe [20]. A 90 cubic inch, four cylinder engine exhaust study included a test system of 48 in. long, 1-1/2 in. diam pipes that discharged into an expansion chamber. Torque peaked at 4000 and 5000 rpms. See Fig. 1.

The lower peak was expected, but the higher point was passed off as if "some other factor besides the exhaust is effecting the volumetric efficiency at this speed (5000 rpm)... some favorable wave in the intake tract." ([20] p. 1743). Using the model described below, this manifold is a one degree of freedom system. The 4000 rpm point is the result of a mass wave timed by the system dynamics scavenging the cylinder, with an average flow velocity in the pipe of 170 ft/s. As Fig. 10 shows, 200 ft/s matched to the Helmholtz governed pressure excursion gives maximum boost: 212 ft/s exists at 5000 rpm. In this case, the resonator and velocity points are relatively close (1000 rpm apart), but far enough apart that both are distinct. If the two design speeds were closer, a single torque peak would exist. An analysis of an Edelbrock Streetmaster manifold on a 350 cid engine showed the same 212 ft/s velocity at its single torque peak at 3500 rpm ([12] p. 9). A recent drag race engine test also had separate speeds, but perhaps because they were closer than the four cylinder (only 6-700 rpm difference) and/or because of the high performance cam used, the apparent torque peak came half way between the other points, at 7200 rpm [21].

In Blair and Goulburn's four cylinder study, both resonator and flow boost points exist. As demonstrated by Thompson [6] and Eberhard [7] at Ohio State, boost is optimized when the resonator and velocity points coincide. The Blair study showed a best improvement over the stock system of 1.9 percent. A common rule of thumb given this author is that 3–5 percent improvement is the best that can be

Contributed by The Technical Division of THE AMERICAN SOCIETY OF MECHANICAL ENGINEERS and presented at the Energy Technology Conference and Exhibition, February 3–7, 1980, New Orleans, Louisiana. Manuscript received at ASME Headquarters October 26, 1979. Paper No. 80-DGP-6. This paper was originally presented at the CIMAC Conference, Stockholm, Sweden, May 24–27, 1971.

expected with exhaust tuning when a "mild" street cam is used. A 1600 cc stock Ford Pinto powered Formula Ford race car developed 12 percent more torque when a closer resonance-velocity match was made [22]. Eberhard experienced volumetric efficiency as high as 118 percent (comparable to a gear driven supercharger) in a naturally aspirated diesel engine intake test. Too often, the cylinder is only considered a source of boundary conditions for the pipe. Important engine parameters are ignored completely: cylinder displacement volume, compression ratio, valve timing, pipe areas and lengths, idle pipe and plenum volumes, and the degrees of freedom of the system.

Theory

At the University of Wisconsin, Engelman pursued a Helmholtz model of the pipe to gain the great separation of the primary from the harmonic frequencies: the ratio of first harmonic to primary is commonly 20-to-1 or more. This ratio in a quarter wave organ pipe model is only 3-to-1. In Teeter's study [3], the manifold alone was modeled as the Helmholtz volume and pipe. Because only a 4 percent improvement was made, Engelman concluded that some other model was necessary. He proposed the two mode model where the cylinder became part of the resonator system. A "filling factor" was anticipated to account for the moving piston, but that was found to be unnecessary. Using a graphical technique, Cambi demonstrated that there is only a 0.3 percent change in the period of an L-C circuit with a ± 20 percent change in the value of the capacitor [4]. The mechanical analog of an L-C is the Helmholtz resonator. It describes the motion of a mass in the pipe moving on the spring mass in the cylinder. The first studies were aimed at verifying the major breathing model with the valve opened but recognized that the closed valve period would impose some minor effect on the system.

The two modes are easily seen in the intake trace in Fig. 2. Damping nearly kills the closed valve oscillations, so it is unreasonable to credit that period with the substantial opened valve period pressure excursion. The natural frequencies of the two periods are noticeably different. Properly, air is not displaced in the manifold because it is a resonator. Rather, the positive and negative peaks are timed to the breathing period according to the system dimensions. The pressure and velocity effects combine for best breathing.

The 2390 rpm trace in Fig. 3 is similar to "proofs" commonly offered to show the continuous oscillations in the pipe. At this speed, damping hasn't reduced the closed valve period signal significantly, so it may be misunderstood. No breathing occurs with the valve closed, but the effect of the pressure oscillation is a boundary condition on valve opening. This matter has been studied before, and it was shown that the familiar ripples in a torque curve are directly related to the opening conditions ([12] p. 6). A shorter pipe, resulting from a higher design speed, will greatly reduce the ripples, leaving the broad Helmholtz defined curve.

The exhaust trace in Fig. 4 shows a similar time history. Blowdown is followed by a vacuum in the cylinder that draws in the next intake charge without waiting for piston motion, and pulls the piston through its stroke, reducing pump work. The design rpm of the system was 2020 rpm while the engine was run at 900 rpm. This ratio of 2020/900 = 2.24 explains the multiple oscillations while the valve is opened. The Edelbrock mentioned above peaks on just such a 2-to-1 resonator to

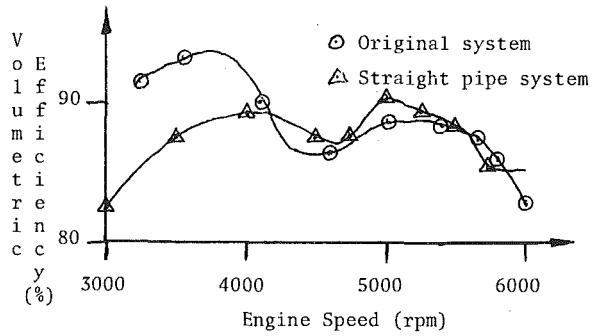

Fig. 1 Lotus-Cortina test data using various exhaust manifolds

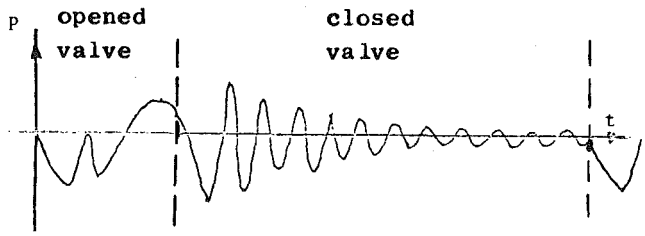

Fig. 2 Pressure-time data in the intake at 985 rpm [1]

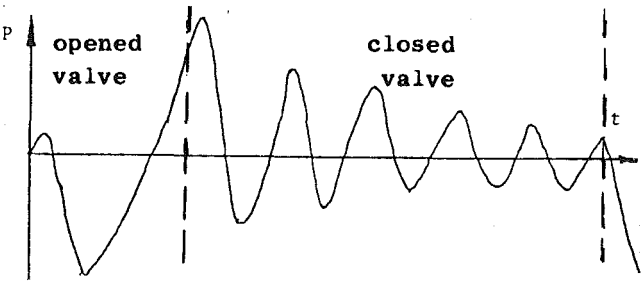

Fig. 3 Pressure-time data in the intake at 2390 rpm [1]

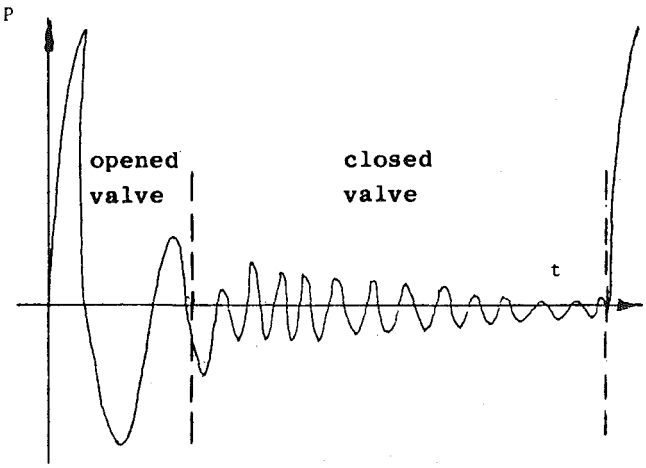

Fig. 4 Pressure-time data in the exhaust at 900 rpm [11]

Nomenclature

a = ratio of secondary to primary lengths to areas
$a_{1,2}$ = primary and secondary pipe areas, in.^{2} (cm^2)
a_p = port area at the manifold flange, in.^{2} (cm^2)
b = ratio of secondary to primary volumes
C_s = speed of sound in the pipe, ft/s (m/s)
H = ratio of Helmholtz rpm to engine torque rpm
k = cam timing factor
$L_{1,2}$ = primary and secondary pipe length, in. (cm)
L_p = port length, from valve stem to manifold flange, in. (cm)
N_p = single pipe torque speed, rpm
$N_{1,2}$ = lower and higher two degree of freedom system torque speeds, rpm
R = compression ratio
V_1 = cylinder displacement volume, in.^{3} (cm^3)
V_{p1} = additional plenum volume, in.^{3} (cm^3)
V_2 = secondary volume, includes idle pipe and plenum volumes, in.^{3} (cm^3)
$V_{1ave,2ave}$ = average primary and secondary runner velocities, ft/s (m/s)
$X_{1,2}$ = ratio of lower or higher torque speed to single pipe torque speed

Subscripts

1 = primary cylinder system dimension or data
2 = secondary dimension or data

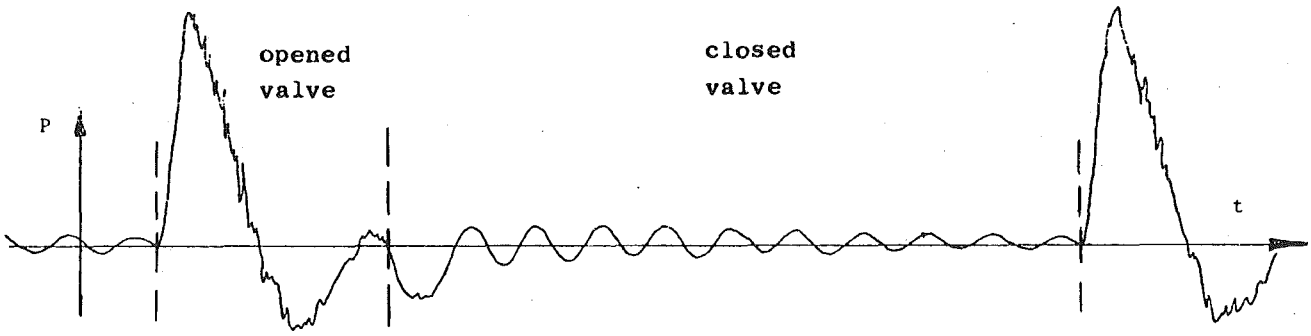

Fig. 5 Pressure-time data in the exhaust at the valve, 900 rpm [2]

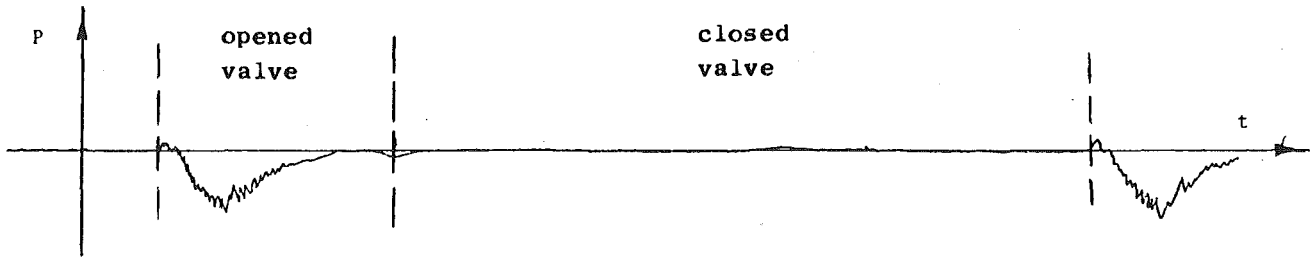

Fig. 6 Pressure-time data in the exhaust at the opened end, 900 rpm [2]

torque rpm ratio. Experiments with the Formula Ford at a 1-to-1 ratio gave 8, 10, and 12 percent improvements at 4500 rpm when various tailpipes were tested against the stock Shenkle Tri-Y racing exhaust. Interesting though, the 12 percent boost engine was the slowest on the track of the four runs made; the 10 percent setup was the fastest. Here, various velocities combined with the resonances to provide boost.

Information in Fig. 5 reconfirms the above earlier studies. This data was taken in the exhaust of a CFR engine being motored at 900 rpm. A 50 psi shop air line was attached to the intake to simulate exhaust pressures on valve opening; the system was not firing. During the opened valve breathing period, however, noise is superimposed over the primary signal. The ripples are most likely caused by air passing over the end of the transducer. The isolation of each breathing excursion, eliminating any carryover from cycle to cycle, is again demonstrated.

Fig. 6 was taken near the end of the same pipe. Two modes are again seen, but without a positive pressure peak. When the valve is closed, the air is bouncing in and out on the air near the valve. No pressure excursion is involved, and none is seen. The pressure depression during the opened period is similar to the events in a venturi. As the velocity goes up, the static pressure goes down. Piecing data in Figs. 5 and 6 together gives a clearer picture of breathing. A dense slug exits the cylinder and accelerates down the pipe. As it exits, it has some velocity but is near atmospheric pressure. The vacuum it pulls will help do pump work for the next intake stroke. By timing the vacuum peak and matching it to an optimum velocity, maximum work is done by the air in the pipe.

The direct application of the Helmholtz equation:

$$N_p = C_s \sqrt{a_1/L_1 V_1} \tag{1}$$

includes all engine parameters. The equation is based on the acceleration of mass in the pipe. Vibration theory accepts multiple degrees of freedom; two degrees are the maximum for a manifold system. A one degree of freedom model has the primary pipe breathing off of the free air. In a manifolded one degree system, all of the primary pipes (five or more) breathe from a common box which is then opened to the free atmosphere. See Fig. 7.

In a two degree of freedom system, the secondary pipe is opened to the free air. See Fig. 8. A group of two degree systems may share a common supply box that is opened to the free air. Depending on the design, a six cylinder engine may perform like two three-cylinder groups or like six individual cylinders. Another possibility is a man-

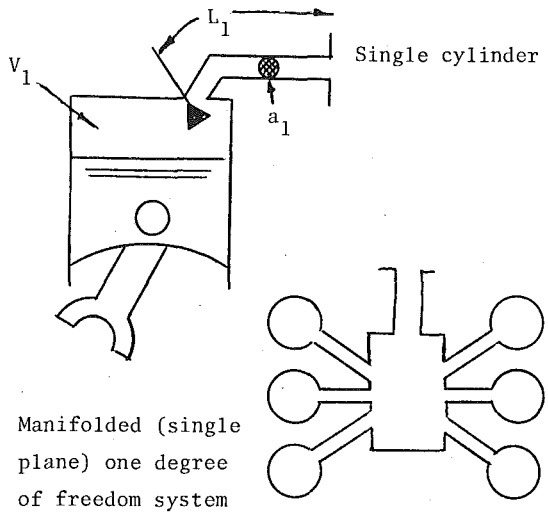

Fig. 7 One degree of freedom resonators

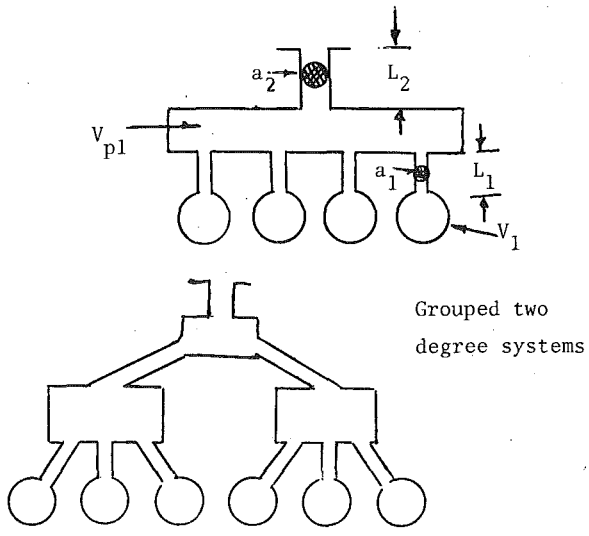

Fig. 8 Two degree of freedom resonators

ifold that acts like both a one and two degree system depending on the engine speed. Undoubtedly the changeover from one model to the other would cause a performance loss when compared to a system that was a consistent one or two degree system throughout its speed range.

Dimensionless parameters useful in design work include the following:

$$a = (L_2/a_2)/(L_1/a_1) \quad (2)[7]$$

$$b = 2V_2(R-1)/V_1(R+1) \text{ intake} \quad (3)[7]$$

$$= V_2(R-1)/V_1R \text{ exhaust} \quad (4)[11]$$

In a two degree of freedom system, a and b relate the higher and lower torque rpms to the natural frequency of the primary pipe system. Data reported to date has had values of $a \geq 0.2$ and $b \geq 5.0$. A Harley-Davidson motorcycle engine with $a = 0.291$ and $b = 2.503$ [23] and one Formula Ford test with $a = 0.044$ and $b = 4.92$ [22] both tuned at their respective N_p rather than N_1 and N_2 as expected. These two degree manifolds collapsed back to a one degree model. Development of this might lead to a small, lightweight manifold.

Model Development

Engelman's work at Wisconsin with a single cylinder intake yielded the modified Helmholtz equation:

$$N_p = 77\, C_s \sqrt{a_1(R-1)/L_1V_1(R+1)} \quad (8)([1] \text{ p. } 109)$$

which sets the resonator frequency approximately equal to 2.1 times the crank speed. The compression ratio factor, R, adjusts the resonator volume to piston at midstroke for an intake design and to bottom dead center for an exhaust design. Bottom center coincides with the end of sonic blowdown, which allows the pressure waves to travel upstream into the cylinder and control the timing of the useful vacuum peak. Metric units: 77 = 642.

Thompson [6] added k, the cam timing factor, to include the effect of different cam profiles. Generally, k is high (2.1–2.3) for a low speed cam and low (1.65–1.75) for a high speed racing cam. This number is an empirical fit to the data from a dynamometer run. In a two degree manifold system, the cam timing factor is used for calculations at N_1; Mother Nature seems to like $k = 2.1$ at N_2. When the k is included into equation (5), the form changes to:

$$N_p = 162\, C_s/k \sqrt{a_1(R-1)/L_1V_1(R+1)}$$

Intake [6] (6)

$$N_p = 162\, C_s/k \sqrt{a_1(R-1)/2L_1V_1R}$$

Exhaust [11] (7)

Metric units: 162 = 1351

For a tapered section, the mean diameter is used to calculate the area of that section. For a pipe of varying cross section, it was found that:

$$L/a_{\text{effective}} = \sum_{i=1}^{\infty} L_i/a_i \quad (8)[6]$$

Abrupt corners or bends are undesirable because of losses, but Thompson demonstrated that no change in tuning rpm results because of a bend. Another rule of thumb is that an area change of 2-to-1 or more be made on entering or leaving a plenum. The resultant velocity change will thus distinguish between a tapered pipe and the transition from a volume to a runner. If the radius of curvature of the entrance is 20—25 percent of the radius of the runner entered, good flow characteristics will exist. Area is significant while shape (round or rectangular) is not. Casting considerations or the availability of a "proper" tubing shape are eliminated.

Eberhard [7] used parameters a and b with the equations:

$$X_{1,2} = \sqrt{\frac{ab + a + 1 + \sqrt{(ab + a + 1)^2 - 4ab}}{2ab}} \quad (9)[7]$$

$X_1(-)\ X_2(+)$

$$N_1 = X_1N_p \quad (10)[7]$$

$$N_2 = X_2N_p(k/2.1) \quad (11)[11]$$

to define N_1 and N_2, the two torque speeds in a two degree of freedom system. See Fig. 9. These speeds are matched to average flow velocities to develop maximum boost. At N_1, V_1 and V_2 have pressure excursions that are in phase; V_{2ave} is dominant. At N_2, the excursions are 180° out of phase; V_{1ave} is used. These average velocities are defined by the equations:

$$V_{1ave} = N_2V_1/360\, a_1 \quad (12)$$

$$V_{2ave} = N_1(0.14V_2 + V_1)/360\, a_2 \quad (13)$$

N_p replaces N_2 in equation 12 when a single pipe system is considered. Metric units: 360 = 3002.

Data relating the average velocity to boost are presented in Fig. 10. These are fairly general data as they cover tests of various pipe areas, therefore tuning speeds, and present smooth curves. Corners and the substantial area changes needed to connect pipes together in a manifold cause flow discontinuities. These losses help create the greater sensitivity to precise flow velocity matching in a two degree of freedom system compared to a one degree system, as noted by the narrower peaks. Demand for small size and a broad operating range may demand the use of a two degree system even though a one degree system might be more powerful at a given speed. The data indicates that 200 ft/s gives optimum volumetric efficiency in a one degree system at the Helmholtz speed. The Edelbrock (intake) and Blair (exhaust) manifolds with 212 ft/s at the peak support this velocity.

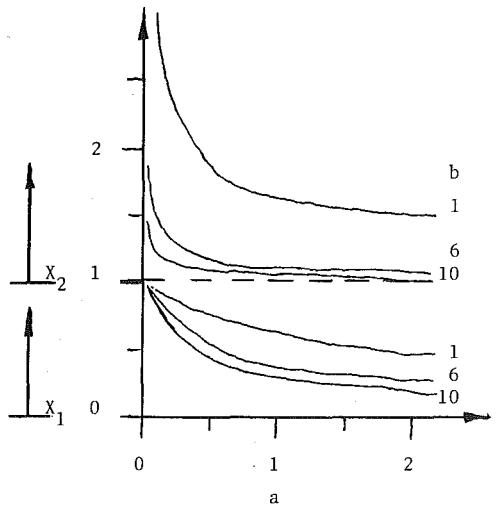

Fig. 9 $X_{1,2}$ **versus** a **versus** b

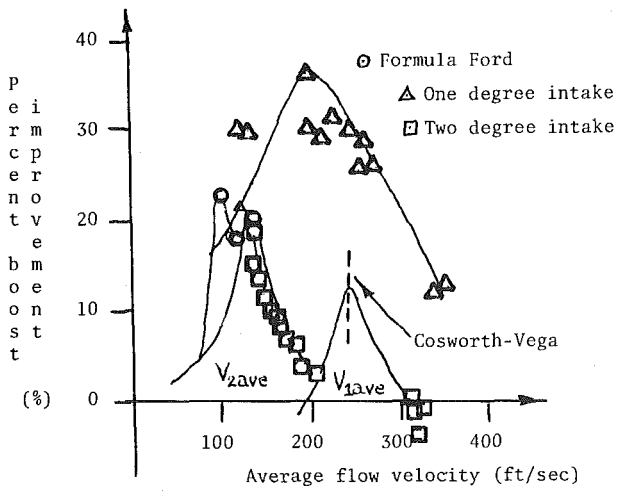

Fig. 10 Average flow velocity versus Boost improvement

In Fig. 11, a comparison of one and two degree systems is seen. The two exhausts produced nearly equal torque at 5000 rpm, but the manifolded system produced 17 percent more at 3000 rpm than the eight individual pipes did. Since the engine was run from 4400 to 6400 rpm, this deficit meant nothing.

Two situations exist with a two degree model: intake and exhaust systems. In the intake system, V_{2ave} = 130 ft/s at N_1 and V_{1ave} = 245 ft/s at N_2 are indicated as best velocities. Eberhard's study confirms the lower speed match point. A Cosworth-Vega log-runner manifold peaked with 245.7 ft/s at N_2. That system was a poor resonator that peaked instead at the appropriate flow match speeds, like the Blair exhaust did at 5000 rpm. N_1 tuned at V_{2ave} = 150 ft/s, perhaps because the gasoline had to be whipped harder when the resonator failed to contribute much to the performance.

Very noteworthy is that the Cosworth-Vega tuned at the same speeds when run naturally aspirated and turbocharged. The familiar performance map of a turbomachinery element will effect breathing, but the Cosworth tuned according to the intake manifold. The common habit of ignoring the manifolds because a turbocharger produces so much power is obviously a mistaken one. A steady pressure level without major oscillations was observed when a transducer was placed more than 1/2 in. from the exhaust face of a radial compressor [24]. Clearly the tuning characteristics of a turbocharger and manifold are independent. Significant power can be developed when they are designed to compliment one another. Performance improvements of a manifold can nearly meet the output of a Roots blower [25, 26]. The advantages of fewer moving parts and lower build and operating costs are obvious. In a recent report [33], Cser reported the use of combined charging on a six cylinder automotive diesel. Increases of 30 percent in torque above the production turbocharged engine were accompanied by reduction in smoke and improved driveability. The improvements came with an improved manifold design matched to the turbocharger.

In a one degree exhaust system, 200 ft/s is again the match point, as evidence by the Blair experience. In a two degree system, two different velocity points exist at N_1. In the Formula Ford tests, 12, 8, and 10 percent improvements of torque were made with V_{2ave} = 98, 115, and 145 ft/s, respectively, over a stock Shankle Tri-Y exhaust. See Fig. 12.

The 12 percent—98 ft/s tailpipe was the slowest on a road course; the 10 percent—145 ft/s pipe was the fastest. Apparently the 12 percent pipe has a gentle "puff" of gas that clears the cylinder efficiently. The mass moves down the pipe without drawing the cylinder down behind it. A lack of friction produces power at a constant speed but acceleration is poor. The boost with 145 ft/s comes from a more dense slug moving down the pipe. Acceleration is good because the vacuum behind the charge induces the next intake cycle when both valves are opened. Performance drops off around N_2, 7200 rpm, when compared to the stock system because what was a flow velocity defined manifold has been forced back partially into a Helmholtz model. The V_{1ave} = 290 ft/s at N_2 is too high to produce power as a resonator manifold, so the power drops.

The above exhaust studies were opened systems. By design, a muffler kills pressure oscillations in the pipe. The Cosworth intake, and Formula Ford and Blair exhausts tuned at speeds defined by flow velocities. Use can be made in a muffled exhaust system of the flow velocities there to provide some measure of performance improvement in an engine speed range. Also, in a six cylinder exhaust, the point where all pipes meet is the effective end of the resonator manifold. This point can be used as the maximum length of a resonator manifold to extract work from the gas as it heads for the muffler.

Resonance Ratio

Optimum velocities and engine block and head dimensions are fixed. Pipe lengths can be adjusted by varying the speed at which the engine tunes or by having one, two, three, or more pressure excursions during each opened valve period. Use of an integer factor, H, in equations (6) and (7) introduces these multiple pressure oscillations and can adjust pipe length according to the formula:

$$N \sim \sqrt{a_1/L_a V_1} = 1/H\sqrt{a_1/L_b V_1}$$

or

$$L_a = H^2 L_b \tag{14}$$

For a given engine speed, pipe lengths may differ by a factor of four, nine, or more in length. A sample of this is the comparison of a Chrysler Cross Ram intake (L_1 = 33 in., H = 1) and an Edelbrock Streetmaster (L_1 = 4 in., H = 2). These two manifolds are on similar sized engines, have torque peaks close together, and develop similar performance curves. See Fig. 13. Edelbrock experience with a still shorter pipe gave equal peak torque, but the drop off of performance on either side of that speed (3500 rpm) was more rapid than with the production four inch "long" pipe.

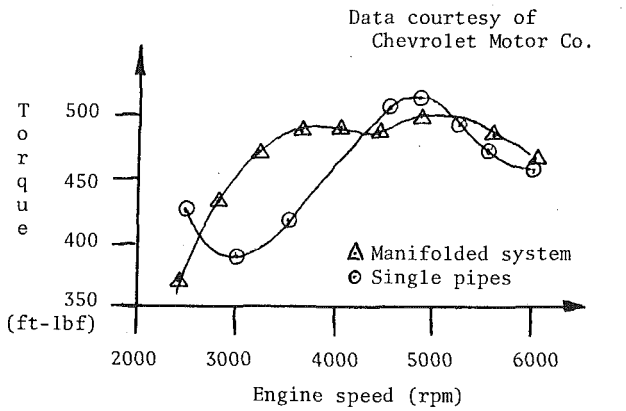

Fig. 11 427 Chevrolet with various exhaust systems

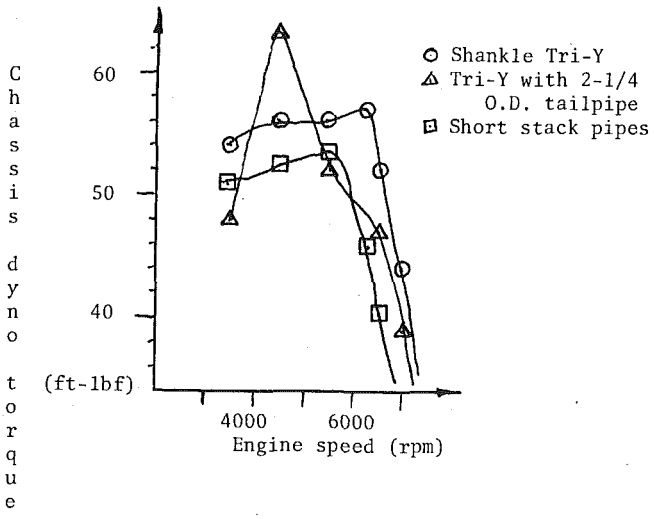

Fig. 12 Formula Ford data with various exhausts [22]

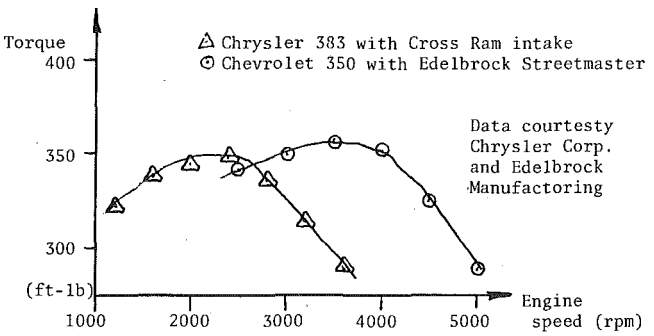

Fig. 13 Comparison of manifolds having one and two pressure excursions per valve period

Conclusion

The discrete modal model is valid for examining the intake and exhaust manifold of a single or multicylinder engine. Specific average flow velocities can be matched to one, two, or more pressure oscillations to provide maximum ram supercharge on intake and scavengine on exhaust. The intake and exhaust points can be paired or offset to compliment one another. Use of a turbocharger, Roots blower, or other supercharger will enhance the system already defined by the manifolds. Inclusion of all engine parameters assures a speedy design sequence at the designers wish to provide a manifold of any desired size and speed range. Improvements in performance, economy, and emissions characteristics will result from the proper design of the intake and exhaust systems.

Acknowledgments

To Ron Alexander, Harley-Davidson Motorcycle Company, Earl Ayers, owner of the Formula Ford, Ernie Helms, student at Ohio State who assisted in experiments presented here, and Warren Elkins, Diamond Racing Engines, and James D. McFarland, Jr., Edelbrock Manufactoring for their help in obtaining data from test programs. To Dr. Helmuth W. Engelman, Associate Professor of Mechanical Engineering at Ohio State for his continued interest in this subject.

References

1 Engelman, Helmuth W., "Surge Phenomena in Engine Scavenging," Ph.D. Dissertation, University of Wisconsin, 1953.

2 Helms, E., student at Ohio State University, aided in tests reported here.

3 Teeter, C. L., "Increasing the Horsepower of Gasoline Engines by Means of a Tuned Intake System," M. S. Thesis, University of Wisconsin, 1951.

4 Cambi, E., "Trigonometric Components of a Frequency Modulated Wave," *Proceedings of IRE*, Vol. 36, 1942, pp. 42–49.

5 Ricardo, H. R., "Internal Combustion Engine," U.S. Patent 1,834,473, 1931.

6 Thompson, Michael P., "Non-Mechanical Supercharging of a Four-Stroke Diesel Engine," M.S. Thesis, Ohio State University, 1968.

7 Eberhard, W. W., "A Mathematical Model of Ram-Charging Intake Manifolds for Four-Stroke Diesel Engines," M.S. Thesis, Ohio State University, 1971.

8 Schwallie, A. L., "Verification of a Mathematical Model of Intake Design," M.S. Thesis, Ohio State University, 1972.

9 Kauffman, J. C., "Investigations of the Influence of Gasoline Induction System Parameters on the Exhaust Emissions," Ph.D. Dissertation, Ohio State University, 1972.

10 Thompson, M. P. and Engelman, H. W., "The Two Types of Resonances in Intake Tuning," *ASME Diesel and Gas Power Proceedings*, 1969.

11 Vorum, P. C., "Short Pipe Tuning of the Exhaust of a Four-Stroke Engine," M.S. Thesis, Ohio State University, 1975

12 Vorum, P. C., "Short Pipe Manifold Design for Four-Stroke Engines," (Part 1) ASME Paper No. 76-WA/DGP-4, 1976.

13 Engelman, H. W., "Design of a Tuned Intake Manifold," *ASME Diesel and Gas Power Proceedings*, 1974.

14 Personal communications with Dr. N. A. Rubayi, Southern Illinois University, Carbondale, Ill.

15 Personal communications with Professor Emeritus Edward S. Taylor, M.I.T., Lincoln, Mass.

16 Morse, P. M., Boden, R. H., and Schecter, H., "Acoustic Vibrations and Internal Combustion Engine Performance," *Journal of Applied Physics*, Vol. 9, January, 1938.

17 Boden, R. and Schecter, H., "Dynamics of the Inlet System of a Four-Stroke Engine," NACA TN 935, May 1944.

18 Personal communications with Dr. Robert H. Boden, Sedona, Ariz.

19 Personal communications with Dr. Harry Schecter, Carlisle, Mass.

20 Blair, G. and Goulburn, "An Unsteady Flow Analysis of Exhaust Systems for Multicylinder Automobile Engine," SAE Paper 69-0469.

21 Personal communications with Warren Elkins, Diamond Racing Engines, Warren, Mich.

22 Personal communications with Earl Ayers, Formula Ford owner, Middletown, Ohio.

23 Personal communications with Ron Alexander, Harley-Davidson Motor Cycle Company, Milwaukee, Wisc.

24 Personal communications with Captain R. Durniak, Air Force Institute of Technology, Wright-Patterson AFB, Ohio.

25 Personal communications with Ernie Marsh, U.S. Army Tank/Automotive Command, Warren, Mich.

26 Personal communications with Bruce Chrisman, Cooper Energy Services, Springfield, Ohio.

27 Personal communications with James D. McFarland, Jr., Edelbrock Manufactoring Company, El Segundo, Calif.

28 Hoche, A., "Intake Equipment on Vehicular Diesel Engines and Effects on Engine Behavior," Dresden Technical University, Dresden, East Germany.

29 Personal communications with Franz K. Vail, Anchorage, Alaska.

30 Treyser, D. A., Greske, J. A., Fisher, R. D., and Creswick, F. A., "A Study of the Influence of Fuel Atomization, Vaporization, and Mixing Processes on Pollutant Emissions from Motor-Vehicle Powerplants," EPA Office of Air Programs, CPA 70-20, 1972.

31 Obert, E., *Internal Combustion Engines*, 3rd ed., 1968.

32 Smith, P. H. and Morrison, J. C., *The Scientific Design of Exhaust and Intake Systems*, 3rd ed., 1971.

33 Cser, Dr. Gy., "Combined Charging Systems for Commercial Vehicles," *Diesel and Gas Turbine Progress Worldwide*, Nov-Dec 1978, pp. 104–8.

A. Voorhies, Jr.
Visiting Professor,
Chemical Engineering Department

L. R. Daniel, Jr.
Professor,
Mechanical Engineering Department
Mem. ASME

Louisiana State University,
Baton Rouge, La.

L. Long
Project Engineer,
Vulcan Materials Company,
Geismar, La.
Assoc. Mem. ASME

The Effect of Percent Hydrogen in Fuel on Smoke Emissions of a Compression-Ignition Engine

Six diesel fuels, varying in percent hydrogen from 12.36 to 14.38 percent and in cetane number from 37.5 to 55.5, were evaluated for percent opacity as a function of fuel-air ratio—both at 800 and 1000 rpm—in a Waukesha CFR diesel engine. In both cases, at a given fuel-air ratio, the smoke emissions (measured by percent opacity) decreased with increasing percent hydrogen in the fuel. In these studies, percent hydrogen was both a satisfactory and a unique parameter, since neither cetane number nor volatility of the various fuels could be correlated with smoke emissions. In these studies, percent hydrogen is apparently the essential index of diesel fuel quality for satisfactory smoke emissions.

Introduction

The percent hydrogen in passenger-car diesel fuel was varied to determine its effect on visible smoke emissions, as measured by percent opacity. One set of three fuels was based on a commercial fuel having 12.36 percent hydrogen (Fuel A). Another set of three fuels was based on a commercial fuel having 13.38 percent hydrogen (Fuel D). In each case (Fuel A and Fuel D), blending agents[1] were used to make two synthetic combinations:

- Same percent hydrogen as the commercial fuel
- 1 percent more hydrogen than the commercial fuel

This is summarized in the following tabulation.

Fuel	Percent Hydrogen	Fuel	Percent Hydrogen
A	12.36	D	13.38
B	12.36	E	13.38
C	13.36	F	14.38

The rationale for Fuels B and E was to find the effect of including tetralin, which has a very low percent hydrogen (9.19), and compensating by adding diesel reference fuel T-15 so that the overall percent hydrogen was unchanged.

As will be evident from the presentation of the data, Fuel B had the same emission characteristics as Fuel A; and Fuel E had the same emission characteristics as Fuel D. This strongly suggests that the overall percent hydrogen is the essential parameter, irrespective of the molecular complexity in the diesel fuel. This would appear to have considerable commercial significance as exemplified below.

Typical diesel fuels produced in the oil refineries contain varying percentage of tetralin compounds, which contribute significantly to a low percent hydrogen, and hence to smoke emissions. Even more objectionable than tetralin compounds are the bicyclic aromatics, which have an even lower percent hydrogen. The required catalyst and operating techniques for hydrogenation of bicyclic aromatics and tetralin compounds (naphtheno-aromatics) are presently available. This presents an interesting possibility for upgrading the smoke-emission characteristics of commercial diesel fuels.

The rationale for Fuels C and F was to find the effect on emissions of an increase of 1 percent hydrogen in Fuel A (13.36 versus 12.36 percent and also 1 percent in Fuel D (14.38 versus 13.38 percent). The data, subsequently presented, show in both cases a significant decrease in emissions for a 1 percent increase in percent hydrogen. In every case studied, the percent hydrogen was both a satisfactory and a unique parameter since neither cetane number nor volatility of the various fuels could be correlated with smoke emissions.

Fuel Blends

As already summarized, comparative studies were made with two commercial diesel fuels and four fuel blends. The composition of these six fuels is shown in Table 1. A commercial diesel fuel (Fuel A) was blended with a small percentage of tetrahydronaphthalene (a typical naphtheno-aromatic) plus a small amount of high cetane number reference fuel (T-15) to give about the same cetane number as Fuel A. This blend (Fuel B) had the same percentage hydrogen as the commercial diesel fuel. The third fuel (Fuel C) consisted of the same

Table 1 *Comparison of test fuels*

Test Fuels	Blending Components % Fuel A	% Fuel D	% T-15	% U-8	% Tetralin	Cetane# of Fuel	% Hydrogen in Fuel
A	100.0					45.7	12.36
B	40.0		38.0		22.0	43.2	12.36
C	20.0		70.6		9.4	55.5	13.36
D		100.0				40.9	13.38
E		40.0	50.2		9.8	41.8	13.38
F		36.7		63.3		37.5	14.38

[1] These blending agents were one or more of the following: diesel reference fuels T-15 and U-8; tetrahydronaphthalene (tetralin).

Contributed by the Diesel and Gas Engine Power Division of THE AMERICAN SOCIETY OF MECHANICAL ENGINEERS and presented at the Energy Technology Conference and Exhibition, New Orleans, La., February 3–7, 1980. Manuscript received at ASME Headquarters November 6, 1979. Paper No. 80-DGP-15.

components as Fuel B. The cetane number was much higher due to the large percentage of T-15.

A second batch of fuels was mixed with a different commercial diesel fuel (Fuel D). It contained a higher percentage of hydrogen than Fuel A. The fifth fuel (Fuel E) contained a small percentage of tetrahydronaphthalene (tetralin), and much high cetane-number reference fuel. This fuel has the same percentages of hydrogen as Fuel D, and about the same cetane number. The sixth fuel (Fuel F) was made with Fuel D and a low cetane-number diesel fuel. The low cetane-number fuel had the highest percentage of hydrogen, and this was needed to raise the hydrogen content of Fuel D one percent. There was no tetralin added to this blend since tetralin has a low percentage of hydrogen. This presented an opportunity to see how the smoke levels of this fuel without added tetralin compared with other fuels with added tetralin. Since this blend was made with a low cetane-number fuel, it was possible to determine how a low cetane-number fuel affected the opacity.

The reference fuels used in these blends were T-15 and U-8. These fuels were manufactured by Shell Oil Company and are predecessors to the current secondary reference fuels. The cetane number, the percentage by weight of hydrogen and carbon, the distillation range of the reference fuels, and the details of the fuel blends are discussed in Appendix I.

Experimental Apparatus

Single cylinder Waukesha, cetane-rating diesel engine was used in the tests. The CFR engine has a large number of parameters which can be varied including compression ratio, engine speed, load and injection timing over a wide range.

The bore and stroke of the engine are 3.25 in. (8.26mm) and 4.50 in. (11.42mm), respectively. The head of the engine is of the turbulence type. The bore of the turbulence combustion chamber is 1.625 in. (4.13mm) and its length is adjustable from 0.375 in. (0.95mm) to 2.750 in. (6.99mm).

A Waukesha ignition delay meter was used to measure the injection advance and the ignition delay in crank angle degrees. This was accomplished by using several magnetic transducers, one on the injector nozzle pin, one in the combustion chamber, and two measuring a calibrated 12.5 deg on the flywheel. The output of the transducers was sent through the ignition delay meter to obtain the readings.

The fuel rate was determined by measuring the amount of time needed for a given amount of fuel to flow through a graduated burette. The amount of fuel burned was usually 13 ml.

The smoke emissions of the engine exhaust were measured with a Clayton Model DA-111 opacimeter. The smoke meter is of the light extinction type. A beam of light is passed through the path of smoke from the exhaust pipe. The light that passes through hits a photoelectric cell where it is converted into an electric voltage which is then measured by a millivoltmeter on the scale reading from 0 to 100. A zero reading indicates no smoke in the exhaust and 100 indicates total light extinction due to smoke. A Hewlett/Packard Model 7100 B strip chart recorder monitored the output of the opacimeter.

Experimental Procedure

After an initial period of approximately one hr, to allow the engine parts and fluids to reach stability, the measurements were taken. The engine was run at two speeds: 800 rpm and 1000 rpm. The injection advance was set at crank angle 13 deg BTDC. The compression ratio was set at 23:1, since this is an average of those being used in current production passenger cars. The compression ratio of the Oldsmobile Cutlass is 22.7:1; the Volkswagen Rabbit is 23.5:1; and the Mercedes 300SD is 21.5:1.

The test procedure was designed to obtain a good correlation of data on each fuel at different fuel-air ratios. One fuel-air ratio was selected

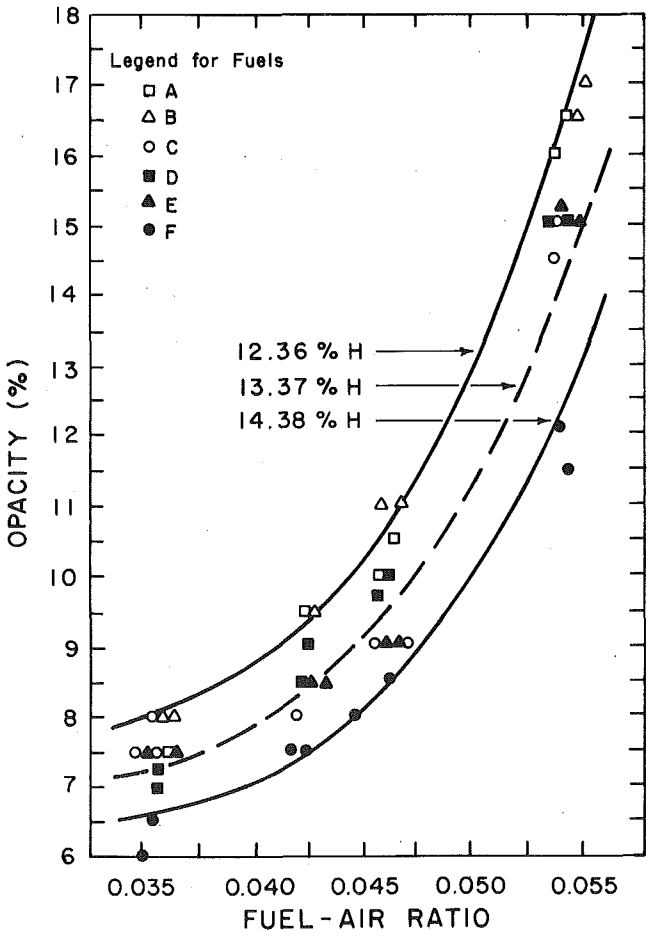

Fig. 1 The effect of fuel-air ratio on exhaust smoke at 800 rpm, comp. ratio 23:1, injection advance 13 deg BTDC

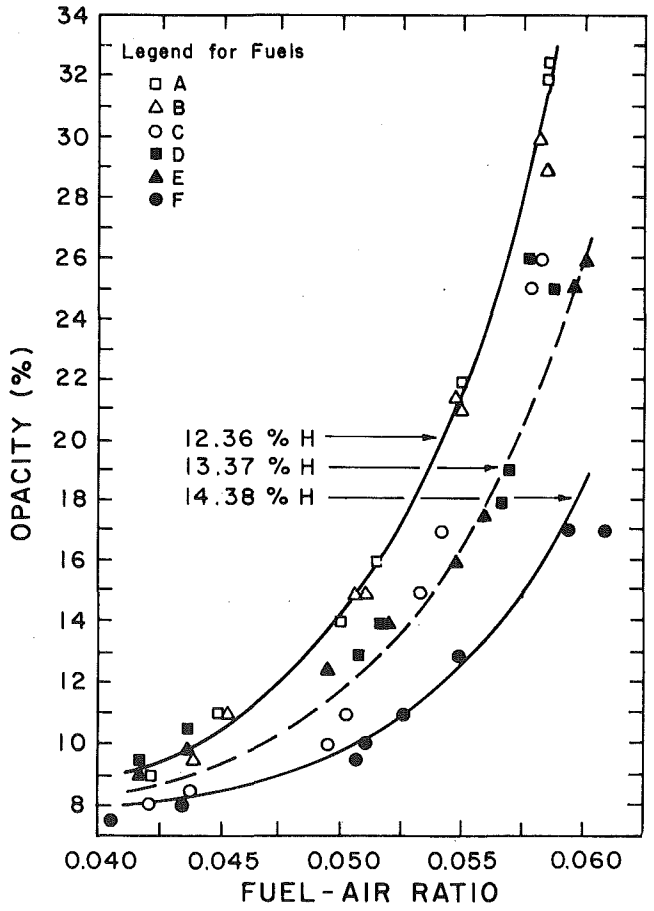

Fig. 2 The effect of fuel-air ratio on exhaust smoke at 1000 rpm, comp. ratio 23:1, injection 13 deg BTDC

and the test fuels were run one after another at the same engine conditions. Each fuel was run for approximately ten minutes to allow for engine stability before measurements were taken. This method proved to be satisfactory at both speeds since an immediate comparison among the fuels was made at a steady set of engine conditions. The opacity levels for each data point were read directly from the opacimeter. A hard copy was also made on a strip chart recorder, which easily defined the time that the engine became stable.

Results and Conclusions

The six fuels were run at the same engine conditions. The actual data are plotted in Figs. 1 and 2. The lines drawn over the data represent an empirical relation which describes the actual data and can predict any values in the range of the data. The data points are listed in Tables 2 and 3. The mathematical model which was used in the correlation is shown in Appendix II.

Fuels A and B have the same percentage of opacity at any given FA ratio. The cetane numbers of these two fuels are similar. They have the same weight percentage of hydrogen. Fuel B contains 22 percent tetralin.

Fuel C has the highest cetane number of the fuels. It has a lower level of opacity than Fuels A and B. Originally, it was not known whether the higher percentage of hydrogen or the higher cetane number caused the difference in smoke density.

A second commercial fuel, Fuel D, was used to make two additional blends. Its hydrogen content is almost identical to that of Fuel C, but its cetane number is much lower.

Fuel E has approximately the same percentage of hydrogen as Fuels C and D. Its cetane number is similar to that of Fuel D. Fuels C, D, and E have approximately the same opacity levels, and also approximately the same percent hydrogen.

Fuel F is a blend which has the highest percentage of hydrogen and the lowest cetane number. The data show that this blend has the lowest opacity level of the fuels. Since the cetane number is lower than that of all the fuels, and Fuel C has the highest cetane number, it can be said that the cetane number did not exhibit any correlation to smoke density.

Table 2 Experimental data at 800 rpm, comp. ratio 23:1, injection advance 13 deg BTDC

Fuel	FA Ratio	Opacity Percent
A	0.0404	8.0
A	0.0409	7.5
A	0.0480	9.5
A	0.0519	10.0
A	0.0527	10.5
A	0.0614	16.0
A	0.0620	16.5
B	0.0409	8.0
B	0.0412	8.0
B	0.0483	9.5
B	0.0524	11.0
B	0.0534	11.0
B	0.0624	16.5
B	0.0632	17.0
C	0.0388	7.5
C	0.0391	7.5
C	0.0462	8.0
C	0.0502	9.0
C	0.0516	9.0
C	0.0593	14.5
C	0.0598	15.0
D	0.0398	7.0
C	0.0400	7.25
D	0.0472	8.5
D	0.0474	9.0
D	0.0510	9.5
D	0.0517	10.0
D	0.0603	15.0
D	0.0607	15.0
E	0.0392	7.5
E	0.0399	7.5
E	0.0471	8.5
E	0.0480	8.5
E	0.0513	9.0
E	0.0514	9.0
E	0.0602	15.25
E	0.0606	15.0
F	0.0370	6.0
F	0.0376	6.5
F	0.0443	7.5
F	0.0448	7.5
F	0.0472	8.0
F	0.0489	8.5
F	0.0573	12.0
F	0.0578	11.5

Table 3 Experimental data at 1000 rpm, comp. ratio 23:1, injection advance 13 deg BTDC

Fuel	FA Ratio	Opacity Percent
A	0.0478	9.0
A	0.0509	11.0
A	0.0568	14.0
A	0.0584	16.0
A	0.0624	22.0
A	0.0624	22.0
A	0.0664	32.0
A	0.0668	32.5
B	0.0500	9.5
B	0.0514	11.0
B	0.0578	15.0
B	0.0581	15.0
B	0.0624	21.5
B	0.0628	21.0
B	0.0666	30.0
B	0.0668	29.0
C	0.0463	8.0
C	0.0483	8.5
C	0.0546	10.0
C	0.0554	11.0
C	0.0589	15.0
C	0.0598	17.0
C	0.0638	25.0
C	0.0641	26.0
D	0.0464	9.5
D	0.0488	10.5
D	0.0566	13.0
D	0.0577	14.0
D	0.0634	18.0
D	0.0637	19.0
D	0.0647	26.0
D	0.0659	25.0
E	0.0462	9.0
E	0.0482	10.0
E	0.0549	12.5
E	0.0574	14.0
E	0.0608	16.0
E	0.0621	17.5
E	0.0662	25.0
E	0.0667	26.0
F	0.0428	7.5
F	0.0459	8.0
F	0.0536	9.5
F	0.0539	10.0
F	0.0557	11.0
F	0.0580	13.0
F	0.0630	17.0
F	0.0644	17.0

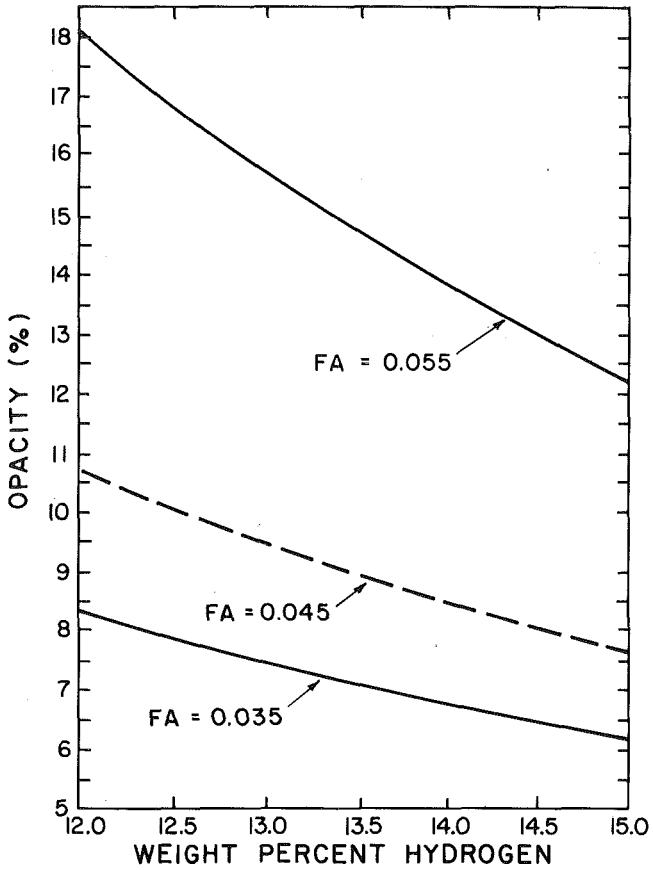

Fig. 3 The effect of hydrogen on exhaust smoke at 800 rpm, comp. ratio 23:1 injection advance 13 deg BTDC

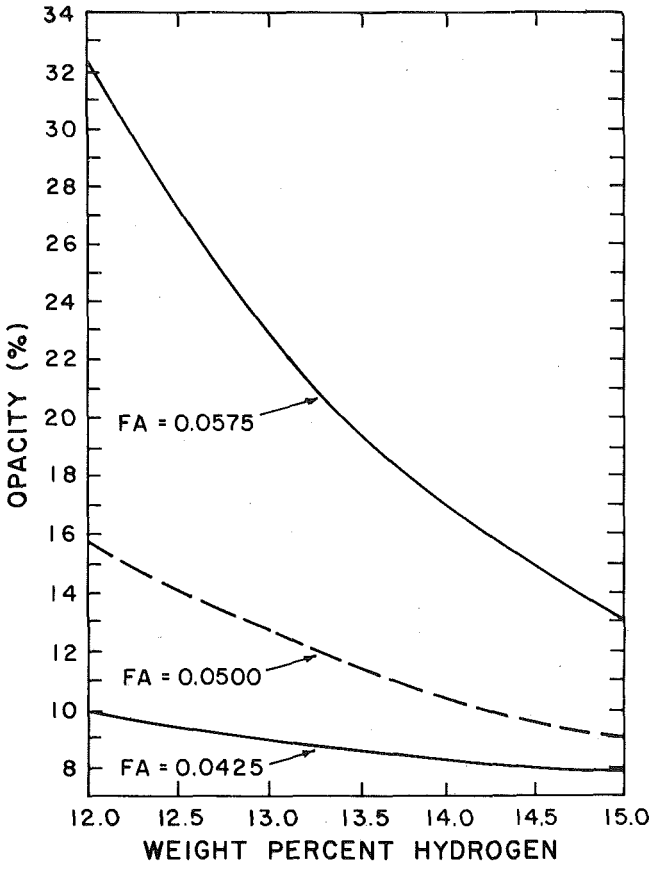

Fig. 4 The effect of hydrogen on exhaust smoke at 1000 rpm, comp. ratio 23:1, injection advance 13 deg BTDC

Within the limited scope of this study, the hydrogen content of the diesel fuel was apparently the most significant parameter in determining smoke emissions. This does not deny the influence of other parameters which were not specifically investigated. For example, the boiling range of a diesel fuel of a given percent hydrogen may have a significant effect on smoke emissions. With respect to the influence of hydrogen content on smoke emissions, the rationale probably resides in the molecular structure of hydrocarbons. A higher percent hydrogen means a higher ratio of hydrogen to carbon, and a faster rate of carbon combustion.

The following remarks summarize the principal conclusions.

- The results indicated that there was no change in the opacity levels of the fuel blends with added tetralin as compared to that of the blends without added tetralin—provided that there was no change in percent hydrogen.
- The cetane numbers of the six fuels ranged from 37.5 to 55.5. A correlation of cetane numbers versus opacity was attempted, but there was no correlation among the six test fuels based on cetane number.
- The volatility, as expressed by distillation data (Appendix III), was checked to determine its correlation, if any, with the opacity. Based on the 50 percent distillation point of the test fuels, which range from 420°F (216°C) to 516°F (269°C), no correlation was found between opacity and volatility of the fuel.
- The smoke emissions data showed a very strong relationship of percent hydrogen with opacity, in which a fuel with the higher percent hydrogen produced less smoke. This correlation is very good even though the six fuels included two different commercial fuels.
- Several FA ratios were chosen to determine the correlation of opacity as a function of percent hydrogen. At lower FA ratios, there is almost a linear relationship. The higher FA ratios exhibit a trend toward a steeper slope at lower percent hydrogen.

Future Plans

The results of this investigation give strong indication that there is a relationship between percent hydrogen in the fuel and opacity of the exhaust of a compression ignition engine.

Of the six fuels studied, only two were commercial diesel fuels,—whereas the other four fuels were synthetic modifications of the two commercial fuels. It would be more realistic to have confirmatory data on the role of percent hydrogen on smoke emissions, based entirely on nonsynthetic commercial diesel fuels of different hydrogen content and cetane numbers. These fuels would be obtained from a petroleum refinery. Funds have been obtained for this investigation.

In at least one instance, the literature reveals that an increase in cetane number will either reduce or increase smoke depending upon combustion chamber design (Breaze and Stillebroer, "Smoke in High Speed Diesel Engines," *SAE Journal,* Mar. 1959, p. 64). Pending funding it is planned to investigate the effect on smoke of changing the percent hydrogen in the fuel of an open combustion chamber diesel in order to compare the results with the results of the present study.

Acknowledgment

This is to gratefully acknowledge the financial assistance of Exxon Research and Engineering Co. in the studies reported in this paper.

APPENDIX I

Fuel Blends

The first blend, Fuel B, was made to have the same percent hydrogen as Fuel A. This blend consists of 40 weight percent Fuel A with

60 weight percent of a blend of T-15 and tetralin. The percentage by weight of hydrogen in each fuel is shown in Table 1. The following equation was used to determine the amount of T-15 and tetralin required:

$$14.20x + (0.6 - x)\,(9.19) + (0.4)\,(12.36) = 12.36 \text{ percent}$$

$$x = 0.380 = \text{fraction of } T\text{-}15$$

$$0.6x = 0.220 = \text{fraction of tetralin} \qquad (1)$$

Proof:

$$(0.380)\,(14.20) + (0.220)\,(9.19) + (0.4)\,(12.36) = 12.36 \text{ percent}$$

Fuel C has a one percent higher hydrogen content than Fuel A and Fuel B. The percent of Fuel A is decreased from 40 to 20 percent. The remainder is a blend of the T-15 and tetralin. The composition of C is calculated as follows:

$$14.20x = (0.8 - x)\,(9.19) + (0.2)\,(12.36) + 13.36 \text{ percent}$$

$$x = 0.706 = \text{fraction of T-15}$$

$$0.8 - x = 0.094 = \text{fraction of tetralin}$$

Proof:

$$(14.20)\,(0.706) + (0.8 - 0.706)\,(9.19) + (0.2)\,(12.36) = 13.36 \text{ percent} \qquad (2)$$

The new commercial fuel, Fuel D, contained 13.38 percent hydrogen. So Fuel E was blended with Fuel D, T-15, and tetralin to have this same percent hydrogen. The calculation of E is as follows:

$$14.20x + (0.6 - x)\,(9.19) + (0.4)\,(13.38) = 13.38 \text{ percent}$$

$$x = 0.502 = \text{fraction of T-15}$$

$$0.6 - x = 0.098 = \text{fraction of tetralin}$$

Proof:

$$(14.20)\,(0.502) + (0.6 - 0.502)\,(9.19) + (0.4)\,(12.36) = 13.38 \text{ percent} \qquad (3)$$

Fuel F has one percent higher hydrogen content than Fuel D and Fuel E. It contains a mixture of Fuel D and U-8 reference fuel. The calculation for its composition is:

$$14.96x + (1 - x)\,(13.38) = 14.38 \text{ percent}$$

$$x = 0.633 = \text{fraction of U-8}$$

$$1 - x = 0.367 = \text{fraction of Fuel D}$$

Proof:

$$(0.633)\,(14.96) + (1 - 0.633)\,(13.38) = 14.38 \text{ percent} \qquad (4)$$

APPENDIX II

Mathematical Model for Data

In order to obtain the best mathematical model for the data, several different functions were used which appeared to be a possible fit for the shape of the curves. A statistical computer program was used to determine how close the relation fits the data. The one which was found to best correlate with the data is the following.

$$z = a_0 + a_1x + a_2y + a_3x^2 + a_4y^2 + a_5xy$$

x = ln percent hydrogen, y = fuel rate, ml/min, z = ln percent opacity.

The coefficients at 800 rpm are: $a_0 = 3.89570$, $a_1 = 0.0$, $a_2 = -0.07329$, $a_3 = -0.09843$, $a_4 = 0.01353$, $a_5 = -0.07342$.

The coefficients at 1000 rpm are: $a_0 = -4.57480$, $a_1 = 0.0$, $a_2 = 0.91487$, $a_3 = 1.41760$, $a_4 = 0.01392$, $a_5 = -0.50680$.

The plot of percent opacity as a function of hydrogen shows that there is a somewhat linear relationship. This is the reason for assuming hydrogen to be a linear function. The FA ratio appears to behave similarly to a parabolic or exponential function. Each of these was tested, and the exponential function worked the best. The multiple correlation coefficient at 800 rpm is 0.9998 and at 1000 rpm is 0.9996. The standard deviation at 800 rpm is 1.047 percent and at 1000 rpm is 1.087 percent.

APPENDIX III

Properties of test fuels and blending components (all temperatures are in °F)

	Test Fuels						Other Blending Components		
	A	B	C	D	E	F	T-15	U-8	Tetralin
Source	Commercial			Commercial			Shell	Shell	
Gravity, API	34.7	33.9	39.4	37.4	38.7	47.0	45.1	52.9	
Gravity, Specific	.8338	.8378	.8100	.8208	.8146	.7775	.7857	.7531	
Cetane Number	45.7	43.2	55.5	40.9	41.8	37.5	22.7	71.0	
Hydrogen Percent	12.36	12.36	13.36	13.38	13.38	14.38	14.20	14.96	9.19
Carbon Percent	86.65			86.30					90.63
Initial Boiling Point	361	367	400	410	406	372	407	356	
10% Evaporation	426	407	435	450	434	379	444	367	
20% Evaporation	454	430	446	467	446	388	455	370	
30% Evaporation	474	440	454	484	460	398	467	374	
40% Evaporation	494	453	467	497	468	410	474	376	
50% Evaporation	510	466	477	516	480	420	484	381	
60% Evaporation	526	480	490	535	498	442	489	390	
70% Evaporation	545	500	501	558	520	472	500	397	
80% Evaporation	562	524	518	588	536	511	511	414	
90% Evaporation	588	550	540	623	568	558	528	451	
95% Evaporation	612	578	559	653	600	596	546	459	
Final Boiling Point	630	608	594	662	633	628	569	553	
Recovery Percent	98.0	99.0	99.0	98.0	98.5	98.5	98.5	99.2	
Residue Percent	1.5	1.0	1.0	1.6	1.4	1.4	1.3	0.8	
Loss Percent	0.5	0.0	0.0	0.4	0.1	0.1	0.2	0.0	

D. R. Garner
Manager,
Rotating Plant Section

R. D. James
Manager,
Automotive Research

J. F. Warriner
Manager,
Diesel Engine Bearing Section

The Glacier Metal Company Ltd.,
Middlesex, England

Cavitation Erosion Damage in Engine Bearings: Theory and Practice

Cavitation erosion damage in engine bearings has assumed increasing importance during the past 5–10 years, probably as a result of the design trends towards higher rotational speeds, and, in some cases, higher rates of change of cylinder pressure rise. In many instances the damage is merely cosmetically undesirable, and of only minor functional significance; this is particularly so when the bearing is overlay plated. In more extreme cases extensive loss of lining material will result, and the consequential adverse effects on oil film conditions will reduce reliability and life of the bearings and associated parts. This paper presents a general background to cavitation erosion damage and examples of specific forms of this type of damage in plain bearings are given. A number of commonly applied palliatives and their effectiveness, based on engine experience, are discussed. A description of computer-based methods for predicting crankshaft journal locus, oil film pressure profile, and film extent is provided. An attempt has been made to rationalize several typical forms of cavitation damage on the basis of the theoretical model. An ultrasonic vibratory test facility used by the authors to determine the relative erosion resistance of the more commonly used bearing materials is described, and results presented.

Introduction

Cavitation erosion damage in engine bearings is a phenomenon which has assumed increasing significance during the past five to ten years, probably as a result of the design trends towards higher rotational speeds and, in some cases, higher rates of change of cylinder pressure rise. In many cases the damage is restricted to local attack of the overlay and the performance of the bearing is virtually unaffected (Fig. 1). However, in more extreme cases extensive loss of overlay and interlayer material occurs, and the consequential adverse effects upon oil film conditions will reduce the service reliability and life of the bearings and their associated components (Fig. 2).

In the past, the damage observed in engine bearings has been treated on a symptomatic basis by the application of relatively simple, and usually effective, palliative measures. These have included reduction in the operating clearance, increase in the oil supply pressure, and the use of harder lining materials. There may be occasions when these measures are not totally effective, or when they cannot be applied due to other design considerations. Therefore, a general solution to the problem is required and to this end a fundamental understanding of the cavitation phenomenon is sought.

Cavitation in liquids will occur when the local fluid pressure falls below the vapor pressure. In effect it is boiling of the liquid by pressure reduction rather than by increase in temperature. Damage to solid surfaces may result from the rapid and violent collapse of vaporous cavities adjacent to the surfaces. A qualitative assessment of the forces involved in cavity collapse can be gained by observing the behavior of a liquid in a "banger" tube (Fig. 3). This consists of a tube partially filled with a liquid, typically water, with the pressure of the air above the liquid surface reduced below atmospheric. Shaking the tube to produce a violent disturbance in the liquid results in a sharp audible crack due to the formation and collapse of cavities; this provides clear evidence of the severity of the phenomenon.

In the past, attempts have been made to calculate the magnitude of local pressure developed by the collapse of a vaporous cavity [1], and even assuming a finite value of final cavity radius local pressures as high as 2000 MN/m^2 are predicted. Such pressures seem surprisingly high, but examination of specimens which have been subjected to cavitation attack reveals considerable plastic deformation of the surface even before material has been lost (Fig. 4).

There has been considerable debate over the years as to the precise mechanism whereby the energy of cavity collapse produces physical damage to an adjacent solid surface. Initially the connection was somewhat tenuously made by reference to cavity implosion [1], but a more credible explanation was suggested by Kornfeld and Suvarov [2] who referred to the impingement by micro-jets of fluid. A possible sequence of events in the collapse of a vaporous cavity leading to the formation of a high intensity micro-jet is shown in Fig. 5, [3]. Subsequently, Benjamin and Ellis [4] lent substantial support to the micro-jet explanation with impressive photographic evidence.

Damage in Plain Bearings. Cavitation erosion damage is seen predominantly in diesel engine bearings, and on the rare occasions when such damage occurs in gasoline engines it is normally as a result of operating under conditions of sustained overspeed or with incorrect ignition timing (Fig. 6). The fact that diesel engine bearings are more prone to cavitation erosion damage is attributed to the more severe combustion conditions, and, additionally, to the necessity for more complex oil feeding arrangements with greater chance of flow discontinuities. In order for cavitation-induced damage to the bearing lining to occur, it is necessary for vaporous cavities in the lubricant

Contributed by the Diesel and Gas Engine Power Division of THE AMERICAN SOCIETY OF MECHANICAL ENGINEERS and presented at the Energy Technology Conference and Exhibition, New Orleans, La., February 3–7, 1980. Manuscript received at ASME Headquarters November 9, 1979. Paper originally presented at the 13th CIMAC Congress, Vienna, Austria, May 8, 1979. Paper No. 80-DGP-28.

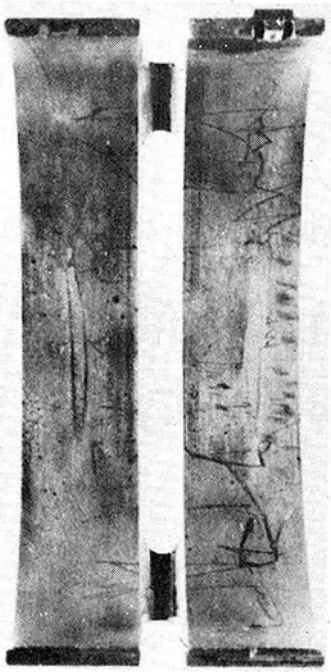

Fig. 1 Mild overlay cavitation damage

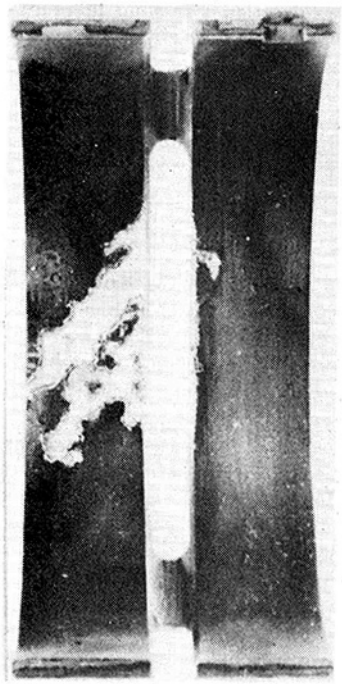

Fig. 2 Severe cavitation damage

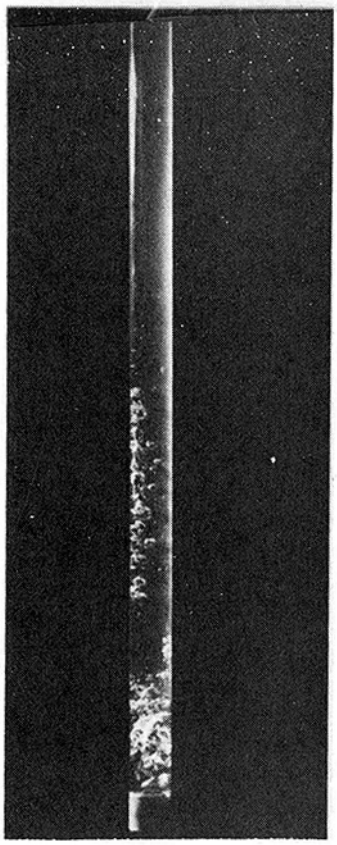

Fig. 3 Cavitation effects in "banger" tube

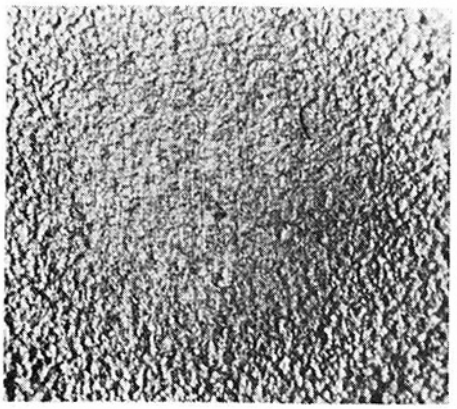

Fig. 4 Plastic deformation in test rig specimen

to collapse in close proximity to the surface, but it is important to recognize that the site of the damage could be remote from the point of inception of the cavities. Vaporous cavities will form when the lubricant pressure locally falls below the vapour pressure, as the result of:

1 *fluctuations in flow arising from the interaction of bearing and* journal features, such as grooves and drillings

2 transient oil film pressures, resulting, perhaps, from changes *in journal eccentricity*

In an attempt to categorize the various forms of cavitation damage that commonly occur, in a wide range of engine types, and to give some insight into the theoretical assessment described later in the paper, a series of specific examples and case histories are examined, together with possible explanations of the damage mechanisms involved.

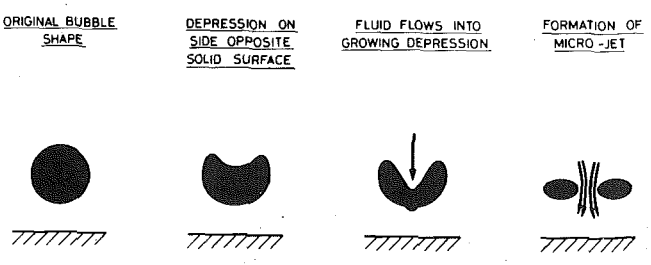

Fig. 5 Mechanism of micro-jet formation

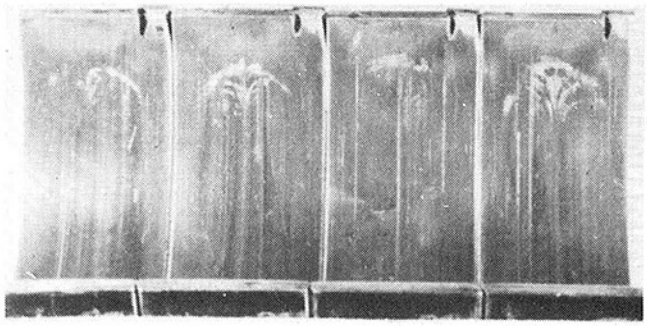

Fig. 6 Overlay erosion in gasoline engine large-end bearings resulting from incorrect ignition timing

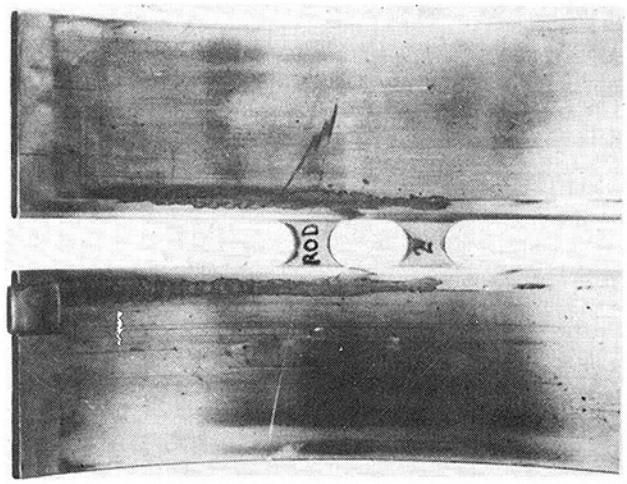

Fig. 7 Groove edge erosion in large-end bearing

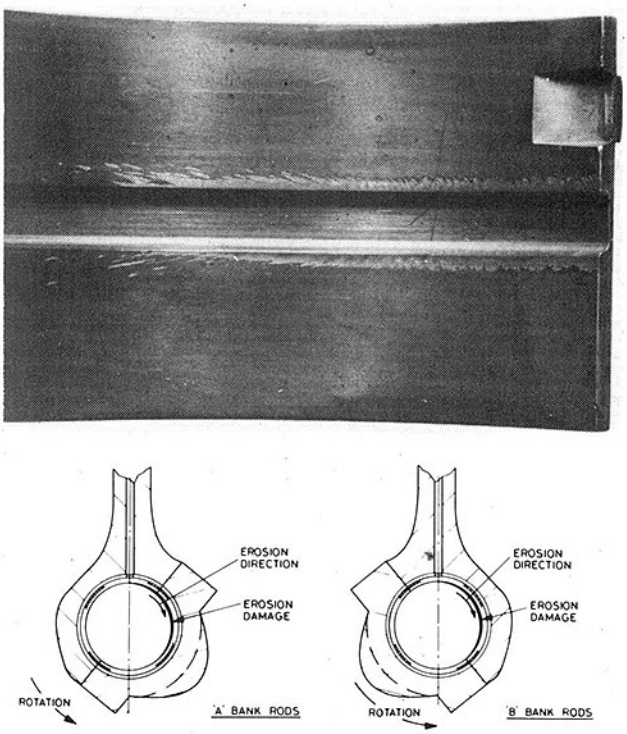

Fig. 8 Relationship between position of groove edge erosion and shaft rotation

Service Experience

Large-End Bearings: Fully Grooved. The commonest form of damage occurring in large-end bearings appears at first sight to be due more to flow erosion than to cavity collapse, but detailed examination of the damage confirms a cavitation effect. This can occur in either fully grooved or partially grooved bearings.

In fully grooved bearings, the damage occurs predominantly at the groove edges, but can ultimately spread into the bearing lands. There is strong evidence that the damage is caused by inertia effects on the column of oil in the connecting rod drilling which is supplied from the large-end bearing groove to provide top end lubrication and piston cooling. In one particular engine with fully grooved bearings such damage occurred when the operating speed was increased by 20 percent, and consequently the inertia effects by 44 percent. An initial modification of providing a compound blend radius at the groove edges was not effective (Fig. 7) whereas fitting a nonreturn valve in the bottom end of the rod drilling eliminated the damage.

The nonreturn valve opens when oil flows from the large-end bearing up the rod, but closes under any reverse flow. The success of this device, fitted immediately adjacent to the large-end groove, proved that inertia forces on the oil column in the connecting rod drilling were significant, and that oil flow back into the bearing, and not out of it, was directly causing the damage.

The nonreturn valve has a proven reliability on engines up to 600 rev/min but it is suspected that at higher speeds the inertia of the moving parts could cause mechanical damage.

On another engine, a Vee type with side by side, but handed, connecting rods, the groove edge damage was consistent on all the rods from one bank, but different from those in the other bank. The similarity lay in the fact that the position of the damage was the same relative to the direction of rotation and to the rod shank drilling (Fig. 8). In this instance, the damage was diminished when the groove cross-sectional areas in both the main and large-end bearings were increased, thus allowing the oil column fluctuation to be better absorbed by the oil in the grooves rather than producing an excessive flow across the bearing lands.

Large-End Bearings: Partially Grooved. On partially grooved large-end bearings, damage frequently occurs at the groove run-out, either at the end of the partial groove (Fig. 9) or at the side of the run-out (Fig. 10). The problem occurs at the end of the partial groove in the direction of shaft rotation, regardless of the position of the oil feed connection to the rod drilling. In the example shown in Fig. 10, in which the damage had occurred within 400 hr, the oil feed to the rod was adjacent to the damaged groove ending. The problem was overcome by the simple expedient of drilling a radial hole in the

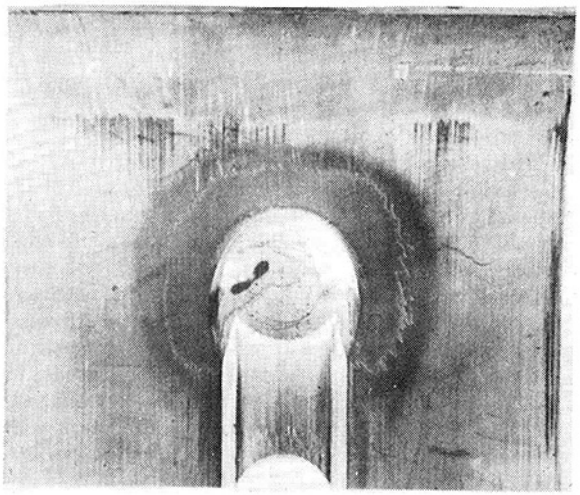

Fig. 9 Cavitation damage at end of smoothly blended groove in large-end bearing

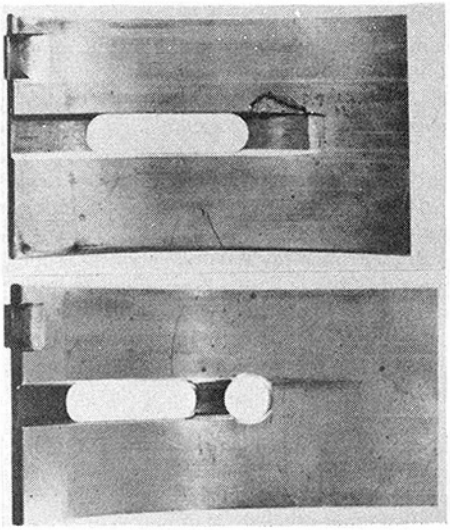

Fig. 10 Cavitation damage associated with groove run-out in large-end bearing, together with effective solution

run-out section, as shown by the lower bearing in Fig. 10 which had run for 1500 hr. Several other cases of similar damage have been successfully treated, including applications where the feed to the rod drilling was adjacent to the opposite end of the partial groove, either by provision of a radial hole or by terminating the groove conveniently at the end of a bridge-piece slot.

The only explanation the authors can put forward for the effectiveness of such solutions is that it results from a combination of the damping effect of a relatively stagnant additional volume of oil and a change in oil flow conditions out of the end of the groove.

All attempts to overcome the damage at the end of partially grooved large-end bearings by gently blending the groove ending, including the use of tangential blends or spoon-shaped indents, have been generally unsuccessful.

In a similar manner to which the damage to the fully grooved bearing shown in Fig. 7 was overcome by fitting a nonreturn flow valve at the base of the connecting rod, the damage shown to the partially grooved bearing in Fig. 9 was overcome by fitting a restrictor in a comparable position. This consisted of an insert in the shank drilling with a smaller diameter hole than the rod drilling. The precise length and diameter of the restrictor have to be determined by heat balance tests on the engine to insure that sufficient oil is supplied for piston cooling. Once correct, it has the advantage that, unlike a valve, it cannot be damaged by inertia effects. A sophistication of this insert would be a tapered hole, allowing easier flow into the rod from the connecting rod bearing when inertia forces on the oil column are upwards, and a restricted flow when they reverse.

High speed diesel engines (above approximately 2000 rev/min) generally use ungrooved large-end bearings and do not supply piston cooling oil via a connecting rod shank drilling. Large-end cavitation erosion damage is not a common problem in these engines, but the increasing level of turbocharging being applied will put further demands on present piston cooling methods. If additional cooling is to be achieved by a rod drilling arrangement, rather than by fixed jets, then similar cavitation problems to those described above would be expected to occur.

One form of cavitation damage which has been noted on the large-end bearings in several different types of high speed diesel engines incorporating horizontally split connecting rods, is shown in Fig. 11. In each case, the damage occurs in cap half bearings close to one joint face only. It is believed that this particular type of damage is influenced by local flexibility of the cap, causing collapse of vaporous cavities formed within the oil film.

Main Bearings: Partially Grooved. The majority of modern medium speed diesel engines use partially grooved main bearings in which the ungrooved arc is symmetrically placed in the bottom half,

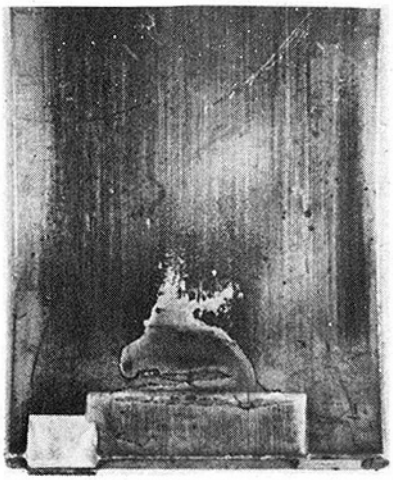

Fig. 11 Suction damage in high speed diesel engine large-end bearing

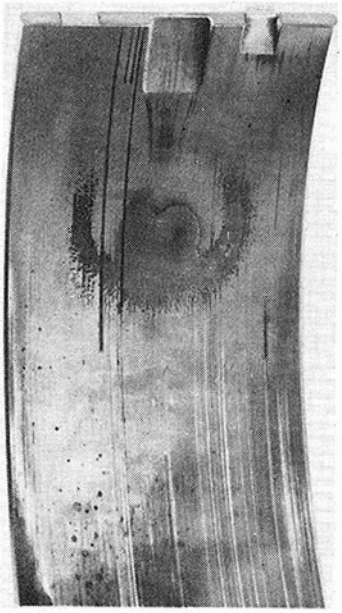

Fig. 12 Mild overlay damage in partially grooved main bearing

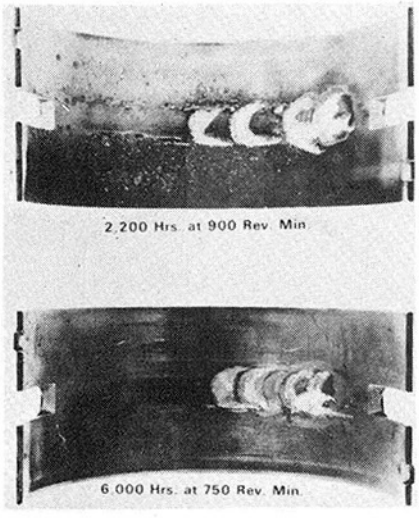

Fig. 13 Severe damage in partially grooved main bearing

and is approximately 120 deg in extent. Such bearings provide an acceptable oil film thickness within the narrow confines dictated by the overall design, but, at today's high ratings, are those most likely to suffer from cavitation erosion damage. This occurs downstream of, but usually close to, the groove run-out and typically takes the form shown in Fig. 12.

In this instance, the damage was found after only 400 hr of operation, and was restricted to the soft overlay plated surface of the bearing, which was of the order of 0.03 mm thick. The stronger bearing lining underneath had not been attacked. This form of damage is characterized by a crescent form, sometimes with an extended zone of damage. The crescent form usually mirrors the outline of the blend radius of the journal drilling which transfers oil to the crankpin bearing. In the particular example shown, after the initial short term damage, further progression was slow. Bearings in this condition after several thousand hours operation may quite safely be refitted. However, in some instances the damage can be much more severe; that shown in Fig. 13 had propagated through the lining material which was of the order of 1 mm thick. Again, the damage exhibits the classic crescent form, but with sufficient severity to be repeated four times, albeit of gradually reducing extent. When this repeated form of damage was first noticed on engine main bearings, it was thought that each position of damage had occurred at a discrete operating speed. However, the engines from which the bearings of Fig. 13 were removed operated at constant speed; the top bearing in the picture was from a 900 rev/min engine, and the lower one from a 750 rev/min engine.

Various palliatives have been tried on different engine types to alleviate this type of damage. These have usually consisted of modifications to the ending of the partial groove. Abrupt groove endings have been tried, as have square end and round end profiles, and groove run-out positions have been moved in both directions around the bearing. In one engine case, a hole was deliberately drilled through the bearing at the point of damage. This merely moved the damage further round the bearing. Spoon-shaped depressions have also been tried in the bearing surface at the groove ending. However, the most effective palliative so far adopted has been a tangential blend from groove to bearing surface, with a square profile. When this was first applied to the bearings of Fig. 13 it was not entirely successful, but when additionally the through slot was terminated in the top half bearing, as shown diagrammatically in Fig. 14, the damage was totally eliminated. This same technique has been applied successfully in several cases, including the first example shown, Fig. 12.

The effectiveness of the above measures suggests that hydrodynamic conditions are not the controlling factor, since they will not be significantly affected by such local changes to groove geometry. This view is reinforced by evidence from certain other types of engines where the load patterns and corresponding journal orbits differ significantly. In a particular engine type produced in Vee 12, 16 and 18 cylinder configurations, all main bearings were similarly damaged, except those not incorporating oil feeds to large-end bearings, or those employed simply as outrigger bearings.

The overwhelming evidence therefore, is that the damage is a function of the rapid termination of oil supply from the main bearing groove to the journal drilling.

The physical appearance of the damage, and its sensitivity to the form of the groove ending, effectively the rate of oil supply shut-off, suggests that the controlling mechanism may be analogous to the well-known water-hammer phenomenon. Briefly, if a valve in a hydraulic circuit is rapidly closed, pressure waves will be reflected in the circuit at acoustic velocity, Va. If the value of Va can be determined from the relationship $Va = \rho K$ where K = bulk modulus for the fluid and ρ = density of the fluid, then the time taken for reflection of the pressure wave in a pipe of known length may be calculated.

Based upon values [5] of $K = 1.70 \times 10^3$ MN/m^2 and $\rho = 900$ kg/m^3 for mineral oil, the time taken for the pressure wave to be reflected at the two operating speeds of 750 rev/min and 900 rev/min was calculated, and from these values the circumferential distance between damage sites was derived.

Very close agreement between observed and predicted damage positions was obtained at both engine speeds when the active pipe length was taken as the length of the crankshaft drilling from main to large-end bearing, together with the length of the connecting rod drilling to the small end.

It must be stressed that the close correlation between theory and practice is regarded as somewhat fortuitous especially in view of the considerable effect that undissolved air or gas in the lubricant can have upon the value of K [5], and also the assumptions made regarding active pipe length. Nonetheless, the fact that the damage shows evidence of energy decay with successive impacts, and that the spacing of the impact sites is clearly dependent upon rotational speed of the crankshaft, strongly supports the view that pressure wave reflection is the controlling mechanism in this form of cavitation erosion.

It is probable that as the oil drilling in the shaft traverses the groove run-out, cavities are formed at the intersection of groove run-out edge and the oil hole blend radius, as depicted diagrammatically in Fig. 15. Progression of the oil hole across the run-out to complete closure results in the pattern of cavity formation shown in Fig. 16. This cavity

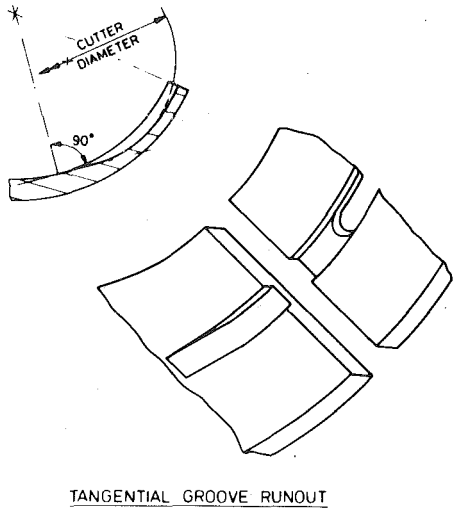

Fig. 14 Design detail of successfully applied modification to groove ending

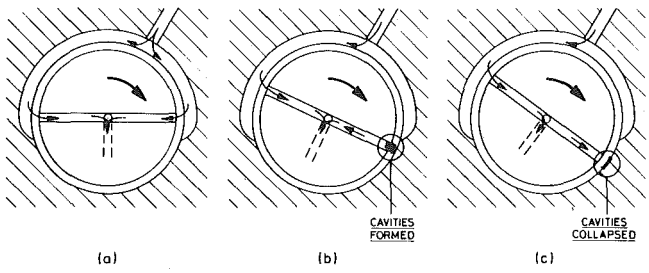

Fig. 15 Cavity formation associated with interaction between journal drilling and partial groove

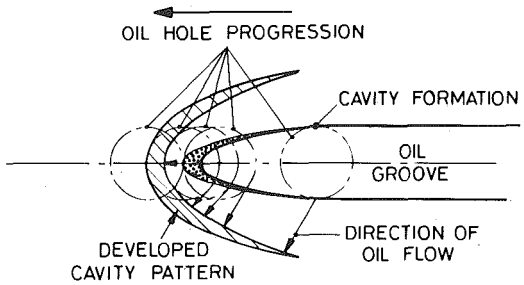

Fig. 16 Suggested mechanism of 'crescent' pattern formation

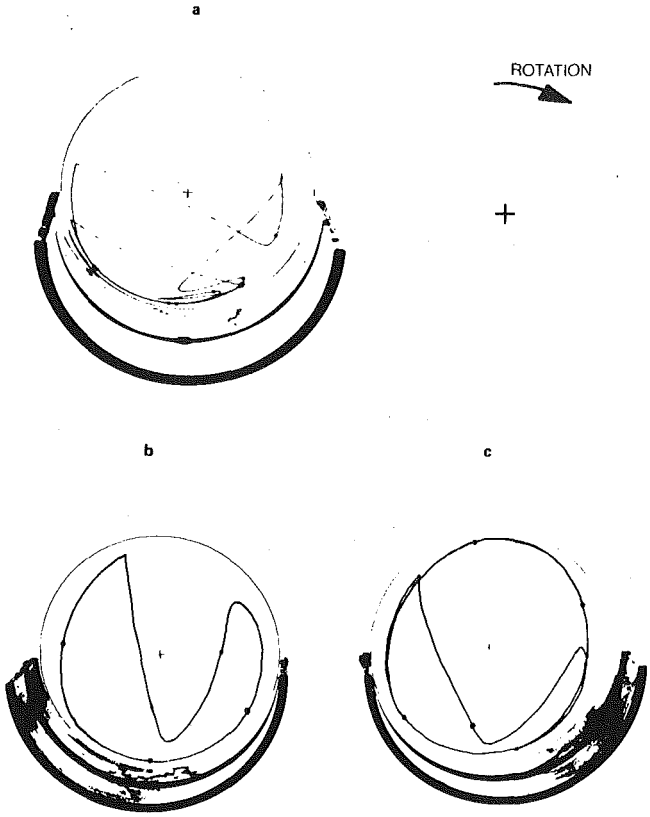

Fig. 17 Influence of journal orbit upon discharge damage in main bearings

pattern continues to flow around the bearing, under the influence of the more general oil flow, forming the broader crescent pattern also shown in Fig. 16. The travelling cavities are forced to collapse by the reflected pressure wave, producing the characteristic pattern of damage shown in Figs. 12 and 13.

The tangential run-out and general groove form of Fig. 14 has the effect of reducing the rate of deceleration of the oil flow into the shaft drilling by means of the more gradual cut-off. In addition, the extended overlap between the opening of one end of the through drilling and the closing of the other end means that the shaft drilling is more likely to remain filled. The combination of these two effects generally overcomes this form of damage.

Main Bearings: Fully Grooved. Fully grooved main bearings on medium speed diesel engines very rarely exhibit cavitation erosion problems. However, at the higher speeds of operation, a form of "discharge" damage has been known to occur. Fig. 17 shows three bearings which exhibit this type of damage. The first bearing is the center main from a Vee 8 engine after 2000 hr at 1800 rev/min, and the second and third bearings are the center main and end main respectively from an in-line six cylinder automotive diesel after 30000 mi at rotational speeds of up to 2400 rev/min. The center journal of the in-line six cylinder engine did not contain an oil drilling. Based on this fact, it is reasonable to presume that the damage bears some relation to the journal orbit. The predicted orbits for all three bearings are superimposed on Fig. 17. The position of damage relative to the orbit suggests that a correlation exists.

There is a striking similarity between the damage in large-end bearings, as typified by Figs. 7–10, and that in the fully grooved main bearings of Fig. 17. Thus it is logical to consider the possibility that this particular type of main bearing damage also results from high oil flow. The damage is again initiated at a surface discontinuity, in this case the groove edge. Its position corresponds to a marked change in the journal center orbit (Point C in Fig. 24(*a*)). The direction in which the damage, once initiated, progresses across the bearing surface appears to be influenced by the direction in which the journal subsequently moves (Fig. 17). Possibly the formation of this damage can be better appreciated if, rather than considering the two dimensional journal orbit, the movement of the whole of the journal surface relative to the bearing surface can be visualized with time. It can then be seen that a rapidly forming divergent clearance space is created between the two surfaces, thus creating a rapid local flow over the groove edges and across the bearing lands, back against the direction of rotation.

A solution, if feasible within other engine design limitations, would be to modify the bearing load diagram, and hence journal orbit, by a change in rotating and/or reciprocating masses, particularly counter-weights.

Further verification of this proposed damage mechanism was provided by results obtained from experiments with an ultrasonic vibratory rig (described in detail in Section 4). Bearings incorporating different groove cross-section forms were substituted for the standard ungrooved specimens. In all cases, the inclusion of grooves had no effect upon the severity or pattern of damage compared with the standard ungrooved specimens (Fig. 18). In the rig, damage is generated purely by rapid approach and separation of two surfaces in a viscous coupling medium in the absence of a circulating flow of oil. The fact that groove edge damage does not occur in such a system suggests that in the engine case flow of oil across the groove is a significant factor.

A characteristic form of suction cavitation erosion damage commonly occurs in the relatively lightly loaded top halves of main bearings in both high and medium speed diesel engines. The bearing in this region almost invariably contains a central groove, and the damage occurs in the center of each land as shown by the example in Fig. 19, where the line of damage is virtually parallel to the groove edge. It may occur on isolated bearings in an engine set, or, in some instances, it has been known to be present on every top half bearing regardless of whether the journal contains an oil drilling or not. It has long been considered that this type of damage occurs due to rapid movement of the journal across its clearance space, and as such is influenced by clearance. Where this damage consistently occurs, it has been alleviated by a reduction in clearance. Reduction of housing flexibility has also been found effective in some instances, due to its influence upon the dynamic clearance.

Further correlation between this type of suction cavitation erosion and clearance is shown in Fig. 20. In this instance, the wall thickness towards the joints was less than in the crown, resulting in a larger clearance in the horizontal plane.

During a series of development tests on a medium speed two-stroke engine, standard wall thickness bearings were fitted to a slightly undersize crankpin, resulting in a clearance approximately 50 percent greater than the design maximum. This arrangement resulted in suction cavitation erosion of the cap half bearing (Fig. 21) within a 50 hr period, whereas, at standard clearance, after operation for several thousand hours, no damage occurred.

Hydrodynamic Considerations

A full mathematical analysis of dynamically loaded journal bearings would be highly complicated, involving the consideration of distortion and flexibility locally within the bearing and grossly within the engine, and also the history and viscosity variation of the oil within the clearance space as temperature and pressure vary. For practical design purposes certain simplifications have to be made and it is common to assume rigid, perfectly cylindrical shaft and bearing surfaces, isoviscous Newtonian lubricants, and a full, perfectly replenished, oil film. A direct approach to the governing film equations can still require an inordinate amount of computer time for the solution of a full set of engine bearings, so the inverse methods of solution [6, 7] offer distinct advantages. In particular the Mobility method has proved to be invaluable in visualizing and analyzing the dynamic behavior of a journal within a bearing.

The Mobility method uses the fact that at any instant in time the journal center position relative to the line of action of the load precisely defines the hydrodynamic conditions.

Referring to Fig. 22, the velocity of the journal center can be determined by considering two components. If the journal is not rotat-

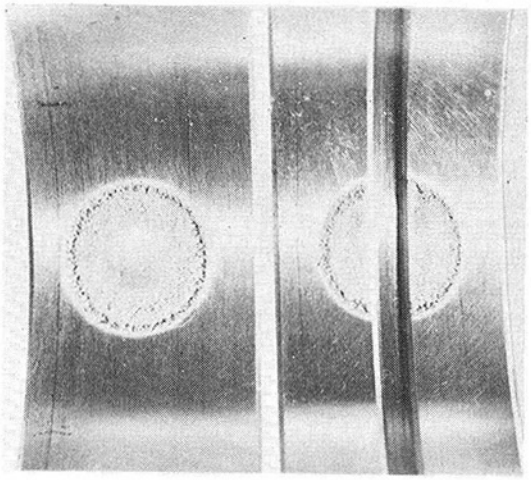

Fig. 18 Comparison between grooved and ungrooved rig specimens

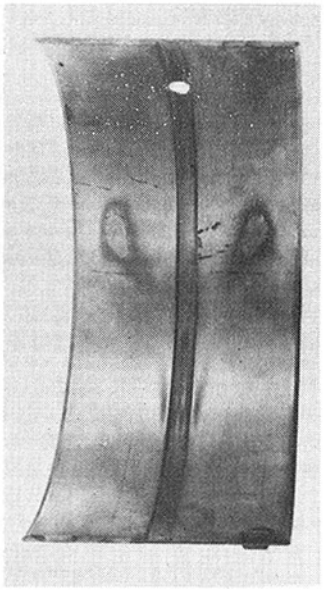

Fig. 21 Suction damage in large-end bearing associated with large clearance

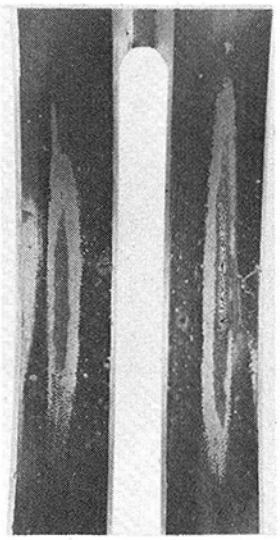

Fig. 19 Suction damage in upper half main bearing of high speed diesel engine

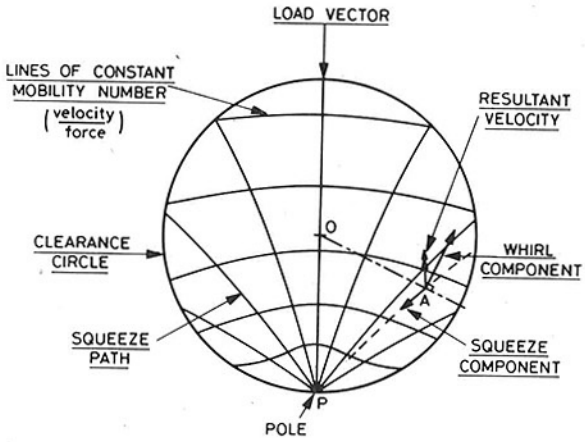

Fig. 22 Mobility map

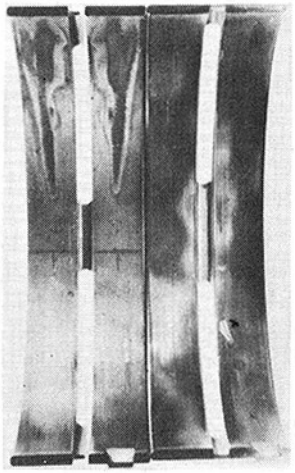

Fig. 20 Suction damage in eccentric wall main bearing of medium speed diesel engine

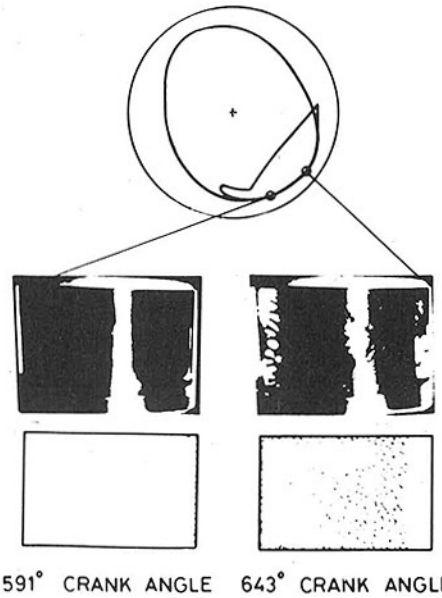

Fig. 23 Comparison between predicted film extent and that observed in dynamic similarity rig

ing, and is acted upon by a force vector in the direction shown, it will move along the squeeze-path indicated, by an amount depending on the local value of the Mobility number, towards the pole position (P). Additionally, the relative angular velocities of the journal, bearing, and load give rise to a whirl component normal to the line of bearing and journal centers ($0A$). The vector resultant of the squeeze and whirl components determines the instantaneous direction and magnitude of the journal movement. By taking suitable discrete time steps the complete journal locus may be marched out. As described, the resulting orbit is relative to the load line, but a simple transformation gives the orbit relative to the bearing itself.

The value of the mobility number throughout the map may be calculated using short or finite bearing theory, and when these data have been curve-fitted the resulting computer solution is very rapid. In this study, short bearing theory has been used since it has already been shown [8] that the approximation gives good qualitative results. An advantage of this approximation is that the theoretical oil film pressures may be determined easily; an important point in work on cavitation.

In an attempt to gain extra confidence in the predicted film pressures some comparisons have been carried out against observed oil film extents in a transparent bearing running in a dynamic similarity rig. Figure 23 shows observed and predicted film boundaries at two crank angles in a typical large-end cycle. Because of the poor definition of one of the theoretical boundaries too much should not be read into these comparisons.

Since the mechanism of cavitation damage depends on cavity formation and collapse, pressure variations below and above the vapor pressure of the lubricant are clearly important. The basic theory used allows positive or negative pressures to be developed within the oil film as dictated by the hydrodynamics. For the purposes of balancing loads and integrated pressures, i.e. in predicting the journal center orbit, it has been assumed, as is common practice, that negative pressures cannot be sustained by the lubricant. However, it is considered that predicted negative pressures will indicate the position and intensity of any cavity formation.

This method was used to examine the hydrodynamic conditions of the bearing showing the suction damage in Fig. 19. The applied load line and resulting orbit are shown in Fig. 24(a), and it can be seen that a rapid journal movement takes place between points B and C. While experience suggests that rapid fluctuations in pressure are associated with such movements, the initial plot of rupture zones within the bearing (Fig. 24 (b)) failed to show anything significant at the top of the bearing (0 or 360 deg). It was only when the time step of the solution was refined (from 10 deg to 1 deg crank angle) that intense 'negative' pressures were predicted (Fig. 24(c)). The regions of predominant cavity formation will be the centers of the bearing lands, and it is here that cavity collapse will take place as the feed pressure is rapidly restored from the adjacent groove. The palliatives mentioned previously—reduced clearance, stiffer bearing caps—help to reduce the rapid journal movement and hence the cavity formation.

The same orbit (Fig. 24(a)) is also known to cause discharge erosion damage (Fig. 17) in the lower half of the bearing. The damage appears to be associated with point C on the orbit, where a reversal takes place, but due to the higher journal center velocities at other points in the orbit it is unlikely to be due purely to flow effects. Reference to Fig. 24(b) and Fig. 25 show that cavity formation and collapse in the region of the damage are occurring. The map in Fig. 25 shows an unwrapped bearing surface (bearing angle) against crank angle. On this are plotted the path of the load line, the predicted journal center movement, and oil film extent. Short bearing theory always predicts a 180 deg region of positive pressure, and consequently a 180 deg rupture extent. On the map the positive pressure zone is the one containing the load line. Cavities are formed at point A in the orbit (at approximately 230 deg bearing angle and 180 deg crank angle, see Figs. 24(b) and 25) as the film thickness increases, and proceed around the bearing in the direction of rotation at approximately half journal speed. As the combustion loads come onto the bearing, a region of positive pressure effectively moves back against shaft rotation, sweeping the cavities

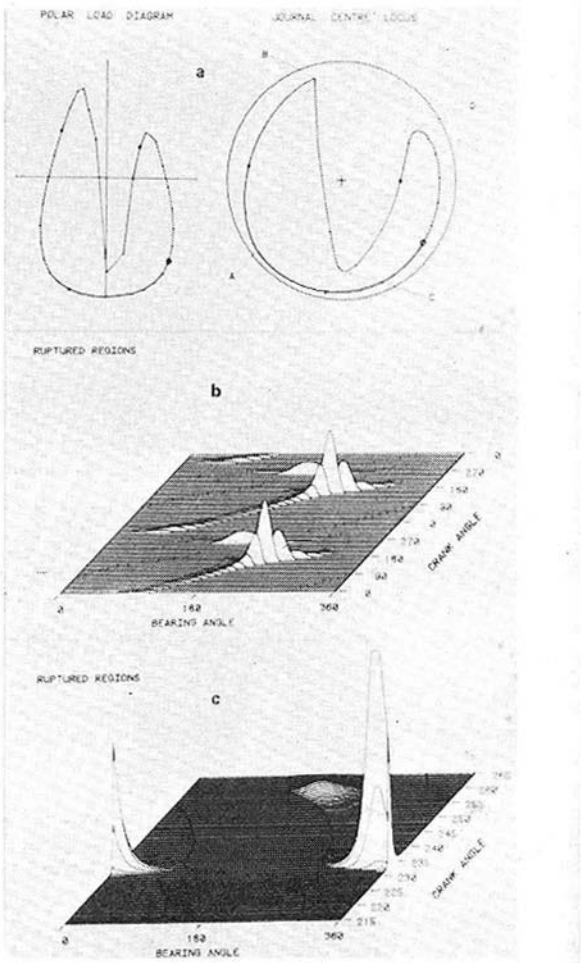

Fig. 24 Predicted hydrodynamic conditions associated with occurrence of cavity damage

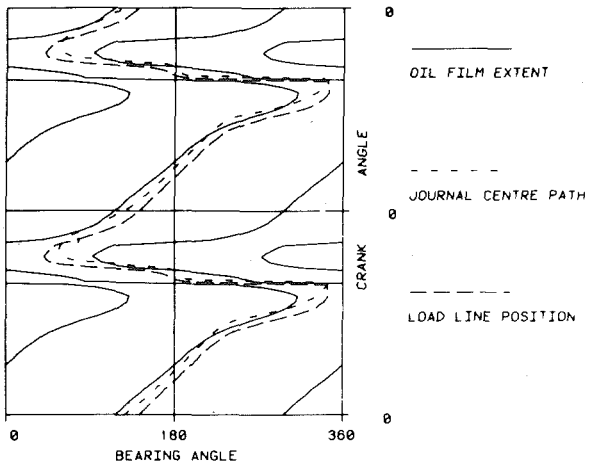

Fig. 25 Predicted oil film conditions throughout the operating cycle

back and forcing them axially out of the bearing lands (point B to point C). Those that are forced into the central groove will collapse at its edge due to the presence of oil at supply pressure. Once started, this damage will progress at an increasing rate because of secondary cavity formation and collapse associated with turbulent flow over the damage site. The velocity of this flow will be directly influenced by

the subsequent movement of the journal away from the bearing surface (point C to point D), and it is thought that the form of the characteristic V-shaped damage is a function of the form of the journal center locus with respect to space. Figure 17 shows journal orbits associated with cavitation damage in lower half main bearings where this point is illustrated.

Determination of Relative Erosion Resistance

It has been known for many years [9], that erosive attack of most materials could be induced by placing a solid specimen, submerged in a fluid, in close proximity to a rapidly vibrating surface. Under these conditions intense localized cavitation of the fluid occurs and the collapse of the resulting vaporous cavities leads to removal of material from the surfaces of even such hard substances as Stellite. Two basic types of vibratory apparatus have been employed to produce cavitation erosion under controlled and accelerated conditions. These employ magneto-strictive or piezo-electric effects to produce the necessary vibration of a tube or specially profiled rod.

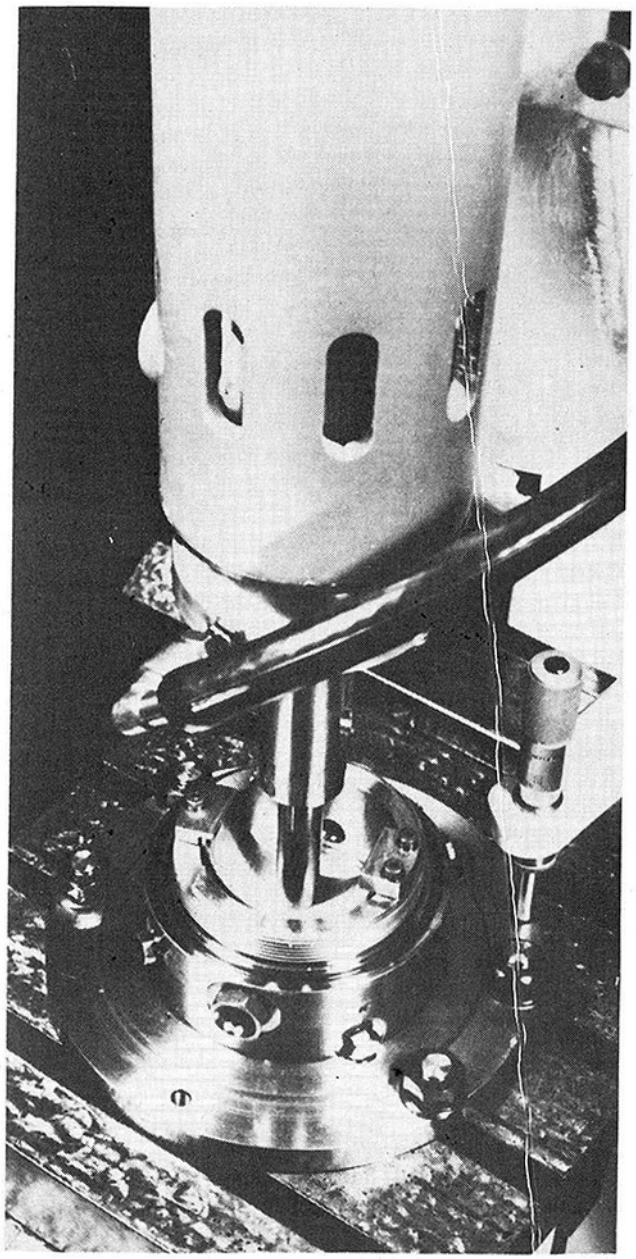

Fig. 26 Ultrasonic vibratory test rig

The authors' work has been conducted with an apparatus depending on piezo-electric effects and operating at 20 kHz (Fig. 26).

A deliberate decision was made to use a typical diesel engine lubricant as the coupling fluid, and to simulate shaft/bearing geometry by providing a cylindrical end to the aluminum-bronze amplifying horn. From the photograph of the apparatus it will be apparent that the form of the test specimen is a thin walled half bearing. This form of specimen was chosen because it was readily obtainable in a wide range of lining materials, with a surface topography and metallurgical structure representative of those normally encountered in engine bearings.

For each test the specimen was carefully cleaned and weighed on a balance accurate to 0.1 mg. It was then mounted in the test rig and the static separation set at 0.75 mm by means of a micrometer attachment. The test cell was filled with Shell Rotella 30 oil to a level to completely immerse the specimen, and the vibrator power adjusted to 150 W at an amplitude of 0.016 mm. During the course of all tests the temperature of the oil increased from room temperature to 66/70° C.

At the end of each test the specimen was thoroughly cleaned in a solvent to remove the oil, and re-weighed. The volume loss was derived from the weight loss and the specific gravity of the particular lining material.

Initial tests were carried out with specimens in overlay plated form for a period of 30 min with an amplitude of 0.016 mm. However, it was soon apparent that with such specimens it was very difficult to discriminate between overlay and interlayer weight loss, and that a clearer assessment of relative erosion rates of different overlay/interlayer combinations would be better achieved in the first instance by examining each layer in isolation.

Initially the test procedure for unplated specimens was as described above with a standard duration of 30 min, but it was subsequently decided that a shorter test would be more realistic since the likelihood of the damage extending down to the steel backing would be minimized. A test duration of 10 minutes was eventually adopted, although certain tests were extended to 50 min duration to investigate the time dependency of the erosion damage.

Experimental Results. Results obtained from tests with a representative range of bearing materials are presented in terms of relative volume loss in Fig. 27, together with the appearance of actual specimens after test in the rig. It is immediately apparent that very great differences exist in the erosion resistance of different bearing materials, and the difference between tin-based and lead-based

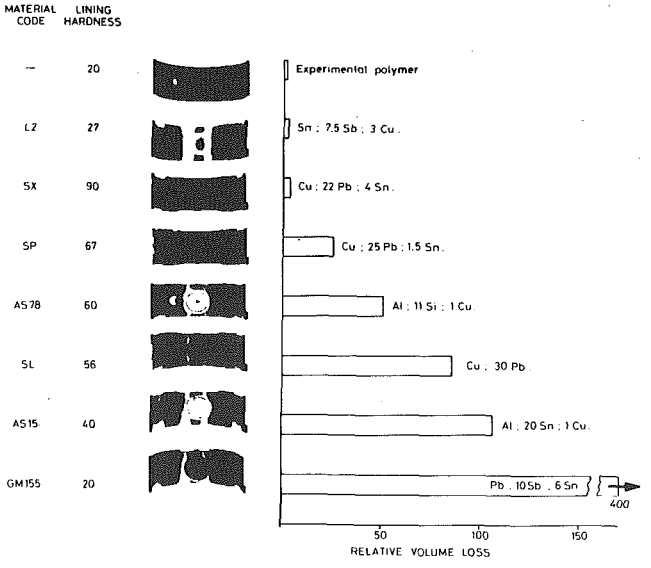

Fig. 27 Relative erosion resistance of plain bearing materials

Table 1

Material	Ultimate resilence MN/m^2	Relative volume loss
Experimental Polymer	<1	<1
Sn; 7.5 Sb; 3 Cu.	58	1
Cu; 22 Pb; 4 Sn.	88	2
Cu; 25 Pb; 1.5 Sn.	68	3
Al; 11 Si; 1 Cu.	224	50
Cu; 30 Pb.	57	85
Al; 20 Sn; 1 Cu.	103	103
Pb; 10 Sb; 6 Sn.	30	400

whitemetals, first reported by Schaeffer, et al. [10], is very striking especially in view of the fact that their bulk mechanical properties, including hardness, are similar. It has long been assumed that a clearly defined relationship between erosion resistance and hardness exists, but the results presented suggest that this is not the case, and that one must look to other mechanical properties, either singly or in combination, for a correlation. An examination of the more obvious physical characteristics such as ultimate tensile strength (UTS), Young's modulus (E), notched impact resistance, fatigue strength, elongation, and hardness does not provide a suitable correlation. Of the more complex relationships postulated, that of ultimate resilience proposed by Hobbs [11] appears the most promising (Hobbs defined ultimate resilience as $UTS^2/2E$). Ultimate resilience has the attraction of taking account of the strain energy to failure, which recognizes the beneficial effect of the resilience of a material or, more graphically, its ability to sustain repeated strain without cracking; Hobbs reports fair correlation taking the results of tests with a number of steels and aluminum bronzes. Experiments carried out by the authors with certain high resilience polymeric materials have shown these to have extremely high resistance to erosion—higher, in fact, than any of the metallic materials presented in Fig. 27.

Although the resilience of the material is recognized as an important factor in its resistance to erosion, the experimental results unfortunately show no general trend towards a direct relationship between ultimate resilience (UR) and erosion resistance of bearing materials (see Table 1). This is almost certainly because such materials invariably comprise more than one phase, and the erosion resistance will, therefore, be closely linked to the relative volumetric presence and continuity of each phase, and, of course, the mechanical properties of the phases in isolation and in concert. One can imagine, for example, that a soft continuous phase within a relatively hard matrix could be eroded rapidly, leaving areas of the harder phase unsupported and, therefore, prone to collapse under oil film conditions (Fig. 28). It should be borne in mind that individual impact sites may be small enough to fall within an individual phase at the bearing surface.

As regards the mechanism of material loss by cavitation attack from a solid surface it seems probable that

1 undulations of the surface result from impingement of micro-jets of fluid.

2 with continued impingement, the undulations become deeper and more numerous such that craters with raised lips are formed and will, in some cases, overlap.

3 material will be torn form the crater lips, with successive fluid impacts, by a process of ductile rupture.

In order to explore in more detail possible failure mechanisms, eroded samples were examined using conventional metallographic techniques and later a Scanning Electron Microscope (SEM). Considerable surface undulations were observed both with rig specimens and bearings damaged in service (Fig. 29), but the transition from the initial incubation stage to the point at which material loss occurs is generally so rapid as to make precise determination of the mechanism very difficult.

It was decided to collect erosion debris from the test rig and examine it using the SEM. The results of this exercise, although not entirely conclusive, have provided valuable indications as to the way in which loss of material occurs. With several of the materials examined the debris exhibited deformed, but nonetheless recognizable, surface features typical of ductile rupture (Fig. 30). In addition, a number of quasi-spherical particles, which have been described as characteristic of erosion debris [12] were observed. Of particular interest is the surface appearance of such particles, which strongly suggests that they are formed from initially irregularly shaped debris

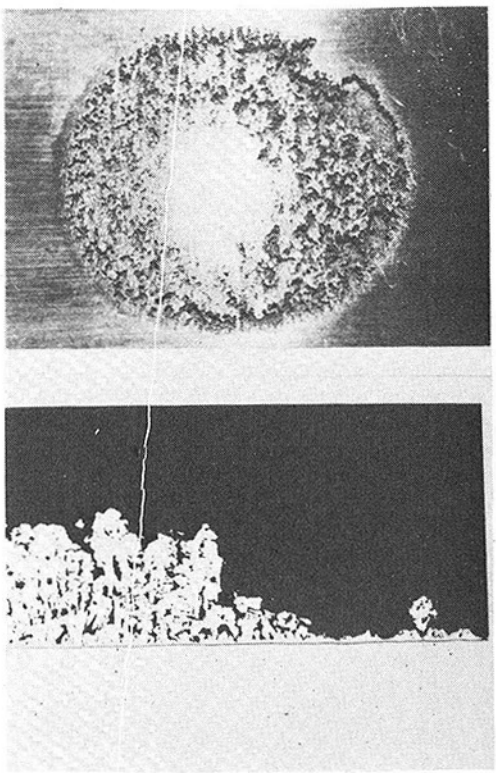

Fig. 28 Preferential erosion of lead phase in cast copper-lead specimen

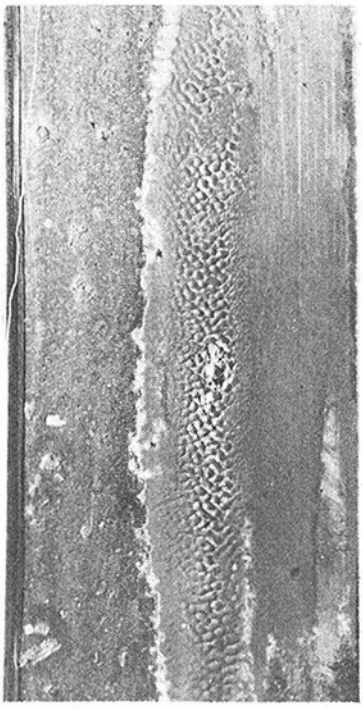

Fig. 29 Surface undulations at early stage of suction erosion damage

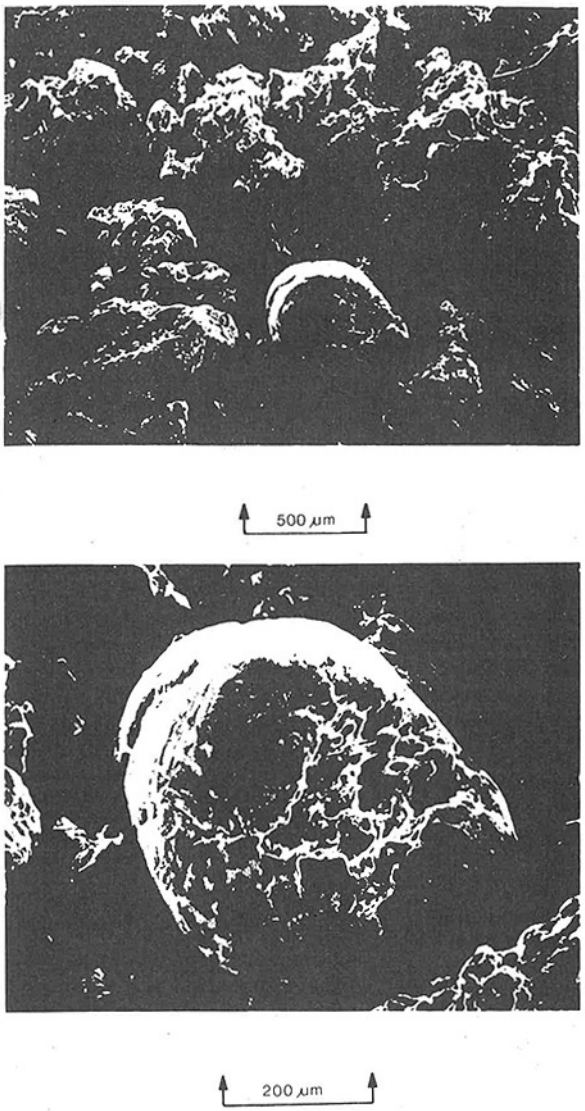

Fig. 30 Scanning electron microscope photographs of debris from erosion rig

by a process of mechanical swaging and abrasion. It would follow that, with time, the number of such particles in a sample would increase, as would their tendency to become more spheroidal.

At one time it was thought that the presence of such particles of bearing materials in lubricant samples taken from engines in service would be characteristic of the occurrence of erosion damage, but this seems unlikely because

1 erosion debris particles are unlikely to remain sufficiently long in the region of erosive attack for the necessary mechanical deformation to occur.

2 debris from bearing linings generated by processes other than erosion would seem to be equally likely to form spheroids.

The fact that spherical particles are seen in debris from erosion rigs is no doubt because the nature of the accelerated test procedure employed provides intense agitation within a closed cell from which the debris cannot escape, which would not be the case in the lubrication system of an engine.

Conclusions

Cavitation erosion damage in diesel engine bearings appears to fall broadly into three categories, associated with

- interactions between bearing surface features and crankshaft drillings
- inertia effects of the oil within connecting rod drillings
- journal movements within the bearing clearance space leading to adverse transient oil film conditions

Relatively simple modifications to the detail design of the bearing and its associated components can usually obviate problems from the first two catagories but often not from the third. However, these more intractable problems do seem to show some correlation with predicted oil film conditions. A more detailed theory than that considered here will probably be needed before damage can be reliably predicted at the design stage.

When considering the erosion resistance of a wide range of bearing materials no relationship involving their simple mechanical properties emerges. However the resilience possessed by certain polymeric materials appears to be very beneficial.

Acknowledgments

The authors wish to thank the Directors of The Glacier Metal Co. Ltd. for permission to publish this paper, to recognize the assistance provided by colleagues within the Associated Engineering Group of Companies and the cooperation of numerous engine manufacturers.

References

1 Lord Rayleigh "On the Pressure Developed in a Liquid During the Collapse of a Spherical Cavity," *Phil Mag*, 34, 1917, pp. 94–98.

2 Kornfeld, M., and Survarov, L., "On the Destructive Action of Cavitation" *Journal of Applied Physics*, 15, 1944, pp. 495–506.

3 Knapp, R. T., Daily, J. W. and Hammitt, F. G., *Cavitation* McGraw-Hill, New York, 1970.

4 Benjamin, T. B., and Ellis, A. T., "The Collapse of Cavitation Bubbles and the Pressures Thereby Induced against Solid Boundaries," *Proceedings of the Royal Society Philosophical Transactions*, 1966.

5 Pearsall, I. S., "The Velocity of Water-Hammer Waves," Symposium on Surges in Pipelines, *Proceedings of the Institution of Mechanical Engineers*, 1965–1966.

6 Booker, J. F., "Dynamically Loaded Journal Bearings: Mobility Method of Solution," ASME *Journal of Basic Engineering*, Vol. 87, No. 3, 1965, pp. 537–546.

7 Blok, H., "Full Journal Bearings Under Dynamic Duty: Impulse Method of Solution and Flapping Action," ASME *Journal of Lubricating Technology*, Vol. 97, No. 2, pp. 168–179.

8 Campbell, J., Love, P. P., Martin, F. A., and Rafique, S. O., "Bearings for Reciprocating Machinery: A Review of the Present State of Theoretical, Experimental and Service Knowledge," *Proceedings of the Institution of Mechanical Engineers Conference on Lubrication and Wear*, London, 1967.

9 Gaines, N., "A Magnetostriction Oscillator Producing Intense Audible Sound and Some Effects Obtained," *Physics*, 1932, 209

10 Schaeffer, R. A., Cerness, J. F. and Thomas, H. A., "The Resistance of Some Cast and Plated Sleeve-Bearing Materials to Cavitation Erosion," *Transaction Institute Metallurgical Finishing*, Vol. 31, 1954, pp. 454–463.

11 Hobbs, J. M., "Experience with a 20 kc Cavitation Erosion Test," *ASTM Special Technical Publication 408*, 1967, pp. 159–185.

12 Kenkeremath, D. and Thiruvengadam, A., "Characterization and Analysis of Particles Produced by Cavitation Erosion," US Office of Naval Research AD-AO11-374, 1975.

L.-A. Nordstroem
Swiss Federal Institute for Reactor Research
Würenlingen, Switzerland

H. Fischli
R. Naegelin
Sulzer Brothers Ltd.,
Winterthur, Switzerland
CH-8400

Recuperators for the HHT-Demonstration Plant

Recuperators of closed cycle gas turbine plants are characterized by large heat transfer areas accommodated in rather small volumes. Clean gas conditions, moderate operating temperatures and modest requirements with respect to tightness have resulted in generally good operational records. In the case of recuperators for direct cycle high temperature reactors, more stringent boundary conditions are being imposed than for conventional plants. In this paper studies and experiments performed for the recuperator of the HHT demonstration plant (670 MWe) are described. Five different design concepts are discussed and mutually compared. All designs use straight tubes. The main concept is a proposal with longitudinal flow on the shell side, but also the proven cross-counterflow concept has its merits. Special subjects are sensitivity to temperature streaks and optimum subdivision into modules.

Introduction

HHT is a German-Swiss project for closed-cycle gas turbine plants heated directly by high-temperature reactors. A project for a reference plant of 1230 MWe capacity was completed in 1977; an overall description is given in [1], while [2] deals with the corresponding heat exchangers. A demonstration plant for 670 MWe is being planned [3]. This paper deals with the recuperator for such a plant. Different design concepts will be discussed in the light of the boundary conditions and the other selection criteria.

Two recuperators are foreseen in parallel loops. They are to be arranged in vertical pods of a prestressed concrete pressure vessel. The connections of hot and cold low-pressure gas are on opposite sides at the bottom of the pod, while the high-pressure gas enters and leaves through concentric ducts in the upper part of the pod. The vertical distance between the low- and high-pressure connections is determined by the overall arrangement of the plant and is available for the recuperator. The diameter of the pod is to be as small as practicable. A specific feature of the HHT-project is the warm liner concept. It means that the pod liner should be swept by gas not warmer than about 150 °C; in this way the liner will not require any insulation and is thus accessible for inservice inspection.

It is expected that the authorities and customers will impose stringent requirements with respect to quality assurance and inservice inspectability despite the fact that the apparatus is not an outer boundary of the reactor coolant circuit. The ultimate stringency of these requirements will depend on the consequences of eventual ruptures of recuperator parts on the rest of the plant and also on the role the recuperator will have to play for residual heat removal. Repairability and exchangeability of the apparatus will have to be provided.

As the size of the recuperator will be quite large, the possibilities of transporting it to the site must be considered. Only road or rail transport will be available. The erection time within the reactor building is to be of short duration.

A preliminary set of thermal design data is summarized in Table 1. Only the sum of the pressure drop ratios on the primary and on the secondary side has been specified; the distribution on both sides does not influence the plant efficiency and may be chosen in order to realize optimum heat exchanger configuration.

Table 1 Thermal design data (per recuperator)

Fluid		Helium
Recuperator primary side:		
Mass flow		411 kg/s
Inlet temperature	T_1	488 °C
Outlet temperature	T_2	148 °C
Inlet pressure		24.6 bar
Recuperator secondary side:		
Mass flow		395 kg/s
Inlet temperature	T_3	107 °C
Outlet temperature	T_4	461 °C
Inlet pressure		72.2 bar
Recuperator effectiveness	η_r	92.9 percent
Sum of pressure drop ratios	ϵ	4.1 percent
Turbine inlet temperature	T_5	850 °C

No strong transients have been specified for normal operating conditions. Two peculiarities of a closed cycle gas turbine circuit, however, may have an impact on the design of the recuperator. Firstly, the bypass control—by which cold gas is added on the low-pressure side between turbine and recuperator—could result in local hot and cold streaks at the heat exchanger inlet. Secondly, rapid pressure equalization resulting from the rupture of a barrier between high and low pressure anywhere in the circuit may cause high transient stresses in the apparatus.

The recuperator is an important part of a gas turbine plant both from its size as well as its influence on the overall efficiency. This may be illustrated by introducing the numbers of Table 1 in the equations given in the appendix. The overall plant efficiency is about 40 percent. An increase of 1 percent in the effectiveness of the recuperator would improve this value by 0.4 percent, provided the gas pressure drop stays unchanged. Such an improvement would require an increase of more than 20 percent in the heat exchange area. Although it would be possible to achieve the higher recuperator effectiveness by the same heat transfer area and greater pressure drop, it would result in a decrease of the overall efficiency.

Review of Design Concepts

General. In this chapter five different recuperator design concepts

Contributed by the Gas Turbine Division of THE AMERICAN SOCIETY OF MECHANICAL ENGINEERS and presented at The Gas Turbine Conference and Products Show, New Orleans, La., March 10–13, 1980. Manuscript received at ASME Headquarters November 26, 1979. Paper No. 80-GT-3.

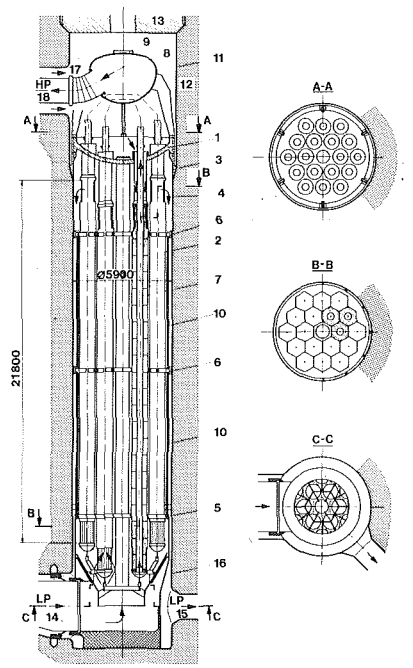

Fig. 1 Recuperator with 18 hexagonal modules, longitudinal counterflow: (1) supporting cover, (2) hexagonal modules staggered with each other and nested, (3) high-pressure connections to the modules, (4) high-pressure outlet pipes, (5) low-pressure seal, (6) lateral bracing for modules, (7) central tube, (8) high-pressure gas collector, (9) access door, (10) tubular lateral bracing, (11) liner (12) prestressed concrete reactor vessel (PCRV), (13) cover of recuperator pod, (14) low-pressure gas inlet, (15) low-pressure gas outlet, (16) low-pressure gas box, (17) high-pressure gas inlet, (18) high-pressure gas outlet

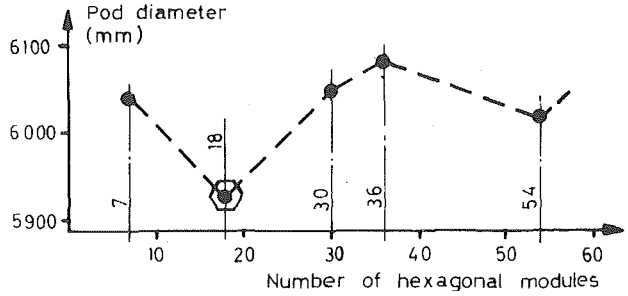

Fig. 2 Pod diameter as a function of the number of hexagonal modules

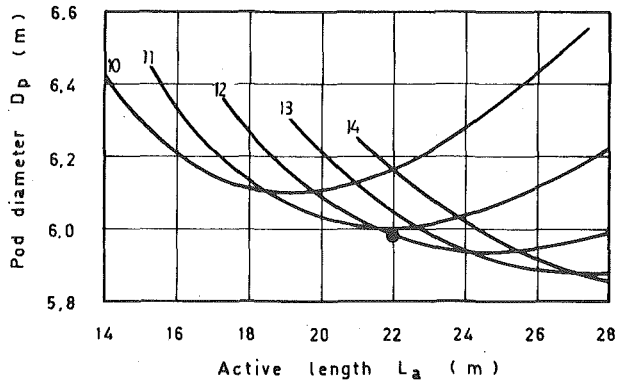

Fig. 3 Pod diameter of the longitudinal counterflow HX as a function of its active length (Parameter: tube outer diameter (mm)). The curves show pod diameter dimensions for an array with seven circular modules. The values for an array with 18 hexagonal modules are about 0.1 m smaller than shown in this figure

are described. Two types are built as longitudinal counterflow heat exchangers (HX's). This arrangement of the gas flow leads to small pod diameters. The heat transfer area is subdivided into hexagonal or circular modules. The thermodynamical layout is the same for both cases (see Fig. 3). Two further design concepts are realized by means of a cross-counterflow arrangement. Such designs are well known from previous closed cycle gas turbine plants [5, 6]. An array of only one module and another with seven modules are described; here, the thermodynamical layout is not the same for the two variants because of a different optimum number of baffles.

The fifth design concept is a longitudinal counterflow arrangement, but in contrast to the other designs the HP-gas flows outside the HX-tubes.

Longitudinal Counterflow Heat Exchanger with Hexagonal Modules and HP-Helium inside Tubes. The correlation between pod diameter and active length of the HX as deducted from thermodynamical layout and simple design rules is shown in Fig. 3. The maximum active length which can be arranged in the given pod is 22 m. With this boundary condition, there is a minimum pod diameter for a tube of 12 mm OD.

A HX with hexagonal modules is shown in Fig. 1. From the turbine, the hot helium flows into the pod at bottom left and is led to the shell side of the bundle. It leaves the tube bundle at the top with a temperature of 148 °C, keeping the steel liner of the pod at this temperature as it flows down to the outlet at the bottom right of the pod. Inflow and outflow of the high-pressure helium are coaxial at top left; heating-up takes place during the downward flow through the tubes.

The exchanger is subdivided into 18 hexagonal modules. One feature of these is the return flow of the HP helium in a central tube. Another characteristic of the proposed design is the supporting cover, which not only carries the weight of the modules but is also loaded by the pressure difference between the HP and LP helium. The modules are positioned horizontally to each other and to the liner by lateral bracings; at the bottom end of the shell they are sealed against each other and also against the hot gas box to prevent LP bypass. This box is insulated at the inside and fixed to the liner by claws and guides or socketed stanchions. The HP gas collector located above the supporting cover has a sliding connection with the hot gas return lines.

The pod diameter has been calculated for different numbers of modules as shown in Fig. 2. The total of 18 hexagonal modules constitutes a minimum in pod diameter. Numbers greater than 54 were not considered any further because of the higher weight attributed recently to inservice inspection.

In the case of the reference plant (1230 MWe) investigated before the demo plant, the minimum pod diameter was found to result from 54 hexagonal modules. The smaller optimum number for the demo plant is due to two reasons. Firstly, the smaller heat exchanger results in a tendency toward less modules, because these should not be too small for inspection reasons. Secondly, the need for space at the inner and outer peripheries of the bundle to prevent bypass flow leads to a reduction of the length of these peripheries, realized by lowering the number of modules.

Heat exchangers composed of hexagonal modules can be designed in many ways. Staggering of the modules as shown in Fig. 1 is no longer necessary, if axial inflow to the modules is made possible by compact module headers, whereby the tubes have to be bent near their ends [7]. Omitting the shrouds around each module avoids a delicate problem of bypass flow. Corresponding designs may have no wall at all between modules or show one wall in the form of a honey-comb structure in order to support the modules. The additional compactness made possible by such variations of hexagonal modules has to be paid for by more accurate and more expensive fabrication.

Longitudinal Counterflow Heat Exchanger with Circular Modules and HP-Helium inside Tubes. The result of the thermodynamical layout is summarized in Fig. 3.

The design, as shown in Fig. 4, is basically similar to that with the hexagonal modules. Sealing against LP bypass flow is effected not directly between the individual modules, but by a sealing grid. Since the modules are not in contact with each other, this arrangement facilitates possible replacement of defective modules. The LP gas flow sweeps the modules all around, so that less staggering is necessary. Thanks to the large and straight HP connecting and central tubes,

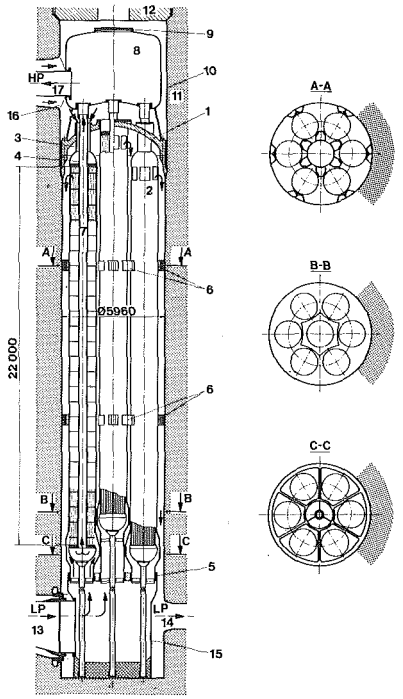

Fig. 4 Recuperator with seven circulator modules, longitudinal counterflow: (1) supporting cover, (2) circular modules, (3) high-pressure ducts to the modules, (4) high-pressure outlet ducts, (5) low-pressure seal, (6) lateral bracing for modules, (7) central tube, (8) high-pressure gas box, (9) access door, (10) liner, (11) prestressed concrete reactor vessel, (12) cover of HX pod with access door, (13) low-pressure gas inlet from turbine, (14) low-pressure gas outlet to precooler, (15) low-pressure gas box, (16) high-pressure gas inlet from compressor, (17) high-pressure gas outlet to reactor

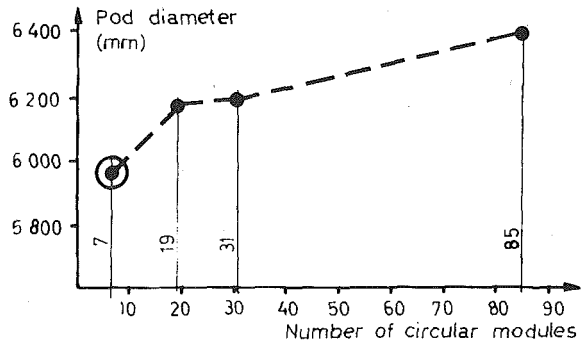

Fig. 5 Pod diameter as a function of the number of circular modules

the tube end plates afford good accessibility.

As for hexagonal modules, the pod diameter has been evaluated for different numbers of modules, see Fig. 5. Seven circular modules result obviously in a minimum pod diameter. The radial space required for gas inlet, shells, insulations and central tubes is lower than that for module numbers of more than seven.

Cross-Counterflow Heat Exchanger with One Module and HP-helium inside Tubes. The pod diameter and active length shown for the cross-counterflow HX with one module in Fig. 6 are based on the results of the thermodynamic calculation.

The fabrication of tubesheets and baffles becomes problematic if the pitches are too small. Consequently, solutions with NC = 6 cannot be selected. The layout-point was finally chosen with NC = 8 and IDB = 2.9 m.

The design concept is shown in Fig. 7. As in the case of the longitudinal counterflow HX, the return of hot HP-helium takes place in a central tube in the middle of the HX. The entering LP gas flows between the lower head cover and an outer spherical shell to the tube bundle.

It is then directed radially toward the inside space. Afterwards it flows upward in a wavy line through a disk and doughnut array of

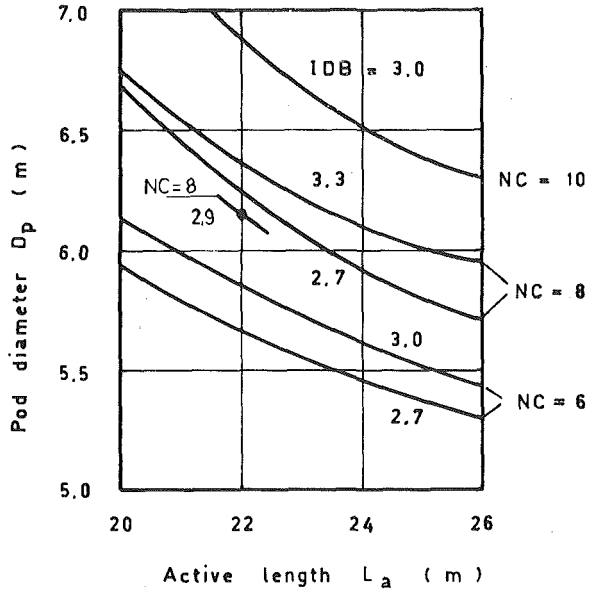

Fig. 6 Cross-counterflow recuperator with one module. Pod diameter as a function of active length. (Parameters: number of passages (NC) and internal diameter of bundle IDB (m).)

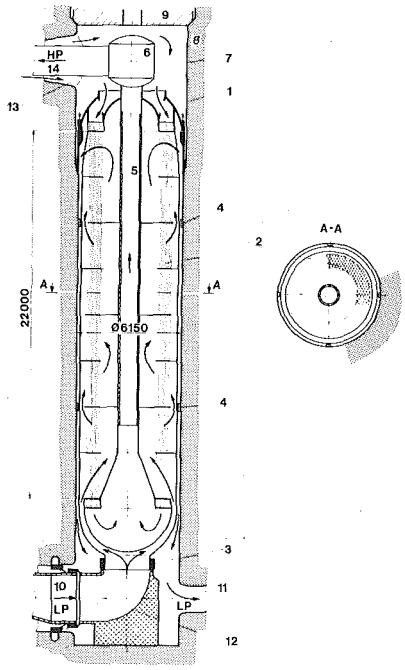

Fig. 7 Recuperator with one module, cross-counterflow: (1) supporting cover, (2) circular module, (3) low-pressure seal, (4) lateral bracing, (5) central tube, (6) high-pressure gas box, (7) liner, (8) prestressed concrete reactor vessel, (9) cover of HX pod with access door, (10) low-pressure gas inlet from turbine, (11) low-pressure gas outlet to precooler, (12) low-pressure gas box, (13) high-pressure gas inlet from compressor, (14) high-pressure gas outlet to reactor

baffles through the HX. After an even number of passages, it leaves the bundle at the top and is redirected and guided back along the liner toward the LP exit.

The large size of a single module gives rise to two problems. Firstly, the large wall thickness of the supporting cover, lower head cover and tubesheets may limit the admissible temperature transients. Secondly, the fabrication of the whole module has to be effected in a workshop on the plant site.

Cross-Counterflow Heat Exchanger with Several Modules and HP-Helium inside Tubes. The modules consist each of a tube bundle with annular cross section and a hexagonal shell, see Fig. 8.

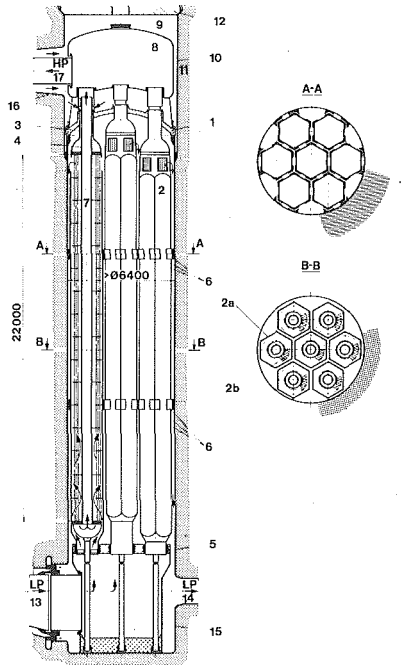

Fig. 8 Recuperator with seven modules, cross-counterflow: (1) supporting cover, (2) module, (2*a*) hexagonal shell of the module, (2*b*) annular bundle, (3) high-pressure ducts to the modules, (4) high-pressure outlet ducts, (5) low-pressure seal, (6) lateral bracing for modules, (7) central pipe, (8) high-pressure gas box, (9) access door, (10) liner, (11) prestressed concrete reactor vessel, (12) cover of HX-pod with access door, (13) low-pressure gas inlet from turbine, (14) low-pressure gas outlet to precooler, (15) low-pressure gas box, (16) high-pressure gas inlet from compressor, (17) high-pressure gas outlet to reactor

The overall arrangement of the apparatus is similar to the longitudinal counterflow HX with seven modules, especially the low pressure sliding seal.

An arrangement with more than seven modules leads to larger pod diameters, as in the case of longitudinal counterflow HX's with round modules.

A workshop on the site is no longer necessary and replacement of individual modules is possible. The thermal inertia of the heavy structures is comparable with those of the longitudinal counterflow HX. One significant disadvantage of this HX is its space requirement.

Longitudinal Counterflow HX with Circular Modules and HP-Helium outside Tubes. In order to avoid the hypothetical problem of a rupture of the supporting cover, it has been proposed to make the large HP/LP-barrier an integral part of the PCRV.

Results of a thermal design study are shown in Fig. 9.

The active length given by the boundary condition as shown in Fig. 10 and the minimum practicable tube sheet ligament, chosen here to be 4 mm, determine the design point in Fig. 9.

The cold HP-helium flows downward along the liner and then upward through the modules (Fig. 10) where it is heated up. The hot helium is collected in the HP gas box and returns via coaxial gas duct.

The number of seven modules is chosen for the same reasons as shown in Fig. 5.

The small pitch necessitates a thick tubesheet with a rather high thermal inertia. Shells and other structures are subjected to pressure from the outside.

Tasks and Effects of the Spacers in a Bundle with Longitudinal Flow

The spacer grids constitute an essential and delicate part of heat exchangers with shell side, longitudinal flow. Their main tasks are:

- Holding the HX-tubes in their proper position, in order to maintain regular flow distribution over the cross section of the bundle
- Preventing buckling of the tubes in the case of different axial stresses

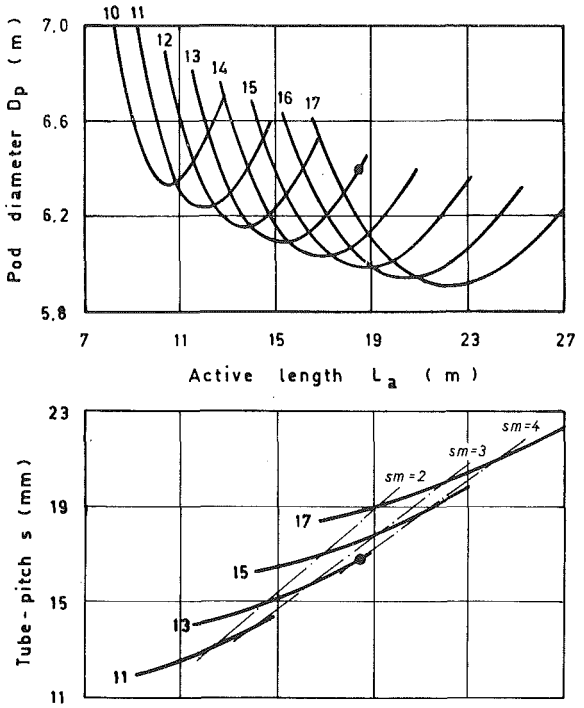

Fig. 9 Pod diameter and tube pitch of the recuperator with circular modules and HP-helium outside tubes as a function of its active length. (Parameter: tube diameter (mm), minimum distance between tubes: sm (mm).)

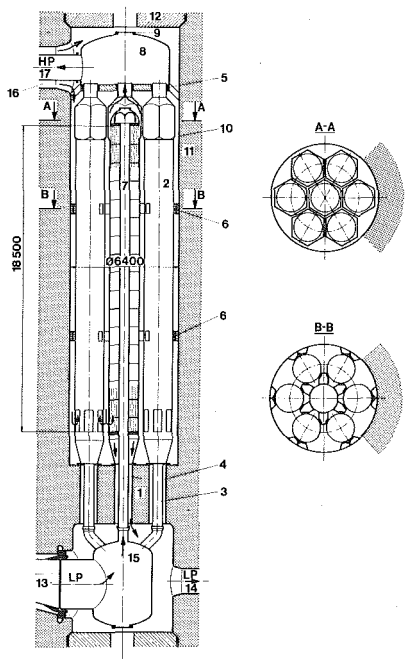

Fig. 10 Recuperator with HP-helium outside tubes: (1) large high pressure/low pressure barrier, (2) circular elements (3) low-pressure ducts to the elements, (4) low-pressure outlet ducts, (5) high-pressure seal, (6) lateral bracing for modules, (7) central pipe, (8) high-pressure gas box, (9) access door, (10) liner, (11) prestressed concrete reactor vessel, (12) cover of HX pod with access door, (13) low-pressure gas inlet from turbine, (14) low-pressure gas outlet to precooler, (15) low-pressure gas box, (16) high-pressure gas inlet from compressor, (17) high-pressure gas outlet to reactor

- Preventing excessive vibration of the tubes under the effect of gas flow.

The main criteria in designing the spacer grids for the recuperator have to be sufficient mechanical stability and minimum gas pressure drop. Several types of spacers have been taken into consideration. Mechanical stability, fretting behavior and pressure drop coefficients were investigated experimentally and analytically.

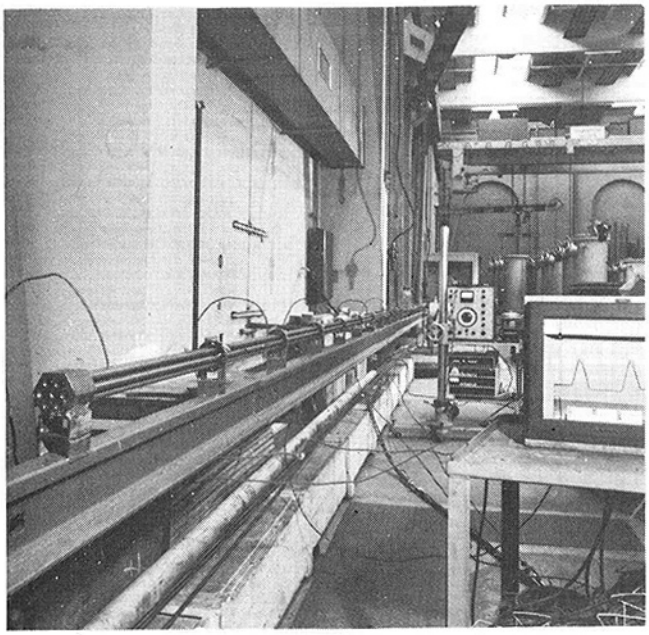

Fig. 11 Test rig for mechanical testing of tubes and spacers

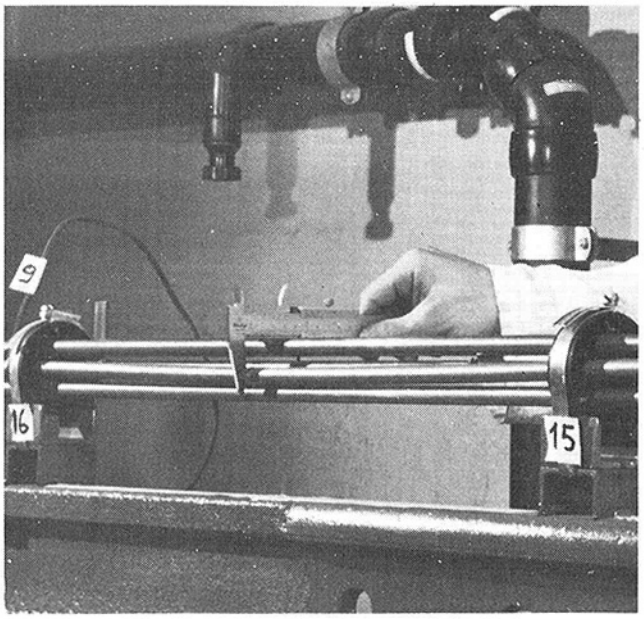

Fig. 12 Detail of Fig. 11, one tube is buckled

Criteria for the Longitudinal Distance between the Spacers. The criteria which determine the interval between successive spacers are accuracy of tube position, vibration amplitude of the tubes, fretting between tube and spacer, and tube buckling due to compressive stress. This last criterion has been found to prevail in our case.

The origins of the stresses are different average temperatures of the tubes caused by gas temperature streaks in the bundle. Such streaks may be produced by bypass control whereby cold gas is mixed to the hot turbine outlet gas at different operational and transient condition cases.

These streaks flow essentially undamped through the heat exchanger. Since they are in touch with the same tubes along their whole way in the bundle, the wall temperatures of these tubes are strongly influenced. Strong hot streaks may thus cause buckling of singular tubes.

Tests are being planned, in order to establish the size of the streaks at the HX inlet. Another test, which will allow to quantify the mixing effects of such streaks within the bundle is in preparation.

A special test has been made to establish and analyze the mechanical behavior of the tubes with different spacers. The test rig employed is shown in Fig. 11. A small HX-bundle with seven tubes is set up on a strong beam. 15 spacers are mounted at equal intervals between tubesheets at the ends of the bundle.

In a first test, a single tube was fixed at the two tubesheets and heated until buckling occurred, see Fig. 12.

A small lateral deplacement of the tube was observed before the theoretical buckling load was reached, probably due to excentric load. Stresses in the tubes caused by temperature differences are of secondary character. Consequently, buckling loads even greater than the theoretical ones may be acceptable, as long as there is no contact between the neighboring tubes.

In a second test, the natural frequency of a tube was observed at different stress loads. It was established that there is significant reduction in the natural frequency at the theoretical buckling load.

It is expected that the type of fixation for the tubes influences the buckling characteristics (Fig. 13). Only one fixation plane was used for the tests mentioned. Further tests with two planes will be investigated later.

The greater the temperature streaks at the inlet of the HX, the smaller the distance between spacers has to be selected in order to avoid buckling. Nevertheless, at the same time the axial force of the tube causes stresses in the weld-connection tube to tube-sheet. The admissible stress of this weld determines another limit for the size of temperature streaks.

Influence of the Spacer Design on the Dimensions of the Recuperator. In order to obtain minimum spacer pressure loss, some attention has been given to the optimization of the spacer geometry. The importance of this problem may be illustrated by the fact that, for the current HHT-recuperator layout, the spacers produce about half of the shell-side pressure loss.

Different spacer types (hexagonal grids as well as ring types) have been designed and analyzed. The pressure drop coefficient z_s may be calculated using the blocked area, wetted perimeter and wetted area [8]. Hydraulic and structural analysis is supplemented by tests.

The influence of z_s on the HX-dimensions is shown in Fig. 14. Thereby shell- and tube-side pressure losses are kept constant, as well as the longitudinal spacer distance.

A variation of the longitudinal distance between the spacers has, in a first approximation, the inverse effect of the variation of the pressure drop coefficient. Therefore, the consequences of such a variation may be read from Fig. 14. Exact measurements of the pressure drop coefficient show an influence of spacer distance. This effect is due to the flow perturbation caused by the spacer. There is also a beneficial consequence, namely a local increase of the heat transfer coefficient. For the spacers of the hexagonal grid type a local maximum of about 10 percent or an average increase of a few percents can be expected [9].

Comparison of the Different Design Concepts

Criteria. The main criteria for the selection of the design concept are:

- feasibility
- space requirement
- accessibility for inservice inspection
- repairability
- sensitility to cold gas streaks
- testability
- cost.

A summarized valuation of the five recuperator concepts as described in Section 2 is given in Table 2, the corresponding arguments are discussed in the following sections.

The criterion cost has not been considered in Table 2. The different space requirements and overall arrangements of the various HX-concepts entail substantial variations of cost for the PCRV etc. Consequently, consideration of heat exchanger costs alone cannot be conclusive.

Table 2 Dimensions, weights and preliminary ratings of the different design concepts—rating scale: (0): Impossible, (1): Bad, (2): Feasible, open problems, (3): Good, (4): Very good

		Longitudinal counterflow HP-helium inside tubes		Cross-counterflow HP-helium inside tubes		Longit. counterflow. HP-helium outside tubes.
		18 hexagonal modules	7 circular modules	1 circular module	7 modules with hexagonal shells	7 circular modules
MAIN DIMENSIONS AND WEIGHTS						
Active length	m	21.8	22.0	22.0	22.0	18.5
Pod diameter	m	5.86	5.96	6.15	>6.4	6.4
Tube diameter	mm	12	12	12	12	13
Tube pitch	mm	16.7	17.8	18.6	16.9	16.9
Number of tubes	–	49'200	40'200	45'900	39'100	47'000
Heat transfer area	m^2	40'500	33'300	38'100	32'400	35'500
Weight	Mg	830	810	640	800	780
RATING OF THE HEAT EXCHANGERS CONCEPTS						
Criteria						
Feasibility		2	3	2.5	3	2
Space requirement		2.2	2	1.5	1	1
Inspectability		2	2.5	3	2.5	2.5
Repairability		1.5	2.5	2.5	2.5	2.5
Sensibility to temperature streaks		1.5	1.5	3	3	2
Testability		2.5	2	1	2	1

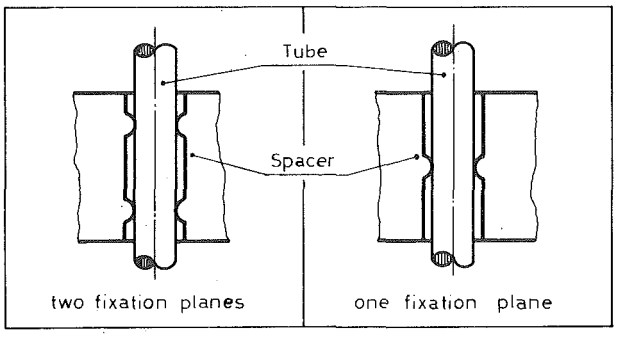

Fig. 13 Types of fixation for the tube by the spacer

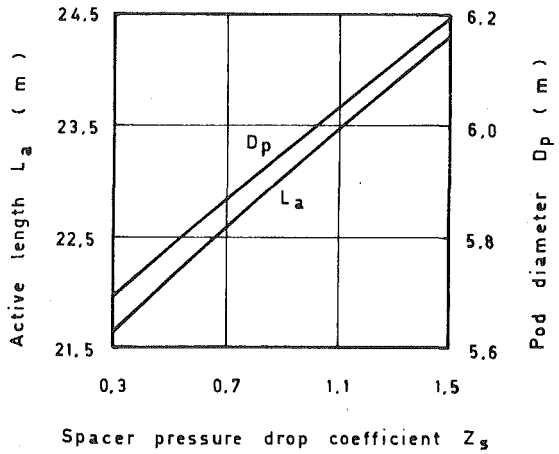

Fig. 14 Active length and pod diameter as a function of the spacer pressure drop coefficient

Longitudinal Counterflow HX with Hexagonal Modules and HP-Helium inside Tubes. The longitudinal counterflow HX will best satisfy the geometrical boundary conditions with slender and high pods.

In the case of hexagonal modules, the LP seal is formed only by the gaps between modules, see Fig. 15.

With a gap width of 1.7 mm, there is a bypass of LP gas around the HX of about 3 percent of the total flow rate. To compensate this effect, the heat transfer area has to be extended and the pod diameter increases correspondingly.

The requirements for inservice inspection of the recuperator because of reactor safety are low. However, because of operational reasons, it is desirable for the structures to be readily accessible at least on the first installation, in order to allow supervision of the operational behavior and examination of any damage sustained. With the present design, it is possible to inspect the supporting cover and to gain access to the tubesheets of the modules as well as to the heat transfer tubes by means of special devices. These can also be used for plugging tubes. An exchange of singular modules would not be impossible, but probably difficult.

As indicated in the preceding section, the feasibility of the longitudinal counterflow HX depends on sufficiently small hot gas streaks on the LP side.

By the criterion testability the possibility for testing a prototype module in a loop such as HHV [10] shall be judged. The smaller the module is, the more easily such a test could be made.

Longitudinal Counterflow HX with Circular Modules and HP-Helium inside Tubes. The circular modules have distinct advantages with respect to fabrication and inservice inspection. In addition, the LP sliding seal produces an internal bypass which is considerably smaller than in the case of the hexagonal modules. The pod diameter is only about 10-cm larger. An individual module could be changed with fewer complications than an hexagonal module because the modules do not touch each other.

Testing a prototype of a circular module will be somewhat more difficult because of its dimensions.

Cross-Counterflow HX with one Module and HP-Helium inside Tubes. Due to the fact that the gas flows perpendicularly to the tubes and mixes after each passage, hot streaks are well damped and the wall temperatures of the tubes are largely equalized.

The pod diameter resulting from our first design calculations is clearly larger than for the longitudinal counterflow HX's. Further development of design and calculation methods for this type of cross-counterflow HX may result in a reduction of this diameter.

An obvious problem of a single module recuperator is given by the necessity of site fabrication. Supporting cover, tubesheets, baffles and high pressure gas collector are delivered to the site as complete parts. However, connection of tube to tubesheets and assembly of the structures take place in a workshop on the site. The implications of such a fabrication are being studied. Site workshops larger than needed in the case considered have been in use [11].

The access to all parts of the HX is quite good. An exchange of the

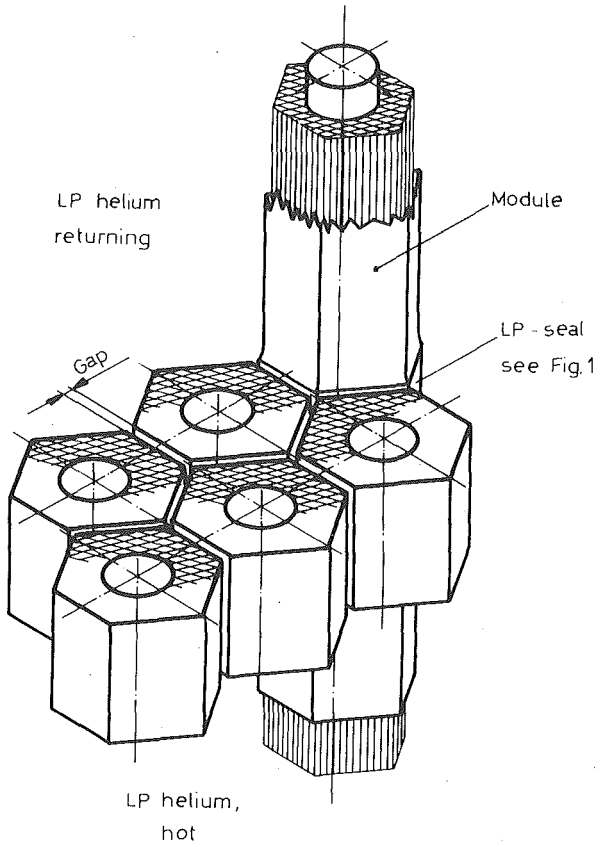

Fig. 15 Gap seal of the longitudinal counterflow HX with hexagonal modules

apparatus would require a suitable lifting equipment in the containment.

The chances for testing a whole prototype are rather small for this design concept.

Cross-Counterflow HX with Several Modules and HP-Helium inside Tubes. The same advantages with respect to fabrication, inspection, repair and testing are offered as in the case of the longitudinal counterflow unit with seven circular modules.

A further advantage is the favorable behavior against temperature streaks as in the case of the type with one module.

The resulting large pod diameter would be the principal disadvantage for an application of this concept in the HHT-project.

Longitudinal Counterflow HX with Circular Modules and HP-Helium outside Tubes. The design with the HP-gas outside the HX-tubes may result in a favorable plant layout through elimination of the steel support cover and better access to the HX-modules. Hot streaks coming from the LP inlet are damped by flowing through the long central tubes.

The small pitches of this design and the resulting thick tubesheets are unfavorable for fabrication and also for transient operation. At the inner and outer periphery of the module, the smaller pitch necessitates very small and well observed distances to the shell and central tube. Otherwise bundle internal temperature streaks could result.

Stresses caused by the rigid connection of HX tubes, tubesheets and central tube are higher. Therefore, bellows will probably have to be provided between the upper tubesheet and the central tube. As can be seen in Table 2, heat transfer area and pod diameter are comparatively large.

The good access from above is impaired by the higher contamination of the warm LP-side, which is now at the upper part of the HX. At present no experimental loop is available which would allow to simulate the HP-gas-flow on the shell side of this HX.

Summary and Conclusions

Recuperators for fossil-fired closed cycle gas turbine plants have been built, after various stages of development, as cross-counterflow heat exchangers with straight tubes, and have demonstrated their maturity by good operating experience. Recuperators for GT-HTGR plants may profit by this record, but have to fulfill some different and additional requirements. The unit size becomes larger as does the pressure difference, fretting problems in helium of reactor quality are more difficult to handle, tubes and other critical parts need to be accessible for inservice inspection and some contamination of the apparatus has to be expected. Integrated arrangement of the entire gas circuit in a prestressed concrete reactor vessel leads to the requirement of even more compact design and the especially small diameter of the apparatus.

Hence, the search for an optimum type of heat exchanger must be considered open again for this new application.

Despite the use of high pressure helium and the splitting of the 670 MWe demo plant in two loops, the adoption of the proven cross-counterflow heat exchanger concept results in a considerable size of the apparatus, so that site fabrication is necessary. This complication can be avoided by dividing the recuperator in seven modules, at the price of the large diameters of the two recuperator pods in the PCRV.

Comparatively small pod diameters can be achieved by adoption of the longitudinal-counterflow heat exchanger concept. Such recuperators are sensitive to temperature streaks, but this problem can be solved within a certain range. Important parts of these heat exchangers are the spacer grids, which have to provide high mechanical stability and low pressure drop. In order to get favorable flow conditions, only modular designs come into question. A heat exchanger comprising seven round modules has become the reference design. A small gain in pod diameter could be achieved by an apparatus composed of 18 hexagonal modules, at the price of additional design problems.

An alternative plant layout results in the high pressure helium on the shell side of the recuperator. There is no advantage from the pure heat exchanger point of view, as long as only conventional design elements are applied.

Acknowledgments

This report describes work carried out by cooperation between:
BBC, Aktiengesellschaft Brown Boveri & Cie, Baden
Brown Boveri & Cie, AG, Mannheim
Swiss Federal Institute for Reactor Research, Würenlingen
Sulzer Brothers Limited, Winterthur
Hochtemperature-Reaktorbau GmbH, Mannheim
Kernforschungsanlage Jülich GmbH, Jülich
Nuklear-Chemie und Metallurgie GmbH, Wolfgang
Schweizerische Aluminum AG, Zurich,
in connection with the development program for nuclear power stations with high temperature reactor and helium turbine (HHT), which is sponsored by the Federal Republic of Germany, the State of Nordrhein-Westfalen, and the Swiss Government.

Valuable contributions to the contents of this paper have been made by S. Amacker, A. Corthay, R. Félix, G. Gobbi and M. Weber of Sulzer Bros. Ltd.

References

1 Haferkamp D., Schneider K. U., Hodzic A., Schwarz H., "Anlagenkonzept HTR-Einkreisanlage (HHT)," *Deutsches Atomforum,* Reaktortagung 1977, Vortrag 704.

2 Naegelin R., Bieri H., Fischli H., Nordström L. A., "Heat Exchangers for HHT-Plants," *Nuclex 1978,* Technical Meetings, Paper A4/16.

3 Arndt E., Kirch N., Sarlos G., "Demonstration Power Plant with High-Temperature Reactor and Helium Turbine," European Nuclear Conference, Hamburg 1979, Paper a 45.

4 Naegelin R., Varadi G., "Thermohydraulic Design of Heat Exchangers for Direct-Cycle Integrated Gas Turbine Plants," *Symposium* July 13–Oct. 17 1975, IAEA-SM-200/6.

5 Bammert K., and Deuster G., "Das Heliumturbinen-Kraftwerk Oberhausen, Auslegung und Aufbau," *Energie und Technik,* Heft 1/1974, S. 1–6.

6 Haas W., Frutschi H. U., "Operating Closed Cycle Plants," *Gas Turbine International,* Mar–Apr 1972

7 Van Hagan T. H., McDonald C. F., Creek R. B., "Heat Exchanger Designs for Gas Turbine HTGR Power Plants," ASME Paper 79-WA/GT-2, 1979.

8 Barroyer P., "Analytical Model For the Prediction of Spacer Pressure Drop Coefficients," Paper A.N.S. 1978 Winter Meeting, Washington, D. C., Nov. 12–17, 1978.
9 Hudina M., Nöthiger H., "Experimental Study of Local Heat Transfer Under and Near Grid Spacers developed for GCFR," EIR internal report TM-IN-526, 1.10. 1973.
10 Krämer H., Noack G., "Hochtemperatur-Helium-Versuchsanlage HHV," Jahresbericht 1973 Kernforschungsanlage, July.
11 Rippon S., "Creys-Malville: Super progress on Super Phénix," *Nuclear News,* Mar 1979, p. 63 ff.

APPENDIX

Simplified Relations between Plant Efficiency, Recuperator Effectiveness, Relative Pressure Drop and Heat Transfer Area

Using the temperature nomenclature of Table 1, the recuperator effectiveness is defined as

$$\eta_r = \frac{T_4 - T_3}{T_1 - T_3} \tag{1}$$

With the net plant power N and the thermal power Q of the reactor the plant efficiency is

$$\eta = \frac{N}{Q} \tag{2}$$

Variations of thermal power Q and of available mechanical power N result in the following change of plant efficiency

$$\Delta\eta = \frac{\Delta N}{Q} - \eta \cdot \frac{\Delta Q}{Q} \tag{3}$$

An increase of the outlet temperature on the high pressure side of the recuperator enables a decrease of the reactor thermal power

$$\frac{\Delta Q}{Q} = \frac{-\Delta T_4}{T_5 - T_4} \tag{4}$$

from (1):

$$\Delta T_4 = \Delta\eta_r \cdot (T_1 - T_3) \tag{5}$$

Additional pressure drop Δp in the recuperator would have to be compensated by additional power of the compressor. With the gas pressure p, the relative pressure drop $\epsilon = \Delta p/p$, the specific volume of the gas v, the specific heat c_p, the gas constant R and the compressor efficiency η_c (about 90 percent) one gets

$$\frac{\Delta N}{Q} = \frac{-\Delta\Delta p \cdot v}{\eta_c \cdot c_p \cdot (T_5 - T_4)} = \frac{-\Delta\epsilon \cdot R \cdot T}{\eta_c \cdot c_p \cdot (T_5 - T_4)} \tag{6}$$

For helium we have $R/c_p = (\kappa - 1)/\kappa = 0.398$.
From (3) to (6):

$$\Delta\eta = \Delta\eta_r \cdot \frac{\eta \cdot (T_1 - T_3)}{T_5 - T_4} - \Delta\epsilon \cdot \frac{0.44 \cdot T_3}{T_5 - T_4} \tag{7}$$

In [4] an equation (18c) for the heat transfer area F in longitudinal flow is given. Neglecting other terms, the relation between F, ϵ and the temperature difference ΔT over the heat transfer area becomes

$$F \sim \frac{1}{\Delta T^{1.4} \cdot \epsilon^{0.4}} \tag{8}$$

Assuming equal mass flows on both sides of the heat exchanger, which is approximately the case with the recuperator, the driving temperature difference is constant over the area and may be deducted from [1]

$$\Delta T = T_1 - T_4 = T_2 - T_3 = (1 - \eta_r) \cdot (T_1 - T_3) \tag{9}$$

equations (8) and (9) combine to

$$F \sim \frac{1}{(1 - \eta_r)^{1.4} \cdot \epsilon^{0.4}} \tag{10}$$

L. S. Langston

Associate Professor,
Mechanical Engineering Department,
University of Connecticut,
Storrs, Conn.
Mem. ASME

Crossflows in a Turbine Cascade Passage

Measurements of the subsonic flow in a large scale plane turbine cascade, that were given in an earlier paper, are examined in more detail from the standpoint of the endwall boundary layer. Representative data are presented in terms of normal and streamwise velocities, flow angle deviations, and polar plots, that can be used to substantiate analytical models of the endwall flow. The qualitative behavior of the endwall crossflow was found to be correlated by a relatively simple expression, based on the flow angle deviation.

Introduction

An important problem that arises in the design of modern gas turbines and in the analysis of their performance, is the understanding and prediction of the nature and influence of secondary flows. Based on the current state-of-the-art, a turbine designer might well define secondary flows as those three-dimensional flow effects in a turbine that he had not planned on. One of the simplest of geometries in which to study these three-dimensional effects is a plane cascade of turbine airfoils.

Background. In an earlier paper, Langston, Nice, and Hooper [1] gave an experimental description of the secondary or three-dimensional flow in a large scale, low aspect ratio plane cascade of turbine airfoils. In their work, detailed measurements of subsonic flow were made at axial planes in front of, within and behind the cascade. The three-dimensional flow that they measured is shown schematically in Fig. 1. This figure shows that at the endwall of the cascade, the inlet boundary layer separates and forms a horseshoe (or leading edge) vortex, with one leg of the vortex in one airfoil passage and the other leg in the adjacent passage.

One leg merges with and becomes part of the *passage vortex*. Thus in a cascade flow, that part of the secondary flow that is called the passage vortex (a term first used by Herzig, et al. [2]) is an amalgamation of one leg of the horseshoe vortex (and hence part of the inlet boundary layer), the crossflow from the endwall boundary layer formed within the cascade, and entrained fluid from the mainstream flow in the cascade passage.

As shown in Fig. 1, the other leg of the horseshoe vortex which has been labeled the *counter vortex* remains in the suction surface-endwall corner. The counter vortex has a sense of rotation opposite to the passage vortex. It is much smaller than the passage vortex and may be dissipated by viscosity.

The ribbon arrow representation of both vortices in Fig. 1 has been drawn to exaggerate the vortex rotation, in order that the sense of rotation of each vortex would be clearly shown. The core of the passage vortex studied in reference [1] approximated a Rankine vortex. A particle of fluid that was near the viscous-inviscid interface of the Rankin vortex would actually have a total gross rotation of one or two revolutions about the center line of the passage vortex, as it passed through the cascade passage.

Crossflow Approach. While reference [1] gave an overall picture of the flow in a turbine cascade, it is the purpose of this paper to examine the data in greater detail, in terms of a three-dimensional crossflow boundary layer approach. The three-dimensional boundary layer referred to here is on the cascade endwall, inside the cascade passage. Regions of the endwall flow that are near singular points or separation and attachment lines are excluded from consideration. Also, the term *boundary layer* is used here in the spirit of the bounded boundary layer defined by Horlock [3], that is, endwall effects can be of the order of magnitude of the passage dimensions. It will be shown that it was not possible to use Horlock's concept exactly.

A bit of three-dimensional boundary layer history is in order at this point. Investigators have found that a convenient way to represent a three-dimensional boundary is to project the velocity profile onto two mutually perpendicular planes, one in a nominal free stream streamwise direction and one normal to the free stream streamwise direction. The latter is called the crossflow component.

Early on it was found that for small crossflows, the streamwise component of a three-dimensional boundary layer could be fairly

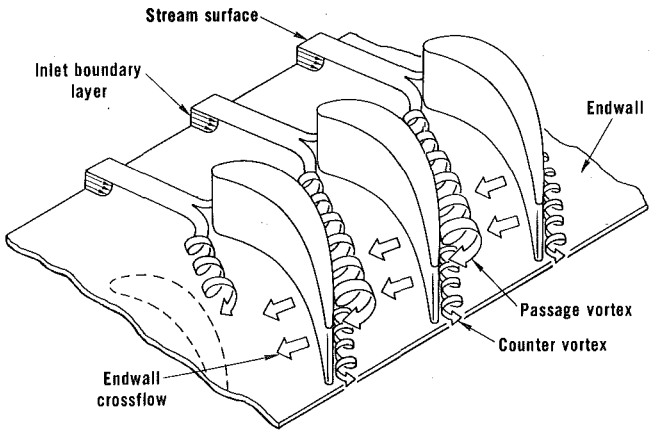

Fig. 1 The three-dimensional separation of a boundary layer entering a turbine cascade. The saddle point occurs where the vortex is formed

Contributed by the Gas Turbine Division and presented at the Gas Turbine Conference and Products Show, New Orleans, La., March 10–13, 1980, of THE AMERICAN SOCIETY OF MECHANICAL ENGINEERS. Manuscript received at ASME Headquarters, December 3, 1979. Paper No. 80-GT-5.

accurately represented by an equivalent two-dimensional boundary layer, with a velocity profile of the form

$$\frac{u_s}{u_{s_{ms}}} = \left(\frac{z}{\delta}\right)^{1/n} \tag{1}$$

where n is a specified constant.

The problem of predicting the crossflow component was treated by using a polar plot of the two velocity components, i.e., a plot of the crossflow velocity component versus the streamwise component. This plot in effect places an imaginary observer atop the velocity profile, watching the loci of the tips of the velocity vectors in the boundary layer below him.

Johnston [4] was one of the first to use the polar plot, and a typical Johnston triangular polar plot is shown in Fig. 2(*a*). It is given by the expression

$$\left.\begin{aligned} \frac{u_n}{u_{s_{ms}}} &= \frac{u_s}{u_{s_{ms}}} \tan \epsilon_w, \qquad z < z^+ \\ \frac{u_n}{u_{s_{ms}}} &= \left(1 - \frac{u_s}{u_{s_{ms}}}\right) \tan \alpha, \qquad z > z^+ \end{aligned}\right\} \tag{2}$$

where u_n, u_s and $u_{s_{ms}}$ are the crossflow, streamwise, and free stream velocities, respectively. The region $z > z^+$ usually accounts for 95 to 99 percent of the boundary layer. Given values of z^+ and α, equation (2) has been shown many times to be a good representation of small crossflows on flat plate geometries. Other small crossflow models are discussed by Nash and Patel [5].

An example of another type of crossflow polar plot is shown in Fig. 2(*b*). This is called a crossover, crossflow plot and can represent crossflow in a flow that earlier in its history had been skewed in the opposite direction, so that u_n changes sign. Klinksiek and Pierce [6] observed this type of flow on the endwall of the second bend in an S-shaped duct. Both Shanebrook [7] and Eichelbrenner [8] have proposed various polynomial expressions to describe the crossover, crossflow polar plot. One form given by Eichelbrenner is a polynomial of the form,

$$\frac{u_n}{u_{s_{ms}}} = \frac{u_s}{u_{s_{ms}}} \tan \epsilon_w \left\{1 + c_1\left(\frac{u_s}{u_{s_{ms}}}\right) + c_2\left(\frac{u_s}{u_{s_{ms}}}\right)^2 + \ldots\right\} \tag{3}$$

where $c_1, c_2, \ldots$ are evaluated from boundary conditions at the edge of the boundary layer and at the wall. Almost any kind of crossflow can be described by equation (3), provided that enough terms in the polynomial are used.

During the 1960's a good deal of work was done in an attempt to find "the best" representation of a general polar plot that would apply to a wide range of three-dimensional boundary layers. Two conclusions came out of this work:

1 In a summary of this work, Johnston [9] concluded that there is no general universal crossflow profile. The flow in three-dimensional boundary layers is dependent in each case on boundary conditions and flow history.

2 As Wheeler and Johnston [10] have pointed out, without a so-called universal crossflow profile, three-dimensional prediction methods using integral techniques cannot be general enough to work on a variety of geometric configurations.

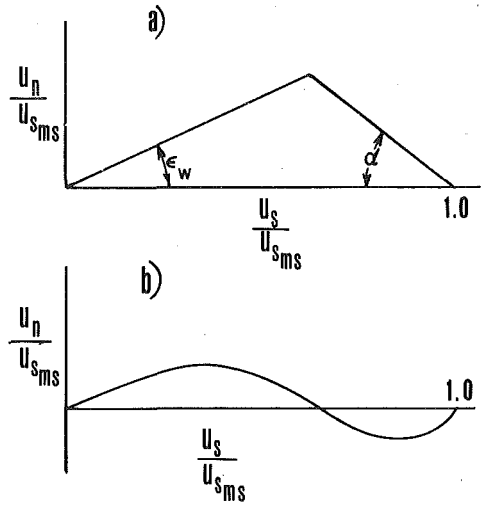

Fig. 2 Polar plots. (*a*) Johnston triangular; (*b*) crossover, crossflow

This then has led to an abandonment of integral methods in favor of methods that use finite difference approximations to the differential boundary layer equations. Examples of this latter approach are the work of Pratap and Spalding [11], Briley and McDonald [12], Dodge [13], and Ghia, et al. [14].

However, the crossflow boundary layer approach and the polar plot still provide a useful and simple picture of a three-dimensional boundary layer which is not conveyed by other representations. It is a convenient way of categorizing or "botanizing" a three-dimensional flow. It is very difficult to represent truly three-dimension flows, which if described through experimental results, may mean several thousand data points (as in the case of reference [1]), or if predicted, may mean many pages of computer printout. The polar plot provides a simple way of summarizing these results.

Objectives. It is the purpose of this paper to present the crossflow characteristics of the endwall boundary layer of a plane turbine cascade. Based on a correlation of the flow angle deviation data, a new empirical crossflow model for endwall flow in a turbine cascade is presented.

This presentation is important for the following reasons:

1 As far as the author is aware of, there are no data available in the open literature that give a complete picture of the turbine cascade endwall boundary layer in a crossflow boundary layer format. Waterman and Tall [15] showed measurements of total pressure in the throat and exit plane of turbine nozzle cascades, but gave no velocity measurements. Sjolander [16] took velocity measurements in a passage of a low-turning inlet guide vane annular cascade. However, all

Nomenclature

a = constant in equation (5)
b_x = axial chord
c = constant in polynomial polar plot
c_{p_t} = total pressure coefficient, $(P_{to} - P_t)/{}^1/_2\rho_0 U_0^2$
n = exponent in equation (1)
P = pressure
u = velocity
U_0 = upstream inlet velocity to cascade
u_n = crossflow velocity
u_s = streamwise velocity
x = coordinate normal to cascade leading edge, nondimensionalized on b_x
y = coordinate parallel to cascade leading edge, nondimensionalized on b_x
z = coordinate prependicular to endwall, nondimensionalized on b_x
z_0 = value of z where $\epsilon = 0$
z_1 = values of z where ϵ is a minimum
z^+ = apex coordinate of Johnston triangle polar plot
α = angle of inviscid portion of Johnston triangle polar plot
β_1 = airfoil mean camber line inlet angle, measured from y axis
β_2 = airfoil mean camber line exit angle, measured from y axis
γ = constant in equation (5)
δ = boundary layer thickness
ϵ = yaw angle deviation, $\theta - \theta_{ms}$
θ = yaw angle
ρ = density
ϕ = pitch angle

Subscripts

ms = midspan or free stream
t = total
x = component in x-direction
w = wall
0 = upstream
1, 2 = indices

of his measurements were taken using a cobra probe, with no provision made for pitch angle variation in the flow. Carrick [17] took extensive measurements inside a low-turning plane cascade passage, but did not report his results in a way that one could make a quantitative assessment of the crossflow in the endwall boundary layer. Marchal and Sieverding [18] took detailed velocity measurements in both a nozzle and a rotor plane cascade. They showed secondary velocities and area-averaged flow angles, but they did not give complete velocity data.

2 The crossflow characteristics to be presented are based on a survey of the entire flow field of a cascade passage. This is very important, especially in internal flows. Wrong conclusions can be drawn if only a few traverses are made in a passage.

3 There is more and more evidence that the endwall flow shown in Fig. 1 is a very general picture of turbine cascade endwall flows for a wide range of cascade geometries and inlet conditions. Sjolander [16] found a similar endwall flow at the i.d. of an annual cascade. Marchal and Sieverding [18] report the same flow picture for both a nozzle (with two different inlet boundary layers) and a rotor cascade. Carrick [17] got the same qualitative endwall flow, even for cases of high inlet boundary layer skew produced by a moving belt at the inlet of his cascade. The author has observed soot and ceramic coating discoloration patterns in the nozzles of turbines in aircraft jet engines after many hours of operation, that suggest the same flow picture.

Thus a case can be made here that, because of the strong favorable pressure gradients in turbine cascades, the endwall boundary layer flow is qualitatively the same over a wide range of conditions. Hence any crossflow models and polar plots based on cascade data can in turn be expected to be quite general.

Experimental Apparatus

Testing was conducted in a large-scale, low-speed cascade wind tunnel that is described in more detail in reference [1]. Measurements were taken at various axial locations through one of the cascade passages, using conventional instrumentation that will be described in the following. The cascade geometry is as follows:

Axial chord, b_x = 11.08 in. (0.2813 m)
Chord/axial chord = 1.2242
Pitch/axial chord = 0.9555
Aspect ratio (span/axial chord) = 0.9888
Airfoil mean camber line angles
β_1 = 43.99 deg
β_2 = 25.98 deg

The airfoil sections, cascade coordinate system and measurement plane positions are shown in Fig. 3. All lengths shown are normalized on the axial chord, b_x. As illustrated in Fig. 3, $x = 0$ is at the leading edge plane and $y = 0$ is at the trailing edge plane tangency point on airfoil 2. The coordinate $z = 0$ is in the endwall plane, with the z axis positive into the flow. Also shown is the yaw angle, θ, measured in xy planes from the x-axis. The pitch angle of the flow, ϕ, defined as the angle between an xy plane and the local velocity vector, is taken as positive away from the endwall.

Most of the flow field in the cascade was mapped by using a five-hole probe that enabled the measurement of total pressure, static pressure, and velocity direction in the flow field, to within 0.1 in. (0.25 cm) of the endwall. Details of the probe are given in reference [1].

Flow velocities near the endwall were measured using both a single sensor hot wire probe and single sensor hot film probe. The data, used here, will deal only with measurements taken with the hot film probe. These were made with a Thermo-Systems Model 1210-20 hot film probe that had a cylindrical sensor with a diameter of 0.002 in. (0.05 mm) and a length of 0.040 in. (1.0 mm). The hot film was located off the wall by noting when electrical contact occurred between a downstream probe foot and a thin, very smooth layer of aluminum foil that covered the entire endwall for the hot film tests. Hot film positioning normal to the endwall was done with a micrometer drive. Flow measurements were taken 0.02 cm (0.008 in.) from the wall as measured from the hot film cylindrical sensor center line, to a sufficient distance away from the endwall so that hot film and five-hole probe data overlapped.

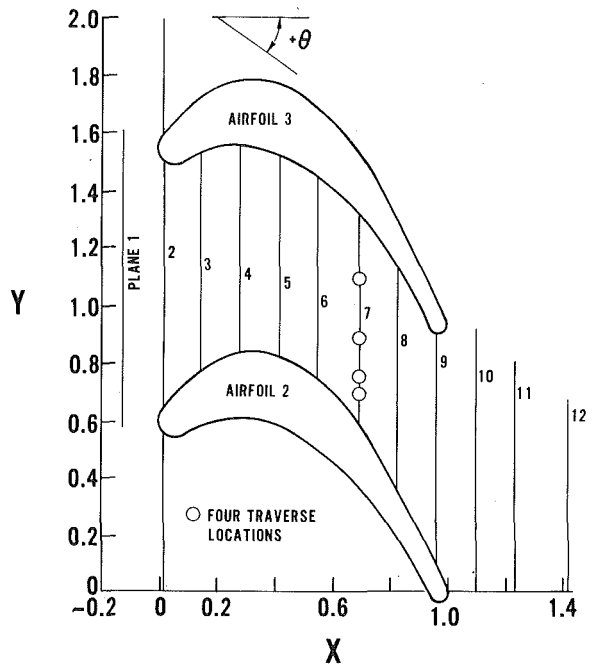

Fig. 3 Airfoil section and *xy* coordinate system. The *z* coordinate is positive into the plane of the page

Test Conditions

All tests were run with the cascade set at an inlet air angle of 44.7 deg. The upstream inlet velocity, U_0, was 110 ft/s (33.5 m/s) corresponding to inlet and exit Reynolds numbers based on blade axial chord of 5.9×10^5 and 10×10^5, respectively.

The characteristics of the equilibrium boundary layer entering the cascade were measured at a point upstream of the cascade (see reference [1]) and were found to have the following values:

Boundary layer thickness	1.3 in. (3.30 cm)
Displacement thickness	0.148 (0.376 cm)
Momentum thickness	0.110 (0.279 cm)
Shape factor	1.35
Momentum thickness Reynolds number	5338

The values for displacement thickness, momentum thickness, and momentum thickness Reynolds number are slightly different from those given in reference [1], due to an error found after the publication of the latter.

Experimental Results

The purpose here is to show the general characteristics of the endwall flow downstream of the endwall saddle point and its separation lines, and unstream of the cascade passage trailing edges. This excludes about 5–10 percent of the passage endwall area. In this way the complexities of the three-dimensional flow separations occurring at or near these locations are avoided, so that the details of a major part of the endwall flow can be treated with an added degree of simplicity.

Because of the large amount of data taken, only the results of flow measurements taken in plane 7 at an axial position of $x = 0.69$ (see Fig. 3) will be presented. Four selected spanwise traverses taken from the endwall to midspan at the gapwise positions of $y = 0.692$, 0.766, 0.903, and 1.106, all in plane 7, will be examined in detail to illustrate crossflow characteristics. Since the entire flow field in front of the passage, at eight planes within the passage and at three planes downstream of the passage, was surveyed, it can be stated with confidence that plane 7 data are representative of the endwall boundary layer. Again the purpose here is to present the dominant streamwise and crossflow features of the endwall boundary layer.

Flow Field Measurements. The distribution of total loss in plane 7 is shown in Fig. 4, as an isobar plot of the total loss coefficient, c_{p_t}. In this plane the observer is looking upstream, into the flow. The passage vortex is evidenced by the closed isobars or Bernoulli surfaces, near the suction surface side of the passage. As shown by the plot, the viscous region of endwall boundary layer is very thin. High losses appear on the endwall near the suction side corner where the endwall boundary layer separates from the endwall (at about $y = 0.7$) and where the suction surface boundary layer separates from the airfoil (at about $z = 0.23$). Also shown in Fig. 4 are the locations of the four spanwise traverses that will be examined in detail. These were chosen out of the total of 14 traverses that were made in plane 7, to show the characteristics of the endwall flow, (a) near the pressure surface, (b) near the inviscid-viscous region of the passage vortex, (c) at the pressure-side of the passage vortex core, and (d) at the suction-side of the passage vortex core.

Figure 5 is a plot of some of the velocity vector components in plane 7, showing the details of the secondary flow in the suction side of the passage. This plot was obtained by calculating the in-plane components of the measured velocity and for each spanwise probe traverse, vectorially subtracting the midspan component from the in-plane velocities of that traverse. Since the midspan static pressure distribution was shown in reference [1] to agree well with a two-dimensional potential flow calculation, the velocity vectors in Fig. 5 also show the deviation from potential flow.

One can see the motion of the passage vortex in Fig. 5, with its center of rotation at approximately $y = 0.73$, $z = 0.1$. This closely coincides with the center of the closed Bernoulli surfaces in Fig. 4, and, although not shown here, with the location of lowest static pressure measured in the plane. To delinate the viscous and inviscid parts of the vortex, the isobar $c_{p_t} = 0.1$ from Fig. 4 has been replotted in Fig. 5. It can be seen from the velocity vectors and the isobar that the passage vortex in plane 7 has the features of a distorted Rankine vortex. Part of this distortion is due to the fact that plane 7 is not a Trefftz plane. Also shown in Fig. 5 are the locations of three of the four traverses that will be treated below.

Velocity Profiles. Figure 6 shows a plot of the normal and streamwise velocity distributions at each of the four selected traverses in plane 7. Normal velocities are taken as positive towards the suction side. The data shown closest to the wall for values less than $z = 0.01$, are taken from the hot film measurements. For each spanwise traverse shown in Fig. 6, the free stream velocity magnitude and direction is taken as the midspan velocity, $u_{s_{ms}}$. The values of the midspan velocities and their associated yaw angles are listed in Table 1, so that the normalized velocities in Fig. 6 can be converted and compared in absolute values to one another.

As shown by the secondary flow velocity vectors in Fig. 5, the crossflow is smallest in the pressure side of the passage, and this is also shown in Fig. 6(a) for a position close to the pressure side. The crossflow profile in Fig. 6(a) is typical of small crossflows of the Johnston-triangular plot variety discussed in the introduction. The streamwise profile shown in Fig. 6(a) shows a decrease in velocity at about $z = 0.04$. However, this is not a true indication of a boundary layer thickness, since no change in total pressure was measured, even for the closest 5-hole probe position at $z = 0.01$. This was true for much of the endwall on the pressure side of the passage, i.e., that the viscous boundary layer was very thin.

Both of the crossflow profiles in Figs. 6(b) and 6(c) exhibit the presence of the passage vortex, and each show a crossover crossflow profile, i.e., in addition to the endwall crossflow toward the suction side, there is a return flow toward the pressure side. These have the same shape as some of the crossover, crossflow profiles measured by Klinksiek and Pierce [6], mentioned earlier.

When the streamwise velocity profiles in Figs. 6(a) and 6(b) are compared, one is tempted to say that there is a thickening of the endwall boundary layer as the suction side is approached, since u_s seems to show conventional boundary layer behavior at about $z = 0.08$ in Fig. 6(b) as opposed to $z = 0.04$ in Fig. 6(a). However, it would be incorrect to use two-dimensional boundary layer concepts for the data shown in Fig. 6(b). The total pressure-results at this gapwise position

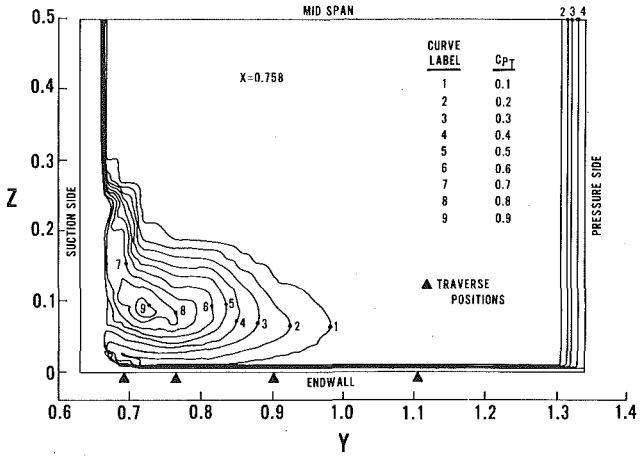

Fig. 4 Isobar plot of total pressure loss coefficients in plane 7. Four traverse positions are indicated

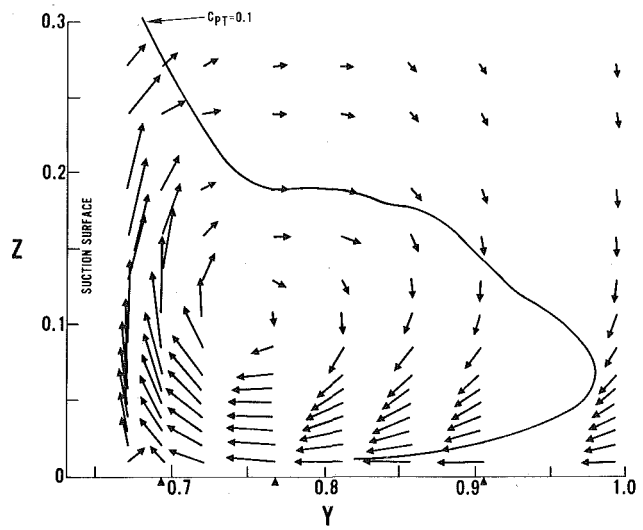

Fig. 5 Secondary flow velocity vectors in plane 7, near suction side. Loss contour $c_{p_t} = 0.1$ is shown for the passage vortex.

(see Fig. 4) show that total pressure is not a monotonic function of distance away from the wall, due to the passage vortex. The streamwise velocity profiles in Fig. 6(c) also clearly shows the effect of the passage vortex and certainly could not be modeled by a two-dimensional equilibrium boundary layer profile, such as given by equation (1).

The velocity profiles that are typical of the region in the suction side of the passage vortex core are shown in Fig. 6(d). No hot film data were taken at this position because of their proximity to the passage vortex separation line in the suction side-endwall corner. In this region the flow near the endwall had high pitch angles, and, since the hot film could only be traversed in a spanwise direction, hot film measurements would have been inaccurate. Again, the streamwise profile is far from a two-dimensional flow. When compared to Figs. 6(b) and 6(c) the crossflow profile on the suction side of the vortex shows smaller positive crossflows, as the endwall flow approaches separation.

The data presented in Fig. 6 represent measurements of the mean flow field only. As was stated in reference [1], turbulence intensity measurements were taken, but due to the extreme thinness of the endwall boundary layer, it was not possible to ascertain its state, i.e., whether it was laminar or turbulent. All that could be said was that there was a rise in turbulence intensity as the wall was approached. Also, any hot film or hot wire measurements made near a separation line or near the core of the passage vortex showed a sharp rise in intensity values over free stream values.

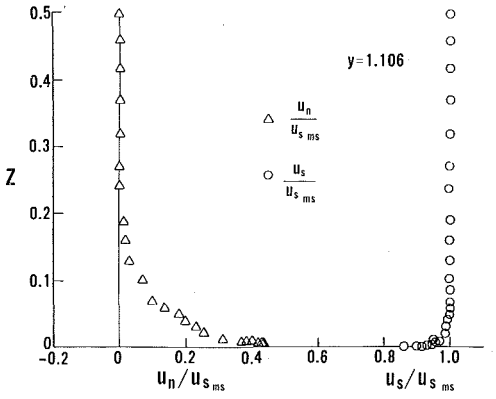

Fig. 6 (*a*)

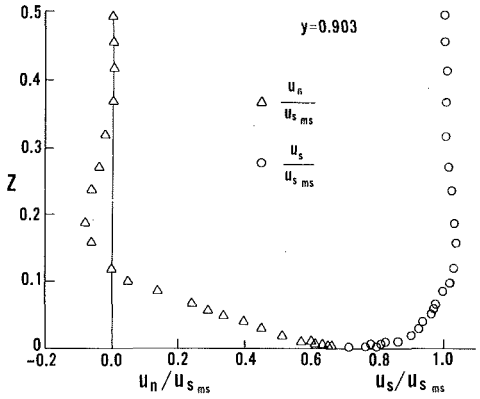

Fig. 6 (*b*)

Yaw Angle Deviation. The yaw angle deviation, ϵ, is an important variable in three-dimensional boundary layers, because ϵ determines the relationship between the streamwise velocity and the normal velocity, i.e.,

$$\frac{u_n}{u_s} = \tan \epsilon. \tag{4}$$

The yaw angle deviation for each of the four traverses in plane 7 is shown in Fig. 7 as a function of normalized distance from the endwall, z. The absolute yaw angles can be calculated from these plots by using the midspan absolute yaw angles listed in Table 1. The angles were measured with the five-hole probe nulled in yaw, and with the hot film by noting the yaw angle at which velocity was a maximum. Positive values of ϵ represent flow towards the suction side of the passage.

The limiting streamline or wall angles shown at $z = 0$ in Fig. 7 were calculated by carefully extrapolating the hot film angle measurements to $z = 0$, on a separate, large-scale plot. The possible underprediction of the limiting streamline angle by using this extrapolation method has been pointed out by Johnston [9]. However it was felt that this method was adequate for the present study for the following reasons:

1 Considering the scale of the channel, hot film measurements were taken very close to the endwall, to within 0.02 cm (0.008 in.), closer than the case that Johnston cited to prove his point.

2 Endwall flow visualization measurements were made using ink injected onto the endwall (see reference [1]). However it was felt that ink traces tended to give lower values of ϵ, whenever the skew was high, due to higher inertia forces on the ink droplet. Values of wall angles measured from the ink traces are given in Table 1, and it can be seen that they are lower than those obtained by extrapolation.

Figure 7(*a*) shows the yaw angle deviation for $y = 1.106$, the position nearest the pressure side, where the crossflow is small. Figures 7(*b*) and 7(*c*) show the deviation for positions closer to and to the right of the passage vortex center line. Both show a typical crossover crossflow behavior. The yaw angle deviation for the position to the left of the passage vortex center line in Fig. 7(*d*) shows a similar behavior, except that near the wall, the values of ϵ start to decrease, possibly because of its close proximity to the suction side endwall separation line. No wall value was calculated for Fig. 7(*d*) since no hot film data were taken at this position because of the high pitch angles.

The yaw angle deviations shown in Fig. 7 are representative of the endwall flow in the passage. An examination of all of the yaw angle deviation data showed that the *qualitative* behavior of the yaw angle deviation could be correlated by a single equation,

$$\epsilon = (\epsilon_w - az)e^{-\gamma z} \tag{5}$$

where ϵ_w—wall value of ϵ

a—crossover crossflow coefficient

γ—crossflow strength coefficient

z—nondimensional distance from the endwall

Also, ϵ is defined in the interval $-\pi/2 < \epsilon < \pi/2$, since values outside of this interval would signify three-dimensional separation.

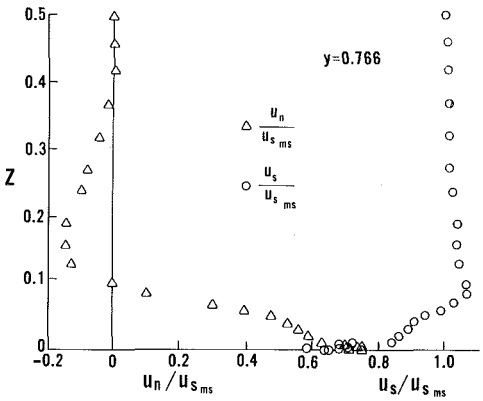

Fig. 6 (*c*)

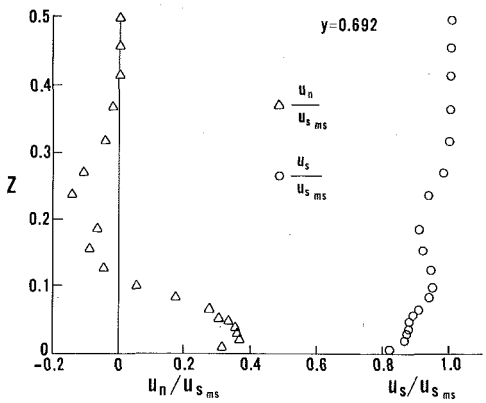

Fig. 6 (*d*)

Fig. 6 Streamwise and crossflow velocities in plane 7 at four traverse locations, as a function distance from the endwall

Table 1 Midspan values and equation (5) constants for four traverses in plane 7, $x = 0.758$

y	0.692	0.766	0.903	1.106
$u_{s_{ms}}/U_0$	1.884	1.796	1.568	1.149
θ_{ms}	51.5°	47.0°	42.6°	42.9°
ϵ_w	—	60°	51°	33°
a	—	612°	405°	0
γ	—	16.13	15.63	19.49
$(\epsilon_w)_{\text{ink}}$	5°	45°	47°	26°

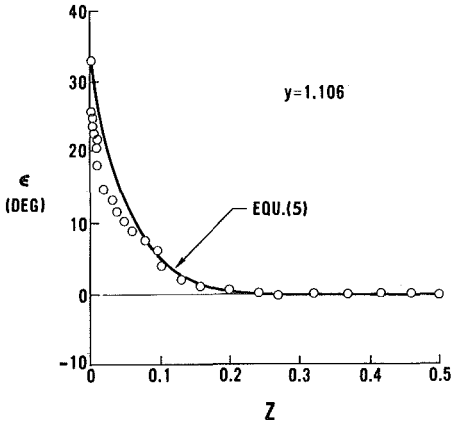

Fig. 7 (a)

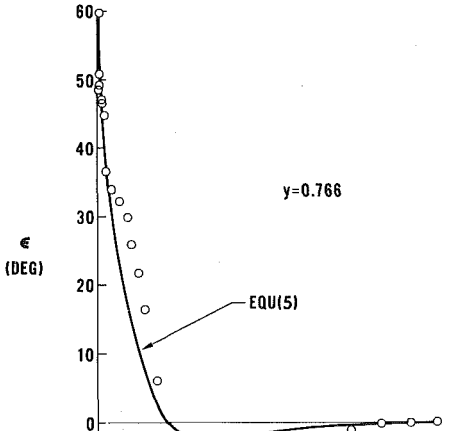

Fig. 7 (c)

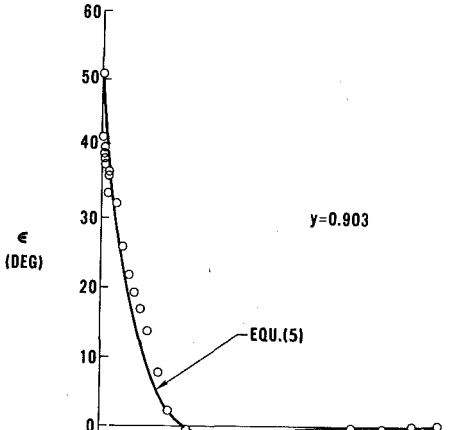

Fig. 7 (b)

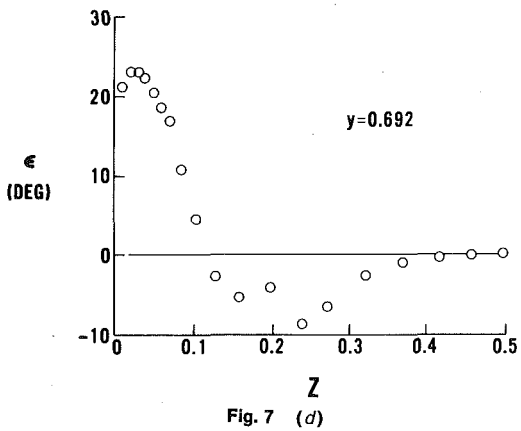

Fig. 7 (d)

Fig. 7 The yaw angle deviation as a function of distance from the endwall for four traverse locations in plane 7

Equation (5) is plotted in Figs. 7(*a*), 7(*b*) and 7(*c*). It is not plotted in Fig. 7(*d*) because it was found to be inadequate to describe regions of the flow that were near the separation line. The crossover, crossflow coefficient, a, was calculated from equation (5) at the point $\epsilon = 0$, or

$$a = \frac{\epsilon_w}{z_0} \tag{6}$$

where z_0 is the value of z where $\epsilon = 0$. In the case of Fig. 7(*a*) (the case of simple crossflow) this occurred essentially at $z \to \infty$, so that from (6), $a = 0$ for this case. For the case of Figs. 7(*b*) and 7(*c*), where there is a cross-over crossflow profile, the values are given in Table 1.

The crossflow strength coefficient was evaluated at the point where the data showed a minimum value of ϵ, i.e., where

$$\frac{d\epsilon}{dz} = 0 \text{ at } z = z_1. \tag{7}$$

The combination of equations (5) and (7) gives an expression for γ,

$$\gamma = \frac{a}{az_1 - \epsilon_w} \tag{8}$$

For the data shown in Fig. 7(*a*), where ϵ decreases monotonically with increasing z, γ was calculated by using equation (5) and the value given by the data at $z = 0.1$. Values of γ are listed in Table 1.

With three experimentally determined constants in equation (5), there are other ways that the data in Fig. 7 could have been fitted. As it is, equation (5) described the data in Figs. 7(*a*), 7(*b*) and 7(*c*) in a reasonably qualitative way. Taking the limit as z gets large in equation (5) and using L'Hospital's rule yields

$$\lim_{z \to \infty} \epsilon = 0 \tag{9}$$

This condition of zero crossflow at large values of z is seen to be in good agreement with the data at the midspan value of $z = 0.5$. One could also speculate that equation (5) might provide a better quantitaive fit of the data for the case of a higher aspect ratio passage, rather than the rather low aspect ratio passage of this study.

Equation (5) also yields a constantly turning velocity vector, right down to the wall; that is, from equation (5)

$$\left.\frac{d\epsilon}{dz}\right|_{z=0} = -(a + \gamma\epsilon_w), \tag{10}$$

which is what the data presented in Figs. 7(*a*), 7(*b*), and 7(*c*) seem to indicate.

Polar Plots. The polar plots that represent the endwall flow (except near regions of three-dimensional separation) in the passage are shown in Fig. 8. In this figure the data points have been connected by straight line segments to show the data point sequence. Thus the angle of the line connecting the origin and the nearest data point should not be interpreted as representing the wall angle, ϵ_w.

Figure 8(*a*) shows the polar plot for the transverse position near the pressure side of the passage. As was seen in Fig. 6(*a*), the crossflows are small in this region, and the plot in Fig. 8(*a*) exhibits a typical Johnston triangular polar plot type of behavior, given by equation (1).

The polar plots in Figs. 8(*b*), 8(*c*) and 8(*d*) exhibit crossover, crossflow behavior. In these regions closer to the suction side of the passage the flow is strongly affected by the passage vortex. All exhibit a "hooked" shape. This is characteristic of a traverse made through some part of a vortex, i.e., there is crossflow in both directions. Positive values on the polar plot indicate flow towards the suction side of the passage.

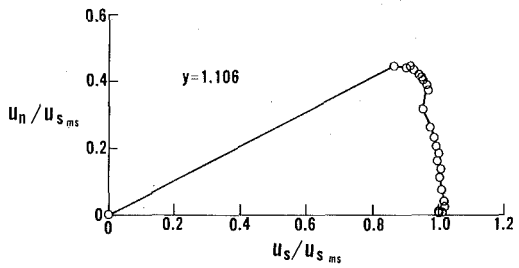

Fig. 8 (*a*)

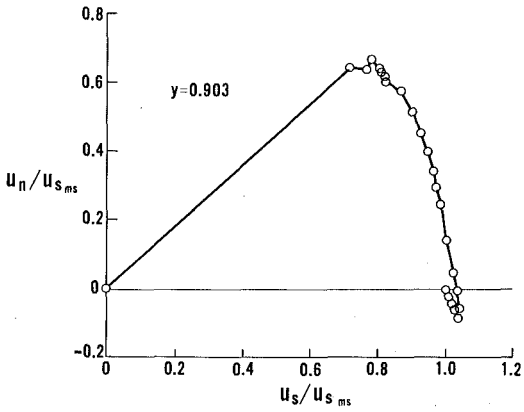

Fig. 8 (*b*)

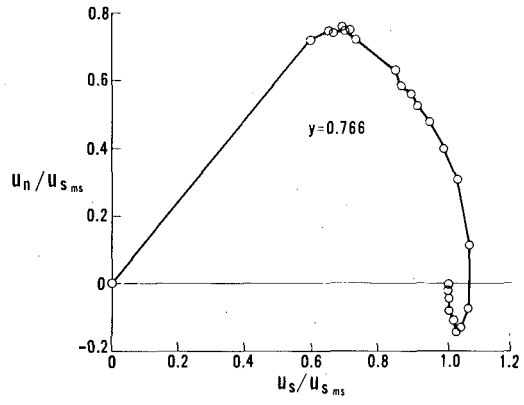

Fig. 8 (*c*)

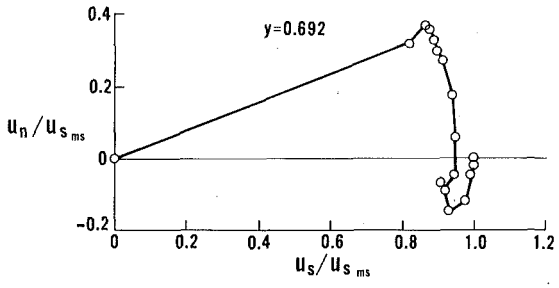

Fig. 8 (*d*)

Fig. 8 Polar velocity plots for four traverse locations in plane 7

Figures 8(*b*) and 8(*c*) show traverses made to the right of the vortex center and they both show a "backward hooked" behavior. That is, for each of these traverse positions, the flow represented by the hooked region is accelerated relative to the midspan velocity at that gap position. In both of these plots the hot film velocity values at the apex of the polar plot (i.e., the region of highest positive crossflow velocity) show that the viscous region of the endwall boundary layer is very close to the wall.

Figure 8(*d*) shows the polar plot for the traverse position close to the endwall separation line and to the left of the passage vortex center, as viewed in Fig. 5. As was stated earlier, no hot film data were taken at this position. This polar plot shows that flow has been decelerated relative to midspan. This type of behavior could be called a "forward hooked" polar plot.

Discussion

Combining equations (4) and (5) yields an expression for the crossflow in terms of the streamwise flow,

$$\frac{u_n}{u_s} = \tan[(\epsilon_w - az)e^{-\gamma z}] \tag{11}$$

This expression qualitatively describes the two types of polar plots found in this study of the endwall flow. These are shown in the sketch shown in Fig. 9.

For values of $a = 0$, $\epsilon_w \geq 0$ and $\gamma > 0$, Fig. 9(*a*) shows the Johnston-like polar plot that equation (11) would yield for crossflow near the pressure side of the passage, i.e., the region of small crossflow, furthest away from the influence of the passage vortex. For values of $a > 0$, $\epsilon_w > 0$ and $\gamma > 0$, equation (11) yields the crossover polar plots shown in Figs. 9(*b*) and 9(*c*), for the suction side of the passage, where the passage vortex is dominant. Figure 9(*b*) typifies the pressure side of the passage vortex, while Fig. 9(*c*) typifies the suction side of the vortex.

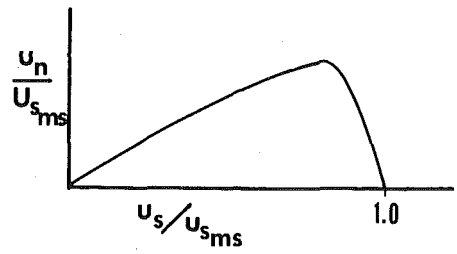

Fig. 9 (*a*)

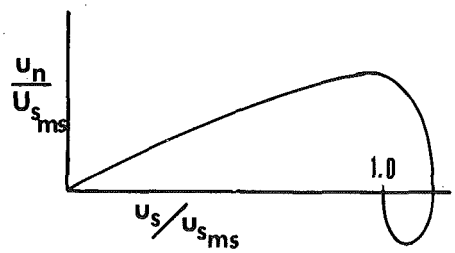

Fig. 9 (*b*)

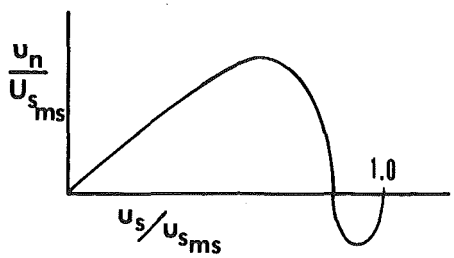

Fig. 9 (*c*)

Fig. 9 Polar plots for crossflow in a turbine cascade given by equation (11)

It should be stated here that equation (11) is simply a correlation of the crossflow data of this study. The range of the constants a, ϵ_w, and γ given in Table 1 is typical of the rest of the endwall data considered, and since equation (11) is a qualitative rather than a quantitative correlation of this very complicated, low aspect ratio endwall flow, there is no need to list additional values of these constants. Equation (11) has three experimentally determined constants, and, as such, is no more general than, say, a third-degree polynomial proposed by Eichelbrenner [8], given by equation (3). Also, as pointed out in the section on velocity profiles, no simple two-dimensional approximation could be made for u_s, the streamwise component of velocity, so that equation (11) cannot be used in a predictive fashion without knowledge of the spanwise variation of u_s.

However, equation (11) does qualitatively correlate the crossflow aspect of the endwall flow, something that Klinksiek and Pierce [6] were unable to do with the polar plot polynomial models of Shanebrook [7] and Eichelbrenner [8] (equation (3)) for their flow in an S-shaped duct. It is felt that this correlation of the endwall flow in a turbine passage is valuable, given that the endwall flow seems always to have the same character over a wide range of conditions, as was brought out in the introduction of this paper.

This correlation can provide a check of other data and analytical models of endwall flow. For instance, in one of the first attempts to do a turbine endwall boundary layer analysis, Dring [19] used an integral boundary layer approach. Booth [20] later extended this analysis to include the effects of compressibility and heat transfer. Both of these analyses used a small crossflow model, i.e., Fig. 9(a), with $a = 0$ in equation (11). The predicted losses that they reported were well below measured values. It is suggested here that one factor contributing to this discrepancy was caused by not using a crossflow model that included the case of $a > 0$. (Figs. 9(b) and 9(c)).

Another area in which equation (11) would be useful is in the evaluation of duct flows that are used to simulate flow in a turbine cascade. Because of the simpler geometry of a duct, it is frequently used for this purpose (see Barber and Langston [21]). For instance, the integral method models of Dring and Booth are duct flow models, as well as the more recent finite difference analyses of Briley and McDonald [12], and Dodge [13]. One of the most extensive experimental duct flow studies done to simulate flow in the turbine nozzle passage was carried out by Stanitz [22]. Had these investigators reported their data in a crossflow format (which they did not), the duct flow polar plots (and ranges of a, γ, and ϵ_w) could have been compared to those given here.

Some of the features of the endwall flow presented here are shared by the bounded boundary layer model proposed by Horlock [3]. By using the secondary flow model of Mellor and Wood [23], Horlock was able to derive gap-averaged expressions for the crossflow velocity in a turning passage. He was able to calculate a polar plot similar to that shown in Fig. 8(d) and to obtain a gap-averaged yaw angle deviation similar to Figs. 7(b) and 7(c).

No direct comparison could be made to his model because one of the key assumptions made was that the boundary layer thickness (defined as the point where total pressure begins to decrease) was of the same order as the passage width. This was not the case in the present study where, as has been shown, the actual endwall boundary layer (using Horlock's definition), was very much smaller than any passage dimension. Also, as he pointed out, the analysis was for small turning where the rotation of Bernoulli surfaces was not large, which was not the case for the data presented here. In addition, the cases that he calculated were for a large aspect ratio passage, while the present study is for a relatively low aspect ratio.

One other point that can be made here is the need for complete measurement surveys of a cascade passage or a duct when three-dimensional boundary layer measurements are made. In their measurements of the endwall boundary layer on the second bend of an S-shaped duct, Klinksiek and Pierce [6] obtained crossover, crossflow polar plots similar to Figs. 9(b), 8(b), and 8(c). The skewing that they reported was less than in the present study, but this is to be expected, since secondary flows in ducts are in general lower in magnitude than in a cascade of the same turning (see reference [21]). They explained their results using external flow boundary layer arguments to account for the phenomenon of flow reversal in the endwall boundary layer of the second duct, with simultaneous skewing occurring in two lateral directions. Their measurements were taken along the center line of the duct, only.

It is suggested here that what they observed in the second duct was actually the passage vortex of the first duct, and that, in internal flows, the occurrence of a crossover, crossflow profile signals the presence of a vortex. The flow visualization studies of Herzig, et al. [2] in tandem cascades support this view. Their work shows that the passage vortex of the upstream cascade passed through the downstream cascade (corresponding to the second bend of Klinksiek and Pierce) completely intact, and showed a high resistance to being turned by the second cascade. Had Klinksiek and Pierce taken more extensive measurements in their duct, this question might have been answered.

Summary and Conclusions

In this paper features of the endwall flow in a plane turbine cascade were examined in detail, using a crossflow boundary layer approach. Regions of the endwall that were near areas of three-dimensional separation were excluded. The following was concluded:

1 The endwall boundary layer region is characterized by small crossflows near the pressure side of the passage and large crossflows near the suction side. Extensive crossflows occur in inviscid parts of the flow and make the usual definition of a boundary layer difficult to apply. The actual portion of the flow that was effected by viscous forces near the endwall, was very thin and was characterized by the highest values of crossflow velocity and yaw angle deviation.

2 The crossflow data showed a Johnston triangular polar plot behavior near the pressure side and a crossover crossflow polar plot behavior in the suction side of the passage. The streamwise flow was found to be not similar to a two-dimensional boundary layer flow.

3 The qualitative behavior of the endwall crossflow was found to be correlated by a relatively simple expression (equation (11)). This expression for crossflow requires knowledge of the streamwise velocity, and three experimentally determined constants that specify the limiting streamline angle (ϵ_w), the relative crossflow strength (γ), and the extent of reverse crossflow (a). Ranges of these constants have been given.

One final conclusion of this paper is that further experimental work in high aspect ratio passages with smaller and simpler crossflows is needed, to evaluate how accurate the crossflow model presented is, in a quantitative sense.

Acknowledgments

The author wishes to express his gratitude to M. L. Nice for the many discussions that were held on this work and to R. M. Hooper for his spirited efforts in the experimental work. The experimental work reported here was supported by Pratt and Whitney Aircraft, Commercial Products Division.

References

1 Langston, L. S., Nice, M. L., and Hooper, R. M., "Three-Dimensional Flow Within a Turbine Cascade Passage," ASME JOURNAL OF ENGINEERING FOR POWER, Vol. 99, Jan. 1977, pp. 21–28.

2 Herzig, H. Z., Hansen, A. G., and Costello, G. R., "A Visualization Study of Secondary Flows in Cascades," NACA Report 1163, 1953.

3 Horlock, J. H., "Cross Flows in Bounded Three-Dimensional Turbulent Boundary Layers," *Journal of Mechanical Engineering Science,* Vol. 15, No. 4, 1973, pp. 274–284.

4 Johnston, J. P., "On the Three-Dimensional Turbulent Boundary Layer Generated by Secondary Flow," ASME *Journal of Basic Engineering,* Vol. 82, 1960, pp. 233–248.

5 Nash, J. F. and Patel, V. C., *Three-Dimensional Turbulent Boundary Layers,* SBC Technical Books, Atlanta, 1972.

6 Klinksiek, W. F. and Pierce, F. J., "Simultaneous Lateral Skewing in a Three-Dimensional Turbulent Layer Flow," ASME *Journal of Basic Engineering,* Vol. 92, 1970, pp. 83–92.

7 Shanebrook, J. R., "An Approximate Method of Treating the Three-Dimensional Incompressible Boundary Layer Equations when Crossflow is Small," Ph.D. Thesis, Syracuse University, Sept. 1965.

8 Eichelbrenner, E. A., "Theoretical Investigation and Control by Measuring Tests on the Behavior of the Three-Dimensional Turbulent Boundary

Layer on an Annular Wing at Various Incidences," Bureau Technique Zborowski, Brunoy, 1963.

9 Johnston, J. P., "Experimental Studies in Three-Dimensional Turbulent Boundary Layers," Report MD-34, Dept. of Mechanical Engineering, Stanford University, July 1976.

10 Wheeler, A. J., and Johnston, J. P., "An Assessment of Three-Dimensional Turbulent Boundary Layer Prediction Methods," ASME *Journal of Fluids Engineering,* Sept. 1973, pp. 415–421.

11 Pratap, V. S., and Spalding, D. B., "Fluid Flow and Heat Transfer in Three-Dimensional Duct Flows," *International Journal of Heat and Mass Transfer, 19,* 1976, pp. 1183–1188.

12 Briley, W. R., and McDonald, H., "Computation of Three-Dimensional Subsonic Flow in Curved Passages," United Aircraft Research Laboratory Report R75-911596-8, 1975.

13 Dodge, P. R., "A Numerical Method for Two and Three-Dimensional Viscous Flows," AIAA Paper No. 76-425, AIAA 9th Plasma and Fluid Dynamics Conf., San Diego, CA, 1976.

14 Ghia, K. N., Ghia, V., and Studerus, C. J., "Analytical Formulation of Three-Dimensional Laminar Viscous Flow through Turbine Cascades using Surface Oriented Coordinates," ASME Paper No. 76-EE-22, 1976.

15 Waterman, W. F., and Tall, W. A., "Measurement and Prediction of 3-D Viscous Flows in Low-Aspect-Ratio Turbine Nozzle," ASME Paper No. 76-GT-73, 1976.

16 Sjolander, S. A., "The Endwall Boundary Layer in an Annular Cascade of Turbine Nozzle Guide Vanes," Tech. Report No. ME/A 75-4, Dept. Mech./Aero. Engr., Carleton University, Ottawa, Canada, Dec. 1975.

17 Carrick, H. B., "Secondary Flow and Losses in Turbine Cascades with Inlet Skew," Ph.D. Thesis, Cambridge University, Oct. 1975.

18 Marchal, Ph., and Sieverding, C. H., "Secondary Flow within Turbine Bladings," AGARD-CPP-214 (Netherlands), *Secondary Flow in Turbomachines,* Mar. 1977.

19 Dring, R. P., "A Momentum-Integral Analysis of the Three-Dimensional Turbine Endwall Boundary Layer," ASME JOURNAL OF ENGINEERING FOR POWER, Vol. 93, Oct. 1971, pp. 386–396.

20 Booth, T. C., "An Analysis of the Turbine Endwall Boundary Layer and Aerodynamic Losses," ASME Paper No. 75-GT-23, Mar. 1975.

21 Barber, T. J., and Langston, L. S., "Three Dimensional Modelling of Cascade Flows," 79-0047 AIAA, Jan. 1979.

22 Stanitz, J. D., Osborn, W. M., and Mizisin, J., "An Experimental Investigation of Secondary Flow in an Accelerating, Rectangular Elbow with 90° of Turning," NACA TN 3015, 1953.

23 Mellor, G. L., and Wood, G. M., "An Axial Compressor End-Wall Boundary Layer Theory," ASME *Journal of Basic Engineering,* June 1971, pp. 300–316.

L. Reid
R. D. Moore
Lewis Research Center,
Cleveland, Ohio

Experimental Study of Low Aspect Ratio Compressor Blading

Introduction

The attainment of improved cycle efficiency for advanced gas tubine engines requires increased pressure ratios for the core compressor. During the past few years NASA-Lewis has been conducting an extensive research program on axial flow compressors with high pressure ratio transonic stages. As a part of this program, four single-stage compressors, that are representative of the inlet stage of a multistage core compressor, were designed and evaluated experimentally.

The stage designs feature two levels of rotor aspect ratio (1.19 and 1.63) and two levels of pressure ratio (1.82 and 2.05). The aerodynamic designs as well as the comparisons of overall performance data for the four stages are given in reference [1]. This paper presents a more detailed investigation of the flow phenomena for the four stages utilizing selected blade element parameters. Comparisons of blade element parameters are presented for the two different aspect ratio configurations at each of the design pressure ratio levels. Blade loading levels (diffusion factors) are compared for the near-stall conditions at all speeds tested. Comparisons are made of loss and diffusion factors (D-factors) over the operating range of incidence angles at several span locations. The axial distributions of rotor tip static pressure are presented for three flow conditions at design speed for all four stages.

Apparatus and Procedure

Test Facility. The compressor stages were tested in the Lewis Research Center single stage compressor test facility, which is described in detail in reference [2]. A schematic diagram of the facility is shown in Fig. 1. Atmospheric air enters the facility at an inlet located on the roof of the building and flows through the flow-measuring orifice and into the plenum chamber upstream of the test stage. The air then passes through the experimental compressor stage into the collector and is exhausted to the atmospheric exhaust system. The rotor is driven by a variable-speed electric motor through a gearbox.

Test Compressors. The detailed aerodynamic and mechanical designs of the compressors used in this investigation are presented in reference [1] and thus only a brief description will be presented herein. The basic designs feature two levels of stage pressure ratio, two levels of rotor aspect ratio, and two levels of stator aspect ratio. The designs are summarized in Table 1. Stages 35 and 36, having a design pressure ratio of 1.82, were designed for rotor blade aspect ratios of 1.19 and 1.63, respectively. Similarly, stages 37 and 38, having a design pressure ratio of 2.05, also had rotor blade aspect ratios of 1.19 and 1.63, respectively. Stator vane aspect ratios were 1.26 and 1.78. All of the rotor and stator blades have multiple circular arc airfoils. Careful positioning of the blade rows allowed all four stages to be tested with the same flow path geometry (Fig. 2). The design specific flow (100.1 kg/s/cm^2) and rotor tip speed (455.0 m/s) were the same for all four stages. These are relatively high values of mass flow and tip speed for core type stages.

Test Procedure. The stage survey data were taken over a range of flows for speeds from 50 to 100 percent of design speed. For each flow, data were recorded at nine radial positions upstream (station 1) and downstream (station 3) of the test stage. At station 3, the instrumentation was also circumferentially traversed to nine positions across the stator gap. The axial locations of the survey stations are shown in Fig. 2. The survey measurements consisted of total pressure, static pressure, total temperature, and flow angle. Flow was measured with a thin plate orifice. A more complete description of the survey instrumentation and test procedure is given in reference [1].

The estimated errors in the data, based on inherent accuracies of the instrumentation and recording system, are as follows:

Flow, kg/s	±0.3
Rotative speed, rpm	±30
Flow angle, deg	±1.0
Temperature, K	±0.6
Rotor-inlet (station 1) total pressure, N/cm^2	±0.01
Rotor-inlet (station 1) static pressure, N/cm^2	±0.03
Stator-outlet (station 3) total pressure, N/cm^2	±0.17
Stator-outlet (station 3) static pressure, N/cm^2	±0.10

Calculation Procedure. Because of the close spacing between the rotor and stator, no instrumentation could be used at station 2 (see Fig. 2). The values of pressure, temperature, and flow angle at this station were obtained as follows: At each radial survey position, total pressure and total temperature were translated along design streamline from station 3. The circumferentially mass-averaged total temperatures from station 3 were used as the total temperatures at station 2. The arithmetic mean of the three highest total pressure values from the circumferential distributions at station 3 were used as the total pressures at station 2. The radial distributions of static pressure and flow angle were calculated based on continuity of mass flow and radial equilibrium. Measured airflow and rotative speed were inputs. Design values of streamline curvature and blockages were also used in the calculations.

All data are corrected to standard day conditions based on the rotor inlet conditions. Overall total pressure ratios and total temperature ratios are based on an energy average of the pressures and temperatures obtained from the calibrated survey instrumentation. Blade element data are translated along design streamlines to the blade leading and trailing edges. Details of the calculation procedure are given in reference [1].

Results and Discussion

An assessment of the effects of blade aspect ratio is made by comparing some of the basic flow phenomenon for the two aspect ratio configurations for each level of design pressure ratio. The overall performance comparisons are presented to show the overall effects of blade aspect ratio on the performance characteristics. Radial dis-

Contributed by the Gas Turbine Division and presented at The Gas Turbine Conference and Products Show, New Orleans, La., March 10–13, 1980 of THE AMERICAN SOCIETY OF MECHANICAL ENGINEERS. Manuscript received at ASME Headquarters December 3, 1979. Paper No. 80-GT-6.

Table 1 Design overall performance parameters for stages 35, 36, 37 and 38

Parameters	Stage			
	35	36	37	38
Rotor total pressure ratio	1.865	1.863	2.106	2.105
Stage total pressure ratio	1.820	1.820	2.050	2.050
Rotor total temperature ratio	1.225	1.227	1.270	1.269
Stage total temperature ratio	1.225	1.227	1.270	1.269
Rotor adiabatic efficiency	0.865	0.858	0.877	0.878
Stage adiabatic efficiency	0.828	0.822	0.842	0.844
Rotor polytropic efficiency	0.877	0.870	0.889	0.890
Stage polytropic efficiency	0.842	0.837	0.857	0.859
Rotor head rise coefficient	0.273	0.272	0.333	0.331
Stage head rise coefficient	0.262	0.261	0.319	0.318
Flow coefficient	0.451	0.447	0.453	0.448
Weight flow per unit frontal area	100.808	100.464	100.950	100.525
Weight flow per unit annulus area	199.989	198.640	200.549	198.877
Weight flow	20.188	20.188	20.188	20.188
RPW	17 188.700	17 188.700	17 185.700	17 188.700
Tip speed	454.456	455.233	454.136	455.096
Hub-tip radius ratio	0.70	0.70	0.70	0.70
Rotor aspect ratio	1.19	1.63	1.19	1.63
Stator aspect ratio	1.26	1.78	1.26	1.77
Number of rotor blades	36.6	48.0	36.0	48.0
Number of stator blades	46.0	62.0	46.0	62.0

tributions of performance parameters are compared for the peak efficiency conditions at design speed to show how the difference in overall performance manifests itself over the blade span. Rotor tip and stator hub diffusion factors for the four stages are compared for the near-stall conditions over the entire speed range. This comparison is made in an attempt to determine which blade row is controlling the flow range and to assess the effects of blade aspect ratio on blade loading limits. Blade element performance comparisons are made to assess the effects of blade aspect ratio on typical blade element parameters over a range of flow conditions. Axial distribution of rotor tip static pressures are presented at design speed to assess the effect of blade aspect ratio on end wall flow conditions when shocks are present.

Overall Performance Comparisons. The effects of aspect ratio on overall performance are presented in Fig. 3. For both design pressure ratio levels, the overall rotor and stage performances for the lower aspect ratio configurations are substantially better than those for the higher aspect ratio configurations. The lower aspect ratio configurations achieved a higher peak pressure ratio and efficiency and a larger flow range over the range of speeds tested. The largest increase in flow range occurred at the design speed.

For the higher design pressure ratio configurations the peak rotor efficiency, at design speed, for the lower aspect ratio configuration (stage 37) is about 2.5 points higher than that for the higher aspect ratio configuration (Fig. 3(a)). However, the difference in stage efficiency is about one point.

Similar trends are shown for the lower design pressure ratio configurations (Fig. 3(b)). At design speed, the peak efficiency for both rotor and stage is approximately 2 points higher for the lower aspect ratio configuration.

The highest overall rotor and stage efficiencies were obtained with the lower aspect ratio higher-pressure configuration (stage 37) and they occurred at 90 percent design speed. The maximum rotor and stage efficiencies are 91.6 percent and 89.3 percent, respectively. The corresponding pressure ratios are 1.775 and 1.751.

The peak efficiencies at design speed along with the corresponding pressure ratios for rotor and stage for all four configurations are summarized in Table 2. Also shown are the values of stall margin based on conditions at peak efficiency and stall.

Radial Distributions of Performance Parameters. Comparisons of the radial distributions of rotor performance parameters, for the peak rotor efficiency at design speed, are presented in Fig. 4. Some

Nomenclature

D = diffusion factor
i_{ss} = suction surface incidence angle, angle between inlet air direction and line tangent to blade suction surface at the leading edge, deg
K_{ss} = angle between a line tangent to blade suction surface and meridional direction, deg
M = Mach number
P = total pressure, N/cm^2
p = static pressure, N/cm^2
r = spanwise radius in meridional plane, cm
T = total temperature, K
W = mass flow, kg/s
V = air velocity, m/s
β = air angle, angle between air velocity and meridional direction, deg
β'_c = relative meridional flow angle based on cone angle, deg
γ = ratio of specific heats, 1.40
δ = ratio of pressure to standard day pressure
η = efficiency
θ = ratio of total temperature to standard day temperature
σ = solidity, ratio of chord to blade spacing
$\bar{\omega}$ = total loss coefficient
$\bar{\omega}_p$ = total loss parameter

Subscripts

ad = adiabatic
id = ideal
le = leading edge
te = trailing edge
θ = tangential direction
1 = instrument station upstream of rotor
2 = calculation station downstream of rotor
3 = instrument station downstream of stator

Superscript

′ = relative to blade

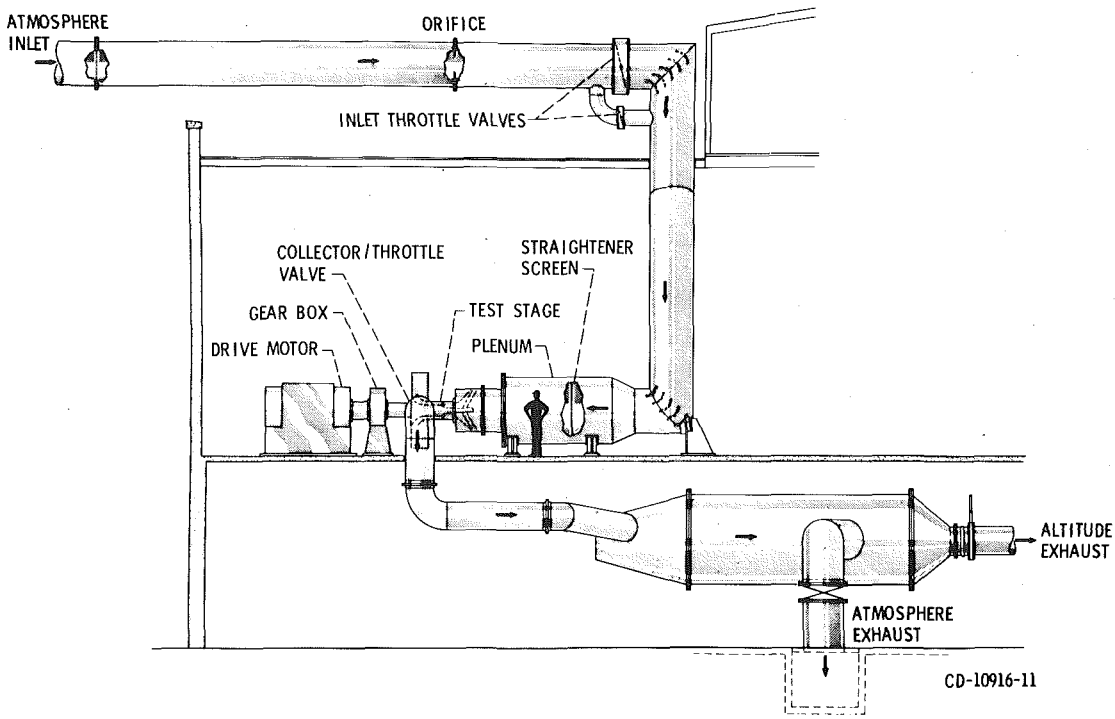

Fig. 1 Compressor test facility

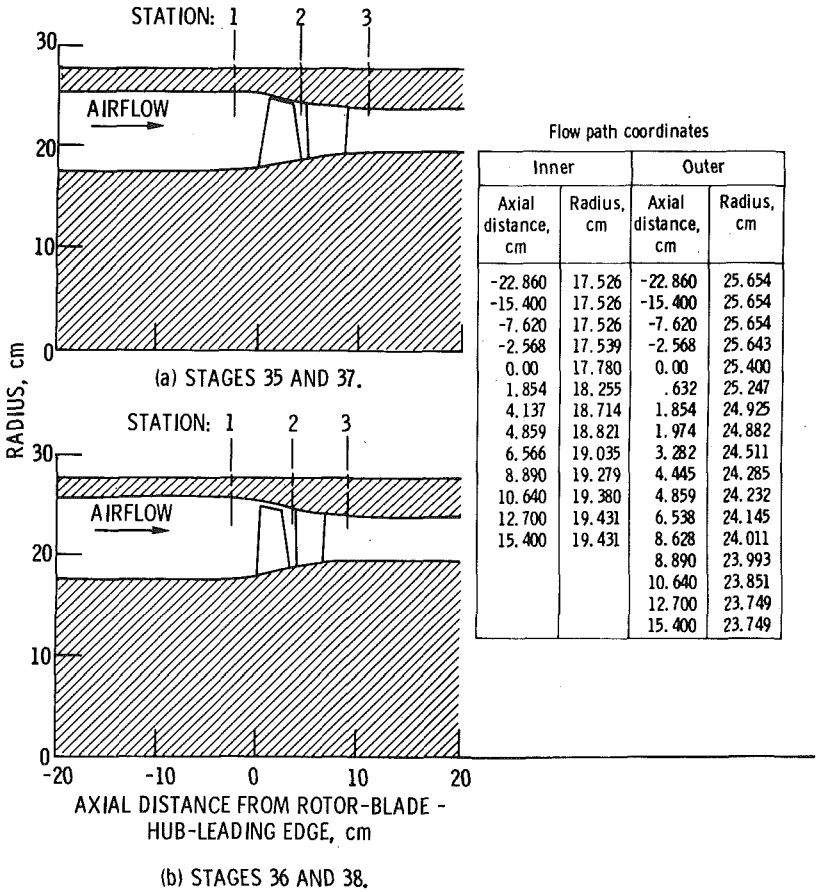

Flow path coordinates

Inner		Outer	
Axial distance, cm	Radius, cm	Axial distance, cm	Radius, cm
-22.860	17.526	-22.860	25.654
-15.400	17.526	-15.400	25.654
-7.620	17.526	-7.620	25.654
-2.568	17.539	-2.568	25.643
0.00	17.780	0.00	25.400
1.854	18.255	.632	25.247
4.137	18.714	1.854	24.925
4.859	18.821	1.974	24.882
6.566	19.035	3.282	24.511
8.890	19.279	4.445	24.285
10.640	19.380	4.859	24.232
12.700	19.431	6.538	24.145
15.400	19.431	8.628	24.011
		8.890	23.993
		10.640	23.851
		12.700	23.749
		15.400	23.749

Fig. 2 Flow path geometry

general trends common to both aspect ratio configurations, are noted. The radial distributions of total pressure ratio are similar for all four rotors. The highest pressure ratio and efficiency occurred in the hub region. For both levels of design pressure ratio, the lower aspect ratio rotors (35 and 37) achieved higher efficiencies and higher pressure ratios over practically the entire blade span. The radial distribution of rotor inlet relative Mach number is practically identical for all four configurations. The rotor inlet relative Mach numbers are supersonic over the entire span and the exit relative Mach numbers (not shown) are subsonic over the entire blade span. It is apparent that the distributions of efficiency and total loss parameters are strongly influenced by the shock losses.

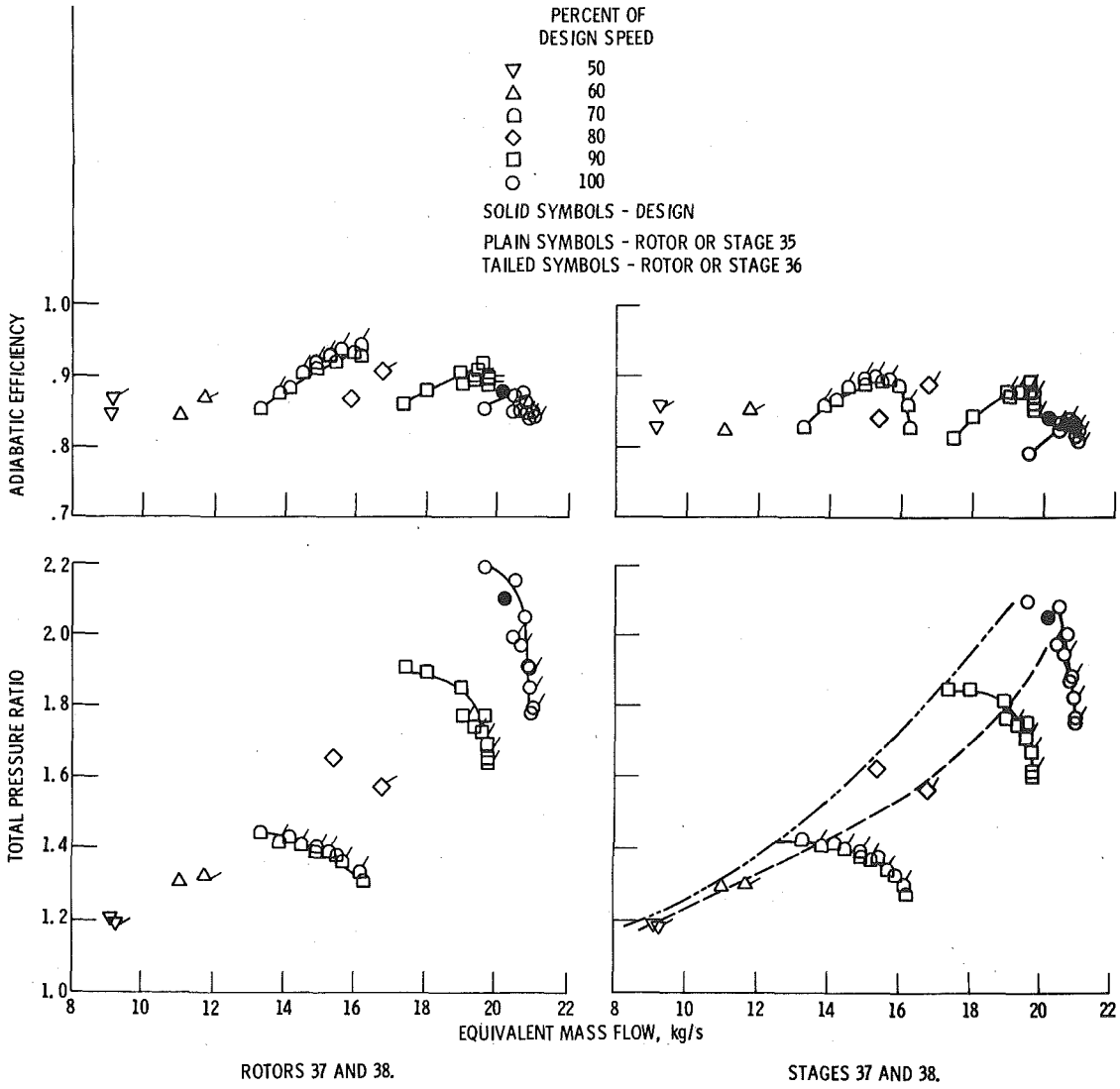

Fig. 3(*a*) Design stage pressure ratio of 2.05

In comparing the lower design pressure ratio configurations (Fig. 4(*a*)), the efficiency difference is most pronounced in the region from 30 to 85 percent span. There is a noticeable inflection in the efficiency distributions at the 50-percent span location for both rotors. This could be a result of large shock losses associated with the high inlet relative Mach (1.4) and high blade loading for this spanwise location. For the lower aspect ratio rotor (rotor 35), the efficiency varies from about 0.80 in the tip region to 0.927 at the 85-percent span location. For the higher aspect ratio rotor (rotor 36), the efficiency varies from about 0.79 in the tip region to 0.902 at the 85-percent span location. In comparing the higher design pressure ratio rotors (rotors 37 and 38), the efficiency for the lower aspect ratio rotor (rotor 37) varies from about 0.77 in the tip region to 0.938 at the 85-percent span location. For the higher aspect ratio rotor, the efficiency varies from 0.76 in the tip region to 0.904 at the 85-percent span location.

Effects of Aspect Ratio on Stall D-Factor. Although the diffusion factor (D-factor) was developed to represent blade loading in a flow field that is totally subsonic, it is commonly used to correlate data from blade rows that operate in a transonic flow field. For flows with shocks, it is recognized that the diffusion factor is questionable for expressing local diffusion (blade loading) on the blade surfaces. However, D-factor has been used with some success in correlating losses and stall margin for transonic blade rows. This indicates that comparative results utilizing D-factor correlations for transonic blade rows can be useful when applied in a consistent manner. This section shows, on a relative basis, how the D-factors for the near-stall conditions vary with blade aspect ratio.

Table 2 Summary of overall performance

Stage number	Rotor aspect ratio	Rotor peak efficiency	Stage peak efficiency	Rotor pressure ratio	Stage pressure ratio	Stall margin
37	1.19	0.876	0.840	2.056	2.000	10
35	1.19	.872	.845	1.875	1.842	21
36	1.63	.852	.821	1.766	1.730	11
38	1.63	.849	.831	1.969	1.944	0

The diffusion factor and inlet relative Mach number are plotted in Fig. 5 as a function of percent design speed at the near-stall condition for all stages. Data are shown for the rotor tip (10 percent span) and stator hub (90 percent span). Considering that the rotor tip diffusion factors are substantially higher than the corresponding stator hub diffusion factors and that the maximum stator hub Mach number is about 0.83, it is reasonable to assume that the flow range is limited by the flow conditions in the rotor tip region for all four stages. For the rotor tip (Fig. 5(*a*)), the inlet relative Mach numbers at the near-stall conditions are practically the same for all four rotors. However, the rotor diffusion factors at the near-stall conditions show that the stalling D-factors are substantially larger for the lower aspect ratio rotors (rotors 35 and 37) than those for the higher aspect ratio configurations at all speeds with a possible exception of the 50-percent speed. For all rotors, the largest value of diffusion factor at near-stall

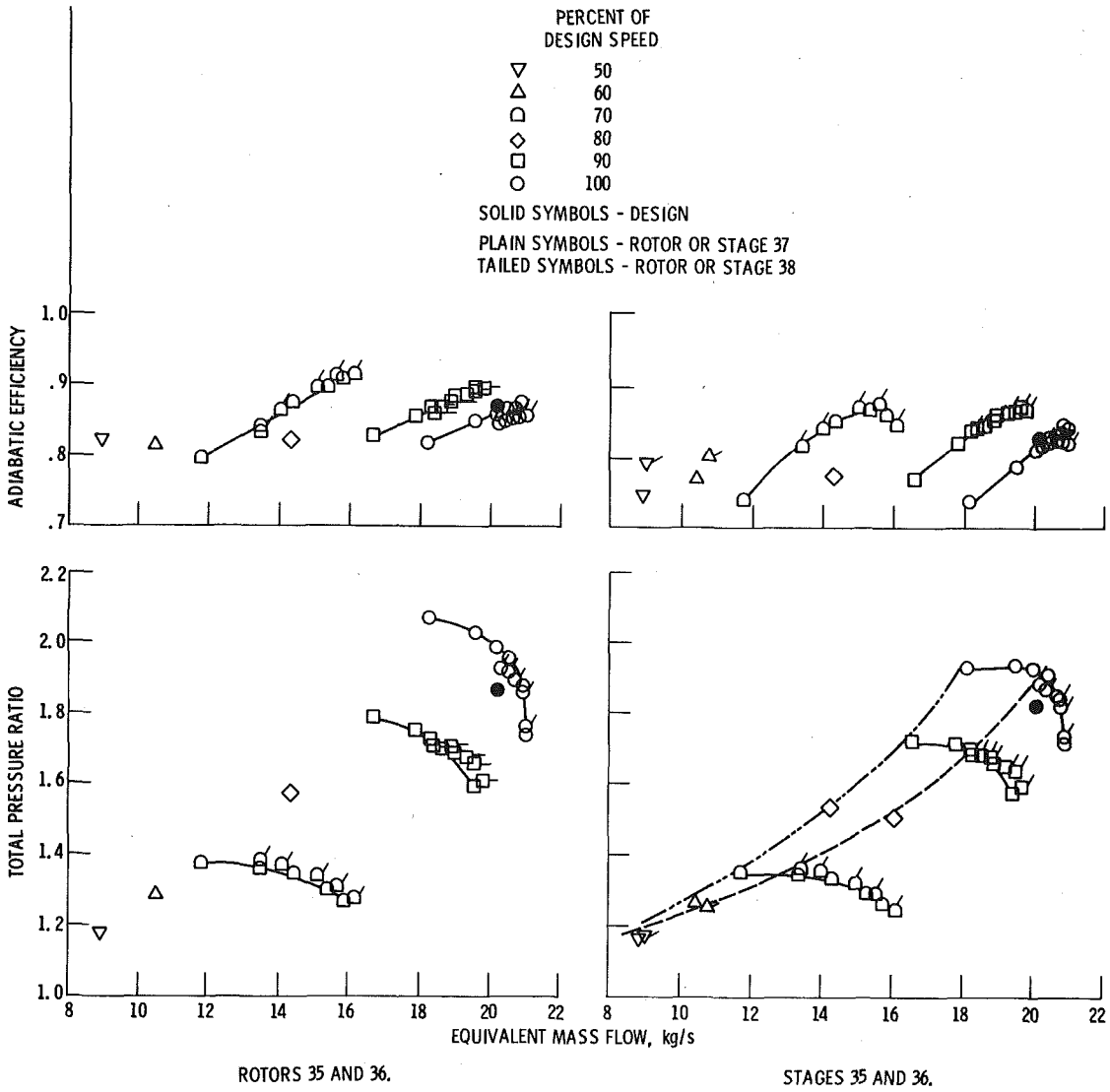

Fig. 3(*b*) Design stage pressure ratio of 1.82

Fig. 3 Effects of blade aspect ratio on overall performance

conditions occurred at design speed. The higher design pressure ratio low aspect ratio rotor (rotor 37) had the highest stall diffusion factor of 0.645. This value of diffusion factor is higher than that for other inhouse higher aspect ratio rotors with comparable inlet relative Mach numbers.

The diffusion factor and inlet Mach number at the stator hub (90 percent span from tip) are plotted as a function of design speed in Fig. 5(*b*). The trends of Mach number and *D*-factor variations with percent design speed are similar to those for the rotor. However, the diffusion factor values are not considered to be stall values for these stators. It is of interest to note, however, that at an inlet Mach number of approximately 0.83 stator 37 (lower aspect ratio) operated at a diffusion factor of approximately 0.575. Based on NASA experience, this is an unusually high value of stator hub diffusion factor for this level of inlet Mach number.

Blade Element Performance Comparisons. Comparisons of rotor blade element performance parameters for the high and low aspect ratio configurations and for each level of design pressure ratio are presented in Fig. 6. Data are presented for the 10-, 50-, and 90-percent span locations at design speed. Total loss parameter and diffusion factor are plotted as a function of suction surface incidence angles. The lower aspect ratio rotors operated over a wider range of incidence angles than the higher aspect ratio rotors for all three blade elements. For the lower aspect ratio rotors, the 10- and 50-percent elements operated to higher diffusion factors levels than the higher aspect ratio rotors. For the 10- and 50-percent span, the blade elements for the low and high aspect ratio rotors operated along the same incidence angle loss characteristics.

Axial Distributions of Rotor Tip Static Pressure. For rotor blade rows operating in a transonic flow environment, the axial distribution of the time-averaged static pressures over the rotor tips is strongly influenced by the shock patterns within the blade passage. In an attempt to qualitatively relate these axial distributions of static pressure to the shock patterns within the blade, data from another transonic rotor are presented [3]. These data include both the axial distributions of rotor tip static pressures and shock patterns within the blade passage. The shock patterns were obtained from intrablade flow field measurements made with a Laser Anemometer (LA) system. The blade passage shock patterns along with the axial distributions of rotor tip static pressure are presented in Fig. 7 for the maximum flow and near-stall conditions. The shock patterns derived from the LA system measurements are for the 15-percent span (from the tip) location. The axial distributions of static pressures measured on the casing over the rotor tips are ratioed to rotor inlet total pressure and plotted as a function of percent of rotor projected chord. At the maximum flow condition (Fig. 7(*a*)), there is a weak shock at the blade

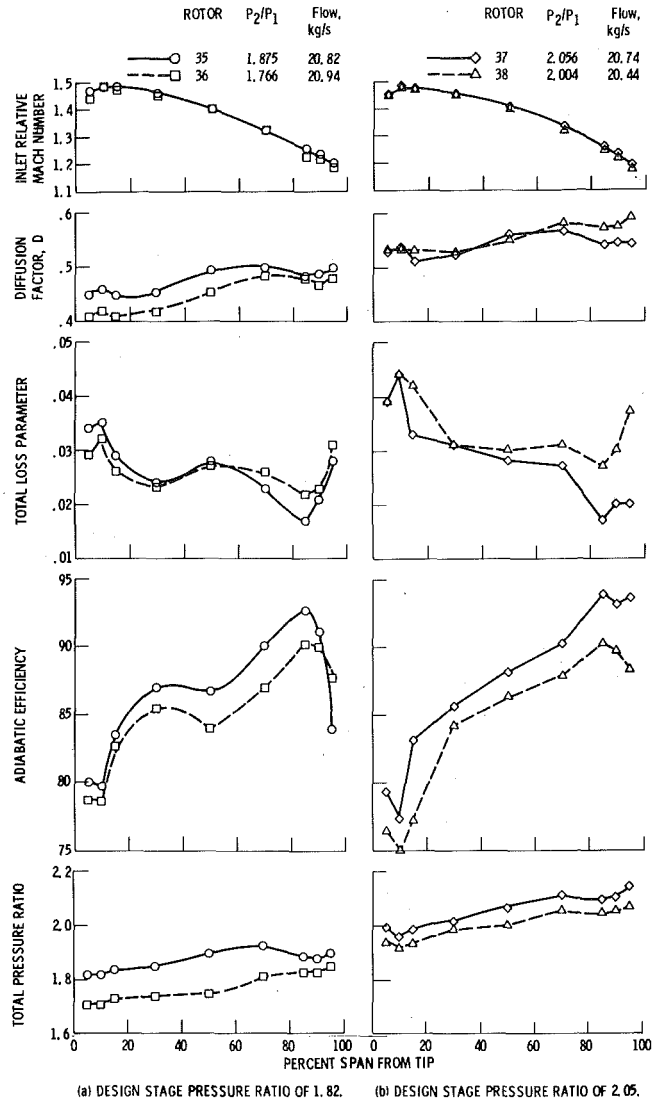

Fig. 4 Radial distribution of performance parameters

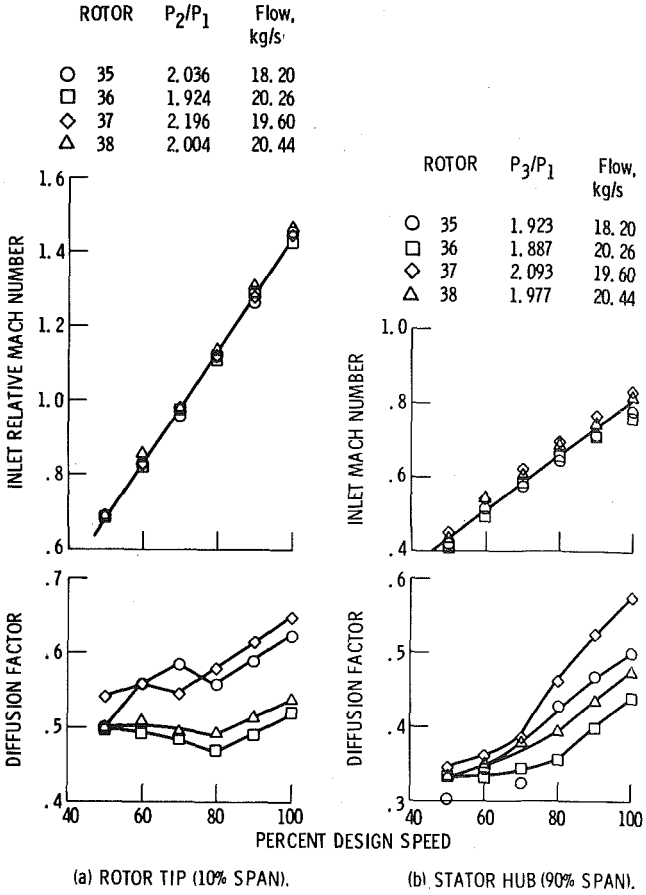

Fig. 5 Diffusion factor and inlet Mach numbers at near-stall conditions

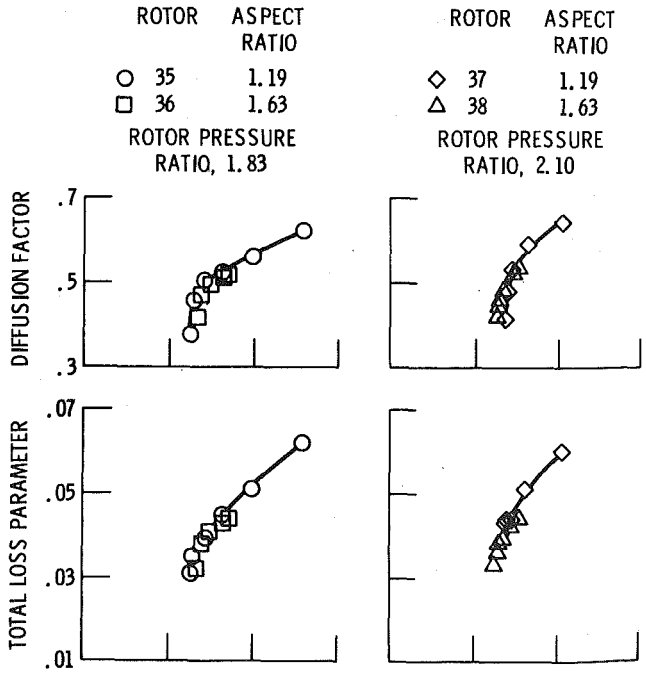

Fig. 6(*a*) Ten percent span from tip

entrance region and a strong shock at the exit of the blade passage. The static pressure gradients in the front and rear portions of the blades are indicative of these passage shock strengths. For the near-stall condition (Fig. 7(*b*)) there is a strong passage shock at the blade entrance region. The strength of the shock is represented by the steep static pressure gradient in the front portion of the blade. However, just downstream of the shock the gradient decreases. These data provide a qualitative assessment of how the axial distribution of time-averaged rotor tip static pressure is influenced by the shock patterns within the blade passage. Based on this assessment the shock strengths will be inferred from the axial distributions of rotor tip static pressure for the rotors evaluated in the low aspect ratio study.

The axial distributions of rotor tip static pressure are presented in Fig. 8 for all four rotor configurations. Data are presented at design speed for three flow rates; maximum flow, peak efficiency, and near-stall conditions. These curves (Fig. 8) show quite similar static pressure gradients for rotors with the same aspect ratio even though the blade rows are designed for different total pressure ratios. This implies that the shock patterns for the low aspect ratio rotors (rotors 35 and 37) are similar and the shock patterns for the higher aspect ratio rotors (rotors 36 and 38) are similar.

For the lower aspect ratio rotors, as the back pressure is increased (lower flow), there is a substantial increase in the static pressure gradient over the front portion of the blade. This indicates that the strength of the shock is increasing and the shock is moving forward in the blade passage. The smooth and continuous static pressure rise on the rear portion of the blade indicates good subsonic diffusion even behind a strong shock.

For the higher aspect ratio rotors, as the back pressure is increased (lower flow), the increase in static pressure gradient over the front portion of the blade is small. However, the static pressure gradients in the 50- to 60-percent chord region increases very rapidly, and then

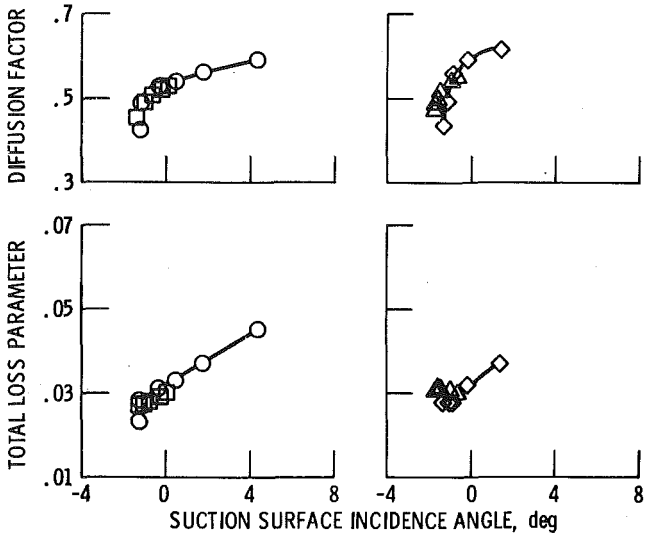

Fig. 6(*b*) Fifty percent span from tip

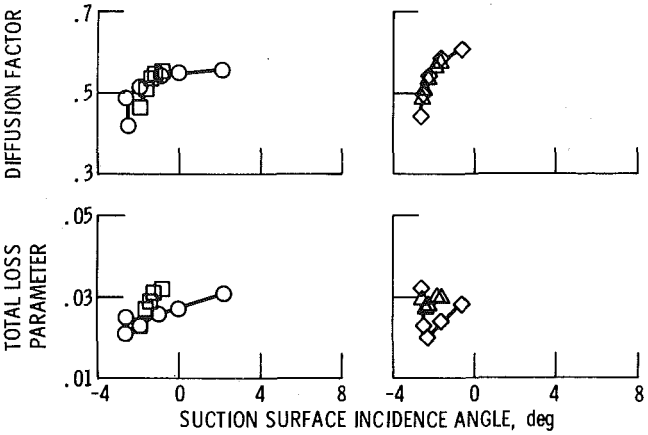

Fig. 6(*c*) Ninety percent span from tip

Fig. 6 Effects of blade aspect ratio on rotor blade element performance parameters

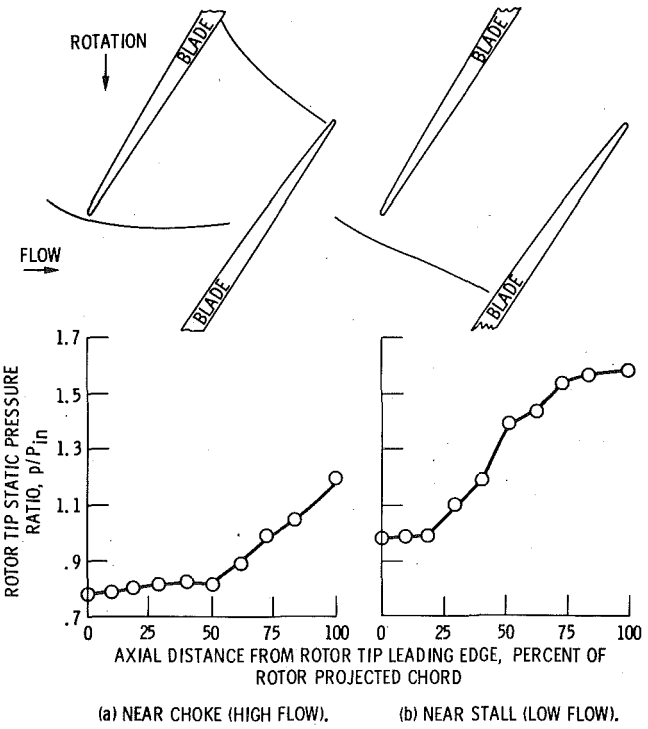

(a) NEAR CHOKE (HIGH FLOW). (b) NEAR STALL (LOW FLOW).

Fig. 7 Axial distributions of rotor tip static pressures and rotor shock patterns; rotor 33, design speed

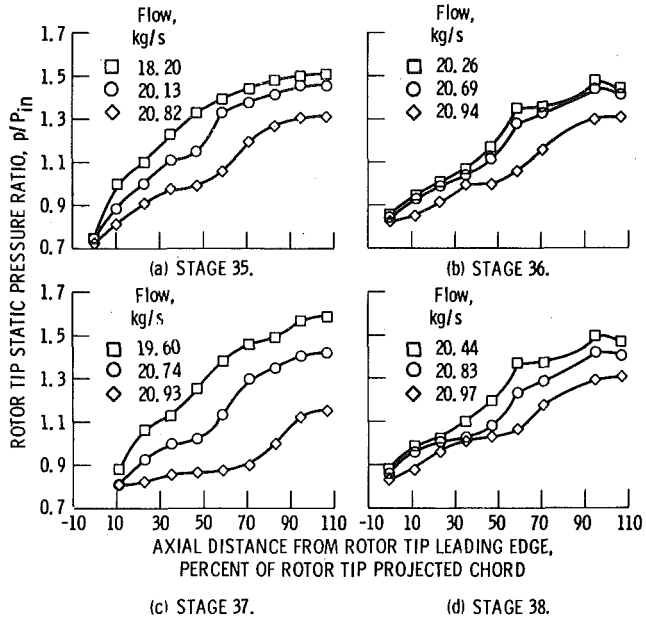

(a) STAGE 35. (b) STAGE 36.

(c) STAGE 37. (d) STAGE 38.

Fig. 8 Axial distribution of rotor tip static pressures, design speed

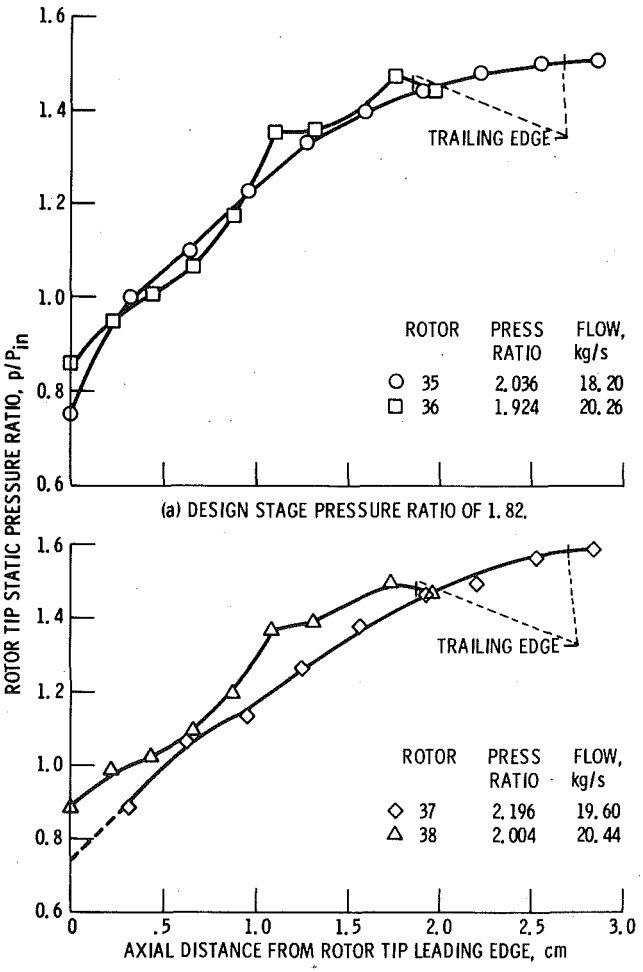

(b) DESIGN STAGE PRESSURE RATIO, 2.05.

Fig. 9 Axial distribution of rotor tip static pressure, near-stall condition design speed

drops off substantially just downstream of the 60-percent chord location. This indicates a strong shock and poor diffusion caused by flow separation and recirculation just downstream of the shock.

A comparison of the axial distribution of rotor tip static pressures for the near-stall conditions is presented in Fig. 9 for the low and high aspect ratio configurations. The comparison shows that the higher aspect ratio rotors have steeper static pressure gradients than the lower aspect ratio configurations. This indicates that it is the steeper static pressure gradient, caused by the shock patterns, that is responsible for the relative poor flow range for the higher aspect ratio configurations.

Remarks

Benefits of lower aspect ratio blading for achieving good efficiency at higher loading levels have generally been demonstrated with stages designed for subsonic flows. In this study the application of low aspect ratio blading to rotors with high loading and high supersonic inlet relative Mach numbers over the entire blade span was investigated. The good efficiency and relatively higher flow range achieved with the lower aspect ratio configuration demonstrates that low aspect ratio blading is highly beneficial for transonic blade rows. For advanced high pressure multistage core compressor the inlet stages must operate at high loading level and high inlet relative Mach numbers. There has been a question whether sufficient flow range can be obtained with stages of this type such that they would be suitable for multistage application. Results of this study indicate that through the use of low aspect ratio blading, high Mach number, highly loaded stages can achieve a performance level suitable for multistage compressor applications.

Summary of Results

This paper presents a study of low aspect blading for inlet stages of a high pressure ratio, high-speed core compressor. The basic overall design variables were stage pressure ratio and blade aspect ratio. These four stages represent two levels of total pressure ratio (1.82 and 2.05), two levels of rotor blade aspect ratio (1.19 and 1.63) and two levels of stator vane aspect ratios (1.26 and 1.78). Comparisons of overall performance, radial distributions of performance parameters, diffusion factors at the near-stall conditions, blade element data, and axial distribution of rotor tip static pressures have yielded the following results:

1 Higher peak pressure ratio, high stage and rotor efficiencies and greater stall margin were obtained with the lower aspect ratio blading.

2 The lower aspect ratio blading showed improved performance over the entire blade span.

3 The lower aspect ratio rotors operated at higher diffusion factors and higher incidence angles over the entire blade span.

4 Better subsonic diffusion downstream of the passage shock was obtained in the lower aspect ratio rotors.

APPENDIX

Suction surface incidence angle:

$$i_{ss} = (\beta_c')_{le} - (K_{ss})_{le}$$

Diffusion factor:

$$D = 1 + \frac{V_{te}'}{V_{le}'} + \left|\frac{rV_\theta)_{te} - (rV_\theta)_{le}}{(r_{te} + r_{le})\,(V_\cdot)_{le}}\right|$$

Total loss coefficient:

$$\bar{\omega} = \frac{(P_{id}')_{te} - (P')_{te}}{(P')_{le} - (P)_{le}}$$

Total loss parameter:

$$\bar{\omega}_p = \frac{\bar{\omega}\cos(\beta')_{te}}{2\sigma}$$

Adiabatic efficiency:

$$\eta_{ad} = \frac{\left[\frac{(P)_{te}}{(P)_{le}}\right]^{\gamma-1/\gamma} - 1}{\frac{(T)_{te}}{(T)_{le}} - 1}$$

Equivalent mass flow:

$$\frac{W\sqrt{\theta}}{\delta}$$

Stall margin:

$$SM = \left[\frac{(P_3/P_1)_{\text{stall}}\left(\frac{W\sqrt{\theta}}{\delta}\right)_{\text{ref}}}{(P_3/P_1)_{\text{ref}}\left(\frac{W\sqrt{\theta}}{\delta}\right)_{\text{stall}}} - 1\right] \times 100$$

References

1 Reid, L., and Moore, R. D., "Design and Overall Performance of Four Highly Loaded, High-Speed Inlet Stages for an Advanced High-Pressure-Ratio Core Compressor," NASA TP-1337, 1978.

2 Urasek, D. C., and Janetzke, D. C., "Performance of Tandem-Bladed Transonic Compressor Rotor with Rotor Tip Speed of 1375 Feet Per Second," NASA TM X-2484, 1972.

3 Powell, A. J., Strazisar, C. J., and Seasholtz, R. G., "Efficient Laser Anemometer for Intrarotor Flow Mapping in Turbomachinery," Paper to be presented at the conference.

P. W. McDonald
C. R. Bolt
Pratt and Whitney Aircraft,
East Hartford, Conn 06108

R. J. Dunker
H. B. Weyer
DFVLR, Institut fur Antriebstechnik,
5000 Cologne 90,
West Germany

A Comparison between Measured and Computed Flow Fields in a Transonic Compressor Rotor

The flow field within the rotor of a transonic axial compressor has been computed and compared to measurements obtained with an advanced laser velocimeter. The compressor was designed for a total pressure ratio of 1.51 at a relative tip Mach number of 1.4. The comparisons are made at 100 percent design speed (20,260 RPM) with pressure ratios corresponding to peak efficiency, near surge, and wide open discharge operating conditions. The computational procedure iterates between a blade-to-blade calculation and an intra-blade through-flow calculation. Calculated Mach number contours, surface pressure distributions, and exit total pressure profiles are in agreement with the experimental data demonstrating the usefulness of quasi three-dimensional calculations in compressor design.

Introduction

Continued improvement of aerodynamic efficiency in gas turbine fans and high Mach number compressors requires an increased understanding of the aerodynamic losses in transonic rotating flow fields. These losses include (1) the direct effects of the shock structure in the primary flow field, (2) viscous shear, shock interaction and mixing losses on the airfoil and endwall surfaces and (3) tip clearance and endwall scraping losses. A better understanding of these losses can be achieved through the continuing development of experimental techniques and computational models. The experimental determination of the detailed flow field ahead of, within and downstream of a transonic fan or compressor is required to verify computational models of the flow field which compute the intrinsic losses of the shock structure. The computational flow field can then be used to develop models for the remaining losses which can also be verified by experimental data. The development of these experimental techniques and computational models are important objectives and the value of each is dependent upon accomplishment of the others.

The need for experimental transonic compressor flow field data has been met, in part, by the efforts of DFVLR in Cologne, West Germany. The Laser-2-Focus Velocimeter (L2F) data from a transonic compressor rotor have been described in detail in references [1–3]. Laser Velocimetry measurements have also been described by Wisler in [4]. The data acquired by DFVLR have been reduced to blade-to-blade Mach number contours at various spanwise locations. These data have been reported for various speed and pressure ratio conditions. A simultaneous effort at Pratt & Whitney Aircraft has led to a working computational quasi-3D procedure which is capable of accurately predicting these complex three-dimensional transonic flow fields. This quasi-3D procedure consists of an iteration between (1) a set of time-marching calculations of the supersonic and/or subsonic flow fields on conical surfaces between airfoils, and (2) an axisymmetric streamline calculation. Solutions from this procedure in the form of blade-to-blade Mach number contours and pressure distributions will be compared to the DFVLR data at 100 percent design speed for three pressure ratio conditions. The development of loss models based on the L2F data and flow field computations is a continuing effort at both DFVLR and Pratt and Whitney Aircraft.

Experimental Method

The test compressor which has been investigated using advanced measuring techniques is a transonic axial single-stage machine, designed for a total pressure ratio of 1.51 and a mass flow of 17.3 kg/s at 20,260 rpm. The rotor consists of 28 blades with an inlet tip diameter of 399 mm and a hub-to-tip radius ratio of 0.5. The rotor blades are composed of MCA-profiles [1].

In order to measure the mean average of the fluctuating total pressure downstream of the rotor, a new hydraulic probe has been developed and used which avoids the integrating errors produced by oridinary pneumatic Pitot probes. Correct average total pressures are absolutely needed to identify the mean axisymmetric flow for detailed performance calculations [5].

The measurement of the velocity vectors ahead, within, and downstream of the fast moving rotor blade channels was performed using the L2F-velocimeter. This technique is quite different from the well known Doppler velocimeter insofar as the fringe pattern within the probe volume is replaced by two discrete parallel light beams forming a light gage. This permits the concentration of the available laser light to a very high intensity in the measuring volume and leads to favorable signal-to-noise ratios even in unfavorable test conditions such as those in a turbomachine. In order to carry out measurements within the channels of turbomachine blades, a synchronizing trigger unit (controlled by a signal from the rotor) times the laser beam release to illuminate preselected points in successive blade channels. The circumferential position of those points is controlled by an adjustable time delay unit. Axial and radial position of the probe volume can easily be changed by a remotely-controlled displacement of the L2F apparatus. Fundamentals and more details on the technique are given by Schodl in references [2] and [3].

Contributed by the Gas Turbine Division and presented at the Gas Turbine Conference and Products Show, New Orleans, La., March 10–13 of THE AMERICAN SOCIETY OF MECHANICAL ENGINEERS. Manuscript received at ASME Headquarters December 3, 1979. Paper No. 80-GT-7.

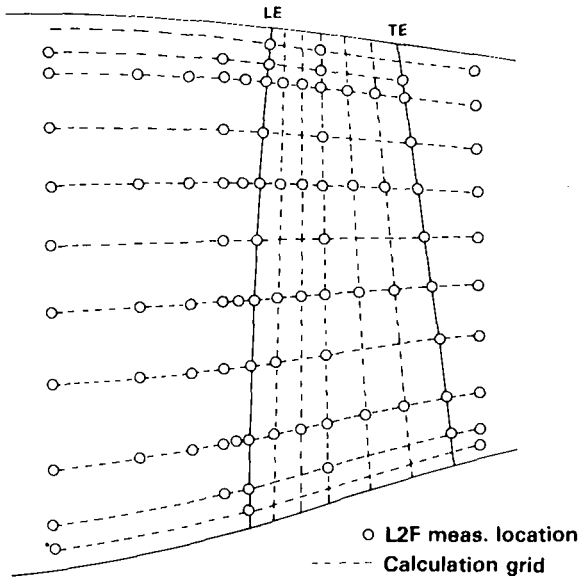

Fig. 1 Calculation grid and L2F measurement locations

For the compressor tests, up to 15 circumferential measuring positions were chosen across the blade gap, giving adequate flow field definition to localize the shock wave system and to analyze the rotor blade wakes in detail. The axial and radial locations of the selected measuring points are shown in Fig. 1.

Computational Method

The computational flow fields which will be presented were obtained by iteration between an axisymmetric through-flow calculation and a two-dimensional transonic blade-to-blade calculation. The combination will be referred to as the quasi-3D calculation. The method is being applied at Pratt & Whitney Aircraft in the current design and analysis process.

The basis of the quasi-3D calculation is that the input of each of the two computer programs can be obtained from the output of the other as shown in Fig. 2. A third element, an interpolation of known airfoil coordinates, must be included in the iteration when the streamlines move to a significantly different radial position or cone angle. The boundary conditions were imposed in both flow field solutions over a 9 radial X 9 axial computational grid (Fig. 1) which corresponds to the L2F measurement locations. Convergence occurs in approximately five cycles of the iterative procedure.

The through flow calculation which has been used in the quasi-3D procedure is the standard compressor design and analysis program which has been developed at Pratt and Whitney by H. K. Carr. This program defines an axisymmetric flow at the grid points given in Fig. 1, based upon the boundary conditions imposed at these locations. The flow properties chosen as input to the through flow program at intrablade stations are spanwise distributions of: (1) relative total pressure recovery, (2) angular momentum, and (3) total blockage (endwall blockage and profile blockage). Flow properties on streamlines in the through flow calculations are obtained by interpolating these input flow properties. The resulting flow field provides the required boundary conditions for the blade-to-blade analysis. The initial through flow calculation uses estimated values of RCu, recovery and total blockage that approximate the overall performance of the rotor.

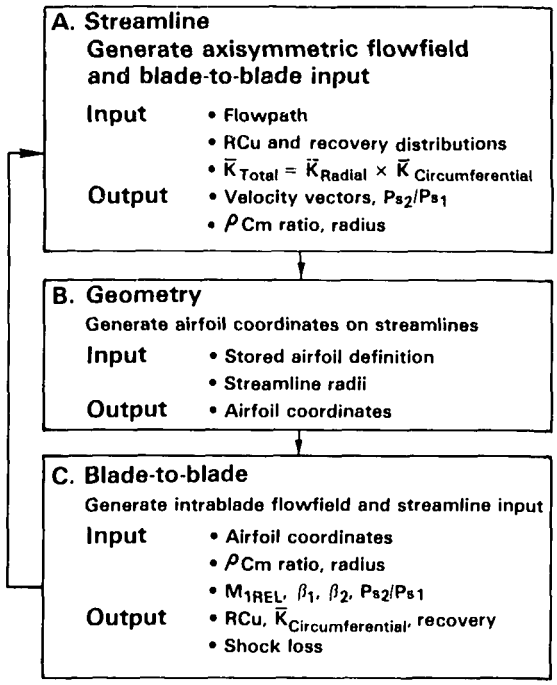

Fig. 2 Quasi-3D iteration

The blade-to-blade transonic flow calculation which has been used is essentially that which has been defined in reference [6]. The Time Marching Finite Area Program has been modified such that the pressure is determined from the relative total temperature, $P = f(\rho, U, V, To(r))$. The original formulation used an isentropic relationship between the pressure and density. The capabilities of modeling radius change, nonlinear streamtube height variation, and surface viscous losses have also been added. The blade-to-blade transonic flow calculation uses input data from the through flow calculation in the form of inlet Mach number and angle, exit angle, static pressure ratio, cone angle, and streamtube height axial distribution. The blade-to-blade solution is used to define the total recovery, RCu, and profile blockage distributions for input into the through flow calculation.

The total pressure recoveries shown in Fig. 3 include both direct shock and surface viscous loss. This viscous loss is modeled in the blade-to-blade solution by applying a surface skin friction which together with the shock loss produces the spanwise total pressure recovery estimated for the trailing edge. The skin friction loss is modeled in the blade-to-blade solution as a transport of momentum across the airfoil surface. The rate of momentum removed from the flow is proportional to the product of the local velocity and an input skin friction coefficient. The magnitude of the skin friction coefficient which will be discussed subsequently is intended only as a means of modeling an approximately valid level of internal loss and blockage. The axial and spanwise distribution for RCu is obtained by computing

Nomenclature

Cm = meridional velocity
Cu = tangential component of the absolute velocity
h = streamtube height
$\bar{K}$ = blockage factor = ratio of actual flow/ideal flow
M_r = relative Mach number
N_c = corrected rotor speed
P = static pressure
P_{Tr} = relative total pressure
R = radius
RCu = angular momentum
Recovery = actual P_T/ideal P_T (independent of reference frame)
Tor = relative total temperature
U = meridional momentum or mass flux
V = relative tangential momentum or mass flux
Wc = corrected mass flow
Wu = tangential component of relative velocity
β = relative air angle measured from tangential
ϕ = streamline slope angle
ρ = density
$\rho_1 Cm1/\rho_2 Cm2$ = velocity density ratio
τ = distance between similar points on adjacent airfoils in a blade row
ω = angular velocity

Subscripts

1 = rotor inlet station
2 = rotor exit station

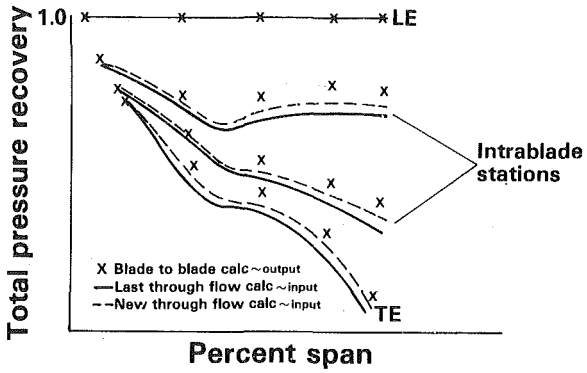

Fig. 3 Total pressure recovery output from blade-to-blade calculation and input to through flow calculation

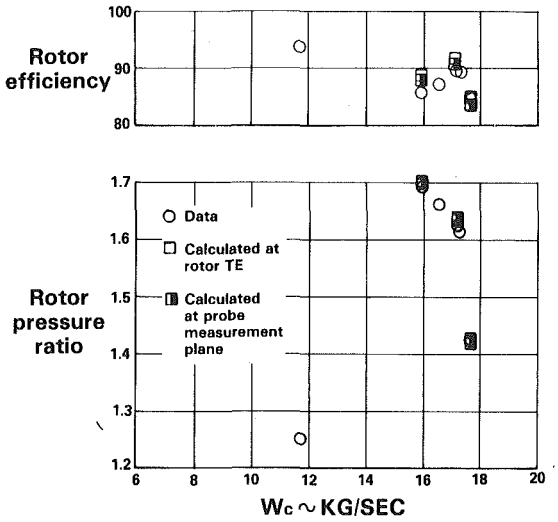

Fig. 4 Measured and calculated rotor performance

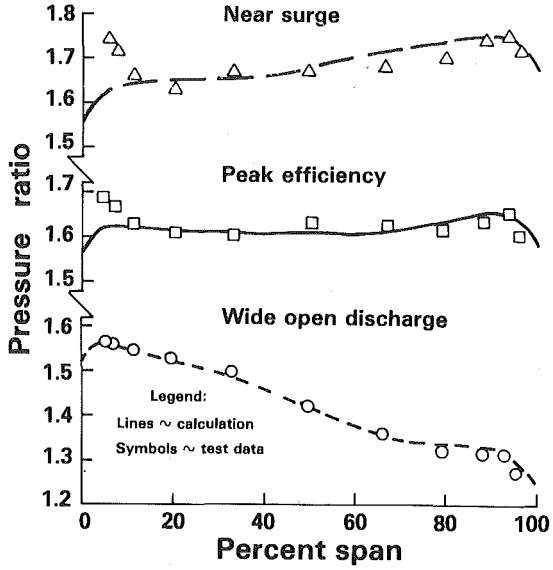

Fig. 5 Measured and calculated total pressure

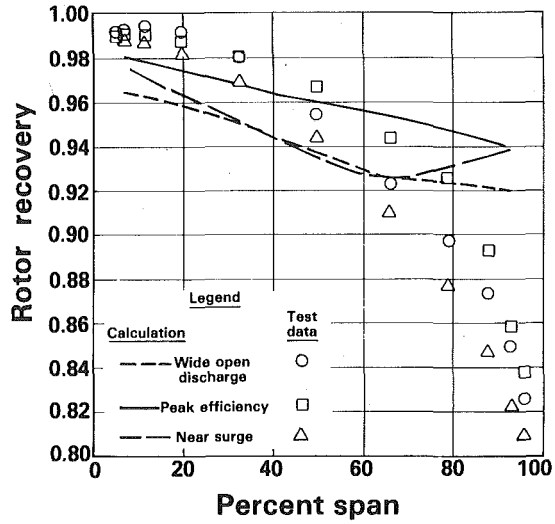

Fig. 6 Measured and calculated recovery

the gapwise mass averaged value of relative tangential velocity in the blade-to-blade calculation with a known radius and wheel speed ($RCu = (R) \times (\omega R - Wu)$). The result is influenced by the surface skin friction coefficient. The circumferential blockage is obtained from the ratio $\int_0^1 \rho Cmd\tau/\tau\rho av\ Cm\ av$, where the ρ_{av} and Cm_{av} depend upon the mass averaged total pressure, total temperature and RCu together with the area averaged static pressure. This blockage includes the effect of blade thickness, surface velocity deficit and nonuniformity of the core flow. The iterative quasi-3D computation procedure was damped (see Fig. 3) as information was passed from one program to another and the iterations were continued until the output of the last iteration matched its input.

Comparison between Experimental and Computational Results

The pressure and efficiency characteristics from the data and the quasi-3D analysis are shown in Fig. 4. The three computed points correspond to the wide open discharge, the peak efficiency, and the near surge operating conditions at 100 percent design speed. At the peak efficiency and near surge conditions the mass flow was imposed on the calculation and the pressure ratio was obtained as part of the solution. At the wide open (choked flow) condition the pressure ratio was imposed and the mass flow was determined by the analysis. The leading edge endwall blockage factor was chosen based on the measured upstream Mach number and was constant for all three operating conditions. The accurate definitions of mass flow and leading edge blockage are of primary importance in predicting the correct shock structure.

To produce the approximate measured efficiency level the spanwise distribution of airfoil surface skin friction coefficient was set to have linear radial variation between 0.005 at the hub and 0.015 at the tip for all operating conditions. From these input conditions the spanwise exit pressure, temperature and recovery profiles were computed together with the intrablade flow field Mach numbers for comparison to the L2F measurements. Fig. 5 shows the comparison between the measured and calculated total pressure profiles. This result indicates that the quasi-3D calculation is able to define the appropriate spanwise distribution of total pressure. Fig. 6 shows the computed radial distribution of recovery compared to the test data.

This method attempts to model an estimated recovery profile at the trailing edge plane. It has been assumed that the large losses in the outer region of the span cannot be modeled as surface viscous loss. The tip clearance and end loss are modeled in the computational procedure as an endwall blockage effect. Supplementary loss calculations are required (which add viscous, endwall and tip clearance losses to the computed shock loss from this model) to predict the measured recovery profile. The computed flow field can be used to obtain boundary conditions for these calculations. More detailed intrablade viscous loss and wake data are needed to further develop this aspect of the prediction. To evaluate the effect of the uncertainty in trailing edge recovery, the magnitude and distribution of the skin friction coefficient have been varied. The conclusion thus far is that so long as the overall level of blockage and recovery is retained, moderate variations in the skin friction coefficient will not significantly alter the inviscid flow field.

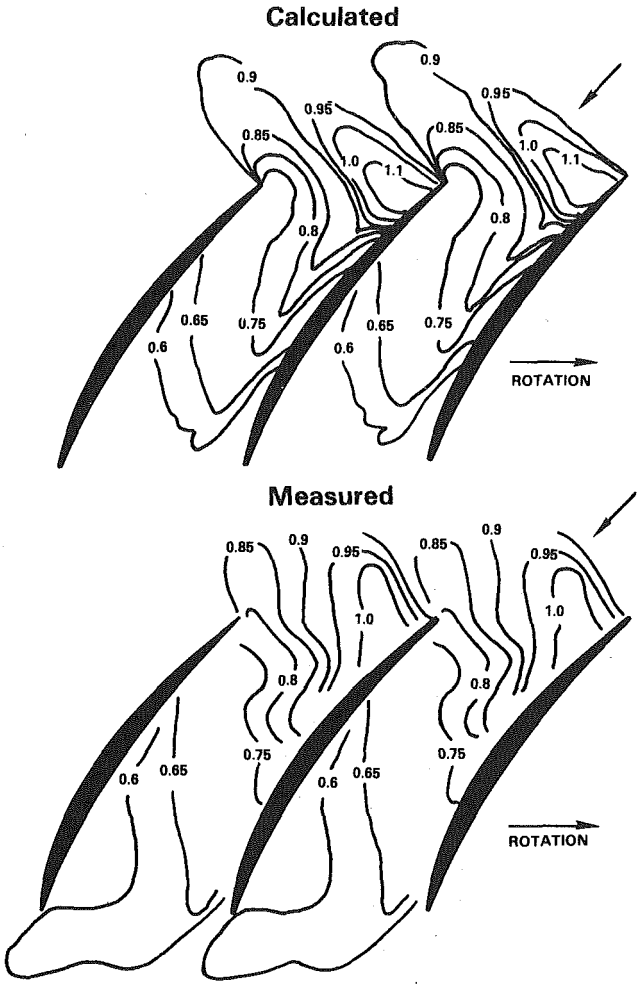

Fig. 7 Fan Mach number contours—18 percent span—peak efficiency—100 percent *Nc*

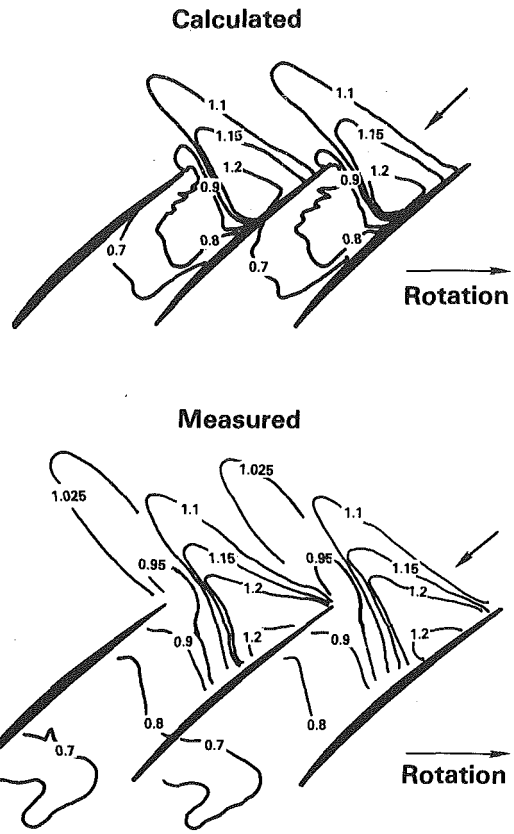

Fig. 8 Fan Mach number contours—45 percent span—peak efficiency—100 percent *Nc*

The measured and computed flow fields for the peak efficiency condition are shown by relative Mach number contours in Figs. 7–10. The comparisons are considered quite good in that both the character of the flow field and the indicated shock strength are approximately the same in the measured and calculated Mach number fields. This occurs even though four distinctly different types of flow fields exist simultaneously along the span. These are: (1) a subsonic inlet with a local supersonic region at 18 percent span, (2) a slightly supersonic inlet with a detached shock at 45 percent span, (3) a moderate supersonic condition with a strong attached shock at 68 percent span, and (4) a higher supersonic inlet Mach number with a weak oblique-normal (λ) shock configuration at 89 percent span. The most noticeable discrepancy between the computed and measured flow fields is the stronger Mach number falloff near the airfoil surface in the computed result. This surface loss is the result of the skin friction model which removes momentum from the flow near the airfoil surface. In general, these comparisons suggest that the level of the skin friction coefficient is high causing the Mach number falloff to be too severe.

Figure 7 defines the flow field at 18 percent span. The computed boundary conditions on this section are $M_{1r} = 0.9215$, $\beta_1 = 35.41$, $P_2/P_1 = 1.438$, ρCm ratio = 0.82, $\phi = 10.13$. The resulting flow field includes a local supersonic region behind the leading edge which terminates ahead of the subsonic passage diffusion. Figure 8 defines the flow field at 45 percent span. The computed boundary conditions here are $M_{1r} = 1.086$, $\beta_1 = 31.59$, $P_2/P_1 = 1.558$, ρCm ratio = 0.88, $\phi = 3.06$. The slightly supersonic inlet flow is accelerated to a local Mach number level in excess of 1.2 before terminating with a detached leading edge shock. Subsonic diffusion occurs from a Mach number level of 0.9 to 0.7. The flow field at 68 percent span is shown in Fig. 9. The computed boundary conditions are $M_{1r} = 1.217$, $\beta_1 = 28.08$, $P_2/P_1 = 1.615$, ρCm ratio = 0.88, $\phi = -1.96$. The flow accelerates to a Mach number greater than 1.25 before reaching the attached leading edge shock which diffuses the flow to the 0.95 Mach number level. The $L2F$ measurements suggest the possibility of boundary layer interaction at this section. Figure 10 defines the flow field at 89 percent span. The boundary conditions are $M_{1r} = 1.307$, $\beta_1 = 24.04$, $P_2/P_1 = 1.63$, ρCm ratio = 0.855, $\phi = -7.52$. At this section the Mach number level is sufficiently high and the leading edge is sufficiently thin and well aligned to the flow that a weak oblique shock can form bringing the Mach number down to 1.15 before the internal passage shock reduces the Mach number level below 1.0. In the measured flow field the diffusion through the Mach 1.0 level is more gradual than in the computed flow field. It is possible that the shock system is more complex than that which is computed, therefore allowing a lower diffusion. This effect is not believed to be the result of an unsteady shock.

Figure 11 shows the computed pressure distribution at the peak efficiency conditions as compared to values interpreted from the $L2F$ Mach number data. The comparisons at 45 percent and 68 percent span are excellent. At the 18 percent span location the computed leading edge suction surface pressure is low when compared to the level indicated by the measurement. The single value from the data may, however, be insufficient to conclude that the very local high Mach number region does not exist. (This overspeed is observed in the data at the near surge condition.) It is also possible that the overspeed terminates earlier than indicated by the computation. At the 89 percent span location the difference between the computed and measured pressure distributions is on the pressure side behind the computed oblique and normal shocks. The data show a more gradual pressure rise which has been discussed as resulting from a more complex shock structure.

Figure 12 defines the measured and computed flow fields at the near surge operating condition for the 68 percent span location. The

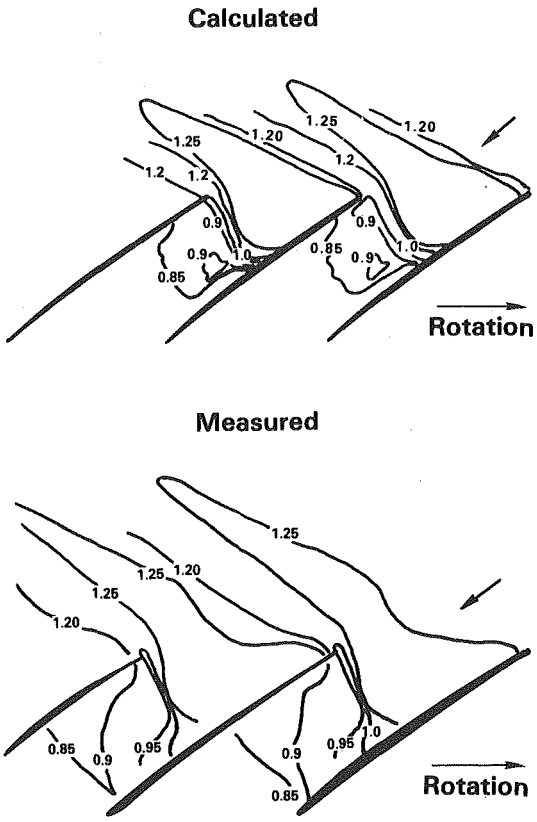

Fig. 9 Fan Mach number contours—68 percent span—peak efficiency—100 percent *Nc*

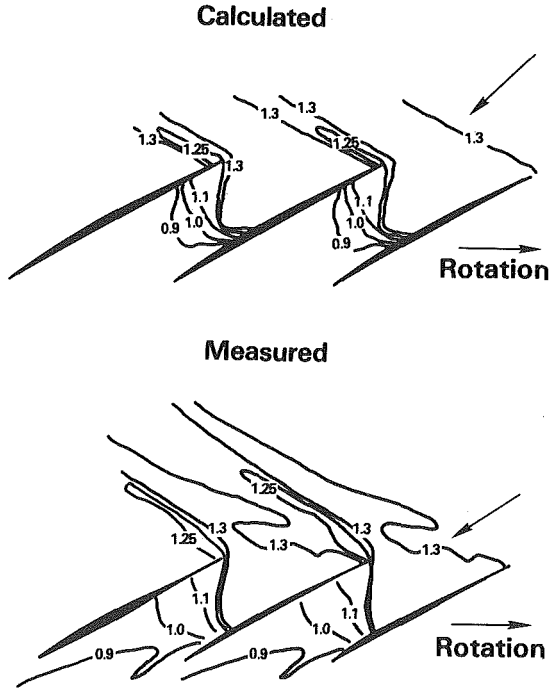

Fig. 10 Fan Mach number contours—89 percent span—peak efficiency—100 percent N_c

computed boundary conditions are $M_{1r} = 1.195$, $\beta_1 = 25.92$, $P_2/P_1 = 1.628$, ρCm ratio = 0.873, $\phi = 0.3$. Here the shock structure is spilled or detached from the leading edge. This condition exists over the full span in both the computed and measured flow fields. Here again there is evidence of possible boundary layer interaction. Pressure distributions from the full span $L2F$ velocity measurements and the computation of the near surge point are shown in Fig. 13. Here the 18 percent span overspeed is observed by the $L2F$ measurement. Except

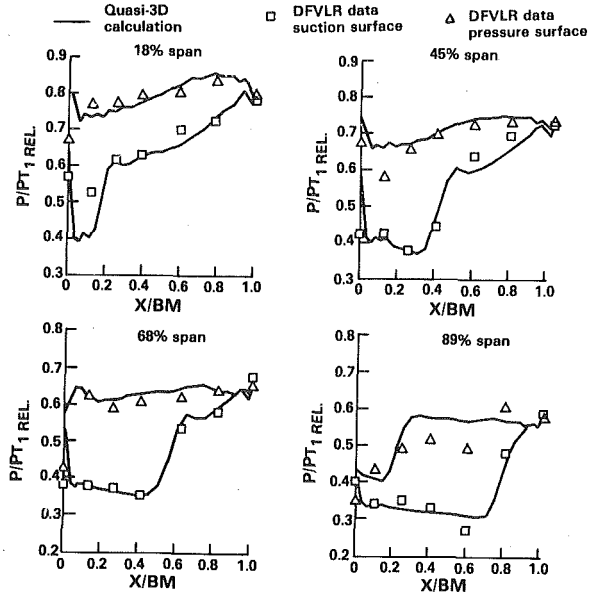

Fig. 11 Surface pressure distributions—peak efficiency

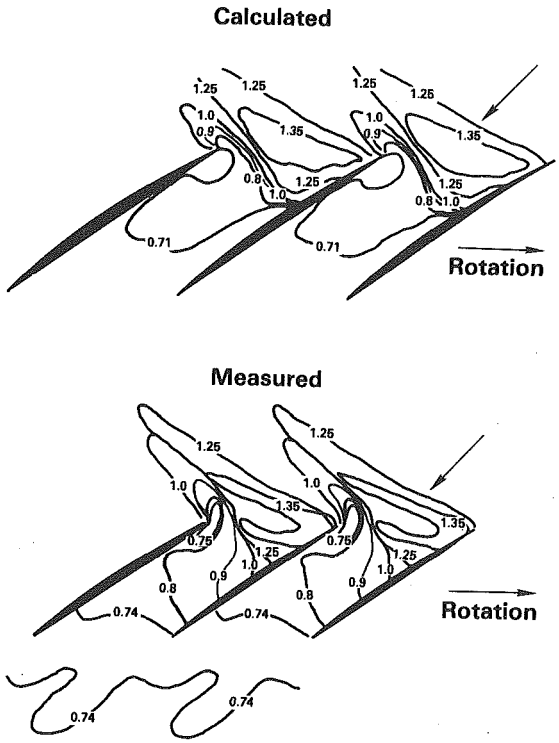

Fig. 12 Fan Mach number contours—68 percent span—near surge—100 percent *Nc*

for the 68 percent span location the computed shock position is too far rearward.

Figure 14 defines the measured and computed flow fields at 89 percent span for the wide open discharge condition. The computed boundary conditions are $M_{1r} = 1.3208$, $\beta_1 = 24.49$, $P_2/P_1 = 1.325$, ρCm ratio = 0.913, $\phi = -10.81$. Both the computed and measured flow fields indicate a weak leading edge shock with a reacceleration to a Mach number level of about 1.4 before the stronger trailing edge shock. This choked condition exists over the full span in both the measured and computed solution. The pressure distribution comparisons in Fig. 15 indicate that the computed solution is generally more choked than the measured flow field.

Examination of the pressure distribution and Mach number con-

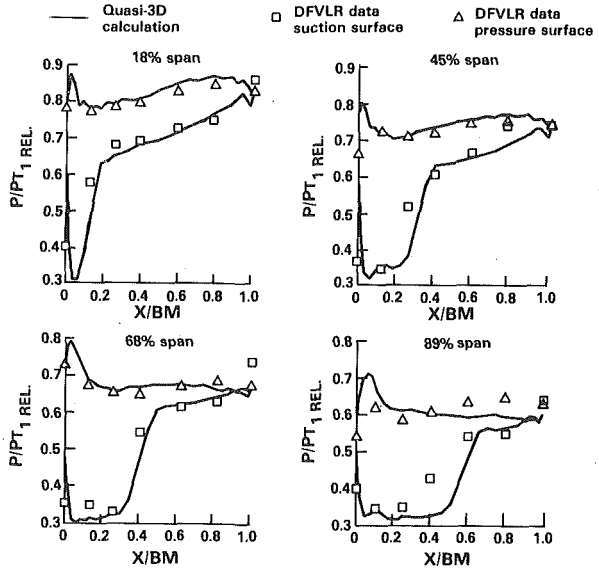

Fig. 13 Surface pressure distributions—near surge

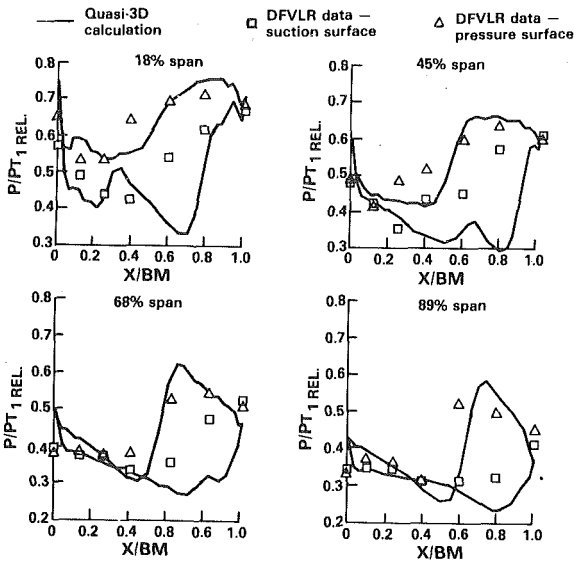

Fig. 15 Surface pressure distributions—wide open discharge

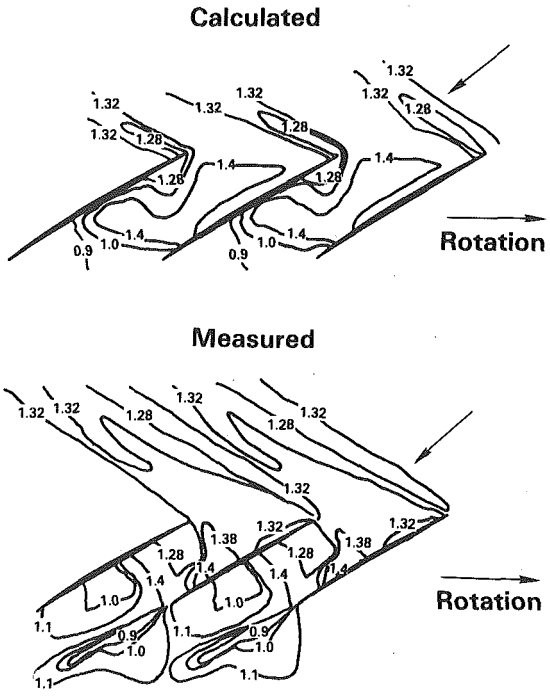

Fig. 14 Fan Mach number contours—89 percent span—wide open discharge—100 percent *Nc*

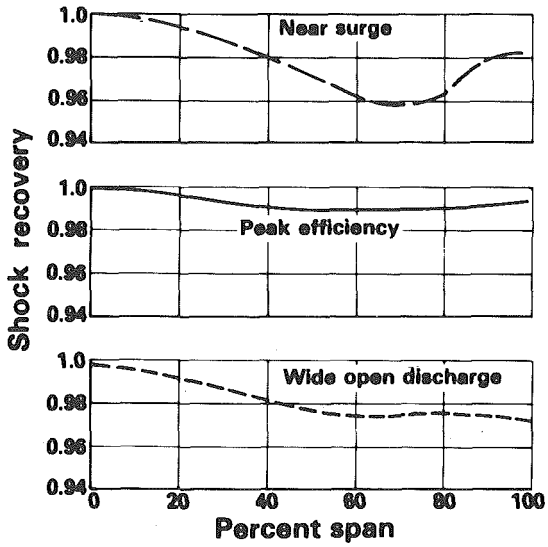

Fig. 16 Calculated shock loss

tours in Figs. 7–15 suggests that the shock strength indicated by the computational model approximates that which is measured by the *L2F* system. The computed spanwise shock total pressure recovery is given in Fig. 16 for three operating conditions. The recovery shown is the integrated value of shock loss interpreted from local static pressure ratios throughout the flow field. At the near surge and peak efficiency conditions the maximum shock loss occurs in the 60–70 percent span region. Closer to the hub the shock strength is reduced by lower inlet Mach number. Near the tip the shock structure becomes oblique resulting in reduced shock loss. An alternative explanation of the distribution of shock strength is given in reference [7].

Conclusion

The computed Mach number contours are in agreement with the measured values at the peak efficiency and near surge operating conditions. The calculated strength and position of the shock structure is valid. The shock loss of this rotor can, therefore, be determined from either the measured or calculated flow field. At these operating conditions the computed and measured surface pressure distributions are essentially the same. Either the measured or calculated pressures can be used as the boundary condition for computing surface viscous loss. At the wide open discharge operating condition the computed flow field shows a stronger shock field closer to the trailing edge compared to the data. A slightly higher pressure ratio boundary condition would undoubtedly improve this comparison.

The comparisons indicate that at unchoked flow conditions the predicted level and shape of the exit pressure profiles are valid when the measured mass flow is given as the boundary condition. Similarly, the computed choking mass flow is verified by the measured wide open discharge mass flow measurement. Under choked flow conditions the shape of the exit pressure profile is correct when the level is given as a boundary condition.

The comparisons between the recovery profiles used in the computational model and the measured values are not in agreement. This is due in part to error in the computational loss model. It is also possible that losses are redistributed between the trailing edge plane where the computed values are given and the downstream measuring plane. The discrepancy between measured and predicted recovery profiles could then be less than indicated by this analysis. An improved model for computing and distributing the viscous loss is required to improve this aspect of the analysis. This suggests the need

for a full three-dimensional boundary layer calculation with shock wave interaction. The development of such a complex computational model will require additional laser velocity measurements. These measurements should focus increased attention on the boundary layers and wakes. Data must be acquired on different fans at a variety of operating conditions.

References

1 Dunker, R. J., Strinning, P. E., and Weyer, H. B., "Experimental Study of the Flow Field within a Transonic Axial Compressor Rotor by Laser Velocimetry and Comparison with Through-Flow Calculations," ASME Paper No. 77-GT-28, 1977.

2 Schodl, R., "Laser-Two-Focus Velocimetry (L2F) for Use in Aero Engines," *Laser Optical Measurements Methods for Aero Engine Research and Development,* Agard-LS-90, 1977.

3 Schodl, R., "Development of the Laser-Two-Focus Method for Non-Intrusive Measurement of Flow Vectors, Particularly in Turbomachines," ESA-TT-528, 1979.

4 Wisler, D. C., "Shock Wave and Flow Velocity Measurements in a High Speed Fan Rotor Using the Laser Velocimeter," ASME Paper No. 76-GT-49, ASME JOURNAL OF ENGINEERING FOR POWER, Apr 1977.

5 Weyer, H. B., "The Determination of Time-Weighted Average Pressures in Strongly Fluctuating Flows, Especially in Turbomachines," Technical Translation, ESRO-TT-161, 1974, p. 141.

6 McDonald, P. W., "The Computation of Transonic Flow Through Two-Dimensional Gas Turbine Cascades," ASME Paper No. 71-GT-89, 1971.

7 Epstein, A. H., Kerrebrock, J. L., and Thompkins, Jr., W. T., "Shock Structure in Transonic Compressor Rotors," *AIAA Journal,* Vol. 17, Apr 1979, pp. 375–379.

for a full three-dimensional boundary layer calculation with shock wave interaction. The development of such a complex computational model will require additional laser velocity measurements. These measurements should focus increased attention on the boundary layers and wakes. Data must be acquired on different fans at a variety of operating conditions.

References

1 Dunker, R. J., Strinning, P. E., and Weyer, H. B., "Experimental Study of the Flow Field within a Transonic Axial Compressor Rotor by Laser Velocimetry and Comparison with Through-Flow Calculations," ASME Paper No. 77-GT-28, 1977.

2 Schodl, R., "Laser-Two-Focus Velocimetry (L2F) for Use in Aero Engines," *Laser Optical Measurements Methods for Aero Engine Research and Development*, Agard-LS-90, 1977.

3 Schodl, R., "Development of the Laser-Two-Focus Method for Non-Intrusive Measurement of Flow Vectors, Particularly in Turbomachines," ESA-TT-528, 1979.

4 Wisler, D. C., "Shock Wave and Flow Velocity Measurements in a High Speed Fan Rotor Using the Laser Velocimeter," ASME Paper No. 76-GT-49, ASME JOURNAL OF ENGINEERING FOR POWER, Apr 1977.

5 Weyer, H. B., "The Determination of Time-Weighted Average Pressures in Strongly Fluctuating Flows, Especially in Turbomachines," Technical Translation, ESRO-TT-161, 1974, p. 141.

6 McDonald, P. W., "The Computation of Transonic Flow Through Two-Dimensional Gas Turbine Cascades," ASME Paper No. 71-GT-89, 1971.

7 Epstein, A. H., Kerrebrock, J. L., and Thompkins, Jr., W. T., "Shock Structure in Transonic Compressor Rotors," *AIAA Journal*, Vol. 17, Apr 1979, pp. 375–379.

Discussion

D. C. Prince, Jr.[1] In a recent paper (reference [8]), I proposed a pattern of characteristic features observed in experiments on a number of transonic compressor rotors. Table 1 is reproduced from reference [8], summarizing these features. I am gratified to see that the material covered in the present paper appears to be in general agreement with the material used in establishing that pattern and I hope that the authors may comment on their experience as it relates to this pattern.

The material in the paper provides evidence particularly relevant to items (1) and (3) of Table 1. Table 2 has been prepared from material in the present paper. Upstream vector angles given in the text were plotted in Figs. 10 and 14. Wave angles from the upstream vector to Mach number contours were measured with a protractor and used in the table. Recognizing the difficulty of obtaining reliable values from small scale figures, it is hoped that the authors can confirm these values or supply a more accurate replacement.

Figure 17 has been prepared using standard shock equations (e.g. reference [9], Chapter 10) and the data given for Fig. 10 ($M_{1R} = 1.307$, $\beta_1 = 24.04$) to assist in discussion of these items. Knowledge of the upstream Mach number and the wave angle provides enough information for a prediction of the discontinuity level to be expected. Applying Fig. 17 to the 55 deg wave angle upstream of the rotor for the measured data of Fig. 10 shows that the shock downstream Mach number is expected to be 1.19. Deceleration from Mach number 1.307 to Mach number 1.19 appears to require about double the pressure discontinuity shown on Fig. 10. The 53 deg wave angle upstream of the rotor in the calculated data of Fig. 10 calls for deceleration to Mach number 1.24, which is much more consistent with the discontinuity shown in the figure. It is surprising that both the calculated and the measured data should show larger upstream wave angles (54 and 56 deg) with wide open discharge than the 53 and 55 deg values at peak efficiency.

Inside the passage, the 62 deg wave angle for the measured data in Fig. 10 calls for deceleration from the upstream Mach number to 1.05. If the shock downstream Mach number is to be 1.15, as given in the text, the wave angle should have been 57 deg. The measured data in Fig. 14 for the region near the leading edge show deceleration from a Mach number above 1.38 to a Mach number slightly below 1.28 across a front nearly perpendicular to the flow, which is rather surprising in view of the data in Figure 17. For the calculated data of Fig. 10, the 61 deg wave angle calls for deceleration to Mach number 1.075, which is a substantially larger discontinuity than is shown on the figure. The calculated data in Fig. 14 show an oblique shock discontinuity extending about one-third of the way across the passage from the leading edge and then disappearing. It would be interesting to explore momentum and continuity balances for control volumes defined upstream of the discontinuity, along a selection of mid passage streamlines, back to the pressure surface along the Mach number 1.4 contour, and closed along the pressure surface.

In reference [8] I reported on the use of laser velocimeter (LV) data from reference [4] to infer the true wave angle. The fringe-type LV system had given direct measurements of momentum change components across the leading edge shock in axial and circumferential directions. The axial momentum was constant across the shock within a resolution of ±3 percent. If the axial momentum is constant, the wave orientation should be axial, so that the momentum change vector can be perpendicular to the wave. Analysis using the equations of Fig. 17 showed that a 5 deg inclination of the wave in either direction from the axial should correspond to 10 percent change in the axial momentum, so that the measurements defined a wave direction within 2 deg of axial. I hope that analysis of the L2F data for the present paper has included similar definition of the wave direction. Fig. 1 suggests that L2F measurements of the shock discontinuity were made for at least three axial positions along the 89 percent span stream surface. The data of Fig. 17 have been resolved into axial and circumferential components of the velocity discontinuity and presented as Fig. 18. From Fig. 18 one may infer that the axial velocity should have increased 3 percent to support the 62 deg wave angle from the measured data of Fig. 10. It is hoped that the authors will supply some detail on their measurements of the discontinuity, so that the wave angle and the uniformity of the shock strength can be confirmed.

[1] Consulting Engineer, General Electric Company, Aircraft Engine Group, Cincinnati, Ohio 45415.

Table 1 Supersonic compressor shock structure features

1	Wave angles approximate maximum deflection.
2	Suction surface pressures near the leading edge are below 80 percent of upstream.
3	Shock discontinuities are substantially below expectation.
4	Pressure surface pressures in supersonic passages respond to back pressure.
5	Passage and downstream shocks disappear at supersonic pressure levels.

Table 2 Flow properties deduced from Figs. 10 and 14

		Peak Efficiency		Wide Open Discharge	
Upstream Mach number (from text)		1.307		1.321	
Mach angle		49.9		49.2	
Shock branch		Upstream	In Passage	Upstream	In Passage
Shock wave angle	L2F measurement	55	62	56	67(?)
	Time marching computations	53	61	54	42(?)

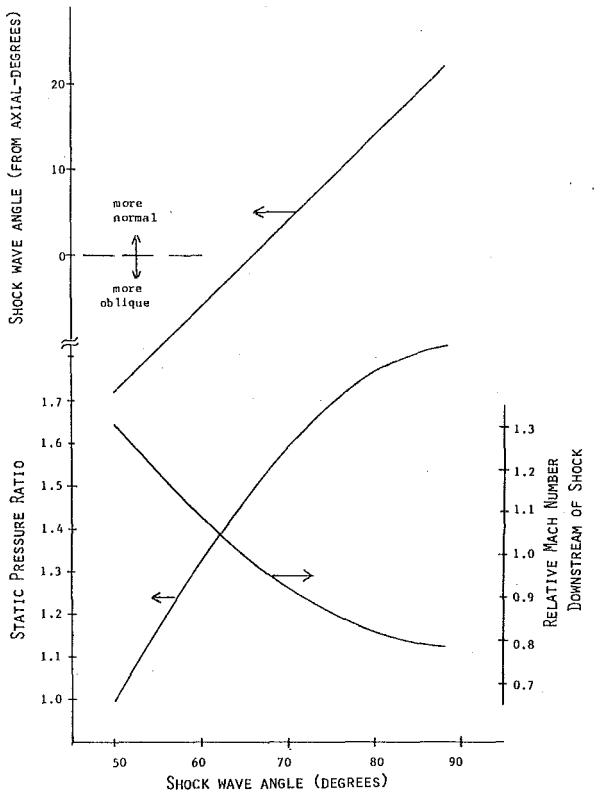

Fig. 17 Predicted wave discontinuities—relative Mach number and static pressure ratio (M_{1R} = 1.307; β_1 = 24.04 deg)

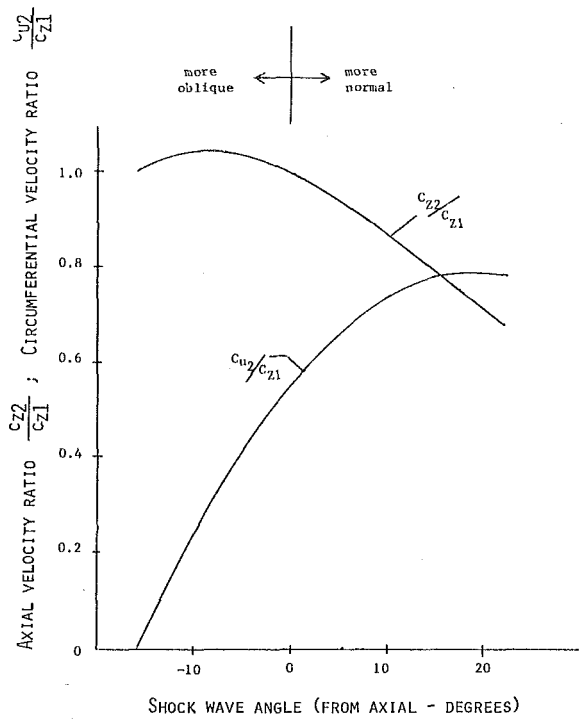

Fig. 18 Predicted wave discontinuities—axial velocity ratio and circumferential velocity ratio (M_{1R} = 1.307; β_1 = 24.04 deg)

Experimental data included in the paper also seem to provide some support for items 4 and 5 of Table 1. I assume that Figs. 10 and 14 each show supersonic pressure surface velocity over the first 50 percent chord, which is presumably isolated from the downstream condition by the "Zone of Silence" concept. However, the Mach number at 25 percent chord on the pressure surface changes from 1.28 in Fig. 14 to about 1.08 in Fig. 10 as a result of throttling. Figure 14 shows a well-defined shock on the pressure surface at 50 percent chord, which has disappeared during throttling to Fig. 10. The experience behind reference [8] suggests that the static pressure rises across the rotor might be substantially less than those required for deceleration from Mach number 1.321 to Mach number 1.1 in Fig. 14, and from 1.307 to 0.9 in Fig. 10, so that this shock disappearance would have occurred at supersonic pressure levels. It would be helpful to know what total pressure loss distributions were used to infer the measured static pressures of Figs. 11, 13, and 15, and how these static pressures compare with measured profiles at rotor exit.

The experimental data in this paper could be used to formulate some requirements that should be met by a realistic blade-to-blade calculation procedure. According to my experience, the suction surface pressure near the rotor tip from the leading edge to the shock incidence does not vary with back pressure for Mach numbers higher than about 1.2. Pressure surface pressures, while remaining supersonic, may respond violently to back pressures. The large pressure surface variations in this paper have just been discussed. The suction surface pressures shown on Figs. 11, 13, and 15 seem indeed to be independent of the back pressure. However, integration of $dp/dr = \rho v^2/r$ along an orthogonal to the flow (taken, for example, at the midpoint of the cascade passage) should be consistent with the difference between the end point pressures. I suppose that these conditions can only be reproduced in a blade-to-blade calculation procedure if the lamina thickness distribution (streamtube thickness in the converging annulus) along the suction surface is independent of back pressure, while that along the pressure surface is a function of back pressure. Probably it is also important to make the strength of the shock discontinuity vary with back pressure. I interpret the text analysis as being restricted to laminae with circumferentially uniform thickness.

The pressure surface response to throttling should be expected, since the back pressure can be felt along the entire pressure surface at midspan, Fig. 8, where the passage flow is clearly subsonic. A rise in the midspan surface pressure should produce a tendency toward radial outflow along the pressure surface, leading to reduced effective lamina thickness near the rotor tip. This is not a viscous flow or secondary flow effect.

Reference [8] observed that obliquity of the passage shock in S_2 surfaces should have substantial influence on the passage shock strength. Figs. 7–10 show the passage shock to be incident on the suction surface at 22 percent chord at 18 percent span, 40 percent chord at 45 percent span, 50 percent chord at 68 percent span, and 70 percent chord at 89 percent span. Consequently, a substantial effect of S_2 surface obliquity might well be expected in this case also. Perhaps the authors would discuss how this effect is induced in their analysis, and in particular whether S_2 deflection across the passage shock has influenced the lamina thickness distribution which they use.

I wish to thank the authors again for publicizing so much useful information on supersonic/transonic rotor shock structure. Clearly, full explanations for all the features are not yet available. Sharing experiences should help to make progress.

Additional References

8 Prince, D. C., Jr., "Three Dimensional Shock Structures for Transonic/Supersonic Compressor Rotors," AIAA Paper 79-0043, *AIAA Journal of Aircraft*, Jan. 1980, pp. 28–37.

9 Shapiro, A. H., *The Dynamics and Thermodynamics of Compressible Fluid Flow*, Ronald Press, New York, 1953.

Authors Closure

The authors wish to thank Dr. Prince for his stimulating and thorough discussion. In general we agree with the observations and conclusions which he has presented. This closure will attempt to answer specific questions which have been raised in the discussion.

1 The interpretation of the magnitude of the wave angles given in the discussion appear to be accurate.

2 We have not devoted sufficient time to the evaluation of the measured or calculated wave angles to be able to explain discrepancies with simple theory. We assume that the differences which exist reflect

the inability of simple models to define a complex three-dimensional fan shock structure. Differences between the calculated and measured results also reflect the limitations of the present quasi three-dimensional model.

3 The increase in the upstream wave angle at the wide open discharge condition is primarily the result of a more negative leading edge suction surface incidence.

4 The total pressure loss used to infer the measured static pressures of Figs. 11, 13, and 15 were obtained from Mach number variations across the shock without considering the local wave angle.

5 We agree that the constraint of circumferentially constant streamtube thickness is undesirable but do not know the magnitude of its adverse effects.

6 The computed radial variation in shock position is influenced most strongly by the leading edge geometry and inlet air angle. The inlet air angle distribution along the span is influenced by the work input and blockage (both reflecting the shock strength) near the leading edge.

The Use of Marine Gas Turbines in an Amphibious Hovercraft, the USN AALC JEFF(B)

A. V. Coles
LC JEFF(B) Test Support Manager,
New Orleans Operations,
Bell Aerospace TEXTRON,
Division of Textron Inc.,
Panama City, Fla 32407

The Navy's air cushion landing craft LC JEFF(B) is one of two full-scale advanced development craft that was developed and is being tested under the Amphibious Assault Landing Craft (AALC) program. The JEFF(B) was designed and built by Bell Aerospace Textron under contract to the Naval Sea Systems Command. The JEFF(B) is powered by six Avco Lycoming TF-40 gas turbines. The engines are coupled together in two sets of three engines each. The loading and control requirements resulting from this configuration, and the associated high-density spray environment, result in some unique capabilities and problems. Initial phases of development and testing of the JEFF(B) have uncovered and solved problems related to control and power matching of coupled engine systems, and to protecting the engines from the deleterious effects of salt-spray ingestion. On-line engine health monitoring systems have been developed to record compressor performance degradation due to salt ingestion.

Description of JEFF(B)

The Navy's air cushion landing craft LC JEFF(B) is one of two full-scale advanced development craft that was developed and is being tested under the Amphibious Assault Landing Craft (AALC) program. The JEFF(B) was designed, built, and initially tested by Bell Aerospace Textron, Division of Textron, Inc., under contract to the Naval Sea Systems Command to provide high-speed amphibious assult landing craft capability for use by the Navy in support of the Marine Corps. The JEFF(B) was delivered to the Navy in July 1978. Bell is currently supporting the AALC Experimental Trials Unit (ETU), a field activity of David W. Taylor Naval Ship Research and Development Center (DTNSRDC), Carderock, Md, in testing the craft at the Naval Coastal Systems Center (NCSC), Panama City, Fla.

The craft is designed to carry an on-deck cargo of 60 short tons (54,431.10 kg) at 50 knots (25.72 m/s) over sea and surf conditions corresponding to sea state 2. In calm water, it can exceed 70 knots (36.01 m/s) and carry a payload of up to 75 short tons (68,038.80 kg). Payloads can roll on and off the craft fore or aft through bow and stern ramps (Fig. 1). Over land the craft can climb 13 percent grades and traverse obstacles up to 3.5 feet (1.07 m) high.

To achieve these operational capabilities, the craft is supported by a cushion of air under its hull, and is propelled by air propellers working in propulsive ducts. Power to drive the lift system fans and the propulsion system is provided by six Avco Lycoming TF-40 marine gas turbines, rated at 3850 hp (2870.94 kW) under standard day conditions. Engine power installed is predicated upon achieving the design operating speeds on a 100°F (38°C) day with a 25-knot (12.86 m/s) head wind in sea state 2 conditions. Directional control of the craft is derived from dual rudders mounted aft of the propeller ducts and from bow thruster nozzles located forward on the craft using air supplied from the lift fans.

Contributed by the Gas Turbine Division and presented at the Gas Turbine Conference and Products Show, New Orleans, La., March 10–13, 1980 of THE AMERICAN SOCIETY OF MECHANICAL ENGINEERS. Manuscript received at ASME Headquarters December 3, 1979. Paper No. 80-GT-8.

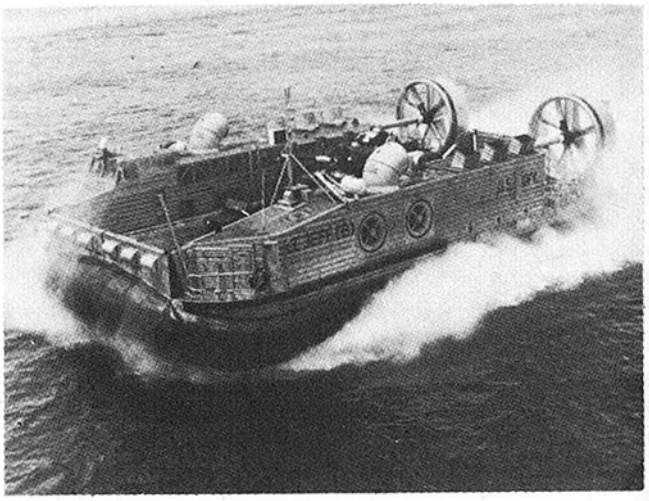

Fig. 1 LC JEFF (B)

The air cushion is contained within a peripheral seal system constructed of a flexible, rubberized fabric inflated with air from the lift fans. The hull is constructed of a welded aluminum raft 80 ft (24.32 m) long by 48 ft (14.63 m) wide, with port and starboard superstructures containing crew stations and machinery. On each side of the craft, three turbine engines are connected to a longitudinal shaft, driving lift fans from the forward end and propellers from the aft end of the shaft.

During cushionborne operation, approximately 10,000 ft^3/s (283.10 m^3/s) of lift air is fed through the peripheral seal into the air cushion. Cushion air is pressurized to 100 lb/ft^2 (4787.68 Pa) and exhausts to atmosphere through a small air gap beneath flexible skirt fingers. The average air gap is 2.5 in. (0.06 m), and the air exhaust velocity is some 170 knots (87.45 m/s).

Underway, the craft is always subject to recirculation of water spray

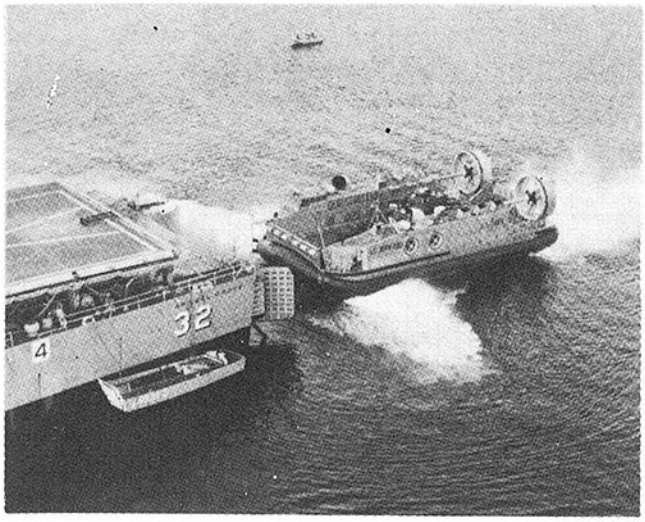

Fig. 2 JEFF(B) entering well deck of LSD

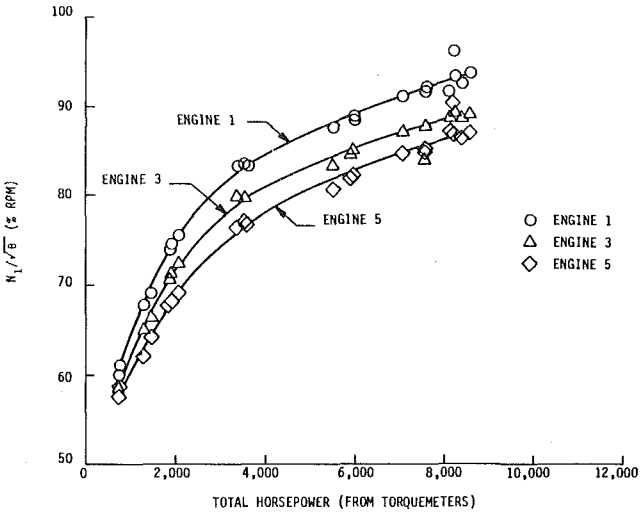

Fig. 3 Engine power matching characteristics (original configuration)

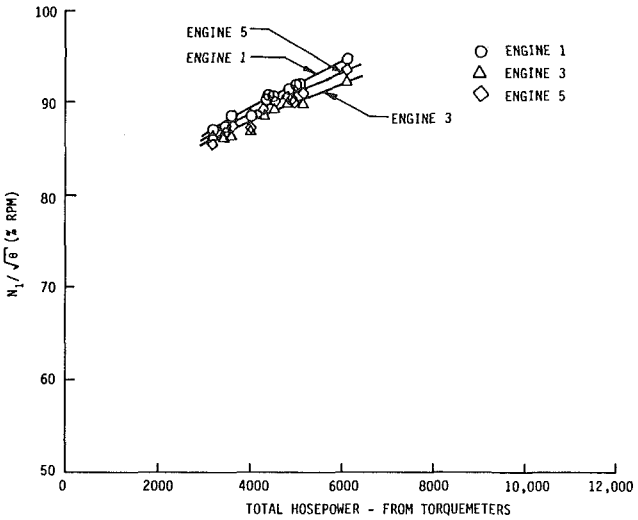

Fig. 4 Engine power matching characteristics (after incorporation of load-sharing system)

or surface dust or sand. Major air inlets feeding engines and lift fans cover a considerable portion of the hull sidewall structure, inboard and outboard.

To perform its prime operational role, the JEFF(B) will transport cargo from a support ship to a beachhead unloading zone. Cargo loading at the support ship may be alongside by crane, or inboard in the well deck of an LSD or similar ship. Well deck operations will be performed with the JEFF(B) with some or all engines operating in an almost completely enclosed area. Recirculation of exhaust and lift fan airflows creates a high-temperature environment during craft transit in and out of the well deck (Fig. 2).

Power Management

The characteristics of an amphibious air cushion vehicle require that the lift fan system be operated continuously to provide airflow for support of the craft. The propulsion thrust required increases with speed to a peak as the craft passes hump speed (19 knots (9.77 m/s) over deepwater), drops to a lower value through 40 knots (20.58 m/s), and then rises again at high speed. In the JEFF(B), thrust is controlled by varying propeller blade angles since the propellers are driven at a rotational speed related to the lift fan speeds.

The operators' controls for propulsion and lift system management include a pair of transmission speed governor/speed set levers and a pair of propeller blade angle command levers. Each engine is controlled through its individual electronic control system, the engine power output being regulated by the controller in response to free turbine governor control loop signals. The governor set speed is normally adjusted by the operator to a value dependent upon craft gross weight for correct lift fan airflow. Engine power output then is modulated through the governor control loop to match the lift fan and propeller aerodynamic loads at the selected speed. Changes in relative wind speed through the propeller and changes in cushion air pressure due to craft motion in a seaway will induce power variations which must be compensated for by the governor. Under typical operating conditions, the power required in the transmission system on either side of the craft may vary from 3000 to 11,000 shp (2,237.09 to 8,202.68 kW) for free turbine speeds selected between 80 and 97 percent of maximum design speed.

Since three engines are connected to a common transmission system, each engine control system registers the same free turbine speed. Therefore, for a commanded set speed, each governor loop will be subject to the same speed-error signal. Actual engine powers reached by individual engines depend upon the degree of parity between engine control loops, engine fuel flows, and engine efficiencies.

In initial craft operations, it was apparent that the matching of engine powers in each set of three engines was poor. The JEFF(B) is not equipped with engine torquemeters, so operators evaluated engine matching on the basis of the compressor speeds shown on cockpit displays. Variations of compressor speeds of up to 15 percent maximum speed were noted, along with the amount of variation depending upon power demanded (Fig. 3). Adjustments made to individual engine controllers effected only slight improvements in power matching. An engine load-sharing system, designed and built by Bell, was therefore incorporated to modulate each engine command set speed signal proportionally to the difference between an individual engine compressor speed and the average compressor speed for the set of three engines. With this system incorporated, the power matching was improved by a factor of 5 with engines operating within a 2 to 3 percent speed band over the full range of powers (Fig. 4).

Engine governor transient response has been rapid and well damped throughout all operations to date. Loss of a single engine is compensated for by increasing the power output of the remaining two engines with little or no effect on craft control or performance. The craft has been operated at all normal speeds using two engines on each side of the craft. In the event of lift fan or transmission malfunctions, provision is made in the design for declutching the rear engine and propeller from the forward parts of the transmission system. The craft may then proceed at reduced speed retaining propulsion thrust on the disabled side of the craft.

Engine Inlet Air Filtration

In anticipation that craft operation would create a heavy spray environment, the engine air inlets are provided with an air filtration system designed to remove water droplets and dust particles. Engine air is drawn through screens on the inside wall of the superstructures.

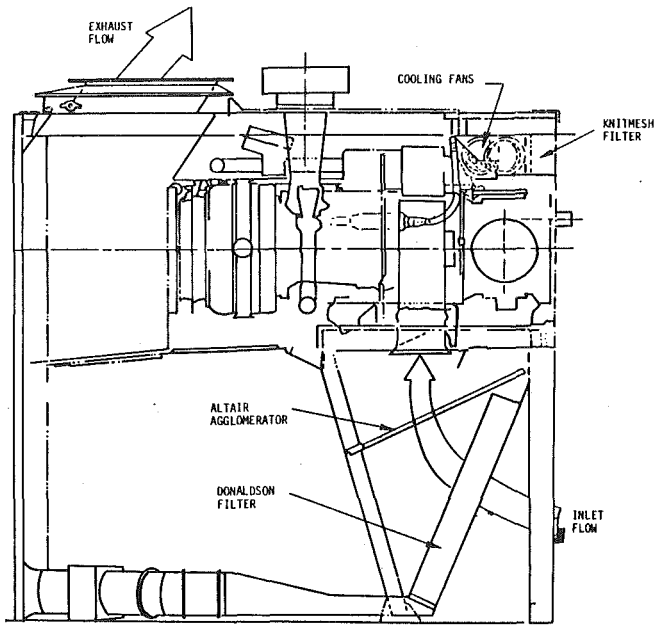

Fig. 5 Original engine air inlet filtration system

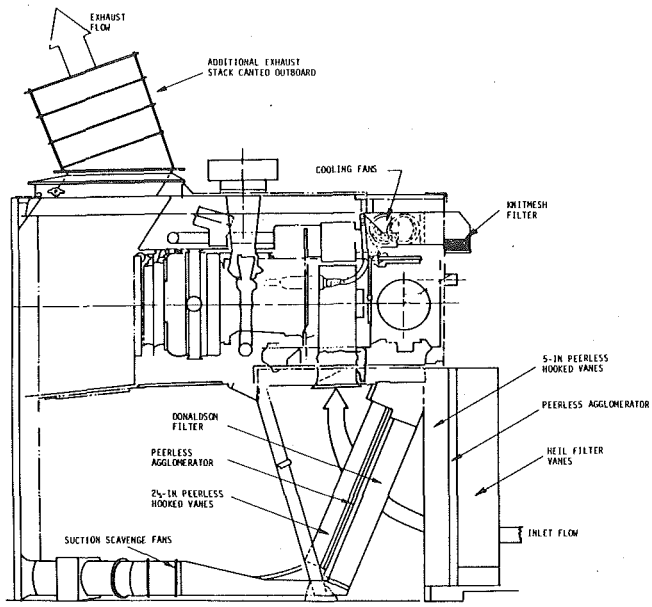

Fig. 6 Improved engine air inlet filtration system

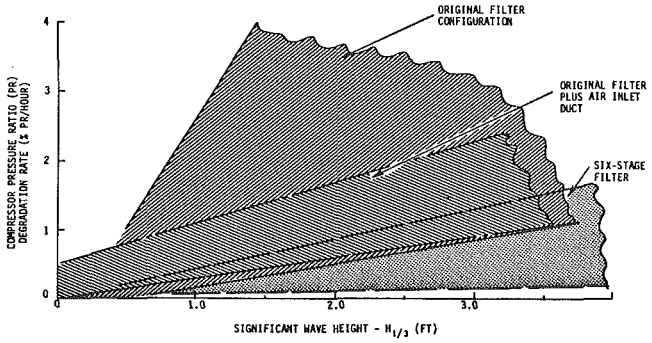

Fig. 7 Engine air inlet filter efficiency in reduction of salt spray ingestion

Each engine inlet contains a series of filter elements, and filtered air passes up through elbow ducts to the engine in the engine bay above the filter bay.

Early operation of the craft over water indicated that engine compressor degradation due to salt ingestion became significant after very short periods of operation. Prior experience with surface effect ships in a similar environment had developed a compressor performance monitoring technique which was employed on JEFF(B). Measurements were made of the compressor inlet and delivery pressures to calculate a pressure ratio. For a clean compressor, this ratio is uniquely related to corrected compressor speed. Underway measurements of pressures, compressor speed, and inlet air temperature enabled a check to be made on pressure ratio versus corrected speed. Based on Avco Lycoming test experience, a 6-percent degradation in compressor ratio was set as a limit to retain an adequate compressor surge margin.

With the initial engine air inlet filtration system, this degradation limit was reached in a period of time as short as 15 min. The engines were equipped with built-in water-wash spray rigs. Injection of 10 gallons (0.04 m^3) of freshwater, while the engine starter is cranking, effectively removes salt deposited on the compressor and restores compressor efficiency.

The original filter system consisted of a Donaldson swirl tube separator followed by an Altair agglomerator pad (Fig. 5). To improve water droplet removal, an additional filter stage of Heil vanes was added upstream of the original system, protruding inboard onto the deck space. With this additional filtration, operations of one or two hours duration were made without excessive compressor degradation. However, overwater operation at low craft speeds still created sufficiently heavy spray at the air inlet face to rapidly degrade compressor performance. Evaluation of the normal spray pattern over the craft underway at speeds above hump speed showed that the aft sidewall areas received heavy spray, whereas the forward deck area was dry. Inlet air ducts were added extending forward to draw engine air from a point inboard of the lift fan inlets. With these ducts installed, a further improvement in operating time without compressor degradation was realized. However, the ducts encroached on the available on-deck cargo space.

A combined Bell/Navy series of tests was performed at the Navy Air Propulsion Center to evaluate alternative multiple-filter combinations. Tests on the craft had established that at the engine inlet area a saltwater concentration of 500 ppm was possible. Avco Lycoming engine tests on a similar engine (TF-35) set limits of 0.14 ppm on the salt ingestion the engine could accept without excessive compressor degradation. Therefore, the required filter efficiency was 99.97 percent water particle removal. The TF-40 engine specification sets a limit of 0.1 ppm salt ingestion. Several filter combinations tested showed filter efficiencies in excess of 99.9 percent, depending upon incoming spray particle size. Measurement of filter efficiencies of the order of 99.98 percent was found to be almost impossible due to the problem of accurately sampling the downstream airflow with extremely low particle counts.

Based on the test data, a six-stage air filter was designed and installed, primarily within the original filter bay, encroaching only 15 in. (0.38 m) on the deck space (Fig. 6). With this filter installed, missions in excess of five hours in sea state 2 have been completed without excessive compressor degradation (Fig. 7). Post-mission water washes are routinely performed to remove accumulated salt and to reduce the probability of a larger accumulation over a series of operations which might not yield to washing. To date, no evidence of permanent engine performance loss has been apparent. One engine turbine section was removed for inspection after 100 hr of operation. No hot-section degradation was noted. Engine operating time at present (Dec. 1979) is 300 hr.

The new engine inlet filter design has two stages of agglomerator screen material which should trap solid particles entrained in the inlet air. The outer stage has been designed to be easily removable for cleaning. In the event that the filter system becomes clogged by particles, blow-in doors are provided downstream of the filter system in the engine air inlet plenum chamber which open when a depression of 15 in. (0.38 m) of water is reached. This permits continued operation for short periods with the filter system bypassed.

Engine Exhaust System

Due to the restrictions on craft overall dimensions, in order to fit within an LSD well deck, the engines are installed with a unique exhaust diffuser duct. This duct consists of a short exhaust diffuser dumping into a vertical exhaust stack. Low-velocity exhaust plumes are discharged upward, with an inboard bias which was imposed by craft structural limitations. At low speeds underway, the exhaust plumes can be deflected by external air movements and reingested in either the engine or lift fan inlets (Fig. 8). Operation within the LSD well deck, with limited ventilation for engine exhaust, results in generally elevated inlet air temperatures. To date, occasional air intake temperature values as high as 180°F (82°C), 100°F (56°C) above ambient, have been noted. Such high inlet temperatures obviously degrade available engine power, but no engine control malfunctions have resulted to date. Exhaust stack extensions which provide a 3-ft. (0.91 m) vertical extension with an outboard deflection of the exhaust have been added to reduce inlet reingestion of exhaust gases. The impact of the longer stacks on the temperature of adjacent structures within the LSD well deck remains to be determined.

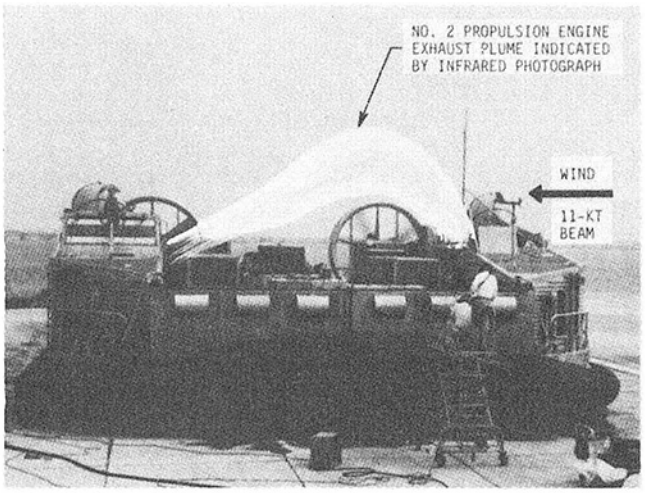

Fig. 8 Engine exhaust plume

Salt-Spray Environment

In the high salt-spray water environment, special care is required to protect engine and control components from corrosion. Although the TF-40 engines are installed internally in the craft sidewall structures, the engine bays must be ventilated with air. Air drawn from the local environment contains salt-water vapor and may be hot. Engine bay air temperature limits of 180°F (82°C) have been set to protect key solenoid fuel valves and to retain a margin for the fire warning system, which can trigger at an area temperature of 220°F (104°C) or a local hot spot of 400°F (204°C). Therefore, the engine bay has all the characteristics of a saltwater sauna. Some minor rusting has occurred on compressor diffuser casings and on bolts in the combustor casings. Avco Lycoming has replaced the combustor bolts with a higher grade stainless steel bolt.

Engine electronic control boxes are located adjacent to the engine bays in access tunnels open to the on-deck environment. High humidity and water from post-mission water washdown of the craft dictates that the engine control boxes must be of submersible quality. External cable connectors must be absolutely watertight at the back closures, and must be made of noncorrosive materials.

Operation of the TF-40 engines in the JEFF(B) has demonstrated the flexibility implicit in a multi-engine, free turbine drive system. Despite an extremely hostile environment, engine serviceability has been excellent.

The salt environment must inevitably result in some accumulation of salt on compressor blades, with attendant performance degradation. Present air inlet filter systems permit 4- to 5-hr mission profiles to be completed before engine water washing is required. In early development operations, compressor ratio degradations of as much as 15 percent were recorded. In some instances engine compressor surges occurred, but engines continued to run without component damage. One engine has incurred over 30 surges during operational and test cell experience. Compressor blades from this engine have been subjected to fatigue testing, and the results indicate no significant reduction in blade life due to surging.

To insure engine operation with acceptably clean compressors, a special Bell-designed engine health monitor (EHM) display has been installed. This display alerts the operator should any engine reach a point at which the engine compressor pressure ratio falls more than 6 percent below the nominal value. A microprocessor is employed to compute pressure ratio and corrected compressor speed, and to compare actual to nominal relationships between these parameters. In addition to the display of pressure ratio degradation in excess of 6 percent, the EHM can be selected to display individual parameters for detailed troubleshooting of a problem engine. Bell and Avco Lycoming engineers are continuing a dialogue to improve the engine control system so that an adequate surge margin can be maintained with a degraded compressor. Engine acceleration fuel scheduling, presently programmed by compressor speed, may be changed by the incorporation of an overriding compressor delivery pressure controller loop which would reduce acceleration fuel available for substandard pressure ratios.

Conclusion

Experience gained to date with the JEFF(B) TF-40 engine installation has confirmed that the marine gas turbine is an acceptable power plant for high-performance air cushion vehicles operating in an unusually severe environment. Future developments of the JEFF craft will provide the Navy and Marine Corps with a unique new assault system, equally at home on water or on land.

Acknowledgments

The author wishes to acknowledge the assistance of the Navy's AALC ETU and fellow Bell Aerospace Textron employees during the development test and trials cycle of the JEFF(B). Avco Lycoming and the Naval Air Propulsion Test Center, Trenton are also recognized for their assistance. With the cooperation of the Naval Sea Systems Command and the David W. Taylor Naval Ship Research and Development Center (DTNSRDC), the JEFF(B) has been developed as a practical working demonstrator of AALC technology which will contribute to the ultimate selection of features for the production design of a follow-on fleet craft designated Landing Craft, Air Cushion (LCAC) in the 1980's.

A. J. Fiorentino
W. Greene
J. C. Kim

United Technologies Corporation,
Pratt & Whitney Aircraft Group,
Commercial Products Division,
East Hartford, Conn. 06108

E. J. Mularz

Propulsion Laboratory,
U.S. Army Research & Technology,
Laboratories (AVRADCOM),
NASA—Lewis Research Center,
Cleveland, Ohio

Variable Geometry, Lean, Premixed, Prevaporized Fuel Combustor Conceptual Design Study

Four lean premixed prevaporized (LPP) combustor concepts have been identified which utilize variable geometry and/or other flow modulation techniques to control the equivalence ratio of the initial burning zone. Lean equivalence ratios are maintained at high power engine operating conditions for low NO_x emissions, while near stoichiometric conditions are maintained at low power for good combustion efficiency and low emissions of carbon monoxide and unburned hydrocarbons. The primary goal of this program was to obtain a low level of NO_x emissions ($\leq$3 g/kg fuel) at stratospheric cruise conditions; additional goals are to achieve the currently proposed 1984 EPA emission standards over the landing/take off cycle and performance and operational requirements typical of advanced aircraft engines. Based on analytical projections made during this conceptual design study, two of the concepts offer the potential of achieving the emission goals. However, the projected operational characteristics and reliability of these concepts to perform satisfactorily over an entire flight envelope would require extensive experimental substantiation before an engine application can be considered.

Introduction

The effects of pollutants released in the stratosphere by aircraft operating at high altitudes may create a hazard to man and his environment. The concern with these pollutants relates primarily to the potentially adverse effect of oxides of nitrogen (NO_x) on the stratospheric ozone layer. The consequences of depletion of this ozone layer have been studied by the U.S. Department of Transportation under the Climatic Impact Assessment Program (CIAP). The "Report of Findings" from this study concludes that the control of oxides of nitrogen at high altitude may be required in the future [1].

As a result of the findings of the CIAP, it has been recommended to the Department of Transportation that research and development be aimed toward a reduction in the emission of oxides of nitrogen by a factor of 10 within the next decade, and that the research programs be aimed at substantial further improvement in emissions to be realized in practical engines during the ensuing decade.

The U.S. Environmental Protection Agency (EPA) has proposed regulations to control aircraft emissions below 3000 ft altitude. These regulations require substantial reduction in exhaust gas emissions of current gas turbine engines. Engine modifications are currently under development to provide substantial improvements in low power combustion efficiency and reductions in carbon monoxide and hydrocarbon emissions. Combustors such as staged and premixed burning have demonstrated potential for providing EPA required reductions in NO_x emissions. Even further reductions in NO_x emissions will be required to obtain the magnitude of reduction desired for stratospheric cruise conditions.

In response to these needs, the National Aeronautics and Space Administration (NASA) initiated the Stratospheric Cruise Emission Reduction Program (SCERP) to develop lean, premixed, prevaporized (LPP) combustor technology capable of reducing critical exhaust emissions over the full range of aircraft operation. The initial phase of a four-phase program was begun in 1976 to examine various aspects of LPP combustion which required more understanding and to establish design criteria for concepts having the potential of meeting program objectives.

This paper summarizes the results of a program in the Phase I effort to identify, conceptually design and analytically evaluate LPP combustor concepts utilizing variable geometry and/or other flow control techniques. More detailed information on this program may be found in the literature [2]. This program was performed under NASA contract NAS3-21256 by Pratt & Whitney Aircraft Group of United Technologies Corporation. The program was directed out of the Combustion and Pollution Research Branch of the Airbreathing Engines Division at the Lewis Research Center.

Program Description

The overall objective of this program was to identify promising lean premixed-prevaporized combustor designs which incorporate variable geometry, and examine their potential for meeting performance, emissions, and operational requirements of advanced aircraft gas turbine engines. The primary goal is a low level of NO_x emissions ($\leq$3g/kg fuel) at stratospheric cruise conditions. The emission and performance goals of the program are shown below.

Program Goals

1 NO_x EI $\leq$ 3 g/kg fuel at subsonic cruise
2 Proposed 1984 EPA emissions standards for T-2 thrust class aircraft over the landing-takeoff cycle
CO EPAP $\leq$ 25 g/kN

Contributed by the Gas Turbine Division and presented at the Gas Turbine Conference and Products Show, New Orleans, La., March 10–13, 1980 of THE AMERICAN SOCIETY OF MECHANICAL ENGINEERS. Manuscript received at ASME Headquarters December 7, 1979. Paper No. 80-GT-16.

UHC EPAP ≤ 3.3 g/kN
NO_x EPAP ≤ 33 g/kN
Smoke No. ≤ 20

3 Combustion efficiency
≥ 99.9 percent at sea level take-off
≥ 99.5 percent at ground idle
≥ 99.0 percent at all other operating conditions

4 Combustor section pressure loss

$$\frac{\Delta P}{P} \leq 5.5 \text{ percent at all operating conditions except idle}$$

5 Altitude relight capability ≥ 10.7 km

Four combustors were defined for the cycle and performance parameters anticipated for the energy efficient engine (E^3), currently being developed under a contract with NASA. The E^3 is configured as a high bypass ratio (6.5:1) engine in the 190,000 Newton thrust class, with a pressure ratio of about 38:1 at the cruise design point. The overall length of the E^3 combustor section (between the trailing edge of the compressor exit guide vane and the leading edge of the first turbine inlet guide vane) is 0.44m, and minimum and maximum diameters are 0.42m and 0.99m, respectively. Representative operating conditions of the E^3 for the design points of the landing/ takeoff cycle and for maximum rated cruise are presented in Table 1.

LPP Combustor Design Considerations

It has been established that the means to achieve low emissions is homogeneous combustion (via premixing and prevaporization) and close control of the gas temperature history in the combustor. To minimize low power emissions of unburned hydrocarbons and carbon monoxide near stoichiometric burning is desirable, while lean combustion is necessary to curtail NO_x emissions. Since the techniques for reducing low power emissions conflict with methods for reducing high power emissions, the apparent solutions are either a multi-stage combustor where each stage is employed and optimized for a particular flight condition, or a variable geometry combustor to accommodate optimization of the stoichiometry by means of airflow modulation. The latter approach is more attractive, if practical, since it can theoretically alleviate the off-design fall-off in performance at intermediate flight conditions and the associated increase in emissions that has been experienced with previous attempts at employing premixed combustors [3].

The ideal variable geometry LPP combustor would be designed to modulate the combustor airflow, mix and vaporize the fuel in air in proper proportions for each engine operating condition, and burn the controlled homogeneous mixture efficiently, thereby minimizing exhaust pollutants. The successful application of LPP combustion to practical engine combustors imposes a number of considerations that often result in contradictory requirements. Some of these factors, such as the characteristics of the compressor discharge flow field, fuel preparation and vaporization, autoignition and flashback, flame stability, and cooling and dilution air requirements will be discussed.

Compressor Exit Flow Characteristics. A basic requirement of the LPP combustor is to supply the combustion zone with a homogeneous mixture of air and fuel vapor over the entire engine power range. The premixing passages should be flowing full, uniform and devoid of recirculating flows. However, the compressor exit aerodynamics in conjunction with flow nonuniformities caused by diffuser case struts, fuel nozzle supports and, possibly, variable geometry devices are in direct conflict with the need to provide the premix passages with uniform, well defined airflow. It is apparent that the tolerance of LPP combustors to variations in combustor inlet flow conditions has to be considered, as is the role of the diffuser in amplifying or damping flow nonuniformities. The unattractive alternative is to design around the flow maldistributions via compartmentalization of the combustor.

Fuel-Air Preparation. It is recognized that even in the ideal case of a uniform flow field feeding the premixing passages, fully premixed and prevaporized mixtures may not be obtainable over the entire engine operating range. In the absence of an external vaporizer, some of the factors that influence fuel vaporization are air temperature and pressure, combustor inlet turbulence level (and possibly scale), and type of fuel injection system, i.e., airblast, air-assist, or pressure atomizer. Figure 1 shows analytical predictions of fuel droplet evaporation as a function of pressure [4]. When the ignition delay characteristics of Jet-A fuel [5] are superimposed, it can be seen that vaporization may also be limited by premixed passage autoignition restrictions.

A spray evaporation model developed during the P&WA/NASA Catalytic Burner Program [6] was used to calculate the degree of fuel vaporization for parametric variations in premixing passage length, velocity and droplet size. The results of this analytical investigation pointed out the importance of ultra fine atomization at the design conditions for high pressure ratio advanced gas turbine combustors. In an attempt to achieve very small droplets, the fuel injectors developed during this program were designed with as many injection sources as practical, without impinging fuel on liner walls and with

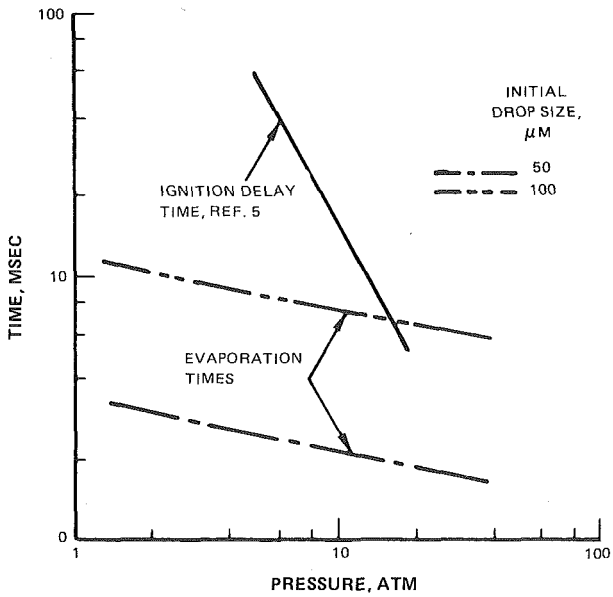

Fig. 1 Effect of pressure on ignition delay and vaporization times for JP-4—inlet air temperature, 833 K

Table 1 Representative Operating Conditions for the Energy Efficient Engine

	Ground[a] Idle	Approach	Climb	Sea-Level Takeoff	Max[b] Cruise
Combustor Inlet Temperature (K)	473	621	777	810	754
Combustor Inlet Pressure (atm)	4.4	11.7	27.0	31.2	13.8
Airflow Rate (kg/s)	14.0	31.6	62.4	70.2	31.7
Combustor Exit Temperature (K)	815	1118	1522	1611	1533
Combustor Exit Pressure (atm)	4.1	11.0	25.5	29.5	13.1
Fuel Flow Rate (kg/s)	0.13	0.43	1.38	1.68	0.74
Overall Fuel-Air Ratio	0.009	0.0137	0.0221	0.0240	0.023

[a] Std. Day—uninstalled (7 percent power)
[b] Alt = 10.7 km, Mn = 0.8

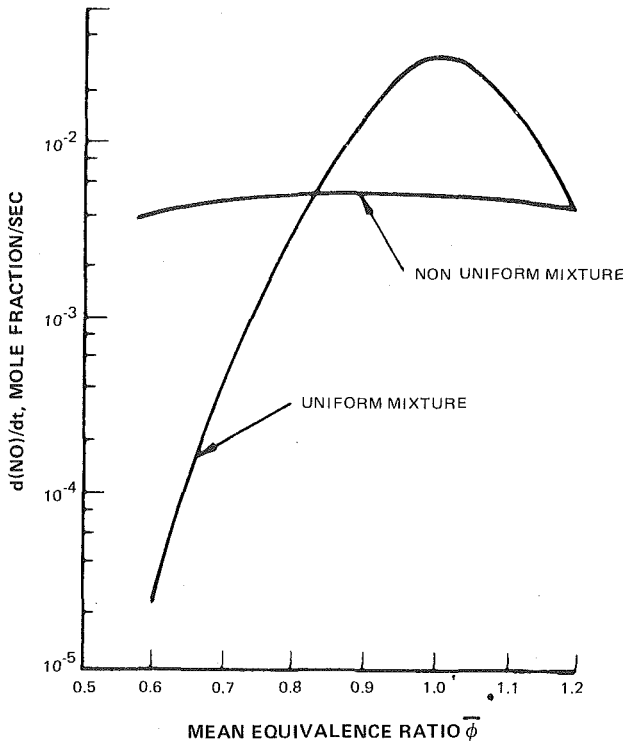

Fig. 2 Effect of mixture uniformity on rate of formation of nitric oxide

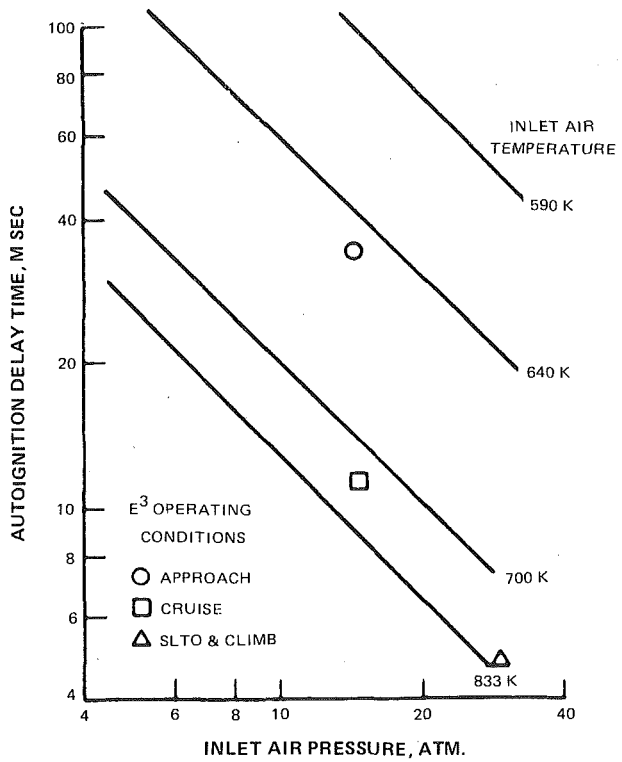

Fig. 3 Autoignition delay times as function of inlet air pressure and temperature

no wakes where fuel could be entrained and possibly exceed autoignition limits. An analytical prediction [7] showing the effect of burning zone uniformity on the rate of NO formation is presented in Fig. 2. It is apparent that the NO_x emission characteristics should be assessed for those engine operating conditions which result in deviations from homogeneous fuel mixing and vaporization.

Autoignition and Flashback. Perhaps the most hazardous characteristics that may hinder the practical application of the LPP combustor in advanced aircraft engines are the phenomena of autoignition and flashback. Many of the experimental rig programs including those sponsored by NASA have experienced autoignition or flashback problems [4]. Autoignition occurs when the residence time of the fuel-air mixture in the premixing passage exceeds the ignition delay time. Flashback occurs when the flame propagation velocity exceeds the mixture velocity, enabling the flame to detach from the intended flameholder and propagate into the premixing passage. In either case, autoignition or flashback, burning takes place in the premixing/prevaporizing passage, resulting in potential damage to the combustor and, possibly, the entire engine.

The autoignition characteristics of Jet-A fuel [8] are presented in Fig. 3. Some of the E^3 operating temperatures and pressures are superimposed on the figure. Clearly SLTO (sea level take-off) operating condition is the power setting that allows minimum margin for autoignition. In defining the premixing passages for the LPP system, precautions have to be taken to avoid potential flow problems, such as wakes behind variable geometry devices, which could increase the residence time of fuel-air mixture in the premixing passage. If flow distortions resulting from variable geometry devices are unavoidable, the design should attempt to restrict these problems to operating conditions corresponding to lower pressures and temperatures, e.g., idle. Reducing the mixture required residence time (mixing length) by preheating or prevaporizing the fuel is another approach to minimizing the potential for autoignition. Incomplete mixing/vaporization, hence higher NO_x emissions at SLTO power conditions, must be weighed against providing adequate margin to avoid autoignition.

Stabilization. The combustor front end airflow required to establish lean combustion during high power operation may result in flame blowout at lower power conditions. There are two approaches to alleviate this design problem. The first is to employ variable geometry to modulate the airflow in order to meet the stability requirements over a wide range of operating conditions. The second approach is to utilize a pilot combustor incorporated into the LPP system. The pilot combustor would be used for starting, ground idle and altitude relight; the LPP system would be staged in the power conditions above idle. This would require a smooth transition between the pilot and LPP stages to ensure proper acceleration and deceleration characteristics. An additional design concern in this application would be fuel nozzle coking after the stage has been shut down.

Cooling and Dilution Air Requirements. The utilization of variable geometry, though desirable from a combustor performance viewpoint, introduces significant complexity and difficulty with respect to combustor design. A typical single stage combustor operating at stoichiometric fuel-air ratio at idle power setting would require approximately 15 percent of the total combustor airflow in the front end. The same stage at cruise or SLTO power setting would require approximately 65 percent of the combustor airflow to maintain an equivalence ratio of 0.55. Utilization of 65 percent of the available combustor airflow in the front end premixing process leaves only 35 percent for dilution and liner cooling. Although a significant side benefit of LPP combustion is a reduction in the potential for hot streaks and a reduction of flame radiation due to lower primary zone gas temperature, the combustor liner design would have to incorporate highly efficient cooling schemes which are also tolerant to variations in liner pressure drop.

Combustor Designs

Four concepts were selected for conceptual design, analysis and evaluation as potential lean premixed prevaporized configurations. The combustors were the axial flow annular type. The concepts selected allowed the evaluation of three variable geometry techniques used in various combinations with advanced burner designs. In order to ensure the ultimate adaptability of the proposed designs to actual engine hardware, it was necessary to restrict the selection process as described below:

1 Simultaneous control of initial burning zone (IBZ) and dilution zone airflow would be required in order to maintain a nearly constant combustor section pressure loss at all operating conditions. Although increasing the complexity significantly, the

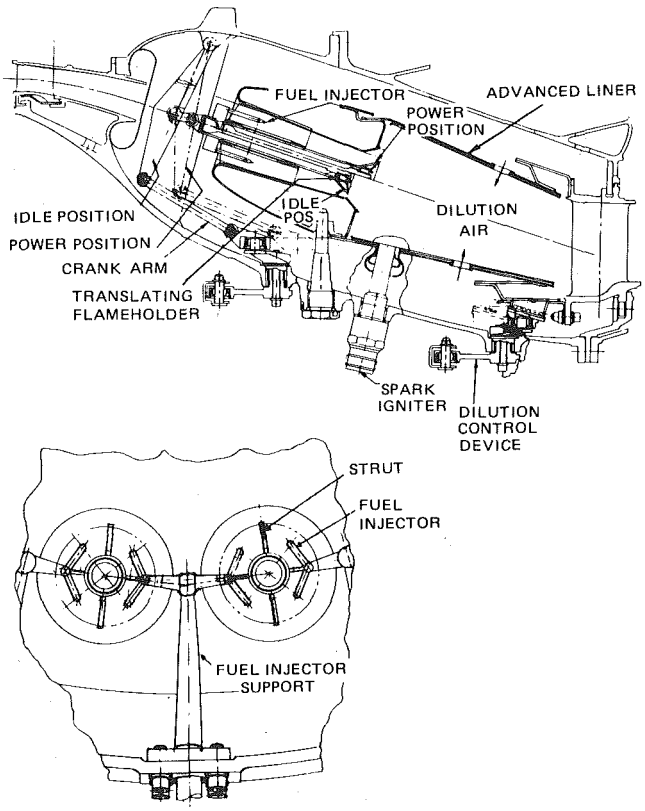

Fig. 4 Variable geometry LPP combustor—concept 1

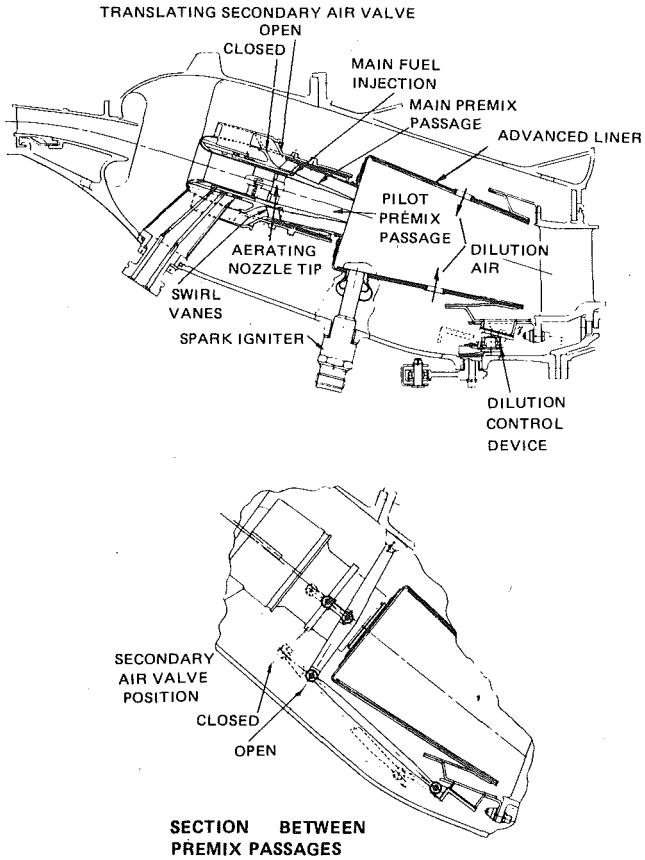

Fig. 5 Variable geometry LPP combustor—concept 2

variation in pressure loss resulting from individual control was felt to be intolerable.

2 Any attempt to control airflow upstream of the IBZ injection plane would have to be carefully designed to minimize wakes.

3 The variable geometry mechanism would have to be capable of fast response.

4 A safety factor of about 2.5 would be applied to autoignition residence time data.

Concept 1. Concept 1 shown in Fig. 4 features 24 premix passages each equipped with a translating centerbody that provides both the desired area modulation between idle and SLTO and a bluff body recirculation zone for flame stabilization. The design evolved from a desire to meter front end airflow at the IBZ injection plane and accelerate the flow in order to minimize the possibility of flashbacks.

The conical flameholder is based on a design evaluated in a NASA program [9] that demonstrated low NO_x emissions and overall good stability. The reference design was used to establish the overall cone size and shape based on a desired degree of blockage, while the number of passages, 24, was selected for compatibility with the 24-strut design of E^3. The outer contour of the passage was sized to allow the annulus area to vary as required for equivalence ratio control. At idle conditions, an IBZ equivalence ratio of 1.0 is maintained to insure high combustion efficiency and low emissions of carbon monoxide and unburned hydrocarbons, while at high power conditions, the equivalance ratio is reduced to 0.55 to control oxides of nitrogen. The test results from previous low emissions combustor programs (3 and 10) were used in selecting an idle IBZ of 1.0 while the experimental premix data of Anderson [11] were used in selecting a value of 0.55 for high power operation.

Each of the 24 premixing passages contains four fuel injectors with two fuel injection holes at the injection plane spraying fuel toward the support struts for the air nozzle plug. These struts serve as splash plates or a filming surface if any atomized fuel droplets impinge on them. Because of the importance of fuel spray quality in the vaporization process, the design of the fuel injector must be considered as a critical design item. The fuel injection system for Concept 1 represents an attempt to maximize the number of fuel source locations to obtain the highest possible degree of vaporization, and premixing.

A dilution control device that meets the design objective of controlling a large quantity of airflow has been incorporated in the Concept 1 design in order to maintain a nearly constant combustor section pressure loss at all operating conditions. The design shown in Fig. 4 utilizes a valving arrangement to bypass combustor inlet air at low power operation. The valve is closed during high power operation and can be partially open at part power to modulate the flow of bypass air. The valve consists basically of a conical ring which is translated axially by a set of crank arms around the combustor outer case. The outer arm of each set is connected to a unison ring rotated by an appropriate actuation device.

Concept 2. Concept 2, shown in Fig. 5, employs fuel staging in addition to variable geometry in an attempt to improve transient stability. Basically, the design consists of 24 premixing tubes, each with concentric inner and outer fuel/air mixing passages. The inner passage, which has fixed geometry and is supplied with fuel through an aerating nozzle, serves as the pilot stage while the outer annular passage, which is equipped with a variable geometry sleeve, serves as the main stage. Swirling flows generated within each passage act to enhance vaporization and mixing of the fuel air mixture and also stabilizes the flame in the combustion zone. An axially sliding sleeve with a conically diverging forward end opens and closes the circumferential secondary mixing tube inlet. Actuation of the sliding sleeves is provided by the ball jointed linkages which are connected to the dilution control valve ring. External actuation of the circumferential unison ring rotates 12 crank arm assemblies to provide axial translation of the exit valve ring. The linkage is designed so that the secondary air premix tube valve is open when the exit bypass valve is closed and vice versa.

The central primary air tube contains an aerating nozzle and swirl vane assembly supported by three struts. Primary and secondary fuel passages in the main support strut feed circular fuel manifolds. Fuel and air schedules are adjusted for stoichiometric combustion at idle

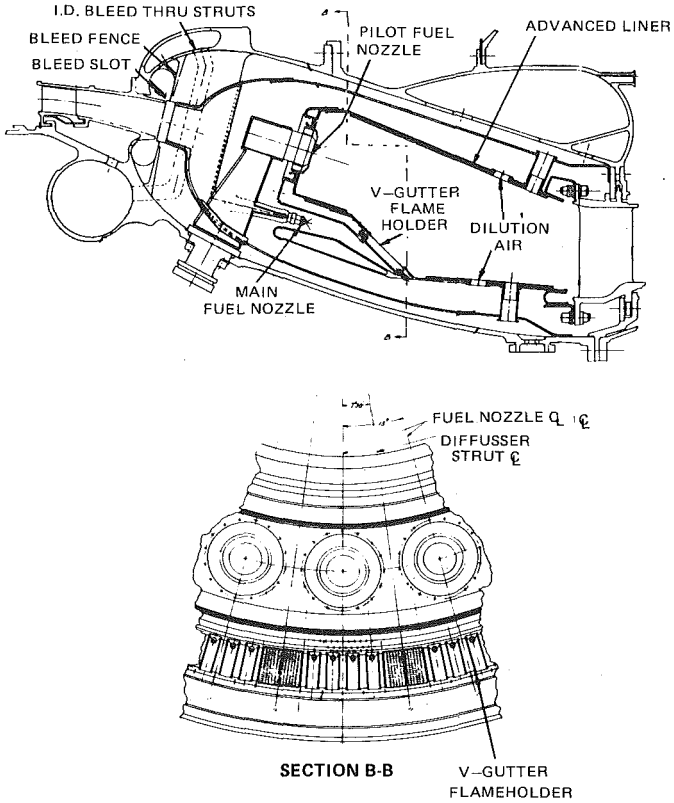

Fig. 6 Variable geometry LPP combustor—concept 3

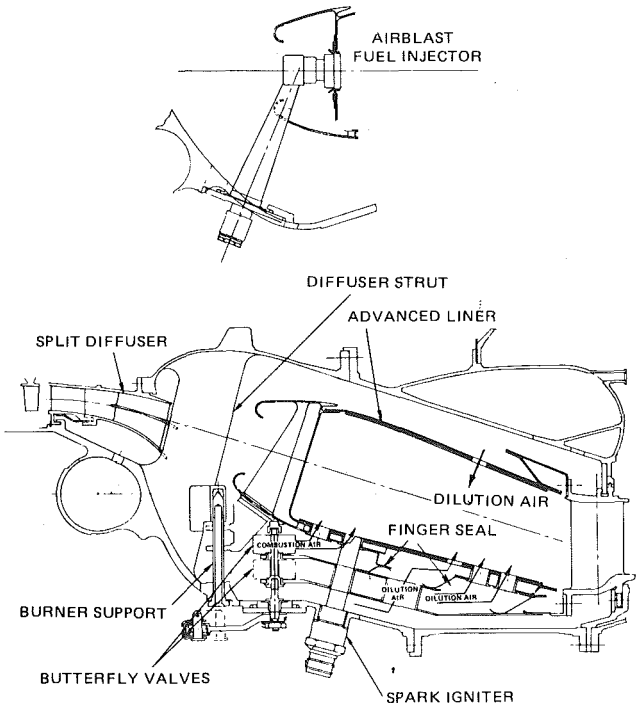

Fig. 7 Variable geometry LPP combustor—concept 4

for high combustion efficiency and low levels of UHC (unburned hydrocarbons) and CO (carbon monoxide) while lean conditions are maintained at high power to reduce flame temperature and limit NO_x production. At idle, fuel and air are supplied through only the inner passage while the outer passage is closed off to both except for a small amount of purge air to prevent recirculation of combustion gases into the tube. At the approach condition both inner and outer passages are fueled with the majority of fuel still supplied through the inner passage. At this condition, outer passage airflow is low, to keep the equivalence ratio sufficiently high for good CO and UHC emissions. At the high power conditions, most of the fuel is supplied through the outer tube and the air passage valve is near full open so that the equivalence ratio will be close to the desired 0.55. During high power operation, the pilot passage equivalence ratio will be maintained above 0.55 to provide protection against lean blow-outs during snap deceleration. Since the percentage of fuel supplied through the pilot is low at these conditions, the pilot contribution and hence the increase in overall NO_x level will be small.

Concept 3. The Concept 3 as shown in Fig. 6 is a radially staged burner design incorporating an aerated nozzle fueled, swirl stabilized pilot zone, located inboard and upstream of a premixed/prevaporized main zone. The main zone premix passage is separated into 24 compartments that occupy approximately 70 percent of the available burner inlet circumferential area. The remaining area between passages is used for structural support to allow a free floating flameholder design. Several flameholder types were evaluated before selecting the V-gutter design presented in Fig. 6. Each compartment contains four individual V-gutters that are free to expand in the longitudinal direction in order to minimize stresses and distortions. The size and spacing within each compartment were selected from the results of a previous NASA program [9] in which a conical V-gutter flameholder was evaluated for stability and emissions. Forty-eight pressure atomizing fuel nozzles mounted on the pilot fuel nozzle supports supply the main zone with fuel.

The concept differs from the previous designs in the method in which front end airflow and equivalence ratios are controlled. Instead of a mechanical type of area modulation, diffuser wall bleeding is used to vary the inlet air velocity profile. Both inner and outer wall bleeds are used to divert airflow from the burner front end at only the approach condition. The design is based on a variable geometry combustor evaluated as part of a research program directed at determining the feasibility of controlling exhaust emissions in a purely aerodynamic manner [12].

Concept 4. The Concept 4, shown in Fig. 7, was patterned after a promising design developed during the NASA/Pratt & Whitney Aircraft Advanced Low Emissions Catalytic Combustor Program [6].

Valves located in the outer diameter shroud area allow simultaneous control of primary and dilution zone airflows. At the idle condition the inner valves are closed and the outer ones are open. This prevents air from entering the primary zone through the side ports, allowing stoichiometric burning for high combustion efficiencies and low levels of CO and UHC. At high power conditions the outer valves are closed and the inner ones are open, allowing the combustion air to enter the primary zone through the side ports, providing very lean combustion for reduced NO_x emission levels. A split diffuser is used to give the desired flow split between inner diameter and outer diameter shroud. To insure adequate cooling of the front end combustor outer liner at all conditions, cooling airflow is provided by double wall construction, with the resultant annulus feed from inside the hood. A separate annulus passage is provided between the outer valves and the outer diffuser case to supply both cooling air necessary for the combustor outer liner aft section and dilution air for temperature distribution control. Twenty four airblast fuel injectors are provided in a conventional externally removable arrangement.

The size and location of the air control valves introduced several mechanical design problems. Physical size restraints required both an outward expansion of the burner case to accommodate the valve assembly and a recontouring of the diffuser to provide an aerodynamically clean feed to the valve inlet tubes. Furthermore, the resultant "one sided" combustor could introduce penetration and mixing deficiencies that would adversely effect both emission and exit temperature distribution. Providing additional air control valves in the inner diameter shroud area was considered as a possible fix, but since it would result in a drastic increase in complexity without eliminating the physical size problems it was not incorporated in the design.

Design Analysis

Gas turbine engine combustors must satisfy many functional requirements simultaneously. The combustor must be capable of burning all the fuel efficiently while constraining exhaust pollutants to stringent limits. The mean temperature of the gases leaving the combustion section has to be commensurate with cycle efficiency requirements, but the maximum local temperature and temperature radial distribution (profile) must be compatible with turbine material limitations. All functions must be performed with minimum pressure loss, since such losses represent a reduction in available energy to the cycle. The combustor must ignite the fuel-air mixture easily and be capable of keeping it lit over wide ranges of fuel temperature, ambient air temperature and ambient pressure. It must not be subject to blowouts resulting from either too rich or too lean fuel-air mixtures, and it must retain its efficiency over the required operating range of the engine. Off-design temperature rise capability has to be compatible with the rotating machinery characteristics so that smooth acceleration of the engine can be achieved. Response of the combustor to throttle movements must be rapid to permit safe flight operations. The combustion section is required to perform all these functions while containing a high temperature combustion process and not compromising the durability of the engine. Each concept was analyzed for its potential in meeting the basic requirements described above and the emission and performance goals of this program shown in the program description section. In these analyses, test data have been used wherever available to assess or substantiate the evaluation.

Emission Estimates. The estimated emissions for the four concepts are presented in Table 2. As indicated, the CO and UHC levels for all four concepts are expected to meet the program goals, except for Concept 3 UHC which is slightly above the EPAP goal of 3.3. The estimates were made from the combustion efficiency relationship by assumming a CO to UHC ratio of 7 to 1 at idle based on several previous emissions programs.

The primary goal of the program was, however, to achieve the NO_x goal at the cruise condition. As shown, only two concepts, 1 and 2, are expected to attain values near the goal EI of 3.0. NO_x emissions for Concept 1 at cruise were estimated by two methods, the first used data generated in a recent NASA program [13] to account for the effect of incomplete vaporization. Using data from this study, a NO_x EI at cruise of 3.1 was predicted for the Concept 1 configuration operating at approximately 70 percent vaporization. The effect of the incomplete vaporization was also estimated by comparing the results obtained with a premix burner design that was evaluated in a Pratt & Whitney Aircraft engine test program [3]. In the reference program, the combustor premix passage was operated at an equivalence ratio of approximately 0.65 and a calculated vaporization of 45 percent. By assuming that the difference between the measured NO_x and the predicted value for 100 percent vaporization and perfect mixing was due to the unvaporized fuel, an estimate was made of the emissions for the Concept 1 configuration operating at 70 percent vaporization with some droplet burning. At the cruise condition, the NO_x emissions index was estimated at 3.9 using this approach. Since this second estimate is based on actual engine data, it is probable that the higher value is the result of poor fuel/air preparation. It is likely that the value for the Concept 1 configuration when tested at E^3 cruise condition will be somewhere in between.

The emission levels predicted for Concept 2 were estimated from the results of a Pratt & Whitney Aircraft rig test program directed at evaluating the configuration from which Concept 2 has been modeled. Variable geometry was simulated by utilizing blockage rings in back-to-back rig tests to vary the airflow through an outer passage which served as the main combustor stage. At idle conditions, fuel and air were supplied through just the inner pilot stage, while at higher power condition, the blockage rings were removed and both the inner and outer passages were fueled. Although testing during this program was limited in scope, the results did demonstrate the excellent potential of this concept toward NO_x emission reduction. When these test data were extrapolated to the E^3 cruise condition, NO_x EI for Concept 2 was estimated at 2.4.

Table 2 Emission Estimates

	Goal	Concept 1	2	3	4
CO EPAP (g/kN)	≤25	12	24	21	12
UHC EPAP (g/kN)	≤3.3	1.7	0.5	3.9	1.7
NO_x EPAP (g/kN)	≤33	<33	<33	>33[1] <33[2]	<33
NO_x EI at cruise (g/kg)	≤3.0	3.1 to 3.9	2.4	30[1] 4.8[2]	7.5
Smoke no.	≤20	<10	<10	<10	<15

[1] With 25 percent front end flow diversion
[2] With 50 percent front end flow diversion

During the preliminary analysis of Concept 3, it was evident that the degree of front end airflow modulation available with a diffuser bleed control was critical in estimating emission levels. The analysis was therefore conducted for different values of airflow diverted from the combustor front end. Specifically, values between 25 and 50 percent were considered even though the higher percentages (over 25 percent) were considered beyond the reach of current technology.

The flow distribution within the combustor was determined by setting the equivalence ratio at approach with bleed sufficiently high to ensure a combustion efficiency of 99.0 percent. The test results from previous emission program [3] were used in establishing a value of 0.70 at approach. The unbled equivalence ratios at cruise were then back-calculated for each bleed condition being analyzed and NO_x emission levels at cruise were estimated following the same theoretical procedure used for Concept 1. The results of the analysis as shown in Table 2 indicate that unless a very high percentage of flow can be diverted, this method does not have much potential for NO_x reduction.

NO_x emissions for Concept 4 were estimated based on an assumed 50 percent variation in IBZ equivalence ratio due to poor mixing and were calculated from pollutant measurements taken from partially mixed turbulent flames during a flame tube study at Pratt & Whitney Aircraft [14].

Comparison of Concepts. As shown in Table 2, Concept 1 and 2 offer the potential of achieving the emission goals while Concepts 3 and 4 are considered to have very little chance for satisfying the program NO_x emission goals at cruise; Concept 3 lacks a sufficient bleed capability and Concept 4 because of poor fuel air mixing.

In comparison with Concepts 1 and 2, Concepts 3 and 4 are considered inadequate in the area of combustor performance, Concept 3, due to probable variations in pressure drop and poor combustion efficiency at approach, and Concept 4 as a result of a potentially troublesome pattern factor and exit radial temperature profile.

Concept 2 was judged slightly superior to Concept 1, because of an expected improvement in stability, relight capability and transient operation with dual staged fuel nozzles.

Concluding Remarks

Based on the analytical projections made during this conceptual design study, two of the four concepts (Concepts 1 and 2) offer the potential of achieving the emission goals while satisfying nearly all of the performance requirements. However, the projected operational characteristics and reliability of any of these concepts to perform satisfactorily over an entire high pressure ratio aircraft engine envelope would require extensive experimental substantiation before an engine application can be considered.

Other fundamental SCERP Phase I activities and this design study program revealed areas of concern as well as the need for technology improvement. The LPP is based on supplying the combustion zone with well mixed and well vaporized fuel-air mixture. Both these goals may prove to be difficult to attain in practice, within reasonable combustor lengths and without incurring autoignition and/or flashback. In the design of the premixing passages for the LPP systems, precautions were taken to avoid potential flow problems, such as wakes behind variable geometry devices and fuel injectors, which

could increase residence time of the fuel air mixture in the premixing passage. Incomplete mixing/vaporization, hence higher NO_x emissions, were weighed against providing adequate margin to avoid autoignition and flashback.

It is evident that future development must concentrate on achieving uniform fuel-air mixture preparation if the full potential of this concept is to be realized. At the present time, the most practical means of achieving rapid fuel vaporization would appear to be ultrafine atomization. The effect of utilizing larger quantities of front end combustion air requires advanced, efficient cooling techniques to achieve the desired liner durability in the more severe operating environment of future aircraft engines. An additional design consideration is the cooling requirements of the flameholders. On the positive side, lean premixed burning should achieve lower primary zone gas temperatures, lower smoke levels and a reduction of flame radiation which in turn should alleviate the cooling requirements.

The anticipated design problems with variable geometry features are their control, operational characteristics and durability. The air staging mechanisms will require control systems and sensors more complex than those used in current engines. Until fabrication drawings are available and construction, testing and final refinements to the combustor hardware have been accomplished, no meaningful estimates can be made of the time and cost to develop one of the LPP fuel combustor conceptual designs into an operational engine combustor.

Although variable geometry introduces complexity with respect to combustor design for emissions reduction, it represents a new degree of freedom for advanced engine designs. Future engine requirements of high thrust-weight ratios, higher temperature rise, smaller combustor volume and extended flight envelopes will make it very difficult to satisfy both emission and performance requirements. Air staging offers the unique potential of significant improvement in both areas.

References

1 Grobecker, A. J., Coroniti, S. C., and Cannon, R. H., "The Effects of Stratospheric Pollution by Aircraft, Report of Findings," U.S. Department of Transportation, DOT-TST-75-50, Dec. 1974.

2 Fiorentino, A. J., Greene, W., and Kim, J. C., "Lean, Premixed, Prevaporized Fuel Combustor Conceptual Design Study—Final Report," NASA CR-159647, Aug. 1979.

3 Goldberg, P., Segalman, I., and Wagner, B., "Potential and Problems of Premixed Combustors for Application to Modern Aircraft Gas Turbine Engines," AIAA/SAE 12th Propulsion Conference, AIAA Paper No. 76-727, July 1976.

4 Rudey, R. A., and Reck, G. M., "Advanced Combustion Techniques for Controlling NO_x Emissions of High Altitude Cruise Aircraft, NASA TM X-73473, 1976.

5 Spadaccini, L. J., "Autoignition Characteristics of Hydrocarbon Fuels at Elevated Temperatures and Pressures," ASME Paper 76-GT-3, Mar. 1976.

6 Sturgess, G. J., "Advanced Low Emissions Catalytic Combustor Program—Phase I," NASA CR-159656.

7 Appleton, J. P., and Heywood, J. B., "The Effects of Imperfect Fuel-Air Mixing in a Burner on NO Formation from Nitrogen in the Air and the Fuel," 14th Symposium (International) on Combustion, University Park, Pa., Aug. 20–25, 1972, pp. 777–786.

8 Marek, C. J., Papathakos, L. C., and Verbulez, P. W., "Preliminary Studies of Autoignition and Flashback in a Premixing-Prevaporizing Flame Tube Using Jet-A Fuel at Lean Equivalence Ratios," NASA TM X-3526, May 1977.

9 Roffe, G., and Venkataramani, K. S., "Experimental Study of the Effects of Flameholder Geometry on Emissions and Performance of Lean Premixed Combustors," NASA CR-135424, June 1978.

10 Roberts, R., Fiorentino, A., and Greene, W., "Experimental Clean Combustor Program Phase III—Final Report," NASA CR-135253, Oct. 1977.

11 Andersen, D. N., "Effects of Equivalence Ratio and Dwell Time on Exhaust Emissions from an Experimental Premixing Burner," NASA TM X-71592, 1975.

12 Adkins, R. C., and Elsaftawy, A. S., "A Double Acting Variable Geometry Combustor," ASME 79-GT-197, Mar. 1979.

13 Cooper, L. P., "The Effect of Degree of Fuel Vaporization Upon Emissions for a Premixed—Prevaporized Combustion System," AIAA Paper No. 79-1320, AIAA/SAE/ASME, 15th Joint Propulsion Conference, June 1979 (NASA TM 79154).

14 Semerijian, H. G., Ball, I. C., and Vranos, A., "Pollutant Emission from Partially Mixed Turbulent Flames," AIAA Paper No. 77–94, July 1977.

Tests of an Improved Rotating Stall Control System on a J-85 Turbojet Engine

G. R. Ludwig
Program Manager.

J. P. Nenni
Senior Aeronautical Engineer.

Aerodynamic Research Department,
Calspan Advanced Technology Center,
P.O. Box 400,
Buffalo, NY 14225

An improved version of a rotating stall control system has been tested successfully on a J-85-5 turbojet engine. Past tests had pointed out the desirability of increasing the response speed of the control. In this study, the installation of the stall control on the J-85 was modified so as to decrease the response time of the control by a factor of ten over that attained in the past tests. The modified control was tested to see if the decreased response time improved the ability to clear rotating stall once it has started, and also to see if rotating stall could be anticipated and prevented by proper selection of the variables in the stall control detection system. The performance of the stall control was tested by closing the bleed doors on the engine until rotating stall occurred or until the control anticipated stall and held the bleed doors open. The tests showed that the control is capable of anticipating stall before it occurs and keeping the engine completely clear of stall at speeds up to 80 percent of design speed. No tests were performed above 80 percent of design speed because opening the bleed doors at such speeds might aggravate the stall rather than clear it.

Introduction

The useful operating range of a turbine engine compressor is greatly influenced by its stalling characteristics. The optimum performance of a turbopropulsion system is usually achieved when the compressor is operating near its maximum pressure ratio. This is generally close to the stall line of the compressor where rotating stall and/or surge will occur. Because of the serious mechanical damage that may result during compressor stall cycles, a factor of safety (stall margin) must be provided between the compressor operating line and the stall boundary. This is usually done by prescheduling the primary engine controls. However, the prescheduling approach has not been entirely successful in that experience has shown that provision of a practical amount of stall margin does not always keep the engine out of stall under all off-design and transient conditions. It is clear, then, that an engine control system that can sense incipient destructive unsteady flow in a compressor and take corrective action would allow for reduced stall margins in the design and thus lead to engine performance gains or increased operational flexibility.

The work reported herein is concerned with the development of a fast acting control system which can sense the onset of rotating stall and keep the engine from operating in the rotating stall mode. The control is an electrical feedback control system which uses unsteady pressure signals produced by sensors within the compressor to detect incipient rotating stall and to provide a correction signal when such conditions occur. In a previous program, [1] and [2], the control was tested on a low speed research compressor and on a J-85-5 turbojet engine. The tests on the J-85 were successful in demonstrating that rotating stall can be controlled at engine speeds up to 70 percent of design speed and that the rotating stall detection system worked very well. However, the test results at 70 percent of design speed showed that, although the control acted fast enough to allow full recovery from rotating stall without engine damage of flameout, there was a noticeable change in engine operating parameters. Moreover the test results did not demonstrate that the stall control system can anticipate stall and prevent its occurrence completely.

In the current program, the installation of the rotating stall control on the J-85 was modified so as to decrease the response time of the control by a factor of ten. This paper summarizes the results of a series of tests of the modified control on the J-85 engine. The test program had two objectives; the first was to investigate how much improvement in stall recovery performance can be obtained by substantially reducing the response time of the control, the second was to determine if rotating stall can be anticipated and prevented by proper selection of the variables in the stall control detection system.

Brief descriptions of the control and its installation on the J-85 engine, and a summary of the test results, are presented in the following paragraphs. Further details and test results can be found in [3].

Description of the Rotating Stall Control System

The operating principle of the rotating stall control system has been presented in [1] and [2]. A condensed description is repeated here for the sake of clarity and completeness.

The control is an electrical feedback control system which uses unsteady pressure signals produced by pressure sensors within the compressor to detect the presence of stall and provide a correction signal when stall occurs. In the prototype system, the correction signal is used to drive a hydraulic actuator which provides a mechanical operation on some variable geometry feature of the compressor to be controlled. In an initial demonstration of the control, the variable

Contributed by the Gas Turbine Division and presented at the Gas Turbine Conference and Products Show, New Orleans, La., March 10–13, 1980 of THE AMERICAN SOCIETY OF MECHANICAL ENGINEERS. Manuscript received at ASME Headquarters December 7, 1980. Paper No. 80-GT-17.

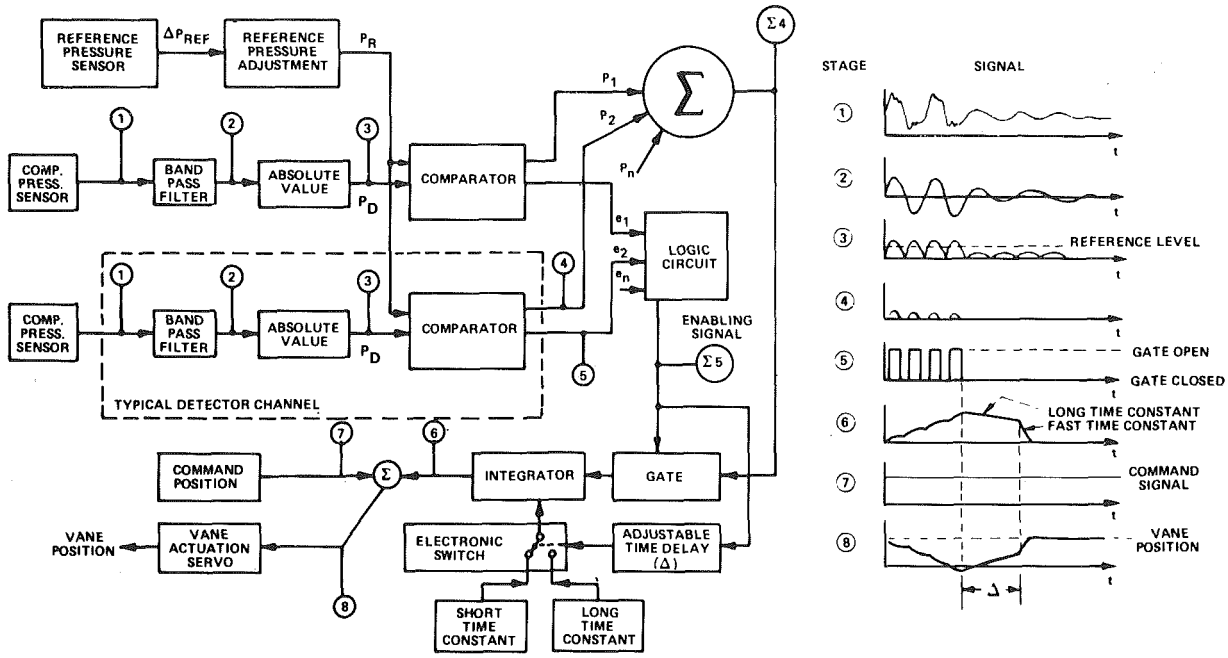

Fig. 1 Block diagram of rotating stall control system

geometry was the stagger angle of stators in a low-speed research compressor. In tests on an aircraft J-85 jet engine, the controlled variable geometry features are compressor bleed doors and inlet guide vane flap deflection. In principle, the stall control may be applied to any compressor or engine which has the variable geometry required to eliminate rotating stall.

The signal conditioning and processing subsystems of the stall control are shown in block diagram form in Fig. 1. The signals at various stages in the circuit are shown schematically on the right side of the figure. In the following description, stator stagger angle is used as the stall correcting variable for illustrative purposes.

1 Time varying electrical signals are obtained from the pressure transducers within the compressor (Stage 1).

2 These signals are bandpass-filtered to remove steady state and low frequency variations (which are not associated with rotating stall) and high frequency contaminants such as instrument noise and rotor blade passage effects (Stage 2).

3 Each bandpass signal is then processed in an absolute value circuit (rectified) to obtain a conditioned detector signal, P_D (Stage 3).

4 Each conditioned signal, P_D, is then input to a voltage comparator circuit along with a second signal, P_R, which is proportional to the static pressure rise, ΔP_{REF}, across the compressor. The P_R signal is conditioned by a critically damped low pass filter so that it responds only to slowly varying changes. This signal is used to compensate the stall control for changes in compressor operating conditions such as compressor rotational speed and aircraft altitude. The comparator produces two output signals. The first signal, Stage 4, is obtained by comparing the conditioned detector signal, Stage 3, with the reference pressure signal, P_R. Only that portion of the Stage 3 signal which exceeds the reference pressure signal is passed. The second comparator output signal, Stage 5, is used to control an electronic gate. This signal activates the gate whenever the Stage 3 signal exceeds the reference level, P_R. The gate has been included in the circuit to ensure that the next component in the system, the integrator, is referenced to zero voltage whenever the input Stage 3 signal is below the reference level, P_R.

5 The Stage 4 and Stage 5 signals constitute the output from a typical detector channel in the stall control system. The prototype stall control contains ten such channels, each with two outputs. The Stage 4 outputs are summed to produce a composite analog signal (Stage $\Sigma 4$) that represents the combined amount that all pressure sensor signals exceed the system reference pressure. The Stage 5 gate enabling signals are combined digitally in a logic circuit to produce a composite gate enabling signal (Stage $\Sigma 5$).

6 The output from the gate is fed into an integrator. The integrator gain and decay rate are independently adjustable. The output from the integrator (Stage 6) is then a signal which is obtained by integrating only those portions of the conditioned detector signals whose absolute values exceed the reference pressure level, P_R. With proper selection of P_R, the integrator output is nonzero only when stall is occurring or is very close to occurring in the compressor. When stall does occur, the integrator output increases rapidly to provide a correction signal which is proportional to the severity of the stall which is occurring. The Stage 6 electrical signal is the basic stall correction signal.

7 The output of the integrator, Stage 6, is summed in opposition with a command position signal, Stage 7. This command position signal is obtained from the primary engine control system and represents the normal (unstalled) operating schedule for the variable geometry on the compressor. The output of the summer, Stage 8, is fed back into the primary engine control to move the compressor away

Nomenclature

B = detector bias level used in conditioning of compressor static pressure rise (see Fig. 2)

K = detector level gain used in conditioning of compressor static pressure rise (see Fig. 2)

N = engine speed

N^* = rated speed of J-85 engine, (16,560 rpm)

P_D = detector signals—amplitude of conditioned pressure fluctuations from control transducers

P_R = system reference pressure used by stall control system

q_o = inlet dynamic pressure measured upstream of compressor face

T = ambient temperature

Δ = time delay factor in rotating stall control, (0.2 seconds)

ΔP_{REF} = compressor static pressure rise measured on outer casing

θ = ambient temperature ratio, $\frac{T\ (\text{Kelvin})}{288.2}$

from the stalled condition. In the illustration of Fig. 1, the primary engine control is assumed to be a stator vane actuation servo. In this case, the servo would act to move the stator vanes away from the stalled condition (reduce angle of attack). When the stall has been removed, the Stage 3 detector signals decrease below the reference level, P_R, causing the integrator input, (Stage $\Sigma 4$), to drop to zero. The output voltage of the integrator, Stage 6, then decays in a way which is controlled by the integrator decay circuitry, which consists of a time delay circuit, and two decay time constant circuits. When the Stage 6 signal has decayed sufficiently, the original command signal, Stage 7, resumes control allowing the engine to resume normal operation (stator vanes move to their original position in the illustration).

The integrator decay circuitry in Fig. 1 is designed to prevent over-control of the engine after stall has been eliminated. The circuitry produces a short time constant when the electronic switch is closed and long time constant when the switch is open. Stall pressures in excess of the reference level, P_R, cause the electronic switch to open and, thereby, establish the long time constant which is maintained as long as the stall pressure signal is in excess of P_R. If the stall pressure signal falls below the reference level, the integrator is switched to the short time constant after a specific time delay. Thus, the system selects the fast recovery time (short time constant) only if the pressure signal remains below the reference level longer than the delay time, Δ.

In the prototype control system, the mechanical operation commanded by the electronic console is performed by an electro-hydraulic servomechanism. In general, the servo consists of a flow control valve, a feedback potentiometer and a linear actuator. Two different servo systems have been used in tests on the J-85 engine. In the original installation, [1], a small actuator was used in the mechanical feedback link of the J-85 fuel control system. The bill-of-material actuators on the engine were used to operate the variable geometry. In the current installation two larger, high-speed actuators were used to replace the bill-of-material engine actuators. Both servo systems are described in the following section.

Installation of Stall Control on J-85-5 Engine

Stall control tests on the J-85 engine have been performed with two different installations for the variable geometry actuators on the engine. In both cases, the stall control detection system was the same, only the actuation system was changed. In this section, the features of the stall detection system, common to both test series, will be described first. This is followed by a description of the original actuation system of [1] and [2]. Finally, a description of the improved high-speed actuation system used in the current study is presented.

Stall Detection System. As described earlier, the inputs to the stall control are unsteady pressure signals produced by sensors mounted in the compressor. On the J-85 engine, eight pressure transducers are used to provide rotating stall control signals. All of the transducers are mounted to measure the pressure fluctuations on the inner surface of the compressor casing at four axial locations near the front of the compressor. Two transducers, separated circumferentially, are used at each axial location. The axial locations are governed by the geometry of the existing compressor casing which includes stiffener flanges on the external surface and stator support rings on the inner surface. The four axial locations are as follows:

1 Near the first stage rotor mid-chord

2 Near the quarter-chord of the first stage stator, as close to the stator suction surface as possible

3 Near the trailing edge of the second stage rotor

4 Between the second stage stator trailing edge and the third stage rotor leading edge

The circumferential locations of the control pressure transducers were selected so they do not interfere with mounting of the accessories and stall control on the compressor casing.

In addition to the eight control pressure transducers, two other pressure transducers were incorporated on the J-85. One of these transducers measured the static pressure rise across the compressor for use as the input reference pressure, ΔP_{REF}, to the rotating stall control system. The other transducer was used to measure the dynamic pressure, q_0, at the throat of the bellmouth upstream of the J-85 compressor. This transducer is not required by the stall control system. It was used simply to provide a measure of the mass flow through the compressor.

The rotating stall control operates by comparing the amplitude of conditioned signals, P_D, from the control pressure transducers in the compressor with the magnitude of a conditioned reference pressure signal, P_R. Prior to conditioning, the unsteady signals from the control transducers contain high frequency fluctuations caused by rotor blade passage and low frequency fluctuations associated with transient operation of the engine. Both of these components, which are associated with normal engine operation, could mask the presence of rotating stall. Thus, it is necessary to filter the control transducer signals to reduce or eliminate the high and low frequency components. The optimum filter characteristics were selected by observing the action of the control in response to tape recorded transducer signals from the engine operating under normal conditions and under stalled conditions. The filter characteristic selected has been presented in [2].

The reference pressure, P_R, used by the control for comparison with the unsteady sensor signals was derived from the static pressure rise ΔP_{REF}, across the compressor. In general, it is desired that the magnitude of the reference pressure after conditioning vary with engine speed and inlet air density in the same way as the conditioned signals, P_D, from the control pressure transducers under normal unstalled operating conditions. The engine test cell at Calspan does not allow for control of inlet air density. (Some stall control tests at simulated altitude conditions have been performed by the U.S. Air Force Aero Propulsion Laboratory, [4].) However, the variation of P_R with engine speed can be selected. Initial tests pointed out a deficiency in varying P_R linearly with ΔP_{REF}. At low compressor speeds, the system reference pressure became very small and the control took action even in the absence of rotating stall. To prevent this occurrence, the system reference pressure circuit was modified so that the reference signal was always maintained above a prescribed minimum positive value.

A sketch of the system reference pressure variation in response to an input pressure variation is shown in Fig. 2. The input pressure is shown starting at a negative value and rising to some positive value. Fluctuations in the input pressure are also shown. These fluctuations are removed from the system reference pressure by a one radian/s second-order critically-damped filter. If the input pressure is negative or zero, the system reference pressure is maintained at a positive value, B, selected by a bias control. Once the input pressure becomes positive, the system reference pressure is increased above the bias level by an amount equal to the value of the input pressure multiplied by the detector gain, K. Both the detector bias level, B, and detector gain, K, are variable in this prototype control system. On the J-85 engine, the static pressure rise, ΔP_{REF}, is always zero or some positive value. Thus, the conditioned reference pressure, P_R, is given by

$$P_R = B + K\,\Delta P_{REF}$$

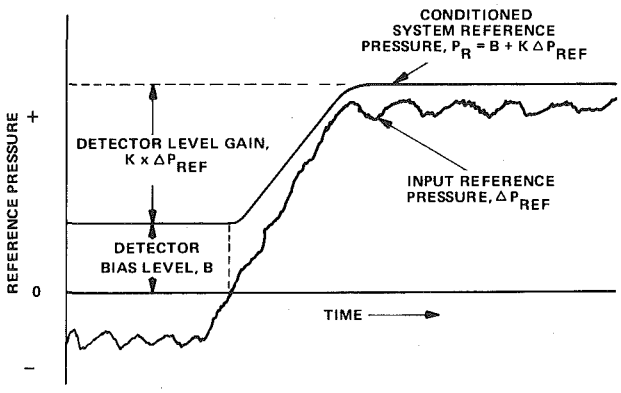

Fig. 2 Sketch showing signal conditioning of input reference pressure

The stall control performance on the J-85 was tested for three different combinations of bias and gain. The variation of P_R with engine speed is shown in Fig. 3 for each combination of B and K. Also shown are measured data points for the on-schedule detection level, P_D, which represent the combined background noise during normal engine operation from all control transducer signals. The reference pressure curve, P_R, must be above the normal background level data to avoid unwarranted action by the stall control system. However, locating the P_R curve too far above the background level will allow stall to develop before corrective action is initiated. In the original stall control tests reported in [1] and [2], the upper P_R curve ($B = 240$ mV, $K = 0.084$) was used in all of the tests. In the current program, all three P_R curves were used to investigate whether rotating stall could be anticipated and eliminated completely.

The above description of the stall control detection system is common to both the original test series of [1] and [2] and the current series. However, the variable geometry actuation system differed in the two test programs. These are described next, with the original system presented first.

Original Variable Geometry Actuation System. The output from the stall detection system is an electrical signal which is used to govern an electro-hydraulic servomechanism for operating some variable geometry features on the compressor to be controlled. On the J-85 engine, which has an eight stage compressor, the variable geometry consists of the inlet guide vanes and bleed doors on the third, fourth, and fifth stages of the compressor. The positions of the guide vanes and bleed doors on the J-85 are normally controlled by the fuel control system as a function of engine rpm and inlet air temperature. A mechanical feedback cable between the variable geometry actuators and the fuel control is used to ensure that the proper position is maintained. In the original installation, the rotating stall control system was incorporated into the main J-85 control system by replacing the mechanical feedback cable with another mechanical cable which was operated by the stall control system. This cable replacement was the *only* change made in the normal J-85 fuel control system. The variable geometry actuators continued to be operated by the fuel control but the response could be modified by action of the stall control on the feedback loop. Essentially the stall control deceived the engine fuel control into performing the desired stall control functions. The principal advantage of incorporating the stall control in this way was that it minimized the engine modifications which were required. A major disadvantage was that response speed of the installation was limited by the response of the J-85 fuel control system.

The response of the original control installation to rotating stall inception on the J-85 engine is illustrated in Fig. 4. The records in this figure were obtained by closing the J-85 bleed doors slowly to induce rotating stall at constant engine speed. This particular set of records is from a test at the highest corrected engine speed (71.8 percent) used in the original test series. The top two records in Fig. 4 show the bleed door position and the compressor static pressure rise, ΔP_{REF}, across the J-85 compressor. The unsteady detector pressure signals generated by half of the eight control pressure transducers are shown in the bottom four records. The high frequency portions of these signals have been filtered as described in [2].

A vertical dashed line labeled "Reference Time Zero" has been included on Fig. 4 to indicate the approximate time at inception of rotating stall. The position of this line corresponds to the first indication of rotating stall in any of the detector pressure signals. Inspection of this set of expanded time records shows that the duration of the stall, measured from time zero until stall has disappeared, was about 310 milliseconds. Inspection of the bleed door position record shows that there is a delay between reference time zero and the time at which the bleed doors begin to open. For this case, which was the most severe stall in the original test series, the delay was approximately 30 ms. At the same time the compressor static pressure rise began to drop after a delay of only 10 ms. Thus, although the control opened the bleed doors fast enough to allow full recovery without damage or flameout there was a noticeable change in engine operating parameters. It was concluded that it would be desirable to increase

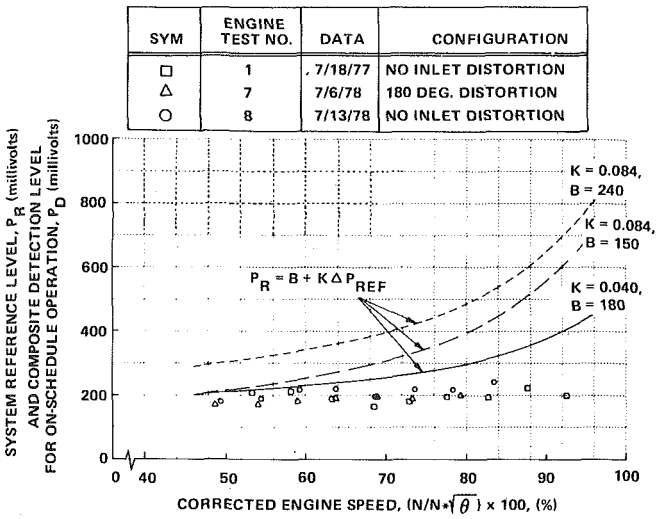

Fig. 3 System reference levels used in stall control tests on J-85 engine

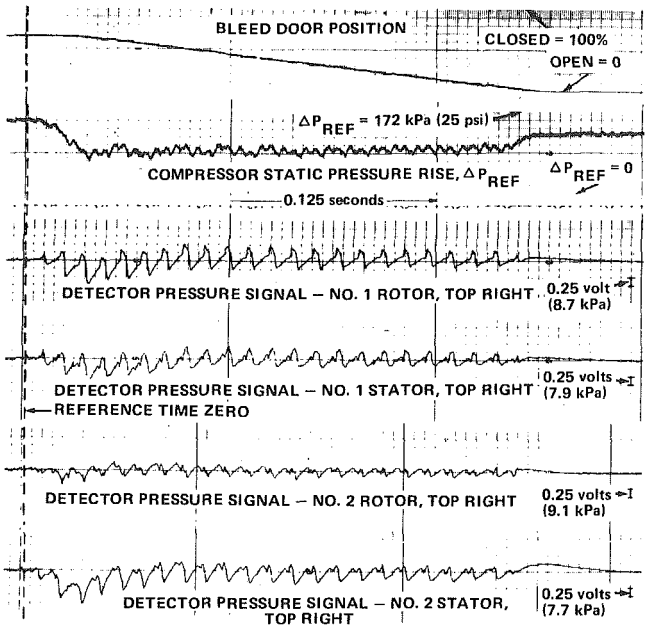

Fig. 4 Performance of original stall control installation on J-85 engine: (expanded time scale), 180 deg circumferential inlet distortion, corrected engine speed ($N/N^*\sqrt{\theta}$) = 71.8 percent

the speed at which the bleed doors open to minimize these variations in engine operating parameters.

Improved Variable Geometry Actuation System. In the current installation of the stall control system on the J-85 engine, the response speed of the system was increased greatly by eliminating the J-85 fuel control from the stall control actuation system. A schematic drawing of the improved installation is shown in Fig. 5. The modified installation is as follows. The hydraulic output generated by the fuel control to provide on-schedule operation of the variable geometry is still used to drive the J-85 variable geometry actuators. However, these actuators are not connected to the compressor variable geometry. Instead, they are used to position a linear potentiometer from which the required electrical signal for normal on-schedule performance is derived. This on-schedule signal, which can be filtered to reduce electrical noise, is combined within the rotating stall control with the existing stall control signal and off-schedule performance signal to give a single electrical output from the stall control console.

This combined signal is used in conjunction with a new flow-control valve (Moog Series 32 Servovalve) to control two new high-speed actuators on the compressor variable geometry system. The new actuators were fabricated at Calspan. The existing hardware links between the new hydraulic actuators and the compressor guide vanes and bleed doors did not require modification. However, a new larger capacity source of hydraulic power for the actuators was required because the small unit on the original installation was not adequate to drive the actuators. The modified variable geometry servo-system was designed to generate 100 percent bleed door travel in about 25 ms. This is substantially faster than the capability of the engine bleed door control servo. The latter was found to generate 100 percent bleed door travel in about 400 ms.

The improvement in the response speed of the bleed doors on the J-85 compressor is shown in Fig. 6 where the original and the current installations are compared. The figure shows the measured time response of the bleed doors to a large amplitude stall which starts with the bleed doors closed 80 percent. The response curves also represent the configuration of the flaps on the inlet guide vanes since these are connected mechanically to the bleed door actuation mechanism. There are two response curves for the current installation: one with a rate limiter on the stall control output and one with the rate limiter removed. The rate limiter was installed for the initial series of tests in the current program to lessen the chance of hardware failure in the bleed door actuation system.

The response curves of Fig. 6 show that the bleed doors do not begin to move immediately when stall inception is detected. Rather, there is a time delay between stall inception and initial bleed door motion. This time delay occurs because of lags in the various components of the mechanical-hydraulic actuation system and should be made as small as possible. Large time delays will allow the stall to develop fully before any corrective action occurs on the compressor. The rate at which the bleed doors move after the initial time delay is also important because the combination of initial time delay plus final rate of motion determines the overall time required for full corrective action on the compressor.

As can be seen in Fig. 6, the current installation of the stall control provides a substantial improvement in response speed of the J-85 bleed doors to correction signals from the stall control system. The total time required to open the bleed doors from an initial position 80 percent closed has been reduced from 376 ms for the original installation to a minimum of 36.5 ms for the current installation without rate limiting. With the rate limiter installed, the corresponding time is 76.6 ms which is still a large reduction in total response time. The first control tests during the present program were performed with the rate limiter installed on the control system. Later control tests were performed with the rate limiter removed.

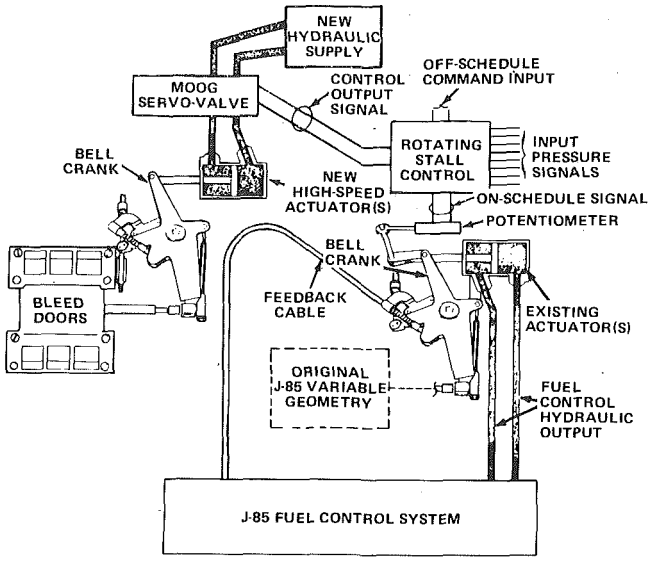

Fig. 5 Configuration of stall control on J-85 engine used to obtain rapid response to stall inception

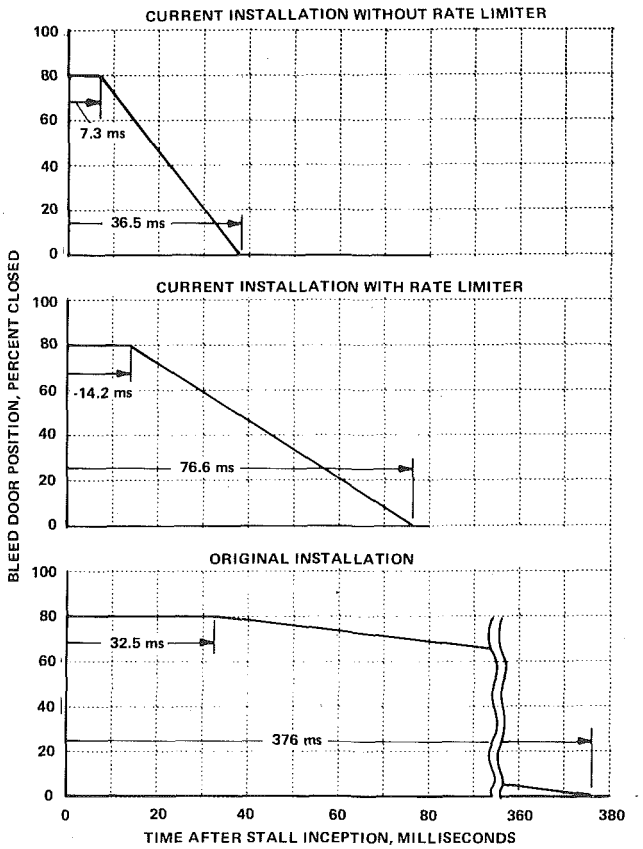

Fig. 6 Comparison of J-85 bleed door response rates to large amplitude rotating stall starting at bleed doors 80 percent closed

Stall Control Tests

The current test program on the rotating stall control system had two objectives. The first objective was to investigate how much improvement in stall recovery performance can be obtained by substantially increasing the response speed of the variable geometry on the J-85 engine. The second objective was to see if rotating stall could be anticipated and eliminated by proper selection of the conditioning parameters for the reference pressure.

The J-85 was stalled in two ways. The majority of the tests were performed by closing the bleed doors at constant engine speed until the engine stalled or the control took action to prevent stall. In addition, some tests were performed by decelerating the engine with the bleed doors partially closed at the beginning of the deceleration. Both types of tests were performed with no inlet distortion and also with 180 degree circumferential inlet distortion. The distortion screen has been described in [1]. Overall, the test results were excellent and sample results will be presented in the following. A more complete presentation of test results is given in [3].

Stall Recovery Tests. Figs. 7–12 are representative multichannel strip recorder charts which illustrate the performance of the control system when the compressor is forced into rotating stall by closing the bleed doors at constant engine speed. In this series of tests, the stall control was intentionally detuned to allow the compressor to stall. The records include corrected engine speeds of approximately 70, 75 and 80 percent of rated speed. Lower speed stalls are not presented since they were not as severe and were cleared rapidly by the stall control system. The data presented in these figures are for cases with 180 degree inlet distortion, and all with the exception of Figs. 11 and 12 have the rate limiter removed from the system. At corrected engine

speeds of 70 and 75 percent the results with clean inlet flow were similar to those presented here. In those tests with the rate limiter in operation, usually two or three more cycles of rotating stall were permitted before the stall was cleared. The engine was allowed to stall only once at a corrected engine speed of 79.4 percent, Figs. 11 and 12, since this was a rather severe stall. In this case the rate limiter was in operation on the stall control system.

Each stall in Figs. 7–12 is presented on two consecutive figures. The first figure presents strip chart records obtained directly while the test was in progress and includes approximately 10 seconds of test results. The second figure presents essentially the same results on a much expanded time scale which covers approximately 320 ms. The expanded time records were obtained by replaying at low tape speed, FM tape records of the tests which were recorded at high tape speed. In each figure six recorded traces are shown as a function of time. The time increases from left to right and the time scale is indicated just below the second record from the top. The upper five records on each of Fig. 7–12 present the same variables. The last record on the directly recorded strip chart is compressor inlet dynamic pressure, q_0. The last record on the expanded time scale chart is the detector pressure signal from one of the control pressure transducers mounted in the compressor outer casing.

The stall control test records for a nominal engine speed of 70 percent (Figs. 7 and 8) show that the effect of the stall on the engine was relatively small. There was a momentary drop in compressor static pressure rise and inlet dynamic pressure. In addition there was a small drop in engine speed, about 2 percent, just after stall was cleared. The small changes observable in the engine operating parameters after the stall has cleared are due to the opening of the bleed doors and are not part of the transient response of the engine to the stall. The expanded time record, Fig. 8, shows that only four small stall cells occurred in a duration of approximately 35 ms. The stall was cleared before the doors were fully open. A similar test with the rate limiter in operation showed that the stall lasted approximately 70 ms. These results are a dramatic improvement over the earlier test results (Fig. 4) where the speed of the bleed door response was limited by the capability of the J-85 fuel control system.

Results for a stall control test at a nominal engine speed of 75 percent are presented in Figs. 9 and 10. With the rate limiter removed, the bleed doors opened in just over 40 ms. Eight stall cells (one very small) occurred over a duration of approximately 90 ms (Fig. 10). In a similar test with the rate limiter in operation, the bleed doors opened in 81 ms, but eight stall cells still occurred and the stall duration was again near 90 ms. With no inlet distortion and the rate limiter removed, only a slight improvement was obtained (seven stall cells over a duration of 78 ms). By themselves, these are excellent results for the performance of the stall control system in eliminating rotating stall once it occurs. However, the stalls did not clear until after the bleed doors were open for a short time, even with the fastest available response of the bleed doors. This suggests that problems may be encountered if rotating stall is permitted to occur at higher engine speeds. The results from one such stall are described below.

Figs. 11 and 12 show the response of the stall control system to a stall at a corrected engine speed of 79.4 percent. This is the highest engine speed for which the bleed doors did not begin to close on their normal schedule under the action of the J-85 fuel control system. This stall was obtained with the 180 degree distortion screen in the engine inlet and with the rate limiter in operation on the stall control system. The presence of the rate limiter means that the bleed doors did not respond at the maximum rate available. However, the results presented previously for 75 percent corrected engine speed suggest that a result similar to that shown in Figs. 11 and 12 would have been obtained with the rate limiter removed. The direct records of this stall (Fig. 11) show that the stall lasted a considerable time (1.06 s) even though the bleed doors were opened completely in about 80 ms. While the stall was occurring, the pressure drop across the compressor caused the engine to decelerate on its own to a corrected speed of approximately 63 percent before the stall was cleared. The additional engine deceleration in Fig. 11 that occurs about a second after the stall was cleared was effected when the test engineer chopped the throttle.

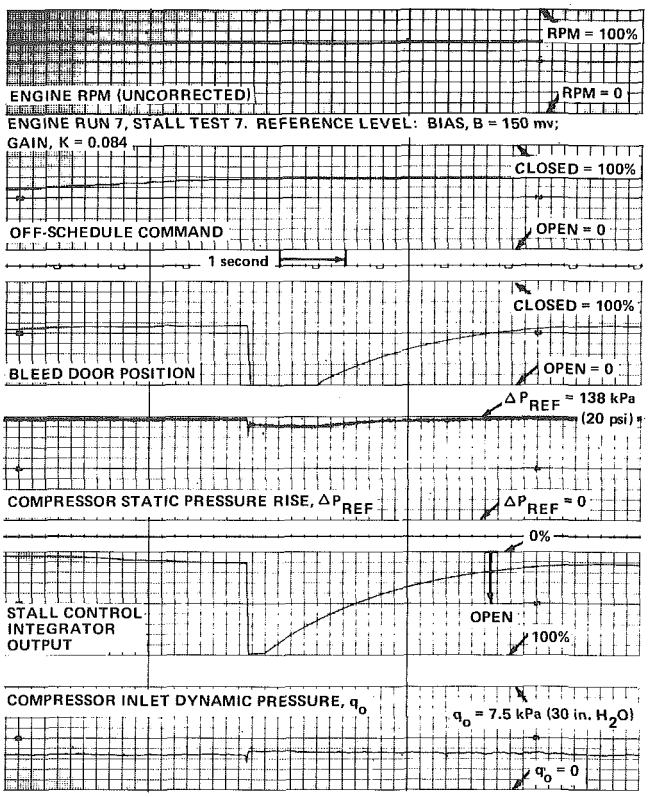

Fig. 7 Performance of modified stall control on J-85 engine: 180 deg circumferential inlet distortion, rate limiter out, corrected engine speed, $(N/N^*\sqrt{\theta})$ = 69.1 percent

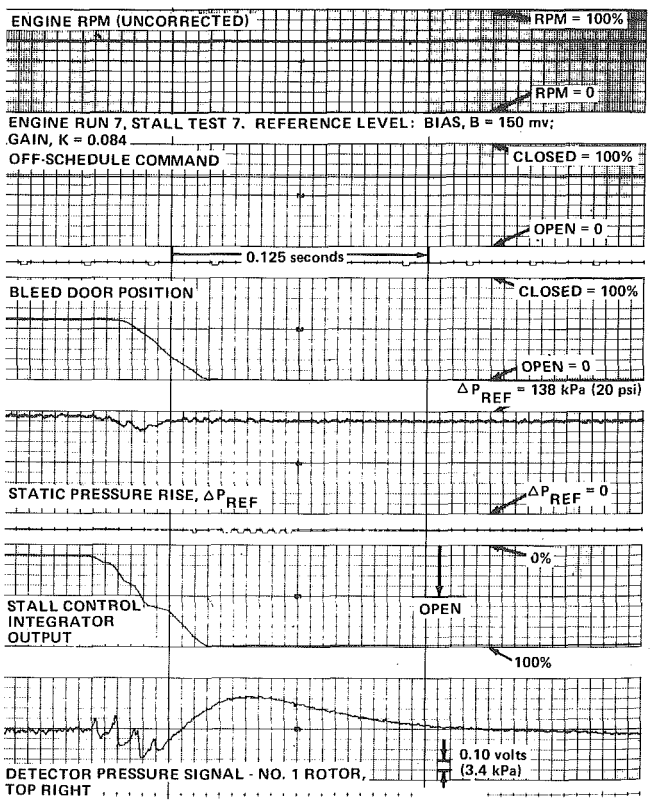

Fig. 8 Stall control performance (expanded time scale): 180 deg circumferential inlet distortion, rate limiter out, corrected engine speed, $(N/N^*\sqrt{\theta})$ = 69.1 percent

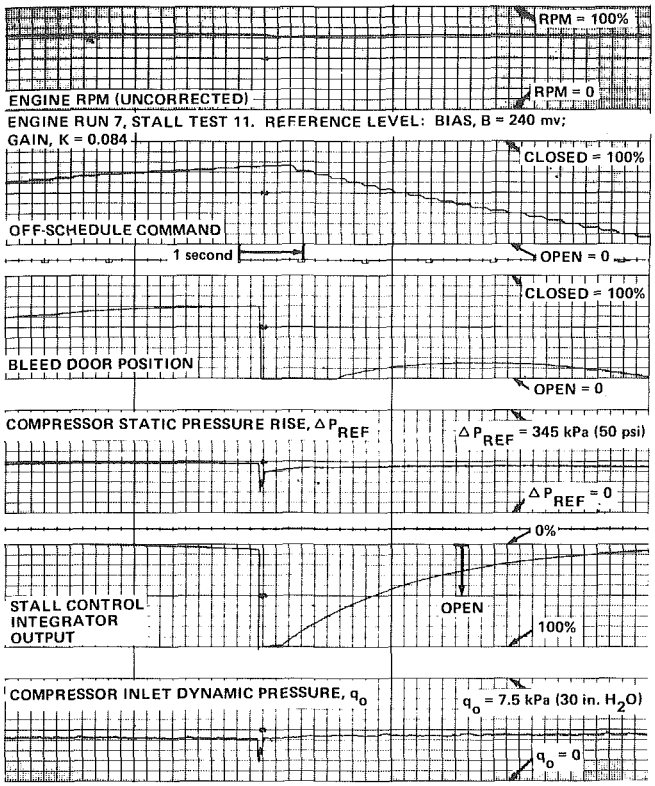

Fig. 9 Performance of modified stall control on J-85 engine: 180 deg circumferential inlet distortion, rate limiter out, corrected engine speed, $(N/N^*\sqrt{\theta}) = 74.0$ percent

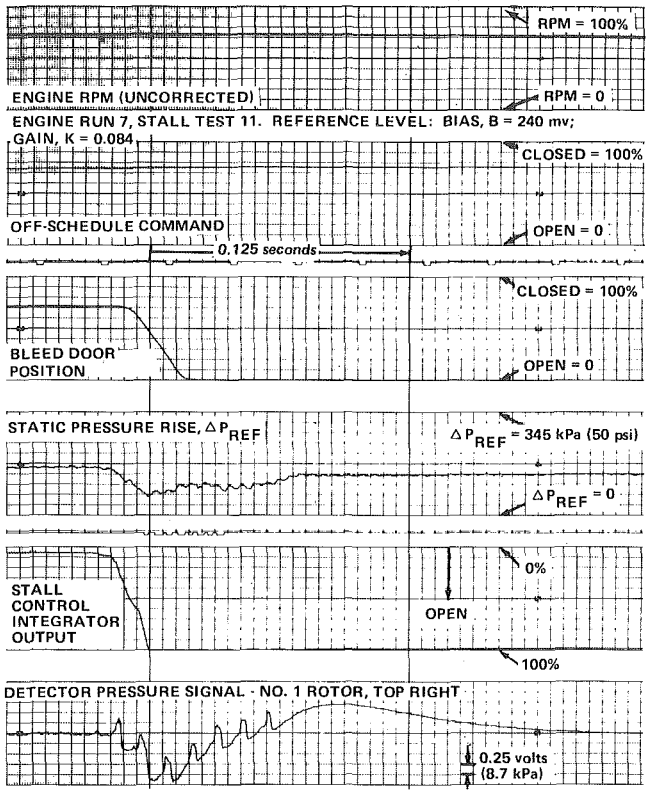

Fig. 10 Stall control performance (expanded time scale): 180 deg circumferential inlet distortion, rate limiter out, corrected engine speed, $(N/N^*\sqrt{\theta})$ = 74.0 percent

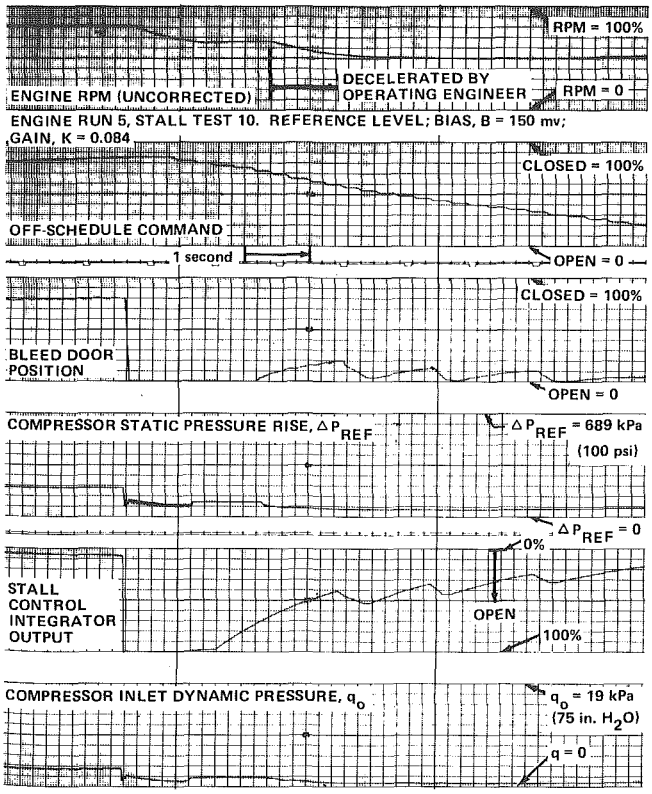

Fig. 11 Performance of modified stall control on J-85 engine: 180 deg circumferential inlet distortion, rate limiter in, corrected engine speed, $(N/N^*\sqrt{\theta}) = 79.4$ percent

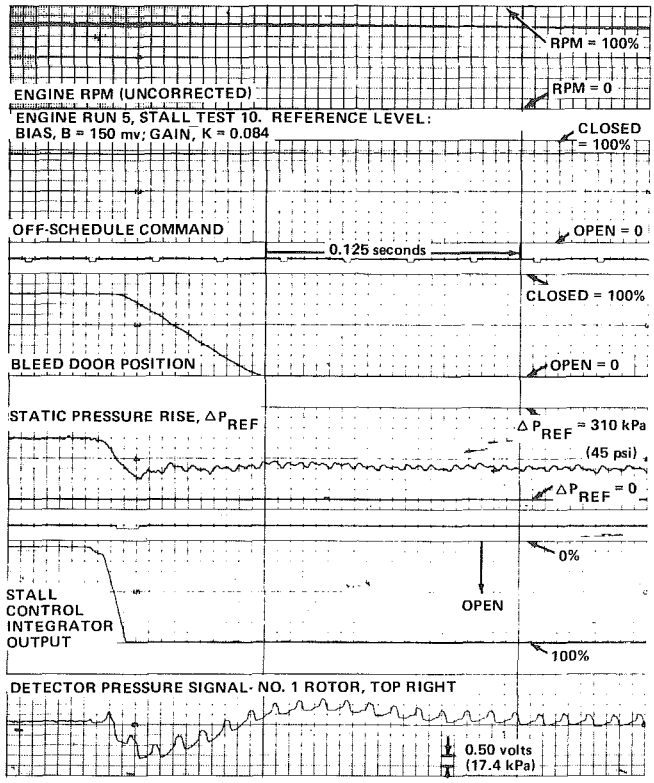

Fig. 12 Stall control performance (expanded time scale): 180 deg circumferential inlet distortion, rate limiter in, corrected engine speed, $(N/N^*\sqrt{\theta})$ = 79.4 percent

In addition to the hard stall, Fig. 11 shows the response of the control to three small amplitude stalls after the throttle was chopped. These occurred because the off-schedule command was not reduced fast enough by the operator to prevent low speed stalls after the engine decelerated. The results suggest that once stall has developed at this high an engine speed, it cannot be cleared by changing the existing geometry on the J-85 engine without first causing a substantial engine deceleration. However once the stall was cleared, engine operation appeared to be normal. In fact three more engine tests were performed after this stall occurred without any indication of engine damage.

Stall Anticipation Tests. The results presented in Figs. 7 12 were obtained with the reference pressure level, P_R, intentionally set at high enough levels to allow the compressor to stall. This was done to investigate the performance of the modified stall control in clearing rotating stall once it had started. The results showed that for engine speeds up to 75 percent (≈12,400 rpm) of rated speed, the stall control acted fast enough to clear rotating stall before it had a noticeable effect on the J-85 engine. However the test at 79.4 percent of rated engine speed showed that the control is not fast enough to clear this stall without first allowing a substantial deceleration of the engine. There are two possible solutions to controlling a high speed stall such as this. The first is to increase the range of control available to the stall control system. On the J-85 this would require increasing the existing bleed air mass flow or including provision for bleeding air at the rear of the compressor, or perhaps, incorporating the stall control in the fuel flow control system. None of these were practical on the existing engine. The second possibility is to have the stall control system anticipate and prevent the stall before it develops. The latter possibility was tested and found to work well at high engine speeds. The results are presented below.

Fig. 13 illustrates the performance of the stall control system when the reference pressure level is set low enough to anticipate rotating stall (B = 180 mV, K = 0.040). These records were obtained by attempting to close the bleed doors at constant engine speed with the stall control reference pressure level set as noted above. The complete strip chart record of this test is very long. It starts with the bleed doors fully open, and both the off-schedule command and the integrator output at zero. The central portion of the test is shown in Fig. 13. Here the off-schedule command is at its maximum (fully closed) and the integrator output has increased sufficiently to hold the bleed doors open far enough to prevent rotating stall inception. The bleed door position at which stall occurs is shown as a dashed line. This position was taken from another test in which rotating stall was allowed to occur by choosing higher values of the reference pressure level, P_R.

Summaries of all the stall anticipation test results are presented in Fig. 14 for 180 deg inlet distortion. As can be seen in this figure, with the bias, B, set at 180 mV and the gain, K, set at 0.040, the stall control held the bleed doors open far enough to prevent stall inception for engine speeds of 70 percent and higher. Similar results were obtained without inlet distortion and are given in [3]. Some additional tests at lower engine speeds and with a higher P_R setting (B = 150 mV, K = 0.084) were also successful in preventing stall inception. However, the results in Fig. 14 for these tests show that the bleed door excursions approach the stall inception boundary close enough that rotating stall may have occurred if the test duration had been extended for a longer time period. In any event, the stall anticipation tests are considered to be successful in that they demonstrated that with proper setting of the reference level, the stall control system is capable of anticipating and preventing the large amplitude rotating stall which occurs at high engine speeds.

Tests with Reduced Number of Stall Detection Transducers. The above test results were all obtained by running the J-85 at constant speed and closing the bleed doors until rotating stall occurred or until the control anticipated stall and held the bleed doors open. The stall control was tested using seven of the eight available pressure transducers in the J-85 compressor casing to detect rotating stall. (The eighth transducer was found to be defective early in the test program and was not used in these tests.) In addition to the test results just presented, some tests were performed to investigate the effect of reducing the number of pressure transducers used to detect rotating

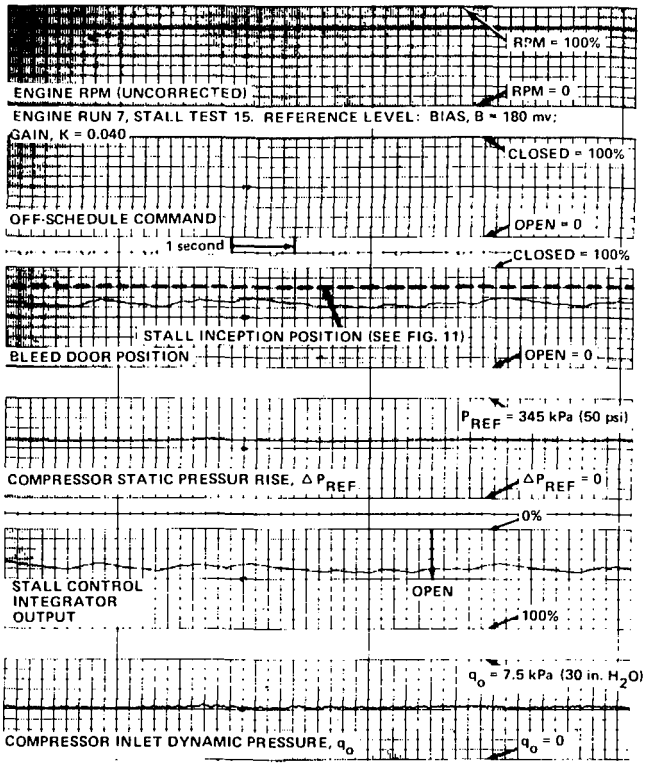

Fig. 13 Elimination of rotating stall control system: 180 deg circumferential inlet distortion, rate limiter out, corrected engine speed ($N/N^*\sqrt{\theta}$) = 78.7 percent

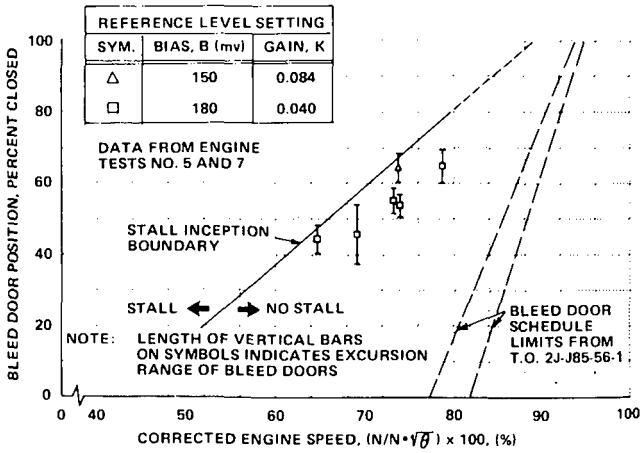

Fig. 14 Bleed door positions during tests in which stall was eliminated on J-85 engine (180 deg circumferential inlet distortion)

stall. It was found that satisfactory performance, almost as good as that presented above, could be obtained by using only two transducers separated circumferentially and situated axially between the second stage stator trailing edge and third stage rotor leading edge. Combinations of other transducers located closer to the front of the compressor did not give the stall control adequate input to provide satisfactory performance. Stalls were detected but were not cleared as fast as they were with the above two transducers.

Tests During Engine Transients. As in [1], some tests were done to study the performance of the control during engine deceleration. In these tests, the engine speed was set at 80 percent of design speed and the bleed doors were closed either a preset amount or else as far as they would go depending on the reference level setting of the stall control. The engine was then decelerated by chopping the throttle to its idle position. The deceleration induced rotating stall in the compressor at some point during the deceleration. With the most sensitive setting for the reference pressure level (B = 180 mV, K = 0.040), it

was found that the highest engine speed at which rotating stall occurred was approximately 70 percent of design speed and that the stall amplitudes and durations were very small; similar to the constant speed results presented in Figs. 7 and 8. Thus it is concluded that the performance of the stall control in clearing stalls induced by moderate transients such as in the engine decelerations is about as good as it is in anticipating or clearing rotating stall under the relatively constant conditions used for the main body of the tests.

In addition to the tests conducted at Calspan, some stall control tests during engine acceleration were performed in a companion test program at the U.S. Air Force Aero Propulsion Laboratory [4]. In this program, stall was induced by a combination of off-schedule geometry and engine acceleration. The engine variable geometry was operated under computer control to be 20 percent more open than the steady state stall inception boundary (Fig. 14). With the stall control deactivated, an acceleration was attempted from 56 percent to 72 percent of design engine speed. The attempted acceleration caused a mild rotating stall 0.2 s after the start of the acceleration which changed to a more severe rotating stall as the engine continued to accelerate and the bleed doors continued to close. As a result of the severe stall, it was not possible to complete the acceleration. Instead the speed began to decay until it reached a stable, steady state rotating stall condition at an engine speed of approximately 55 to 57 percent. A second acceleration run was conducted with the stall control active. Once again a mild rotating stall occurred approximately 0.2 s into the acceleration. However, this stall was detected immediately and the stall control rapidly moved the bleed doors to the full open position where they remained for the duration of the acceleration. When the acceleration was completed, the bleed doors returned to the position commanded by the computer for the final steady state engine speed of 72 percent. Since the bleed doors were fully open for the majority of the acceleration period, the engine completed its speed transient in an entirely normal manner. Thus, the presence of the stall control changed a "hung" acceleration to an approximately normal acceleration in these tests. Further details of the acceleration results and results at simulated altitude conditions will be presented in [4].

Summary and Conclusions

An improved version of a rotating stall control system has been tested successfully on a J-85-5 turbojet engine. Past tests, [1] and [2], had pointed out the desirability of increasing the response speed of the control. In this study, the installation of the stall control on the J-85 was modified so as to decrease the response time of the control by a factor of ten over that attained in the past tests. The modified control was tested to see if the decreased response time improved the ability to clear rotating stall once it has started, and also to see if rotating stall could be anticipated and prevented by proper selection of the variables in the stall control detection system.

The tests were performed under sea level static conditions, both with and without inlet distortion. The stall control was installed to override the normal operating schedule of the compressor bleed doors and inlet guide vanes on the J-85. The tests were limited to engine speeds at or below 80 percent of design speed because of the overall configuration of the engine. The location of the bleed doors on the intermediate compressor stages will only allow control of stalls which originate on the first two or three compressor stages. Such stalls are most likely to occur at engine speeds between idle and approximately 80 percent of rated speed, where the bleed doors are normally scheduled to be open in order to provide matching between the front stages and rear stages. The operation of the stall control system was tested by arbitrarily closing the bleed doors at these engine speeds, and observing if the stall control prevents the occurrence of rotating stall by limiting how far the doors can be closed, or by rapidly opening the doors if a stall does begin to form. A similar procedure was not applied above 80 percent of rated speed because clearing stalls at these speeds would probably require unloading the rear compressor stages. In this case opening the bleed doors on the intermediate stages would only aggravate the stall, not clear it.

The J-85 was stalled in two ways, first by closing the bleed doors at constant engine speed, and second by decelerating the engine with the bleed doors partially closed at the beginning of the deceleration. In the constant speed tests it was found that the control can anticipate and eliminate rotating stall completely at engine speeds between 65 and 80 percent of design. The deceleration tests showed the same capability at engine speeds between 70 and 80 percent of design. At speeds lower than 65 to 70 percent of design, it was possible to stall the compressor but the amplitude and duration of the stalls were very small and had no noticeable effect on the engine. Moreover, with the control set to anticipate stall, normal unstalled operation of the engine was unaffected.

Additional tests were performed in which the stall control was intentionally detuned to allow the compressor to stall. This was done to investigate the performance of the modified stall control in clearing rotating stall once it had started. The results showed that for engine speeds up to 75 percent (≈12,400 rpm) of rated speed, the stall control acted fast enough to clear rotating stall before it had a noticeable effect on the J-85 engine. However, a test at 79.4 percent of rated engine speed showed that the control is not fast enough to clear this stall without first allowing a substantial deceleration of the engine. There are two possible solutions to controlling a high speed stall such as this. The first is to increase the range of control available to the stall control system. On the J-85 this would require increasing the existing bleed air mass flow or including provision for bleeding air at the rear of the compressor or, perhaps, incorporating the stall control in the fuel flow control system. None of these were practical on the existing engine. The second possibility is to have the stall control system anticipate and prevent the stall before it develops. As described above, the latter possibility was tested and found to work well at high engine speeds.

Acknowledgments

This work was supported by the Air Force Aero Propulsion Laboratory, Air Force Systems Command, Wright-Patterson AFB, under Contract No. F33615-76-C-2092 and was under the technical direction of Mr. Marvin A. Stibich, AFAPL/TBC. The authors are indebted to Mr. James N. Dittenhauser, Mr. Alfred F. Gretch and Mr. Mario Urso all of Calspan, and Mr. Rudy H. Arendt of MGA Research Corporation for their contributions to this investigation.

References

1 Ludwig, G. R. and Arendt, R. H., "Investigation, of Rotating Stall Phenomena in Axial Flow Compressors, Volume III—Development of a Rotating Stall Control System," U.S. Air Force Aero Propulsion Laboratory Technical Report No. AFAPL-TR-76-48, June 1976.

2 Ludwig, G. R. and Nenni, J. P., "A Rotating Stall Control System for Turbojet Engines," ASME JOURNAL OF ENGINEERING FOR POWER, Vol. 101, No. 3, 1979, pp. 305–314.

3 Ludwig, G. R., "Tests of an Improved Rotating Stall Control System on a J-85 Turbojet Engine," U.S. Air Force Aero Propulsion Laboratory Technical Report No. AFAPL-TR-79-2060, Aug. 79.

4 Small, Lester L., "J-85 Engine Evaluation of a Rotating Stall Detection and Control System," U.S. Air Force Aero Propulsion Laboratory Technical Report—to be published.

M. J. Scotto
Engineer,
Advanced Instrumentation, AEG,
General Electric Company,
Lynn, Mass.

M. E. Eismeier
Manager,
Instrumentation Design Engineering, AEG,
General Electric Company,
Evendale, Ohio

High-Speed Noncontacting Instrumentation for Jet Engine Testing

This paper discusses high-speed, noncontacting instrumentation systems for measuring the operating characteristics of jet engines. The discussion includes optical pyrometers for measuring blade surface temperatures, capacitance clearanceometers for measuring blade tip clearance and vibration, and optoelectronic systems for measuring blade flex and torsion. In addition, engine characteristics that mandate the use of such unique instrumentation are pointed out as well as the shortcomings of conventional noncontacting devices. Experimental data taken during engine testing are presented and recommendations for future development discussed.

Introduction

This paper is concerned with high-speed, noncontacting instrumentation for the test and evaluation of jet engines. The acquisition of data from rotating components, e.g., temperature, clearance, and vibration is often a difficult task, and is frequently accomplished by placing sensors in contact with the moving parts and coupling out the data through the use of telemetry or slip rings. In order to simplify this type of data acquisition, a substantial effort has been made in recent years to develop noncontacting sensors, i.e., remote sensing devices which do not require physical contact with the component under investigation or the use of intermediate instrumentation to transmit the data. This effort has had considerable success and has led to the development of several types of instrumentation including optical pyrometers for measuring blade surface temperatures, capacitance clearanceometers for measuring blade tip clearance and vibration, and opto-electronic systems for measuring blade flex and torsion. In the following discussion the operating characteristics of these systems will be described, and experimental data from engine tests presented.

Time Response

Before describing the individual systems it is useful to examine the time response, or the electronic bandwidth requirements for the various systems to be considered. In each case a detector with a small sensitive area (typically 0.1 in. (2.5 mm) dia) is placed in the vicinity of a rotating blade. The target area on the blade which the detector senses is often much smaller than the detector area, and for the purpose of this discussion will be regarded as a point.

The required frequency response is determined by the time interval, t, spent by the target in the field of view of the detector. If the target moves past the detector with a velocity V, then the frequency response, f, is given by $f = 1/t = V/d$ where d is the diameter of the detector. For a target at the tip of a rotor, the frequency response, or instrument bandwidth required is

$$f = \pi N (D/d) \text{ Hz} \tag{1}$$

where N = rotor speed (Hz) and D = rotor diameter. This relationship represents the minimum bandwidth required. For practical purposes, however, the bandwidth should be several times greater. As an illustrative example, for a rotor diameter, D = 20 in. (51 cm), a detector diameter, d = 0.1 in. (2.5 mm), and a rotor speed, N = 18,000 rpm (300 Hz), the minimum bandwidth, f, is of the order of 200 KHz.

The general relationship derived for the bandwidth holds for the temperature, clearance, and vibration systems to be described. In the following sections the details of these systems will be discussed along with experimental data obtained from engine tests.

Temperature Measurements

In this section instrumentation will be described for measuring turbine blade temperatures. Since blade life is a critical function of the temperature, it is important to know the temperature profiles over the blades under various operating conditions. Under typical conditions the blade temperatures under consideration range between 1400 − 1800°F.

Radiation Fundamentals. The instrumentation which has been developed to measure the temperature profiles utilizes an optical pyrometer which senses the optical radiation emitted from the blade surface. For any given material the intensity of the emitted radiation is proportional to the blade temperature, and may be used to determine the temperature of the surface in question. For so called black bodies the intensity of radiation is dependent upon the observed wavelength as well as the temperature and is given by the well-known Planck function

$$W_B(\lambda,T) = \frac{c_1}{\lambda^5(e^{c_2/\lambda T} - 1)} \tag{2}$$

where $W_B(\lambda,T)$ is defined as the power radiated per unit wavelength interval at wavelength λ by a unit area of the surface at temperature T K. c_1 and c_2 are universal constants.

When plotted as a function of the wavelength, λ, the radiation intensity $W_B(\lambda,T)$ exhibits a maximum value, $W_{B\,\max}(T)$, as shown in Fig. 1. If the Planck function is integrated over all wavelengths, the

Contributed by the Gas Turbine Division and presented at the Gas Turbine Conference and Products Show, New Orleans, La., March 10–13, 1980 of THE AMERICAN SOCIETY OF MECHANICAL ENGINEERS. Manuscript received at ASME Headquarters December 7, 1979. Paper No. 80-GT-18.

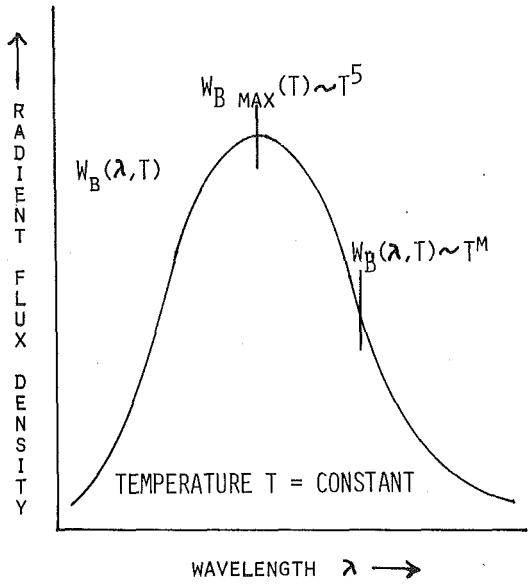

Fig. 1 Planck's function

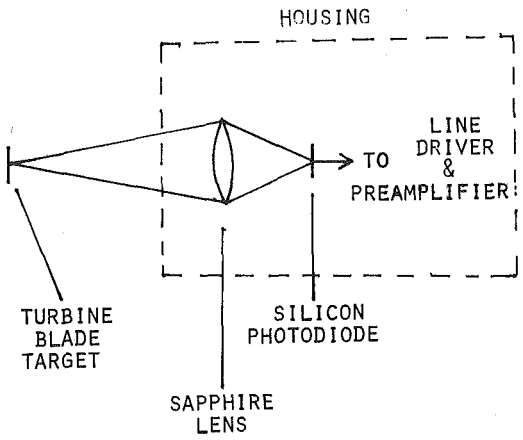

Fig. 2 Optical pyrometer schematic

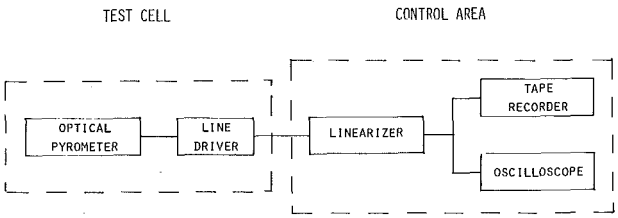

Fig. 3 Schematic of pyrometer system

total radiation $W_B(T)$ is found to vary as the fourth power of temperature, i.e.,

$$W_B(T) = \int_{\lambda=0}^{\infty} W_B(\lambda,T)d\lambda \sim T^4 \tag{3}$$

For narrow-band radiation the intensity varies as $W_B(\lambda,T) \sim T^m$ where the exponent m(λ) depends on the observed wavelength, λ. At the peak of the Planck function the exponent $m = 5$ and the maximum intensity varies as $W_{B\ \max}(T) \sim T^5$.

The Planck function as represented by equation (2) very closely approximates the radiation emitted from certain materials such as carbon black. For most materials, however, it overestimates the magnitude of the radiation. For such "gray" bodies the radiation, W_G, actually emitted is smaller by a factor ϵ known as the emissivity which is defined by

$$\epsilon = W_G/W_B \tag{4}$$

In general, the emissivity factor depends upon the particular material and the condition of its surface. Typical values of the emissivity for turbine blades are of the order of $\epsilon = 0.9$.

Instrumentation. The optical pyrometers which have been developed to measure turbine blade temperatures are opto-electronic devices which collect and sense the radiation emitted, and generate an electronic signal which is proportional to the temperature. The principal elements of the optical system consist of a sapphire lens and silicon photodiode mounted in a stainless steel housing. A schematic diagram of the system is shown in Fig. 2. The housing is mounted directly on the engine casing, where radiation from the turbine blade is collected by the lens and focused onto the photodiode. The photodiode is sensitive to wavelengths in the neighborhood of 1μ and has a bandwidth of approximately 1μ as well. In this arrangement, since the pyrometer is exposed to the high temperature of the engine casing, and contaminants in the gas flowing through the turbine, the pyrometer housing is water cooled to protect the internal electronic components, and the region in front of the lens is continuously purged with a jet of air to minimize the deposition of foreign matter on the optics.

A schematic of the electronic signal processing system is shown in Fig. 3. The principal components of the electronic system consist of a line driver and preamplifier, a linearizer, and data acquisition equipment. The optical pyrometer and line driver are physically located in the test cell. Remaining components may be remotely located in a control area up to 100 ft (30 m) away. In this system the photodiode signal is preamplified by the line driver which also serves as an impedance transformer. The impedance transformation is necessary in order to preserve the time response of the system, which otherwise would be degraded by capacitive loading of the cables between the test cell and the control room. After conditioning by the line driver the output voltage signal is linearized to generate a signal which is directly proportioned to the temperature, and is then recorded on tape or observed on an oscilloscope.

Prior to operation the system is calibrated in the laboratory in a static mode. The calibration is performed by replacing the turbine blade with a hot metal strip which is of the same material and emissivity as the blade. The strip is electrically heated by means of a low voltage transformer, and the linearized output signal recorded as a function of temperature. The strip temperature is determined through the use of a thermocouple, or secondary radiation standard.

The system is capable of operating over a temperature range between 1400 – 2000°F (750-1100°C), and under normal conditions has an accuracy of the order of 5°F (3°C). The system is also quite stable, and during operation requires only minor adjustments.

Engine Data. Optical pyrometers of the type described have been used successfully to measure turbine blade temperatures on a variety of General Electric engines. In this section, representative data will be shown for a selected engine line. In Fig. 4 the data shown were obtained from a J-85 turbine operating a high speed. In Fig. 4(a) the upper trace shows the temperature variation of all the blades during one revolution. The lower trace of Fig. 4(a) represents a voltage signal synchronous with the rotation of the turbine which is used to trigger the oscilloscope, and which occurs once per revolution. The upper trace of Fig. 4(a) essentially shows the envelope of the maximum temperature observed on all the blades. In this test the peak value of the measured temperature is approximately 1800°F (1000°C), which is consistent with analytical predictions.

Fig. 4(b) represents the same data as 4(a), recorded on a rapid time scale in order to observe the temperature profile of individual blades. It is interesting to examine this profile in some detail. As the blade rotates, the pyrometer views a spot on the surface which moves from the tip of the blade to a point near the root, and then to the tip of the next blade where the process repeats itself. As the pyrometer views the surface of the blade a minimum temperature is observed at the tip. The temperature then rises rapidly and exhibits a maximum value at some point intermediate between the root and the tip. The temperature then falls off more slowly as the root is approached, and at this point a discontinuity in the signal is observed as the target of the pyrometer moves to the tip of the next blade. The temperature profile

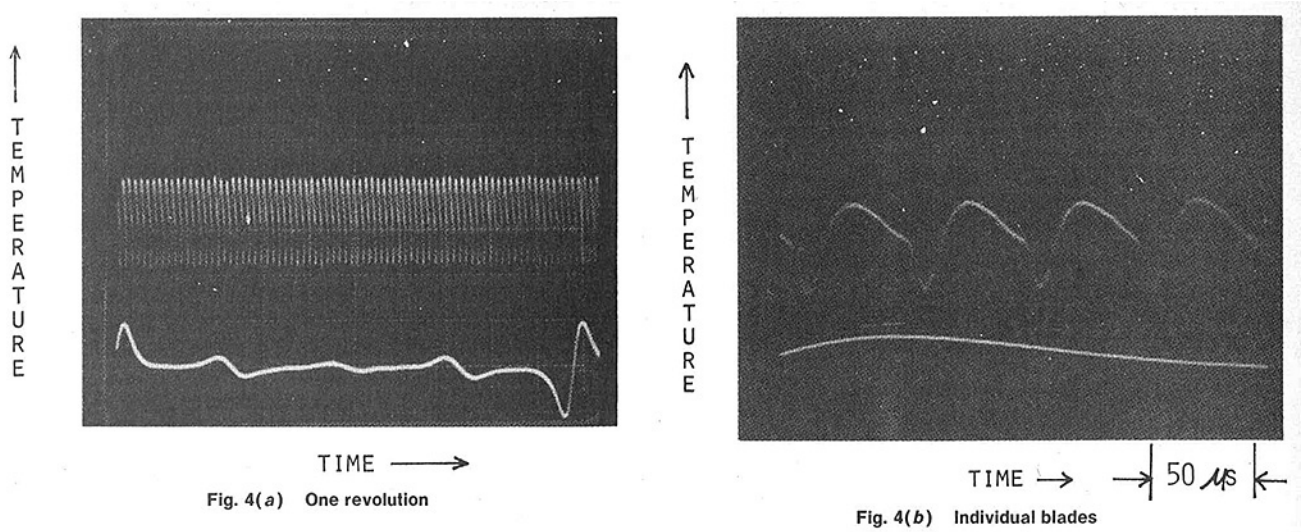

Fig. 4(*a*) One revolution

Fig. 4(*b*) Individual blades

Fig. 4 Optical pyrometer data for J-85 turbine

observed is typical of that exhibited by jet engine turbines.

These type of data have proven very useful in the analysis of blade life times and would be very difficult to obtain by other means such as the application of thermocouples. Optical pyrometry not only provides a continuous temperature profile over every blade surface, but does not require the use of slip rings to couple out the data. In addition, the pyrometer allows data to be acquired over a longer period of time than that permitted by thermocouples, and may be refurbished without the need of engine disassembly.

In addition to optical pyrometers, other categories of instrumentation have been developed which involve the measurement of blade tip clearances and vibration. These instrumentation systems will be discussed in the following sections.

Clearance Measurements

In this section, instrumentation will be described for measuring blade tip clearance which is the gap between the blade tip and the inner wall of the engine casing, or flow path. Since gas flow through the gap degrades both compressor and turbine efficiencies, it is important to know the variation and magnitude of clearance under different operating conditions. Under typical conditions the clearances under consideration range between 0–100 mils (2.5 mm).

Instrumentation. The instrumentation to be described will be limited to devices which measure clearance by sensing the capacitance between the blade tip and the flow path. These so called capacitance clearanceometers are rf devices which incorporate the capacitance of the gap to be measured as part of a tuned circuit. Changes in the gap or capacitance generate a phase shift in the cirucit current which is excited by a 10 MHz rf oscillator. The phase shift produced is detected and processed, and is converted into a voltage signal which is directly proportional to the clearance. Devices which utilize this principle have a time response which is inherently much shorter than other "proximity" devices which depend on eddy current losses or magnetic properties of materials.

A schematic diagram of the capacitance clearanceometer system is shown in Fig. 5. The principal elements of the sensing probe consist of a capacitive tip and an inductive coil mounted in a stainless steel housing. The housing is mounted directly on the engine casing with the probe tip essentially in the plane of flow path. In this arrangement since the clearanceometer probe is exposed to the high temperature of the engine casing, the housing must be water cooled to protect the internal electronic components.

The capacitance probe is coupled to the rf oscillator by a coaxial cable which constitutes an integral part of the rf circuitry. As such there are practical considerations which limit the maximum length of the cable, which in the present system is of the order of 50 ft. This proximity requirement applies to the rf oscillator and signal processing electronics, but not the data acquisition equipment.

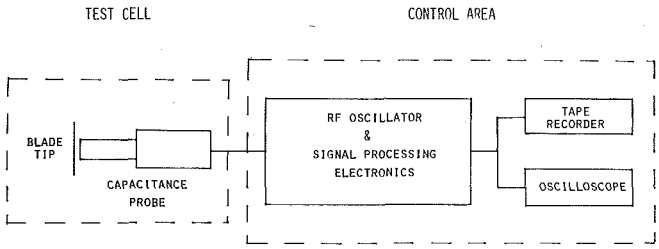

Fig. 5 Schematic of clearanceometer system

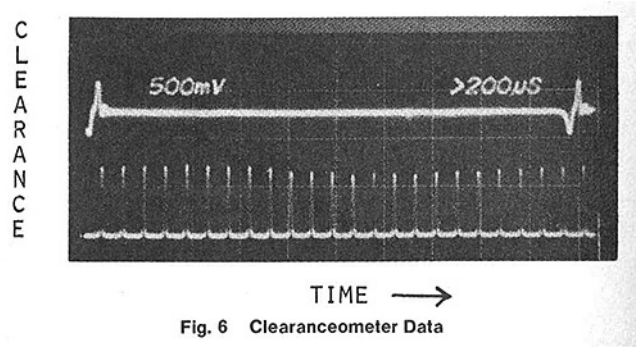

Fig. 6 Clearanceometer Data

Prior to operation the system is calibrated in the laboratory in a static mode. The calibration is performed by mounting the probe in a fixture of material similar to that of the engine casing, and placing a sample blade under the probe tip. The gap is altered by means of a micrometer drive and the output signal recorded as a function of clearance. The calibration can also be performed under dynamic conditions by placing the blades in a rotating fixture.

The system is capable of operating over a clearance range of 0–100 mils (2.5 mm) and under normal conditions has an accuracy of the order of 1 mil (25 m). The system stabilizes after a suitable warm-up time, and thereafter requires only minor adjustments.

Engine Data. Because of temperature limitations, clearanceometers of the type described have been applied mainly to compressor measurements and have been used at temperatures as high as 1000°F (550°C). Clearanceometers have been used to measure clearance and runout, and have also been used for other purposes which will be discussed later. In this section the results of some qualitative measurements will be presented in order to illustrate the type of data that may be obtained. In Fig. 6, data which were obtained from a compressor under development operating at high speed are shown. The upper trace in the figure is a synchronous oscilloscope trigger signal. In the lower trace, the peak amplitudes represent the

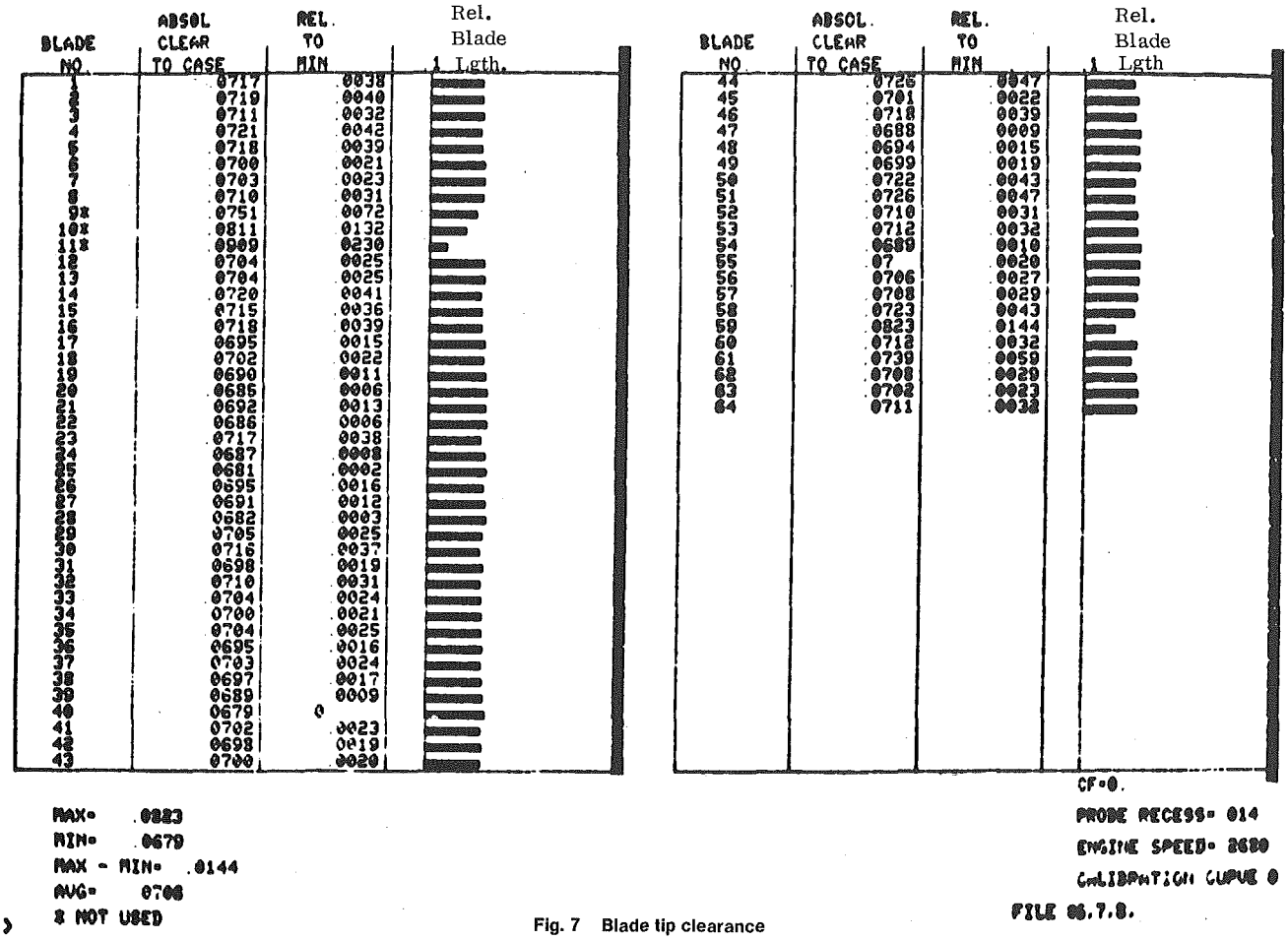

Fig. 7 Blade tip clearance

clearance of each individual blade over one revolution. The lower trace also indicates the blade tip runout which is represented by the overall envelope of the peak amplitudes. In this particular case the magnitude of the runout is approximately 1 mil (25 μ), which is consistent with the predicted value.

In recent capacitance clearanceometer testing, an automatic data reduction system has been developed which utilizes high speed recording of the sensor output. This recording is played back at a 16:1 speed reduction and the analog waveform is digitized at a high speed to find the peak of the signal at each blade plassing. This peak is then representative of the blade clearance and will give the absolute clearance of each blade when combined with the pre-test static calibration. The tape data can thus be automatically reduced to give the clearance of each individual blade in a rotor stage, and the blade clearance arithmetically averaged for the overall stage clearance. Similarly, the blades with maximum and minimum clearances can also be found. Figure 7 shows the output of the system for a single rotor revolution. Data like this can be taken at any series of points to give complete clearance patterns with rotor speed during steady-state or fully transient engine operation. Figure 8 shows data which are representative of this type of capacitance clearanceometer measurement.

It should be pointed out that capacitance clearanceometers are still in a developmental stage, and an effort is being made to increase their temperature range and to improve their ease of handling. For many applications, however, they represent a very convenient way for measuring blade tip clearances and may be used for other types of measurements as well. The clearanceometers provide a continuous record of the clearance and yield information such as runout data which cannot be obtained by other devices such as mechanical touch probes. They can also provide information on other high-speed phenomena which may not be obtained by relatively slow devices such as eddy current proximitors and magnetic pickups. In the next section alternate applications of capacitance clearanceometers will be discussed along with a final category of instrumentation for measuring blade tip vibrations.

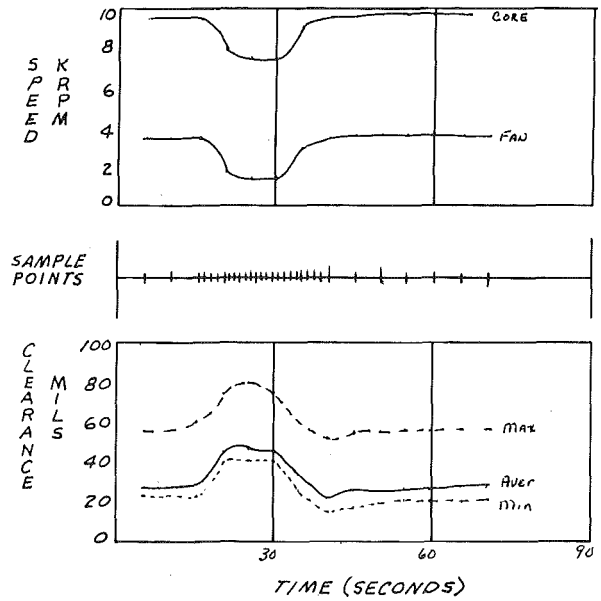

Fig. 8 Transient clearance versus engine speed

Vibration Measurements

In this section instrumentation will be described for measuring

blade vibration characteristics. Since blade fatigue is a sensitive function of the various modes of vibration, it is important to measure the degree to which each of these modes is excited. The instrumentation to be described includes two related systems for accomplishing this task.

Basic Principles. The basic principles of operation are common to both systems. For the sake of simplicity, the measurement of the flexure mode will be described first and will be limited to vibrations which are nonsynchronous with the rotation of the rotor.

A schematic diagram of the system is shown in Fig. 9(*a*). The principal components of the system consist of two high-speed sensors, a ramp generator, signal processing electronics, and data acquisition equipment.

In this arrangement, one sensor is mounted on the engine casing directly over the center of twist of the rotor blades. The other sensor is mounted over a gear having the same number of teeth as blades on the rotor, and which rotates at the same speed. The system operates as follows: Each time a gear tooth passes the sensor, a pulse is generated which starts a ramp generator. The ramp signal increases linearly with time until it is stopped by a second pulse originating from a rotor blade. At this point the ramp resets and the process repeats itself as the next gear tooth and next blade pass the sensor. This sequence of events is illustrated by the solid curve in Fig. 9(*b*). In the absence of vibration, the solid curves are retraced during each subsequent revolution. If the blade has flexed between successive revolutions, however, the ramp will be stopped either earlier or later than the previous stop depending on the direction of flex. The change is amplitude as represented by the dashed line in Fig. 9(*b*) is directly proportional to the instantaneous magnitude of the flex. Over a period of many revolutions the total spread in the ramp height represents the maximum amplitude of vibration. When the flexure plane is normal to the rotor axis the peak-to-peak vibration amplitude, D, may be expressed in terms of the spread in ramp height by the following relation:

$$D = V_t(\Delta V/R)\,\mathrm{Cos}\theta \tag{5}$$

where ΔV = Spread in ramp height (volts), R = Ramp Slope (volts/s), V_t = Blade tip velocity (cm./s), and, θ = Blade pitch angle.

The measurement of torsion is accomplished in a similar manner. For torsion measurements the gear-tooth sensor is eliminated and replaced with a second sensor over the rotor. In this case, however, the two rotor sensors are placed over the leading and trailing edges of the blade, one sensor activating the start ramp and the other stop ramp. This leads to a torsion signal pattern which is similar to the flex pattern.

Sensors. In performing vibration measurements with this type of system any sensor can be used with a sufficiently fast rise time. The system was originally designed to be used with optical sensors of the type shown in Fig. 10. This type of sensor utilizes a bifurcated fiber—optic bundle in which the fibers from the two branches merge into a single bundle. One of the two branches is connected to a light source and the other to a photo diode which is connected to the start or stop channel of the ramp generator. The end of the main stem is mounted over the rotor in the plane of the flow path. In this arrangement, the rotor is illuminated by the light source and as the blade tip passes the fiber optic bundle the light is reflected into a photodiode which triggers the ramp generator. In order to generate a sufficiently strong trigger signal, it is generally necessary to polish the blade tips.

The system nominally operates over a range of vibration amplitudes between 0–100 (2.5 mm) mils and has an accuracy of the order of 1 mil (25 μ). The system is inherently stable and during operation requires only minor adjustments to compensate for changes in engine speed.

Most of the blade vibration data obtained have been acquired through the use of fiber optic sensors. During one test, however, both clearanceometers and optical sensors were installed for the purpose of making simultaneous clearance and blade vibration measurements. Both types of sensors were mounted in the same configuration over the rotor. With this arrangement an opportunity was presented in which the clearanceometers could be used to measure blade vibration

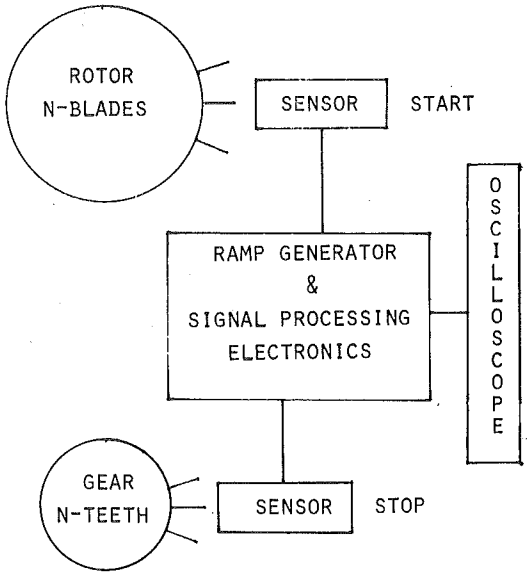

Fig. 9(*a*) Schematic of flex vibration system

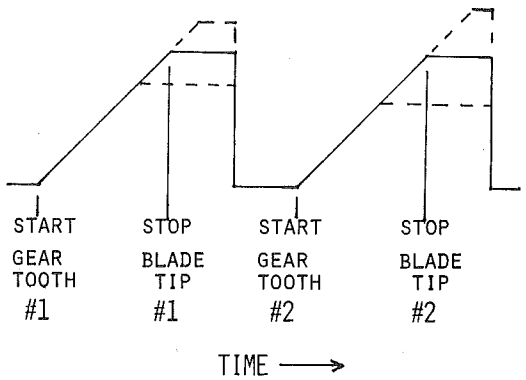

Fig. 9(*b*) Ramp generator signals

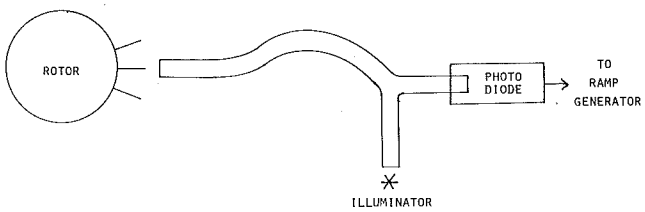

Fig. 10 Fiber optic sensor

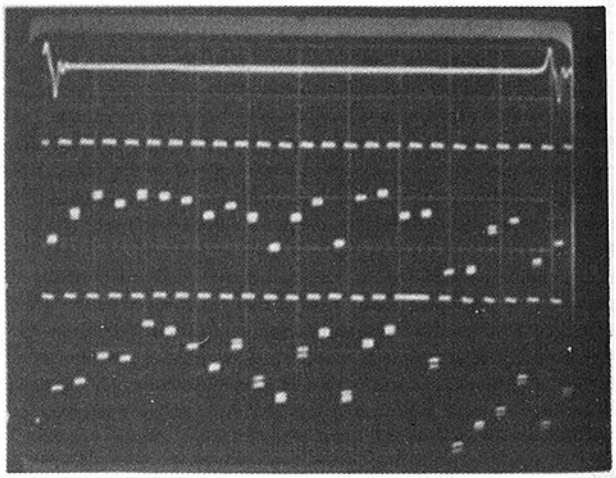

Fig. 11 Comparison of fiber optic and clearanceometer flex vibration data

as well as clearance. This test was performed and the results compared with those obtained from fiber optic sensors.

Engine Data. In the test to be described the two sensors were mounted at different angular positions over the same rotor, but each was located over the center of twist of the blades. Another optical sensor was located over a gear which was directly coupled to the rotor. In this test the flex vibration data generated by the two different sets of sensors could be measured simultaneously. This was accomplished by activating one ramp generator with the gear-tooth and fiber optic signals, and another ramp generator with the gear-tooth and clearanceometer signals. In both cases, the common gear-tooth signal was used to trigger the stop ramps. The results of these measurements are shown in Fig. 11.

In this figure the trace at the top of the photo is a synchronous oscilloscope trigger signal. The upper ramp trace in the photo represents the clearanceometer data while the lower trace shows the fiber optic data. The data shown include the vibration of all blades. The overall pattern exhibited by the ramp signals represents two separate phenomena. The average ramp height which undergoes abrupt changes from blade to blade arises from slight differences in angular spacing of the blades and is of no consequence in the present measurement. The signal which is of interest is the spread in the peak amplitude of each individual ramp height which represents the amplitude of vibration of each blade. The purpose of this test is to compare the spread in amplitudes of the two sets of data. If this comparison is made, it is found that the average spread is the same for both sets, which demonstrates the equivalence of the two different sensors. In this particular test, the average flex vibration amplitude determined from equation (5) is approximately 10 mils (250 μ), which is consistent with other measurements performed by means of strain gage instrumentation.

One of the principal benefits of having a choice of sensors is that costly engine rework can often be avoided. In the present test which required clearance as well as vibration data, for example, the engine rework and installation of the fiber optic bundles would not be necessary.

While the vibration data obtained from noncontacting instrumentation can also be acquired through the use of strain gages, the noncontacting devices provide several advantages. The chief benefits include longer sensor life, data transmission without the use of slip rings, and the ability to refurbish the sensors without the need of engine disassembly.

Summary and Need for Future Development

The instrumentation systems described in this report have included noncontacting systems for measuring temperature, clearance, and vibration of rotating jet engine components. These systems have been developed to overcome some of the shortcomings of conventional contact instrumentation such as the requirement of slip rings or telemetry to couple out the data, and the need to disassemble the engine in the event of sensor failure. While the noncontacting systems are not subject to these limitations, they are nevertheless state-of-the-art devices which require further development. The most important areas in need of development involve an expanded temperature range, more rugged sensors, and the automation of data acquisition. Improvements in these areas would substantially enhance the utility of noncontacting instrumentation systems.

Acknowledgment

Many helpful discussions with Gordon E. Grady and Darrell O. Rowe II are gratefully acknowledged.

References

1 Anderson, B., "An Optical Method of Measuring Compressor Rotor Blade Vibration During Vehicle Operation," General Electric Co. Technical Memorandum, TM No. 74-889, Jan. 22, 1975.

2 Rowe, D. O. II, "Optical Detection of Vibrating Airfoils in Jet Engines," General Electric Co. Technical Memorandum, TM No. 73-185, July 2, 1973.

3 Rowe, D. O. II, "F101 Maintainability Using the C & A Pyrometer With a Transient Recorder," General Electric Co. Technical Memorandum, TM No. 73-184, May 5, 1973.

D. L. Carriere
Engineering and Research Staff,
Ford Motor Company,
Dearborn, Mich.

Differential Split Power Transmissions for a Single Shaft Passenger Car Gas Turbine Engine

Descriptions, schematics, equations, and efficiency curves for a unique single shaft gas turbine engine transmission, consisting of a power splitting differential reduction gear combined with either a variable stator torque converter or variable ratio traction drive as a speed variator, and with a current production automatic four-speed gear box as a ratio expander, are contained in this paper.

Introduction

Ford Research studies [1] indicated that a single shaft gas turbine engine with a suitable speed variator and conventional transmission could equal or surpass the performance of a two-shaft engine using a conventional transmission and a free power turbine with a variable power turbine nozzle as a speed variator.

A Ford study [2] of 16 possible speed variator and transmission concepts for a single shaft engine, concluded with the selection of a power splitting differential gear train, combined with either a variable stator torque converter or a variable ratio traction drive as a speed variator and with a Ford Integral Overdrive (FIOD) transmission gear box as a ratio expander.

Differential Variable Stator Torque Converter Arrangement. Figure 1 illustrates a basic split power variable stator torque converter (VSTC) arrangement.

A fixed speed rotor is connected by a sun gear to a compound epicyclic gear set utilizing two ring gears. The epicyclic gear set functions as both a reduction gear and as a power splitting differential. The normal direction of power flow is illustrated in Fig. 2. Power from the first ring gear goes to a speed reducing and rotational direction changing simple epicyclic gear unit which drives the impeller of a variable stator torque converter. The turbine of the torque converter drives the second ring gear of the compound gear unit if the converter speed ratio is positive. If the speed ratio across the converter is negative, the rotational directional and power flow to the second ring gear are reversed. The planetary carrier acts as the output member of the compound epicyclic gear set and sends the collected power through a drop box to a modified FIOD transmission gearbox. The function of the startup and neutral idle clutches are discussed later in the paper.

Speed and Power Relationships for Differential VSTC. The epicyclic gear differential unit is shown schematically in Fig. 3. For purposes of analysis the schematic shown in Fig. 4 can be utilized to indicate directions of rotation and loading on the various gear members.

The following relationships can be obtained:

$$\frac{Ni}{No} = \frac{R(SR)(Q+1) + QX(R+1)}{R(SR) + QX} \tag{1}$$

$$\frac{Nc}{Ni} = \frac{\frac{No}{Ni}(R+1) - 1}{R(SR)} \tag{2}$$

$$\frac{hpc}{hpi} = \left[\frac{No}{Ni}(R+1) - 1\right] \frac{QX\epsilon^6}{(SR)(R + QX\epsilon^4[TR])} \tag{3}$$

$$\epsilon_o = \left[1 + \frac{RQ\epsilon^3 + RQX\epsilon^6(TR)}{R + QX\epsilon^4(TR)}\right] \frac{No}{Ni} \tag{4}$$

$$\frac{N_p}{Ni} = \left(\frac{2}{R-1}\right)\left(1 - \frac{No}{Ni}\right) \tag{5}$$

$$\frac{To}{Ti} = \frac{R(L + Q\epsilon^3) + (QX\epsilon^4[TR])(1 + R\epsilon^2)}{R + QX\epsilon^4(TR)} \tag{6}$$

$$hpc = \frac{N_c{}^3}{Ki^2(5252)} = \frac{Nc}{\sqrt{Tc}} \tag{7}$$

Variable Stator Torque Converter Parameters. An experimental variable capacity torque converter was designed, built and tested by Ford Research in 1970 for inline use with the Ford Model 820 single shaft gas turbine engine. The torque converter was of the

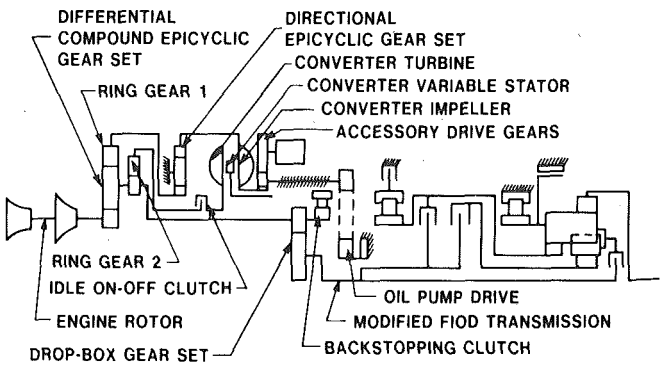

Fig. 1 Differential split power variable stator torque converter transmission for a passenger car gas turbine engine

Contributed by the Gas Turbine Division and presented at the Gas Turbine Conference and Products Show, New Orleans, La., March 10–13, 1980 of THE AMERICAN SOCIETY OF MECHANICAL ENGINEERS. Manuscript received at ASME Headquarters December 7, 1979. Paper No. 80-GT-19.

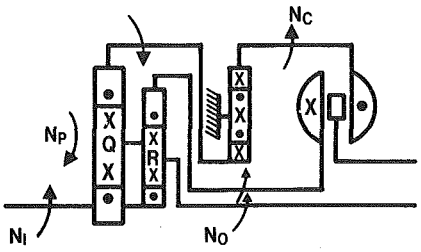

Fig. 2 Differential VSTC power flow

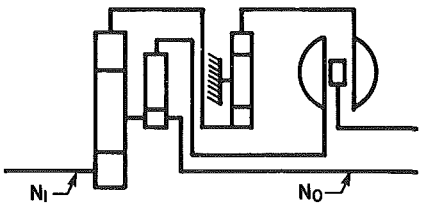

Fig. 3 Differential arrangement

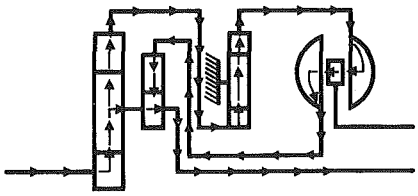

Fig. 4 Equivalent differential arrangement

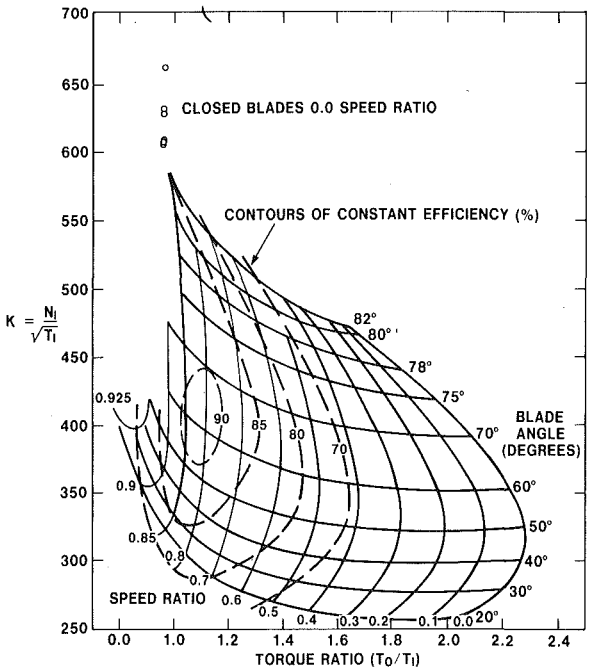

Fig. 5 9.18 in. dia variable capacity torque converter test results

standard three element design except for movable stator blades. A performance map of test results on this 9.18 in. dia converter is shown in Fig. 5. Speed ratio, torque ratio, and capacity factor relationships from this map can be used in the equations contained in this paper.

The map can be scaled for other converter sizes by using the relationship:

$$K_{\text{new}} = \left[\frac{9.18}{D_{\text{new}}}\right]^{2.5}(K_{\text{old}}) \tag{8}$$

where D_{new} is a different converter size expressed in inches.

Selection of *Q, R,* and *X* Gear Ratios. The gear ratio Q should be as large as possible to keep the planet rotational speed low and minimize spin losses. If the gear tooth pitch is [25], a ratio of $Q = 11$ would be the largest practical for a three-planet arrangement.

Gear ratio R essentially determines the output shaft speed range for a fixed input speed as the converter speed ratio varies from minimum to maximum. This ratio R should also be as large as possible consistent with planet pinion gear size limitations and assembly requirements.

Converter input speed is effectively controlled by ratio X as is the maximum amount of negative converter speed ratio required to stall the output shaft. In addition, ratio X shifts the operating line for any given engine power point around on the converter map if the Q and R ratios are held constant.

Example of Differential VSTC Operation. As an example of the use of this arrangement, some basic relationships will be demonstrated for a typical engine. In the interest of simplifying the example, most of the data presented will be good approximations.

Assumptions: Single shaft turbine engine with power and fuel flow characteristics as illustrated in Figs. 6 and 7, respectively. (Note: 130 maximum hp at 100,000 rpm).

A differential gear unit and directional reversing gear unit with ratios $Q = 11$, $R = 47.86$, and $X = 2.244$

A 9.18 in. variable stator torque converter with characteristics as shown in Fig. 5

A vehicle installation in a 3125 lb. inertia weight car with a 2.73 axle ratio and 848 rev/ mile tires

An FIOD transmission with ratios of 2.4, 1.47, 1.0, .67 in the four gear ranges. A ratio of 1.544 is used in the drop box connecting the differential carrier or output shaft with the transmission input.

An assumed gear efficiency of:

$$\epsilon = \left(.9923 - \frac{.75 + \dfrac{Ni}{100000}}{hpi}\right)^{1/2} \tag{9}$$

Figure 8 illustrates the shaft speeds of the example arrangement. The rotor idles at 55,000 rpm and has a 100 percent speed of 100,000 rpm. The corresponding speed ranges of the other members for fixed rotor speeds of 55,000 and 100,000 rpm are also shown on the figure. Note that the converter turbine rotates backward when the output shaft is stalled.

Figure 9 is an example of system operation at low road load horsepower and speed for a constant 55,000 rpm rotor speed. Note that rotor power is varied by inlet guide vane setting as shown in Fig. 6. Since the maximum K factor for the converter is 630, the vehicle will

Nomenclature

hpc = converter input power
hpi = engine power
hpt = traction drive input power
K_i = converter input capacity factor
N_c = converter input or impeller speed
N_i = input speed (engine rotor speed)
N_o = output speed (planetary carrier speed)
N_p = speed of compound planetary about its axis
N_T = traction drive input speed
Q = ring gear to sun gear ratio—mesh 1
R = ring gear to sun gear ratio—mesh 2
(SR) = converter speed ratio
T_c = converter input torque
T_i = input torque (engine torque)
T_o = output torque
T_T = traction drive input torque
(TR) = converter torque ratio
V = traction drive ratio (output speed/input speed)
X = ring gear to sun gear ratio—mesh 3
ϵ = efficiency of one gear mesh or all bearings of a gear unit
ϵ_o = overall efficiency
ϵ_T = traction drive efficiency

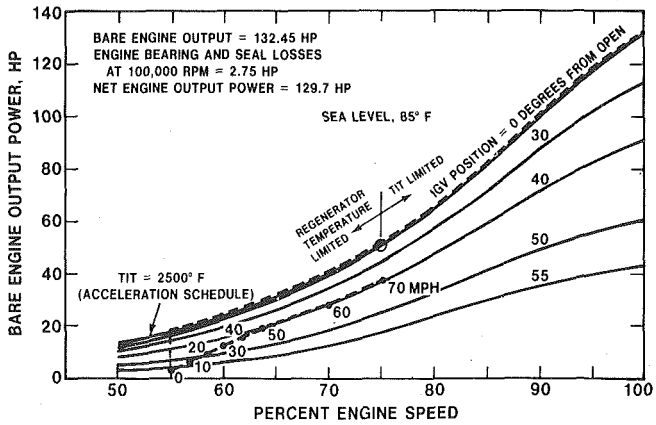

Fig. 6 Power characteristics, ceramic turbine engine

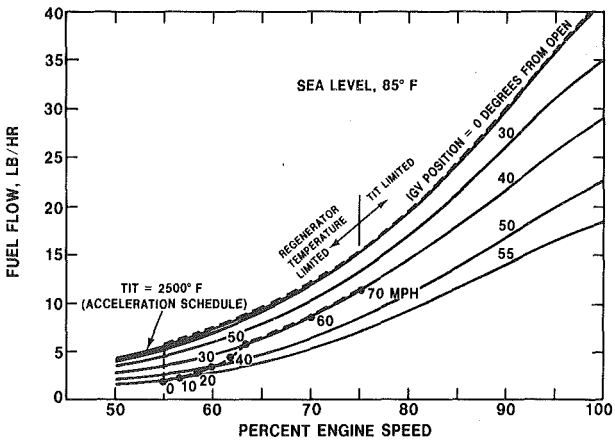

Fig. 7 Fuel flow characteristics, ceramic turbine engine

creep up to 10 mph in first gear with the variable stators in the torque converter closed while moving the engine inlet guide vanes with the engine at idle. A peak speed is possible in fourth gear of 42 mph with the engine at idle speed of 55,000 and the inlet guide vanes at a 0 deg setting and the converter stator set at about 50 deg. The location of the variable stator blades for various power levels for a given road speed can be approximated from this figure. Note that the negative speed ratio condition only occurs at vehicle speeds below 8 mph in first gear at rotor idle speed or up to 14.5 mph at maximum engine speed.

Figure 10 is an expanded operation chart for the entire operating range of the engine-transmission arrangement. Note that large areas of operation are available at maximum turbine efficiency conditions where the inlet guide vanes are at a zero setting. This operation is possible due to the continuously variable operating characteristics of the engine-transmission systems.

Figure 11 illustrates the zones of engine speed, inlet guide vane setting, fuel flow, and variable stator position required to operate an engine with this transmission arrangement. Note that in zone 12 a small area of operation exists at low grades and high vehicle speed where the inlet guide vanes move the engine off the maximum efficiency operating line. This would be at vehicle speeds of over 75 mph, and is not very significant.

Figure 12 indicates where on the torque converter map the system is operating for conditions of:

- 0 percent Road Load
- Constant 10 hp at 55,000 rpm
- Constant 18 hp at 55,000 rpm
- Constant 130 hp at 100,000 rpm

Note the extrapolation of the basic torque converter map for negative speed ratios and stator angles less than 20 deg. Operation in these areas must be verified.

Figure 13 illustrates the component speeds at idle. A clutch called the neutral idle clutch exists in the mechanical path from the converter turbine to the second ring gear of the differential unit. At vehicle idle this clutch is disengaged to prevent churning losses in the converter while still permitting operation of the engine accessories which are driven off the impeller side of the converter. If a negative speed ratio is a problem, this clutch can be slipped to allow for vehicle startup.

Figure 14 illustrates the direction of gear member loading and rotation during engine start and explains the possible need for a backstopping clutch on the differential carrier for a reaction member. The backstopping clutch is engaged only at vehicle start and is energized by the starter circuit.

Figure 15 indicates the accessory shaft speed for various steady state vehicle speeds for a 0 percent grade road load. At vehicle speeds from 15 to 60 mph the accessories have a speed of only plus or minus 14 percent. Accessory speeds are 57 percent high at idle, but the

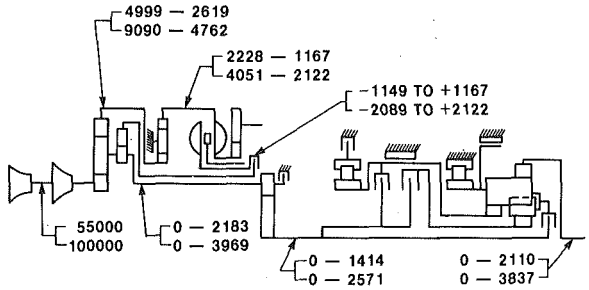

Fig. 8 Single shaft AGT-shaft speeds

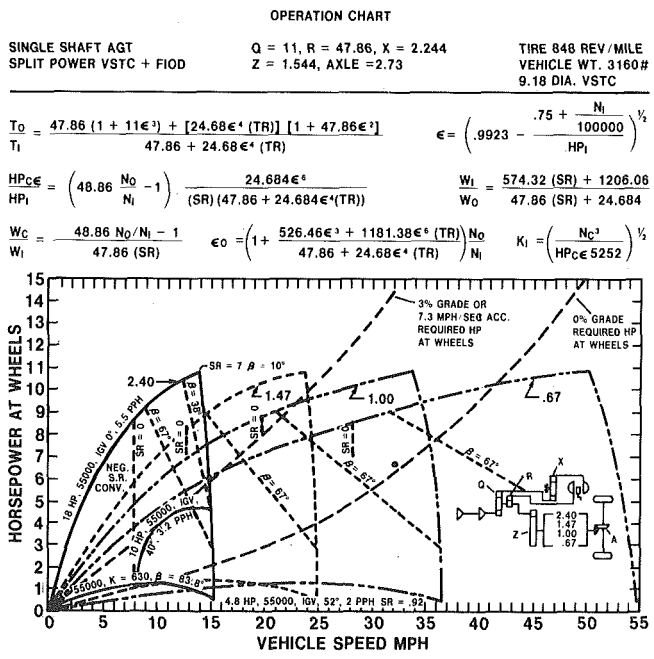

Fig. 9 Operation chart

overall operating range is still less than 2:1, which is very close to a constant speed accessory drive.

Optional Split Power VSTC Arrangement. Numerous possible gear arrangements exist for splitting power to the torque converter. An example is given in Fig. 16 where the second ring gear to the differential is eliminated and the converter turbine is attached to the differential carrier or output shaft. This eliminates negative speed ratios since the output shaft stalls when the converter is stalled, also losses are reduced if a neutral idle clutch is not utilized. However, Ford studies indicate that this arrangement is not as efficient as the dual ring gear approach. Also the dual ring gear arrangement offers growth

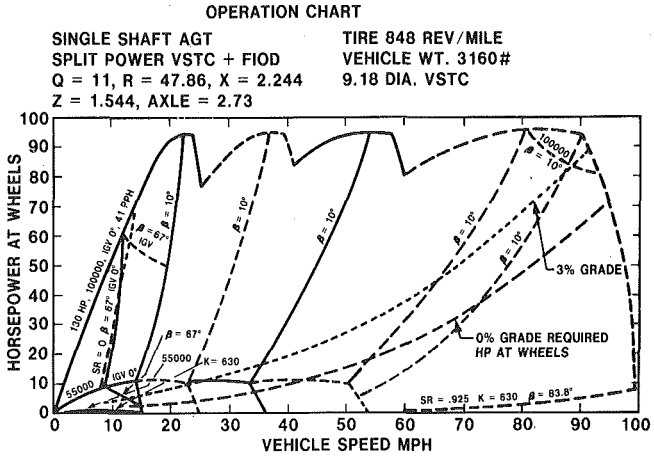

Fig. 10 Operation chart

① FIRST, 55000, IGV 0 TO 52°, B — 15 TO 83.8°, 2 TO 5.5 PPH
② SECOND, 55000, IGV 0 TO 52°, B — 15 TO 83.8°, 2 TO 5.5 PPH
③ THIRD, 55000, IGV 0 TO 52°, B — 15 TO 83.8°, 2 TO 5.5 PPH
④ FOURTH, 55000, IGV 0 TO 52°, B — 15 TO 83.8°, 2 TO 5.5 PPH
⑤ FIRST, 55000 TO 100000, IGV 0°, B — 15 TO 83.8°, 5.5 TO 41 PPH
⑥ SECOND, 55000 TO 100000, IGV 0°, B — 15 TO 83.8°, 5.5 TO 41 PPH
⑦ THIRD, 55000 TO 100000, IGV 0°, B — 15 TO 83.8°, 5.5 TO 41 PPH
⑧ FOURTH, 55000 TO 100000, IGV 0°, B — 15 TO 83.8°, 5.5 TO 41 PPH
⑨ FIRST, 55000 TO 100000, IGV 0 TO 55°, B — 15 TO 83.8°, 2 TO 41 PPH
⑩ SECOND, 55000 TO 100000, IGV 0 TO 55°, B — 15 TO 83.8°, 2 TO 41 PPH
⑪ THIRD, 55000 TO 100000, IGV 0 TO 55°, B — 15 TO 83.8°, 2 TO 41 PPH
⑫ FOURTH, 55000 TO 100000, IGV 0 TO 55°, B — 15 TO 83.8°, 2 TO 41 PPH

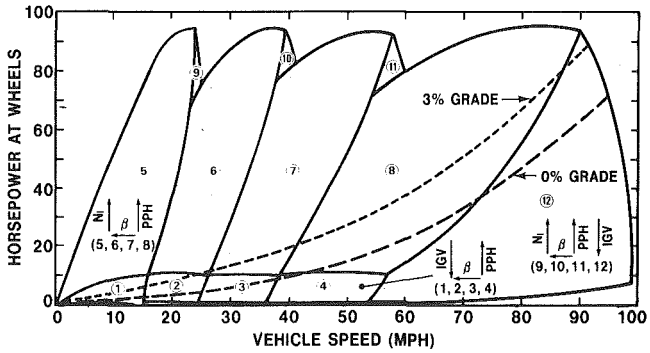

Fig. 11 Operation chart

potential for replacing the VSTC unit with a variable ratio toroidal traction drive while eliminating the directional reversing gear set.

Differential Variable Ratio Traction Drive Arrangement. Figure 17 illustrates a basic split power variable ratio traction drive (VRTD) arrangement.

A fixed speed rotor is connected by a sun gear to a compound epicyclic gear set utilizing two ring gears. The epicyclic gear set functions as both a reduction gear and as a power splitting differential with power flow as illustrated in Fig. 18. Power from the first ring gear goes to the input side of a VRTD, with the output side of the VRTD connected to the second ring gear. The planetary carrier acts as the output member of the compound epicyclic gear set and sends the collected power through a drop box to a modified FIOD transmission gearbox. A combined coupling/clutch is provided for neutral idle, and vehicle startup from rest. The VRTD is repositioned each time a shift occurs in the FIOD transmission gearbox.

Speed and Power Relationships for Differential VRTD. The basic epicyclic gear and VRTD unit is shown schematically in Fig. 19. For purposes of analysis the schematic shown in Fig. 20 can be used to define rotations and gear loadings.

The following relationships can be obtained:

$$\frac{Ni}{No} = \frac{Q(R+1) + RV(Q+1)}{RV + Q} \tag{10}$$

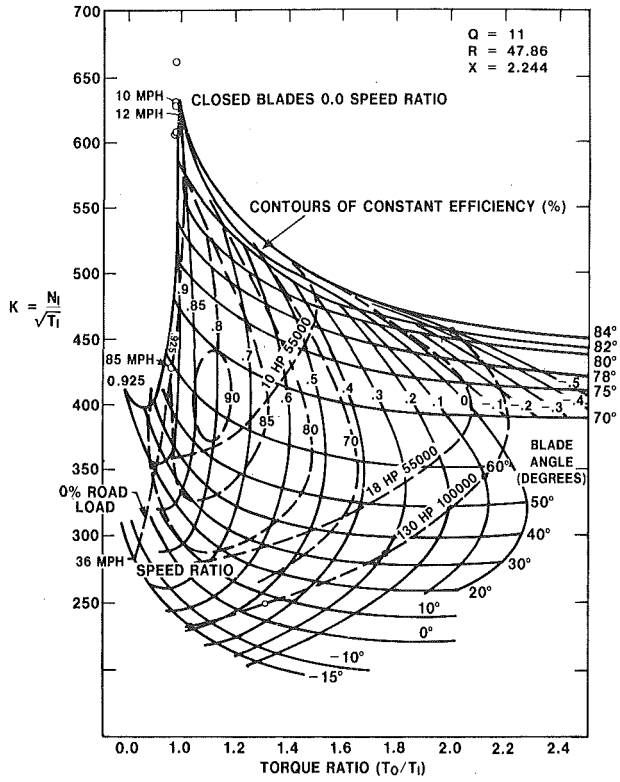

Fig. 12 Converter operation map

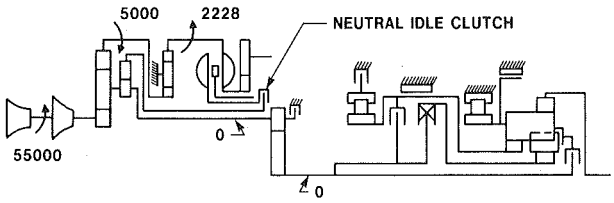

Fig. 13 Neutral idle

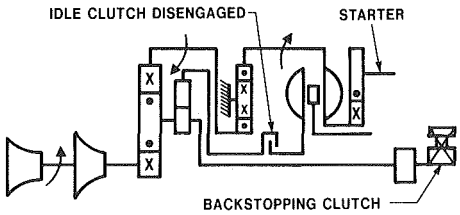

Fig. 14 Engine start

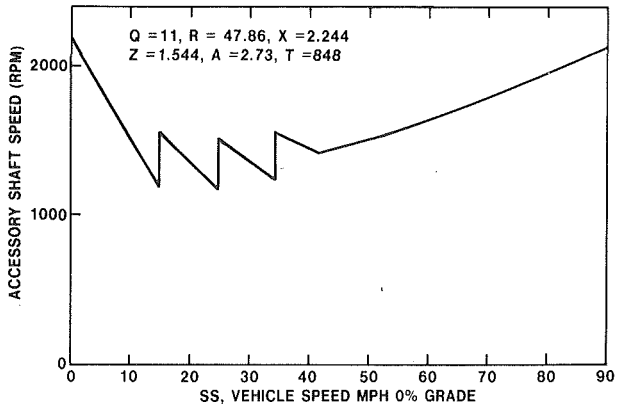

Fig. 15 Accessory versus vehicle speed

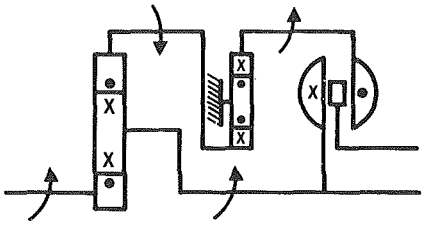

Fig. 16 Optional arrangement

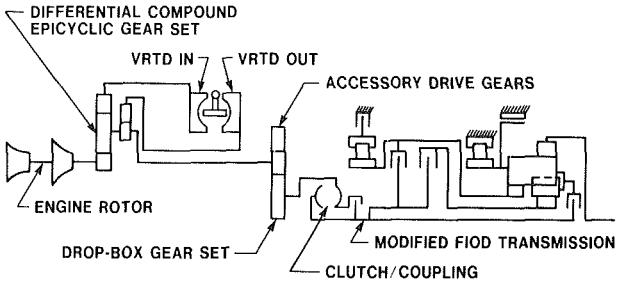

Fig. 17 Differential split power variable ratio traction drive transmission for a passenger car gas turbine engine

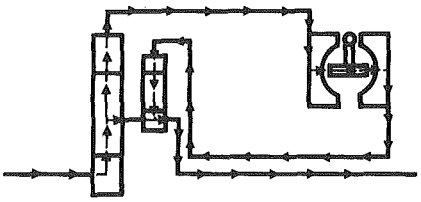

Fig. 18 Power flow VRTD

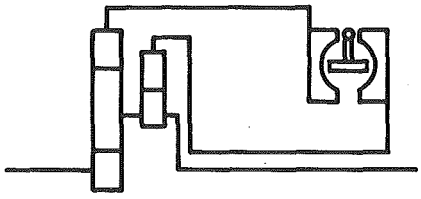

Fig. 19 Basic VRTD unit

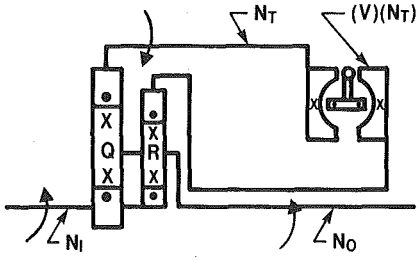

Fig. 20 Equivalent VRTD unit

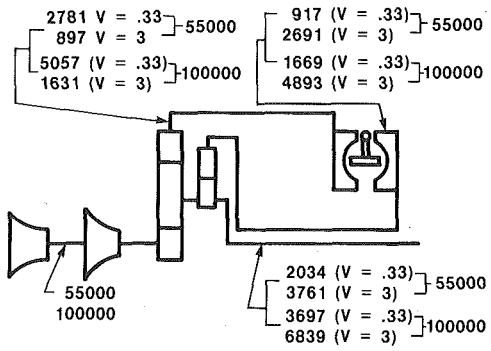

Fig. 21 Shaft speeds VRTD

$$\frac{NT}{Ni} = \frac{1 - \frac{No}{Ni}(1+Q)}{Q} \tag{11}$$

$$\frac{hpt}{hpi} = \left[1 - \frac{No}{Ni}(Q+1)\right]\frac{RV\epsilon^3}{RV + Q\epsilon\epsilon_T} \tag{12}$$

$$Eo = \left[\frac{RV(1+Q\epsilon^3) + Q\epsilon\epsilon_T(1+R\epsilon^2)}{RV + Q\epsilon\epsilon_T}\right]\frac{No}{Ni} \tag{13}$$

$$\frac{T_T}{Ti} = \frac{RVQ\epsilon^3}{RV + Q\epsilon\epsilon_T} \tag{14}$$

Example of Differential VRTD Operation. An example similar to that presented for the VSTC can be made for the VRTD.

Assumptions:

Single shaft turbine engine with power and fuel flow characteristics as illustrated in Figs. 6 and 7.

A differential gear unit with ratios $Q = 11$ $R = 47.86$.

A toroidal traction drive with variable ratio $V = .33$ to $V = 3$.

A vehicle installation in a 3125 lb inertia weight car with a 4.04 axle ratio and 848 rev/mile tires.

An FIOD transmission with ratios of 2.4, 1.47, 1.0, .67 in the four gear ranges. A ratio of 1.842 is used in the gear box connecting the differential carrier or output shaft with the transmission input.

An assumed gear efficiency of:

$$\epsilon = \left(.9923 - \frac{.75 + \frac{Ni}{100000}}{hpi}\right)^{1/2} \tag{9}$$

An assumed traction drive efficiency (ϵ_T) from reference [3].

Sample calculation reveal that when $V = .33$ then $Ni/No = 27.092$ and 33 percent of the power goes through the VRTD. When $V = 3$ then $Ni/No = 14.623$ and 16 percent of the power goes through the VRTD. Thus for a 130 hp engine only a 43 hp traction drive is required, and a 10 percent loss in the traction drive only represents a maximum 3.3 percent loss in overall efficiency. In this example the maximum traction drive input torque is calculated at 68.2 ft-lbs at 1631 rpm ($V = 3$) and minimum torque 45.1 ft-lbs at 5057 rpm ($V = .33$). It is estimated that this torque can be accommodated by a three roller traction unit with a 5.75 in. o.d. and 2.68 dia rollers.

Figure 21 illustrates the shaft speeds of the example arrangement with a rotor idle speed of 55,000 rpm and a 100 percent speed of 100,000 rpm. The corresponding speed ranges of the other members for fixed rotor speeds of 55,000 and 100,000 rpm are also shown in the figure. Note that the output shaft has a speed ratio range of 1.85 for a fixed input speed, and does not go to 0 speed. A slip clutch is required to stall the output shaft.

Figure 22 is an example of system operation at low road load horsepower and vehicle speed for a constant 55,000 rpm rotor speed. Note that maximum horsepower available at the wheels is practically constant for this engine speed, indicating practically a constant efficiency for the system. Note that the slip clutch is required for vehicle

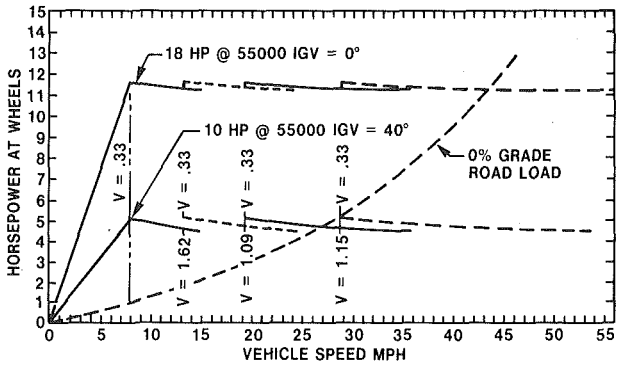

Fig. 22 Differential VRTD operation at low power

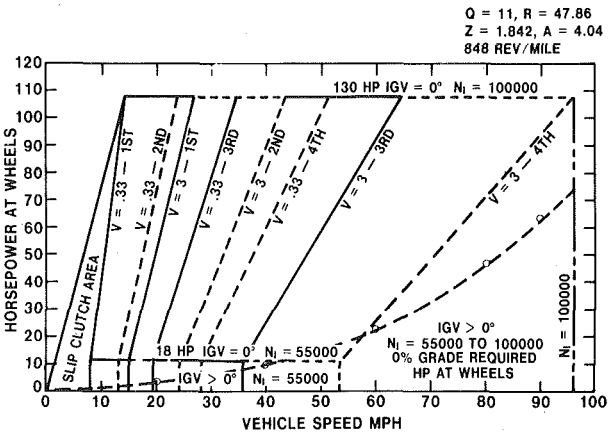

Fig. 23 Operation chart VRTD

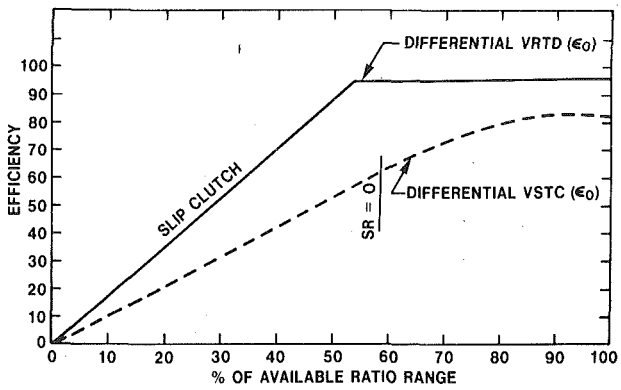

Fig. 24 Efficiency comparison at 100 percent power

speeds between 0 and 8 mph, or once the clutch is engaged and the vehicle has a creep speed of 8 mph. Note that a full stroke of the traction unit of .33 to 3 and back to .33 is not required due to the ratio overlap of the FIOD transmission. If a transmission was available with four speeds as multiples of 1.85 then the full range of the traction unit would be used in all gears and creep speed could be reduced to 4.5 mph for a vehicle with a top speed of 97 mph and a 55 percent idle speed on the engine rotor.

Figure 23 illustrates the complete operating range of the engine transmission system, and illustrates the large area of engine operation available at peak engine operating efficiency with the IGV setting of zero. The amount of power available for accelerating the vehicle in high at all vehicle speeds with no dips, and the slip clutch is required only for vehicle start from rest.

Under steady state operating conditions this appears to be a highly efficient engine-speed variator-transmission system. The response and shift smoothness during transient operation remain unknown and details on this aspect are beyond the scope of this paper.

Comparison of Differential VRTD and VSTC Arrangements. Figure 24 compares the efficiency of full engine power across a normalized full speed ratio range for both arrangements considered in this paper. The efficiency is for the powertrain from engine rotor to speed variator and does not include dropbox, transmission, and axle. It can be seen that the VRTD arrangement is about 12 percent more efficient than the VSTC arrangement at the maximum end of the speed range and increases this efficiency advantage to the point of clutch slip. Part power efficiencies are not included in this paper but the trends are similar, i.e., the VRTD arrangement is more efficient at all power levels.

Summary

A compound epicyclic reduction gear set, utilizing two ring gears for differential power splitting and combined with either a variable stator torque converter or a small variable ratio traction drive as a speed variator, can be combined with a current automatic transmission gearbox to form a highly efficient final drive for a single shaft turbine engine.

Conclusions

Both of the basic transmission arrangements described in this paper are viable concepts for use with a single shaft turbine engine.

Based on efficiency considerations only, the differential VRTD is preferred over the differential VSTC arrangement. However, both arrangements are considered to be of relatively high efficiency due to the power splitting nature of the design.

Practical factors favor the VSTC, since the ability to obtain smooth shifts with the VRTD and to supply traction units in high volume remain unknown. The design of a low cost automatic modulating slip clutch may also prove to be a problem with the VRTD arrangement.

It appears that the VSTC arrangement should be developed first and then the VRTD arrangement evolved as a growth effort of high potential.

Although no comparison with two shaft or multiple shaft turbine arrangements are given in this paper, due to limitations in scope, sufficient data are presented to permit the observation that a single shaft engine with the VSTC arrangement will equal the performance and with a VRTD arrangement will surpass the performance of a two shaft engine when installed in a passenger car. It remains for the reader to confirm that observation.

Acknowledgment

The author wishes to express his thanks to Melody Bornhoft for her assistance in preparing the manuscript for this paper.

References

1 Howes, B. T., "Conceptual Design Study of Automotive Gas Turbine," Department of Energy, Highway Vehicle Systems Contractors Coordination Meeting, Apr. 24, 1979.

2 Carriere, D. L., "Optimum Transmission for a Single Shaft Turbine Engine," Engineering and Research Staff, Ford Motor Company Technical Report No. SR-79-08, Jan., 1979.

3 Christenson, B. C., Frank, A. A., Beachley, N. H., "The Fuel Saving Potential of Cars with Continuously Variable Transmissions and an Optimal Control Algorithm," ASME Paper No. 75 WA-AUT-20, 1975.

Inlet Flow Distortion in Turbomachinery

B. S. Seidel
University of Delaware

M. D. Matwey
University of Delaware

J. J. Adamczyk
NASA Lewis Research Center

A single stage axial compressor with distorted inflow is studied. The inflow distortion occurs far upstream and may be a distortion in stagnation temperature, stagnation pressure or both. The blade rows are modelled as semi-actuator disks. Losses, quasi-steady deviation angles, and reference incidence correlations are included in the analysis. Both subsonic and transonic relative Mach Numbers are considered. A parameter study is made to determine the influence of such variables as Mach Number and swirl angle on the attenuation of the distortion.

Introduction

It is well known [1, 2] that axial flow fans and compressors suffer a loss in performance and a loss in stability if the inlet flow is circumferentially nonuniform. In this study, a stage whose chords are finite length (semiactuator disk) is analyzed. The flow is taken as compressible. Radial effects are ignored. The flow nonuniformities are small perturbations superimposed on a steady mean flow. The distortion occurs at upstream infinity and is in the form of total pressure and/or total temperature. Losses and quasi-steady deviation angle correlations are included in the analysis. The passage of a distortion through the stage is described and the effect on attenuation of Mach number, inlet angle, and other parameters is shown.

In a separate, but related analysis, the same problem is analyzed except that the flow relative to the rotor is transonic.

Background

The first papers in this field were those of Ehrich [3] and Rannie and Marble [4]. Both were linearized, incompressible actuator disk solutions. Later papers have used a parallel compressor model [5], studied compressor-diffuser interaction [6], studied the flow in the annulus from a secondary vorticity plus shed circulation viewpoint [7], considered large flow perturbations [8], considered mixed-flow machines [9], and made and analyzed measurements on a high-speed machine [2]. Quite a thorough search of the literature through 1974 may be found in [1].

There appears to be no previous work in which both velocity and temperature distortions are treated, the blade rows modelled as semi-actuator disks, and losses and quasi-steady deviation angle correlations included in the analysis.

Formulation

Field Equations. The governing equations for the flow field upstream of the rotor, between rotor and stator, and downstream of the stator will be written in an absolute coordinate system. Dependent variables are written as mean value plus perturbation, for example

$$\rho' = \bar{\rho} + \rho = \text{mean value plus perturbation.}$$

The equation of continuity is

$$\frac{1}{\rho'}\frac{D\rho'}{Dt} + \nabla \cdot q' = 0 \tag{1}$$

where ρ, q, and t are, respectively, density, vector velocity ($q' = iu' + jv'$), and time. The velocity perturbation may be written as the sum of rotational and irrotational parts: q^R, q^{IRR}. Further q^{IRR} may be written

$$q^{\mathrm{IRR}} = \nabla\phi$$

Introducing these variables into (1), and linearizing gives

$$\bar{u}\rho_x + \bar{v}\rho_y + \bar{\rho}\nabla^2\phi = 0, \tag{2}$$

where $(\ )_x$ indicates partial derivative with respect to x.

From the momentum equation,

$$\frac{\partial q'}{\partial t} + q' \cdot (\nabla q') = -\frac{g_0}{\rho'}\nabla p'$$

Further, q^R may be written as the curl of a vector potential A

$$q^R = \nabla x A$$

Since the flow is a plane flow, $\nabla x q^R$ is in the z direction, and $\nabla x q^R$ may be written

$$\nabla x q^R = \vec{k}\zeta$$

It may be shown that, to first order,

$$\bar{q}\cdot\nabla\zeta = 0$$

that is, the vorticity perturbation is convected with the mean flow, and one may write

$$\zeta = f\left(\frac{y - x\tan\alpha}{r}\right)$$

where

$$\alpha = \tan^{-1}\frac{\bar{v}}{\bar{u}}$$

r = turbomachine mean radius

Sine ζ must be of period $2\pi/n$, n an integer, an arbitrary function ζ may be written as

$$\zeta = \Sigma A_n \exp^{[\mathrm{in}.(y - x\tan\alpha)/r]}$$

From the definition of A, it follows that

Contributed by the Gas Turbine Division and presented at the Gas Turbine Conference and Products Show, New Orleans, La., March 10–13, 1980 of THE AMERICAN SOCIETY OF MECHANICAL ENGINEERS. Manuscript received at ASME Headquarters December 7, 1979. Paper No. 80-GT-20.

$$u^R = \frac{\partial A_z}{\partial y} \tag{3}$$

$$v^R = \frac{\partial A_z}{\partial x} \tag{4}$$

$$\zeta = -\nabla^2 A_z \tag{5}$$

where A_z is the z-component of A. One may also show that

$$\bar{q}\cdot\nabla A_z = 0 \tag{6}$$

The most general form for A_z which satisfies the above requirements is

$$A_z = \left(\frac{r\cos\alpha}{n}\right)^2 \Sigma A_n e^{\mathrm{in}y - x\tan\alpha/r} \tag{7}$$

Then expressions for u^R and v^R may be found through (3, 4), and (7).

The entropy is next considered. The flow is modelled as isentropic, but not homentropic. Thus, each particle maintains its entropy, but the entropy varies from particle to particle.

$$\frac{Ds'}{Dt} = 0$$

$$\frac{\partial s'}{\partial t} + q'\cdot\nabla s' = 0 \tag{8}$$

Dropping the unsteady term, one has, to first order,

$$\bar{q}\cdot\nabla s = 0 \tag{9}$$

From this requirement and the periodicity, one may conclude

$$s = \Sigma E_n \exp^{[\mathrm{in}(y - x\tan\alpha)r]}$$

From the above conclusion that the entropy perturbation is convected by the mean flow, the assumption of an equation of state of the form

$$p = p(\rho, s),$$

use of the linearized continuity and momentum equations, one may obtain an equation for the velocity potential ϕ:

$$(1 - \overline{\mathrm{M}}_x{}^2)\phi_{xx} - 2\overline{M}_x\overline{\mathrm{M}}_y\phi_{xy} + (1 - \overline{\mathrm{M}}_y{}^2)\phi_{yy} = 0 \tag{10}$$

where

$$\overline{\mathrm{M}}_x = \frac{\bar{u}}{\bar{c}}$$

$$\overline{\mathrm{M}}_y = \frac{\bar{v}}{\bar{c}}$$

and $\bar{c}$ is the sound speed.

Solutions to (10) which fit the current problem are

$$\phi = (B_n e^{Q_1 x} + B_n' e^{Q_2 x}) e^{\mathrm{in}y/r} \tag{11}$$

where

$$Q_1 = \frac{in\overline{\mathrm{M}}_x\overline{\mathrm{M}}_y + \sqrt{n^2(1 - \overline{\mathrm{M}}^2)}}{r(1 - \overline{\mathrm{M}}_x{}^2)}$$

$$Q_2 = \frac{in\overline{\mathrm{M}}_x\overline{\mathrm{M}}_y - \sqrt{n^2(1 - \overline{\mathrm{M}}^2)}}{r(1 - \overline{\mathrm{M}}_x{}^2)}$$

From (11), one may find the velocity components u^{IRR} and v^{IRR}.

If the x-momentum equation,

$$\frac{\partial}{\partial x}(\bar{u}\phi_x + \bar{v}\phi_y) = -\frac{g_0}{\bar{\rho}}p_x,$$

is integrated partially with respect to x, one obtains

$$\bar{u}\phi_x + \bar{v}\phi_y = -\frac{g_0}{\bar{\rho}}p + f(y) \tag{12}$$

Since $\lim p = 0$,

$$x \to \begin{cases} +\infty \\ -\infty \end{cases}$$

then $f(y) = 0$. Thus, (12) gives p (x,y,B_n,B_n', mean flow parameters) using ϕ, given by (11).

A similar level of detail may be obtained for the density. The equation of state, $p' = \rho' RT'$, and the thermodynamic requirement $Tds = dh - dp/\rho$ yield a relationship between the perturbations in density, pressure and entropy.

$$\frac{\rho}{\bar{\rho}} = \frac{1}{\gamma}\frac{p}{\bar{p}} - \frac{\gamma - 1}{\gamma R}s$$

The previously obtained expressions for p and s then permits one to obtain an expression for ρ:

$$\rho = \rho\ (x,y,B_n,B_n',E_n, \text{ mean flow parameters})$$

Boundary Conditions for $\mathrm{M}_2{}^{\mathrm{REL}} < 1$. The stations in the flow are described in Fig. 1. Examination of the above procedures for the flow upstream of the rotor, between rotor and stator, and downstream of the stator reveal that the number of unknowns is 20: B_n; (w,ρ,p,s) at stations 3, 4, 7; B_{n5}, B_{n5}', A_{n5}, E_{n5}, B_{n9}', E_{n9}, A_{n9}. Thus 20 equations, derived from the boundary conditions, are sought. One of these will be given in some detail, to suggest the procedure. The others will be mentioned only by name.

Continuity across the leading edge of the rotor requires that

$$(\rho' u')_2 = \rho_3' w_3' \cos\theta_1 \tag{13}$$

where w is the velocity relative to the blade row and θ_1 is the mean angle of the flow entering the rotor, as shown in Fig. 2.

The first order component of (13) is

$$(\bar{\rho}u + \bar{u}\rho)_2 = (\bar{\rho}w + \rho\bar{w})_3 \cos\theta_1 \tag{14}$$

Nomenclature

A = vector potential, area
A_n = Fourier coefficient for vorticity
A_z = z-component of A
B_n,B_n' = Fourier coefficient for ϕ
c = sound speed, chord
E_n = Fourier coefficients for the entropy
g_0 = constant of proportionality: $F = ma/g_0$
h = enthalpy
$i = \sqrt{-1}$
$\vec{k}$ = unit vector, z direction
L = standoff distance
L_6 = blade row spacing
M = Mach number
n = harmonic number
p = static pressure
$\hat{P}' = (\rho' c' \mathrm{M}^{\mathrm{REL}'})_2$
q = vector velocity
$\hat{R}' = (\rho' c')_{2A}$
Q_1,Q_2 = exponents defined in the text
r = mean radius
R = gas constant
s = entropy, blade spacing
t = time, thickness
T = static temperature
U = wheel speed at the mean radius
u,v = x,y components of velocity
w = relative velocity in the blade passage
x,y = axes

$\alpha = \tan^{-1}\frac{\bar{v}}{\bar{u}}$ (absolute air angle)

β = relative air angle
γ = ratio of specific heats
δ = deviation angle
ζ = magnitude of $\nabla x q^R$
θ = circumferential coordinate
θ_1 = rotor stagger angle
θ_7 = stator stagger angle
ξ_R = rotor chord length
ρ = density
σ = solidity, chord/spacing
ϕ = velocity potential, $q^{\mathrm{IRR}} = \nabla\phi$, camber
χ = loss coefficient
Ω = shaft angular velocity

Subscripts and Superscripts

$(\bar{\ })$ = mean value
$(\ )'$ = mean value plus perturbation
$(\ )^{\mathrm{IRR}}$ = irrotational
$(\ )^R$ = rotational
$(\ )_R$ = rotor
$(\ )_S$ = stator
$(\ )_0$ = stagnation
$(\ )^{\mathrm{REL}}$ = relative to blading

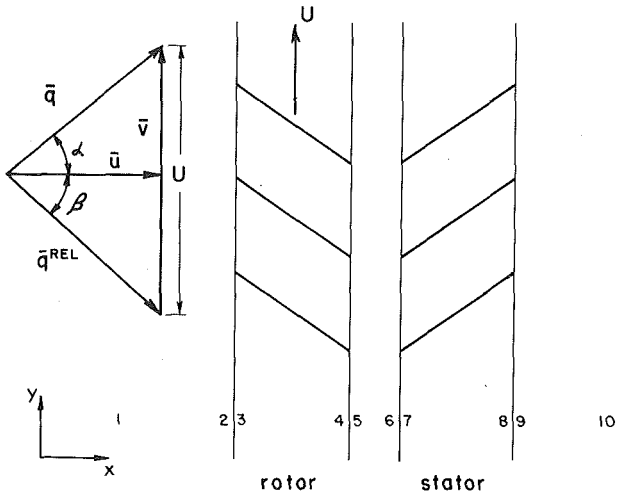

Fig. 1 Coordinates and notation

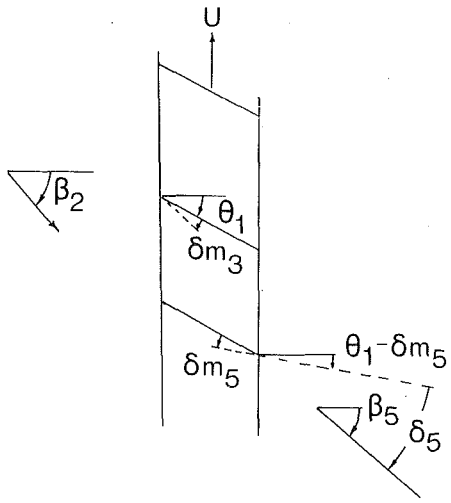

Fig. 2 Definition of various angles; dashed line is the camber line

The unknowns in this equation are u_2, ρ_2, w_3 and ρ_3. The first two, u_2 and ρ_2 are themselves functions of the incoming flow perturbations and the mean flow parameters:

$$u_2 = u_2(A_n, B_n, y, \text{mean flow parameters})$$

$$\rho_2 = \rho_2(B_n, E_n, y, \text{mean flow parameters})$$

Thus (14) can be viewed as one equation in the unknowns B_n, w_3 and ρ_3. A_n and E_n are considered known, since they are fixed by the flow at station 1.

Note that the properties at stations 7 and 8 are assumed equal. The losses in the stator are assumed to occur between 8 and 9. Similarly, the rotor losses are assumed to occur between 4 and 5.

The remaining equations are

- Constant relative stagnation enthalpy from station 2 to station 3, 4 to 5, 6 to 7, 8 to 9
- Constant entropy, 2 to 3, 6 to 7
- Equation of state (p-ρ-s relation) at 3, 4, and 7
- Continuity (4 to 5), (6 to 7)
- Deviation angle, rotor

$$\beta_5 = \delta_{\text{ROTOR}} \tag{15}$$

The deviation angle δ' is taken to be

$$\delta' = \delta'(\beta_{2'}, \mathrm{M}_2^{\mathrm{REL}'}),$$

and (15) becomes

$$\beta_5 = \frac{\partial \delta'}{\partial \beta_{2'}}\beta_2 + \frac{\partial \delta'}{\partial \mathrm{M}_2^{\mathrm{Rel}'}}\mathrm{M}_2^{\mathrm{REL}}$$

The values of the above derivatives may be obtained from correlations such as those in [10].

- Deviation angle, stator

$$\delta_{\text{STATOR}} = \alpha_9 \text{ or}$$

$$\frac{\partial \delta'}{\partial \alpha_{6'}}\alpha_6 + \frac{\partial \delta'}{\partial \mathrm{M}_{6'}}\mathrm{M}_6 = \alpha_9$$

- *Flow through the rotor.* The perturbation properties at the rotor trailing edge are determined from those at the leading by modelling the flow in the blade passages as inviscid one-dimensional, compressible, unsteady flow as described in [11]. The result may be written

$$\begin{Vmatrix} w_4 \\ \rho_4 \\ p_4 \end{Vmatrix} = U\lambda_{\xi R}U^{-1} \begin{Vmatrix} w_3 \\ \rho_3 \\ p_3 \end{Vmatrix}$$

where

$$\Lambda_{\xi R} = \begin{vmatrix} e^{\lambda_1 \xi_R} & & \\ & e^{\lambda_2 \xi_R} & \\ & & e^{\lambda_3 \xi_R} \end{vmatrix}$$

$$\lambda_1 = -\frac{in\Omega}{\bar{c}_3(\bar{\mathrm{M}}^{\mathrm{REL}} - 1)}$$

$$\lambda_2 = -\frac{in\Omega}{\bar{c}_3(\bar{\mathrm{M}}^{\mathrm{REL}} + 1)}$$

$$\lambda_3 = -\frac{in\Omega}{\bar{w}_3}$$

ξ_R = rotor chord length

$$\mathrm{U} = \begin{vmatrix} -\frac{\bar{c}_3}{\bar{\rho}_3} & \frac{\bar{c}_3}{\bar{\rho}_3} & 0 \\ 1 & 1 & -\frac{(\gamma-1)\bar{\rho}_3}{\gamma R} \\ \frac{\gamma\bar{p}_3}{\bar{\rho}_3} & \frac{\gamma\bar{p}_3}{\bar{\rho}_3} & 0 \end{vmatrix}$$

- *Losses in the rotor.* A loss coefficient χ is defined:

$$\chi = \frac{p_{02}^{\mathrm{REL}} - p_{05}^{\mathrm{REL}}}{\frac{\rho_2 q^{\mathrm{REL}^2}}{2g_0}}$$

Also, $\bar{p}_{02}^{\mathrm{REL}} = \bar{p}_{04}^{\mathrm{REL}}$, since it is assumed that the rotor loss occurs across the trailing edge. Then

$$s_{5'} - s_{4'} = -R \ln \frac{p_{05}^{\mathrm{REL}'}}{p_{04}^{\mathrm{REL}'}} = -R \ln\left(1 - \frac{\rho_{2'} q_2^{\mathrm{REL}'^2}\chi'}{2g_0 p_{0_2}^{\mathrm{REL}'}}\right) \tag{16}$$

To first order, we have

$$s_5 - s_4 = G_1,$$

where G_1 is the first order component of the right hand side of (16). We further assume that a lag occurs in s_5, corresponding to the observation that the entropy perturbation travels with the mean relative flow velocity:

$$s_5 = s_4 + \frac{\frac{\bar{w}_3}{\xi_R}G_1}{\frac{\bar{w}_3}{\xi_R} + in\Omega}$$

- *Losses in the stator.* The approach here is similar to that of the previous section. A loss coefficient χ_s for the stator is defined:

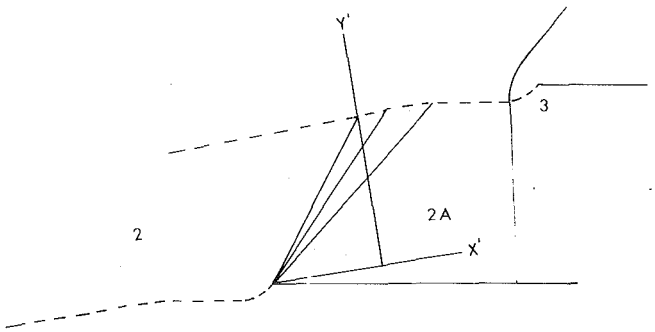

Fig. 3 Bow wave, passage shock, and Prandtl-Meyer expansion

$$\chi_s = \frac{p_{06} - p_{09}}{\frac{\rho_6 q_6^2}{2g_0}}$$

Further, $\bar{p}_{06} = \bar{p}_{08}$, since it is assumed that the rotor loss occurs across the trailing edge. Then

$$s_8' - s_9' = -R \ln \frac{p_{08}'}{p_{09}'} = -R \ln\left(1 - \frac{\rho_6' q_6'^2 \chi_s'}{2g_0 p_{06}'}\right) \tag{17}$$

To first order, we have

$$s_8 - s_9 = G_2,$$

where G_2 is the first order component of (17).

Boundary Conditions for $M_2^{REL} > 1$

In the case $M_2^{REL} > 1$, a bow wave exists at some distance from the blade leading edge, as shown in Fig. 3, and studied in [12]. Figure 3 shows the cascade, two stagnation streamlines (dashed), a Prandtl-Meyer expansion, and a bow wave and shock. This is in accord with [12].

The standoff distance is represented as a mean value plus perturbation:

$$L' = \bar{L} + L$$

Further, this distance is a function of M_2^{REL} and β_2:

$$L' = L'(M_2^{REL'}, \beta_2')$$

The perturbation L, obtained from the above expression, will be periodic in θ:

$$L(\theta) = Ae^{in\theta}$$

Then the rate of change of standoff distance with time will be

$$\dot{L} = \frac{\partial L}{\partial \theta}\frac{d\theta}{dt} = (Ae^{in\theta} in)\Omega$$

That is,

$$\dot{L} = L(\theta) in \Omega$$

The details may be found in [11].

As was done in the previous section, we may then list the unknowns: B_{n2}, B_{n5}, $B_{n5'}$, B_{n9}, A_{n5}, A_{n9}, E_{n5}, E_{n9}, w_{2A}, w_3, w_4, w_8, ρ_{2A}, ρ_3, ρ_4, ρ_8, p_{2A}, p_3, p_4, p_8, s_3, s_4, s_8, L, M_2^{REL}, M_{2A}^{REL}, $\hat{R}$, $\hat{P}$, β_2, T_{2A}

The number of unknowns is 30, and this number of relations among the variables is sought.

We next list these equations.

- Continuity, 2A to 3
- Momentum, 2A to 3
- Constant relative stagnation enthalpy, 2A to 3, 4 to 5, 6 to 7, 8 to 9
- Flow in the rotor, 3 to 4 (similar to previous discussion)
- Losses in the stator
- Losses in the rotor, stator
- State equation (p-ρ-s) at 2A, 3, 4, 8
- Continuity, 4 to 5, 6 to 7, 8 to 9
- Deviation angle for the rotor, stator
- Entropy perturbation carried by the mean flow, 5 to 6
- Prandtl-Meyer turn
- State equation (p-ρ-T) at 2A
- Definition of M_{2A}^{REL}
- The standoff distance L' may be found by adapting the results of [12]:

$$\frac{L'}{s\cos\beta_2'} = \left[1 - \frac{(\rho' c' M^{REL'})_2 \cos(\beta_2' - \theta_1 + \tan^{-1}\sqrt{M_{2A}^{REL'^2} - 1})}{(\rho' c')_{2A}}\right].$$

$$f(M_{2A}^{REL'})$$

where f is a known function. It is from this relation that one achieves $L(\theta)$ and $\dot{L}$.

- Definition of M_2^{REL}
- Definition of β_2
- Entropy rise, 2A to 3
- Definition of $\hat{R}$ occurring in $\dot{L}$ expression
- Definition of $\hat{P}$ occurring in $\dot{L}$ expression

Results

With the theory described in previous sections, there are a number of parameter studies one may make. Also, one may consider upstream distortions in T_0 only, in p_0 only, or in both T_0 and p_0. These are named case 1, 2, and 3, respectively. In this last case, one may also vary the phase angle between p_0 and T_0. In making the study, the parameters are varied about representative values, chosen from [2]:

$\bar{\alpha}_2 = 0$	$\phi_S = 38.34$ deg
$\phi_R = 6.15$ deg	$\frac{\xi_R}{r} = 0.242$
$\bar{M}_{x2} = 0.616$, $\bar{M}_2^{REL} = 1.171$	
$\bar{\beta}_2 = 58.2$ deg	$\frac{L_6}{r} = 0.168$
$\left(\frac{t}{c}\right)_R = 5.74$ percent	$\sigma_R = 1.665$
$\left(\frac{t}{c}\right)_S = 6.88$ percent	$\sigma_S = 1.572$

Figure 4(a) shows the ratio of perturbation magnitudes T_{06}/T_{01} and $T_{010}/T_{01} = T_{06}/T_{01}$ for case 1. Note that for $M_{x2} = 0.527$, $M_2^{REL} = 1$. The ordinate is not monotonic. Attenuation is achieved for M_{x2} greater than about 0.6. Figure 4(b) shows that $p_{06}/p_{05} = 1$, as expected; and that attenuation occurs across the stator. Again, the ordinate behavior is not monotonic.

Next, consider case 2, p_0 distortion only. Figure 4(c) shows that $T_{06}/T_{05} = T_{010}/T_{05} = 1$ for all M_{x2}, as expected. Figure 4(d) shows p_{06}/p_{01} and p_{010}/p_{01} versus M_{x2}. Note that there is attenuation across the rotor and further attenuation across the stator for every M_{x2}. These curves display both a maximum and a minimum.

Next, consider both a p_0 and a T_0 distortion, in phase at station 1. Figure 4(e) shows that T_0 is attenuated by the rotor, (but not by the stator) for all M_{x2}, but the ordinate behavior is not a simple one. If we compare Fig. 4(e) to 4(a), we note that a T_0 distortion alone can be amplified, but, when accompanied by a p_0 distortion, is attenuated (under the conditions examined here). Figure 4(f) shows a considerable attenuation across the rotor and a further attenuation across the stator. If we compare Fig. 4(f) and 4(b), it appears that a p_0 distortion is much more highly attenuated when accompanied by an in-phase T_0 distortion.

The same type of study has been made, but with $\bar{\beta}_2$, chord/mean radius, and phase angle between the upstream p_0 and T_0 distortions as independent variables. The graphs are contained in [11]. A simple summary is difficult, but, at least for the mean flow states examined, attenuation is a monotonic function as follows:

- *Subsonic through transonic.* With a p_0 distortion, increased p_0 attenuation occurs with increasing β_2. With a p_0 and T_0 distortion (in phase) increased p_0 attenuation occurs with increasing β_2.

[1] A second value of M_{x2}, not from [2], was chosen to yield a subsonic M_2^{REL}: $M_{x2} = 0.3$, $M_2^{REL} = 0.57$.

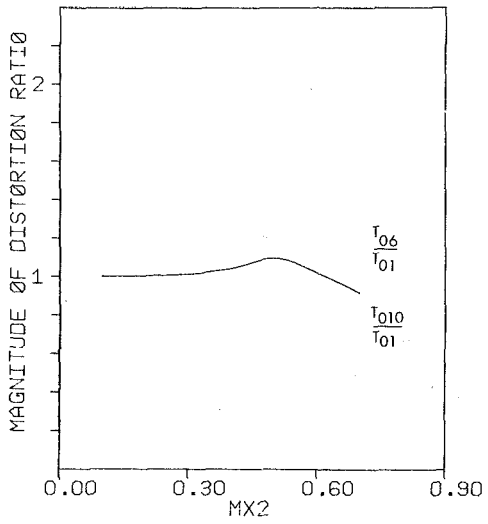

Fig. 4(*a*) Parameter study of attenuation. T_0 distortion, M_{x2} variable

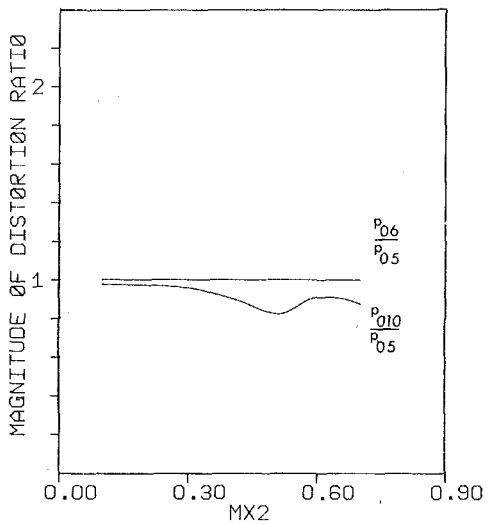

Fig. 4(*b*) T_0 distortion, M_{x2} variable

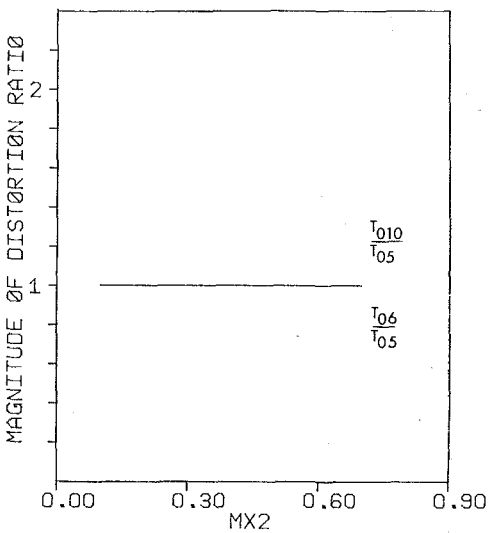

Fig. 4(*c*) p_0 distortion, M_{x2} variable

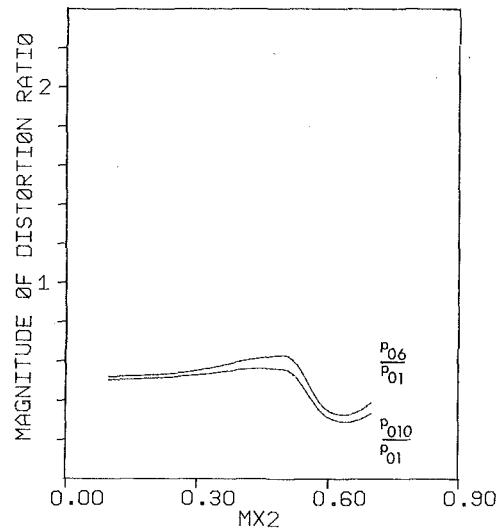

Fig. 4(*d*) p_0 distortion, M_{x2} variable

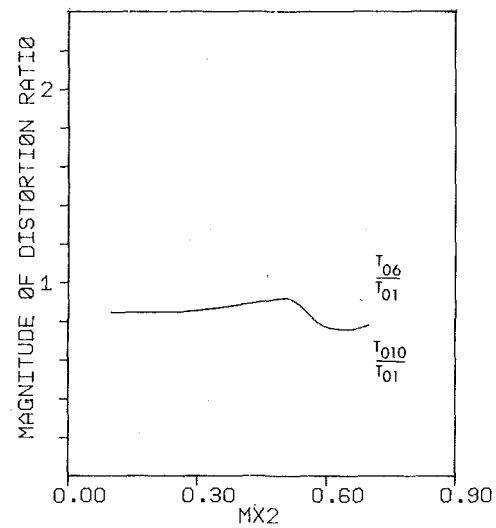

Fig. 4(*e*) p_0 and T_0 distortion, M_{x2} variable

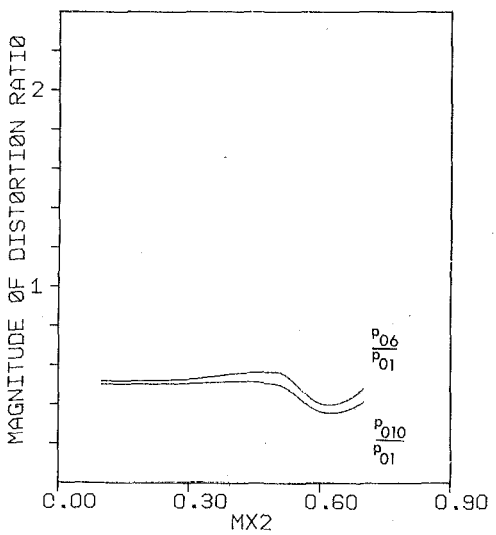

Fig. 4(*f*) p_0 and T_0 distortion, M_{x2} variable

• *Transonic.* With T_0 distortion, increased T_0 attenuation occurs with increasing chord/mean radius. With a T_0 distortion, increased p_0 attenuation across the stator occurs with increasing chord/mean radius. With a T_0 and p_0 distortion (in phase) increased T_0 attenuation and decreased p_0 attenuation occurs with increasing chord/mean radius.

• *Subsonic.* With a p_0 distortion, increased p_0 attenuation occurs with increasing α_2.

With a p_0 and T_0 distortion, increased T_0 attenuation and p_0 attenuation occurs with increasing α_2.

Acknowledgment

This work would not have been possible without the support of NASA (Grant NSG 3189), the programming and checking done by Mr. Larry Perkins, University of Delaware, and the assistance of the University of Delaware Computing Center.

References

1 "Distortion Induced Engine Instability," Advisory Group for Aerospace Research and Development (AGARD) Lecture Series No. 72, Oct. 1974.

2 Sanger, N. L., "Performance of a 1.57-Pressure-Ratio Transonic Fan Stage With a Screen-Induced 90° Circumferential Inlet Flow Distortion," NASA TN D-8163, Feb. 1976.

3 Ehrich, F. F., "Circumferential Inlet Distortions in Axial Flow Turbomachinery," *Journal of the Aeronautical Sciences,* Vol. 24, No. 6, June 1957.

4 Rannie, W. D., and Marble, F. E., "Unsteady Flows in Axial Turbomachines," paper presented at International Days of Aeronautical Sciences, Paris, France, May 1957.

5 Mazzawy, R. S., "Multiple Segment Parallel Compressor Model for Circumferential Inlet Distortion," ASME JOURNAL OF ENGINEERING FOR POWER, Apr. 1977.

6 Greitzer, E. M., and Griswold, H. R., "Compressor-Diffuser Interaction with Circumferential Inlet Distortion," *Journal of Mechanical Engineering Science,* Vol. 18, No. 1, 1976.

7 Hawthorne, W. R., McCune, J. E., Mitchell, N. A., and Tan, C. S., "Nonaxisymmetric Flow through Annular Actuator Disks: Inlet Distortion Problem," ASME JOURNAL OF ENGINEERING FOR POWER, Vol. 100, Oct. 1978.

8 Adamczyk, J. J., "Unsteady Fluid Dynamic Response of an Isolated Rotor with Distorted Inflow," AIAA Paper 74-49, 1974.

9 Tanida, Y., "Inlet Airflow Distortion in Turbomachinery," *SAMP,* Vol. 23, 1972.

10 "Aerodynamic Design of Axial-Flow-Compressors," NASA SP-36, 1965.

11 Seidel, B., and Matwey, M., "Inlet Flow Distortion in Turbomachinery," Mechanical and Aerospace Engineering Department Report No. 229, Nov. 1979, University of Delaware, Newark, Del.

12 Miller, G. R. and Hartmann, J. J., "Experimental Shock Configurations and Shock Losses in a Transonic-Compressor Rotor at Design Speed," NACA RM E58A14b, June 1958.

H. J. Förster

Prof. Dr.-Ing.,
Daimler-Benz AG,
Stuttgart, W. Germany

Continuously Variable Ratio Transmissions for Single-Shaft Gas Turbines

The single-shaft gas turbine was combined with various CVR transmission. Of the three variants studied in detail—purely hydrostatic transmission, hydrostatic transmission with internal power splitting, and hydrodynamic transmission with variable pitch converter—the latter gives the best transmission efficiency. However, comparison with the two-shaft gas turbine shows quite clearly that in practically all cases a large part of the gain in efficiency achieved by increasing the process temperature to 1623 K is absorbed by the losses from the CVR transmissions. Because of the great significance attached today to fuel consumption, the combination of single-shaft gas turbine with CVR transmission—on the basis of these investigations—cannot be recommended. This statement would even apply if it was to be proved that the simple design of the single-shaft gas turbine alone permitted the use of ceramic material and thus the higher process temperatures. This is because the conditions along the traction resistance line for level ground have a much greater effect on everyday fuel consumption than the efficiency ratings at full load. The latter only has an effect during acceleration or when steep gradients are being negotiated.

Gas turbines so far have not been able to replace the reciprocating piston engine in motor vehicles. There are two essential reasons for this: the higher fuel consumption, above all in the part-load range, and the greater construction expenditure. One hopes to improve the fuel consumption by applying the higher process temperatures made possible by the use of ceramic materials. As regards cutting down the construction expenditure, attention is being focused once again on the single-shaft gas turbine. As this can only be made suitable for use in vehicles if a continuously variable ratio (CVR) transmission is employed, these transmissions will have a decisive effect on the future of the single-shaft gas turbine as a drive unit.

With the single-shaft gas turbine (Figs. 1(a) and (b)) the one turbine has to provide not only enough power to drive the compressor, but also enough to drive the vehicle. This results in a relatively simple drive unit with the added advantage that the parts subjected to the high temperature can be constructed in a relatively compact and rotationally symmetrical form. On the other hand, the two-shaft gas turbine (Figs. 2(a) and (b)) has a separate turbine with which to drive the vehicle. In this way the speeds of the vehicle and the gas generator are not directly interdependent, which provides considerable advantages. However, the construction expenditure is greater and central arrangement of the combustion chambers is hardly possible.

The differences are clearly shown by comparing the operational performance maps of vehicles with the performance maps of gas turbines. The single-shaft turbine, (Fig. 3) covers only a very small part of the required map; i.e. it can only be rendered useful by means of CVR transmissions. On the other hand, the two-shaft gas turbine (Fig. 4) in principle requires no additional transmission. However, it appears worthwhile generally to provide a few selectable ratios for purpose of acceleration and to enable steep gradients to be negotiated easily.

The demands made on the CVR transmission by the single-shaft gas turbine are considerable. For example, a fourfold increase in maximum torque is necessary to enable steep gradients to be overcome. However, as maximum torque in the turbine is only produced at the point of maximum output, a limitation of this transmission range would result in very high power dissipation in the start-up zone and is thus unacceptable. Rather, a considerably greater transmission range is necessary to convert even operating points of low output to a high starting torque. A large transmission range, however, can also be recommended for operation at low output levels and low driving speeds. As the idle speed of the single-shaft gas turbine is about 50 percent of its maximum speed, and as the vehicle will be driven at low speeds for a not inconsiderable part of its total operating time, too much slip would be very uneconomical. Consequently, transmission ranges of over 20 are necessary, at least in the part-load range. Unfortunately, the efficiency ratings of all CVR transmissions decrease as the transmission range increases. The efficiency of the transmission, however, is of decisive importance as it greatly influences the fuel consumption of the drive unit.

CVR transmissions are able to extend an operating point on the input shaft to an operating curve on the output shaft. Similarly they can extend an operating curve on the input shaft to a whole operating field on the output shaft. Consequently, a suitable characteristic curve must be selected from the operating field for the single-shaft gas turbine. (Fig. 5). This suitability is judged according to the criteria fuel consumption and acceleration reserve. By acceleration reserve I mean the torque which becomes spontaneously available solely as a result of a change in temperature, without involving any change in

Contributed by the Gas Turbine Division and presented at the Gas Turbine Conference and Products Show, New Orleans, La., March 10–13, 1980 of THE AMERICAN SOCIETY OF MECHANICAL ENGINEERS. Manuscript received at ASME Headquarters December 7, 1979. Paper No. 80-GT-21.

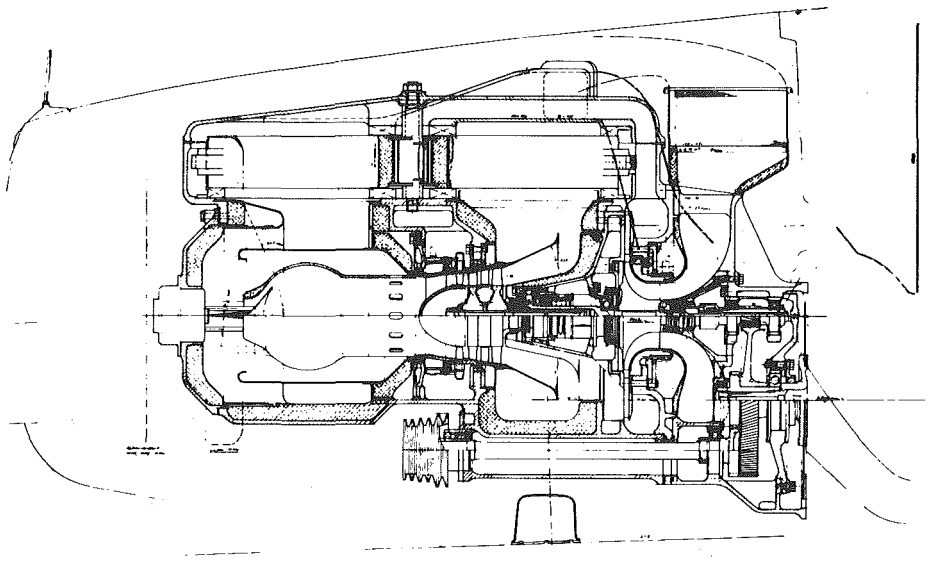

Fig. 1(*a*) Longitudinal section through a single-shaft gas turbine

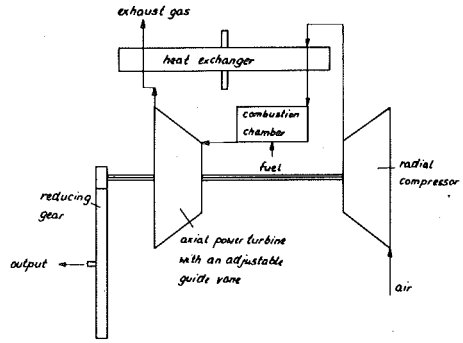

Fig. 1(*b*) Block diagram of a single-shaft gas turbine

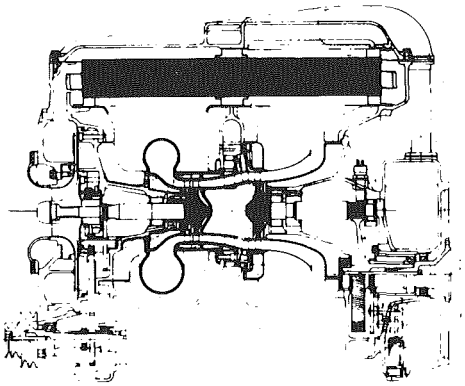

Fig. 2(*a*) Longitudinal section through a dual-shaft gas turbine

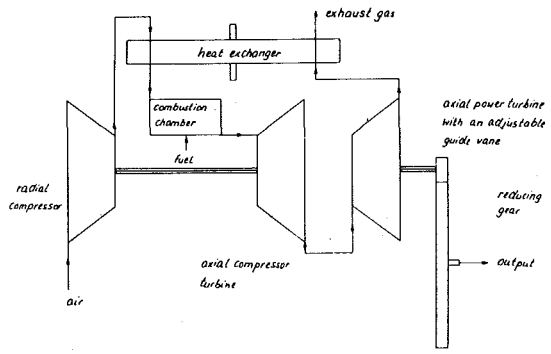

Fig. 2(*b*) Block diagram of a dual-shaft gas turbine

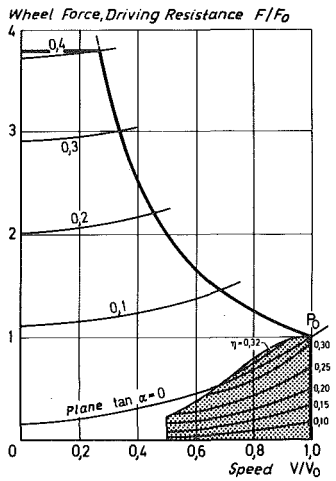

Fig. 3 Performance graphs of a vehicle and a single-shaft gas turbine

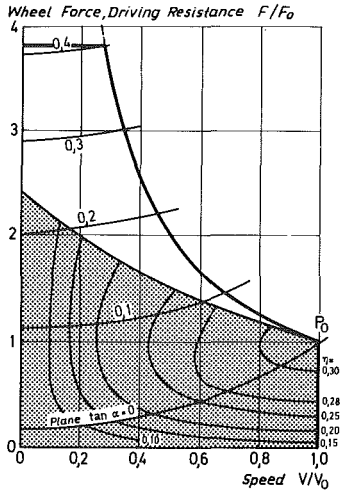

Fig. 4 Performance graphs of a vehicle and a dual-shaft gas turbine

speed. The chosen characteristic curves must all go through the point of maximum output (Fig. 6). The curve "constant $speed_{max}$ = constant" exhibits the greatest acceleration reserve but also the worst fuel consumption. The "best fuel consumption" curve is the full load curve, but it provides no acceleration reserve. A mean characteristic curve between these two extremes was therefore chosen.

Various types of CVR transmission are available: mechanical converters, hydrodynamic converters and hydrostatic converters.

Mechanical Converters

The traction or chain drives used in mechanical converters generally have a transmission range of 4 to 5. The change in conversion during operation is achieved by adjusting the radius of the pitch point. The proposed gas turbine transmission shown in Fig. 7 has toroidal drive system with a high conversion ratio of $I = 9$ (!) and a regenerative power-split arrangement. As a result it is possible to raise the transmission range to over 20. However, the regenerative blind power, which is greater than the input power, reduces the efficiency of the unit (Fig. 8). Despite this, the efficiency ratings given in the available literature—especially the minor difference between the output of 220 DIN/hp and that of 25 DIN/hp—are remarkable. Mechanical CVR transmissions normally also require special start-up devices (clutches) and a reverse gear. The available data are not sufficient to combine a gas turbine with the transmission in a common performance map.

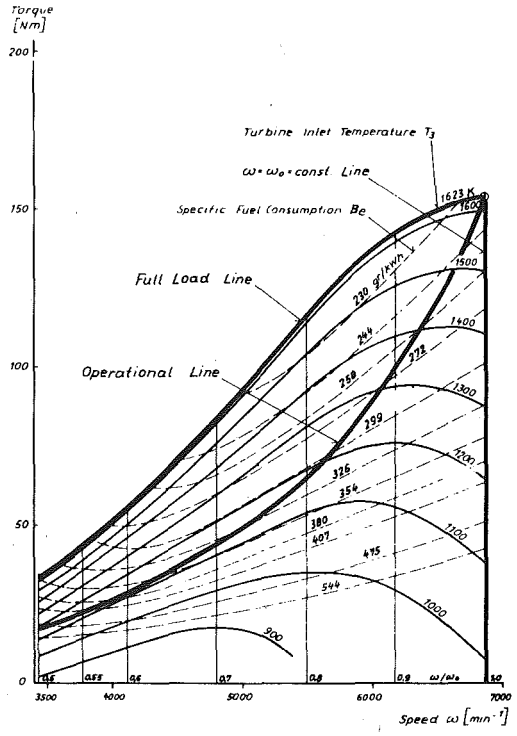

Fig. 5 Performance graph of a single-shaft gas turbine

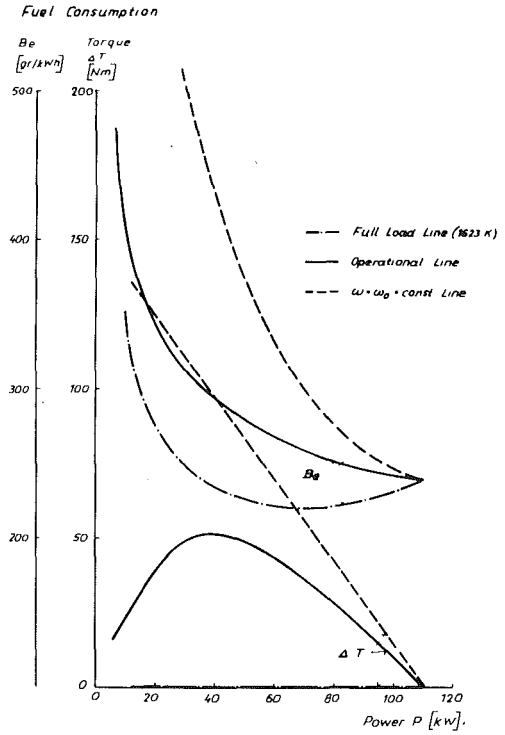

Fig. 6 Operational characteristics of a single-shaft gas turbine

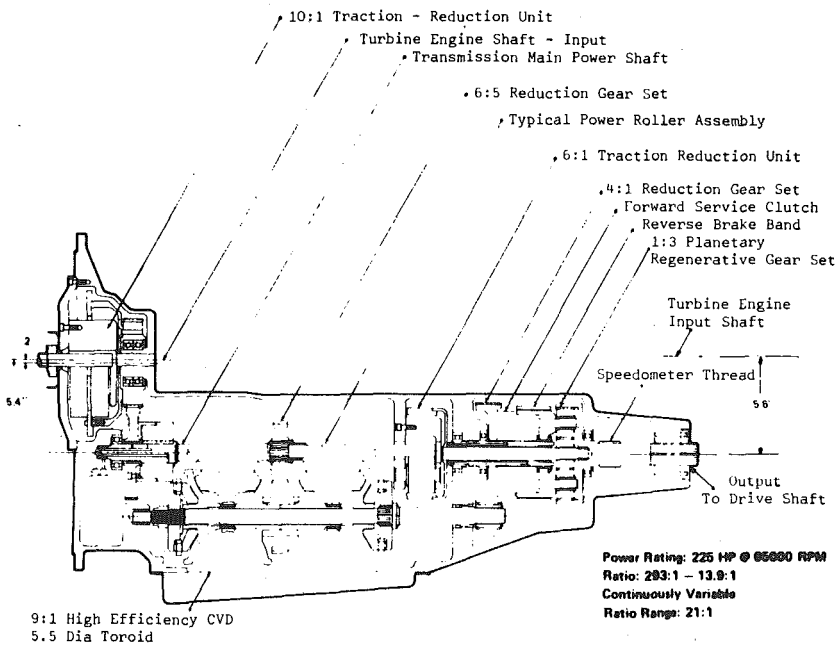

Fig. 7 Tracor transmission, transmission schematic

Hydrodynamic Converters

The torque input curve of a hydrodynamic transmission is a paraboly. If it is taken through the point of maximum output for a single-shaft gas turbine, then this parabola intersects only a part of the performance map (Fig. 9). Now, it has been suggested that a CVR transmission with a conversion range of about 2–3 should be placed between the gas turbine and the converter, because in this way the performance map of the single-shaft gas turbine can be varied so that it can be combined with a fixed-blade converter. However, the efficiency ratings of the CVR transmission and the converter transmission are then multiplied.

Another possibility is to use variable pitch converters, in which case the natural characteristic curve can be altered by means of pivoting reactor blades so as to enable operation along the selected characteristic curve. Adjustment of the reactor blades is dependent on the operating point of the gas turbine and not on the driving condition. Using measured performance maps of a variable pitch converter—although a higher output version—and the performance map for the single-shaft gas turbine as in Fig. 5, a performance map was calculated for the combination single-shaft gas turbine and variable pitch converter (Fig. 10). There is a relatively large area where efficiency is better than 80 percent. The traction resistance curve "road load" corresponds approximately to the best fuel consumption curve.

In order to provide the turbine with good climbing ability at part load, it is necessary to extend this turbine converter performance map by three selectable transmission ratios. The result is the operational performance map in Fig. 11 showing the overall efficiency of engine times transmission. The shift curves between the individual gears were chosen according to minimum consumption. The achievable efficiency ratings are not bad. However, as the traction resistance curve on level

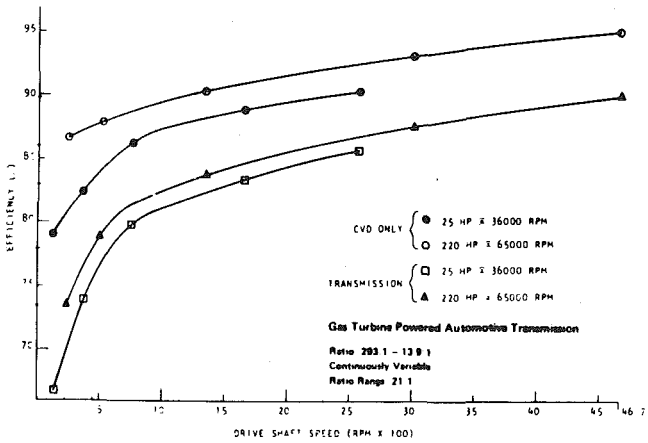

Fig. 8 Tracor transmission, characteristics

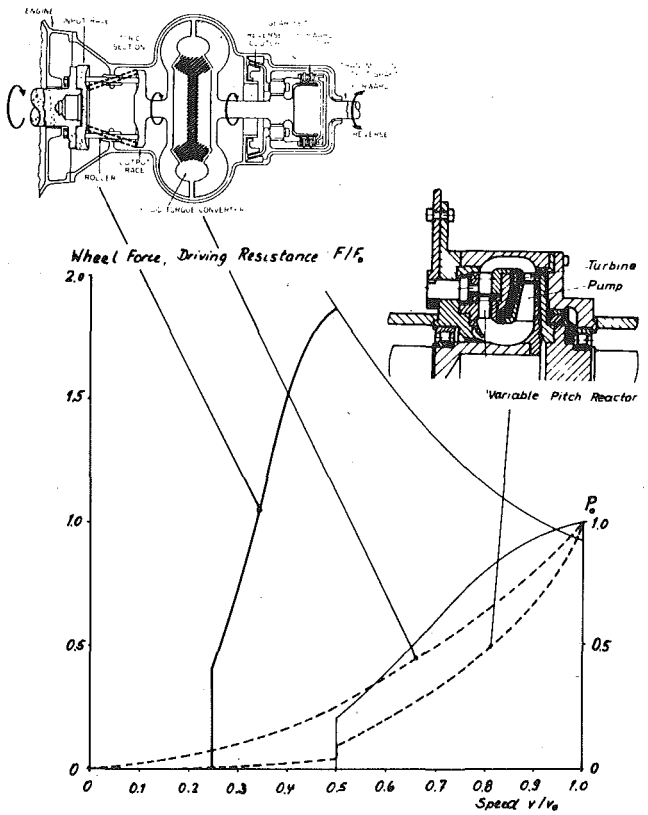

Fig. 9 Single-shaft gas turbine with variable pitch torque converter and variable speed transmission

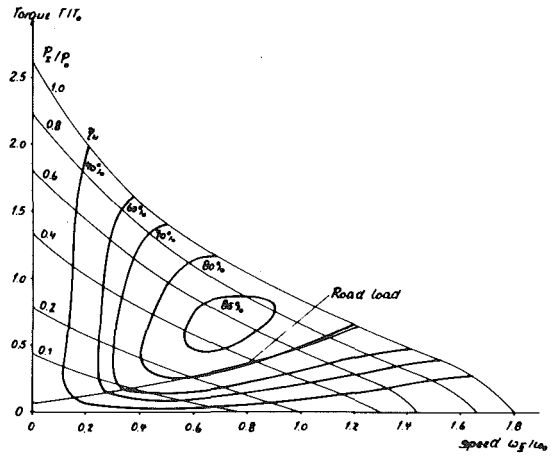

Fig. 10 Performance graph of a single-shaft gas turbine with variable pitch torque converter

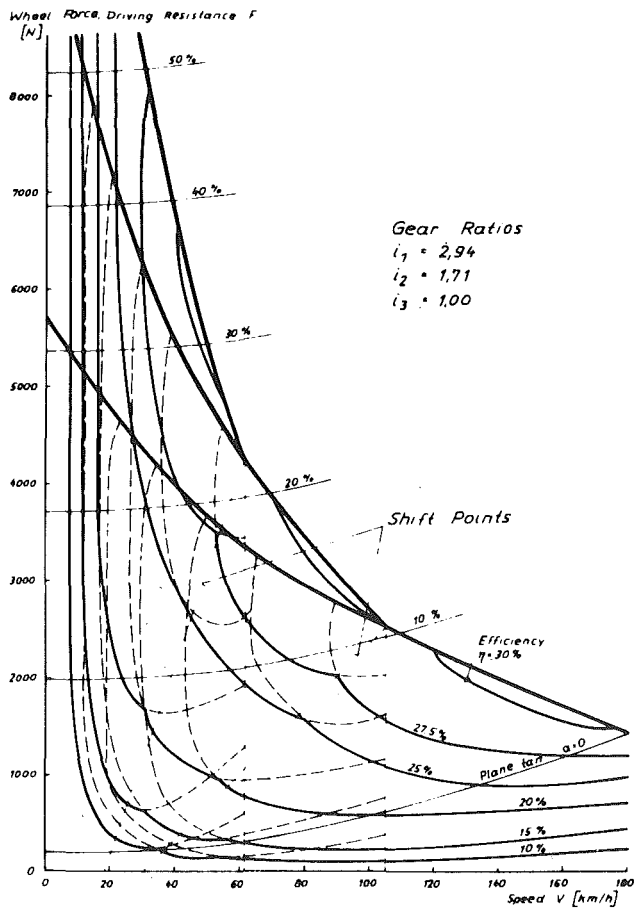

Fig. 11 Performance graph of single-shaft gas turbine and variable pitch torque converter three-speed transmission installed in the vehicle

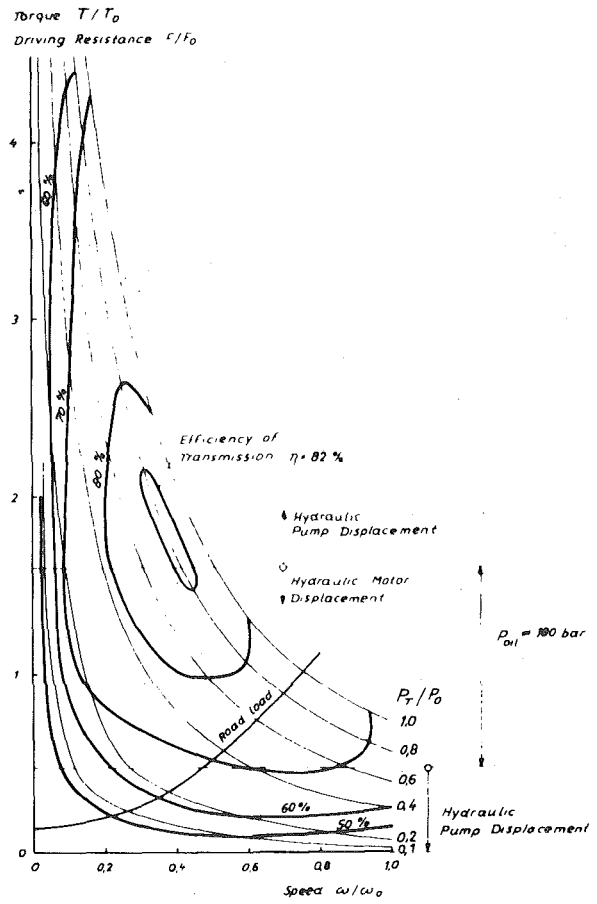

Fig. 12 Performance graph of a single-shaft gas turbine with hydrostatic transmission

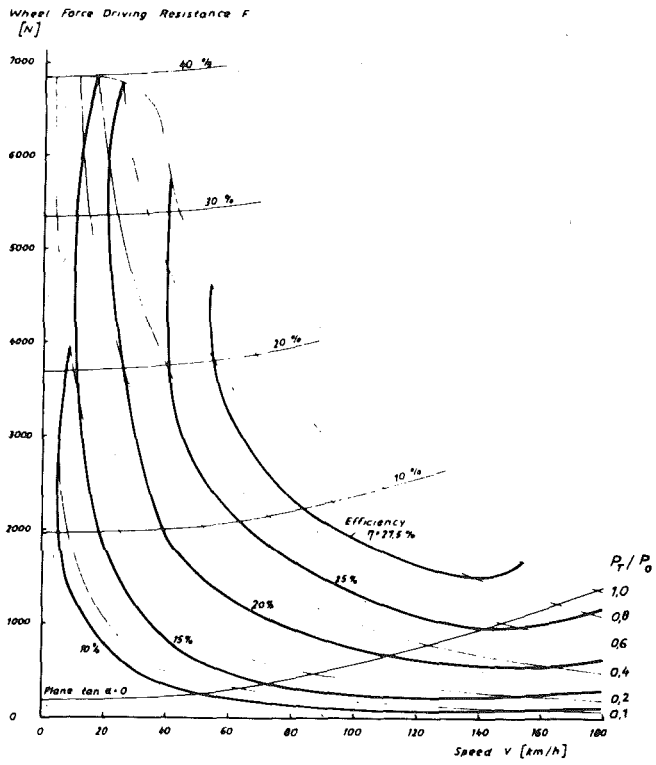

Fig. 13 Performance graph of single-shaft turbine and hydrostatic transmission installed in the vehicle

ground—where the vehicle is driven for most of the time anyway—calls for only a little traction at low road speeds, the efficiency ratings there are really very low. The transmission described here consists of proven elements and will therefore pose no problems in operation. Expenditure as compared with ordinary automatic transmissions is slightly increased by the use of a variable converter, but is quite acceptable nevertheless.

Hydrostatic Transmissions

Hydrostatic transmissions are the most adaptable of all CVR transmissions. The torque conversion is proportional to the volume ratio of hydraulic motor and hydraulic pump. Good efficiency ratings can only be achieved in a relatively narrow conversion range, this being due mainly to flow losses. As the conversion range permitted by the change in swept volume of the hydraulic motor hardly goes above 3; everything beyond this figure must be done via the change in swept volume of the hydraulic pump. At constant output the increase in hydraulic pump volume means a decrease in pressure and an increase in quantity, and this leads very quickly to a clear deterioration in efficiency. A hydrostatic transmission was calculated for the single-shaft gas turbine, using the best hydrostatic machines on the market and assuming that very high pressures of over 400 bar are permissible in special cases. The result is shown in Fig. 12. In the torque range 4 to 1.6, the swept volume of the hydraulic pump is increased, thus lowering the maximum pressure from about 450 to 180 bar. The following range between the conversion 1.6 and 0.5 is completed by adjusting the hydraulic motor. As a further reduction of the swept volume of the hydraulic motor would quickly result in a deterioration in efficiency ratings, the missing range must be completed by a further increase in the swept volume of the pump and thus decreasing pressure. As a result the efficiency in this area deteriorates very quickly. The results achieved are very good and the range of efficiency above 70 percent is remarkably wide. The combination with the vehicle was chosen so that the traction resistance curve for level ground intersects areas of good efficiency wherever possible. The actual performance map in Fig. 13 again shows curves of constant overall efficiency of the transmission. Here too the traction resistance curve for level ground lies in areas of poor overall efficiency for much of the driving speed range.

Hydrostatic Transmission in Power Split Arrangement

Time and time again it is suggested that the efficiency of hydrostatic transmissions should be improved by means of power splitting. In the following investigation no consideration is given to any of those arrangements where the ranges of hydrostatic transmissions are extended by the shifting of servo units instead of purely by continuously variable means. Although the combination of hydrostatic transmissions with such servo units is not impossible, it has a considerably negative effect on the operating characteristics and requires rather precise process control, since in principle the hydrostatic transmission of power is also rigid (shunt characteristic). (The use of gears with hydrodynamic transmissions can be seen in a different light as hydrodynamic transmissions have a series characteristic.)

As regards connecting hydrostatic transmissions to planetary gear sets, combinations can easily be found with the desired transmission range of over 20. However, the achievable improvements in efficiency are normally disappointing, particularly at those points where little hydraulic power is actually transmitted. This is because mostly high speeds are produced at the extreme points for at least one of the hydrostatic units, and these severely reduce the efficiency ratings despite the small amount of hydraulic output.

As a result a transmission arrangement was examined here which goes back to a suggestion from Dr. Ebert, and which was produced for a while by the German firm of Allgaier as a drive unit for tractors. It is a hydrostatic transmission with internal power splitting (Fig. 14).

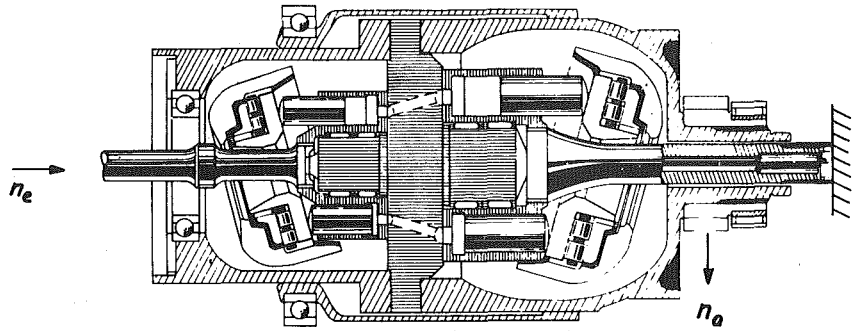

Fig. 14 Hydrostatic transmission (Allgaier)

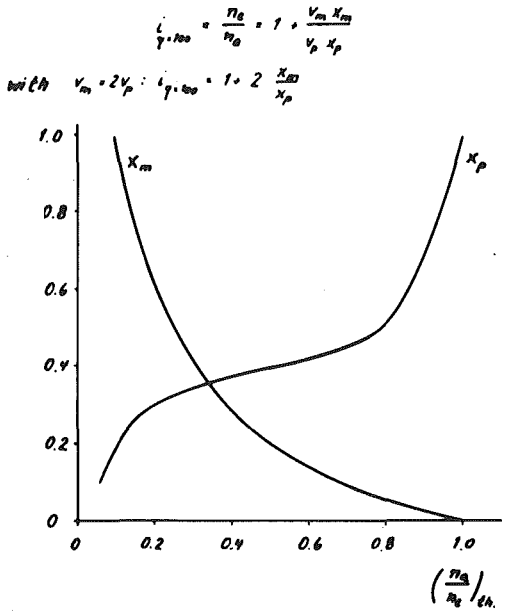

Fig. 15 Rule for hydrostatic transmission from Dr. Ebert

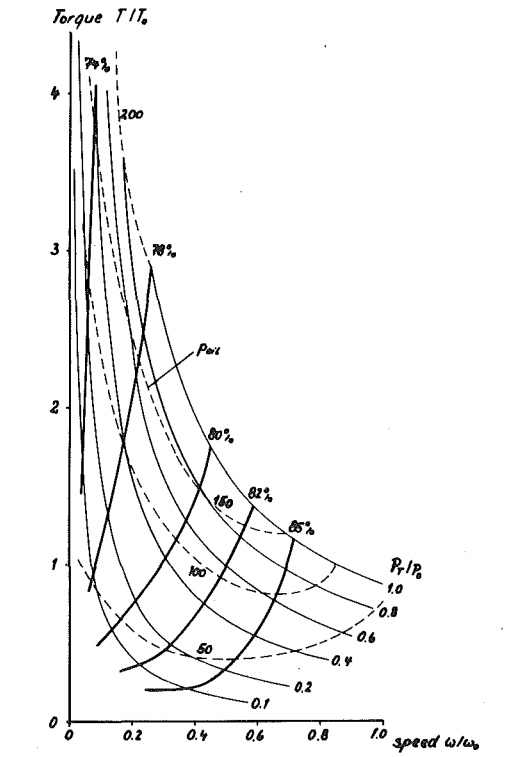

Fig. 16 Performance graph of a single-shaft gas turbine with Allgaier transmission

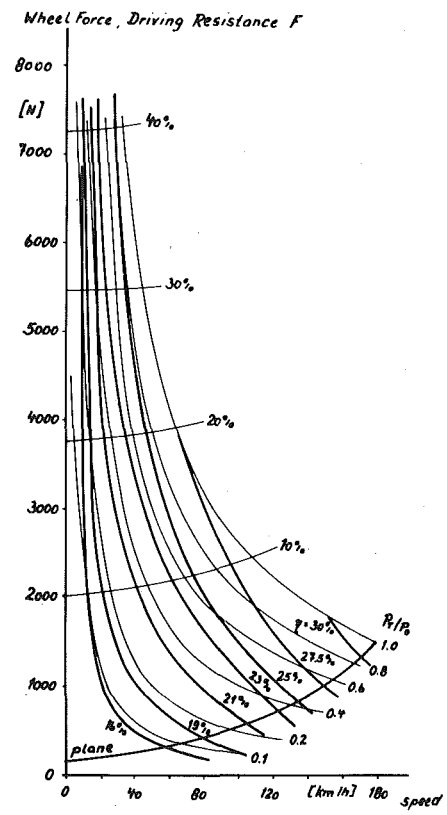

Fig. 17 Performance graph of a single-shaft gas turbine with Allgaier transmission

With this arrangement the input torque is always transmitted mechanically as a reaction torque to the output shaft. The amount of torque exceeding the input torque must be produced by the hydrostatic unit. With this transmission arrangement all the effective speeds are always lower than the transmission input speed. On the pump side the relative speed drops from a maximum during maximum conversion to zero with the transmission ratio 1, while on the hydraulic motor side the speed increases from zero to 1 at maximum road speed. Suitable matching of the swept volumes of pump and motor enable oil quantity and oil pressure to be combined to give a relatively high degree of efficiency over a wide range. The chosen arrangement is shown in Fig. 15. The volume of the hydraulic motor is twice as great as that of the hydraulic pump. This gives, for example, a theoretical overall transmission ratio of 21 for a full motor volume and a pump volume of 10 percent. With approximation to the transmission ratio 1, the pump volume is increased, but because of the decreasing relative speed this does not lead to a corresponding increase in the recirculated quantity. The low pressure ensures that the leakage losses and the friction losses on the motor remain small.

Figure 16 shows the combination of this transmission with the single-shaft gas turbine. The entire area is dominated by relatively low oil pressures. Efficiency is good, and remains remarkably good

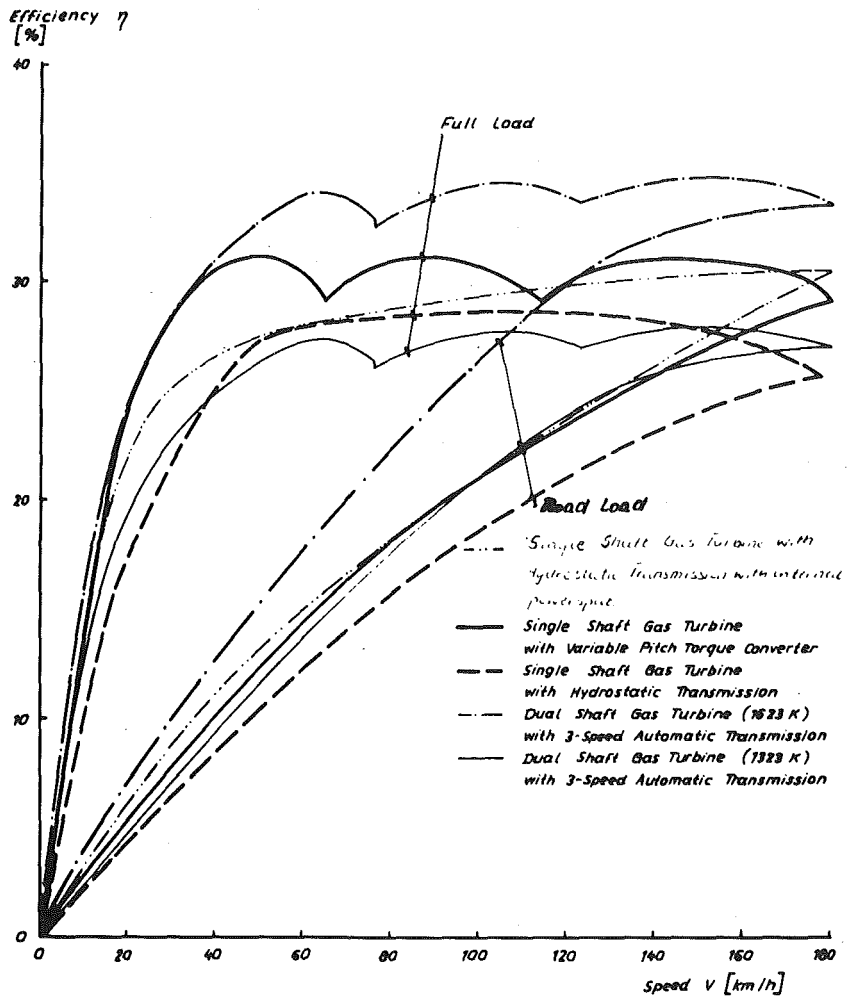

Fig. 18 Comparison of efficiencies

even in the low output range. As a result, the part-load efficiency ratings in the operational performance map (Fig. 17) are better than those of the transmissions examined previously.

Comparison of Single-Shaft and Two-Shaft Gas Turbines with Different Process Temperatures

Figure 18 shows a comparison between selected characteristic curves (full load and road load) for various gas turbine/transmission combinations. In the case of the single-shaft gas turbine—process temperature 1623 K—the results with purely hydrostatic drive are the worst. This applies to both the full load curve and the road load curve. The hydrostatic transmission with internal power splitting gives better values at full load, especially at low and high driving speeds. At road load the efficiency ratings are increased throughout the whole range.

At full load the single-shaft gas turbine and the hydrodynamic transmission with a variable pitch converter is superior to the hydrostatic transmission with internal power splitting. At road load both these types of transmission are approximately equal.

For purposes of completion, the diagram also shows characteristic curves for a two-shaft gas turbine with a three-speed manual transmission, but without a converter. At the process temperature of 1323 K, the efficiency at full load lies below the curves just mentioned. However, the very important efficiency at road load corresponds for a fairly wide range with the combinations single-shaft gas turbine (1623 K) and CVR transmissions; only at low driving speeds is it somewhat less. A two-shaft gas turbine with a process temperature of 1623 K, however, is superior to all the combinations shown: this applies not only to the full load curve, but also particularly to the road load curve at driving speeds above 40 km/h. Below this speed all efficiency data are subject to considerable uncertainty.

Concluding Remarks

The single-shaft gas turbine was combined with various CVR transmission. Of the three variants studied in detail—purely hydrostatic transmission, hydrostatic transmission with internal power splitting, and hydrodynamic transmission with variable pitch converter—the last gives the best transmission efficiency. However, comparison with the two-shaft gas turbine shows quite clearly that in practically all cases a large part of the gain in efficiency achieved by increasing the process temperature to 1623 K is absorbed by the losses from the CVR transmissions. Because of the great significance attached today to fuel consumption, the combination of single-shaft gas turbine with CVR transmission—on the basis of these investigations—cannot be recommended. This statement would even apply if it was to be proved that the simple design of the single-shaft gas turbine alone permitted the use of ceramic material and thus the higher process temperatures. This is because the conditions along the traction resistance line for level ground have a much greater effect on everyday fuel consumption than the efficiency ratings at full load. The latter only has an effect during acceleration or when steep gradients are being negotiated.

The Perbury Transmission

F. G. de B. Perry
Managing Director,
Perbury Engineering, Ltd.
Whitehead, England

The Perbury transmission is a form of toroidal traction drive. This descriptive paper presents a brief overall view of its principles, background, present status of development, applications and future development areas.

Introduction

Ever since the appearance of the first power units and the mechanisms they drove, it was realised that in all but rare cases a fixed speed ratio was merely an expedient compromise in connecting driver and driven components. Prime movers have their efficiency maps to indicate at what rotational speed they give their power most effectively; and driven machines have operating speed requirements forced on them by use and by features of design; so the chances are slim that a one to one speed connection will be operable, let alone optimal.

In the early part of this century, therefore, great efforts and ingenuity were devoted to ways of adjusting speed ratio in a continuously variable way so as to provide the right connection at all times. The mechanisms described in books of that period show how hard and widely engineers looked for the answer. Their schemes divided broadly into mechanical, hydraulic and electrical categories and it is probably true to say that the basic principles of any modern drive can be found already depicted there wholly or in part. Mainly under the pressure of emerging designs for vehicle propulsion, many of these devices were made and tried, but they all failed in performance or durability or both. As a result, the fixed ratio gear wheel won the day. It was simple and cheap; it worked efficiently and lasted; and if one ratio was not right, other options could be added for the operator to engage at his discretion. Ideally, the range would include a one to one direct drive as the optimum and departures from that could be catered for by a choice of indirect gears.

This has long been the situation. The reduction in final performance and the lost efficiency of the prime mover due to departures from instantaneous optimum speeds were not worth bothering about as long as engine size was no problem and users were prepared, or even pleased, to arrange for the engagement of roughly the right speed ratio. But all of a sudden, and very suddenly in terms of technological development times, some vital boundary conditions of power system design have been rewritten, particularly in the field of land transport. A certain performance is still needed to do the job, but fuel consumption, noise and pollution have to be minimised. Weight and cost remain as important as ever but the prime change concerns fuel economy. Henceforth, efficiency lost in the power supply due to running away from the optimum conditions is no longer acceptable without very good reasons and we have returned once more to the predicament of the early vehicle pioneers.

Fortunately, however, the intervening years have seen work progressing quietly on the continuously variable transmission (CVT). Many types have been thoroughly explored and assessed for different applications so that the most advantageous aggregate of pros and cons can be chosen for a variety of technical and commercial reasons. Amongst these, rolling traction drives comprise a specialised category of mechanical torque-converter; the Perbury transmission is only one of a number of possible configurations of traction drive rolling components but its balance of features is well suited in practice and theory to vehicle power units. This paper will try to summarize the main characteristics so that potential users can judge for themselves.

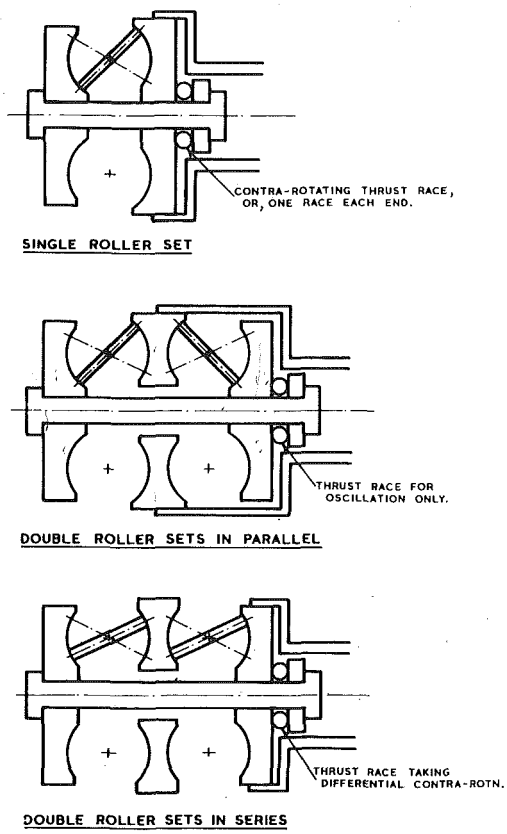

Fig. 1 Perbury transmissions—basic rolling geometry

Basic Description

The basic geometry of rolling components is shown in Fig. 1. A pair of toroidal disks co-operating with a single set of three rollers is referred to as a single-sided unit and is shown in the top diagram. The anchored centre of the roller coincides with the center of the torus cavity so that whatever the angle of the roller, the rolling surfaces are truly normal to each other and no axial movement of the discs is involved. The speed ratio is changed by altering the roller angle so as

Contributed by the Gas Turbine Division and presented at the Gas Turbine Conference and Products Show, New Orleans, La., March 10–13, 1980 of THE AMERICAN SOCIETY OF MECHANICAL ENGINEERS. Manuscript received at ASME Headquarters December 10, 1979. Paper No. 80-GT-22.

to make contact with the input and output disks at different radial distances from the main rotational axis; it can be seen that the ratio could be changed from about 3:1 reduction, through 1:1 at the horizontal, to about 3:1 step-up, giving a range of 9:1, with the output disk revolving in the opposite direction to the input. An end load is applied to the assembly of disks and rollers to provide the traction at the rolling contacts and this is completely contained by tension in the main shaft. In a single-sided unit this means taking the full axial end load at input and output speeds in thrust bearings of some sort or the contra-rotational sum in a single bearing, as shown.

Largely due to the thrust bearing problem, a double sided unit is usual for any high speeds or high powers. As shown in the next diagram, all end loads are balanced and only an oscillating bearing is needed to accommodate movements in some types of axial end-loading device. For hydraulic end-loading, no bearing is needed at all. A comfortable speed ratio range of 5:1 can be obtained from this geometry.

The third diagram in Fig. 1 shows a series set arrangement in which speed ratios of the two sides are multiplied; this is feasible but there are other ways of achieving big ratio ranges.

Historical

The rolling geometry depicted in Fig. 1 is quickly recognized as nothing new. The earliest British Patent found so far on this type of drive was granted to W. D. Hoffman in 1899. But small power single-sided units have been made for years and are still in production; for example, the Swedish Brottby, Belgian Sadivar, French K. S. G. Variator and the little Metron instrument drive in the U. S. Between 1899 and today there is a whole history of effort and invention; names like Hayes, Erban and Erlich in the United States are writ large on much of the prior art.

Through prototype work by the Cloudsley Engineering Company and by consultants Halford, Moult and Brodie (later of the De Havilland Engine Company), the Austin Motor Company produced limited quantities of the Hayes Self-Selector Transmission as a £50 optional extra for their six cylinder saloon cars around 1935. At that time the General Motors Corporation was also active and ran a big test program but no production units followed.

During the war there was little or no activity on this traction drive but interest rekindled afterwards. While investigating simulated gear tooth contacts in 1957, Dr. A. W. Crook of A.E.I. established in a rigorous way the reality of oil film separation in rolling contacts [1, 2] and foreshadowed theories of elastic hydrodynamic lubrication that were to come [3, 4]. General Motors Corporation interest continued and prompted their 1962 symposium [5]. The Lycoming Corporation of the U. S. produced an aircraft constant speed alternator drive which saw service and the then English Electric Company (now part of Lucas Aerospace Ltd.) produced a small Perbury C.S.D. which is still flying.

Perbury Engineering Ltd. was formed in 1956 to put into effect the results of an earlier private study and by 1958 a Rootes Hillman Minx saloon was running with a transmission based on old Austin parts suitably modified. Fig. 2 shows this installation.

There was a forward/reverse lever, two pedal control with a mechanical centrifugal clutch and a control system that gave the highest gearing which matched the engine output. The ratio range was from 3:1 reduction to 1.5 overdrive. Fuel savings were 20–25 percent and the car was very lively and a pleasure to drive. However, the idea did not really appeal to any of the 50 or so companies who showed interest and 25,000 miles later backing was given by the National Research Development Corporation (N.R.D.C.) London, who took control and funded a development programme.

Six test transmissions and four in. roller diameter were designed and built by Perbury Engineering and Plint and Partners at Wargrave were commissioned to design, build and operate the test facilities. Fig. 3 shows the back-to-back performance investigation rig. A six cylinder diesel engine drove through a step-up belt drive which also served as a swinging arm torque meter.

Since the power circulated between the transmissions, only losses were supplied and measured and so the efficiency figures are really accurate. Results from this rig were given in the 1963 Cranfield paper [6]. A second test rig completed four years fatigue life testing to provide data on torque ratings.

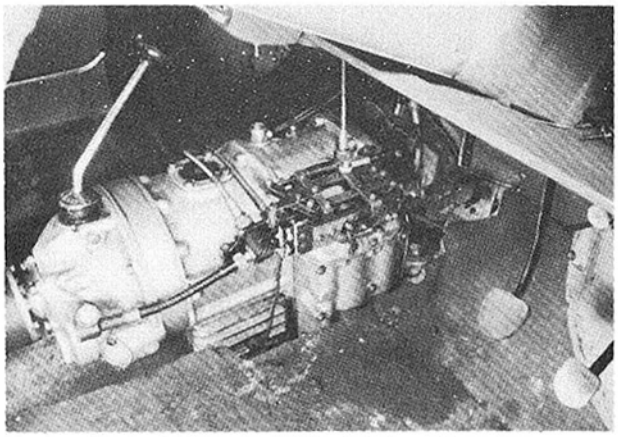

Fig. 2 Prototype installation in Hillman Minx saloon

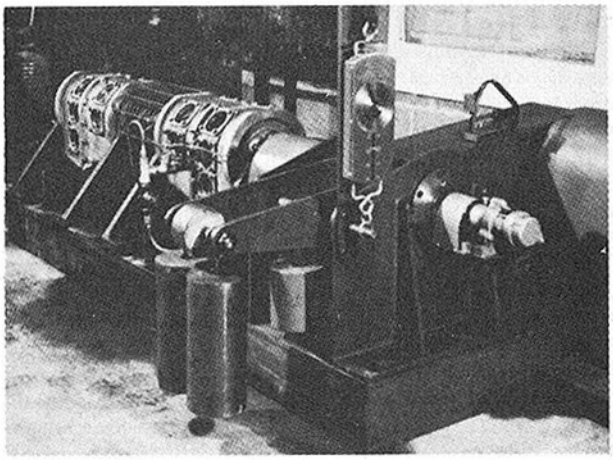

Fig. 3 Back-to-back performance test rig with swinging-arm torque measurement

Space does not permit more than passing mention of these few historical names and landmarks but perhaps enough has been said to indicate that the designs and hardware now under development are not recently discovered and hedged about with uncertainties. Data and know-how have been evolved over many years and the supporting theory and practice are well established in university and learned Society papers and through practical experience.

Mode of Operation

Film Traction. The rolling assembly could be regarded as a large double ball thrust bearing with unused parts of the balls cut away to leave disks of material. The analogy is very close from the design point of view and ball bearing technology is highly relevant. As in rolling bearings, the contact areas are separated by an elastohydrodynamic film of great dependability [1–4] and the traction forces which produce the torque are transmitted by shear in the fluid film [7–9]. The visible result of film shear is a slight movement of the driving surface relative to the driven which appears as a continuous relative rotation or "creep". Creep is one of the two main power losses in the contacts. The other is "spin" loss due to the differential sliding in the contact ellipse which spreads radially over a finite length in the plane of disk rotation. The degree of spin is set initially by the rolling geometry but the power lost is also a function of rotational speed and contact load. Spin and creep losses are both dependent on power transmitted and thus have little effect on the part load efficiency of the rolling assembly. Together they comprise a loss of 6–7 percent but the relative proportions of spin to creep vary.

With rotation but no transmitted power the loss is all from spin as shown by the line through the origin in Fig. 4. If the end-loading is insufficient to support the torque so that gross sliding occurs, then the loss is effectively all due to creep, now become slip, and spin loss is swamped. Inbetween these two extremes there is a graduation of both, but the sum of the two has a fairly flat minimum when the effective coefficient of traction is 75 to 80 percent of its limiting value [8]; at this condition the creep loss can be considerably greater than the spin loss. From the losses and efficiency point of view, there is therefore some latitude in choice of design traction coefficients.

Much more influential on part load efficiencies are parasitic losses of the whole transmission which do not reduce in proportion to transmitted power. As might be expected in a freely rotating assembly, the parasitics of the rolling assembly are very low and there is very modest demand for hydraulic pressure flows. Low power efficiencies thus depend mostly on the rest of the system with its gearing, clutches, brakes and so on.

The mechanism of fluid traction has been under intensive study for many years at certain universities and research establishments and the understanding gained is now used to select and even construct fluid molecules which give greater traction and other desirable properties. To indicate an order of magnitude, if castor oil is put into a traction drive, it will produce practically no power at all; if a typical mineral engine oil is used, some power will be transmitted but this can be roughly doubled for the same unit life by using a specially prepared fluid.

Some fluids also give greater separation of the rolling surfaces than others; increased film thicknesses in hot, slow operation are always welcome since the limiting bulk temperature of the unit can be raised and it can be run still hotter and slower without risk of undue surface contact. When a unit is started from rest there is initial metallic contact but it lasts only a very short time until the roller rotational speed builds up; by two or three hundred rpm, the surfaces are fully apart. In the intervening period there is boundary lubrication in the contacts and mild surface active additives in the fluid give protection from damage as in other mechanisms.

Although early traction drive pioneers could call on no theoretical backing for the concept of fluid films between heavily loaded rollers, they knew from their own experience that some oils were better than others and selected accordingly. The 1935 Austin saloons in England used a fluid called "Drivex" blended by the Sternol Oil Company; further work with Perbury Engineering produced the "Hydratorque" range of fluids in 1956 for the first prototypes and the later N.R.D.C. development program. All the early performance data relate to that type of fluid. A synthetic, high temperature range version of Sternol Hydratorque is still in use for the Harrier jump-jet constant speed alternator drive and forms a useful base fluid for comparing further improvements. Considerable research has been, and is still being done, by the Monsanto Company of St. Louis and the results appear in their "Santotrac" formulations.

Life. Complete separation of the rolling surfaces means that roller or disk wear is not a Perbury phenomenon. Although there are sometimes conditions of full or partial metallic contact, such as in starting from rest and through particles of debris bridging the fluid film, practice bears out the claim that failure of the rolling assembly is by metal fatigue and not by wear. Under the influence of shear stresses below the contact areas, cracks propagate to the surface and a pit appears by a piece of metal detaching itself from the bulk in the classical fashion. However, the fatigued track will still have its final finishing marks, and no dimensional change will be measurable on the components as a whole due to its failure. Some forms of traction drive do remove metal from their running surfaces and cannot operate continuously at one ratio position without trouble, but the causes of their film failure do not exist in the Perbury transmission.

Given film thicknesses exceeding twice the surface composite roughness, fatigue failure can be taken to be the result of sub-surface shear failure; it should not be caused by surface initiated cracking. Deep-shear life is the optimum fatigue performance and can be achieved by careful design and good traction fluids.

From the users' point of view, the effect of pitting failure is to produce grumbling noises when the pits are sufficiently enlarged, or just a "noisy" transmission; the noise gradually becomes worse just as in ball and roller bearings. Failure is thus progressive over a period and ample warning is given of material distress long before any change in operating characteristics or efficiency can be detected even with test bed instrumentation.

The life requirement of a vehicle transmission ranges from 160,000 km for cars to 2,000,000 km for commercial vehicles and the B_{10} life expectancy is adjusted to this by the operating torque rating. Due allowance is made for the number of components in a complete assembly and where possible it is good to under-run small but critical bearings so as to fade them right out of the fatigue liability picture. When used mostly at a fixed ratio, the disks are the life criterion but in vehicles the amount of ratio variation is such that rollers are the failure probability.

Establishing fatigue data is costly and time consuming but has to be done for correct rating. Fig. 5 shows two self-monitoring back-to-back test rigs running at overloads to produce disk and roller failures. Input speeds range from 1000 rpm to over 4000 rpm, the speed ratio can be fixed or cycled and the hydraulic end-loading is adequate for about 300 hp circulation.

Accurate torque rating of a rolling assembly design is needed to ensure minimum cost and weight for reliable performance of a given duty and the life for a 10 percent failure rate expectancy (B_{10} life) has to be found statistically from Weibull plots. About 30 test failures are required for adequate determination of a component failure line and from this information the statistical performance of whole assemblies can be predicted.

Torque Limits. In order to obtain rolling assembly lives of thousands of hours it is necessary to run at quite moderate contact

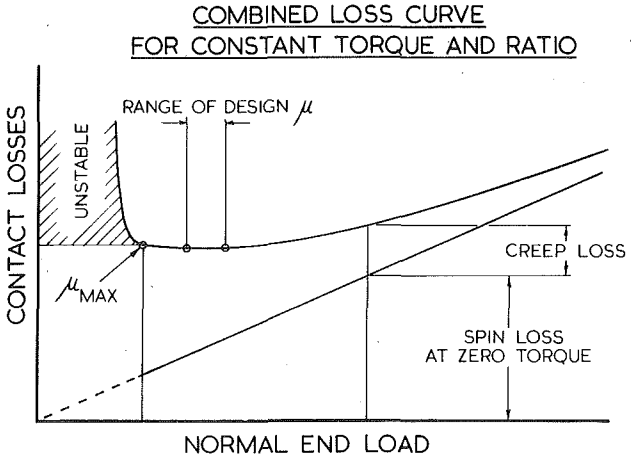

Fig. 4 Combined contact losses

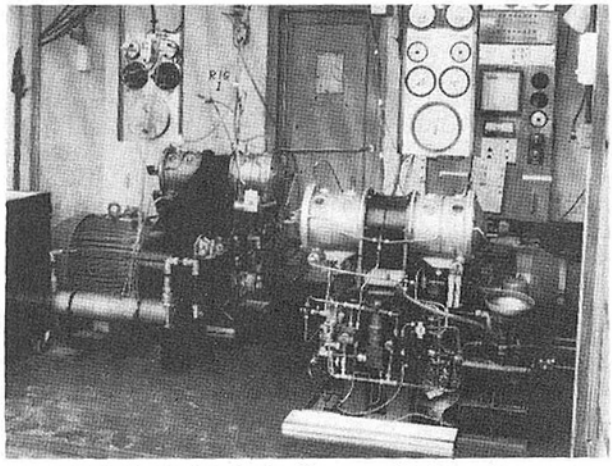
Fig. 5 Back-to-back rolling assembly fatigue rigs

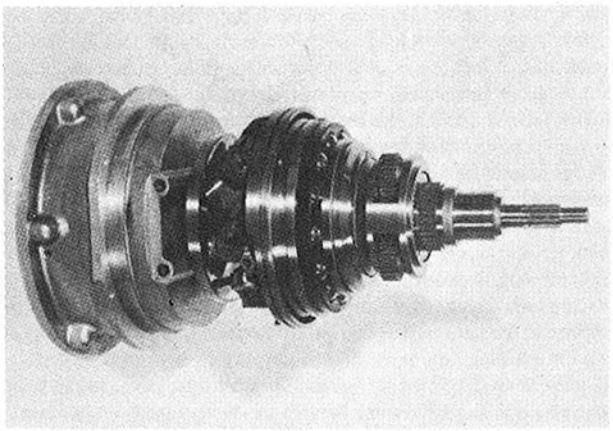

Fig. 6 Simple epicyclic train after-gearing behind an 80 mm single-sided rolling assembly

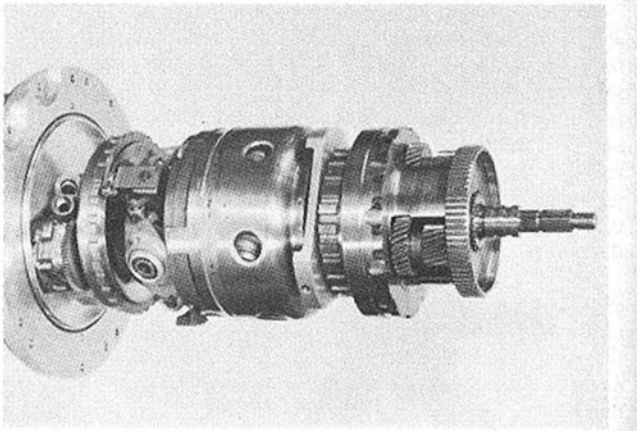

Fig. 7 Two regime after-gearing behind a 100 mm double-sided rolling assembly

stresses. Just as it is normal practice to run an aircraft bearing at a maximum load many times that same bearing's industrial rated load, so the operating stresses in the disk and roller contacts can be increased with impunity by at least 100 percent and still be within the material shake-down stress [10]. But a stress multiplication of two is an end-load factor, and hence a torque increase, of eight. This is often more than the structural strength of drive line components down-stream of the transmission and means that it is difficult to overstress the rolling contacts in a correct vehicle installation.

Overloads are normally of short duration and so have negligible effect on life but if they are maintained for longer periods a different transmission limitation appears in the inability to remove loss heat by the rolling component oil flows. This is a thermal power limit which lies well above normal operating levels but which can be reached in some high duty and short life applications. When cooling improvements have been exhausted, the limit can be raised further by using high temperature fluids and hot-hard steels for the components.

Concerning enforced shocks and slips due, for instance, to engaging after-gearing clutches with incorrect synchronization of ratios, these are of no consequence to the rolling assembly if they are only momentary. No surface damage can be caused unless the fluid film is ruptured; the film thickness in the contact is nearly independent of load but varies with the instantaneous rolling speed (not with creep or slip) and the fluid viscosity at the contact inlet. Viscosity is determined closely by roller surface temperature so only roller heating can thin the film during a shock—and that takes time. Sudden short lived enforced slip can therefore occur within the film without causing metal to metal contact and without leaving any evidence that it happened, as long as the rolling surface temperature rise is not excessive.

Auxiliary Gearing

A double-sided rolling assembly has a convenient ratio range of 5:1 or 6:1 with the greatest reduction ratio, for reasonable contact stresses, of about 3:1. In many applications it is desired to go to a geared idle or zero output condition and convert the CVT into an IVT (infinitely variable transmission). This is easily done with epicyclic or equivalent gearing bridging between the rolling assembly output and an extension of the input shaft, since the output direction has already been reversed. A simple train of this type fitted to a single-sided rolling assembly is shown in Fig. 6 with the annulus connection removed. This unit has a separate reverse train and gives output speeds from zero to about 0.75 × input speed in both directions.

But though cheap and simple, a single train is rather lossy with its high power circulation and where efficiency is important it is best to add another regime and utilize the best parts of both. A compound spur gear equivalent of such a system is shown in Fig. 7, behind a double-sided rolling assembly. "Low" regime goes from a 4:1 reverse ratio, through zero output speed into a low forward speed. At this point the rolling assembly speed ratio is the same as the indirect regime output speed ratio and a clutch and a brake are swopped over synchronously (i.e., a cold shift); "High" regime then takes the output from low forward speed to a 2:1 overdrive straight from the rolling assembly.

Any system that goes through zero output speed, or infinite reduction, needs to be torque sensitive in some way to monitor and control large torques that can circulate internally. The Perbury roller control mechanism feels torque directly and by reacting this with hydraulic pressure in the control system, a simple relief valve can limit the transmission reaction forces. Since the reaction torque is the sum of input and output torques, this implies much less than full engine torque input for a preset maximum stall torque. Stall, in fact, is no problem because only the losses of the transmission are being supplied and a vehicle can hang indefinitely on a gradient without burning anything out.

Recirculation and shunt gearing systems are nothing new and it is not necessary here to go into details of the wide variety of possible arrangements. However, some general comments may be relevant. When the efficiency of the variable speed unit itself is low, gearing arrangements are aimed at reducing the power, and hence the losses, in the variable element branch of power division; such systems seem to come out more complicated mechanically than some recirculating alternatives, where the variable unit takes more than input power. Thanks to inherently high efficiency in the Perbury variable speed link, it is sometimes feasible to increase the variable unit losses by recirculating power in a cheap and simple layout and yet still emerge with acceptable efficiencies in the main operating areas.

With operating economics in mind, it is possible to make special provisions in the rear-end gearing for some applications with major portions of duty at approximately fixed and known conditions, such as long distance cruising. For example, a straight through overdrive or direct lock-up can be provided which leaves the rest of the system free-wheeling at the correct speed but taking no power and incurring little more than parasitic losses. Transmission efficiencies are then around 98 percent and it is a question of engine management as to how far it pays to keep in this by-pass gearing and depart from the optimum engine operating line into areas of slightly increased specific fuel consumption.

Now that engine speeds and torques can be controlled by way of the CVT it is instructive to consider overall engine-plus-transmission specific fuel consumption loops based on fuel consumed for delivered output shaft power at various output speeds. Such data might be more interesting to the vehicle designer than engine-only specific figures which have to be tailored by assumed efficiencies for the different gear ratios and a guess as to what engine speed might be used for a given vehicle situation.

Applications

In any application the two elements of power throughput are torque and speed; these affect the life of the transmission differently. For a given life expectancy, the torque rating of a rolling assembly is nearly

cubic with size; torque rating and weight are thus roughly linear. As regards rotational speed, there is no particular upper limit. Life cycles are consumed pro rata with speed, coefficients of traction decrease gradually as rolling speeds rise but the torques are coming down even faster, so it pays to run fast; in practice, desirable operating speeds are usually decided by other factors such as bearings, seals, centrifugal effects and the gearing arrangements before and after the rolling assembly.

Most applications now are concerned about efficiency. A small transmission of about 30 mm (1.2 in.) roller diameter complete with seals, bearings, pump and control would have an overall efficiency of about 85 percent on load; in a larger straight-through 500 Nm (370 lb ft) unit, the efficiency could exceed 92 percent due to the decreasing influence of parasitics. So what applications are there for variable speed drives of high efficiency, no inherent speed limitation, an almost inaudible white noise level, extremely rapid ratio control response and a torque-size relationship that means large torques for quite moderate bulk?

Areas of application tend to segregate when licensing is considered for manufacture of different final hardware but the rolling assembly technology is usually common to them all with the surrounding casings, gearing, clutches and control arrangements tailored to special requirements; these, however, can constitute more than half the whole transmission.

The smallest Perbury unit made at present is shown in Fig. 8. This is an early prototype of the Lucas Aerospace 12 kVA constant speed alternator drive which is fitted to vertical take-off Harriers, or AV8 B's in the United States. Input speeds are between 7000 rpm and 17,000 rpm and the output speed is held within ±2 percent even with steps of full overload. At the rated electrical output, the variable unit is giving 25 hp and at the 100 percent overload condition that goes up to 50 hp; yet the rolling assembly weighs only 3 kg (6½ lb). This is an example of a weight conscious application with the power transmitted at high speed and low torque in normal aerospace fashion.

But in more mundane machinery the speeds all come down, so the torques go up, and therefore the size, even though the life requirement may be less severe than for aircraft.

Large gains in fuel economy are predicted, and obtained in practice, by running automotive petrol engines on or near the optimum torque-speed relationship. This necessitates a wide torque range transmission (at least 8:1) so that rotational speeds can be held down at low powers, but always have 4000 rpm–6000 rpm available for full power. The larger the capacity of the engine, the less easy it is to run at economical levels of b.m.e.p. in normal motoring conditions; but small engines lack the steady speed torque back-up available merely by depressing the accelerator and the "big car" feel is lost. A Perbury CVT, however, can change speed faster than an engine can follow so that nearly instantaneous torque back-up is felt to be there even with a small engine; but now the torque increase is derived from both higher engine power and extra torque multiplication from the transmission instead of merely using spare torque capacity from the engine. This feature will help car buyers to accept, and later to appreciate, lower installed maximum power and engine capacity. For similar reasons, a CVT is advantageous for battery driven electric vehicles where high torque output is often synonomous with high currents and a heavy armature.

Diesel engines have better part load characteristics than petrol engines but, even so, analysis indicates that worthwhile improvements can be made by keeping to an optimum engine operating line chosen with regard to economy, pollution and noise. Since diesel speeds are lower than for petrol, it seems best to use layshaft arrangements for the transmission and gear up the rolling assembly.

Vehicle drive systems with flywheel energy storage cannot really avoid using an IVT. Though designers' liability legislation makes any energy storage system a source of anxiety for fear of what the unauthorised might do with it, there are outstanding economy gains to be had in stop-start vehicle operation; perhaps commercial fleets will be the first to take advantage.

In spite of low inertia, the high speed of gas turbine rotors makes continuous output speed ratio changes much to be preferred over stepped changes however the shifts may be tailored for quality. Turbine characteristics tend to be peaky and the optimum operating line is therefore more important still. Furthermore, with an IVT a separate stallable power turbine is no longer necessary.

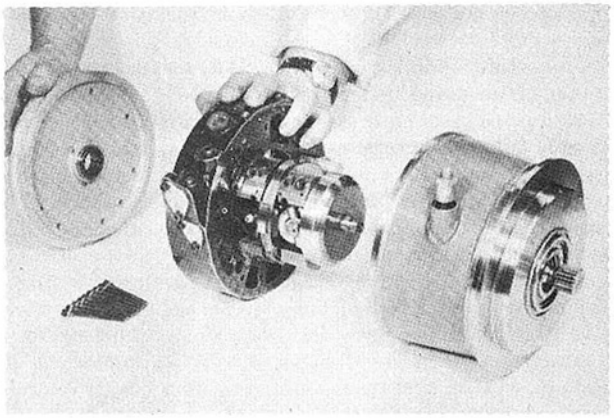

Fig. 8 Prototype English Electric 12 kVA constant speed alternator drive

Small power CVTs of various principles have been marketed for industrial use over many years but the choice thins out markedly above a few tens of horsepower. Some say this is because the market for them does the same but the argument is not convincing. In view of the high specific power and great overload capacity, it would seem that a Perbury industrial drive would be smaller and cheaper than many accepted rivals.

Once the idea is generally accepted that a reliable and efficient, high power potential CVT is here to stay, a host of uses will be able to emerge. The first successful application clears the psychological hurdle. Perhaps no more need be said here about applications as long as the characteristics of the transmission have been appreciated.

Development Areas

There are four main areas in which development can bring about better transmissions. These are:

Traction fluids
Rolling component fatigue life
Regime gearing arrangements
Production packaging.

Traction Fluids. The end-load must be applied for the rolling assembly to transmit torque is inversely proportional to the coefficient of traction; and life is inversely proportional to end-load cubed. Thus an increase in traction coefficient gives a cubic increase in life for the same torque or a pro rata improvement in torque rating for the same life, all for no change in the transmission. Higher traction is therefore the prime goal of the fluid suppliers.

However, other features are important too. The effect of temperature is to reduce the maximum film shear strength which decides the limiting traction, and to decrease the bulk viscosity, giving a thinner film. The design has to assume coefficients and viscosities relating to the worst conditions of use, or abuse, probably with temperatures at a maximum and a deficient high temperature performance will not normally permit advantage to be taken of a good performance when running cooler.

Stress and shear rate have their effects on the fluid film but there must be no anomolous functioning. Oxidation resistance needs to be adequate if a fill-for-life policy is adopted. The fluid will be pumped at pressures up to 300 psi at bulk temperatures from −30 to 130°C and must then lubricate bearings, seals, gear teeth, clutches and control system with minimum parasitic losses. It acts as a heat transfer medium. Despite being violently churned, it has to de-aerate rapidly. It must prevent corrosion during long periods of transmission disuse, perhaps with adsorbed water and it must not react with any of the usual transmission materials. Toxicity is not permitted in fluid or vapor form. Last, but not least, the cheaper it is, the better. A few good

fluids are now available but there still seems plenty of scope for improvement.

Fatigue Life. Since the B_{10} fatigue life for the whole transmission is usually taken as the life required for the rest of the vehicle, there is little interest in the much greater B_{50} life. Of far more concern are the early failures that form part of a typical straight line Weibull distribution; troubles there can activate warranties and reflect unfavorably on reliability. Rogue bearings are rare nowadays on the industrial scene but components with a life shorter than the full B_{10} are tolerated; it is the same for this transmission. So the fatigue life improvements that are to be welcomed and actively sought after are the kind that give the Weibull line a steeper slope and a downward curve at the low failure rate end, indicating reduced life scatter and an expected minimum life. Clean steels, freedom from carbide segregations, uniform heat treatment and rigorous quality control in manufacture all contribute to this end.

Pitting is nucleated in the stressed volume below the surface but failure is not considered to have occurred until a large enough amount of metal has come adrift from the surface; this event is the culmination of a crack propagation process. There are heat treatments and modes of surface stressing which on their own, or in co-operation, can produce compressive residuals at the highly loaded surfaces to discourage or even inhibit crack growth. Big improvements in roller and disk life may be possible this way.

In the search for cheapness with undiminished performance, some of the larger components might have a mixed construction, a cheap material giving general structural rigidity with a more sophisticated and costly layer attached for the rolling surfaces. Once traction drives are in widespread use, such investigations might be expected.

All attempts to improve fatigue durability have to be evaluated in rig running. Full scale rigs are expensive to build and run but there is still doubt as to how to simulate them under small scale and accelerated conditions. Stanhope-Seta four-ball and Unisteel machines are well known but their low rolling speeds make a big difference to the degree of surface separation achieved; in addition, the desire to reduce the test duration often leads to the imposition of stresses well above the material shake-down stress. Are the failures typical and can the lives from these tests be read across to rolling components of ten times the size and rolling speed? A possible answer lies in the failure mode. Perbury fatigue is of the sub-surface shear type normally associated with surfaces running well separated. If this form of fatigue failure is reproduced in the rig simulation, it would appear relevant. In this respect, the NASA five-ball fatigue tester and the Plint and Partners high-speed four-ball machine would seem to offer better simulation than those with lower operating speeds.

It may be that the fatigue performance of full film rolling components can still be rated correctly in a comparative way by low speed boundary contact testing. This would be quite adequate once a datum fluid/material combination has been tested at full scale and satisfactorily correlated. Work is still needed in this area.

Regime Gearing. Vehicle transmissions are now required to show as high an efficiency as they can within other constraints. Depending on the vehicle duty and specification, there are many forms of shunt, recirculating and by-pass gearing which bring advantages in certain areas of operation and not in others. Correct choice of this part of the transmission can drastically reduce rolling assembly power flows and give lower size and cost, higher overall torque ratings and increased efficiencies. Designing to specification in future should produce some preferred arrangements for certain recurrent needs. Good progress has already been made but there seems more to come.

Production Packaging. The principles of the rolling assembly are now known, as they are of gearing, clutches, controls and so on, but not enough has yet been done in the detailed penny-pinching design of minimum weight, cost and volume packages for particular CVT applications. Production and value engineers have a great deal to contribute in cheap and compact integrations of prototype engine/transmission layouts.

Summary

For several decades the basic rolling geometry of the Perbury transmission has appeared in small production numbers under other names; but only in the last fifteen years or so have the subtle analytical problems been solved of what is happening in the fluid films and contact areas of heavily loaded rolling components. In practice, the performance of past traction drives has been interesting but not enough to break into quantity production.

Now there is a full theoretical background to rolling traction: materials are greatly improved and problems of application and packaging have been studied. Above all, there is a need for what a CVT or IVT can do. Whatever the form of prime mover, large improvements in vehicle fuel economy are possible with correct engine management; but correct management demands that engine speed shall not be tied to vehicle speed by fixed ratio compromises. Complete freedom to run the engine at the right speed for any power is the only way to seize the full fuel savings. The Perbury transmission is one of the few ways of doing this at high powers and speeds; perhaps this paper will help convince those concerned that the excellence with which it does so warrants a real hard look.

References

1 Crook, A. W., "Simulated Gear Tooth Contacts: Some Experiments upon Their Lubrication and Sub-Surface Deformations," *Proceedings I Mechanical Engineering* Vol. 171, No. 5, 1957, pp. 187–214.

2 Crook, A. W., "The Lubrication of Rollers," *Philosophic Transactions of the Royal Society of London,* Series A, Pt. I, Jan. 1958, Pts. II and III Dec. 1961, Pt. IV, Jan. 1963.

3 Dowson, D. and Archard, J. F., "Elastohydrodynamic Lubrication," *Proceedings of Symposium,* Leeds, U. K. Sept. 1965.

4 Archard J. F. and Cowking, E. W. "Elastohydrodynamic Lubrication at Point Contacts," *Proceedings I Mechanical Engineering,* Vol. 180, Pt. 3B 1965, pp. 47–55.

5 Bidwell, J. B. Ed. *Rolling Contact Phenomena,* Elsevier, Amsterdam, 1962.

6 Fellows, T. G., Downson, D., Perry, F. G. and Plint, M. A. "The Perbury Continuously Variable Ratio Transmission," *Advances in Automobile Engineering,* Pt. II, 1964, Pergamon Press, Oxford.

7 Johnson, K. L. and Camerson, R. "Four Papers on Traction in Elastohydrodynamic Contacts," *Proceedings I Mechanical Engineering,* Vol. 182, Pt. I, 1967–68, pp. 1–39.

8 Tevaarwerk, J. L. and Johnson, K. L. "The Influence of Fluid Rheology on the Performance of Traction Drives," *Proceedings of ASLE-ASME Lubrication Conference,* Minn. Oct. 1978.

9 Daniels, B. K. "Non-Newtonian Thermo-Viscoelastic EHD Traction from Combined Slip and Spin," *Proceedings of ASLE-ASME Lubrication Conference,* Minn., Oct. 1978.

10 Johnson, K. L. and Jefferis, J. A. "Plastic Flow and Residual Stresses in Rolling and Sliding Contact," *Proceedings of Symposium on Fatigue in Rolling Contact,* paper 5, I. Mech. E., March, 1963.

N. Kyrtatos
N. Watson,

Department of Mechanical Engineering,
Imperial College of Science and Technology,
Exhibition Road,
London SW7 2BX
England

Application of Aerodynamically Induced Prewhirl to a Small Turbocharger Compressor

A design procedure is described which allows the development of an arrangement to aerodynamically impart prewhirl to the inflow of a compressor. The procedure uses compressor performance data and inducer inlet flow distributions together with a mathematical model of the aerodynamic prewhirl inducing arrangement to arrive at the parameters which completely define an arrangement suitable for a particular compressor. The application of the procedure to design an arrangement for a small turbocharger compressor is presented. The effect of the aerodynamically imparted prerotation on the compressor performance was found to be similar to that produced by inlet guide vanes.

Introduction

The performance of a compressor can be controlled by the use of inlet prewhirl, and its flow range can be widened, thus increasing flexibility in operation. Prewhirl is usually imparted through variable inlet guide vanes (V.I.G.V.). However, this mechanical arrangement adds complexity to the machine and an alternative is desirable. It is possible to impart prewhirl aerodynamically to the inlet flow of a compressor, by injecting high pressure fluid at some oblique angle into the inflow, the fluid being derived from the compressor discharge. By varying the amount of fluid injection, variable prewhirl can be obtained. The fluid is ejected through orifices spaced around the periphery of the inlet duct. Hence, prewhirl in the direction of impeller rotation, or opposite to it, is possible, depending on the orientation of the orifices. The arrangement of the orifices presents no structural obstruction to the inflow and does not interfere with the flow or efficiency of the compressor under normal running conditions.

Such a system could emulate I.G.V. if it could be made to work efficiently.

The Design Procedure

A design procedure was formulated, which allows the development of an aerodynamic prewhirl-inducing arrangement, to suit a particular compressor. The design procedure is based on a mathematical analysis and flow modeling of the aerodynamic arrangement [1]. The application of the design procedure on a small radial flow turbocharger compressor is described. This formed part of a more general study of turbocharger and engine matching. In this application, the need for turbomachinery flow control is more pronounced when matching turbochargers to wide speed range engines. Prewhirl may be used to increase the compressor flow range and control the compressor delivery pressure, thus controlling the engine boost pressure.

The design procedure involves two basic assumptions:

The first assumption concerns how stability and efficiency of the compressor are related to the inducer inlet flow angles. It is assumed that inlet flow angle distribution at the best efficiency point—which may, or may not, coincide with the design point of the compressor—represents a set of optimum angle values.

Hence, the best efficiency point is taken as the reference point in the design process, and the corresponding angles as the "reference angles". However, it is not certain that the angle distribution at the best efficiency point, is the optimum incidence distribution for the inducer. The jet-arrangement design point is chosen on the surge line, because this region of incipient flow instability is more critically dependent on the design, than the stable high flow—high pressure ratio region, where prewhirl may also be used (e.g. to limit the boost in vehicle engine turbocharger applications). Of course any other distribution of inlet angles can be defined as the design point of the device.

The single, unbounded, round jet in a cross-flow theoretical model is used to define the jet needed to provide such a deflection to the inflow (prewhirl) so that the resulting relative flow angles at the jet-arrangement design point, match the compressor best efficiency point (b.e.p.) reference flow angles.

When a multitude of jets interact in a confined space (as in the case with the jet arrangement), additional parameters are introduced, complicating the situation. Most of them are only dealt with qualitatively in the design process, based on experience with former designs of the jet arrangement. It may be possible to quantitatively examine selected parameters or use information from related cases (e.g. multi-jet impingement cooling of turbine blades). Some other influencing factors may still be unidentified in this extremely complicated flow situation.

The design procedure in its present form is flexible, consistent, and relatively easy to use, and it is desirable to retain these qualities.

The second assumption is, therefore, that the result of the design procedure, i.e., the parameters which define the jet arrangement, is a reasonable approximation to the ideal solution, which would be achieved if all influencing factors could be accounted for.

The following parameters completely define the jet arrangement (see Fig. 1).

1 Ejection orifice diameter (D_j)

Contributed by the Gas Turbine Division and presented at the Gas Turbine Conference and Products Show, New Orleans, La., March 10–13, 1980 of THE AMERICAN SOCIETY OF MECHANICAL ENGINEERS. Manuscript received at ASME Headquarters December 7, 1979. Paper No. 80-GT-23.

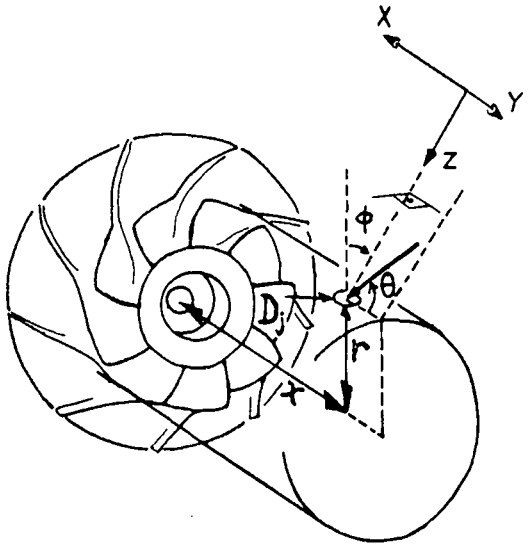

Fig. 1 Parameters defining the jet arrangement

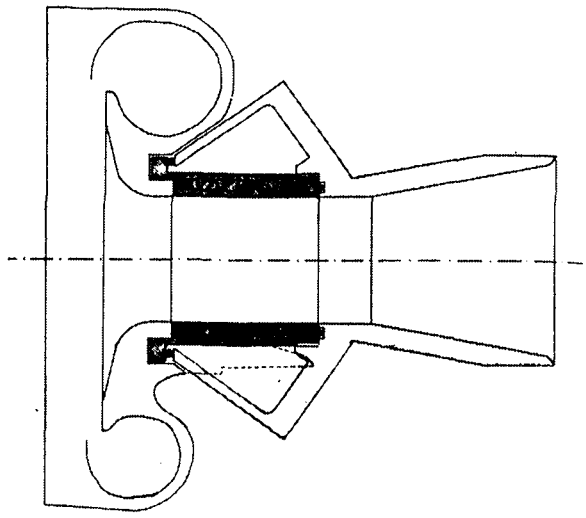

Fig. 2 Inlet casing adaptor and nozzle ring assembly

2 Distance of ejection point from compressor face (x)

3 Distance of ejection point from compressor centerline (r)

4 Jet inclination in ($x - z$) plane (θ) (positive anti-clockwise)

5 Jet inclination in x = const. plant (θ) (positive anti-clockwise)

6 Number of jets (N)

The steps in the design procedure are as follows:

1 Obtain compressor aerodynamic design and performance data.

2 Determine inlet velocity triangles along surge line and at best efficiency point. Determine required flow deflection (Assumption 1), hence required prewhirl profile.

3 Assume approximately available jet to cross flow velocity ratio (R) near surge and determine jet trajectory and growth, for different ejection angles. Find distance (x) giving required deflection at inlet. Assume ejection diameter (Dj) and check parameters of expanded jet to be within compressor inlet spatial constraints. Thus determine final, Dj, θj, x.

4 For the same initial parameters but different (R) determine off-design performance of jet.

5 Determine number of jets (N) and ejection axis (ϕ) to insure circumferential profile uniformity at inlet.

6 Check that the compressor can provide the mass flow and pressure ratio required for the total jet flow and velocity ratio at the design point.

The above procedure was applied to a small turbocharger compressor resulting in two alternative jet arrangement designs. The application is described in Appendix 1.

Compressor Performance Experiments

A series of experiments was conducted to test the performance of the compressor, using the two aerodynamic prewhirl inducing arrangements.

An adaptor was designed to fit the jet arrangement assembly to the compressor casing. The jet issuing orifices were formed in independent interchangeable "nozzle-rings". All the orifices were fed from a common scroll. The adaptor-casing assembly is shown in Fig. 2. The

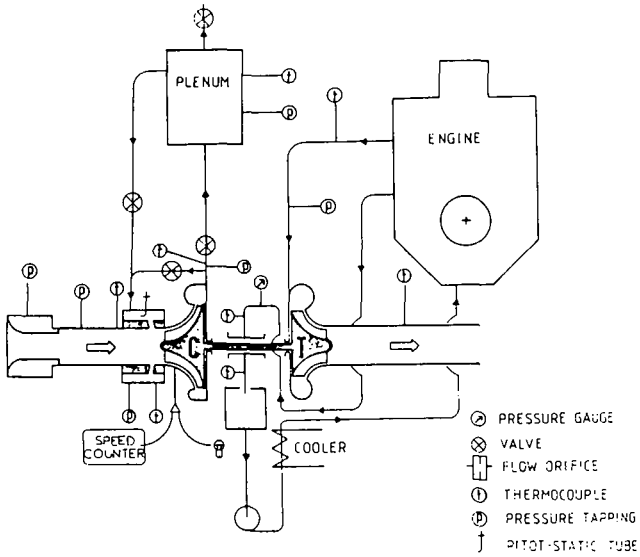

Fig. 3 Experimental rig set-up

experimental set-up is shown diagramatically in Fig. 3. A diesel engine was used as a gas generator to drive the turbocharger turbine. The turbine power could be controlled by the gas generator speed or load. The turbocharger speed was measured using an optical tachometer [2]. The jet flow was provided by recirculating compressor discharge air. The compressor mass flow was measured using two BS1042 nozzles to cover the whole flow range and the recirculation mass flow was measured using a calibrated pitot-static tube and a micromanometer. The compressor stability limits were defined using a sound level meter in front of the compressor inlet duct (see Appendix 2).

Two sets of experiments were conducted, with θ = 70 and 90 deg design jet arrangements. The testing schedule was as follows.

For a chosen compressor speed and a given back pressure valve setting, the recirculation valve was opened in pre-determined steps.

Nomenclature

C = absolute velocity
D_j = ejection orifice diameter
$\dot{m}_e$ = net compressor flow, inlet flow, cross flow or engine flow
m_j = jet flow or recirculation flow
N = rotational speed; number of jets
r_p = pressure ratio
r = distance of ejection point from compressor axis
R = ratio of jet velocity to cross flow flow velocity
U, u = peripheral velocity
x = distance of ejection point from compressor face
X, Y, Z = Cartesian co-ordinates
β = relative flow angle
η_c = compressor efficiency
η_T = system efficiency
θ = prewhirl angle, local jet trajectory angle, inclination angle
ρ = density
ϕ = inclination angle
ω = relative velocity

Table 1

Speed (rpm)	Engine Flow at Normal Surge $\dot{m}_{s_N}$ (kG/s)	Engine Flow at Inhibition Surge $\dot{m}_{s_i}$ (kG/s)	Percent Improvement in Surge margin $\left(1-\frac{m_{s_i}}{m_{s_N}}\right)*100$	Recirculation Flow (Jet Flow) $\dot{m}_j$ (kG/s)	$\dot{m}_{s_N}-\dot{m}_{s_i}$	$\frac{\dot{m}_j}{\dot{m}_{s_N}-m_{s_i}}$	Percent Contribution of Prewhirl
30000	0.00794	0.00126	84	0.00471	0.00668	0.71	29
40000	0.01137	0.00307	73	0.00656	0.00830	0.79	21
50000	0.02263	0.01403	38	0.00745	0.00860	0.87	13
60000	0.02479	0.01602	35	0.00800	0.00877	0.91	9
70000	0.03333	0.02603	34	0.00994	0.01123	0.89	11
80000	0.03391	0.02603	23	0.00494	0.00788	0.63	37
60000 Special Min. Flow Point (r_p = 1.27)	0.02479	0.00972	60	0.00757	0.01507	0.50	50

The speed was regulated, and after a settling time of five min. the readings were taken. This was repeated until a "critical condition" where the prewhirl is excessive, creating stability problems, was reached, or the recirculation valve was fully open. The back pressure was then increased in steps and the whole procedure repeated until the unstable range was entered.

The compressor stability limit without recirculation at that speed, was defined using the noise meter. Then the procedure was repeated but both the back pressure and recirculation were changed in smaller steps.

Results from the Experiments

From the two sets of experiments it was concluded that the performance of the compressor was best overall when using the $\theta = 70$ deg jet arrangement. Hence the following sections refer to that arrangement. A comparison of the two different arrangements will then follow.

Improvement in Surge Margin. (N.B., The term "surge" is adopted here as equivalent to the defined stability limit).

Shown in Fig. 4 is the projection of the (three-dimensional) "variable performance" compressor map (see Appendix 3) on the $r_p - \dot{m}_\epsilon$ plane. The net compressor flow would be the engine flow in a turbocharging application and is denoted as such in Fig. 4. The movement of the surge line to the left can be seen. The surge line on the left (with jets) corresponds to the locus of the points of minimum compressor flow achieved adjusting the jet flow, for the defined stability limit at each speed.

The percentage improvement in surge margin at any speed may be defined as:

$$\left[1-\frac{(\dot{m}_s)_i}{(\dot{m}_s)_N}\right]^{*100}$$

where $(\dot{m}_s)_i \equiv$ minimum mass flow rate with surge inhibiting device

$(\dot{m}_s)_N \equiv$ minimum mass flow rate for standard compressor

The improvement in surge margin for different speeds is shown in Table 1, column 4. The percentage of prewhirl to this improvement was found by subtracting the recirculation flow from the surge flow $(\dot{m}_s)_N$ and is shown in the final column of Table 1.

In general, fairly conservative stability limits were defined, to prevent mechanical damage. However, the compressor was brought to full surge at N = 60,000, under carefully controlled conditions, since the system was in an unstable balance, which could be destroyed by any sudden changes to the setting. The recirculation was adjusted as the net flow was decreased, to avoid reaching a critical condition.

The operating point SP is shown in Fig. 4 and the results in Table 1, row 7. A 60 percent improvement in surge margin was obtained, with prewhirl contributing 50 percent to it.

The contribution of prewhirl to the improvement in surge margin can be seen to vary for different speeds. It seems that the prewhirl

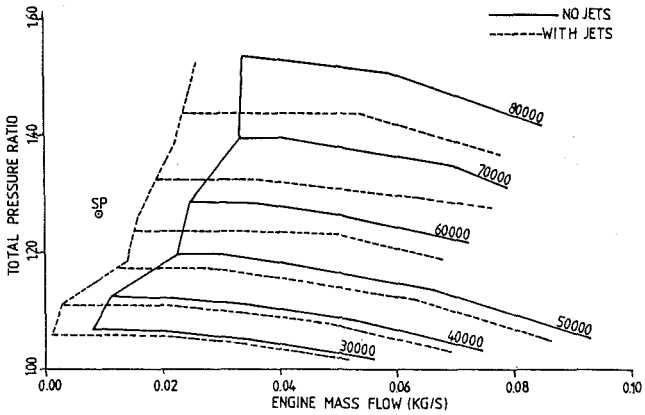

Fig. 4 Variable performance compressor map

induced by the jet arrangement becomes more effective in stabilizing the compressor as the speed drops below N = 50,000, in which case it is possible that the inducer is stabilized.

Drop in Pressure Ratio. The projection of each speed surface on the $\dot{m}_\epsilon - r_p$ plane can be seen in Fig. 4 (see also Fig. 13). As the jet flow is increased at constant speed the pressure ratio decreases. This drop in pressure ratio becomes larger at higher speeds. The net compressor flow decreased as the jet flow was increased. This throttling effect of the jets to the cross flow had also been observed in earlier experiments.

Recirculating Jet Flow. Shown in Fig. 5 are the projections of the speed surfaces on $\dot{m}_\epsilon - m_j$ planes, assembled so as to give an impression of the (three-dimensional) compressor map (axonometric) (see also Fig. 13). The dots in Fig. 5 correspond to experimental points. The solid lines joining groups of dots show the movement of the operating point when the jet flow was increased at a constant compressor delivery valve setting.

The dashed lines enclose the operating region obtained with this particular design. The left hand side of each region denotes the surge limit. (Surge surface in Fig. 13.) It can be seen that, in terms of compressor total flow, the recirculating jet mass more than compensates for the drop in net flow due to the throttling effect of the jets. It would appear then that the action of the jet increases the absolute approach velocity of the flow to the compressor, in addition to presenting "easier" inflow angles for the inducer. The latter however is reflected as a drop in discharge pressure.

Efficiencies. The compressor efficiency (η_c) contours for the different constant speed surfaces of the v.p. compressor, projected on $\dot{m}_\epsilon - \dot{m}_j$ planes are shown in Fig. 6, assembled so as to give a (three-dimensional) impression (axonometric). (See also Fig. 13.) The dashed lines enclose the operating region. It can be seen that near

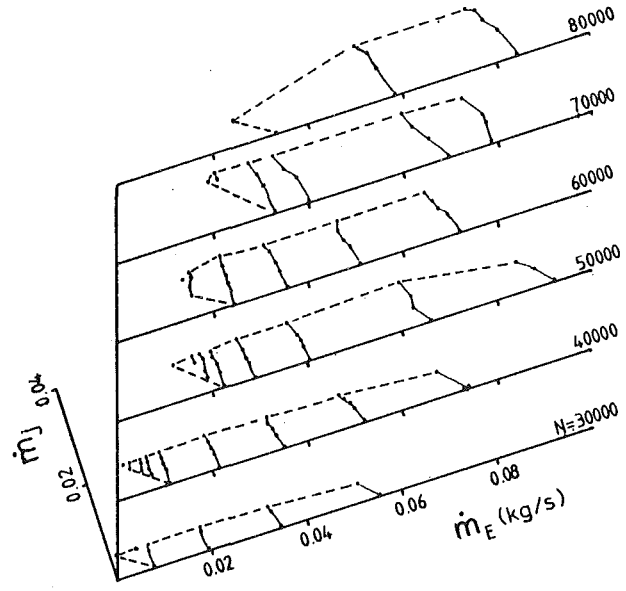

Fig. 5 Variable performance compressor map

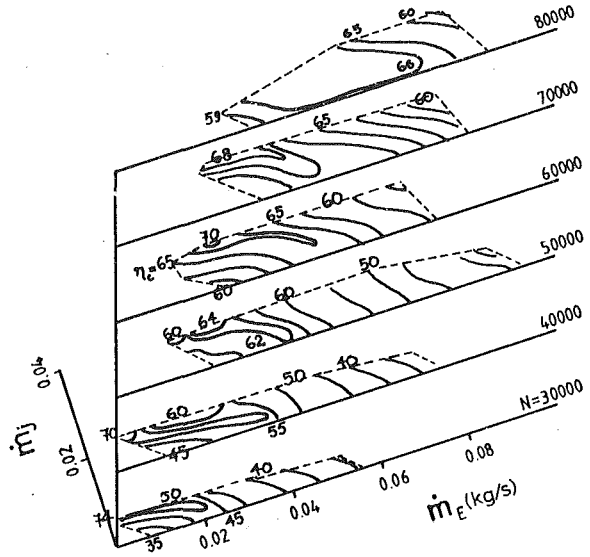

Fig. 6 Variable performance compressor efficiency contours

surge the compressor efficiency increases as the jet flow is increased.

The contours exhibit two distinct patterns. At low speeds (N = 30,000; 40,000) the maximum efficiency is where the ratio of jet flow to "engine" flow is at a maximum. A long thin high-efficiency island extends from that point towards the maximum efficiency point of the standard compressor at that speed. As the speed increases a second high efficiency region is created at higher "engine" flow, but still maximum recirculation. Eventually the first region disappears and the maximum efficiency point shifts to the second region. The efficiency islands grow in size as the speed increases.

Shown in Fig. 7 are the overall system efficiency (η_T) contours for the different constant speed surfaces of the v.p. compressor, projected on $\dot{m}_\epsilon - m_j$ planes in axonometric assembly.

As the jet flow is increased η_T is reduced, mainly because of the recirculation of hot discharge air which increases the intake temperature. There is also a possibility of inlet flow-blade mismatch under certain conditions.

Velocity Ratios. The contours of maximum available velocity ratio (R) of jet flow to cross flow ("engine" flow) are superimposed on the v.p. compressor map in Fig. 8. High velocity rates are available near the surge line ($R > 7$). In the high flow-high speed region the availability is quite low ($2.5 < R < 3.5$).

Comparison of Jet Arrangements. In Fig. 9 the performance of the θ = 70 deg jet arrangement (A70) and the θ = 90 deg jet arrangement (A90) design is compared.

The background in Fig. 9 is the A70 compressor performance map. Near the surge line the minimum values of "engine" mass flow that was achieved with the two designs, i.e., the movement of the surge line, is compared. It can be seen that the deficit of A90 increases as the speed is decreased. As the velocity ratio increases, A90 has backflow problems while A70 can tolerate much higher velocity ratios without becoming "critical". Another possible explanation for the poor performance of A90 in that region, is that the jets are situated very close to the inducer and their wakes may adversely influence impeller stability. In the high flow-high speed region, A90 performs better and the resulting drop in pressure ratio is larger. With this jet arrangement the penetration into the cross flow achieved for a certain velocity ratio is better, hence the deflection (or prewhirl) larger.

Comments on the Experiments

The experiments gave a complete (three-dimensional) v.p. compressor map for speeds up to 80,000 rpm. It was established that high velocity ratios hence high deflection (prewhirl) of the inflow are possible near the surge line. Conservative stability limits were chosen

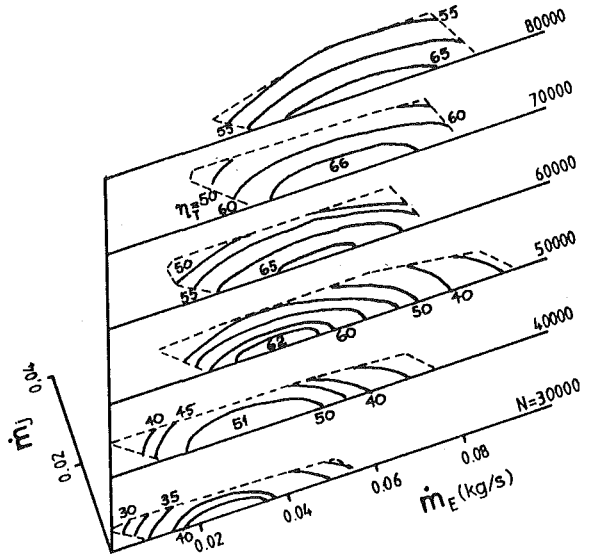

Fig. 7 Variable performance compressor system efficiency contours

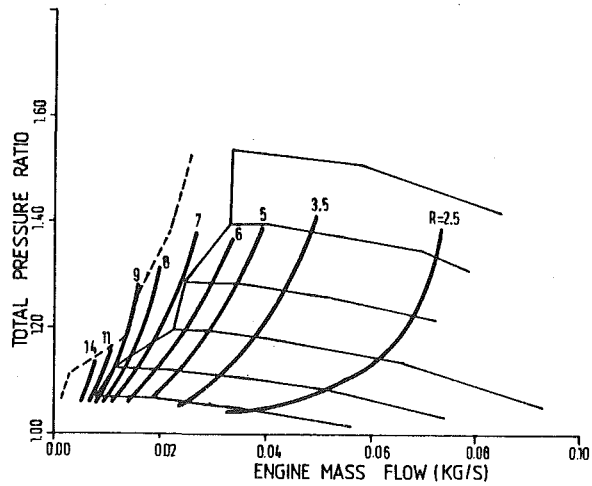

Fig. 8 Constant velocity ratio lines on compressor map

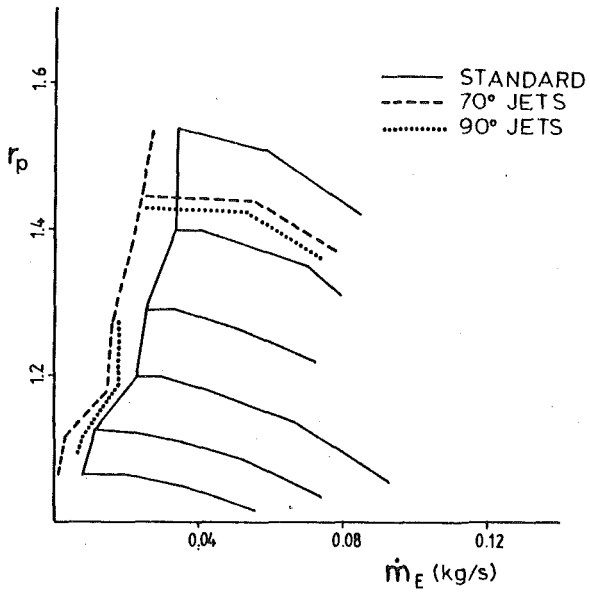

Fig. 9 Comparison of the performance of two jet designs with $\theta = 70$ and 90 deg initial ejection angle

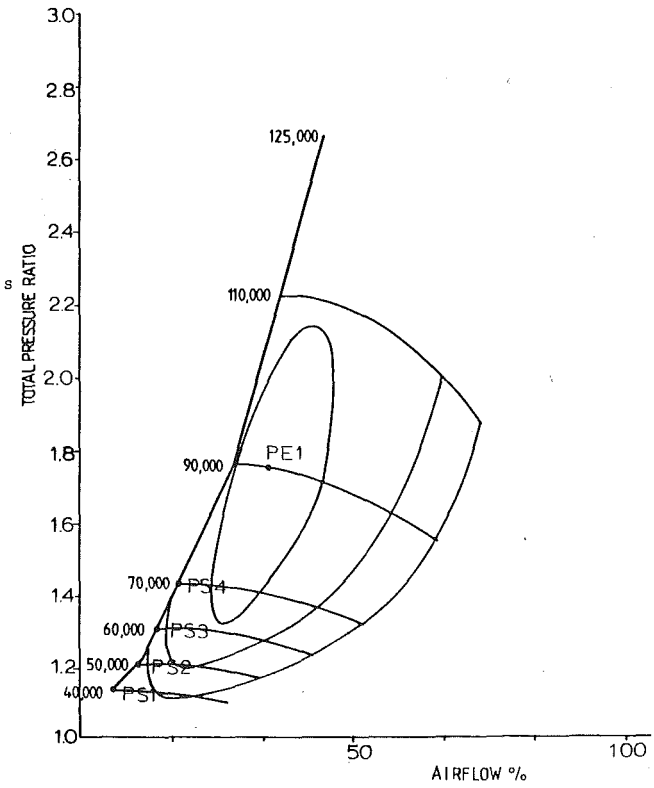

Fig. 10 Standard compressor performance map

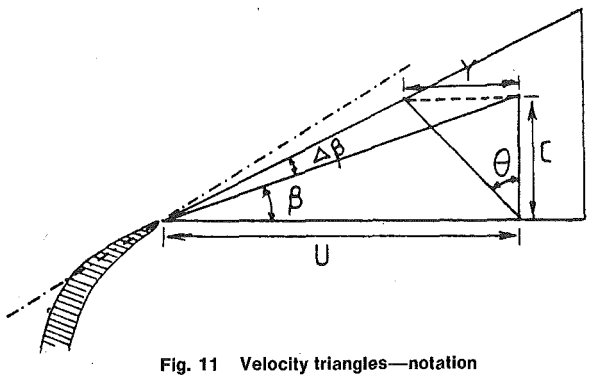

Fig. 11 Velocity triangles—notation

and all pairs of minimum stable flow, with and without recirculation, were consistent, in each case, with the definition of the noise level-stability limit relation.

It was assumed that the improvement in surge margin was due to the effects of recirculation and prewhirl only. All other factors possibly introduced by the jet arrangement and influencing the stability limit (e.g., turbulence) were not accounted for.

The contribution of prewhirl to the improvement in surge margin was generally low. The potential for better performance was however demonstrated by the special point at 60,000 rpm. The influence of prewhirl would have possibly been greater, if the compressor was designed accordingly.

The compressor efficiency was improved with recirculation. However, relatively little detail is known about the flow situation to rigorously explain the shape of the efficiency contours obtained.

Despite the low available velocity ratios at high flows, the potential for pressure drop with recirculation was satisfactory in the high flow—high speed region. Larger or more orifices would enable higher recirculation rates to be achieved at this region and thus improve the potential performance. The flow must then be appropriately regulated near the surge line to keep recirculation within acceptable limits.

Conclusions

A design procedure has been described, which allows the tailoring of an aerodynamic prewhirl-inducing jet arrangement to suit a particular compressor. The procedure uses an analytical model of the flow situation, specifically developed for this purpose. Each design is also partly based on knowledge accumulated from previous investigations. Examples of applying the procedure to design prototype prewhirl inducing devices have been described.

The investigations were based on small radial flow turbocharger compressors with relatively wide flow range and low maximum pressure ratio. High pressure ratio compressors will have larger velocity ratio (R) availability at the upper end of their range, allowing greater design flexibility. If the compressor range is affected by choking, prewhirl should be beneficial.

The device would be more successful on a compressor designed so as to benefit from prewhirl. Further, the variable prewhirl option would introduce an additional degree of freedom to an initial compressor design.

References

1 Kyrtatos, N., Watson, N., "An Aerodynamic Method for Control and Range Improvement of Rotary Compressors," To be presented, New Orleans, ASME, 1980.

2 Goulas, A., Baker, R. C., An Optical Tachometer for Turbocharger Research, International Journal of Mechanical Engineering, Vol. 5, No. 5, pp. 347–350.

APPENDIX 1

The Design

Compressor Inlet Velocity Triangles. The manufacturers' compressor performance map for the compressor is shown in Fig. 10. The velocity triangles at the compressor inlet were evaluated based on velocities calculated from mass flows from the compressor map. Velocity triangles for the points PS1, PS2, PS3, PS4 on the surge line, as well as at the point of best efficiency PE1 (reference point), were constructed using one-dimensional theory, for three positions along the inducer blade.

Referring to Fig. 11, the relation between the prewhirl angle θ required for a change $\Delta\beta$ in the relative flow angle β is as follows:

$$\frac{C}{U - Y} = \tan(\Delta\beta + \beta) \tag{1}$$

$$\frac{Y}{C} = \tan\theta \tag{2}$$

$\therefore C \tan\theta = Y$

Hence

$$\frac{C}{U - C\tan\theta} = \tan(\Delta\beta + \beta)$$

$$\therefore \frac{U}{C} - \tan\theta = \frac{1}{\tan(\Delta\beta + \beta)}$$

$$\therefore \tan\theta = \left[\frac{1}{\tan\beta} - \frac{1}{\tan(\Delta\beta + \beta)}\right]$$

$$\therefore \theta = \tan^{-1}\left[\frac{1}{\tan\beta} - \frac{1}{\tan(\Delta\beta + \beta)}\right] \quad (3)$$

Table 2

			Inducer Blade Position		
		Point	Root	Midpoint	Tip
Block 1	Relative Flow Angle β_{FL} Degrees	PS1	17.92	10.98	7.89
		PS2	24.97	15.61	11.29
		PS3	26.80	16.86	12.21
		PS4	29.00	18.40	13.37
		PE1	40.44	27.08	20.06
Block 2	Inducer Angle β_B Suction Side (SS)		52.0	39.5	33.5
	Pressure Side (PS)		66.0	49.0	36.0
Block 3	Incidence Mismatch $\Delta\beta_\eta = \beta_B - \beta_{FL}$ @ PE1	SS	11.56	12.42	13.44
		PS	25.56	21.92	15.94
Block 4	Incidence Mismatch $\Delta\beta_s = \beta_B - \beta_{FL}$ (Degrees) @ Surge Line — Suction Side	PS1	34.08	28.52	25.61
		PS2	27.03	23.89	22.21
		PS3	25.20	22.64	21.29
		PS4	23.00	21.10	20.13
	Pressure Side	PS1	48.08	38.02	28.11
		PS2	41.03	33.39	24.71
		PS3	39.20	32.14	23.79
		PS4	37.00	30.60	22.63
Block 5	Incidence Difference $\Delta\beta = \beta_{B_s} - \beta_{FL_s} + \beta_{FL_\eta} - \beta_{B_\eta}$ (Degrees)	PS1	22.52	16.10	12.17
		PS2	15.47	11.47	8.77
		PS3	13.67	10.22	7.85
		PS4	11.44	8.68	6.69
Block 6	Required Prewhirl Angle, θ (from eq. (3)) (Degrees)	PS1	62.48	72.64	77.41 ← Design Point
		PS2	44.25	58.37	66.23
		PS3	38.88	53.35	62.03
		PS4	32.24	46.40	55.75

The subscripts used:

β ≡ relative flow angle
s ≡ surge point
η ≡ best efficiency point
B ≡ blade
FL ≡ flow

The steps to determine the required prewhirl profile which would change the inlet flow incidence angles at surge to the reference angles are shown in Table 2.

Notes

Block 1 It can be seen that at points PS2, PS3, PS4, there is only a small difference in incidence especially at the blade tip.

Block 3 For the suction side there is only a small variation in the value of $\Delta\beta_\eta$.

Block 4 The values for point PS1 are quite different from those at higher speeds. At higher speeds the values vary between 2–4 deg. On the suction side, which is more critical for flow separation, surge coincides with an incidence mismatch of approximately 22.5 deg. At this incidence the inducer may be stalled. Although it is not necessary that surging is a result of inducer stall, a destabilized inducer may affect the stage stability.

Block 6 This is the required prewhirl profile to change the relative inlet flow angle from the surge angle to that of maximum efficiency. In this case equation (3) becomes

$$\theta = \tan^{-1}\left[\frac{1}{\tan\beta_{FLs}} - \frac{1}{\tan(\Delta\beta + \beta_{FLs})}\right] \quad (4)$$

where $\Delta\beta + \beta_{FLs} = \beta_{FL\eta}$ (5)

The design "target" profile was chosen at point PS2, $N = 50{,}000$, $r_p = 1.22$.

Choice of Design Velocity Ratio. In previous experimental investigations it was found that high velocity ratios were available near the surge line. These velocity ratios were in excess of 10. $R = 6$ was chosen as the design preliminary velocity ratio. Using the jet in cross-flow theoretical model a computational scanning of the region round the design point was made.

The variation of the principal parameters was:

- Velocity ratio (R). From $R = 4$ to $R = 8$.
- Initial jet ejection angle (θj). From $\theta_j = 30$ deg to $\theta_j = 150$ deg.
- Initial jet diameter (Dj). From $D_j = 0.003$ m, to $D_j = 0.004$ m.

For every point on the jet trajectory the model gives the following information:

- Cartesian coordinates of the point
- Angle of trajectory to the x-axis
- Rate of change of angle of trajectory
- Mean jet velocity
- Mean jet density
- Equivalent circular cross section radius

The Two Alternative Designs. From the results of the computational scanning, two alternative design initial ejection angles were chosen $\theta_j = 90$ deg and $\theta_j = 70$ deg. Table 3 is from the loop to determine D_j, θ_j, x, in the design procedure and shows the values of parameters for a set of initial conditions $D_j = 0.003$ m and $Z/D = 4.33$, with Z determined from the impeller dimensions. It can be seen that at the required Z/D, $\theta_j = 80$ deg gives a gradient $\theta = 58.33$ deg which is exactly the blade midpoint prewhirl angle required ($\theta = 58.37$), at the design point (see Table 2). The two design initial ejection angles were chosen on either side of $\theta_j = 80$ deg. Tables 4 and 5 show the off-design parameters for a specific θ_j and D_j at the appropriate x/D shown in Table 3.

Table 3

Velocity Ratio $R = 6$		Initial Diameter $D_j = 0.003$ m		$Z/D = 4.33$	
Ejection Angle θ_j	Trajectory Slope θ	x/D	x mm	Velocity u m.s.$^{-1}$	Equivalent Diameter $D_{eq.}$ mm
70	49.5	2.499	7.50	55.69	8.65
80	58.33	1.627	4.88	54.13	8.65
90	66.58	0.847	2.54	52.52	8.65

Table 4

θ_j = 70 deg		x/D = 2.4999			
Velocity Ratio R	z/D	z mm	Trajectory Slope θ	Velocity um.s.$^{-1}$	Equivalent Diameter $D_{eq.}$ mm
4	3.63	10.89	42.41	43.2	7.95
5	4.03	12.09	46.58	49.3	8.29
7	4.60	13.80	52.42	61.8	8.94
8	4.8	14.40	54.40	68.1	9.14

Table 5

θ_j = 90 deg		x/D = 0.847			
Velocity Ratio R	z/D	z mm	Trajectory Slope θ	Velocity um.s.$^{-1}$	Equivalent Diameter $D_{eq.}$ mm
4	3.26	9.78	60.09	41.5	6.12
5	3.80	11.40	64.10	47.34	8.12
7	4.83	14.49	68.45	57.30	9.16
8	5.26	15.78	70.28	62.01	9.62

With the 90 deg ejection angle the jets will be ejected very close to the compressor face. The ejection angle ϕ of the following jet must be chosen so that on expansion, the latter jet fills as much as possible of the low pressure region of the former jet (Fig. 12). Again because of the close proximity to the inducer, some degree of jet to jet interaction, tending to push the jets towards the wall, is expected with this design. This is aggravated further because of the presence of the centrifugal field due to the inducer and may lead to the jet's attaching to the wall because of differential entrainment. This would be undesirable as the increased friction would consume jet energy and must be avoided by suitable choice of ϕ angle.

With θ_j = 90 deg the shift of the trajectory in the z-direction for different velocity ratios R is large which means that the off-design conditions may differ considerably from the design point. However the 90 deg ejection gives the maximum jet expansion at the compressor inducer face (except from the backward ejecting jets, which may lead to flow breakdown and were not adopted). Thus the inducer annulus can be provided with a fairly uniform circumferential velocity profile, with a minimum number of jets. In this way the recirculation is minimized. Very large flow deflections are potentially available and the velocity ratio must be carefully controlled to avoid adverse flow conditions which cause the aerodynamic performance of the blades to deteriorate.

The jets with initial ejection angle θ_j = 70 deg have the advantage that the trajectory shift in the z-direction at off-design velocity ratios, is relatively smaller hence the deviation from the design point is smaller. Also, with the θ_j = 70 deg jet there is less danger of flow breakdown and backflow in the inlet pipe from excessive prerotation, because of the jet action towards the impeller. However the lower angles that are potentially available may mean that the θ_j = 70 deg jet will perform less satisfactorily at the high flow-high speed region on the compressor map where low velocity ratios would be available. The θ_j = 70 deg jet will have less opportunity to expand before reaching the inducer, so more jets are needed to avoid "patches" i.e., nonuniform circumferential velocity profile round the inducer face. More jets also mean more recirculation, which is undesirable, but the higher flow will help the arrangement performance in the high flow-high speed region on the compressor map.

Unlike the assumption in the theoretical model, the velocity profile across the section of the jet is not uniform, but would resemble a Gaussian distribution. This must also be accounted for when choosing the ϕ angle. Another factor to be considered is that the jet ejection is oblique to the cross flow. This results in one side of the jet being subjected earlier to the cross flow.

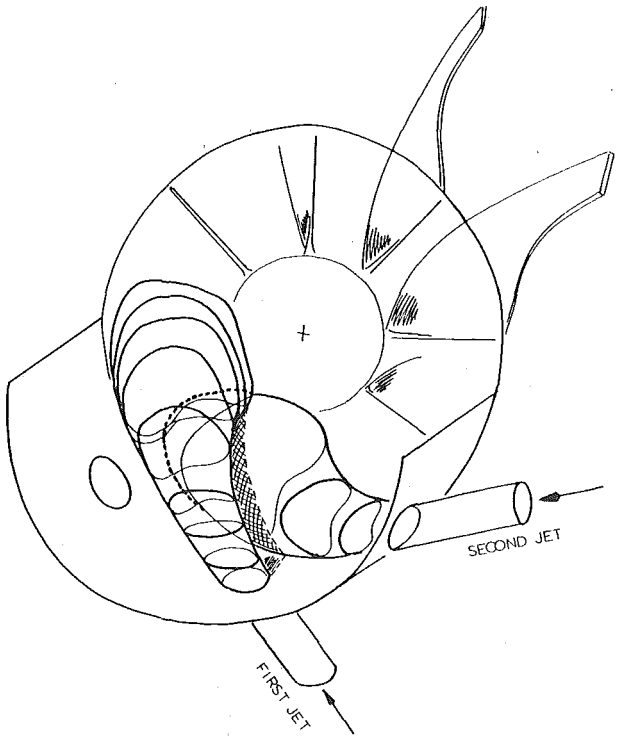

Fig. 12 Impression of flow situation (jets near compressor face)

The two final designs for the jet arrangement were:

Design 1	Design 2
N = 7 (Angular dispersion = 51.43°)	N = 8 (Angular dispersion = 45 deg)
θ_j = 90 deg	θ_j = 70 deg
D_j = 0.003 m	D_j = 0.003 m
ϕ = 35 deg	ϕ = 40 deg
x = 0.00254 m	x = 0.0075 m
Design point 1	Design point 2
z/D = 4.33	z/D = 4.33
z = 13 mm	z = 13 mm
R = 6	R = 6
x/D = 0.847	x/D = 2.5
θ = 66.58 deg	θ = 50.17 deg

APPENDIX 2

Definition of Compressor Stability Limit

A sound level meter (Bruel and Kjaer Type 2203) was used in combination with an Octave Filter Set (B & K Type 1613) to determine the stability limit. The microphone of the instrument has positioned near the entry of the compressor inlet pipe. A certain frequency band, not affected by the jet noise was chosen, and the instability initiation point was defined as a sharp increase in sound level followed by a fluctuating reading, as the flow rate reduced. This fluctuation was associated with flow pulsations characteristic of compressor instability.This sound level was taken as a threshold, and the jet flow was regulated to keep the sound level below the threshold, as the main flow was then throttled further.

APPENDIX 3

The "Variable Performance Compressor" Map

The prewhirl-inducing jet arrangement introduces a new variable in the presentation of compressor performance: the jet mass flow. The most convenient way to account for the effect of the jet flow in the compressor performance map is to introduce a third axis, the jet flow axis, while the compressor mass flow axis should preferably represent the net compressor through flow (or engine flow).

Since the jet flow can be continuously variable, the performance of the compressor will also be continuously variable and "lines" on the two-dimensional compressor performance map will become surfaces on the three-dimensional map, as shown schematically in Fig. 13. The unit was named a "variable performance compressor" (v.p. compressor).

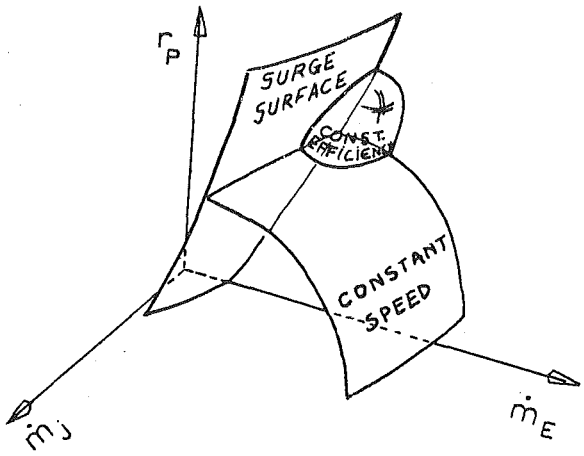

Fig. 13 The (three-dimensional) variable performance compressor map

Bottoming Gas Turbine-Electric Plant by Immiscible Liquid Cycle

B. M. Burnside
B.Sc., Ph.D., M.I. Mech.E., C. Eng.,
Senior Lecturer,
Mechanical Engineering Department,
Heriot-Watt University,
Edinburgh, U.K.

The use of the immiscible liquid binary cycle (ILBC) to recover exhaust heat from electric utility gas turbine plant is described. In simple dual pressure plant without L.P. turbine admission, increase in specific work output compared with the steam cycle and its variation with condenser pressure, turbine efficiency and exhaust gas temperature is presented. The penalty of larger condenser surfaces is quantified. A dual pressure steam—ILBC cycle with L.P. turbine admission, which should improve on the corresponding steam cycle, is proposed.

Introduction

Moral and economic opinion today dictate more efficient use of fuels. A particular responsibility rests on manufacturers and users of prime movers, not least gas turbine electric utility manufacturers, who consume high quality fuel. Modern electric utilities powered by vapor power cycle-bottomed gas turbines are the sophisticated result of the ingenuity of the manufacturers in discharging this responsibility. In today's climate of rising fuel costs every scheme which promises an increase in efficiency must be examined.

There is no doubt that it is possible to design sophisticated steam bottoming plant which can extract a maximum amount of heat from the gas turbine exhaust. The "exhaust-fired-boiler cycle" [1] is an example of a suitable plant cycle. It is a fully integrated combined cycle whose steam part is similar to conventional steam power plant with high boiler pressure, a chain of feed-heaters and a requirement for very low feedwater oxygen levels. There is, however, a market for combined plant with much simpler and cheaper steam part [2], and which operates at lower steam temperatures and pressures which require simple deaeration only.

Between these extremes there is a grey area in which the competing factors—specific fuel consumption, capital cost, load variation, availability of skilled operators, accessibility for service—have an influence on an acceptable degree of complication in the bottoming plant. The object of this paper is to present and analyse a means of increasing the efficiency of simple bottoming plant by using the immiscible liquid binary cycle (ILBC) [3, 4].

Background

The principle that organic vapor power cycle working fluids with higher molecular weight than steam, because of their low latent heats and liquid specific heats, match gas turbine exhaust heat loads better than steam in simple cycles, is well established. The analysis of organic fluid bottoming plant for gas turbines [5] indicates some major advantages, Table 1, over steam plant.

It is not always possible to find a working fluid which permits all of these advantages simultaneously and there are many attendant disadvantages which are critical in large plant, Table 2.

For manufacturers of gas turbine electric utilities these problems seem to have ruled out further consideration of organic cycle bottoming.

The question then arises—is it possible to find a design compromise which permits the advantages of the organic cycle and of the steam cycle to be obtained simultaneously? If the working fluid is a mixture of steam and an organic vapor which are immiscible in the liquid phase then this compromise can be achieved at least in part.

(a) Sealing problems are eliminated because steam and water can be used in all external rotating seals. The thermodynamically correct composition can be restored after condensation where the liquids can be separated readily.

(b) The heat transfer characteristics of the binary fluid should lie between the high water and low organic values. Heat exchangers—particularly the condenser, while larger than the steam units can be smaller than the organic ones.

(c) Use can be made of very stable organic fluids which on their own have unsuitable thermodynamic properties—e.g., alkanes and perfluorocarbons.

(d) Control can be exercised over the slope of the T-s saturated vapor line to provide a dry more efficient expansion than in the steam turbine, Fig. 1.

The Immiscible Binary Cycle

Liquid-Vapor Equilibrium. Immiscible liquids form a heterogeneous azeotrope, Fig. 2. When the mixed vapor is cooled three types of behavior are observed on the dew line.

Table 1 Advantages of organic cycle bottoming

Choice of condenser pressure
Volume flow rate to optimise turbine design
Dry expansion in turbine without necessity for regeneration
Superior matching to cooling gas heat loads resulting in higher heat recovery and cycle efficiencies.

Table 2 Disadvantages of pure organic cycles

Fluid instability
Corrosion problems
Shaft sealing problems
Large heat exchangers
Unfamiliarity

Contributed by the Gas Turbine Division and presented at the Gas Turbine Conference and Products Show, New Orleans, La., March 10–13, 1980 of THE AMERICAN SOCIETY OF MECHANICAL ENGINEERS. Manuscript received at ASME Headquarters December 7, 1979. Paper No. 80-GT-24.

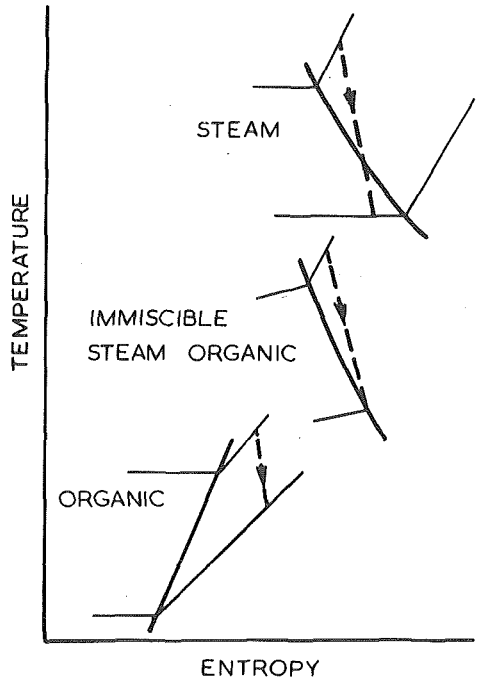

Fig. 1 Expansions relative to dew lines

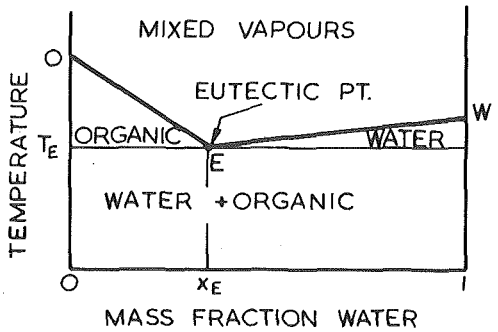

Fig. 2 Vapor-liquid equilibrium of binary immiscible liquids—constant pressure

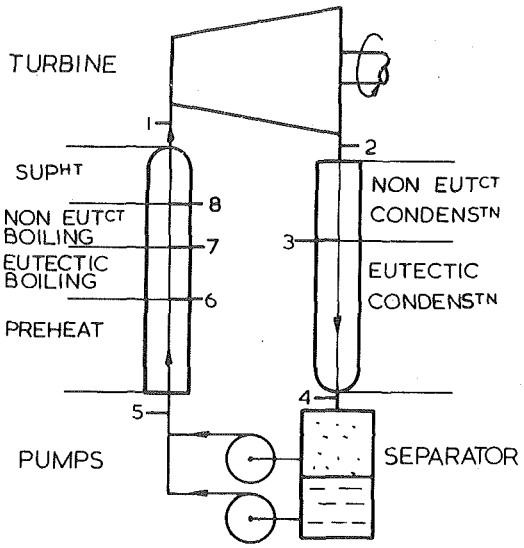

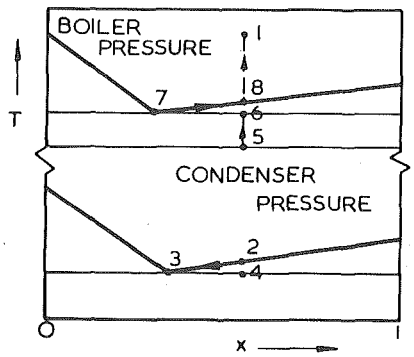

Fig. 3 ILBC plant and *T-x* diagram

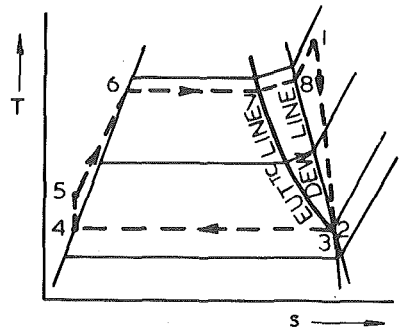

Fig. 4 *T-s* diagram for the ILBC

(a) $x = x_E$ the eutectic point. The vapor condenses to liquid of the same composition at T_E.

(b) $x > x_E$ water only condenses at the dew point. On further cooling the temperature decreases with x until $x = x_E$ at T_E, then as (a).

(c) $x < x_E$ organic only condenses until $x = x_E$ at T_E, then as (a).

On heating, the liquids evaporate at T_E producing vapor of the eutectic composition x_E until one of the liquids disappears. The other then evaporates at increasing temperature, the composition following the dew line until all the liquid disappears at the initial composition of the liquid. The equations required to determine the locus of the dew lines *WE*, *OE* and the eutectic point *E* have been developed [3].

The Cycle. The simple ILBC plant is shown in Fig. 3 together with *T-x* diagrams at boiler and condenser pressures. The cycle thermodynamics has been explained [3, 4].

Figure 4 shows the *T-s* diagram for the cycle. The *T-s* diagram shown is the "optimum" one in the sense that eutectic and dew points are coincident at the condenser pressure and simultaneously the dew line has negative slope which permits a dry turbine expansion terminating on the dew line. It has been shown [4], that this condition is satisfied only when low volatility, i.e., high normal boiling point, organics are used.

Nomenclature

A = area, m^2
h = film coefficient of heat transfer, kW/m^2-K
Q_r = heat rejected, kJ
s = specific entropy, kJ/kg-K
T = temperature, K
t = temperature, °C
W = specific work output, kJ/kg gas
x = mass fraction
η_T = turbine isentropic efficiency

Subscripts

BM = binary mixture
C = condenser
E = eutectic
G = gas
s = steam
w = water

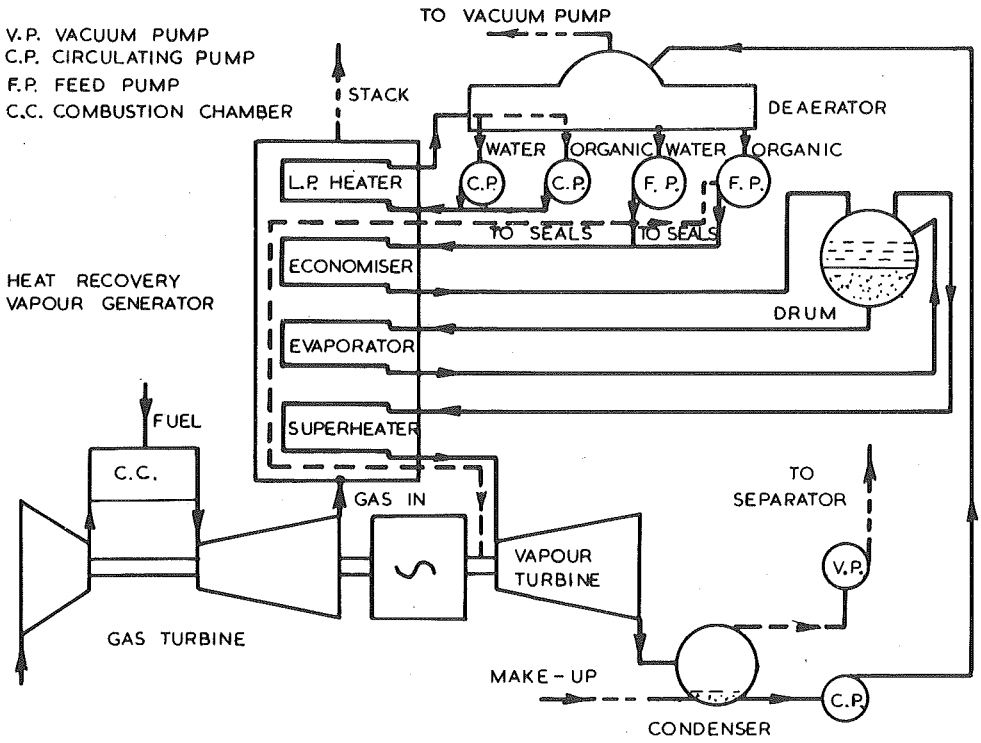

Fig. 5 Simple dual pressure ILBC heat recovery

Choice of Organic Fluid. The organic must be stable in the presence of water and normal plant materials. Perfluorocarbons and the alkanes are in this category although the former are very expensive at present. The thermodynamic restriction mentioned above restricts normal boiling point to the range 100–150°C—the compounds perfluorodecalin and perfluoromethyldecalin, in the perfluorocarbon series, and *n*-octane, *n*-nonane and *n*-decane, of the alkanes, [6], have suitable boiling points. Before using perfluorocarbons, extensive realistic degradation and corrosion tests in the presence of plant materials and small concentrations of air will be necessary. Although the C—F bond is strong there must be some fear of degradation which could lead to catastrophic corrosion in the plant. Tests conducted by the author, [7], however, have indicated no such breakdown.

The alkanes are much more promising. There is extensive experience of handling them in process plants and although they are inflammable the risk is considerably less than experienced daily in oil refineries and petrol stations.The alkane is contained with water and in the heat recovery boiler, where most danger lies, any leak is diluted by such large quantities of exhaust gases that risk of explosion is remote.

Gas Turbine Exhaust Heat Recovery

Simple Bottoming Plant—ILBC versus Steam. Analysis of the performance of ILBC and steam bottomers for gas turbine plant exhausting at 513 and 350°C, has shown significant advantage to the ILBC plant, [8], particularly at the lower exhaust temperature. The simple case of dual pressure operation, with the L.P. fluid used only for deaeration, was examined. The maximum steam temperature was assumed to be 400°C and of the binary vapor, 350°C. The ILBC bottomed plant is shown in Fig. 5.

The corresponding steam cycle plant has one circulating and one feed pump only and an L.P. boiler replaces the L.P. heater. Matching diagrams of the bottoming cycles are compared in Fig. 6. The following features of the comparison are noteworthy.

(a) Because the ILBC can reduce, the gas temperature to near 110°C the L.P. section of the vapor generator becomes a liquid heater. For low temperature gas turbine exhaust, 350°C, stack temperature is higher and an L.P. boiler is possible.

(b) Apart from (a) not much increase in ILBC heat recovery generator transfer area is envisaged. Heat transfer in the unit is gas side controlled except possibly in the superheater where the temperature difference is 50K higher than in the steam cycle.

(c) Based on the channeling flow theory of condensation the reduction in condensation heat transfer coefficient predicts a condenser tube surface considerably larger than the steam condenser.

(d) If the turbine is of conventional design with the same exhaust Mach number as the steam turbine the exhaust area of the octane/steam turbine is the same as the steam turbine and the area may be increased by increasing the molecular weight of the organic. This will be an advantage in moderate sized plants because the turbine efficiency increases with volume flow, [9].

(e) Very little complication of the plant is involved. Two feed and circulating pumps are necessary instead of one, the flow paths of sealing steam are complicated and a circulator in the evaporator section is required to maintain noneutectic flow.

(f) The prediction that the ILBC combines some of the best features of pure organic and steam cycles is correct.

(g) The performance comparisons made above refer to the optimized cycles in each case, in particular to the optimum boiler pressure. At the higher gas inlet temperatures, however, due to uncertainty about the properties of the binary at pressures near the critical pressure of the organic, boiler pressure has been set below the optimum, [Fig. 6]. Higher ILBC efficiencies are therefore possible when more information on binary properties is available.

Effect of Change in Cycle Conditions. The effect on the comparison between steam and ILBC plants of changes in condenser temperature, turbine efficiency and gas turbine exhaust temperature are now examined. The discussion, based on calculations for the binary *n*-octane/water is general. Table 3 shows the basis of the comparison. In all the binary cycles considered the tubine expansion terminates on the dew line.

Condensing Temperature. The variation of specific work output difference between the cycles is plotted in Fig. 7 as a function of condensing eutectic temperature, t_c. t_c has little effect on the comparison except at low gas inlet temperature where ILBC efficiency is reduced disproportionately at high condenser temperature. It is worth noting that at the low gas inlet temperatures the optimum ILBC output is obtained with very little superheat whereas, because of

moisture corrections, the steam cycle requires the maximum superheat.

The effect of t_c on condensing surface area is shown in Fig. 8. As a first approximation the condensing surface area ratio was based on the heat transfer resistance from the vapor-liquid interface to cooling water only. No account was taken of the positive effects of vapor shear and splashing or of the negative effect of diffusion in the binary vapor. On the vapor side the Nusselt film coefficient was used for steam condensation and a volume weighted channeling flow theory, [10], coefficient for the binary mixture. The ratio of the pure component film coefficients, h_s/h_{oct}, was assumed constant (6:1 for water:octane), independent of film temperature difference. Assuming that the condensers are designed with equal condensing and cooling water side film coefficients these assumptions lead to the expression for relative condensing areas.

$$\frac{A_{BM}}{A_s} = \frac{1 + h_w/h_{BM}}{1 + h_w/h_s} \cdot \frac{Q_{RBM}}{Q_{Rs}}$$

where (Q_{RBM}/Q_{Rs}) is the ratio of heats rejected by the cycles. The disproportionate rise with t_c of A_{BM} at 300°C gas inlet temperature is a result of the lower ILBC cycle efficiency already mentioned. Fig. 8 sets out deliberately to show the ILBC condensing requirements in their worst light in order to emphasize the penalty paid for higher output. This penalty is severe at low gas temperatures both because the optimum plant output is so much greater than the steam plant and because the optimum ILBC, while extracting more heat from the gas, rejects much more heat to the condenser. A trade-off between ILBC output and condenser surface area is obviously possible. For example at t_G = 400°C, t_c = 50°C the optimum boiler pressure and temperature are 19.2 bar and 190°C giving specific work of 65 kJ/kg gas. An increase of pressure and temperature to 24 bar, 225°C reduces the specific work to only 63 kJ/kg gas, still 11 percent higher than the optimum steam cycle, but the condenser area is reduced by over 20 percent. The stack temperature in this cycle is 140°C compared with 110°C in the optimum cycle. Thus in the optimum cycle a small gain in overall efficiency requires a large increase in heat extraction from the gas most of which is rejected in the condenser.

There is another sense in which Fig. 8 shows the ILBC to least advantage. The eutectic mass fraction of water in the water/octane binary is lower than that in the water/nonane binary, 20 and 43 percent, respectively [8]. Thus the average water content by volume of the latter is higher and its condensing surface area lower. In fact calculation shows that a change to the water/nonane binary can produce the same 20 percent saving in condensing surface in the example above without significant loss in output. Here the "trade-off" is between condensing surface area and turbine volume flow. Except for very large turbines, however, the increase in volume flow which accompanies decrease in condensing surface requirement should be an advantage.

Turbine Efficiency. The advantage in output of the ILBC over steam is enhanced slightly at high gas inlet temperature by increase in turbine efficiency but reduced at low ones, Fig. 9.

The enhancement is caused by relative reduction in steam turbine efficiency due to increased wetness corrections. At low gas temperature this effect is offset by reduction in ILBC efficiency.

Care should be exercized in interpreting Fig. 9. The turbine overall efficiency, η_T(DRY), is the actual turbine isentropic efficiency when referring to the ILBC turbine where the vapor is always dry but is the hypothetical "dry" efficiency of the steam turbine without wetness corrections. In comparing the cycles it is assumed that the binary vapor turbine efficiency is equal to the dry efficiency of the steam turbine and the former is assumed to be of conventional design with similar stage loading and compressibility effects. Because of the

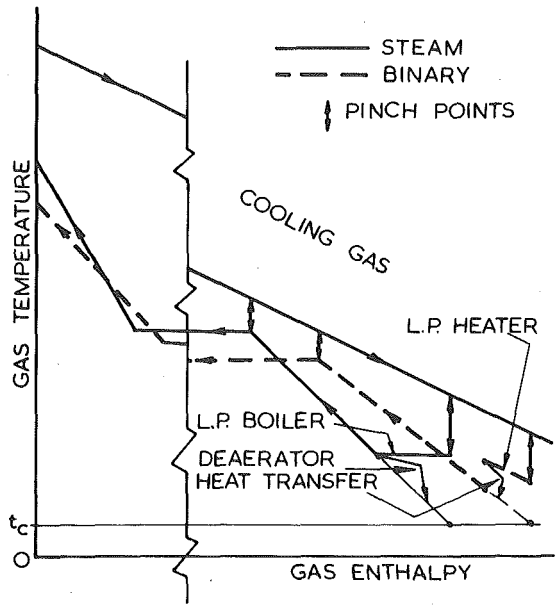

Fig. 6 Matching of bottoming cycles to exhaust gas

Table 3 Basis of ILBC versus steam cycle comparison

Gas inlet temp., °C	500	400	300
Minimum gas outlet temp., °C	110	110	110
Available gas enthalpy, kJ/kg	408	304	199
Pump efficiency	0.70	0.70	0.70
Pinch point temp. diff., K	30	30	30
Maximum cycle temp., °C	400	350	250

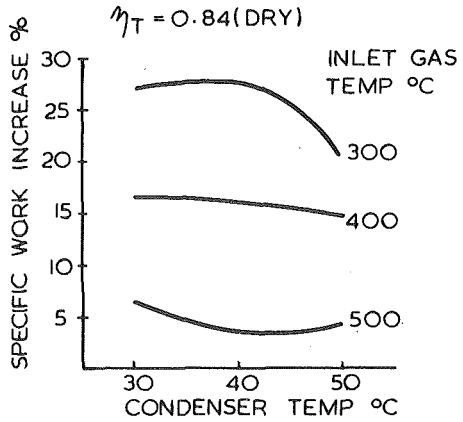

Fig. 7 Improvement in specific work (ILBC-steam)/steam as a function of t_c—octane/steam binary

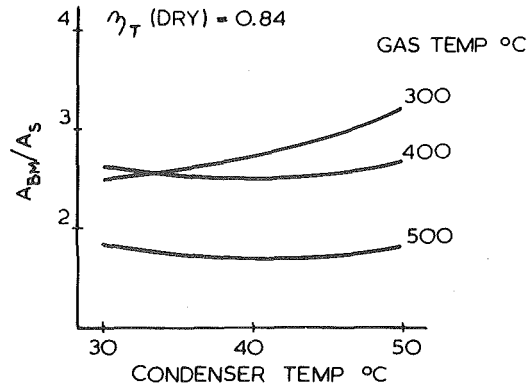

Fig. 8 Ratio of condensing surfaces A_{BM}/A_s as a function of t_c—octane/steam binary

generally larger flow area of the binary vapor turbine and because of certain changes in the turbine design which may be possible due to a novel method of handling part-load conditions in the ILBC which will be referred to below, there is reason to believe that this is a conservative assumption.

The details of the wetness correction method applied are set out in reference [11]. A Baumann correction of 1 percent reduction in stage efficiency was made for each 1 percent average wetness in a stage. No allowance was made for utilizing increased reheat by separa- moisture since the losses incurred, [12], may be self-defeating and the plant complicated unnecessarily.

Gas Temperatures. Figure 7 shows a rapidly decreasing difference between steam and ILBC plant as gas inlet temperature rises. Clearly there is a point at which the ILBC cycle can no longer compete with the steam cycle in the dual pressure-H.P. only admission cycle. At present it is not possible to say at what level of gas inlet temperature this transition should occur because lack of knowledge of the binary properties at high pressure confines calculations to boiler pressures below the optimum.

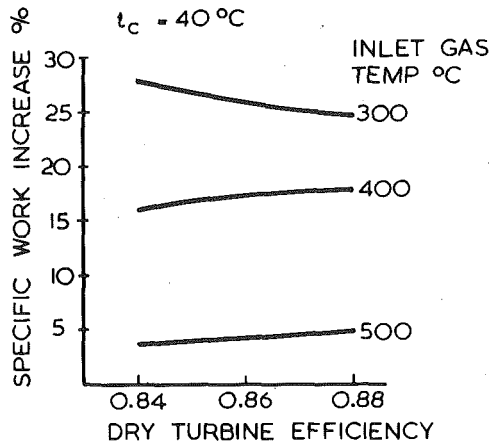

Fig. 9 Improvement in specific work (ILBC-steam)/steam as a function of η_T-octane steam binary

The Dual Pressure Cycle

Gas turbine exhaust temperatures of 510°C are common in electric utility plant and higher temperatures are likely as top temperatures are raised to improve efficiency. Further, there is increasing pressure to reduce stack temperatures below the dew point where premium fuels are used. This extension of the range of heating gas temperatures and a rising ratio of fuel:capital cost has dictated the increased plant complication of the dual pressure cycle with L.P. steam admission to the turbine and higher steam conditions. The question therefore arises—is the ILBC relevant to gas turbine electric utilities under these conditions?

In principle there is no reason why not. It has been established that the ILBC has higher output than the steam plant when fired by low temperature gas. Therefore if a means can be devised of using the ILBC as the L.P. stage and the steam cycle as the H.P. stage of a dual pressure plant, improved performance may be possible. A suggested arrangement is shown in Fig. 10. A typical dual pressure steam cycle with condenser deaeration is modified by placing a separator unit between L.P. drum and H.P. economizer. The ILBC circuit is similar to the arrangement in Fig. 5. Control over the proportion of organic in the L.P. vapor mixture allows dry expansion in the L.P. turbine stages. A number of other possible variations in plant layout are possible.

Concluding Remarks

It has been established in principle that the ILBC offers gains in specific work output/kg of gas turbine exhaust in simple cycles. Gains are highest when exhaust temperature is lowest and the gas turbine cycle with one stage of regeneration bottomed by the ILBC should be a strong combination in maximizing overall efficiency. The penalty is a large increase in condensing surface. Although a detailed analysis has yet to be made it seems likely that the dual pressure steam—ILBC

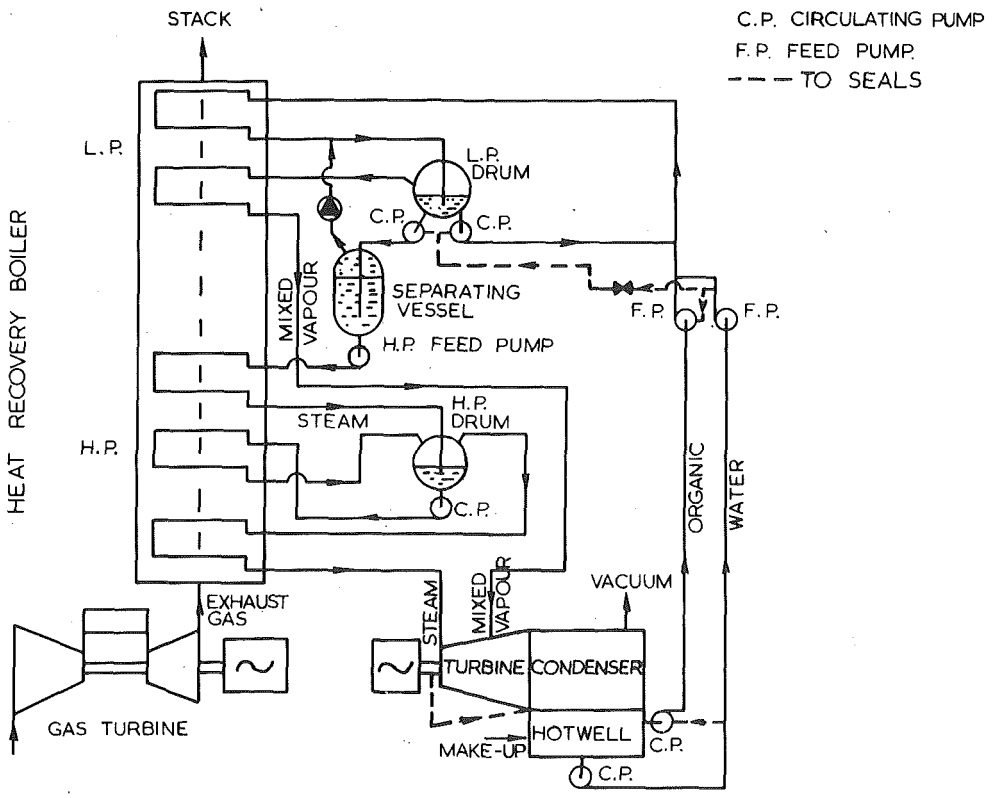

Fig. 10 Dual pressure steam—ILBC cycle

plant with L.P. turbine admission will show an improvement in specific work output compared with the all-steam version currently in use. Detailed design studies by the manufacturers must resolve these issues.

ILBC plants offer some interesting possibilities in turbine design. It has been shown that the absence of moisture corrections in the ILBC turbine is a big factor in the higher output of the cycle. Another advantageous feature is the flexibility offered by the possibility of varying binary composition in matching the turbine to part load operation. By increasing the proportion of organic in the mixture the overall enthalpy drop is reduced and the turbine inlet area may be kept high maintaining high efficiency while the power output is reduced. This change in fluid composition will result in superheated turbine exhaust conditions since the slope of the T-s dew line becomes positive, Fig. 1. An important factor in using this method of part load operation is the balance between the smaller heat rejection required to the condenser and the decrease in heat transfer/unit area of the condensing surface.

References

1 Bartlett, R. L., *Steam Turbine Performance and Economics,* McGraw-Hill, New York, 1958, p. 211.

2 Coats, R., "The Efficient Use of Gas Turbines for Electricity Production," *Institute Engineers and Shipbuilders in Scotland,* Paper No. 1405, Jan. 1977.

3 Burnside, B. M., "The Immiscible Liquid Binary Rankine Cycle," *Journal of Mechanical Engineering Science,* Vol. 18, No. 2, 1976, pp. 79–86.

4 Burnside, B. M., "Research Note: Temperature—Entropy Diagrams of the Immiscible Liquid Binary Cycle", *Journal of Mechanical Engineering Science,* Vol. 19, No. 3, 1977, pp. 131–132.

5 Bindon, J. P. and Carmichael, A. D., "A Preliminary Assessment of the Combined Gas Turbine and Vapour Turbine Engine," *Journal Institute Fuel,* Vol. 41, 1968, pp. 28–36.

6 Burnside, B. M., "Immiscible Liquid Binary Cycle with Aqueous Binary Working Fluids in the n-saturated Aliphatic Hydrocarbon Homologous Series," Report No. 4 on S.R.C. grant B/RG/23530, Aug. 1976, Dept. Mech. Eng., Heriot-Watt University, U.K.

7 Burnside, B. M., "Final Perfluorocarbon-Water Degradation Tests," Report No. 4, ibid., Nov. 1976.

8 Burnside, B. M., "Gas Turbine Exhaust Heat Recovery by using the Immiscible Liquid Binary Cycle," *La Termotecnica,* Vol. 33, No. 1, 1979, pp. 11–19.

9 Hegetschweiler, H. and Bartlett, R. L., "Predicting Performance of Large Steam Turbine-Generator Units for Central Stations," *Trans. ASME,* Vol. 79, No. 5, 1957, pp. 1085–1114.

10 Bernhardt, S. H., Sheridan, J. J. and Westwater, J. W., "Condensation of Immiscible Mixtures," *AIChE Symposium Series,* Vol. 68, No. 118, 1971, pp. 21–37.

11 Burnside, B. M., "A Professional Exercise in Applied Thermodynamics," IJMEE, Vol. 8, No. 1, 1980.

12 Beldecos, N. A. and Smith, A. K., "Comparative Performance of Turbine-Generator Units in Saturated—Steam Cycles," ASME, Paper No. 54-SA-65, 1954.

H. Hempel
R. Friedrich
S. Wittig

University of Karlsruhe,
Institute of Thermal Turbomachinery,
West Germany

Full Coverage Film-Cooled Blading in High Temperature Gas Turbines: Cooling Effectiveness, Profile Loss and Thermal Efficiency

Extending data obtained from hot gas cascade measurements on the cooling effectiveness and profile loss coefficients of full coverage film-cooled blading, use is made of similarity considerations to determine the heat transfer characteristics under actual engine conditions. Of primary interest are stationary gas turbines. Calculations are made for a four-stage single shaft gas turbine with air preheat and common component efficiencies. As a representative result it is found that for a pressure ratio of $\pi = 10$ a relative cooling air flow of approximately 8 percent will be required in rising the temperature from 1173 to 1573 K. The resulting relative improvement of the thermal efficiency is 24 percent and that of the specific work about 70 percent.

Introduction

In recent years, attention increasingly has been directed towards high temperature gas turbine technology in jet aircraft engine propulsion as well as in stationary power plants. Various new programs have been initiated in the U.S. and in Europe for rising the turbine inlet temperature up to approximately 1800 K. Modified air cooling techniques and water-cooled turbines, therefore, are presently under intensive study [1].

The present investigation is concerned with relatively far-advanced air cooling techniques. A qualitative comparison of the effectiveness of various air cooling methods reveals the strong dependence of the cooling effectiveness $\eta_{bl,cr}$ on the coolant mass fraction especially for low cooling air flow rates [2]. While the data for convection, impingement and film cooling are relatively well established, information on transpiration cooling and its modifications such as effusion or full coverage film cooling is scarce. In a preceding study [3, 4] we were able to demonstrate considerable improvement of $\eta_{bl,cr}$ by full coverage film cooling of blades which were equipped with arrays of holes inclined 30 deg to the surface tangent.

The present study and analysis of overall thermal efficiencies is based on these measurements.

Experimental Apparatus

The hot gas tunnel used for the experiments has been described in detail by Hempel [4]. The test section of 200 mm width and 100 mm height holds a four channel—i.e. three blades-cascade with 50 mm spacing. The center blade is full coverage film-cooled and made of CrNi-alloy. The material of the two other blades is Nimonic 80 A.

The experiments were performed at main inlet flow Mach numbers of 0.18 and 0.26, gas temperatures of 673 K and 823 K and at a pressure of approximately 1.1 bar. The relatively modest temperature level was chosen to protect the instrumented blades and to assure sufficient measurement accuracy. The sequence of measurements was controlled by a mini-computer which also was used for on-line processing of the data and printing of the results.

The cross-sectional view of one of the test blades (blade No. 2) is shown in Fig. 1. The core profile of 100 mm height, 61 mm chord and inlet and exit angle of 90 deg and 36 deg, respectively, is equipped with cooling passages. The center body is covered with a perforated, blade shaped sheet metal "jacket" of 0.3 mm thickness welded by an electron welding procedure to the core. Perforation of the blade jacket was achieved by electron beam drilling.

In selecting the hole distribution over the blade's surface the following criteria were considered: Czaja [5] in preliminary cold flow experiments with a blade made of plastics but with identical dimensions found a drastic reduction of the profile loss when the holes were inclined to the surface's tangent. An angle of 30 deg was desirable which could be obtained with an electron beam without beam reflection. The lowest achievable hole diameter in this case is 0.2 mm.

Holes with 30 deg inclination cannot be realized at the blade's leading edge. The angles in this region amount to 90 or 60 deg, respectively.

Goldstein, Liess and Metzger [6–8] found the cooling to be effective over a jet width of 3 d (d = hole diameter) for flat plate flow. A downstream effect was observed up to 40 d. The hole distribution was selected in accordance with these considerations.

Two blades with slightly different characteristics were investigated. Blade No. 1 was equipped with 14 cooling passages. The spacing at the leading and at the trailing edges was 1.4 mm, with 2 mm over the rest of the blade's surface with a stagger of one half and one third spacing respectively.

Contributed by the Gas Turbine Division and presented at the Gas Turbine Conference and Products Show, New Orleans, La., March 10–13, 1980 of THE AMERICAN SOCIETY OF MECHANICAL ENGINEERS. Manuscript received at ASME Headquarters December 10, 1979. Paper No. 80-GT-37.

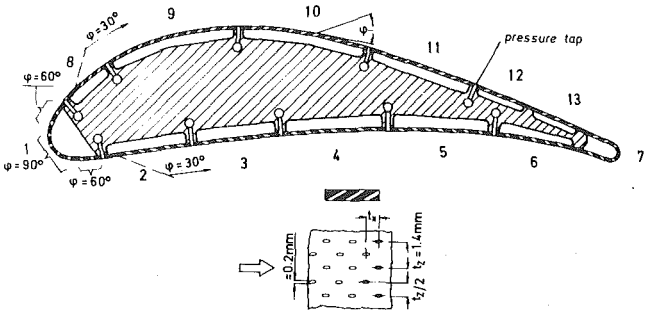

channel	Nr.	1	2	3	4	5	6	7	8	9	10	11	12	13
surface $b_c \cdot l$	10^2 mm^2	9.25	8.45	8.20	9.85	9.95	7.10	8.00	5.05	13.4	13.2	11.0	4.85	4.85
t_z	mm	1.4	1.4	1.3	1.4	1.4	1.4	1.3	1.2	1.3	1.3	1.3	1.5	1.5

Fig. 1 Cross-section of blade No. 2

Blade No. 2 (Fig. 1) was equipped with 13 cooling passages. The spacing was 1.4 mm over the blade's surface with a stagger of one half spacing. Fifteen thermocouples were used in the mean section, and five at both the root and tip of the blade for determination of the surface temperature. In addition, there were five thermocouples at both the root and the tip of the blade for measuring the main body temperature and 13 thermocouples in the air supply tubes to measure the temperature of the entering cooling air.

The pressure distribution was determined with pressure taps around the profile's mean section. The axial holes leading to the pressure taps were drilled by means of spark erosion. The surface temperature was determined with shielded miniature thermocouples of 0.25 mm in diameter, which are welded by means of a laser-beam to the blade's surface.

At constant main flow Mach numbers and gas temperatures the following parameters were recorded:

- The state in front of the cascade by means of a three hole pressure probe and a temperature probe.
- The blowing rate distribution necessary for constant wall temperature at different coolant flow rates. Reference plane is the mean hight blade section.
- The pressure distribution around the profile's mean section.
- The wake structure and total pressure variation to determine the profile losses.

The amount of cooling air supplied to each blade cooling passage was independently adjusted and measured by means of calibrated orifice meters.

Blade and Cooling Air Temperatures, Cooling Effectiveness and Profile Loss Coefficients

The cooling air temperature at the root and the surface temperature at the mean blade section are shown in Fig. 2 for test blade No. 2 as a function of the relative coolant flow rate with hot gas temperature and Mach number as determining parameters. The air flow rate in the cooling channels was controlled such that the blade temperature around the profile was constant within ±1.5 K.

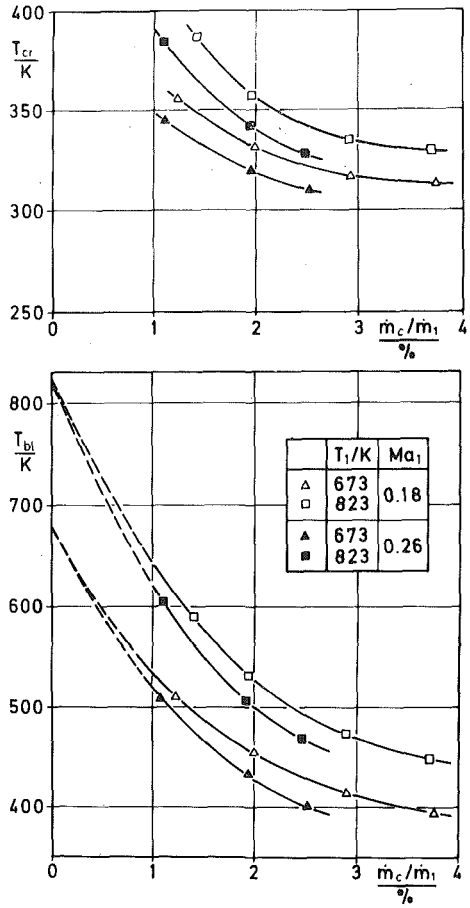

Fig. 2 Coolant and blade surface temperature (blade No. 2)

From Fig. 2 it is obvious, that the surface temperature initially is decreasing fairly rapidly with increasing relative coolant flow. At blowing rates exceeding 3 percent, however, the influence is reduced. A similar effect is observed with the cooling air entrance temperature, as the upstream effects become of minor importance at higher coolant flow rates. It should be noted that the temperature decrease was more pronounced with blade No. 2 than with blade No. 1.

In addition to the surface (jacket) temperature an attempt was made to determine the temperature of the main blade body.

Fig. 3 illustrates the temperature change along the blade. It can be seen that at the blade's tip the "body" temperature is considerable higher than the surface temperature. This is due to heat transferred from the outer wall which is unperforated to the blade and should be

Nomenclature

a_N = specific work, KJ/kg
b_c = width of cooling channels, m
c = gas velocity, m/s
c_p = specific heat of hot gas, J/kg K
c_{pc} = specific heat of coolant, J/kg K
ℓ = length of cooling channels, m
Ma = Mach number
$\dot{m}$ = mass flow, kg/s
Nu_0 = Nusselt number without blowing
p, p_t = static, total pressure, N/m^2
Pr = Prandtl number
Re = Reynolds number
T = gas temperature, K
T_{bl} = blade surface temperature, K
T_{cr} = cooling air temperature at the blade's root, K
T_{TI} = turbine inlet temperature, K
T_S = blade body temperature, K
v = ideal velocity normal to plate's or blade's surface (as with porous wall), m/s
z = coordinate along the blade, m
α_0, α = heat transfer coefficient without and with blowing, W/m^2 K
κ = specific heat ratio
λ = heat conductivity, W/m K
μ = relative blowing rate, percent
ν = kinematic viscosity, m^2/s
π = pressure ratio
ρ = density, kg/m^3
η_{bl} = cooling effectiveness formed with the local surface temperature and local coolant temperature
$\eta_{bl,cr}$ = cooling effectiveness formed with the $\eta_{s,cr}$ surface temperature, i.e. body temperature in a section of the balde and with the coolant temperature at the blade's root
η_{th} = thermal efficiency
ζ, ζ^* = profile loss coefficient with and without consideration of coolant energy

Subscripts

1 = plane in front of cascade
3 = plane far behind cascade
′ = operating state

compensated by additional cooling. The gas temperature profile, however, was essentially flat over the hight of the blade.

In summarizing the experimental results, the average cooling effectiveness in the mean section was determined as shown in Fig. 4. As the difference between the free stream gas temperature and the recovery temperature is negligable in the Mach number region here considered, we can define:

$$\eta_{bl,cr} = \frac{T_1 - T_{bl}}{T_1 - T_{cr}} \tag{1}$$

From Fig. 4 it is obvious that the cooling effectiveness is considerably higher for blade No. 2 due to smaller hole spacing and the different design of the leading edge cooling channel. For both blades it was found that the cooling effectiveness at constant Mach number will decrease with increasing gas temperature but will increase at constant temperature with the Mach number. This can readily be explained with the fact that with constant Mach number and increasing gas temperature at constant relative cooling air flow rate the blowing rate decreases inducing a reduction of the cooling effectiveness. On the other hand, with constant temperature and increasing Mach number an improvement of the cooling effectiveness is obtained due to the increasing blowing rate. This will be discussed in detail in the next section. Only minor improvements are obtained with relative coolant flow rates exceeding 3 percent.

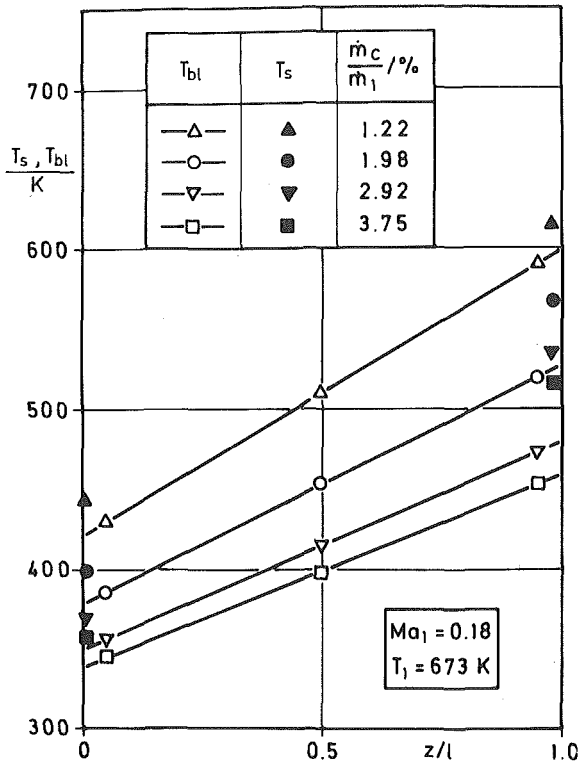

Fig. 3 Temperature change along blade No. 2

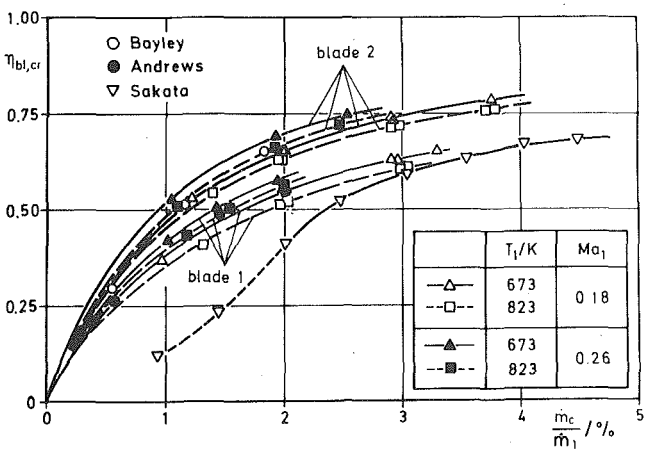

Fig. 4 Cooling effectiveness of the blades

Good agreement with the results of blade No. 1 are found in Andrews' [9] measurements at 770 K gas temperature with a wire mesh shell. Bayley [10] reports higher values at 370 K with a porous bronze shell, but they are in good agreement with the results of blade No. 2. A comparison of these results seems to indicate, that the cooling effectiveness with blowing through a porous wall is not differing drastically from the full-coverage blade cooling with 30 deg inclined holes and a spacing/hole diameter ratio of about 7.

For comparison, additional results from a recent study by Sakata [11] have been added to Fig. 4. Here, hot air of 400 K was blown into the cold main air flow. It should be noted, though, that Sakata's results show deviations of $\Delta\eta = \pm 0.15$.

For design purposes, a complete analysis of the cooling effectiveness for blade No. 2 is presented in Fig. 5. In addition to the data in the mean section discussed earlier, the cooling effectiveness for the blade's jacket and the body of the blade is shown for the root and mean section. As expected, the highest values are obtained for the root. From a designer's point of view this is desirable as in engine applications the maximum strain will be found in this region. It should be noted that the cooling effectiveness as shown in Fig. 5 can be increased—i.e., matched to the design requirements over the hight of the blade by decreasing the spacing of the holes towards the tip.

In evaluating various cooling techniques as described earlier a parameter of dominant importance is the profile loss coefficient. In the present study, the wake profile was determined over the length of one pitch approximately 8 mm from the blade's trailing edge in steps of 0.3 mm to 0.5 mm. The measurements were evaluated by means of the modified mass-averaged momentum procedure for determination of the profile loss coefficient ζ_3 as defined

$$\zeta_3 = \frac{P_{t1} - P_{t3}}{P_{t3} - P_3} \tag{2}$$

Fig. 6 shows the profile loss coefficient for blade No. 2. In applying the profile loss coefficient as defined in equation (2) it should be noted that in accordance with generally accepted procedures the energy of the cooling air has not been considered. It, therefore, is possible to obtain negative profile loss coefficients as reported in the preceding study by Czaja [5]. Alternatively, the energy of the cooling air can be estimated and added to the main flow as shown by Hempel [4]. The profile loss coefficient ζ^* thus determined is compared in Fig. 6 with ζ. It can be seen that ζ^* increases almost linearly with the relative coolant mass flow rate whereas ζ changes degressively.

A comparison of the profile loss coefficients of the present study

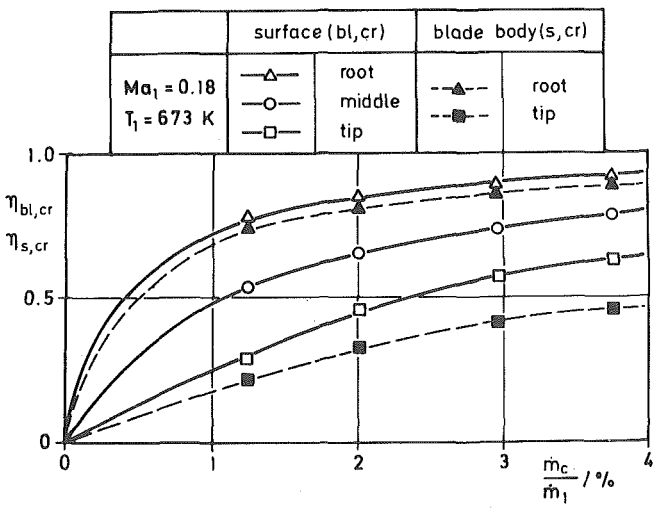

Fig. 5 Cooling effectiveness of blade No. 2 (surface and blade body)

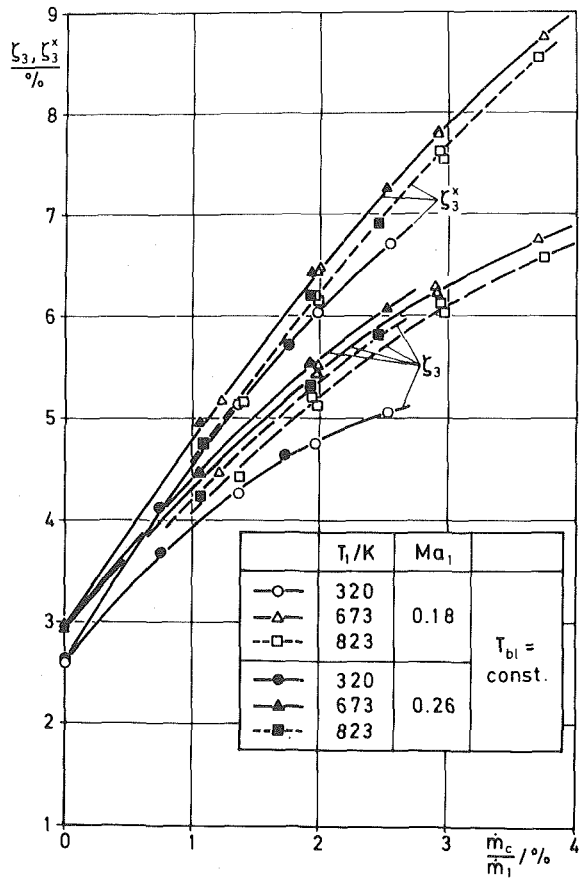

Fig. 6 Profile loss coefficient of blade No. 2

with those of other investigations has been presented by Hempel [4]. It was found that the profile losses with blowing from arrays of holes—i.e., full coverage film cooling—inclined 30 deg to the blade surface tangent will not deviate considerably from blowing through porous walls—i.e., transpiration cooling.

Application and Discussion

As the experimental results were obtained at relatively modest temperatures and pressures, the question of their extension and applicability to real design conditions of stationary gas turbines or aircraft jet engines must be considered. To assure clarity and to reduce large number of influence parameters, the analysis will be made utilizing the flat plate as example. For laminar flow without mass addition the following relations for the heat transfer coefficient hold:

$$\mathrm{Nu}_{ox} = 0.322 \sqrt{\mathrm{Re}_x}\, \sqrt[3]{\mathrm{Pr}} = \frac{\alpha_0 x}{\lambda} \tag{3}$$

$$\alpha_0 = \frac{0.322\, \lambda\, \sqrt[3]{\mathrm{Pr}}\, \sqrt{\mathrm{Ma}}\, (\kappa R T)^{0.25}}{\sqrt{x}\, \sqrt{\nu}} \tag{4}$$

Assuming that the gas constant R and the Prandtl number are constant over wide temperature ranges, the heat transfer coefficients at different states of the fluid at a certain position x are related by:

$$\frac{\alpha_0}{\alpha_0'} = \frac{\lambda}{\lambda'} \sqrt{\frac{\nu'}{\nu}} \left(\frac{T}{T'}\right)^{0.25} \sqrt{\frac{\mathrm{Ma}}{\mathrm{Ma}'}} \left(\frac{\kappa}{\kappa'}\right)^{0.25} \tag{5}$$

where α_0 and α_0' are the heat transfer coefficients at the reference and the operating state, respectively. The same applies to the other properties.

For tubulent flow without blowing we obtain

$$\mathrm{Nu}_{ox} = 0.0292\, \mathrm{Re}_x^{0.8}\, \sqrt[3]{\mathrm{Pr}} \tag{6}$$

respectively

$$\frac{\alpha_0}{\alpha_0'} = \frac{\lambda}{\lambda'} \left(\frac{\nu'}{\nu}\right)^{0.8} \left(\frac{T}{T'}\right)^{0.4} \left(\frac{Ma}{Ma'}\right)^{0.8} \left(\frac{\kappa}{\kappa'}\right)^{0.4} \tag{7}$$

Applying the continuity equation and the ideal gas equation the mass flow rate at the two states can be expressed for constant cross sectional area A as follows:

$$\frac{\dot{m}}{\dot{m}'} = \frac{\rho c}{(\rho c)'} = \frac{\mathrm{Ma}}{\mathrm{Ma}'} \frac{p}{p'} \sqrt{\frac{T'}{T}} \sqrt{\frac{\kappa}{\kappa'}} \tag{8}$$

If μ is the relative coolant flow rate in percent we obtain

$$\dot{m}_c = \frac{\mu}{100} \dot{m} \tag{9}$$

and with the total heated faced area of the plate A_h

$$(\rho_c v_c) A_h = \frac{\mu}{100} (\rho c) A \tag{10}$$

Hence, for the two states considered with equation (8) and A/A_h = constant

$$\frac{\rho_c v_c}{(\rho_c v_c)'} = \frac{\mu}{\mu'} \frac{\mathrm{Ma}}{\mathrm{Ma}'} \sqrt{\frac{T'}{T}} \sqrt{\frac{\kappa}{\kappa'}} \frac{p}{p'} \tag{11}$$

As shown by Hempel [4] the heat balance on a permeable wall considering the cooling effectiveness yields for the ratio of the heat transfer coefficients with blowing α and without blowing α_0

$$\frac{\alpha}{\alpha_0} = \frac{\rho_c v_c c_{pc}}{\alpha_0} \left(\frac{1 - \eta_{bl}}{\eta_{bl}}\right) \tag{12}$$

Equation (12) implies an internal wall thermal effectiveness of 100 percent (ideal porous wall assumption). For turbulent flow the ratio of heat transfer coefficients with and without blowing Mukherjee [12] found in good agreement with experimental results

$$\frac{\alpha}{\alpha_0} = \frac{\dfrac{\rho_c v_c c_{pc}}{\alpha_0}}{e^{\dfrac{\rho_c v_c c_{pc}}{\alpha_0}} - 1} \tag{13}$$

If we assume general applicability of equation (13) and

$$\frac{c'_{pc}}{c_{pc}} = \frac{c'_p}{c_p} \tag{14}$$

we obtain for the cooling effectiveness with equations (12) and (13)

$$\frac{\eta_{bl}}{\eta'_{bl}} = 1 + \frac{(1 - \eta_{bl})\,[1 - e^B]}{e^B - (1 - \eta_{bl})} \tag{15}$$

with

$$B = \ln(1 - \eta_{bl}) \left(1 - \frac{(\rho_c v_c)'}{(\rho_c v_c)} \frac{c'_p}{c_p} \frac{\alpha_0}{\alpha_0}\right)$$

The error induced by applying equation (14) is small, i.e., approximately 5 percent. It should be noted that T and p are Mach number dependent for given total pressure and temperature conditions. However, for the low Mach numbers under consideration—although desirable in principle—a formulation in terms of total parameters will not lead to major deviations. Temperature, pressure and Mach number, therefore, may be treated under the present assumptions as independent parameters.

The influence of pressure, temperature and Mach number on the cooling effectiveness now can be estimated using equations (5, 7, 11) and (15). This is demonstrated in Figs. 7 and 8 with the reference state defined by:

Entrance flow Mach number	M = 0.18
gas temperature	T = 673 K
pressure	p = 1 bar.

An underlying assumption is a constant relative blowing rate ($\mu = \mu'$), i.e. in changing the reference state μ will remain constant.

Fig. 7 illustrates the dependence of the cooling effectiveness on the temperature at constant pressure and Mach number. Furthermore, the influence of the Mach number is shown assuming constant pressure and temperature for laminar and turbulent flow. The cooling

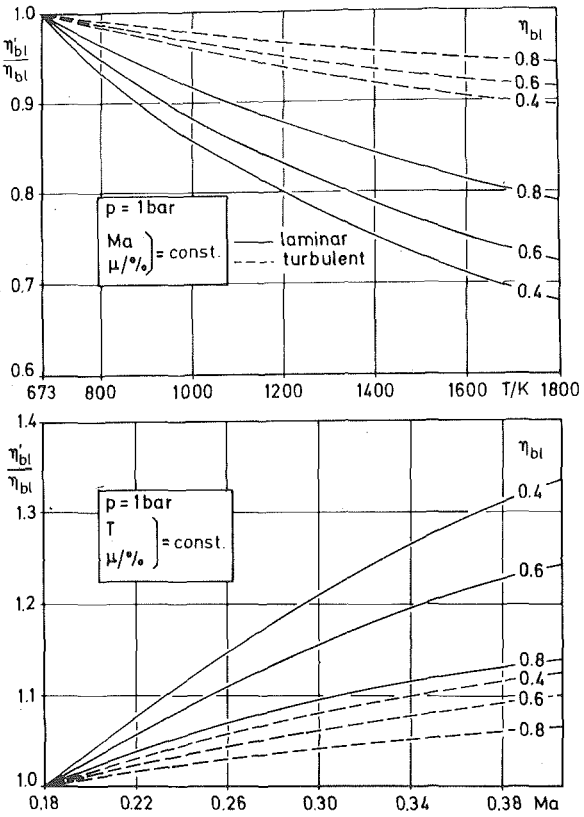

Fig. 7 Influence of gas temperature and Mach number on cooling effectiveness

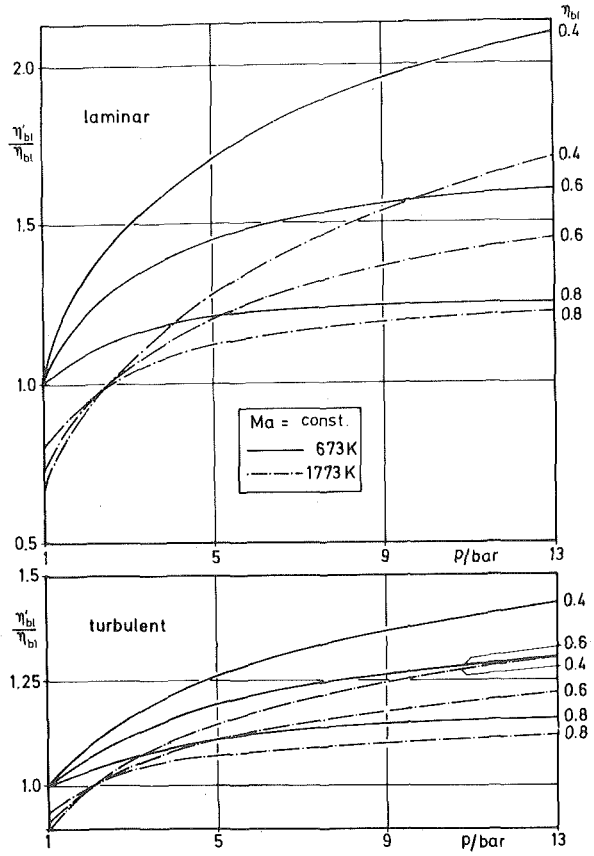

Fig. 8 Influence of pressure on cooling effectiveness

effectiveness at the reference state (η_{bl}) appears as parameter. An obvious result is the decrease of the cooling effectiveness with increasing temperature, the change being more pronounced for laminar flow than for the turbulent case as readily can be seen from equations (5) and (7). Increasing Mach number at constant temperature yields higher η_{bl}—a result which is supported by our experiments with both blades as shown in Fig. 4.

The decrease of the cooling effectiveness with increasing temperature readily will be compensated by higher pressures as found in stationary gas turbines and jet engines. Fig. 8 illustrates the change in η_{bl} with pressure. Parameters are the gas temperature and η_{bl}. It is found that particularly in the pressure range 1 bar $< p <$ 10 bar—especially of importance to the design of stationary gas turbines—the increase of η_{bl} due to a pressure rise is stronger than the decrease due to rising temperatures. Generally, the effects are more pronounced with laminar than with turbulent flow.

In the foregoing discussions all calculations were performed assuming constant relative blowing rate. However, for design purposes the required change of the blowing rate for constant cooling effectiveness is of interest, i.e., (see equations (12–14))

$$\frac{(\rho_c v_c)'}{\rho_c v_c} = \frac{c_p}{c_p'} \frac{\alpha'_0}{\alpha_0} \tag{16}$$

With equation (11) we obtain

$$\frac{\mu'}{\mu} = \frac{\dfrac{(\rho_c v_c)'}{\rho_c v_c}}{\dfrac{\mathrm{Ma}'}{\mathrm{Ma}} \dfrac{p'}{p} \sqrt{\dfrac{T}{T'}} \sqrt{\dfrac{\kappa'}{\kappa}}} \tag{17}$$

The dependence of the blowing rate on temperature and Mach number is shown in Fig. 9. Finally, the effect of rising pressures on the blowing rate is plotted in Fig. 10. It is interesting to note that for laminar as well as for turbulent flow a pressure rise to approximately 2.6 bar is sufficient for all temperatures below 1773 K to maintain the cooling effectiveness of the reference state. Increasing the pressure levels even further—as is common to all gas turbine designs—yields considerably lower blowing rates.

The primary emphasis of the analysis presented here was to clarify the influence of pressure, temperature and Mach number on the cooling effectiveness and the blowing rates using simplified models. It should be noted that, for example, the local distribution of the blowing rate along the blade's surface and subsequently the influence on the cooling air channels has not been considered. May [13], for example, points out that the pressure and velocity distribution and hence the local heat transfer coefficients especially on the suction side will change with increasing temperatures.

Hempel [4] compared the effects on the properties and the heat transfer in the cooling channels for the following reference and operating states:

		Reference State	Operating State
Gas temperature	T	673 K	1773 K
Mach number	Ma	0.18	0.18
Pressure	P	1 bar	9 bar
Temperature of cooling air	T_{cr}	313 K	670 K

Similar heat transfer characteristics were found for the reference and the operating state. However, changing Mach and Reynolds numbers altered the blowing rate and temperature distribution over the height of the blade.

In summarizing the experiments and analysis, the results are applied to a cycle calculation of a single-shaft stationary gas turbine with air preheat and four-stage full coverage film-cooled turbine. The following assumptions were made:

(a) Mean blade temperature T_{bl} = 973 K
(b) Compressor inlet temperature T_{CI} = 288 K
(c) Component efficiencies and relative pressure losses constant: Compressor efficiency η_C = 0.885, turbine efficiency η_T = 0.88,

mechanical compressor and turbine efficiency $\eta_m = 0.995$, combustion chamber efficiency $\eta_{CC} = 0.97$, recuperator efficiency $\eta_R = 0.8$, pressure losses $\Sigma\Delta p/p = 0.07$.

(d) Cooling effectiveness at reference state ($M = 0.18$, $T = 673$ K) following Fig. 4.

(e) Cooling air temperature at the blade's root (T_{cr}) equal to compressor exit temperature (T_{CE}) plus 10 percent of the difference between hot gas temperature and compressor exit temperature:
$[T_{cr} = T_{CE} + 0.1\,(T - T_{CE})]$

(f) Predominantly turbulent flow in the operating state.

(g) Increase of the profile loss coefficients with increasing coolant flow (see Fig. 6) considering the energy of the cooling air exiting the blades.

Furthermore, it should be noted that blade profiles similar to the base profile studied in the experimental investigation were assumed to be used in the turbine. Also, an increase of the Mach number within the turbine was not considered at this would lead to improved cooling effectiveness (see Fig. 4). The present results, therefore, represent lower bound values for the improvements to be expected.

Following the results of Fig. 11 it is possible to increase the thermal efficiency for stationary plants with a pressure ratio of approximately $\pi = 10$ by approximately 24 percent (from 37 to 46 percent) in rising the gas temperature from 1173 K to 1573 K. The relative coolant flow is approximately 8 percent. The gain in specific power will be close to 70 percent. At even higher temperatures, the additional gain will not be as pronounced with the thermal efficiency whereas the specific power rise is still considerable.

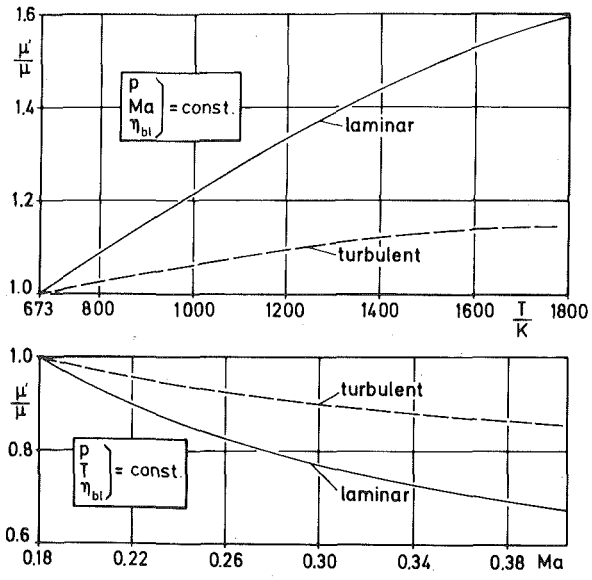

Fig. 9 Influence of temperature and Ma on the relative blowing rate

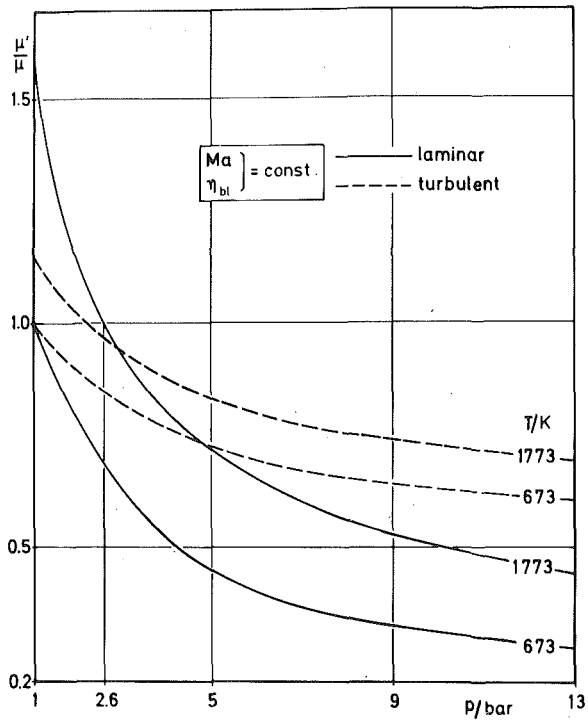

Fig. 10 Influence of pressure on the relative blowing rate

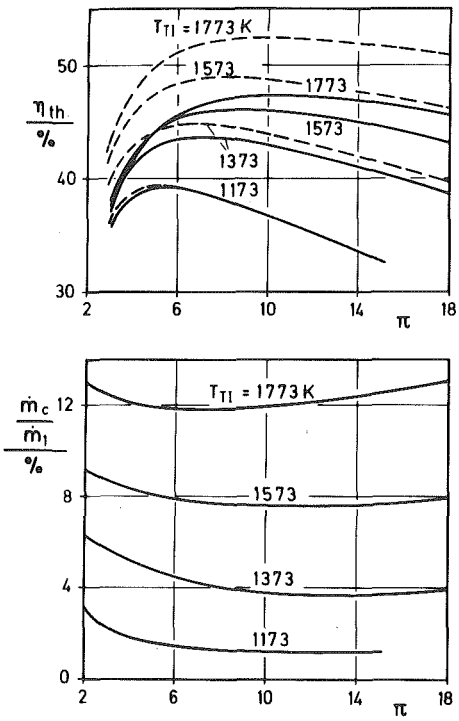

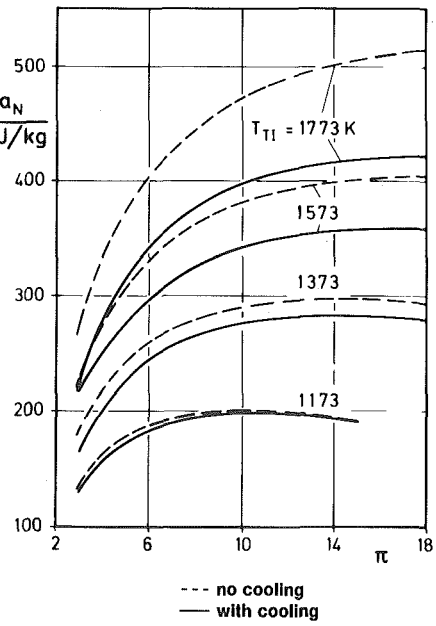

Fig. 11 Thermal efficiency, cooling rate and specific work for a gas turbine cycle with recuperator and full coverage film-cooled blading

Conclusions

The cooling effectiveness of effusion of full coverage film-cooled blades is strongly dependent on the geometrical arrangement—i.e., primarily the spacing—of the holes over the perforated wall. With hole diameters of 0.2 mm and spacing of 1.4 mm the cooling effectiveness is close to values obtained with transpiration cooling. With relative coolant flow rates of 3 percent, the cooling effectiveness will exceed 0.7.

Similar to porous walls, the profile loss coefficient rises with increasing coolant flow and will double in comparison to flow without blowing at relative cooling air flow rates of 3 percent.

A detailed analysis shows that under conditions found in engines of the latest design the relative cooling air blowing rate is considerably smaller than under the experimental conditions chosen. Calculations were made for a single shaft gas turbine with heat exchanger. As a representative result it was found that for a pressure ratio of $\pi = 10$ a relative cooling air flow of approximately 8 percent will be required in rising the temperature from 1173 K to 1573 K. The resulting relative improvement of the thermal efficiency is 24 percent and that of the specific work about 70 percent. At even higher temperatures, improvement of the thermal efficiency is reduced with the specific work still rising as expected.

Under certain conditions full coverage film-cooling approaches the cooling effectiveness of transpiration cooling. Its major advantage, however, is the possibility—advanced by modern manufacturing processes—of matching the required cooling air flow by proper arrangement of the hole distribution over the blade's surface.

References

1 Horner, M. W., Day, W. H., Smith, D. P. and Cohn, A., "Development of a Water-Cooled Gas Turbine," ASME Paper No. 78-GT-72, 1978.

2 BBC-Nachrichten, 1974, Heft 10

3 Hempel, H. and Friedrich, R., "Profile Loss Characteristics and Heat Transfer of Full Coverage Film-Cooled Blading," ASME Paper No. 78-GT-98, 1978.

4 Hempel, H., "Untersuchungen zur Entwicklung einer effusionsgekühlten Gasturbinenschaufel," Dissertation Universität Karlsruhe 1978.

5 Czaja, W., "Theoretische und experimentelle Untersuchung zur Turbinengitterströmung mit Ausblasung aus der Schaufeloberfläche," Dissertation Universität Karlsruhe 1975.

6 Goldstein, R. J., Eckert, E. R. G. and Ramsey, J. W., "Film Cooling with Injection through Holes: Adiabatic Wall Temperatures Downstream of a Circular Hole," ASME JOURNAL OF ENGINEERING FOR POWER, Oct. 1968.

7 Liess, C., "Experimental Investigation of Film Cooling with Ejection from a Row of Holes for the Application to Gas Turbine Blades," ASME JOURNAL OF ENGINEERING FOR POWER, May 1974.

8 Metzger, D. E., Takeuchi, D. I. and Kuenstler, P. A., "Effectiveness and Heat Transfer with Full-Coverage Film Cooling," ASME JOURNAL OF ENGINEERING FOR POWER, July 1973, pp. 180–184.

9 Andrews, S. J., Odgen, H. and Marshall, J., "Some Experiments on an Effusion Cooled Turbine Nozzle Blade," A.R.C. Technical Report C.P. 267, 1956.

10 Bayley, F. J. and Turner, A. B., "The Heat Transfer Performance of Porous Gas Turbine Blades," *The Aeronautical Journal* 72, 1968, p. 1087.

11 Sakata, K., Usui, H. and Takahara, K. "Cooling Characteristics of Film Cooled Turbine Vane Having Multi-Row of Ejection Holes," ASME Paper No. 78-GT-21, 1978.

12 Mukherjee, D. K., "Beitrag zur Effusionskühlung," *Z. Flugwiss.*, 21, 1973, Heft 7.

13 May, H., "Prüfstand zur Untersuchung von Schaufelgittern und Druckverteilungsmessung bei hohen Gastemperaturen," *Allgemeine Wärmetechnik*, Band 12, Folge 3, 1964.

S. Ito
Assistant Professor,
Ikutoku Technical University,
Atsugi, Kanagawa-ken,
Japan

E. R. G. Eckert
Regents' Professor Emeritus.

R. J. Goldstein
Professor and Head,
Department of Mechanical Engineering,
University of Minnesota,
Minneapolis, Minn 55455

Aerodynamic Loss in a Gas Turbine Stage with Film Cooling

Experiments have been performed to measure the total pressure loss of the flow through a two-dimensional turbine cascade with "coolant" injection from a single row of holes on the suction or pressure side of the blades. The tests were performed in a low speed tunnel. Air and carbon dioxide were used as secondary fluids, the latter to provide a large density difference between the gas in the mainstream and the injected gas. Both gas streams had the same temperature. The measured pressure loss is in good agreement with analytical predictions based on a model introduced by Hartsel. The results thus provide information which can be incorporated in a program which predicts the influence of injection on the aerodynamic efficiency of a gas turbine.

Introduction

The performance of a gas turbine increases in general with increasing inlet temperature. However, the attainable temperature of the structural components is restricted because of the potential of mechanical failure. This holds especially for the turbine blades and vanes. Film cooling alone or combined with other cooling methods is now widely used to maintain the skin of blades and vanes at acceptable temperatures. The coolant injected into the gas stream in the film cooling method is effective in reducing the skin temperature of the blade. However, it also influences the aerodynamic loss of the flow through the turbine stage and this in turn affects the overall efficiency of the gas turbine.

The Heat Transfer Laboratory of the University of Minnesota has a wind tunnel in which the film effectiveness in a cascade of turbine blades has been investigated [1]. The large size of the blades makes it possible to perform also accurate surveys across the wake of the blades and in this way to determine the aerodynamic loss. The present paper represents such measurements and compares the results with an analytic investigation.

Only a few theoretical studies on the effect of coolant injection from the surface of blades on the aerodynamic loss are available in the literature. Tabakoff and Earley [2] and Tabakoff and Hamed [3] considered the effect of coolant injection on boundary layer growth assuming that the coolant flow is completely immerged into a two-dimensional boundary layer. For injection from a row of holes, however, it has been found that often the coolant flow penetrates completely or in part through the boundary layer. In this situation the analysis becomes very difficult and the problem has not been solved by a method which considers the boundary layer character of the flow.

Prust [4] studied the aerodynamic loss using a one-dimensional analysis with the assumption that the injected coolant mixes with the main gas flow at the blade row exit. Hartsel [5] improved this analysis with the assumption that the ejected coolant mixes with a part of the mainstream, called the "mixing layer," at the location of injection and that this mixing layer then mixes with the rest of the main stream at the exit of the blade row. The thickness of the mixing layer was chosen so that agreement with experiments was obtained. The present analysis is a modification of Hartsel's method. It will be presented in Section 3. Experiments with a two-dimensional cascade of turbine blades are reported in Section 2 and a comparison of analytic and experimental results is the content of Section 4.

Experiments

Apparatus. The present experimental study has been carried out in the low velocity wind tunnel shown in Fig. 1.

Air at room temperature, delivered by a fan, flows to the turning vanes, and then through screens and flow-straighteners to the contraction section (entrance: 102 cm × 97 cm, exit: 46.9 cm × 60 cm). The flow then enters the two-dimensional turbine blade cascade with an approach velocity of 14 m/s and leaves through an exit duct.

There are seven threaded holes in the tunnel ceiling at a distance 0.76 times the chord length upstream of the leading edges of the blades which can be used for the insertion of pitot tubes and thermocouples.

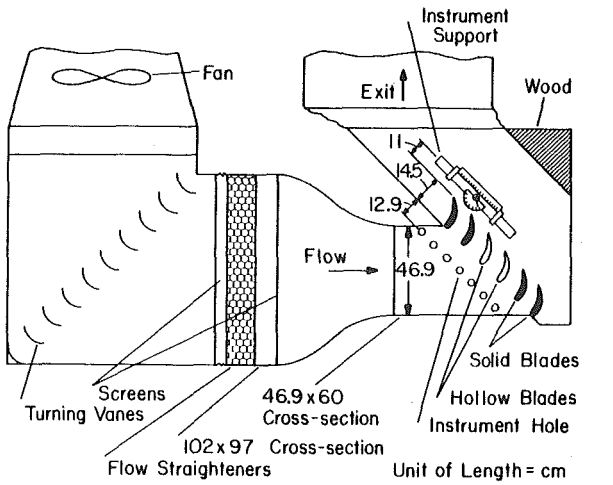

Fig. 1 Wind tunnel for flow and heat transfer studies on a cascade of turbine blades

Contributed by the Gas Turbine Division and presented at the Gas Turbine Conference and Products Show, New Orleans, La., March 10–13, 1980 of THE AMERICAN SOCIETY OF MECHANICAL ENGINEERS. Manuscript received at ASME Headquarters December 10, 1979. Paper No. 80-GT-38.

The inlet flow velocity, angle, and temperature are measured at this position later referred to as Section 1. A MKS Baratron Type 77 Electronic Pressure Meter is used for pressure measurement. A slit is provided in the upper wall at a distance 1.43 chord lengths downstream of the trailing edges. A slide with a protractor can be moved along this slit which is otherwise closed off. The blade outlet flow angle, total pressure and flow velocity are measured across the blade row using a yaw meter, an impact tube, and a pitot tube at this section later referred to as Section 3.

The cascade has six blades—four solid and two (the center ones) hollow ones. One of the hollow blades has a row of holes on the suction side and the other has a row of holes on the pressure side as shown in Fig. 2. The angle between the axis of the holes through the blade skin and the wall surface is 35 deg. The axis of the holes is located in a plane normal to the blade axis. The blade surfaces with holes face each other. The ratio of the span to the chord length is 3.55. This rather long span is designed to avoid end effects. The ratio of chord length L_c, to pitch length, L_s, is 1.289. There are 79 holes for the secondary fluid injection in each of the two blade walls spaced equally over the entire span. The diameter of each hole, D, is 2.38 mm, and the spacing between the centers of adjacent holes is $3D$.

Air and carbon dioxide were used as the injected gas. The second gas provided a large density difference between the two gas streams and thus simulated large temperature differences existing in a gas turbine between the coolant and the main flow. The experiments could in this way be run at uniform temperature. The secondary gas is ducted into the blade interior by a brass tube. It exits through a row of holes in the tube wall to the inside of the blade and from there through the injection holes. The brass tube was rotated and fixed at the position which gave the most uniform flow out of the injection holes. Satisfactory uniformity was obtained.

Results. Figure 3 presents the normalized main stream velocity profile u/U_3 along the blade surface. The local velocity u is obtained from the total pressure p_{t1} measured at Section 1 upstream of the blade row, the static pressure p is measured at the pressure taps along the blade surface and the density ρ_∞ is used assuming that the flow can be considered incompressible. The equation

$$u = \sqrt{2(p_{t1} - p)/\rho_\infty} \tag{1}$$

determines u. The term U_3 indicates the average velocity at the exit of the blade row measured by the probes at station 3. The normalized distance $\overline{X}_n$ is measured in the direction indicated in the figure. The

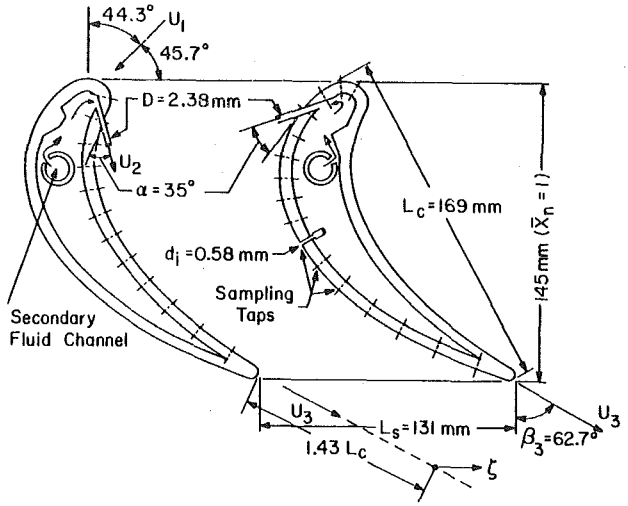

Fig. 2 Turbine blades with film cooling by injection through rows of holes on the suction and pressure sides

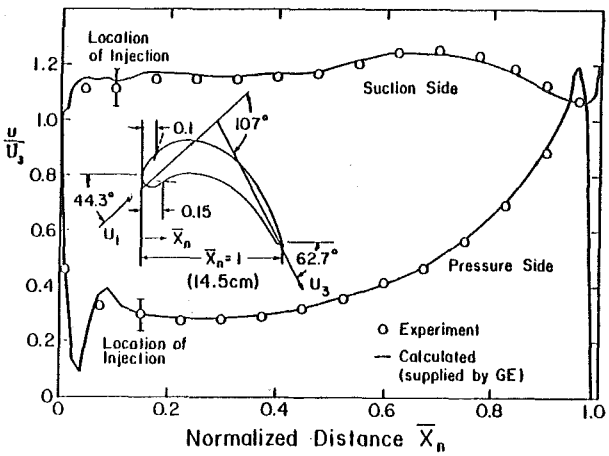

Fig. 3 Measured and calculated velocity distribution around the surface of the turbine blade

Nomenclature

A_1 = inlet cross-sectional area of duct with unit width
A_2 = total area of a slit or a row of injection holes for unit width of duct
A_3 = outlet cross-sectional area of duct with unit width
c_p = specific heat at constant pressure
c_v = specific heat at constant volume
D = diameter of injection hole
d_i = diameter of pressure tap
d_t = diameter of trip wire
k = ratio of specific heats, c_p/c_v
L_c = blade chord length (cf. Fig. 2)
L_s = pitch of blade row (cf. Fig. 2)
Ma = Mach number of main stream
m = mass flow rate, mass flow per unit time
p = pressure
$\overline{p}_t$ = mass averaged total pressure
p_{t1} = total pressure at center of inlet section
$\Delta\overline{p}_t$ = difference of mass averaged total pressures at inlet and exit, $\Delta\overline{p}_t = \overline{p}_{t1} - \overline{p}_{t3}$
$\Delta\overline{p}_{tm}$ = total pressure loss due to mixing with the mainstream flow
$\Delta\overline{p}'_{tm}$ = total pressure loss due to mixing in mixing layer
$\Delta\overline{p}_{tv}$ = total pressure loss due to viscous effect
R = gas constant
Re_3 = chord Reynolds number, U_3L_c/ν_3
T = temperature
ΔT_t = increase of total temperature of stream in duct due to secondary fluid addition
U = mean velocity
U_e = mean velocity of flow in mixing layer at cascade exit
u = local flow velocity
$\overline{X}_n$ = normalized axial distance of cascade (cf. Fig. 3)
α = angle between velocity vector U_2 and tangent to wall at exit of injection (cf. Figs. 2 and A1)
β_3 = cascade exit flow angle (cf. Fig. 2)
λ = mass weighted local pressure loss coefficient (cf. equation (2))
$\overline{\lambda}$ = mass averaged total pressure loss coefficient (cf. equation (4))
$\overline{\lambda}_m$ = mixing loss coefficient, $\overline{\lambda}_m = \overline{\lambda} - \overline{\lambda}_v$
$\overline{\lambda}_v$ = mass average viscous loss coefficient (cf. equation (8))
ν = kinematic viscosity
ζ = distance across blade row at 1.43 times the chord length downstream from the trailing edge (cf. Fig. 2)
ξ = ratio of coolant to total mainstream mass flows, m_2/m_1
ξ_m = ratio of coolant to mainstream mass flows in mixing layer (cf. equation (9))
ρ = density
σ = ratio of mainstream mass flow in mixing layer to total mainstream mass flow before mixing (cf. equation (9))

Superscript

– = mass averaged value

Subscripts

j = flow after mixing in mixing layer
0 = values with absence of coolant flow
t = total or stagnation state
1 = cascade or duct inlet (Fig. 6)
2 = secondary (coolant) flow
3 = cascade or duct exit (Fig. 6)
∞ = local mainstream at location of injection

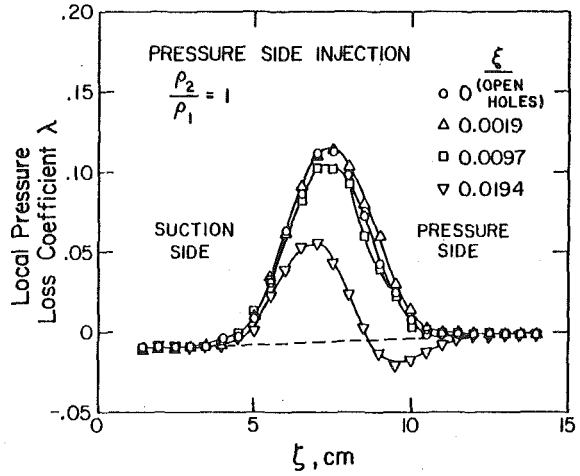

Fig. 4 Mass weighted local total pressure coefficient, measured at 1.43 cord length downstream of the trailing edge of the blade, for injection on the pressure side. Reynolds number, $Re_3 = 2.3 \times 10^5$

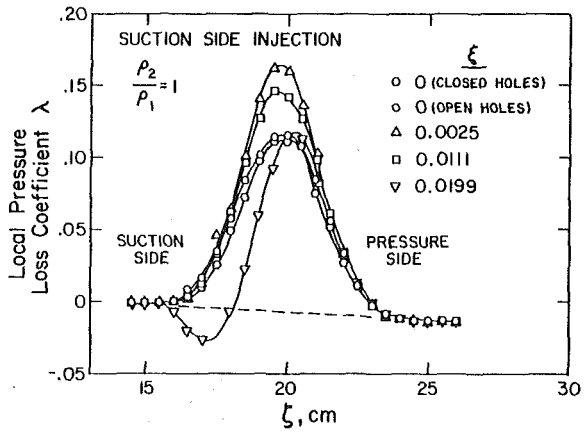

Fig. 5 Mass weighted total pressure coefficient, measured at 1.43 cord lengths downstream of the trailing edge of the blade, for injection on the suction side. Reynolds number, $Re_3 = 2.2 \times 10^5$

experimental points agree well with results calculated for incompressible flow, which were supplied by the Aircraft Gas Turbine Division of the General Electric Company for this blade contour. The location of the injection holes is indicated in the figure of the blade and on the pressure distribution curve. The measured inlet and outlet flow angles were found also to agree within 0.2 to 0.3 deg with the calculated flow angles.

The ratio of the boundary layer displacement thickness at the injection line, δ^*, calculated by the method of Kármán and Pohlhausen [6] to the diameter, D, of the injection hole on the suction surface of the blade has the value 0.09 and the boundary layer Reynolds number $u_\infty \delta^*/\nu$ is 300. The velocity u is practically constant near the injection holes. The critical Reynolds number for this condition is about 660 [6]. The boundary layer on the suction surface at the location of injection is therefore expected to be laminar. On the pressure side of the blade there is an adverse pressure gradient upstream of the injection holes and the boundary layer near the injection hole is expected to be turbulent.

Figures 4 and 5 present the results of wake traverses at Section 3, a distance of 1.43 times the cord length downstream of the trailing edge of the blade. Figure 4 is obtained from measurements with injection on the pressure side of the blade and Fig. 5 injection at the suction side. The local mass weighted pressure loss coefficient λ presented on the ordinate of the figure is defined in the following way:

$$\lambda = \frac{(p_{t1} - p_{t3})\dfrac{u_3}{U_3}}{p_{t1} - \bar{p}_3} \tag{2}$$

p_{t1} indicates the total pressure at station 1 and p_{t3} the total pressure at station 3. $\bar{p}_3$ is the mass averaged pressure, u_3 denotes the local velocity and U_3 the average velocity at station 3. The length ζ is measured at location 3 in the direction parallel to the blade row as shown in Fig. 2. The symbol ξ represents the ratio of the coolant mass flow m_2 to the mainstream mass flow m_1

$$\xi = \frac{m_2}{m_1} \tag{3}$$

Both figures represent the results of measurements in which air was used as coolant. The density ratio of the coolant ρ_2 to the density ρ_1 of the air in the main stream is therefore practically equal to 1.

Figure 4 shows the results with injection on the pressure side. Without injection ($\xi = 0$) the largest loss occurs directly downstream of the trailing edge of the blade. Small values of injection have only a small influence on the pressure loss coefficient. However, a large reduction of this coefficient, especially downstream of the pressure side of the blade, is observed at the highest injection ratio, $\xi = 0.0194$. This obviously is due to the momentum in the flow direction supplied by the injected fluid.

The pressure loss coefficient of the blade with injection on the suction side presented in Fig. 5 exhibits some different characteristics. A small amount of injection increases the loss coefficient, whereas a reduction occurs again at the largest injection rate, $\xi = 0.0199$. Measurements have in this case been performed for two conditions of zero injection because the boundary layer is expected to be laminar at the point of injection on the suction side of the blade. In one, the holes were taped over to provide a smooth surface whereas in the second, the holes were left open. It may be observed that there is a slight difference in the loss coefficient; it has a somewhat smaller value for the smooth surface.

Analysis

Definitions. The pressure loss coefficient averaged over the mass flow at the exit of a cascade is customarily defined by

$$\bar{\lambda} = \frac{\bar{p}_{t1} - \bar{p}_{t3}}{\bar{p}_{t1} - \bar{p}_3} \tag{4}$$

assuming that all the pressures have obtained uniformity in the respective cross-sections by mixing (Fig. 6).

It will be assumed that the total pressure loss due to mixing of the coolant flow with the mainstream $\Delta\bar{p}_{tm}$ and the loss due to viscous effects $\Delta\bar{p}_{tv}$ are separable so that the total loss is given by the equation

$$\Delta\bar{p}_t = \bar{p}_{t1} - \bar{p}_{t3} = \Delta\bar{p}_{tm} + \Delta\bar{p}_{tv} \tag{5}$$

or that

$$\bar{\lambda}_m = \bar{\lambda} - \bar{\lambda}_v \tag{6}$$

where

$$\bar{\lambda}_m = \frac{\Delta\bar{p}_{tm}}{\bar{p}_{t1} - \bar{p}_3} \tag{7}$$

$$\bar{\lambda}_v = \frac{\Delta\bar{p}_{tv}}{\bar{p}_{t1} - \bar{p}_3} \tag{8}$$

The coefficient $\bar{\lambda}_v$ will be assumed independent of the coolant injection rate in the following comparison of experimental and analytical results.

Modification of Hartsel's Method. The following analysis is based on the model introduced by Hartsel and will be discussed with reference to Fig. 6. Mixing layers are postulated to adjoin the blade surfaces with thicknesses larger than the boundary layers. In Fig. 6 the mixing layer is sketched on the suction side of the blade. A similar layer occurs also along the pressure side. The rest of the flow is called the unaffected mainstream. The analysis for the various layers is one-dimensional. The fluid in the mixing layer expands isentropically from the upstream velocity U_1 to the velocity u_∞ approaching the point of injection. There the coolant injected with the velocity U_2 mixes with the fluid in the mixing layer at constant pressure. The

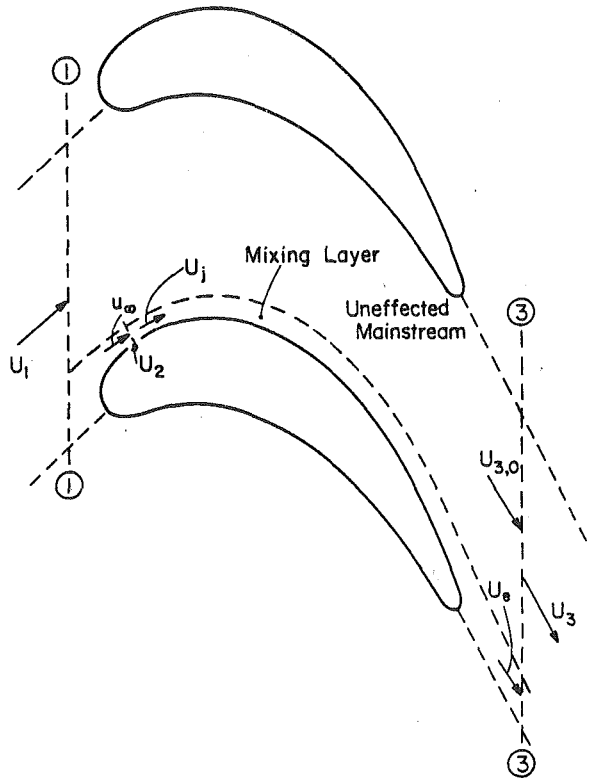

Fig. 6 Sketch of flow through a turbine blade cascade illustrating the mixing layer on the suction side for obtaining the total pressure loss coefficient

resulting uniform velocity is U_j. After mixing, the fluid in the mixing layer continues to expand isentropically to the exit Section 3 reaching the velocity U_e. The unaffected mainstream expands isentropically from the upstream velocity U_1 to the exit velocity $U_{3,0}$ in the exit cross Section 3. The two streams mix at constant pressure, and the resulting uniform velocity is U_3.

The present analysis uses the same model for the flow but bases the analysis on the relations for constant pressure mixing presented in the appendix of this paper; those relations are derived there for an injected gas different from the mainstream and for specific heats of the coolant and the mainstream fluid which are functions of temperature. The presentation in this and the following sections is aimed at providing analytical expressions for the mixing loss coefficient which can be compared with the experimental results. It restricts the expressions given in the appendix to incompressible flow with temperature independent specific heats because this is the condition which was well approximated in the low flow velocity experiments. The mixing loss coefficient, then, is expressed by a simple equation which can be calculated easily, if one knows the ratio of the mainstream velocity at the location of injection without injection to the cascade exit velocity.

Total Pressure Loss Due to Fluid Injection. The following assumptions will be made in addition to those mentioned in the preceding section. Subscript o will be used for values under the condition that no secondary fluid is injected.

1 Coolant and mainstream fluid are perfect gases.
2 The inlet total pressure p_{t1} and the exit static pressure p_3 are not influenced by fluid injection ($p_{t1} = p_{t1,0}$ and $p_3 = p_{3,0}$).
3 The mainstream velocity at the location of injection before mixing is not influenced by fluid injection ($u_\infty = u_{\infty,0}$).

The ratio of the mass flow of the fluid in the mixing layer approaching the blade row to the total mass flow in the mainstream is denoted by the symbol σ. The coolant fraction in the mixing layer is accordingly

$$\xi_m = \frac{m_2}{\sigma m_1} = \frac{\xi}{\sigma} \tag{9}$$

The following equation can easily be obtained by a derivation analogous to that of equation (A20) in the Appendix

$$\frac{\Delta\bar{p}'_{tm}}{p_{t1} - p_\infty} = 1 - \frac{\rho_j}{\rho_1}\left(\frac{U_j}{u_\infty}\right)^2 \tag{10}$$

where

$$\frac{U_j}{u_\infty} = \frac{1 + \dfrac{\xi}{\sigma}\dfrac{U_2}{u_\infty}\cos\alpha}{1 + \dfrac{\xi}{\sigma}}$$

In the above equation, $\Delta\bar{p}'_{tm}$ is the difference of the total pressures in the mixing layer before mixing and after mixing, p_∞ is the static pressure at the location of injection, ρ_j is the density of the fluid in the mixing-layer after completion of mixing, and α is the angle between the coolant velocity vector at the exit of the coolant hole and the tangent on the blade surface. The various velocities are indicated in Fig. 6.

We consider the case when the direction of the flow after mixing, U_j, is the same as that before mixing, u_∞. The following equations hold because of isentropic expansion

$$p_{t1} - \Delta\bar{p}'_{tm} = p_3 + \rho_j\frac{{U_e}^2}{2} \tag{11}$$

$$p_{t1} - p_3 = \frac{\rho_1 {U_{3,0}}^2}{2} \tag{12}$$

From equations (11) and (12) one obtains

$${U_e}^2 = \frac{\rho_1}{\rho_j}{U_{3,0}}^2 - \frac{2}{\rho_j}\Delta\bar{p}'_{tm} \tag{13}$$

The density ratio ρ_1/ρ_j is obtained from the ideal gas equation.

Substituting equation (10) into equation (13) gives

$$\frac{{U_e}^2}{{U_{3,0}}^2} = \frac{\left(1 + \dfrac{\xi}{\sigma}\dfrac{R_2}{R_1}\right)\left(1 + \dfrac{\xi}{\sigma}\dfrac{c_{p2}\,T_2}{c_{p1}\,T_1}\right)}{\left(1 + \dfrac{\xi}{\sigma}\right)\left(1 + \dfrac{\xi}{\sigma}\dfrac{c_{p2}}{c_{p1}}\right)}\left\{1 - \left(\frac{u_\infty}{U_{3,0}}\right)^2\right\} + \left(\frac{u_\infty}{U_{3,0}}\right)^2\left(\frac{1 + \dfrac{\xi}{\sigma}\dfrac{U_2}{u_\infty}\cos\alpha}{1 + \dfrac{\xi}{\sigma}}\right)^2 \tag{14}$$

R denotes the gas constant, c_p the specific heat at constant pressure and T the absolute temperature.

The mass fraction of the flow in the mixing layer to that in the unaffected mainstream after injection is

$$\frac{m_2 + \sigma m_1}{m_1 - \sigma m_1} \text{ or } \frac{\xi + \sigma}{1 - \sigma} \tag{15}$$

The flows in the mixing layer and in the mainstream are assumed to be parallel to each other so that

$$\frac{p_{t3,0} - p_{t3}}{p_{t3,0} - p_3} = 1 - \frac{\rho_3}{\rho_1}b^2 \tag{16}$$

where

$$b = \frac{1 + \dfrac{(\xi + \sigma)}{(1 - \sigma)}\dfrac{U_e}{U_{3,0}}}{1 + \dfrac{\xi + \sigma}{1 - \sigma}} \tag{17}$$

The term $p_{t3,0}$ is the total pressure in the unaffected mainstream before mixing, which is equal to p_{t1} and p_{t3} is the total pressure at cascade exit after mixing. The density ratio ρ_3/ρ_1 is obtained from the ideal gas equation. With this equation (16) becomes

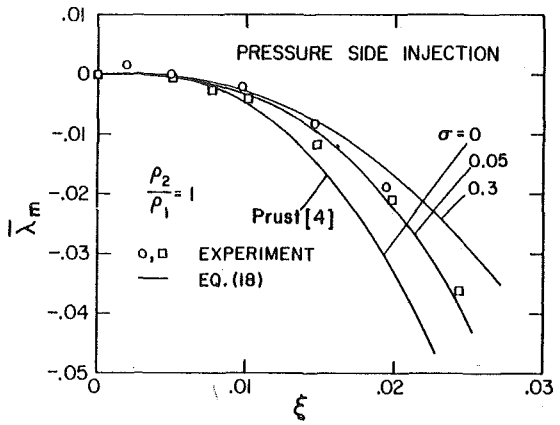

Fig. 7 Mean total pressure loss coefficient for injection from the pressure side (□ with a trip wire on the pressure side near the nose, d_t = 0.9 mm). $U_2 = u_{\infty,0}$ at $\xi = 0.0030$

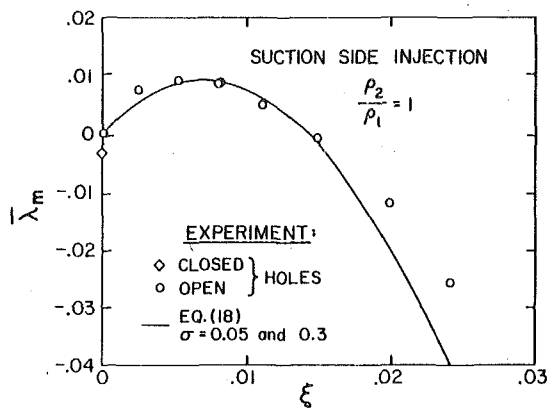

Fig. 8 Mean total pressure loss coefficient for suction side injection. $U_2 = u_{\infty,0}$ at $\xi = 0.012$

$$\bar{\lambda}_m = 1 - ab^2 \tag{18}$$

where a is given by

$$a = \frac{(1+\xi)\left(1+\xi\frac{c_{p2}}{c_{p1}}\right)}{\left(1+\xi\frac{R_2}{R_1}\right)\left(1+\xi\frac{c_{p2}}{c_{p1}}\frac{T_2}{T_1}\right)} \tag{19}$$

The inlet mainstream flow rate will actually be changed by coolant injection, if one assumes that the inlet total pressure p_{t1} and the exit static pressure p_3 are the same with and without injection. This affects the flow velocity of the unaffected mainflow and the static pressure at the exit before mixing. In the present analysis for the mixing loss coefficient, this effect is neglected and the unaffected mainstream at the exit is assumed to be the same with and without the secondary fluid injection. This results in a small error in the loss coefficient unless $\bar{\lambda}_m$ is very large. Equation (18) will be used to compare the experimental results described in Section 2 with results of the present analysis. Before doing this, however, the effect of fluid injection on the mainstream flow rate and on the exit kinetic energy will be calculated.

Effect of Fluid Injection on Mainstream Flow Rate and on Exit Kinetic Energy Flux. The total pressure loss due to viscous effects will be assumed unchanged by coolant injection. The ratio of the mass flows at the blade row exist with and without coolant injection is then given by the following equation

$$\left(\frac{m_3}{m_{3,0}}\right)^2 = \frac{\rho_3}{\rho_{3,0}}\frac{(p_{t3}-p_3)}{(p_{t3,0}-p_3)}$$

or

$$\left(\frac{m_3}{m_{3,0}}\right)^2 = \frac{\rho_3}{\rho_{3,0}}\left(1-\frac{p_{t3,0}-p_{t3}}{p_{t3,0}-p_3}\right) \tag{20}$$

Substitution of equation (16) results in

$$\frac{m_3}{m_{3,0}} = ab \tag{21}$$

where $U_e/U_{3,0}$ in the term b is given by equation (14).

The ratio of the mainstream flow rate with and without coolant injection is

$$\frac{m_1}{m_{1,0}} = \frac{m_1}{m_{3,0}} = \frac{m_3 - \xi m_1}{m_{3,0}} \tag{22}$$

From equations (21) and (22) follows

$$\frac{m_1}{m_{1,0}} = \frac{1}{1+\xi}ab \tag{23}$$

The relative change in blade row exit kinetic energy flux is computed from the following equations

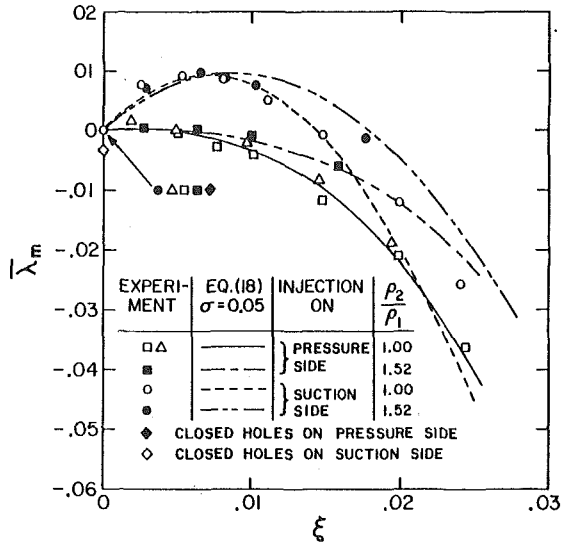

Fig. 9 Effect of density ratio on mean pressure loss coefficient

$$K = \frac{m_3 U_3^2 - m_{3,0}U_{3,0}^2}{m_{3,0}U_{3,0}^2} = \frac{\rho_{3,0}^2 m_3^3}{\rho_3^2 m_{3,0}^3} - 1 \tag{24}$$

$$K = ab^3 - 1 \tag{25}$$

Comparison of Experimental and Analytical Results

The averaged pressure loss coefficients measured for the blade cascade used in the experimental part of the program are presented in Figs. 7–9. Figures 7 and 8 are for the condition that air as "coolant" is injected into air in the mainstream and that both have the same temperature ($\rho_2/\rho_1 = 1$). Figure 9 illustrates the effect of density ratio ρ_2/ρ_1. Carbon dioxide at room temperature is used as "coolant" in these experiments, resulting in a density ratio $\rho_2/\rho_1 = 1.52$. The ordinate of the figure is $\bar{\lambda} - \bar{\lambda}_v$. The loss coefficient $\bar{\lambda}$ for any injection rate ξ is obtained from the area enclosed by the respective curve and the straight dashed line shown in Figs. 4 and 5. The friction loss coefficient $\bar{\lambda}_v$ has been assumed to be equal to $\bar{\lambda}_{v,0}$, consistent with the assumption that the frictional pressure loss does not depend on the amount of injection. The experimental points in the figures are compared with analytical results obtained by Hartsel's method as modified in Section 3.

Figure 7 presents the pressure loss coefficient for injection from the pressure surface of the blade. It is observed that the ratio σ of the fluid mass in the mixing layer to that in the mainstream has little effect for $\xi < 0.01$ ($U_2/u_\infty < 3.0$), but a considerable effect for the larger ξ on the pressure loss coefficient. The prediction agrees best with the experimental results for a value $\sigma = 0.05$.

The situation is different for coolant injection at the suction surface of the blade (Fig. 8). Analytical results obtained from equation (18) for $\sigma = 0.05$ and 0.3 practically coincide indicating that the mass flow ratio σ has practically no effect on the pressure loss coefficient. The explanation for this difference is obtained from a comparison of the mainstream velocity profiles along the two surfaces of the blade shown in Fig. 3. On the suction side the mainstream velocity, and therefore the pressure, are practically constant along the blade surface. Therefore, it makes little difference whether the mixing of the coolant with the mainstream occurs at the point of injection or at the blade row exit. On the pressure side, the mainstream velocity along the blade surface is smaller at the location of injection than at the blade row exit. The coolant mixes with part of the mainstream at a lower velocity causing the mixing loss to be smaller than that on the suction side.

No explanation can be offered why the two experimental points in Fig. 8 at the large injection rates deviate from the calculated curve. Figure 8 presents two experimental values on the ordinate (for zero coolant injection) indicating that the presence of the holes constitutes a surface roughness and increases the turbulence in the flow even without coolant injection. The higher value of the pressure loss coefficient was assumed to represent the frictional loss coefficient for the evaluation of the experimental results with fluid injection.

Figure 9 compares analytical predictions based on equation (18) with experimental results for two values of the density ratio ρ_2/ρ_1 at $\sigma = 0.05$. The prediction is in good agreement with experimental results even at density ratios different from 1.

Conclusions

The total pressure losses in the flow through a cascade of turbine blades can increase or decrease with coolant injection in the downstream direction. An analysis based on the model introduced by Hartsel predicts this loss in agreement with experimental results for small coolant injection, which is the situation in film cooling. The loss coefficient varies considerably with σ at $\xi > 0.01$ for pressure side injection and agrees best with experimental results at $\sigma = 0.05$. The change in the mainstream flow rate and in the kinetic energy flux change at the blade row exit can also be predicted from the equations in Section 3. The analysis can now be incorporated in a program which predicts the aerodynamic efficiency at a gas turbine.

Acknowledgment

The authors want to express their appreciation to the Power Branch of the Office of Naval Research for support under contract No. N 00014-76-0246.

References

1 Ito, S., Goldstein, R. J., and Eckert, E. R. G., "Film Cooling of a Gas Turbine Blade," ASME, JOURNAL OF ENGINEERING FOR POWER, Vol. 100, 1978, 476.

2 Tabakoff, W., and Earley, R., "Two-Dimensional Flow Losses of a Turbine Cascade with Boundary Layer Injection," ASME Paper No. 72-GT/46, 1972.

3 Tabakoff, W., and Hamed, A., "Theoretical and Experimental Study of Flow Through Turbine Cascade with Coolant Flow Injection," AIAA Paper No. 75-843, 1975.

4 Prust, H. W., Jr., "An Analytical Study of the Effect of Coolant Flow Variables on the Kinetic Energy Output of a Cooled Turbine Blade Row," AIAA Paper No. 72-12, 1972.

5 Hartsel, J. E., "Prediction of Effects of Mass Transfer Cooling on the Blade-Row Efficiency of Turbine Airfoils," ASME Paper No. 72-11, 1972.

6 Pohlhausen, K., "Zur näherungsweisen Intergration der laminaren Grenzschicht," *Zeitschrift fuer Angewandte Mathematik und Mechnik*, Vol. 1, 1921, 252.

7 Ito, S., "Film Cooling and Aerodynamic Loss in a Gas Turbine Cascade," Ph.D. Thesis, Univ. of Minnesota, Dec. 1976.

8 Shapiro, A. H., and Hawthorne, W. R., "The Mechanics and Thermodynamics of Steady One-Dimensional Gas Flow," ASME *Journal of Applied Mechanics*, 1947, pp. A-317-A-336.

APPENDIX

Constant Pressure Mixing of a Compressible Fluid. The total pressure loss of one-dimensional flow is given by the following equation for constant pressure mixing and for constant area mixing when the effect of friction is neglected [8].

$$\frac{dp_t}{p_t} = -\frac{k}{2}\mathrm{Ma}^2\frac{dT_t}{T_t} - k\mathrm{Ma}^2\left(1 - \frac{U_2}{U_1}\cos\alpha\right)\frac{dm}{m} \tag{A1}$$

Figure A1 sketches this mixing process at constant pressure in a channel. With a small coolant flow and therefore a small change in the flow from cross section 1 to cross section 3, the above equation can be approximated by

$$\frac{p_{t1} - p_{t3}}{p_{t1}} = \frac{k}{2}\mathrm{Ma}_1^2\frac{\Delta T_t}{T_{t1}} + k\,\mathrm{Ma}_1^2\left(1 - \frac{U_2}{U_1}\cos\alpha\right)\xi \tag{A2}$$

It is evident from the above equation that the difference in the total pressure loss for a given ξ between constant area mixing and constant pressure mixing is small when the coolant injection is small so that the change of the Mach number Ma, due to injection is small for given inlet total pressure and exit pressure. The analysis, presented here for constant pressure mixing because it results in simpler relations, can therefore also be used with good approximation for constant area mixing.

The total pressure can be expressed for a compressible fluid by the equation

$$p_t = p\left(1 + \frac{k-1}{2}\mathrm{Ma}^2\right)^{k/(k-1)} \tag{A3}$$

Expanding this equation in a series and maintaining the first five terms gives

$$p_t = p + \frac{\rho U^2}{2}\left[1 + \frac{1}{4}\mathrm{Ma}^2 + \frac{2-k}{24}\mathrm{Ma}^4 + \frac{(2-k)(3-2k)}{192}\mathrm{Ma}^6\right] \tag{A4}$$

For constant pressure mixing, p_1 is equal to p_3. The pressure loss coefficient can therefore be written as

$$\bar{\lambda}_m = \frac{p_{t1} - p_{t3}}{p_{t1} - p_1} \tag{A5}$$

Using equation (A4), and the abbreviation

$$Y_i = 1 + \frac{1}{4}\mathrm{Ma}_i^2 + \frac{2-k_i}{24}\mathrm{Ma}_i^4 + \frac{(2-k_i)(3-2k_i)}{192}\mathrm{Ma}_i^6 \tag{A6}$$

one obtains

$$\bar{\lambda}_m = 1 - \frac{\rho_3 U_3^2 Y_3}{\rho_1 U_1^2 Y_1} \tag{A7}$$

where the subscript i in equation (A6) has to be replaced by 1 and 3, respectively, in equation (A7).

The terms Ma_3, k_3, U_3, T_3, and R_3 are unknown in the above equation. They are obtained from the following relations.

Continuity equation

$$\rho_1 U_1 A_1 + \rho_2 U_2 A_2 = \rho_3 U_3 A_3 \tag{A8}$$

Momentum equation

$$\rho_3 U_3^2 A_3 - \rho_1 U_1^2 A_1 - \rho_2 U_2^2 A_2 \cos\alpha = 0 \tag{A9}$$

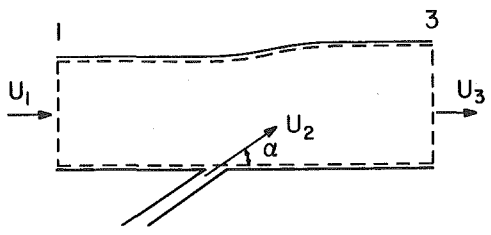

Fig. A1 Sketch of flow channel for constant pressure mixing

Energy equation

$$\int_{T_r}^{T_3} c_{p3}dT = -\frac{U_3^2}{2} + \frac{1}{1+\xi}\left(\int_{T_r}^{T_1} c_{p1}dT + \frac{U_1^2}{2}\right) + \frac{\xi}{1+\xi}\left(\int_{T_r}^{T_2} c_{p2}dT + \frac{U_2^2}{2}\right) \quad \text{(A10)}$$

in which T_r denotes a reference temperature. The velocity U_3 is obtained from equations (A8) and (A9)

$$U_3 = \frac{U_1 + \xi U_2 \cos\alpha}{1+\xi} \quad \text{(A11)}$$

Equation (A10) is used to determine the temperature T_3. From the equation of state results

$$\frac{\rho_3}{\rho_1} = \frac{R_1 T_1}{R_3 T_3}, \frac{\rho_1}{\rho_2} = \frac{R_2 T_2}{R_1 T_1} \quad \text{(A12)}$$

The equations for c_{p3}, R_3, k_1 and Ma_3 are

$$c_{p3}(T) = \frac{c_{p1}(T) + \xi c_{p2}(T)}{1+\xi} \quad \text{(A13)}$$

$$R_3 = \frac{R_1 + \xi R_2}{1+\xi} \quad \text{(A14)}$$

$$k = \frac{c_p(T)}{c_p(T) - R} \quad \text{(A15)}$$

$$\mathrm{Ma}_3^2 = \frac{U_3^2}{k_3(T) R_3 T_3} \quad \text{(A16)}$$

Using the second equation (A12) and equation (A11), one obtains

$$\frac{U_3}{U_1} = \frac{1 + \xi^2 \dfrac{R_2 T_2 A_1}{R_1 T_1 A_2}\cos\alpha}{1+\xi} \quad \text{(A17)}$$

Equations (A13), (A14), and (A15) result in

$$k_3(T_3) = \frac{c_{p1}(T_3) + \xi c_{p2}(T_3)}{c_{p1}(T_3) + \xi c_{p2}(T_3) - (R_1 + \xi R_2)} \quad \text{(A18)}$$

The Mach number at the blade row exit can be obtained by substituting the terms obtained above into the equation

$$\frac{\mathrm{Ma}_3}{\mathrm{Ma}_1} = \frac{U_3}{U_1}\sqrt{\frac{k_1 R_1 T_1}{k_3 R_3 T_3}} \quad \text{(A19)}$$

The pressure loss coefficient $\bar{\lambda}$ is finally obtained from equation (A7)

For incompressible flow, the terms with a Mach number in equation (A6) can be neglected. Therefore, substituting equation (A10) into equation (A7)

$$\bar{\lambda}_m = 1 - \frac{\rho_3}{\rho_1}\left(\frac{1 + \xi\dfrac{U_2}{U_1}\cos\alpha}{1+\xi}\right)^2 \quad \text{(A20)}$$

where

$$\frac{\rho_3}{\rho_1} = \frac{R_1 T_1}{R_3 T_3} \quad \text{(A21)}$$

in which the ratio R_1/R_3 is obtained from equation (A14). For temperature independent specific heat, the temperature T_3 is given from equations (A10) and (A13), where the kinetic energy terms may be neglected:

$$T_3 = \frac{c_{p1} T_1 + \xi c_{p2} T_2}{c_{p1} + \xi c_{p2}} \quad \text{(A22)}$$

Printed in U. S. A.

K. Bammert
Professor.

H. Beelte
Research Assistant.

Institute for Turbomachinery,
University of Hannover,
Hannover, Germany

Investigations of an Axial Flow Compressor with Tandem Cascades

In axial flow compressors with high degrees of reaction the transfer of energy can be increased by using suitable tandem cascade arrangements. The application of multistage tandem cascade systems therefore allows savings in constructional length and blading and thus a very compact compressor design. Therefore a four-stage tandem cascade compressor with 100 percent reaction was built. To determine the operating behavior of the machine, the compressor characteristic on speed control was measured. For optimization and further development of this compressor the characteristics on adjustment of all stator blade rows and speed control were measured. To allow the behavior of the stator blade rows and tandem cascade wheels to be assessed, the channel flow in the axial gaps behind selected wheels was measured. The tandem cascade compressor, its layout and the results of experimental investigations are presented and discussed.

Introduction

The volume flows to be handled by stationary axial compressors are steadily increasing. This is true for all gaseous working media. In particular the handling of light gases, such as helium, leads to larger sizes of the turbo set [1]. However, for economical reasons and in the interest of operational safety and simple manufacture and construction, the dimensions of the turbo machines should be kept as small as possible. This can only be achieved by increasing the degree of power conversion of these machines referred to the volume of construction.

In the case of axial compressors, compact designs are obtained by increasing the suction capacity and the stage pressure ratio [2]. The stage pressure ratio can be raised by increasing the degree of deflection in the cascade. Since there are relatively close limits to the aerodynamic loading of a retarding single cascade, the desired increased deflection has to be obtained by providing tandem cascades.

Relatively high degrees of reaction allow tandem cascade arrangements to be favorably used in multistage axial compressors. In these, then, the pressure rise of the stage is considerably increased by providing tandem rotor blade cascades and single stator blade cascades (Fig. 1). As compared to corresponding axial compressors with the conventional single cascade design, the use of tandem cascade stages in multistage machines allows considerable savings in length and blading and thus a very compact compressor to be built [3].

At the Institute for Turbomachinery of the University of Hannover, a multistage tandem cascade compressor was laid out and designed. It was built in cooperation with Gutehoffnungshütte Sterkrade AG (GHH). For verification of the layout of this machine suitable measurements of the characteristics and speed control were carried out. Subsequently, to facilitate the further development of this machine, characteristics on stator blade adjustment and speed control were measured. Finally, to also allow the behavior of the stator blade and rotor blade wheels in the rotating machine to be assessed with more accuracy, at certain points of the characteristic the operation was repeated and the compressor flow over the channel height in the axial gaps behind selected wheels was measured. The present paper describes the tandem cascade compressor and the relevant investigations made and gives an interpretation of the test results.

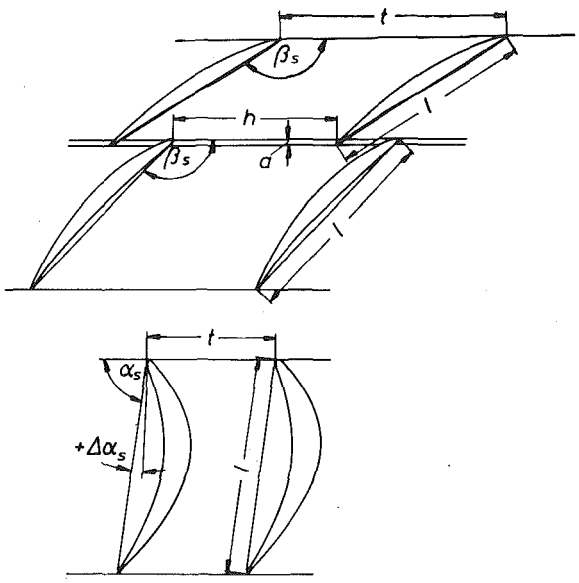

Fig. 1 Tandem cascade stage: (*a*) axial displacement, (*h*) displacement in peripheral direction, (*l*) chord length, (*t*) pitch, (α_s, β_s) stagger angle, ($\Delta\alpha_s$) stagger angle adjustment

Layout and Design of the Compressor

A tandem cascade stage with 100 percent reaction consists of the tandem cascade wheel followed by the impulse stator blade row (Fig. 1). The tandem cascade wheel consists of two retarding single cascades, 1 and 2, mounted immediately one after the other, whose arrangement relative to each other can be optimized according to [3]. In the moving part of the stage a large retardation is achieved and therefore a relatively small total retardation ratio w_2/w_1 is obtained (Fig. 2). Nevertheless the retardation ratios of the single cascades,

Contributed by the Gas Turbine Division and presented at the Gas Turbine Conference and Products Show, New Orleans, La., March 10–13, 1980 of THE AMERICAN SOCIETY OF MECHANICAL ENGINEERS. Manuscript received at ASME Headquarters December 10, 1979. Paper No. 80-GT-39.

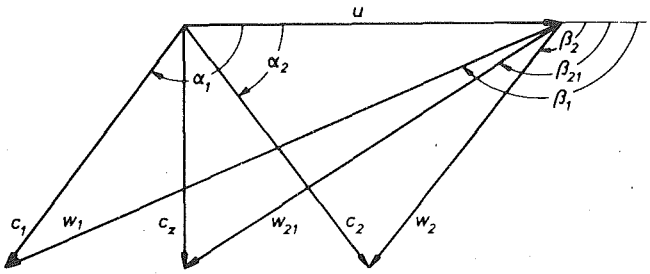

Fig. 2 Velocity triangle of a tandem cascade stage (reaction 100 percent): (c_z) axial velocity, (u) circumferential velocity, (w_1,c_2) inlet velocity, (w_2,c_1) outlet velocity, (w_{21}) outlet velocity cascade 1, inlet velocity cascade 2, (α_2, β_1) inlet angle, (α_1, β_2) outlet angle

Table 1 Design values of the tandem cascade compressor

Name		Dim.	Value
mass flow rate		kg/s	6.58
speed		rpm	11000
number of stages		-	4
hub to tip ratio		-	0.64
internal power		kW	672
total pressure	inlet	bar	1.0
total temperature	inlet	K	288.15
total pressure	outlet	bar	2.51
total temperature	outlet	K	389.9

w_{21}/w_1 of cascade 1 and w_2/w_{21} of cascade 2, of approximately 0.7, are of an order which has been applied many times in practice. The advantage of the tandem arrangement is that, thanks to the division of the high deflection between two single cascades, a new boundary layer is formed on the suction side of the second cascade which can overcome the pressure rise more easily. The stator blade impulse wheel has a deflection from c_2 to c_1, which is relatively high for a compressor stage. Hence to increase the energy transfer by say 100 percent through application of a tandem stage, instead of a single stage, it is necessary to increase the aerodynamic load of the impulse cascade.

The compressor developed on the basis of the described stage arrangement operates with a free vortex blading and a reaction of 100 percent in the tandem cascade stages. Thermodynamically the compressor was laid out based on the mean stream line theory using the documents as per [4]. The layout data are shown in Table 1. The channel dimensions and the arrangement of stages with the appertaining velocity triangles can be seen from Fig. 3. The compression starts with a single cascade stage followed by three tandem cascade stages and an outlet rotor wheel. With the velocity plans chosen here for the tandem arrangement no stator blades are required at the inlet and outlet. Instead of these one can install at the blading inlet the cascade 2 of the tandem wheel as inlet rotor wheel and at the outlet the cascade 1 as outlet rotor wheel. With this arrangement the axial inlet and outlet flow at the rotor ends fits the blading in the design point. In addition the length of the machine is reduced and manufacture is rationalized since now the homogeneous blading only consists of two rotor blade cascades of the tandem wheel and the stator blade row.

By application of a three-dimensional method as per [5] and using the data of Table 1 and the corresponding channel contour, the compressible flow in the tandem cascade test compressor was calculated. Taking into account the radial equilibrium, the method yielded the distribution of flow over the channel height in the bladeless axial gap behind the wheels. The distribution figures served as bases for the detailed theoretical and experimental developments of the tandem cascade rotor blade and the stator blade wheels described in [3] and [6]. For the rotor blades suitable NACA profiles of the series 65 were chosen in [3]. The stator blade row was newly designed as an impulse cascade in [6]. With 85 deg at the hub decreasing to 65 deg at the stator blade carrier it has a deflection effect which is relatively high for compressor blade profiles.

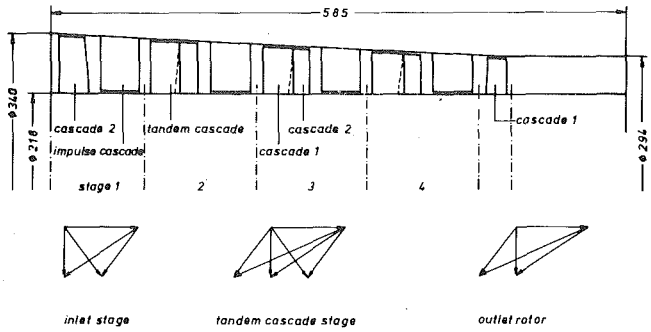

Fig. 3 Channel contour and arrangement of stages

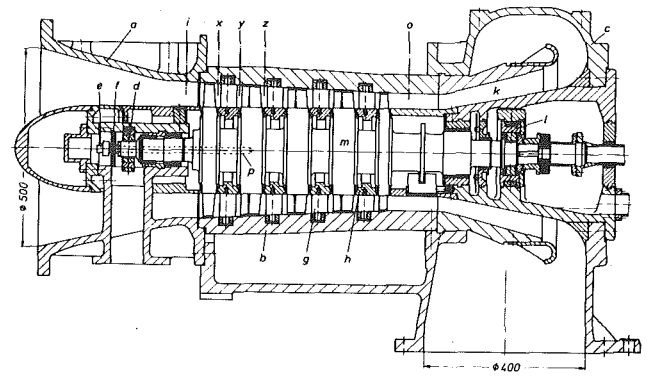

Fig. 4 Tandem cascade compressor: (a) inlet casing, (b) stator blade carrier, (c) outlet casing, (d) journal bearing, (e) co-rotational transmitter, (f) receiving antenna, (g) stator blade, (h) shroud, (k) diffuser, (l) double thrust bearing, (m) rotor with rotor blades, (p) boring for transmitter line, (i, x, y, z, o) measuring plane for scanning

Figure 4 shows a longitudinal section of the built tandem cascade compressor. This machine consists of three axially separable parts with horizontal partition joint, the inlet casing (a), the stator blade carrier (b) and the outlet casing (c). The inlet casing holds the journal bearing (d). At the free shaft end the co-rotational single-channel transmitter (e) of the telemetering system for monitoring the rotor blade vibrations is fixed. The receiving antenna (f) installed in the inlet part encloses the transmitter. The stator blades (g) are inserted in axially and radially divided rings in the stator blade carrier and fixed in their stagger angle position. To reduce clearance losses the stator blades are provided with shrouds (h) in the rotor hub area.

In the top part of the inlet casing and in the stator blade carrier, in planes i and o, probe bores for measuring the characteristics are located before and behind the blading. After completion of the measurements, for the subsequent wheel scannings radial bores were also provided in planes x and z and a longitudinal groove was provided in peripheral direction in plane y, over two blade pitches, for fitting measuring probes.

Nomenclature

A = area, m^2
$\dot{m}$ = mass flow rate, kg/s
n = speed, rpm
p = pressure, bar
P = power, kW
u = circumferential velocity, m/s
$\dot{V}$ = volume flow rate, m^3/s
Δh = enthalpy rise, kJ/kg
η = efficiency, percent
π = pressure ratio
φ = flow coefficient
ψ = pressure coefficient

Subscripts

h = hub, inner
i = inlet, in front of the blading
o = outlet, behind the blading
s = isentropic
tot = total
w = wall, outer

Table 2 Measured characteristics and scannings

Type	Stagger angle change $\Delta\alpha_s$ of stator blade No. 1	2	3	4	Speed ratio n/n_d	Scanning at speed ratio
I	0^o	0^o	0^o	0^o	0.6	n/n_d = 0.5, 0.83, 1.0
II	4^o	4^o	4^o	4^o	0.5, 0.7	n/n_d = 1.0
III	8^o	8^o	8^o	8^o	0.83, 0.9	n/n_d = 1.0
IV	8^o	8^o	4^o	4^o	1.0	no
V	-4^o	-4^o	-4^o	-4^o		no

The blading and the measured section with constant channel height are followed by the diffuser (k). The inner shell of the diffuser is fixed in the outlet casing and supports the undivided fixed bearing (l). The diffuser leads the compressed gas into the curved space of the outlet casing, which is connected with the nozzle of the discharge pipe. The rotor (m) is machined from the solid and has a constant diameter at the blade root. From the inlet side a central bore (p) in the rotor extends to the first tandem cascade to accomodate the line between strain gauge and transmitter. The photo of Fig. 5 shows the compressor rotor placed in the casing. One can clearly see the blading arrangement starting on the left with the inlet wheel, followed by three tandem cascade wheels and the outlet wheel, and also the compact tandem arrangement with the gap between cascades 1 and 2.

Test Program

The test program was divided into two successive portions, measurement of the characteristics and wheel scannings. It was started with verification of the design point and measurement of the nominal characteristic field on speed control. Subsequently, characteristic fields were measured also on stator blade adjustment combined with speed control. A survey of the measured characteristics, their designations and the various adjustments made is given in Table 2. The speed ratios

$$n/n_d = 0.5, 0.7, 0.83, 0.9 \text{ and } 1.0,$$

and for the nominal characteristic I also $n/n_d = 0.6$, were adjusted. n_d is according to Table 1 the nominal speed of 11,000 rpm.

The stagger angles of the stator blades could be changed by simple design changes to their connection in the stator blade carrier but only with the machine uncovered. Therefore the angle variations $\Delta\alpha_s = \alpha_s - \alpha_{s,d}$ (Fig. 1) were limited with regard to their extent and stepping. $\Delta\alpha_{s,d}$ is the designed stagger angle. However, with a stepping of $\Delta\alpha_s = \pm 4$ deg and a maximum adjustment of $\Delta\alpha_s = 8$ deg they give a good survey of this possibility of compressor optimization. Altogether four characteristic fields with different stator blade adjustments were measured (Table 2). For the three characteristics II, III and IV the stagger angles were increased according to the counting direction of Fig. 1 in the direction of the circumferential velocity. These adjustments are counted positively and are called positive prerotation adjustments. With the fourth variant, V, the stagger angle was reduced. This adjustment is counted negatively and called negative prerotation adjustment.

The testing facility and the appertaining measuring tap arrangement are described in [2, 7]. During the test the measuring points were adjusted on a characteristic curve from the throttling line to the surge line by gradual closing of a throttle valve at the discharge end. The throttling line corresponded to the resistance characteristic of the machine with the throttle valve fully opened. Operation at the surge limit was performed at all speeds with the exclusion of the nominal speed.

At each point the values for calculation of the mass flow rate, power requirement, pressure ratio and efficiency were measured. The quantities required for graphical representation were obtained by radial flow scannings at the blading inlet and outlet in planes i and o (Fig. 4). These measurements were taken with a probe which allowed the total pressure, the static pressure, the temperature and the angle of flow to be determined at the same time. In addition through bores in the stator blade carrier after each wheel, in the diffuser and at the outlet nozzle the wall pressures in the compressor could be measured.

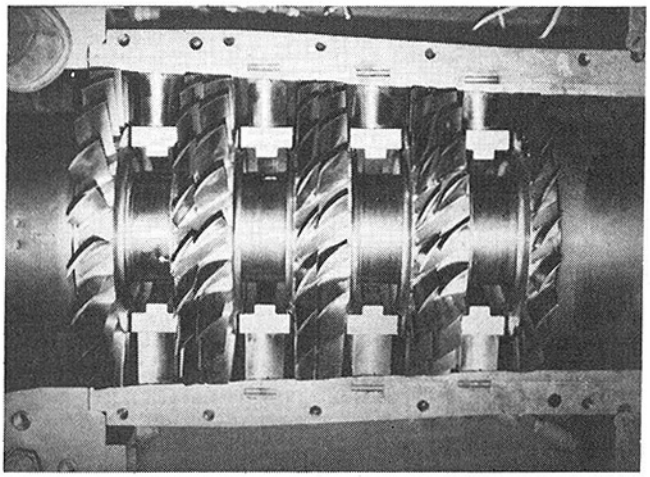

Fig. 5 View of opened tandem cascade compressor

Apart from the results of the characteristic measurements, knowledge of the local flow data occurring during operation of the machine before and after the rotor and stator blade wheels is of particular interest. Therefore the machine was operated again at various points of the previously measured characteristics I, II and III for speed control and stator blade adjustment (Table 2) and detailed distribution measurements were taken. As before, the flow was measured at the blading inlet and outlet, in planes i and o, radially between the hub and tip diameter. These measurements were supplemented now by radial scannings in plane x after the inlet wheel and plane z after the first tandem cascade wheel and by radial and peripheral distribution measurements over one pitch in plane y after the first stator blade row (Fig. 4). For these scannings the channel was divided in all planes by 10 measuring radii, in plane i by 11 radii. At the stator blade carrier and hub a closer spacing was chosen than in the middle of the channel.

Measuring Results

Since the tandem cascade compressor handled atmospheric air, the values found under varying suction conditions had to be converted to a uniform reference state by application of the laws of similarity. As reference state the design values at the inlet were chosen. The quantities describing the characteristic field were formed from integral mean values of the scanned flow distributions corresponding to the measured mass distributions.

Characteristic Results in Design State. For verification of the layout the characteristic values were compared (Fig. 6). The related pressure coefficient ψ/ψ_d and the related total efficiency η/η_d were

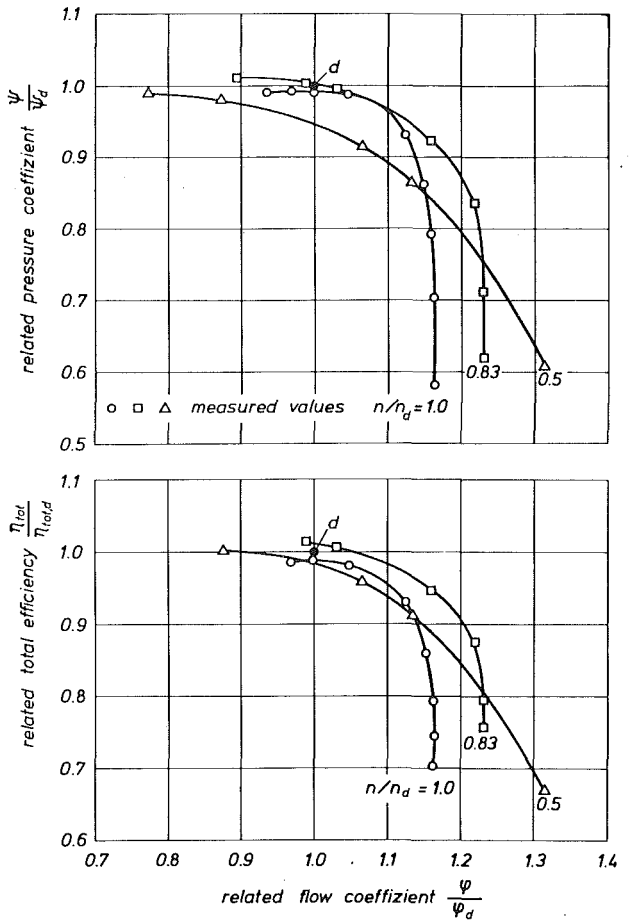

Fig. 6 Related pressure coefficient and related total efficiency as a function of the related flow coefficient: (*d*) design point, (*n*/*n*$_d$) speed ratio

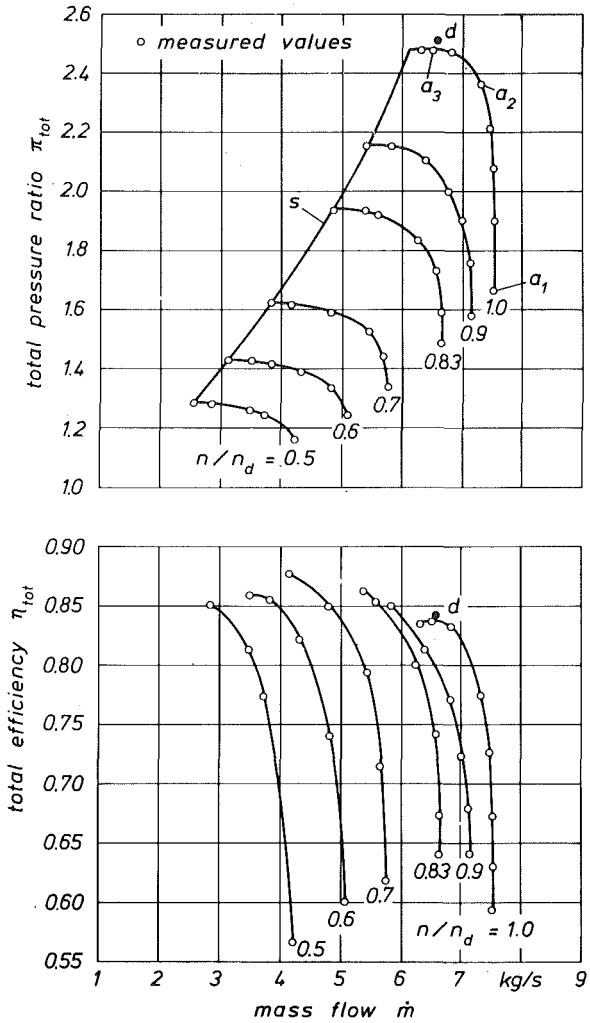

Fig. 7 Characteristics for the tandem cascade compressor: (*d*) design point, (*s*) surge line, (*n*/*n*$_d$) speed ratio

plotted against the related flow coefficient φ/φ_d. Selected for this comparison were the speed ratios $n/n_d = 0.5$, 0.83 and 1.0. The pressure coefficient characterizes according to equation

$$\psi = 2 \cdot \Delta h_{s,\mathrm{tot}}/u^2 \tag{1}$$

the total isentropic enthalpy rise $\Delta h_{s,\mathrm{tot}}$ of the machine which is made nondimensional with the square of the circumferential velocity u. The total efficiency

$$\eta_{\mathrm{tot}} = \dot{m} \cdot \Delta h_{s,\mathrm{tot}}/P \tag{2}$$

is calculated with the aid of the mass flow rate $\dot{m}$ and the compressor power P. P corresponds to the difference between the driving power and the mechanical power losses in a gearbox and in the compressor. The flow coefficient

$$\varphi = \dot{V}_{\mathrm{tot},i}/(A_i \cdot u) \tag{3}$$

is the flow coefficient in the inlet plane i, which is calculated from the total volume $V_{\mathrm{tot},i}$ and the cross-sectional area A_i. d characterizes the design values to which relations were established too. ψ and η_{tot} designate the work of the blading from the inlet plane i to the outlet plane o (Fig. 4).

In Fig. 6 the deviations between measurement and design are about 1 percent in the case of the pressure coefficient and approximately 1.1 percentage points for the total efficiency. Taking into account that the compressor under consideration is an unusual, highly loaded machine with a firstly developed blading and stage arrangement, it may be said that the design values show good correspondence with the measuring results. It is true that the design values are not achieved throughout the stable nominal characteristic range, but at high pressure coefficients in the direction of partial load with $\varphi/\varphi_d < 1$ a very flat characteristic curve is measured. This has its cause in the high degree of deflection in the tandem cascade stages.

When the compressor is running in the overload range with $\varphi/\varphi_d > 1$ the nominal characteristic and the appertaining efficiency drop very quickly. In the end there is only a pressure drop with no increase in mass flow. The reason for this is that the influence of the Mach number increases with increasing mass flow. Because of the high degree of reaction due to the high deflection effect of the stator blades, and still low temperatures, the critical Mach number at which losses start to increase, is first reached in cascade 1 of the first tandem cascade wheel. This leads to increasingly faulty inlet flow and relative volume increase in the succeeding stages, whose operating points are shifted more and more on their characteristic curves into the overload range. These stages then work under increasingly unfavorable conditions near the throttling line. If the speed is reduced the influence of the Mach number decreases. For example, at 0.83·n_d higher pressure coefficients and in particular higher efficiencies are measured. Furthermore the drop in the characteristic line starts later. On further reduction of the speed the influence of the Mach number disappears and the curves becomes relatively flat in the entire range, such as with $n/n_d = 0.5$. However, now the compressor flow no longer suits the channel so that the design values are only achieved at a high degree of throttling. The working range of the compressor between the limits of the characteristic field increases with decreasing speed.

These curve forms, depending on the speed, are also found in the characteristic field of the tandem cascade compressor (Fig. 7). Here the total pressure ratio π_{tot} and the total efficiency η_{tot} are shown as functions of the reduced mass flow measured at the orifice. The total pressure ratio

$$\pi_{\mathrm{tot}} = P_{\mathrm{tot},o}/P_{\mathrm{tot},i} \tag{4}$$

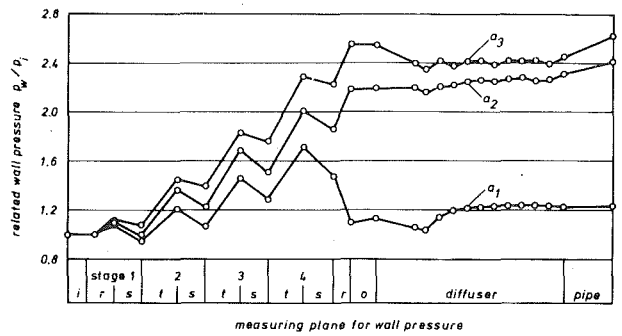

Fig. 8 Wall pressure in the tandem cascade compressor at design speed: (a_1, a_2, a_3) see Fig. 7, (*i*) inlet, (*o*) outlet, (*r*) single cascade rotor blade, (*s*) stator blade, (*t*) tandem cascade rotor blade

is the mean value of the total pressures p_{tot} in planes i and o (Fig. 4) and characterizes the pressure rise of the blading.

At nominal flow the compressor develops a total pressure ratio of 2.48 at a total efficiency of 83.7 percent. The measured surge points result in a slightly curved line as the surge line s, which cuts the nominal characteristic line relatively close to the design poind d. As a result the operating range of high pressure ratio and high efficiency is restricted here. The reason for this are the high degrees of energy transfer of the tandem cascade stages. The nominal characteristic reaches its maximum shortly after passing the design point. Hence compared to the design values the nominal characteristic of this compressor has no mass flow and pressure reserves. With decreasing speed the surge line is shifted into the part load range.

Because of the small stage outlet angle β_2 which was chosen, the maximum efficiency is measured on all characteristics in the vicinity of the surge line [8]. The ranges of highest efficiency are thus relatively close to the surge line. Owing to the decreasing influence of the Mach number the highest characteristic efficiency of 88 percent is reached at $0.7 \cdot n_d$.

In the case of axial compressors the static pressure generally does not change very much over the channel height. So the wall pressures measured at the stator blade carrier, diffuser and discharge nozzle are very suitable for verifying the wheel and stage behavior and the machine tuning under different operating conditions. For this purpose the wall pressure p_w referred to the static pressure p_i of the inlet plane i was plotted against the distance assigned to the particular measuring planes (Fig. 8). Three measuring points of the nominal characteristic were selected. a_1 is at the throttling line, a_2 is the point at medium throttling, and a_3 corresponds to the design point (Figs. 7 and 8).

The wall pressure curve of a_3 shows that in all of the four stator blade rows designed as impulse cascades the static pressure is markedly reduced. This effect increases with increasing mass flow from a_3 to a_1. The reasons for this are inevitable wheel losses and an inlet flow concentrated too much on the suction side already in the design point. The tandem cascade wheels develop the wall pressure at almost all measuring points of a characteristic relatively uniformly and more intensively than the single cascade wheels at the inlet and outlet of the blading. Particularly interesting is the behavior of the outlet rotor. At points a_2 and a_3 of the throttled compressor it works as a retarding wheel as expected. However, with a_1 at the throttling line with the low back pressure this wheel reduces the pressure very much. This phenomenon is due to the poor adaptability of the tandem cascade stages to pressure and mass flow variations. Their flat stage characteristics, which hardly allow pressure control, have the effect that the compressor at point a_1 develops a pressure ratio of approximately 1.7 before the flow enters the fourth stator blade row. However, the consumer, which begins at the outlet nozzle, only requires 1.2 times the inlet pressure. To this level now the excessively compressed gas has to be expanded by the outlet wheel. During this expansion very high velocities are produced at the wheel outlet, which cause high losses. The steep pressure and efficiency drop observed in the characteristic field in the vicinity of the throttling line is still intensified by this effect at the outlet wheel.

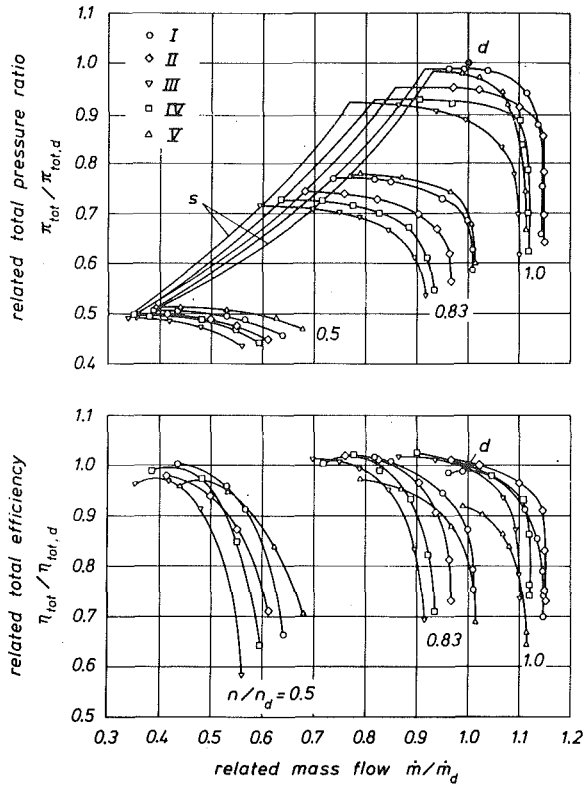

Fig. 9 Comparison of measured characteristics: (*d*) design point, (n/n_d) speed ratio, (I, II) see Table 2 (*s*), surge line

Characteristic Results on Stator Blade Control. Adjustment of the stagger angle of a stator blade row for deviation from its layout leads to a changed channel geometry in this wheel and to changes in the stage behavior, which depend on the layout data and the direction of adjustment. By an adjustment for positive prerotation (Fig. 1, Table 2) the operating point of a stage is changed to smaller mass flows and smaller pressure rises, the degree of reaction is reduced and a steeper stage characteristic is caused. Adjustment for negative prerotation has the opposite effect.

The influence of stator blade adjustment on the work of the tandem cascade compressor is shown in Fig. 9, where all measured characteristics are entered. The variables π_{tot}, η_{tot} and $\dot{m}$ were referred to their design values. In order to make the superimposed characteristics more transparent, the curves of only three speed ratios were selected for the purpose of representation.

With increasing positive adjustment from the design case I via the 4 deg adjustment at II and the 8 deg and 4 deg adjustment at IV, to the 8 deg adjustment at III (Table 2), the characteristic moves away from the design point d and the operating range is shifted into the part-load range towards smaller flow rates. The pertinent surge line too is shifted in this direction, while the specific throttling line of the machine undergoes hardly any change. Since a positive adjustment reduces the inlet velocity of the rotor wheel and thus the influence of the Mach number, the steep drop in the high-speed curves which occurs in the overload range begins later and later. The ranges of relatively good and almost constant pressure ratio therefore increase here from I to IV. The characteristics themselves hardly become any steeper. However, at nominal speed and high-pressure ratios the efficiency is increased by the positive adjustment compared to I, by 1 to 2 percentage points to values above 85 percent. This is also mainly due to the decrease in the inlet flow Mach numbers, for with smaller speed ratios the tendency is reversed in favor of I. The −4 deg negative adjustment of V deteriorates the operating behavior of the compressor in every respect. The characteristic range is markedly restricted by the location of the characteristic curves and by early approach to the surge line. Moreover, the lowest efficiencies are measured here.

Of all variants measured, II with the positive adjustment of $\Delta\alpha_s = 4$ deg in all stages is doubtless the most favorable. The compressor

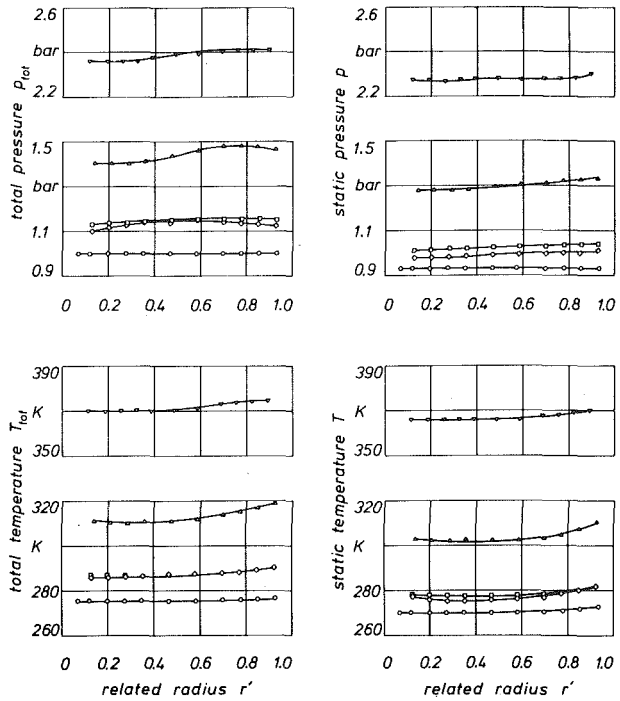

Fig. 10 Radial distribution of pressure and temperature: (○) measuring plane *i* for scanning, (□) measuring plane *x* for scanning, (◇) measuring plane *y* for scanning, (△) measuring plane *z* for scanning, (▽) measuring plane *o* for scanning

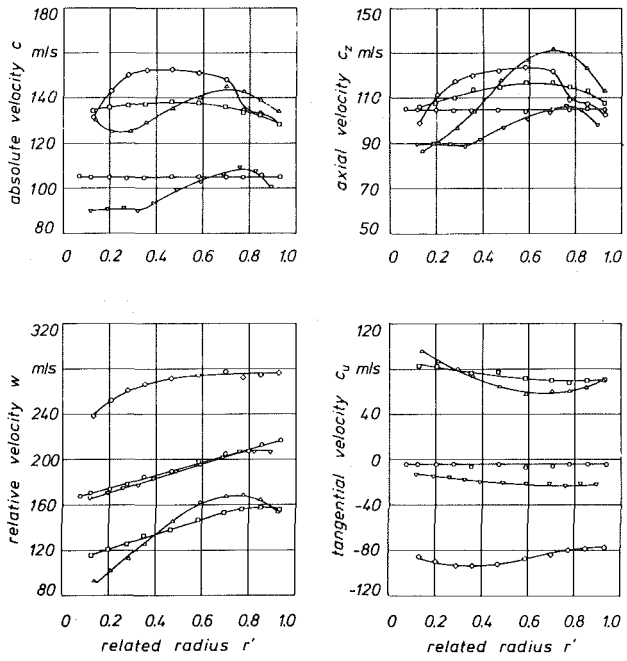

Fig. 11 Radial distribution of velocity—Legend see Fig. 10

here achieves—with an increased operating range compared to I—still high pressure ratios and good, even partly improved, efficiencies. A larger positive adjustment causes the pressure ratio to drop too much; a negative adjustment is out of the question.

Wheel Scannings. In order to get an insight into the flow distributions at nominal conditions in the five measuring planes *i*, *x*, *y*, *z* and *o* (Fig. 4) for the wheel scannings the operation was repeated also at point a_3 of the nominal characteristic field. At a_3 the compressor handled almost exactly the nominal mass flow on the curve with $n/n_d = 1$ (Fig. 7). To analyze the compressor flow at this measuring point, in the following two pictures the pressure, temperature and velocity curves were plotted against the radius r' referred to the channel height according to equation

$$r' = \frac{r - r_h}{r_w - r_h} \tag{5}$$

wherein r is the particular measuring radius adjusted, r_h the hub radius and r_w the wall radius.

Fig. 10 shows the distribution of the total pressure p_{tot} (r'), the static pressure $p(r')$, the total temperature T_{tot} (r') and the static temperature $T(r')$. The symbols pertaining to the measuring planes in Fig. 10 also mark each individual radial measuring value. In plane *y*, in which the flow at the outlet of a stator blade was measured over one pitch in peripheral and radial direction, the mean peripheral value per radius had to be determined.

The radial distribution of the total pressure is almost constant in planes *i* and *x* before and after the inlet rotor wheel and at *y*. In the tandem cascade wheel from *y* to *z* however there is a marked rise in total pressure in the upper channel half. This rise can also be seen in a less pronounced form at *o*. The static pressure is only constant over the channel height at *i*. At the outlet of the wheels it slightly rises toward the wall due to the centrifugal forces based on the circumferential components of the absolute velocity.

The total temperatures also rise particularly behind the tandem cascade blading at *z* and *o* above the mean radius. The constant total radial enthalpy increase of the free vortex flow which was assumed in the design is thus not fully reached. The total temperatures at *x* and *y* before and after the stator blade row must be constant. The slight deviations in Fig. 10 at the hub are within the limits of the measuring accuracy. The distributions of the static temperatures are similar to those of the total temperatures.

Fig. 11 shows the distributions of the absolute velocity $c(r')$, their components in axial and circumferential direction, $c_z(r')$ and $c_u(r')$, and the relative velocity $w(r')$ in the measuring planes.

Since the absolute and relative velocities are composed of the velocity components, only $c_u(r')$ and $c_z(r')$ are considered here.

The circumferential component $c_u(r')$ of the absolute velocity has a distribution which virtually corresponds to a free vortex flow. Only in plane *z* after the tandem cascade wheel it slightly rises towards the wall, after a minimum at $r' = 0.7$. At the blading inlet and outlet the axial inlet and outlet flow assumed in the design, i.e., $c_u(r') = 0$, is not fully established. Particularly at *o* the air leaves the blading in the vicinity of the design point with a negative prerotation (a_3 in Fig. 7), which slightly impedes the pressure buildup by the outlet wheel.

The most remarkable distributions have the axial component $c_z(r')$. In the layout an almost constant c_z value both over the channel height and in axial direction was assumed, as shown at *i* at the inlet. However, the axial velocity already rises parabolically over the channel height when the air flows through the inlet wheel from *i* to *x*. The form of the increase indicates a reduction of cross-sectional area by wall boundary layers. Furthermore this wheel has not the optimum setting according to the analyses of its outlet angle distributions. This increase in velocity in the inlet wheel causes a changing of the incident angle of the first stator blades from three to four degrees over the channel height, directed to the suction side. This in turn cause an axial acceleration of the air in a middle of the channel. The wall flow however is decelerated very much by friction. However, the greatest changes in c_z over the radius are measured behind the tandem cascade wheel. Here, in plane *z*, the axial velocity decreases very much toward the hub from a pronounced maximum before the stator blade carrier. This leads to excessive velocities and localized increased mass flow rates in the upper channel half and also contributes to the intensified pressure rise observed in this area as per Fig. 10. At the outlet at *o* the c_z distribution is of a similar nature. Hence the air will be displaced in all tandem cascade wheels in outward direction toward the stator blade carrier. As the analyses of the outlet flow angle and efficiency distributions have shown, this displacement has its cause in the fact that the deflection in the hub area of the tandem cascade wheel is excessive in relation to the inlet flow velocity. The tandem cascade is subjected to localized excessive loads so that at the blade root great secondary and wall influences may become effective which in the first approximation are proportional to the cascade loading. The results of this flow

displacement are relatively high-pressure rises and good wheel efficiencies in the upper channel half and the contrary in the lower channel half. Furthermore the displacement leads to faulty flow to the succeeding wheels and has an unfavorable influence on the work of the rear part of the blading.

Summary

In this paper the concept and design of a multistage tandem cascade compressor have been presented. Characteristic measurements on this axial compressor at the rated operating conditions have shown that the layout is in good correspondence with the test results. However the characteristic field at design conditions of all wheels was unfavorably influenced by certain phenomena. For example, at high speeds the part load range was, relatively early, limited by the surge line, while under overload conditions the pressure ratios and efficiencies were reduced by an increasing influence of the Mach number. The ranges of optimum efficiency were close to the surge line.

These influences could be reduced by a suitable stator blade adjustment, without giving up the idea of developing a compact and economical compressor design. The optimum stagger angle increase proved to be 4 deg in all stator blade rows. With this adjustment the tandem cascade compressor still achieved high-pressure ratios and good efficiencies in a wider characteristic field compared to the layout.

The results of the characteristic measurements were supplemented and substantiated by flow measurements during machine operation in the axial gaps behind selected rotor and stator blade wheels. This allowed assessment of the work performed by the measured wheels under rated operating conditions and on speed control and stator blade adjustment.

The many machine tests have proved that operation with the tandem cascade compressor does not raise any problems. Moreover these tests have indicated many possibilities of improvement and further development.

References

1 Bammert, K., and Twardziok, W., "Kernkraftwerke mit Heliumturbinen für großе Leistungen," *Atomkernenergie* 12, No. 9/10, 1967, pp. 305–326.

2 Bammert, K., and Turanskyj, L., "Untersuchungen an einem Axialverdichter mit kleinem Nabenverhältnis und hoher Stufenbelastung," *Konstruktion* 24, 1972, pp. 121–126.

3 Bammert, K., and Staude, R., "Optimization for Rotor Blades of Tandem Design for Axial Flow Compressors," ASME Paper No. 79-GT-125, 1979.

4 Traupel, W., *Thermische Turbomaschinen,* Vol. 1, Springer-Verlag, 1966.

5 Bammert, K., and Fiedler, K., "Die Strömung in axialen Turbomaschinen," Ing.-Archiv 33, No. 1964, pp. 322–329.

6 Bammert, K., and Ahmadi, B., "Investigations on Impulse Blade Cascades with Medium Deflection," ASME Paper No. 78-GT-12, 1978.

7 Beelte, H., "Untersuchungen an einem Tandemgitterverdichter," Diss. Uni. Hannover, 1979.

8 Horlock, J. H., *Axialkompressoren,* Verlag G. Braun, Karlsruhe.

K. Bammert
Professor,
Institute for Turbomachinery,
University of Hannover, Germany

H. Sandstede
Dr.-Ing.,
Gutehoffnungshütte Sterkrade AG,
Oberhausen, Germany,
formerly Research Assistant at the Institute for Turbomachinery

Measurements of the Boundary Layer Development along a Turbine Blade with Rough Surfaces

During the operation of turbines the surfaces of the blades are roughened by corrosion, erosion and deposits. The generated roughness is usually greater than that produced by manufacture. The quality of the blade surfaces determines the losses of energy conversion in turbine cascades to a great extent. The loss coefficient can be found theoretically by a boundary layer calculation. For rough surfaces there are no boundary layer measurements along the profiles of a turbine cascade. Therefore in a cascade wind tunnel measurements of the boundary layer development were carried out. The chord length of the blades was 175 mm. The cascade represented a section through the stator blades of a 50 percent reaction gas turbine. For smooth surfaces and three different roughnesses up to $3.3 \cdot 10^{-3}$ *(equivalent sand roughness related to chord length) the boundary layers were measured. The momentum thickness is up to three times as great as that on smooth surfaces. Especially in regions with decelerated flow the effects of roughness are high. A rough surface causes a rise of the friction factor and a shift of the transition of laminar to turbulent flow. The results of the measurements are shown. Correction factors are worked out to get good agreement between measurement and calculation according to the Truckenbrodt theory.*

Introduction

Efficiency and operational behavior of a fluid flow machine are influenced to a high degree by the surface finish of the blading. Small flow losses necessitate certain surface finish qualities which can sometimes be realized only at high fabricational expense. During operation, however, the blading surface is impaired and changed by soiling, erosion and corrosion [1, 2]. The surfaces thus brought about very often cause a considerable loss in efficiency and compressor map range [3–5]. Since the characteristic cascade values of blades with a rough surface which are required for the calculation of these influences are very rarely available from measurements, the cascade loss values are usually determined theoretically.

The theoretical methods are based on a boundary layer calculation for which certain factors have to be assumed, such as the position of the transition point from laminar to turbulent flow, the magnitude of the resistance coefficient, the shape of the velocity profile, or the kind of generation and dissipation of turbulences. For the purpose of comparison and evaluation, measurements were carried out for clarification of the flow around rough acceleration cascades. For this, the boundary layer along the contour of rough turbine blades was measured in a two-dimensional cascade wind tunnel and the pressure distribution around the blades was determined.

Cascade Wind Tunnel

The wind tunnel is operated in suction service. The cascade used has an inlet cross-section of 0.51 m^2. The air mass flow amounts to about 11 kg/s and can be varied by throttling. The inlet flow velocity upstream the cascade just about reaches 20 m/s, resulting in an outlet flow velocity of approx. 50 m/s, a Reynolds' number of $5.6 \cdot 10^5$, and a Mach number of 0.14. The degree of turbulence in the intake is 2 percent.

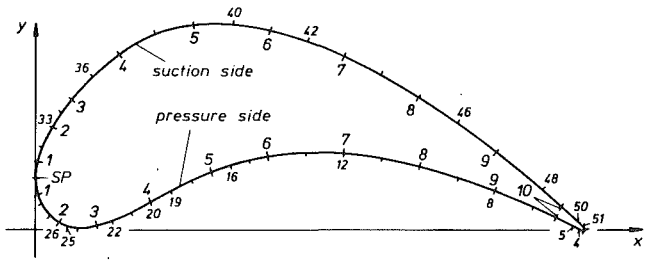

Fig. 1 Profile: 4 . . . 51 profile coordinates; 1 . . . 10 pressure tappings; *SP* stagnation point

The test cascade is made up from 9 blades with a height, H, of 530 mm and a profile chord length, l, of 175 mm. At a pitch ratio, t/l, of 0.685 the pitch, t, is 119.875 mm. The stagger angle, β_S, is 56.5 deg. The blades correspond to a guide blade mean section of a gas turbine with 50 percent reaction. Fig. 1 shows the profile as well as the positions of the measuring points for boundary-layer scanning and of the pressure tappings. The two central blades of the cascade are provided with ten pressure tappings each at the pressure and suction sides. These tappings are arranged at half the blade height and serve for measuring the pressure and velocity distribution around the profile.

Contributed by the Gas Turbine Division and presented at the Gas Turbine Conference and Products Show, New Orleans, La., March 10–13, 1980 of THE AMERICAN SOCIETY OF MECHANICAL ENGINEERS. Manuscript received at ASME Headquarters December 10, 1979. Paper No. 80-GT-40.

The blades were produced by casting. A mould with an extremely smooth surface was treated with a parting compound to prevent the blades from sticking, and was filled with epoxy resin. Ground slate was used as filling material. The blades were strengthened by steel frames to prevent distortion and bending. The achieved surface finish of the blades was very good. With similarly made blades, a peak-to-valley height of about 1 μm was measured with a Hommel tester.

To provide an adequate thickness of the boundary layers for measurements with probes, the blades were produced with a comparatively large chord length of 175 mm, corresponding to magnification at a scale of 3 to 1 as compared to the original profile dimensions in the turbine. The boundary layers increase to the same extent so that at the trailing edge of the rough blades, boundary layer thicknesses of approx. 10 mm are brought about. The blade ratio of H/l greater than three insures two-dimensional flow in the middle of the tunnel.

Roughness

The rough surface of the profiles was produced with the aid of loose emery powder. The use of sandpaper glued to the blades was decided against as this would make the profiles unnecessarily thick. Emery powder grains are classified to the same sizes as the emery paper for which they are used. The size of the grains is defined by an emery grade number which stands for the number of meshes counted over a length of one inch of a screen which just still permits the grains to fall through. The test screens are standardized, in the German standard DIN 4188. A higher emery grade number thus means a smaller grain size and consequently a smoother surface than a lower grade number.

In addition to the peak-to-valley height, both the shape and distribution of the roughness elements have an effect on the flow conditions. Not the absolute peak-to-valley height of roughness is therefore used as a measure for roughness, but instead the equivalent sand roughness, k_s, which was employed in the tests for studying the laws of flow in rough pipes, serves to describe the fluidic effect of surfaces [6]. The interrelation between sandpaper of a defined grain size and sand roughness is known, from experiments [7, 8]. In order to insure that the blade surfaces produced by sticking on loose emery powder correspond to those of usual commercial emery paper, test surfaces were measured with a Hommel tester thus proving coincidence of the roughness measures.

The blades were roughened in the following way: First, the cleaned blade surfaces were sprayed with a very thin coat of a water-soluble adhesive which was then sprinkled with the desired emery grade. When all superfluous grains had been shaken off, the surface was left with a single and uniformly thin layer of emery grains. When the blades had dried, they were mounted in the cascade wind tunnel. Upon completion of the measuring series with one roughness grade, the rough layer was washed off with water and the new roughness grade applied as described above.

The emery grades used for the tests, the sand roughness and the related sand roughness are compiled in Table 1. The related roughness is referred to the profile chord length of 175 mm. A blade without a sticked-on layer has a peak-to-valley height of approx. 1 μm and is hydraulically smooth, since the admissible related roughness is not reached at a Reynolds' number of $5.6 \cdot 10^5$. The admissible related roughness can be determined from

$$(k_s/l)_{adm} < 100/Re;$$

in this case $k_{s\ adm}$ is 0.03 mm.

Measurements

With test conditions kept constant, the following measurements were carried out on cascades of varying roughness:

- pressure distribution around the profile,
- total losses and outlet flow angle in the wake,
- velocity distribution in the boundary layer and turbulences in the boundary layer.

Table 1 Roughnesses

emery grade No	sand roughness k_s in μm	relative roughness $k_s/l \cdot 10^3$
smooth	1	hydraul. smooth
220	100	0.57
120	180	1.02
40	580	3.31

The pressure distribution supplies information on the static pressure and as such on the velocity of the undisturbed flow at any point of the profile. Evaluation of the flow actions around the profile and calculation of the flow boundary layer is possible only on the basis of the pressure distribution data. For this reason, ten pressure tappings each were provided on the two central blades at half the blade height on the side facing the channel between them. The pressure tappings, whose position can be seen from Fig. 1, have a diameter of 0.5 mm.

The overall losses of the two-dimensional cascade are determined from momentum measurements downstream the cascade. The measurements in the wake establish the direction of flow, the static pressure and the total pressure. On the basis of these data together with the same data ascertained upstream the cascade by means of a Pitot tube which is installed in the intake as a reference probe, the losses and their distribution along the pitch can be calculated.

For evaluation of the development of a boundary layer and calculation of its thickness the pattern of the flow velocity between the value "zero" right at the wall and the unaffected outer flow must be known. This pattern is measured by means of a Pitot tube flattened at its tip to 0.25 mm and provided with an inlet slot of 0.05 mm width and about 1 mm length. These small dimensions in conjunction with the large blade dimensions insure that the tip of the probe is small as compared to the thickness of the boundary layer and can be brought comparatively near to the wall up to half the probe thickness. With the Pitot tube the total pressure in the boundary layer is measured. The second characteristic variable besides the total pressure which is of importance for the determination of the boundary layer is the distance of the probe from the wall. This distance is determined with the aid of a measuring dial of 1/100 mm-accuracy mounted on a probe adjusting gear. With the wind tunnel not in operation, this adjusting gear is fitted in such a way that the probe can be moved at the selected profile point vertically to the contour, assisted by a template with movement markings for the probe which is placed against the profile. When the wind tunnel is then put into operation the probe is moved toward the profile—which in the measuring plane was previously laminated with aluminium foil of 0.02 mm thickness—until contact is established, thus closing an electric circuit. The switch action is made visible on an oscilloscope. In conjunction with a visual check, the zero point for boundary layer measurement can thus be properly set and reproduced. For the measurements with a rough surface the emery powder is removed from the measuring area. In order not to influence the development of the boundary layer before the measuring point by this change in roughness, measurements are started at the trailing edge and only so much emery powder is removed each time that the probe for zero point measurement is positioned right behind the emery grains.

In order to check the pneumatically determined values for the boundary layer velocities, the boundary layer is also scanned with hot-wire anemometer probes. In addition, the degree of turbulence is also ascertained by this measuring method.

Evaluation of Measuring Results

After corresponding conversion and temperature correction, the static pressures, p_k, measured along the profile contour are represented together with the dynamic pressure, q_1, and the static pressure, p_1, in the intake as a nondimensional pressure coefficient, c_p. This pressure coefficient is defined as

$$c_p = \frac{p_k - p_1}{q_1} \tag{1}$$

The pressure coefficients are plotted as a function of the nondimensional profile length, x/l.

The measurements in the wake in particular provide information on the total loss and the outlet flow angle. The efficiency for energy conversion on a streamline is defined as

$$\eta = \left(\frac{w_2}{w_{2s}}\right) \tag{2}$$

where w_2 is the actual outlet flow velocity and w_{2s} the ideal velocity without loss as arising on isentropic expansion. The loss coefficient is

$$\zeta = 1 - \eta \tag{3}$$

Since the losses on the different streamlines vary, the characteristic values can only be determined through integration. The evaluation method takes into account all the conservation laws concerned, such as the equation of continuity, momentum balance, energy law and equations of state. The inhomogeneous flow in the wake is converted to a homogeneous flow. This method supplies at the same time the mean values of flow such as velocity, pressure and temperature as well as the loss coefficient and the direction of outlet flow.

The measurements of the boundary layer with the Pitot tube serve for determination of the velocity distribution in the boundary layer and thus of the boundary layer variables δ, δ_1 and δ_2. The thickness of the boundary layer, δ, is usually defined by the particular distance from the wall where the boundary layer velocity amounts to 99 percent of the outer flow velocity. This represents an arbitrary definition as the transition from the boundary layer velocity to the outer flow proceeds asymptotically. More reliable conclusions than from the boundary layer thickness, δ, can be drawn from the physically defined boundary layer thicknesses δ_1 and δ_2.

The displacement thickness is defined by the following equation:

$$\delta_1 = \int_{y=0}^{\delta} \left(1 - \frac{w(y)}{w_k}\right) dy \tag{4}$$

where y is the coordinate vertical to the profile surface and w_k the undisturbed velocity. The displacement thickness describes the narrowing of the channel brought about by the lower velocity in the boundary layer, and represents the distance by which the outer flow is displaced toward the outside by the formation of the boundary layer.

The momentum thickness, δ_2, covers the reduction of the momentum by the boundary layer, its definition being as follows:

$$\delta_2 = \int_{y=0}^{\delta} \frac{w(y)}{w_k}\left(1 - \frac{w(y)}{w_k}\right) dy \tag{5}$$

The ratio of displacement thickness to momentum thickness is given by the shape factor

$$H_{12} = \delta_1/\delta_2 \tag{6}$$

which characterizes the shape of the velocity profiles in the boundary layer.

Measuring Results

Fig. 2 illustrates the pressure distributions for the profile used. The related profile length, x/l, was used as abscissa, with x representing the running coordinate and l the profile chord length. The surface roughness, k_s/l, served as parameter. Fig. 2 which shows the pressure curves determined by measurements, includes entries of the measuring points for all roughness grades, but only the points for the smooth surface and with maximum roughness were connected by full and broken lines, respectively. The pressure distribution is not changed very much by the roughness. The measured values show a quite definite tendency as a function of the roughness: On the suction side the roughness causes the pressure coefficient to become lower, i.e. the velocity is reduced, whereas on the pressure side, in the back

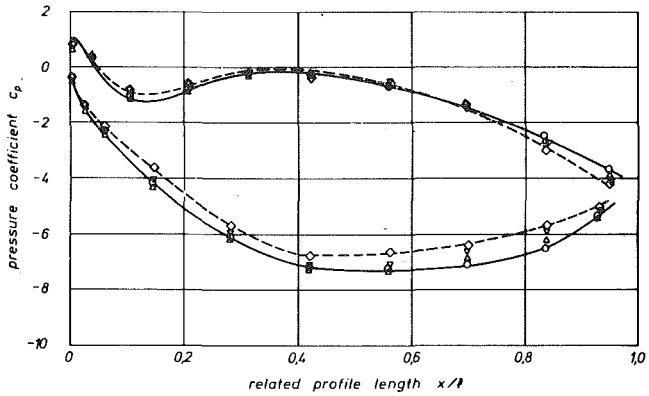

Fig. 2 Measured pressure distribution: (○) smooth, (△) $k_s/l = 0.57 \cdot 10^{-3}$, (▽) $k_s/l = 1.02 \cdot 10^{-3}$, (◇) $k_s/l = 3.31 \cdot 10^{-3}$, (——) smooth, (- - -) $k_s/l = 3.31 \cdot 10^{-3}$

section, the opposite effect can be observed; i.e., the velocity increases. In the central section the pressure distribution remains unchanged, whereas shortly behind the leading edge lower velocities occur. The effects described are the more pronounced, the rougher the surface. The pressure distribution shows very favorable flow conditions. On the pressure side an initial acceleration is followed by a brief retardation. From a related profile length of about 0.35 up to the trailing edge there is a uniform acceleration of flow. On the suction side there is a steady acceleration of the fluid up to about the middle of the blade; there is no suction peak and the pressure minimum is stretched long. Only in the back section of the suction side the flow is retarded down to the outlet pressure. The outlet pressure is not much higher than the minimum pressure, and the retardation therefore is not very large.

The development of the boundary layer along the profile surface can be seen from Fig. 3 and Fig. 4, where the momentum thickness as per equation (5) is entered as a function of the contour length. Fig. 3 shows the momentum thicknesses on the pressure side and Fig. 4 those on the suction side. The relative roughness is always indicated as parameter.

The momentum thickness on the pressure side (Fig. 3) increases from the front stagnation point until it reaches its maximum value at a contour length, s, of 75 to 90 mm. Up to shortly before the trailing edge the boundary layer then becomes thinner again. Especially with the two higher roughness grades, $k_s/l = 3.1 \cdot 10^{-3}$ and $1.02 \cdot 10^{-3}$, the momentum thickness increases near the trailing edge. The curves resulting from a smooth surface and from a relative roughness of $0.57 \cdot 10^{-3}$ are very similar. With a roughness, k_s/l, of 1.02 the boundary layer is about 1.5 times thicker than with a smooth surface or a surface with insignificant roughness. The maximum roughness of $k_s/l = 3.1 \cdot 10^{-3}$ causes the boundary layer to become more than twice its original thickness. At the trailing edge the momentum thickness for $k_s/l = 0.57 \cdot 10^{-3}$ and with a smooth surface is approximately 0.17 mm, for $k_s/l = 1.02 \cdot 10^{-3}$ it comes up to 0.25 mm, and for $k_s/l = 3.1 \cdot 10^{-3}$ it reaches a thickness of approximately 0.4 mm.

The momentum thicknesses at the suction side are considerably greater than at the pressure side (Fig. 4). Up to contour lengths of approximately 75 mm the boundary layers increase only slowly, while from 75 mm onward the growth becomes more marked. On the suction side the flow is accelerated up to a contour length of approximately 100 mm.

The curve for roughness $k_s/l = 0.57 \cdot 10^{-3}$ (emery grade 220) takes a similar course in the front range than that for the smooth surface. Up to a contour length of 100 mm the momentum thickness is less than with a smooth surface. From $s = 75$ mm onward there is a noticeable increase. At the trailing edge the momentum thickness is 1 mm, as compared to 0.4 mm with a smooth surface.

With roughness $k_s/l = 1.02 \cdot 10^{-3}$ (emery grade 120) the boundary layer at the trailing edge is likewise approximately 1 mm thick. In the front range, however, this roughness has a far greater effect. The momentum thickness rises already from a contour length of 20 mm. When s is more than 60 mm, the boundary layer increases to a higher

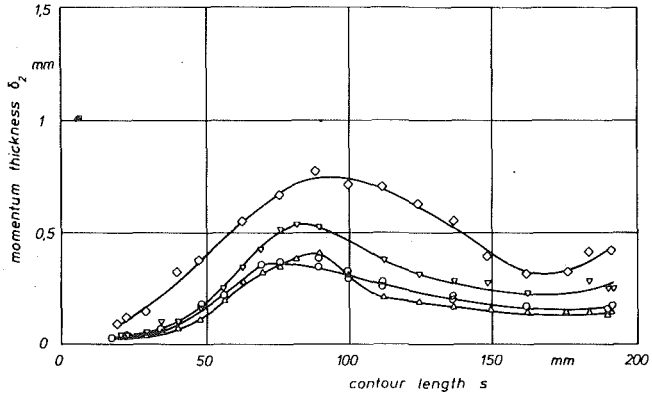

Fig. 3 Momentum thickness at pressure side. Legend see Fig. 2

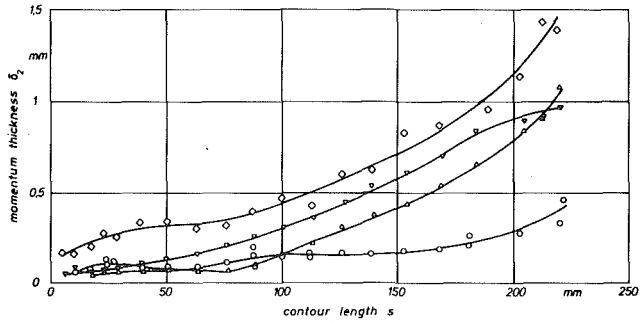

Fig. 4 Momentum thickness at suction side. Legend see Fig. 2

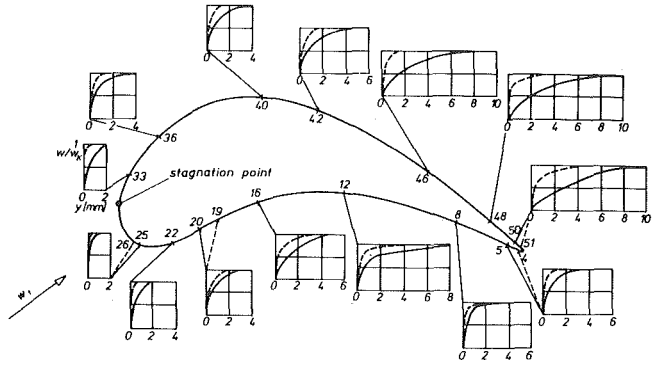

Fig. 5 Velocity distribution along profile: (—) smooth, (-----) rough ($k_S/l = 3.31 \cdot 10^{-3}$)

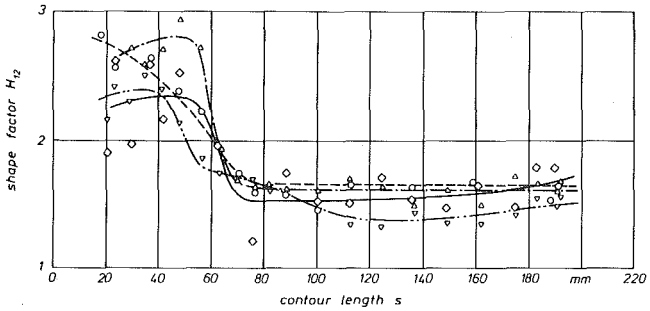

Fig. 6 Shape factor at pressure side. Legend see Fig. 2

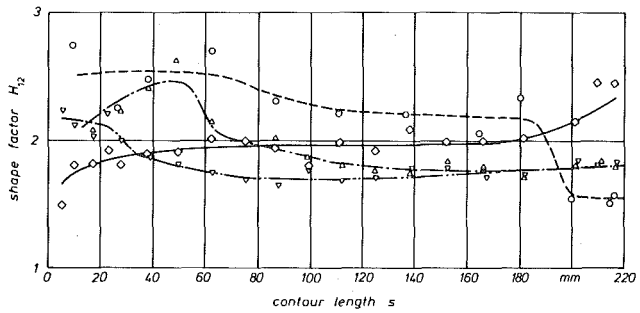

Fig. 7 Shape factor at suction side. Legend see Fig. 2

degree and up to $s = 190$ mm runs parallel to the momentum thickness at $k_s/l = 0.57 \cdot 10^{-3}$, after which the increase is only slight.

The strongest effect is brought about by the maximum roughness, where k_s/l is $3.1 \cdot 10^{-3}$ (emery grade 40). Right behind the front stagnation point the boundary layer has already reached a considerable thickness. From $s = 60$ mm it increases even more, and from the same point onward the acceleration of the outer flow is only very slight. At the trailing edge the momentum thickness comes up to about 1.4 mm.

Figs. 3 and 4 show that the boundary layers on the suction side are considerably thicker than on the pressure side. Corresponding to the momentum thickness the profile flow loss is likewise determined by the suction side by about 2.5 to 3.5 times as much as by the pressure side. The characters of the boundary layer on the pressure side and on the suction side differ. On the suction side the boundary layer gains in thickness up to the trailing edge, whereas on the pressure side the boundary layer decreases again in the back section of the profile contour as a result of the acceleration of flow. Fig. 5 represents a selection of velocity distributions measured in the boundary layer. The velocity ratio w/w_k is plotted as a function of the wall distance, y; w_k stands for the velocity outside the boundary layer while w stands for the local velocity. For some contour points the velocity distributions for a smooth surface and for a related roughness of $k_s/l = 3.1 \cdot 10^{-3}$ have been compiled. By the additionally shown allocation to the measuring point on the blade profile, the development and change of velocity in the boundary layer can be observed.

The velocity curves for smooth and rough surfaces differ. Right from the start, roughness $k_s/l = 3.1 \cdot 10^{-3}$ has a very great influence on the boundary layer. Since it can be assumed that at the beginning of the profile the flow is laminar, an influence of the rough surface on the laminar boundary layer cannot be excluded.

For great contour lengths and in particular on the suction side, the difference between the boundary layers on a smooth surface and on a rough surface becomes more and more pronounced. Contrary to the velocity profiles on the pressure-side profile end, the velocity gradient on the suction-side profile end is very small already near the wall. This causes correspondingly high values for the boundary layer thickness. Such a comparison can be easily made with the help of Fig. 5.

The loss coefficient rises from 1.85 percent for a smooth profile to 6.39 percent for roughness $k_s/l = 3.1 \cdot 10^{-3}$. For the roughness grades between, the loss coefficient amounts to 4.09 and 4.39 percent.

Analysis

The measuring results show the effect of the surface roughness of blades on the boundary layer. Neither the pressure distribution nor the velocity distributions show any sign of a separation of the boundary layer from the examined profile. This means that the boundary layer is essentially laminar and turbulent. The position of the transition point, which is an important parameter for the theoretical calculation of the boundary layer, cannot be recognized directly from the velocity distributions along the profile and the momentum thicknesses derived therefrom. As a further criterion for the position of the transition point, shape parameter H_{12} is plotted as a function of the contour length in Figs. 6 and 7. Shape parameter H_{12} represents the ratio of displacement thickness and momentum thickness and lies between 4.0 and 2.0 for laminar boundary layers and between 2.0 and 1.0 for turbulent boundary layers [9]. Shape parameters of more than 2.0 tend to cause a separation with turbulent boundary layers. A change of the boundary layer character from laminar to turbulent brings about a leap in the shape parameter [10].

On the pressure side (Fig. 6) the shape factor drops considerably for all roughness grades at a contour length, s, of between about 50 mm and 60 mm. The transition from laminar to turbulent flow can thus be allocated to this range. For rough surfaces the transition is steeper than for smooth surfaces. From $s = 70$ mm onward the shape

factor is about 1.6. The transition range comprises an area where the flow, after initial acceleration, is slightly retarded. It can be assumed, therefore, that in the boundary layer on the pressure side the transition point lies for all roughness grades at $s \approx 55$ mm. Up to this point the boundary layer is laminar and from then on turbulent, with no separations occurring.

The boundary layer on the suction side does not show such a uniform behavior. For smooth blades the shape factor is greater than 2 up to a contour length of approximately 190 mm, after which it takes a steep drop. For this surface, transition would only occur in this range shortly before the trailing edge. For the smooth surface on the suction side the transition point from laminar to turbulent flow in the boundary layer is assumed to be at $s = 185$ mm.

With the lowest roughness grade, which has a value of $0.57 \cdot 10^{-3}$ referred to the contour length, the shape factor for $s = 50$ mm drops steeply, as shown in Fig. 7. In spite of the fact that the flow is accelerated in this area, transition occurs from laminar to turbulent flow. As can be seen from Fig. 4, the momentum thickness shows a marked increase only from contour lengths of more than 100 mm as compared to the smooth surface. On account of the acceleration of flow the turbulent flow character does not yet take its full effect. The differences in boundary layer thickness as compared to the smooth surface are correspondingly small up to this contour length. Roughness $k_s/l = 1.02 \cdot 10^{-3}$ causes a drop of the shape factor already at $s = 30$ mm. This is in conformity with the increase of the momentum thickness as shown in Fig. 4.

The maximum roughness grade produces a boundary layer shape factor of less than two right from the start on the suction side (Fig. 7). Even at the leading edge the momentum thickness (Fig. 4) is about 2.5 times as high as for the other roughness grades, with correspondingly great effects on the velocity distribution in the boundary layer, as shown in Fig. 5. Peak values of up to 46 percent were measured for the turbulence grades. Shortly before the trailing edge the shape factor increases again to values of more than two. The turbulent boundary layer stands within short of separation, as becomes also apparent from the velocity distribution in Fig. 5. Near the wall, the gradient is very small. The disturbances caused by roughness are so high that the flow is turbulent almost right from the start. The transition point is to be assumed at $s = 0$ mm.

On the basis of the above transition points the boundary layer was calculated for the measured pressure distributions with reference to Truckenbrodt [11] and the studies by Scholz [9]. For the calculations an integral method was used based on the resistance coefficients c_f on an even plate. The resistance coefficients were calculated for a laminar flow according to

$$c_f = 1.328/\sqrt{\mathrm{Re}} \tag{7}$$

and for a turbulent flow with a smooth surface according to

$$c_f = 0.455 \times (\lg(\mathrm{Re}))^{-2.58} \tag{8}$$

and for a rough surface according to

$$c_f = 0.418 \times (2 + \lg(l/k_s))^{-2.53} \tag{9}$$

Re stands for the Reynolds number of the intake referred to the contour length l, and k_s for the thickness of sand roughness. The calculated results satisfactorily coincide with the measurements only for a smooth surface. The roughness affects the flow around a blade profile to a much greater extent than would be assumed from equations (7–9). A comparison between the calculated and measured momentum thicknesses shows that the laminar boundary layer, too, does not remain unaffected by the roughness. Boundary layers being regarded as laminar here when their shape factor H_{12} is clearly higher than two. As shown by the measurements of the degree of turbulence, these boundary layers are not free from cross movements. The criterion for the difference to the turbulent boundary layers is the attenuating ability towards disturbances [12, 13]. It was suggested to multiply the resistance coefficient obtained from equation (7) for boundary layers defined in this way as "laminar" with a factor depending on the roughness grade. With the available measurements

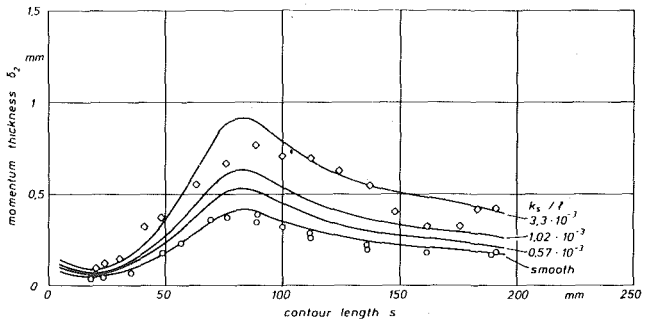

Fig. 8 Calculated momentum thickness at pressure side. Measured points see Fig. 2

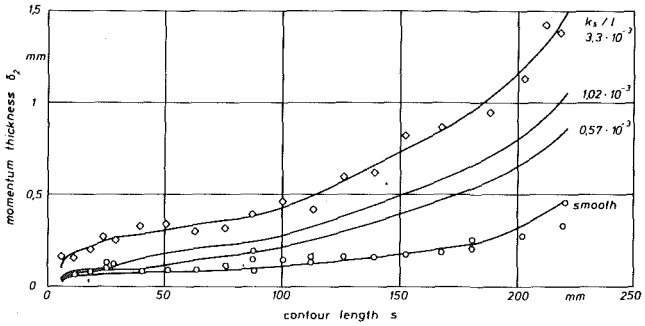

Fig. 9 Calculated momentum thickness at suction side. Measured points see Fig. 2

the effect caused by roughness was not as pronounced as suggested by [12, 13].

With reference to the recommendation of [12, 13] the following formula was developed for the factor k_r with which the resistance coefficient as per equation (7) is to be multiplied, based on the measurements carried out on the turbine profile:

$$k_r = 5.7 + 0.48 \times \ln(k_s/l) \tag{10}$$

Equation (10) applies to related roughnesses of more than $0.2 \cdot 10^{-3}$, whereas $k_r = 1.6$ is to be used for smoother surfaces.

The resistance coefficient for turbulent boundary layers is likewise to be corrected for the flow around turbine profiles. As pointed out already in [14], about 15 to 25 percent higher friction coefficients are to be assumed because of the flow start conditions. From the available measurements the following equation was established for the factor k_r for turbulent boundary layers in dependence on the roughness grade:

$$k_r = 3.4 + 0.26 \times \ln(k_s/l) \tag{11}$$

For roughness grades below $k_s/l = 0.2 \cdot 10^{-3}$ there is to be used $k_r = 1.2$.

The boundary layer calculations were repeated with the resistance coefficients corrected in accordance with equations (10) and (11). The results can be seen from Figs. 8 and 9, where the momentum thickness is plotted as a function of the contour length. For purposes of comparison with the measured results, the measuring points have been entered for a smooth surface and for roughness $k_s/l = 3.1 \cdot 10^{-3}$. There is quite a good coincidence between the measured and calculated values on the suction side, and likewise for the smooth surface on the pressure side. The momentum thickness for roughened surfaces is illustrated satisfactorily. The tendency of the boundary layer course is correctly maintained by the calculations and coincides with the measurements also quantitatively. Coincidence for the intermediary roughness grades, the measuring points of which were not entered, is likewise satisfactory.

Summary

In a two-dimensional cascade wind tunnel in which comparatively large blades with a chord length of 175 mm were installed, boundary layer measurements were carried out in a turbine cascade having a

guide blade mean section profile of a 50 percent reaction turbine. The boundary layers along the contour were scanned with Pitot tube probes and hot-wire probes both for smooth blades and for three different roughness grades of up to $k_s/l = 3.1 \cdot 10^{-3}$ sand roughness related to the chord length. The boundary layer is very much affected by the roughness grade. As compared to smooth surfaces the momentum thickness is up to about three times as high. The roughness produces an increased resistance and shifts the transition point forward. With the higher surface roughness grades, transition could not be prevented even by an accelerated flow.

The friction coefficient is higher than with a corresponding roughness on an even plate. Even in the case of laminar boundary layers increased friction can be observed. On the basis of the measuring results it was possible to specify factors in dependence on the related roughness both for the laminar and for the turbulent boundary layer with which the friction coefficients of the even plate are to be multiplied for obtaining results from boundary layer calculations which correspond to the measurements.

Acknowledgment

The investigations dealt with in this paper have been carried out within the framework of the Special Research Programme (SFB 61) of the German Research Association (DFG). The authors thank them for their support.

References

1 Bammert, K., et al., "Verluste beim Betrieb von Dampfturbinen," *Vereinigung Industrielle Kraftwirtschaft* (V.I.K.), V.I.K.-Berichte, No. 141/142, 1963.

2 Bammert, K., et al., "Über Korrosion, Erosion und Verschmutzung bei Gichtgasturbinen," *Vereinigung Industrielle Kraftwirtschaft* (V.I.K.), V.I.K.-Berichte No. 164, 1965.

3 Bammert, K., and H. Stobbe, "Messungen an einer mehrstufigen Axialturbine mit normalen, verdünnten und verdickten Schaufeln," *Motortechnische Zeitschrift*, 31, No. 5, 1970, pp. 189–198.

4 Bammert, K., and H. Sandstede, "Measurements Concerning the Influence of Surface Roughness and Profile Changes on the Performance of Gas Turbines," ASME JOURNAL OF ENGINEERING FOR POWER, Vol. 94, No. 3, 1972, pp. 207–213.

5 Bammert, K. and G.-U. Woelk, "Der Einfluß der Profilrauhigkeit auf die Strömungsverluste von Axialverdichtern, "*VDI-Berichte*, No. 264, 1976, pp. 119–128.

6 Nikuradse, J., "Strömungsgesetze in rauhen Rohren," *VDI-Forschungsheft*, 361, 1933, pp. 1–22.

7 Speidel, L., "Einfluß der Oberflächenrauhigkeit auf die Strömungsverluste in ebenen Schaufelgittern," *Forschung im Ingenieurwesen* 20, No. 5, 1954, pp. 129–140.

8 Feindt, E. G., "Untersuchungen über die Abhängigkeit des Umschlages laminar-turbulent von Oberflächenrauhigkeit und der Druckverteilung," Jahrbuch der Schiffbautechnischen Ges. 50, 1956, pp. 180–225.

9 Scholz, N., *Aerodynamik der Schaufel-gitter 1*, Verlag G. Braun, Karlsruhe, 1965.

10 Schlichting, H., *Grenzschicht-Theorie*, Verlag G. Braun, Karlsruhe, 1966.

11 Truckenbrodt, E., "Ein Quadraturverfahren zur Berechnung der laminaren und turbulenten Reibungsschicht bei ebener und rotationssymmetrischer Strömung," Ing.-Archiv 20, No. 4, 1952, pp. 211–228.

12 Bammert, K., and R. Milsch, "Boundary Layers on Rough Compressor Blades," ASME Paper No. 72-GT-48.

13 Bammert, K., and R. Milsch, "Das Verhalten der Grenzschichten an rauhen Verdichterschaufeln," *Forschung im Ingenieurwesen* 39, No. 4, 1972, pp. 101–109.

14 Bammert, K., and K. Fiedler, "Der Reibungsverlust von rauhen Turbinenschaufelgittern," BWK (*Brennstoff-Wärme-Kraft*) 18, No. 9, 1966, pp. 430–436.

L. L. Debruge
Air Force Aero Propulsion Laboratory,
Wright-Patterson AFB, OH 45433

The Aerodynamic Significance of Fillet Geometry in Turbocompressor Blade Rows

This paper describes a theoretical investigation of the influence of fillet radius on the aerodynamic behavior of turbocompressors. The fillet is that found at the intersection of an airfoil and a hub or shroud where no relative motion or gap is present. A modified power law velocity is used in conjunction with experimental estimates of the three-dimensional corner boundary layer extent to obtain values of the interference displacement and friction coefficient for the 90 deg corner flow which are in fair agreement with Gersten's experimental results. Likewise, interference displacement and friction coefficient are obtained in the case of a corner flow in a dihedral > 150 deg for which experimental data is unavailable but where the low curvature of the stream surfaces allows the three-dimensional boundary layer extent to be calculated from Bertotti's integral momentum equation. The boundary layer characteristics thus obtained are then applied, by means of a polyhedral approximation, in the evaluation of the influence of 90 deg corner fillet on corner flow separation. Some guidelines are provided relating the fillet radius to physical dimensions of the blading.

Introduction

The following paper is the result of a theoretical investigation aimed at assessing the significance of fillet geometry to the aerodynamic performance of a turbocompressor. The fillet in question is that found at the intersection of an airfoil and its adjacent platform or endwall where no relative motion or significant gap exists. The past tendency has been to strike a compromise between making the fillet as small as possible for aerodynamic benefit and as large as possible for structural and manufacturing benefit. Experience with aircraft design has shown that the fillet geometry at the juncture of a wing and fuselage can have significant impact on the interference drag associated with the intersection of the two bodies [1]. The interference drag is that component of the drag of an assembled wing and fuselage which is greater than the sum of the drags of the two bodies, each measured separately. It seems reasonable to assume that an analogous effect may exist in a turbomachine which might influence the endwall losses. This paper examines the effect of a fillet placed in both acute and obtuse corners. Since the fillet itself is represented by a series of short straight lines intersecting at an obtuse angle, the treatment of flow in an obtuse corner is particularly important to the development of the paper. Hence, it was thought that a short chronological presentation of past work in this subject would help clarify the assumptions inspired by these works.

It is well known that, as early as the thirties, ad-hoc solutions were applied successfully by researchers in the aircraft industry to reduce interference drag. They consisted chiefly in providing a fillet of varying radius along the line where body and wing join.

Although to date, to the author's knowledge, no attempt has been made, even for the simple case of two plates forming a 90 deg corner, to analytically predict the impact of a fillet on the interference drag, some researchers have sought analytical solutions to the three-dimensional corner flow. The first attempts addressed the problem of laminar flow in a 90 deg corner and were followed by analyses of turbulent flows in corners >90 deg. Carrier [2], then Sin-I-Cheng and Levy [3] obtained solutions for laminar flows using series solutions in cartesian and cylindrical coordinate systems. Bertotti [4] obtained a three-dimensional form of the momentum integral equation for both laminar and turbulent corner flows. Adopting Bertotti's method but using a power law for the velocity profile in the corner, Eichelbrenner [5] obtained explicit solutions for the corner boundary layer parameters in the case of zero pressure gradients. In 1959, Gersten [6] published the results of an experimental investigation of corner flow interference effects, taking into account the influence of a pressure gradient. Gersten derived correlations between characteristic interference parameters and the Reynolds number. Bragg [7] experimentally studied the turbulent flow in a 90 deg corner with and without pressure gradient. He used his measurements of velocities, wall shear stress and normal stresses, both in the three-dimensional momentum integral equations and in similarity analyses, to obtain correlations describing the flow over a narrow range of Reynolds numbers.

Paradis [8] conducted an experimental study of 90 deg corner flows to verify the validity of Eichelbrenner's theory and found that the observed velocity profile in the corner differed significantly from that obtained using a power law assumption. This divergence was attributed by Paradis to the presence of secondary flows in the corner. Eichelbrenner and Toan [9] jointly published a theoretical explanation of the secondary flow pattern in the 90 deg corner.

Zamir [10] contested the validity of the boundary layer equations

Contributed by the Gas Turbine Division and presented at the Gas Turbine Conference and Products Show, New Orleans, La., March 10–13, 1980 of THE AMERICAN SOCIETY OF MECHANICAL ENGINEERS. Manuscript received at ASME Headquarters December 10, 1979. Paper No. 80-GT-41.
Copies will be available until November 1980.

in a 90 deg corner on account of the streamsurfaces high curvature in this region. His use of a general boundary layer based on a tensor model using a hyperbolic system of coordinates leads to a system of differential equations whose solution is difficult.

Suter [11] obtained a theoretical estimation of a corner boundary layer growth for an axial compressor channel, under the combined influence of pressure gradients and secondary flows. The method followed is based on the integration of the two-dimensional boundary layer equations assumed valid for the corner, with the velocity profile represented by a power law. The results obtained in the absence of secondary flows and curvature are in agreement with Eichelbrenner's for the symmetrical case.

Finally, Toan [12] published the results of an experimental investigation of corner flows with and without pressure gradients and showed the discrepancy between these results and the solution of the integral momentum equation based on a velocity profile power law assumption. His study showed the total failure of the method of solution which neglects the influence of secondary flows on the primary flow pattern. Toan obtained a satisfactory correlation between the primary and secondary flows in the corner, using an orthogonal system of coordinates based on the isovels, in conjunction with the equations of motion.

Thus, Toan's results seem to corroborate Zamir's observations and establish that boundary layer theory is not applicable to curvilinear boundary layers since in this case it is no longer valid to argue that velocity gradients normal to the surface are much larger than those parallel to it.

In view of this, it appeared that any attempt to derive a correlation at least qualitatively establishing the influence of introducing a fillet on the development of the corner flow would have to use hypotheses for the primary flow velocity justified by experimental results such as Toan's, as well as corner flow parameters whether directly obtainable from experimental data or resulting from a modification of the corner flow configuration by-passing Zamir's objections.

From the review of published works it appears that the failure of former theoretical attempts to predict corner flow parameters in agreement with experimental observations may be attributed to both the three-dimensional nature of the corner boundary layer and to the strong curvature of the steamsurfaces in this region. Also, the comparative study of experimental and theoretical investigations published to date on this subject indicates the possibility of a compromise between an exact treatment of the three-dimensional corner flow and the usual approach to two-dimensional boundary layer problems. Essentially, this compromise utilizes experimental results establishing a relationship between the characteristics of the free flow and the extent of the three-dimensional corner zone. This relationship is then called upon to generate a hypothesis for the form of the three-dimensional boundary layer velocity. The latter is then used in the usual integration procedures which yield parameters of interest in the prediction of flow separation in the corner. For a right dihedral, experimental data is available to verify the accuracy of these parameters for an extended range of Reynolds numbers and pressure gradients. For obtuse dihedrals, such data are unavailable. However, the extension of the hypothesis for primary flow velocity in 90 deg corners to dihedrals >150 deg proceeds on fairly safe grounds since the nature of the corner flow becomes asymptotically two-dimensional.

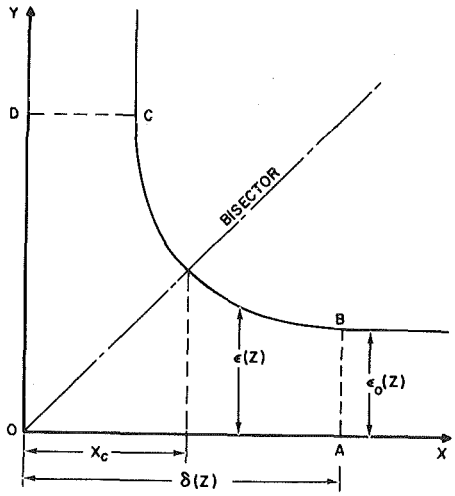

Fig. 1 Theoretical model of 90 deg corner flow

Consequently, the development of three-dimensional corner flows in dihedrals >90 deg can be predicted and the interference parameters D_3' and δ_3' obtained. The combined effect of several dihedrals used in the approximation of a 90 deg corner fillet on the separation characteristics of the corner flow is then assessed. Finally, these results are applied in the evaluation of the adjunction of a fillet on the aerodynamic performance of a turbocompressor.

Analysis

The compromise between an exact treatment of the three-dimensional corner flow and the usual approach to two-dimensional boundary layer problems mentioned in the introduction is obtained through a modification of the familiar velocity power law,

$$\frac{U}{U_e} = \left(\frac{Y}{\epsilon_0}\right)^{1/n} \tag{1}$$

for the two-dimensional boundary layer. The two-dimensional boundary layer thickness ϵ_0 is replaced by ϵ which, as Fig. 1 indicates, is a function of both X and Z.

Nomenclature

C_f = skin friction coefficient
C_f3 = interference skin friction coefficient
d = ratio of endwall to blade boundary layer thickness
D_1 = 90 deg corner total displacement area
D_2 = 90 deg corner two-dimensional displacement area
$D_3 = D_1 - D_2$
$DR1$ = 90 deg corner total drag
$DR2$ = 90 deg corner two-dimensional drag
L = length of dihedral or stator channel
n = inverse exponent in power law for primary velocity profile
p = pressure
r = fillet radius
s = distance measured along channel streamline
U = primary flow velocity in boundary layer
U_0 = free stream inlet velocity
X, Y = coordinates on floor and side-wall respectively
Z = coordinate parallel to the corner apex
X_c = coordinates of intersection of bisector with corner boundary layer surface
α = supplementary angle of dihedral (Fig. 7)
β = parameter governing the inclination of isovels to the wall (Fig. 2)
δ, δ^1 = extent in the X, Y directions of the three-dimensional flow in the corner
δ_1 = displacement thickness
δ_2 = momentum thickness
δ_3 = interference displacement thickness (α = 90 deg)
ϵ = boundary layer thickness
η = distance from stator endwall streamline
ν = Kinematic viscosity
ρ = density of fluid
ψ_1, ψ_2 = streamfunctions, reference [11]

Subscripts

$_c$ = in the corner
$_e$ = in potential flow
$_0$ = in two-dimensional region
$(F)_x' = \frac{\partial F}{\partial X}$ = derivative of function F with respect to the variable X

Superscripts

$'$ (prime) = in dihedral $\neq$ 90 deg

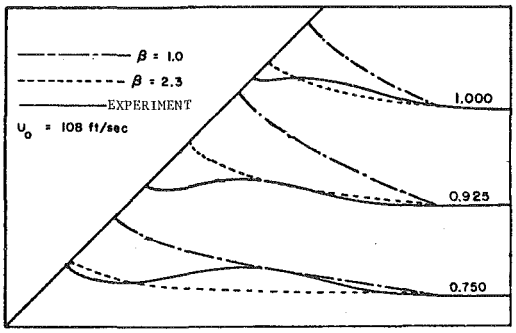

Fig. 2 Distribution of isovels at dihedral station *Z* for zero pressure gradient from Toan [*12*]

Bertotti and Eichelbrenner derived a relationship between ϵ_0, ϵ, X and δ from the requirements of continuity of the primary flow velocity on the corner bisector expressed as

$$\epsilon = \epsilon_0(\delta/X) \tag{2}$$

Toan observed a significant discrepancy between the shape of the isovels obtained from (2) and that obtained from experimental measurements of the velocity (Fig. 2). Furthermore, Toan noticed that for a significant range of pressure gradients an approximate agreement could be restored between the isovels given by a modified version of (2) and those experimentally obtained. The modified version could be written

$$\epsilon = \epsilon_0(\delta/X)^{1/\beta} \tag{3}$$

with β assuming appropriate values for the pressure gradients chosen.

Hence, in analogy with (1), a tentative form for the three-dimensional boundary layer velocity could be introduced as

$$\frac{U}{U_e} = \left(\frac{Y}{\epsilon_0}\left(\frac{X}{\delta}\right)^{1/\beta}\right)^{1/n} \tag{4}$$

with n obtained from the two-dimensional boundary layer parameters δ_1 and δ_2:

$$\frac{\delta_1}{\delta_2} = \frac{(2+n)}{n}. \tag{5}$$

Nonetheless, the appropriate values of β can be obtained only is δ is known. This is obvious when, using (4), the momentum equation describing the net influence of the corner is integrated to yield the correlation obtained by Toan:

$$\frac{\delta}{\epsilon_0} = \left[\frac{\beta(n+1)(n+2)}{\left(\frac{2n\beta}{\beta+1}+1\right)\left(\frac{2\beta n}{\beta+1}+2\right)}\right]^{\frac{(1+\beta)}{(\beta-1)}} \tag{6}$$

This correlation is reproduced from [12] in Fig. 3.
Toan used his experimental values of δ/ϵ_0 to obtain β for the corresponding n.

It remains to show that (4) holds when used in the derivation of three-dimensional boundary layer parameters such as the displacement and momentum thickness. These parameters were calculated by Gersten [6] for the 90 deg corner three-dimensional flow using an experimentally obtained velocity distribution.

They were used, directly, to determine interference parameters which, in turn, supplied useful information on the inception of separation in the corner.

In the following section, definitions of interference parameters, by Gersten, relevant to the development of this paper, are presented. Also, the interference skin friction coefficient and the interference displacement thickness are obtained analytically, using (4) and compared with Gersten's results.

Evaluation of Corner Interference Displacement Thickness and Friction Coefficient Using Toan's Assumptions, and Comparison with Gersten's Results. For the theoretical model shown in Fig. 1, values of the interference thickness and friction coefficient are derived, using (4) and Toan's experimental observation that δ/ϵ_0 is fairly insensitive to moderate changes in n and remains $\simeq 2$. In the subsequent analysis, all lengths and velocities are nondimensionalized with respect to L, the length of the plates, and U_0, the free stream velocity at the plates leading edge. Flow symmetry about the bisector allows one to write for the displacement area D_1 pertaining to region OABCDO of Fig. 1,

$$D_1 = 2\left\{\int_0^{X_c}\int_0^{X}\left[1-\left(\frac{Y}{\epsilon_0}\left(\frac{X}{\delta}\right)^{1/\beta}\right)^{1/n}\right]dY\,dX + \int_{X_c}^{\delta}\int^{\epsilon_0(\frac{\delta}{x})^{1/\beta}}\left[1-\left(\frac{Y}{\epsilon_0}\left(\frac{X}{\delta}\right)^{1/\beta}\right)^{1/n}\right]dY\,dX\right\}, \tag{7}$$

where use has been made of (4) and Ue is the flow velocity at the edge of the boundary layer.

Upon integration of (7), the following expression for the corner displacement area is obtained:

$$D_1 = \frac{Xc^2}{2} - \frac{n^2\beta}{(n+1)}\frac{\epsilon_0^{-1/n}\,\delta^{-1/n\beta}\,X_c^{(\beta(2n+1)+1)/n\beta}}{(1+\beta(2n+1))} + \left(\frac{\beta\epsilon_0\delta^{1/\beta}}{(\beta-1)(n+1)}\right)\left(\delta^{(\beta-1)/\beta} - X_c^{(\beta-1)/\beta}\right) \tag{8}$$

The interference displacement area D_3 is obtained by subtracting from D_1 the displacement area D_2 associated with the two-dimensional flow. The latter can be expressed as

$$D_2 = 2\left\{\int_0^{\epsilon_0}\int_0^{X}\left[1-\left(\frac{Y}{\epsilon_0}\right)^{1/n}\right]dY\,dX + \int_{\epsilon_0}^{\delta}\int_0^{\epsilon_0}\left[1-\left(\frac{Y}{\epsilon_0}\right)^{1/n}\right]dY\,dX\right\}, \tag{9}$$

where $U_e(Y/\epsilon_0)^{1/n} = U$ is the two-dimensional flow boundary layer velocity. Integration of (9) gives:

$$D_2 = \frac{2\epsilon_0\delta}{(1+n)} - \frac{\epsilon_0^2}{(2n+1)} \tag{10}$$

Hence, $D_3 = D_1 - D_2$.

With the remarks made earlier for the calculation of the interfer-

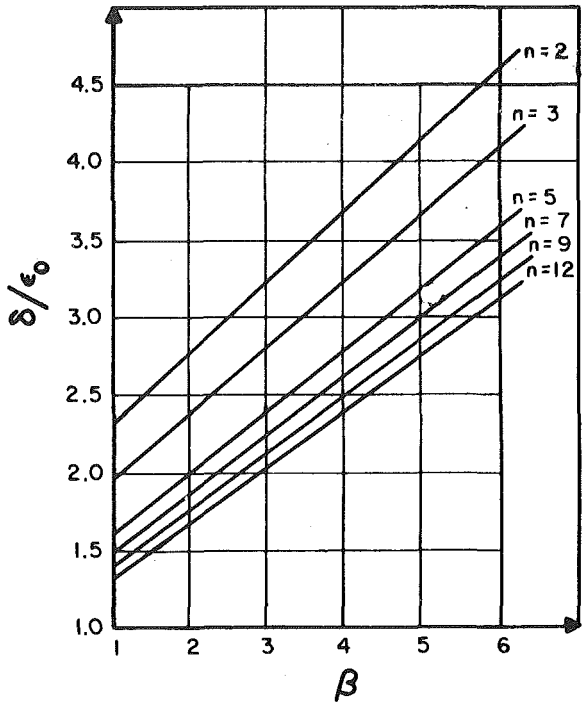

Fig. 3 Relation between β, n and δ/ϵ_0

ence displacement area, the total drag for region OABCDO of Fig. 1 can be expressed as:

$$\frac{DR1}{\rho U_0^2} = 2\int_0^{X_c}\int_0^{x}\left\{\left[\frac{Y}{\epsilon_0}\left(\frac{X}{\delta}\right)^{1/\beta}\right]^{1/n} - \left[\frac{Y}{\epsilon_0}\left(\frac{X}{\delta}\right)^{1/\beta}\right]^{2/n}\right\} dY\,dX + 2\int_{X_c}^{\delta}\int_0^{\epsilon_0(\epsilon/X)^{1/\beta}}\left\{\left[\frac{Y}{\epsilon_0}\left(\frac{X}{\delta}\right)^{1/\beta}\right]^{1/n} - \left[\frac{Y}{\epsilon_0}\left(\frac{X}{\delta}\right)^{1/\beta}\right]^{2/n}\right\} dY\,dX \quad (11)$$

Performing the integration gives:

$$\frac{DR1}{\rho U_0^2} = \frac{2n^2\beta\epsilon_0^{-1/n}\delta^{-1/n\beta}X_c^{(1+\beta(2n+1))/n\beta}}{(n+1)\,(\beta(2n+1)+1)} - \frac{n^2\beta\epsilon_0^{-2/n}\delta^{-2/n\beta}X_c^{2(1+\beta(1+n))/n\beta}}{(2+n)(1+\beta(1+n))} + \left[\frac{2\beta\epsilon_0\delta^{1/\beta n}}{(\beta-1)(n+1)(n+2)}\right]\left[\delta^{(\beta-1)/\beta}X_c^{(\beta-1)/\beta}\right] \quad (12)$$

The total drag for the corresponding two-dimensional flow is:

$$\frac{DR2}{\rho U_0^2} = \frac{2n\epsilon_0\delta}{(1+n)(2+n)}. \quad (13)$$

The values of ϵ_0, δ, Xc, n and β required to obtain numerical values for equations (8, 10, 12) and (13) are derived next from two-dimensional flow theory and (6). From two-dimensional flow theory, the momentum thickness δ_2 for the incompressible, turbulent, two-dimensional boundary layer is obtained from the momentum integral equation

$$\delta_2\left(\frac{Ue\,\delta_2}{\nu}\right)^{1/4} = 0.016\,Ue^{-4}\int_0^Z Ue^4\,dZ \quad (14)$$

given in [13]. Introduction of the Euler number

$$\mathrm{Eu} = -\frac{L}{\rho U_0^2}\frac{dp}{dX}$$

in this equation yields

$$\delta_2 = 0.0087\,\mathrm{Re}^{-1/5}\frac{(8\mathrm{EU}^2Z^3 + 12\mathrm{EUZ}^2 + 6Z)^{4/5}}{(1+2\mathrm{EUZ})^{1.7}}, \quad (15)$$

This analysis is concerned with null and adverse pressure gradients which are identified by the Euler numbers 0, −0.1, −0.18, and −0.25.

The corresponding value of the parameter n results from equation (5). δ_1, the displacement thickness, is obtained from

$$\delta_1 = \frac{0.052}{5\sqrt{\mathrm{Re}}}f_2(\mathrm{EU}),$$

where f_2 (EU) is a function relating the displacement thickness to the Euler number for the two-dimensional flow [6]. Therefore, ϵ_0 is simply:

$$\epsilon_0 = \frac{(n+1)(n+2)}{n}\delta_2.$$

Values of these parameters calculated for air at $Z = L$ and $\mathrm{Re} = 10^6$ are entered in Table 1. Xc is directly obtained from (3), if it is assumed that $\delta/\epsilon_0 = 2$.

It is appropriate, at this point, to introduce some of Gersten's definitions [6] which will be used in deriving expressions for the interference skin friction coefficient and interference displacement thickness to be compared with his experimental results. Referring to Fig. 4, the triangle cde represents the interference displacement area D_3, δ_3, the height of this triangle, defines the interference displacement thickness $\delta_3 = \sqrt{D_3}$.

Referring next to Fig. 5, the difference in total skin friction between configurations (a) and (b) is designated by

$$DR3 = DR1 - DR2$$

so that the interference skin friction $c_f{}^3$ is expressed as

$$C_{f3} = 2DR3/(\rho U_0{}^2 L^2).$$

The values of δ_3 and C_{f3} obtained from (8, 10, 12) and (13) for $\mathrm{Re} = 10^6$ and the Euler numbers chosen are entered in Table 2 with Gersten's experimental results.

It may be seen that the agreement is quite satisfactory and therefore justifies the use of (4) for the specific purpose of obtaining δ_3. The interest in δ_3 stems from the fact that, in analogy with two-dimensional boundary layer flow, Gersten, experimentally, derived a relationship between this parameter and the Euler numbers which, for given Reynolds numbers, determine separation in the 90 corner. This is shown in Fig. 6.

Thus, within the domain assigned to the role of (4) in the present analysis, its usefulness, on the basis of the preceding results, may be safely assumed when α takes values <90 deg. This assertion is, of course, based on the observation that the decrease in α induces a concomitant change of the three-dimensional corner flow toward two-dimensional behavior. The following section concerns the im-

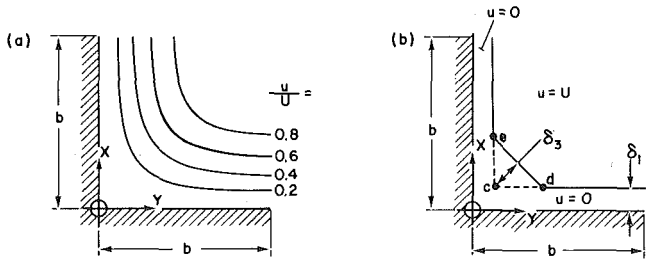

Fig. 4 Displacement of the boundary layer in a 90 deg corner [6] (*a*) curves of constant velocity for the real flow pattern (*b*) simplified flow pattern having the same displacement area as the real flow pattern

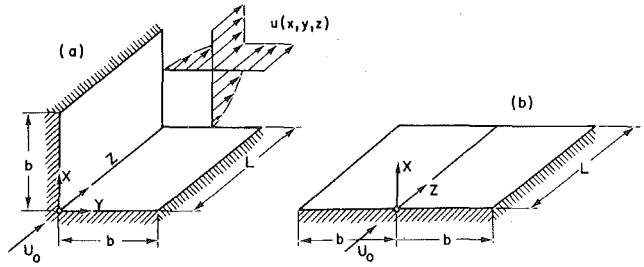

Fig. 5 Skin friction for flow in 90 deg corner from [6] (*a*) flow over two flat plates with corner interference (*b*) flow over two flat plates without corner interference

Table 1

EU	δ_2	f_2	δ_1	H12	n	ϵ_0	β
0.	.0023	1	.0032	1.4	5	.019	2
-.1	.0029	1.303	.0042	1.49	4.32	.0216	1.8
-.18	.0036	1.91	.0063	1.72	2.91	.024	1.2
-.25	.0049	2.75	.009	1.85	2.35	.0303	1.0

Table 2

EU	n	β	δ_3	δ_3 (GERSTEN)	C_{f3}	C_{f3} (GERSTEN)
0.	7	1	.0108	.007		.36 X 10^{-4}
0.	5	2	.00716	∿	.43 X 10^{-4}	∿
-.1	4.32	1.8	.0091	.0084		
-.18	2.91	1.2	.0134	.0131		

plications of this remark with respect to the derivation of δ_3 for obtuse dihedrals, for the Euler numbers already considered.

Extension to a Corner $\neq$ 90 deg. The good agreement between analytically derived results and the values obtained experimentally by Gersten for δ_3 and C_{f^3} would seem to authorize the application of the assumptions made for the 90 deg corner flow to the case where $\alpha \neq 90$ deg. Unfortunately, to our knowledge, experimental data have yet to be published for this case. The immediate consequence is the impossibility of establishing a relationship between β and n for $\alpha \neq 90$ deg since δ/ϵ_0 is now unknown.

Nonetheless, it must be emphasized that, as α decreases, the curvature of the streamsurfaces in the corner decreases also and consequently the main objection to using the integral momentum equation in the corner may be lifted. Also, it might be surmised that, as α decreases significantly, β must differ little from 1 since the behavior of the corner flow comes closer to being two-dimensional. Equation (3) was initially derived by Bertotti and Eichelbrenner for the general case of dihedrals as

$$\epsilon = \epsilon_0 \left(\frac{\delta}{X}\right)^{\gamma}, \tag{16}$$

where

$$\gamma = \frac{(1 - \cos\alpha)}{(1 + \cos\alpha)}$$

Applying Toan's correction to (16) gives

$$\epsilon = \epsilon_0 \left(\frac{\delta}{X}\right)^{\gamma/\beta}.$$

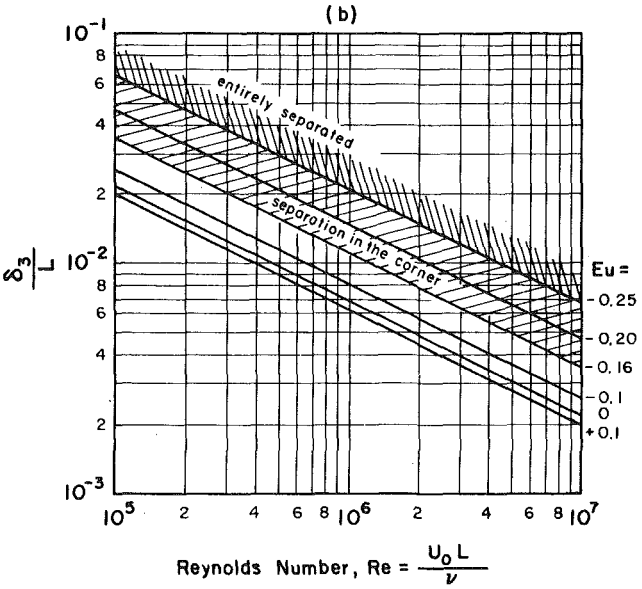

Fig. 6 Interference displacement thickness of turbulent boundary layer in convergent or divergent flow along a corner [6]

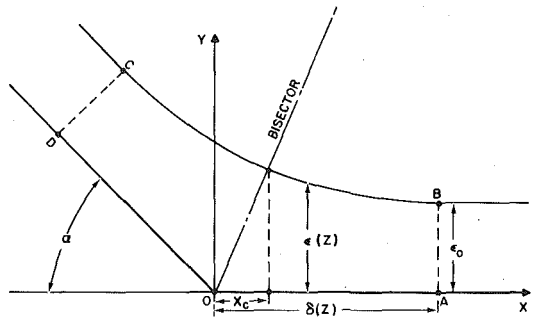

Fig. 7 Theoretical model of corner flow $\alpha \neq 90$ deg

Consequently, the three-dimensional boundary layer velocity for dihedrals >90 deg is written:

$$\frac{U}{U_e} = \left[\frac{Y}{\epsilon_0}\left(\frac{X}{\delta}\right)^{\gamma/\beta}\right]^{1/n}. \tag{17}$$

The procedure followed in the derivation of (6) for $\alpha = 90$ deg is observed, using (17), with the integration carried over the area OABCDO of Fig. 7.

Thus, the following correlation between δ, β, γ and n is obtained:

$$\frac{\delta}{\epsilon_0} = \left[2 + \frac{n(\gamma - \beta)(3\beta(n+1) + \gamma(n+3))}{(2n\beta + \beta + \gamma)(n\beta + \beta + \gamma)} \over 2\gamma/\beta\right]^{(\gamma+\beta/\beta-\gamma)} \text{Tan}\,(\alpha/2). \tag{18}$$

Equation (18) is plotted in Fig. 8 for several values of α.

It may be seen from this figure that for $\alpha < 30$ deg and hence $\beta \simeq 1$, the ratio δ/ϵ_0 conserves the approximate value of 2 experimentally observed for $\alpha = 90$ deg. Therefore, letting $\beta = 1$, the integral momentum equation describing the net influence of the corner

$$\left(\int_c \frac{U}{U_e} I\,dY\,dX - 2\delta \int_0^{\epsilon_0} \frac{U}{U_e} I\,dY\right)_X + \frac{1}{U_e}(U_e)'_Z \left(\int_c I\,dY\,dX - 2\delta \int_0^{\epsilon_0} I\,dY + 2\int_c \frac{U}{U_e} I\,dY\,dX - 4\delta \int_0^{\epsilon_0} \frac{U}{U_e} I\,dY\right) = 0 \tag{19}$$

is numerically integrated, using (17) with $I = (1 - U/U_e)$, and where $\int c$ indicates integration over the area OABCDO of Fig. 6. The values of δ obtained from (19) are listed in Tables 3 and 4 for $\alpha = 22°5$ and

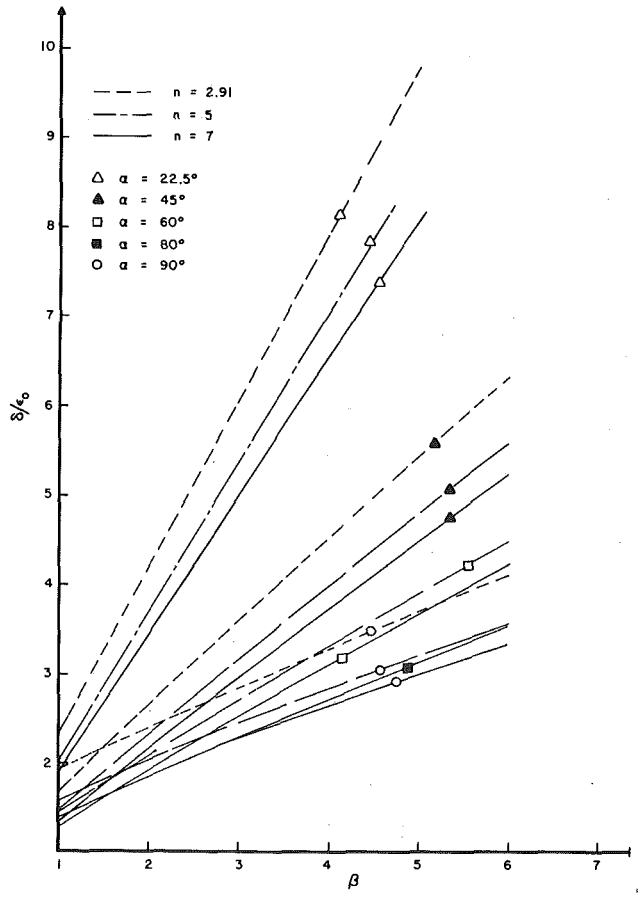

Fig. 8 Relation between δ/ϵ_0, β and n for $\alpha \leqslant 90$ deg

Table 3 (α = 22.5 deg)

EU	n	δ	δ_3	C'_{f3}
0	5	.0397	.00128	.39 X 10^{-7}
-.1	4.32	.0415	.00148	
-.18	2.91	.0418	.00177	
-.25	2.35	.0420		

11°25. As for the case where $\alpha = 90$ deg δ exhibits little sensitivity to variations in the Euler number.

In analogy with the procedure followed for $\alpha = 90$ deg, equations (7, 9) and (11) are used, in conjunction with (17) to calculate, for the region OABCDO of Fig. 7, the total displacement area D_1',

$$D_1' = X_c^2 \cot \alpha/2 - \frac{2n^2\delta^{-\gamma/n}\epsilon_0 - {}^{1/n}X_c{}^{(\gamma+1+2n)/n}}{(n+1)(2n+1+\gamma)} + \left(\frac{2\epsilon_0\delta^{-\gamma}}{(1-\gamma)(n+1)}\right)(\delta^{(1-\gamma)} - X_c{}^{(1-\gamma)}) \quad (20)$$

the displacement area D_2', associated with the two-dimensional flow,

$$D_2' = \epsilon_0^2 \operatorname{Tan} \alpha/2 \left[\frac{2n}{(n+1)(2n+1)} - 1\right] + \frac{2\epsilon_0\delta}{n+1}, \quad (21)$$

the interference displacement area, D_3',

$$D_3' = D_1' - D_2',$$

the interference displacement thickness δ_3', defined in Fig. 9

$$\delta_3' = (D_3' \operatorname{Tan} (\alpha/2))^{1/2} \quad (22)$$

and the interference friction coefficient, C'_{f3},

$$C_f' 3 = 4\left\{\frac{n^2[\cot(\alpha/2)]^{(n+1)/n}}{(n+1)(2n+1+\gamma)}\epsilon_0{}^{-1/n}\delta^{-\gamma/n} \times X_c{}^{(\gamma+2n+1)/n} - \frac{n^2[\cot(\alpha/2)]^{(2+n)/n}}{2(2+n)(\gamma+1+n)} \times \epsilon_0{}^{-2/n}\delta^{-2\gamma/n}\hat{x}_c{}^{2(\gamma+1+n)/n} + \frac{n}{(n+1)(n+2)}\left[\frac{\epsilon_0\delta^{-\gamma}}{(1-\gamma)}(\delta^{1-\gamma} - X_c{}^{1-\gamma}) - \epsilon_0\delta\right]\right\}$$

Tables 3 and 4 list values of δ_3' obtained for null and adverse pressure gradients with $\alpha = 22°5$ and 11°25. Also, values of C_{f3}' obtained for zero pressure gradient.

Introducing a Fillet in the 90 deg Corner. Given the difficulties encountered when attempting to obtain 90 deg corner boundary layer parameters using the integral momentum equations, the adjunction of a fillet, with the associated complexity bestowed on the corner flow seems to forbid a direct analytical approach. Consequently, the effect of introducing a fillet in the 90 deg corner on the interference displacement thickness, and hence on the initiation of corner flow separation, will be evaluated using a polyhedral approximation for the fillet of radius r. Through this approach, the results obtained for the corner flow with $\alpha < 30$ deg may, in principle, be used directly since the fillet is represented by four or eight corners whose interference displacement area is known.

The definition of interference displacement thickness will be consistent with that adopted for the 90 deg corner without fillet. It is represented in Fig. 10 as the height of segment EFG whose area is the interference displacement area for the corner.

Thus, the definition of interference displacement thickness limits the value of the minimum fillet radius to twice the two-dimensional displacement thickness, while the desirability of duplicating a fully developed flow for each corner used in the approximation makes the choice of a minimum fillet radius yielding δ, as obtained from (19), preferable (Fig. 11).

Table 4 (α = 11.25 deg)

EU	n	δ	δ_3	C'_{f3}
0	5	.0685	.00063	.22 X 10^{-7}
-.1	4.32	.0715	.00073	
-.15	3.23	.0707	.00081	

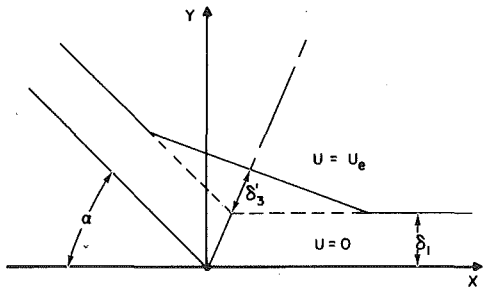

Fig. 9 Simplified flow pattern showing same displacement area as real flow pattern

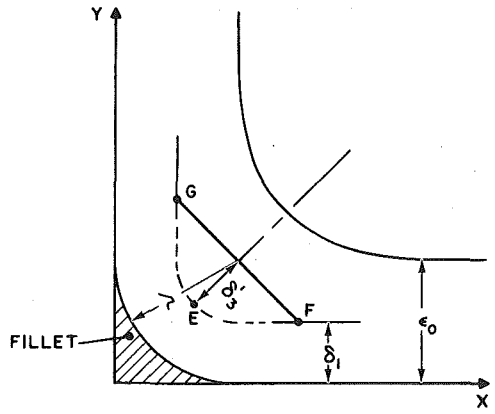

Fig. 10 Simplified flow pattern showing same displacement area as real flow pattern

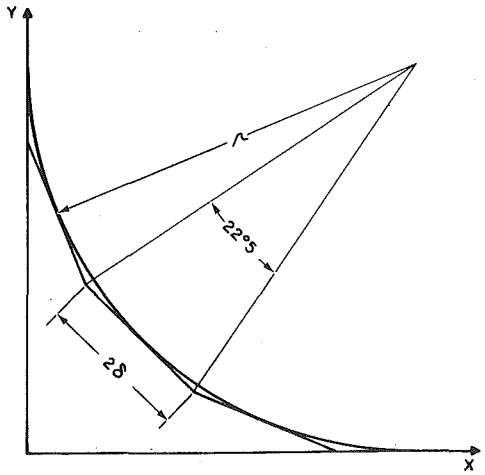

Fig. 11 Polyhedral approximation of corner fillet

However, it may be argued that most of the interference displacement is generated deep in the corner where the secondary vortices occur and that the interference of secondary flows from two adjacent corners occuring at a distance $\delta^1 < \delta$ from the corners produces roughly the amount of interference displacement normally obtained with a fully developed flow over the length $\delta - \delta^1$. Nonetheless, for $2\delta_1 < r < \epsilon_0$, it seems likely that the interference displacement area generated will be the result of a combination of the 90 deg corner and fillet influences and that the values obtained with r taken within this interval are somewhat arbitrary and could be expected to be rather higher.

Table 5 lists values of δ_3 corresponding to a fillet radius equal to multiples of ϵ_0 using four corners for the approximation. The value of δ_3 listed last for each Euler number corresponds to

$$r = \delta/\tan(\alpha/2),$$

where δ is obtained from (19).

Table 6 lists values of δ_3 obtained when eight corners are used to approximate the fillet.

Comparison of results listed in Tables 5 and 6 shows that a four corner approximation to the fillet radius is sufficient. It also indicates the effectiveness of a fillet radius close to $r = \epsilon_0$ on the interference displacement thickness. This is better shown in Fig. 12 which illustrates the drastic decrease of displacement thickness when a fillet is provided in the 90 deg corner. Accordingly, corner flow separation is avoided for the turbulent flow with a constant, adverse pressure gradient considered here when a fillet radius amounting to only a fraction of the two-dimensional boundary layer thickness is provided.

Application to Turbocompressor Blade Row. A somewhat simplified version of the flow of gases in a typical turbocompressor is now considered. To obtain a rough estimate of the influence of a corner fillet on an expected corner flow separation, secondary flow in the channel is initially neglected so that the thickening of the corner boundary layer is solely attributed to the growth of the secondary vortex. The additional effect of secondary flow present in any curved channel can be accounted for and its impact on the rate of growth of the corner boundary layer combined with that of the secondary vortex. This is shown in Suter's paper [11] where equation (25) of the present analysis assumes a form reflecting this effect. Thus, the essential differences between the compressor channel corner flow and the 90 deg corner flow treated previously involve the changes from a symmetrical to an unsymmetrical corner flow and from a constant to a variable pressure gradient. This type of flow was studied by Suter [11], assuming a constant shape factor $H12$ and friction coefficient so that separation in the channel could not be monitored.

In the present analysis, the development of the two-dimensional channel flow with variable pressure gradient is obtained from the simultaneous calculation of the momentum displacement thickness δ_2 using Truckenbrodt's quadrature [13], and the friction coefficient C_f:

$$C_f = 0.013/(U_e\delta_2/\nu)^{1/6}. \tag{23}$$

The shape factor $H12$ is then obtained from Garner's equation [13] and used in evaluating n along the corner according to the relationship

$$H12 = \frac{2+n}{n}.$$

The channel potential flow velocity U_e is expressed as:

$$U_e = \psi_1(s) + \psi_2(s)\eta \tag{24}$$

where s is the distance measured along a streamline and η the distance from the mid-channel streamline referenced by $\eta = 0$.

The strongly unsymmetrical corner flow is schematically represented in Fig. 13. The ratio of the extent of the corner zone influence normal to the endwall to that normal to the blade surface is assumed to be approximately the same as that of the boundary layer thicknesses on the endwall and blade surfaces. Thus, a single parameter δ_c for the extent of the corner zone influence may be obtained through integration of the integral momentum equation and, in turn, the corner boundary layer parameters.

The interference displacement thickness can then be evaluated along the intersection of the blade and endwall using the method described for the 90 deg corner flow, and Fig. 14 used to determine the fillet radius required to prevent separation. The following example

Table 5 (α = 22.5 deg)

r	δ_3 (EU=0)	δ_3 (EU=-.1)	δ_3 (EU=-.18)
ϵ_0	.0027	.0033	.0041
$2\epsilon_0$	.0021	.0024	.003
$3\epsilon_0$	.0018	.0021	.0026
$4\epsilon_0$	.0016	.0019	.0023
$5\epsilon_0$	.0015	.0017	.0021
$6\epsilon_0$	.0014	.0016	.002
$7\epsilon_0$	.0013	.0015	.0017
$8\epsilon_0$	.0012	.0014	
$9\epsilon_0$	.0011	.00134	

Table 6 (α = 11.25 deg)

r	δ_3 (EU=0)	δ_3 (EU=-.1)
$2\epsilon_0$	.002	.00238
$3\epsilon_0$	.00173	.00204
$4\epsilon_0$	.00156	.00183
$5\epsilon_0$	.00143	.00169
$6\epsilon_0$	.00133	.0016

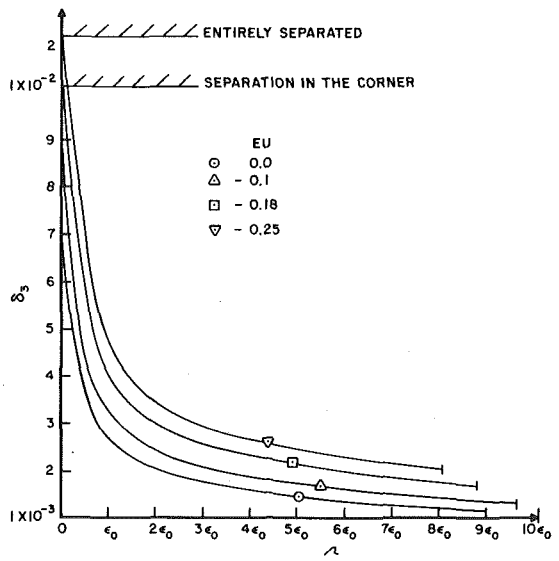

Fig. 12 Variation of interference displacement thickness with fillet radius

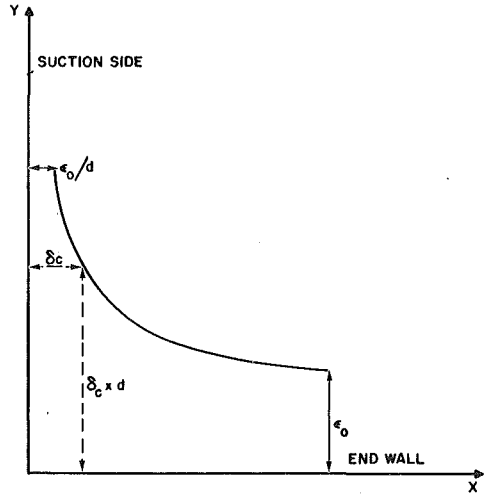

Fig. 13 Schematic representation of unsymmetrical corner flow

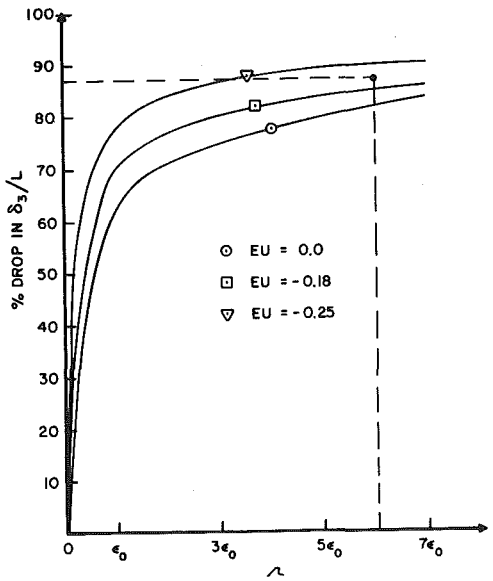

Fig. 14 Percent drop in δ_3/L versus fillet radius

will illustrate the procedure, using data typical for a high performance turbocompressor stator row.

Procedure and Numerical Example. The estimation of a fillet radius preventing separation in the corner formed by the intersection of the stator blade and endwall of a turbocompressor may be obtained as follows: the given data include the channel dimensions, the Reynolds number Re, the meridional velocity (assumed constant), the channel entrance and exit tangential velocities, and the initial momentum thickness. From these, the potential flow velocity distribution may be obtained (24 [11]) as well as the pressure gradient. The momentum thickness is then calculated simultaneously with the friction coefficient and the shape factor $H12$, using Truckenbrodt's quadrature, [13], and Garner's equation.

The calculation of the corner boundary layer parameters is carried out using the following equation from reference [11]:

$$(U_{ec})'_s \frac{\delta_{2c}}{U_{ec}} \frac{(n^3 + 7n^2 + 12n + 4)}{n^2(3 + 2n)} + \frac{2(n+1)}{(3+2n)} (\delta_{2c})_s' = \frac{C_f}{2}\left(\frac{d+1}{d}\right) \quad (25)$$

where U_{ec} is the potential flow velocity in the corner, $\delta_2 c$ the momentum thickness in the corner, and d, the ratio of the endwall and blade boundary layer thicknesses. The interference displacement thicknesses along the corner is then obtained as:

$$\delta_3 = \left[\frac{(1+2n)}{(1+n)^2}\frac{\delta_c{}^2}{4} - \frac{1}{(1+n)}\left(\epsilon_0\delta_c - \frac{\epsilon_0\delta^2}{2}\right)\right]^{1/2} \quad (26)$$

The value of r required to lower the maximum value of δ_3/L in the corner to or just below that indicated in Fig. 12 as separation in the corner is obtained from Fig. 14 where the percent drop in δ_3/L versus r is given for the range of Euler numbers of interest.

By way of example, Fig. 15 contains the complete calculation for the suction and pressure side corners of a compressor stator blade row using the following data: Channel width = 2.54 cm (1 in.); Re = 10^6; initial momentum thickness δ_2 = 0.003683 cm (0.00145 in.); H12 = 1.47; meridional velocity = 233.78 m/s (767 ft/s); initial tangential velocity = 195.68 m/s (642 ft/s); exit tangential velocity = 5.18 m/s (17 ft/s).

For this case, the maximum value of δ_3/L in the pressure corner is approximately 0.085 at X/L = 0.55 so that the drop in interference displacement thickness required to match the value of 0.011 representing separation in the corner in Fig. 12 is 87 percent. Choosing the Euler number in the neighborhood of the highest values obtained in the pressure corner, let $EU = -0.2$. Hence, as indicated in Fig. 14, a fillet radius of 6 ϵ_0 would prevent separation.

ϵ_0 is directly obtained from δ_2 through the relationship:

$$\epsilon_0 = \frac{(n+1)(n+2)}{n}\delta_2$$

since n is known from $H12$. In this example, at X/L = 0.55, $H12$ = 1.96, n = 2.08, δ_2 = 0.01854 cm (.0073 in.) and ϵ_0 = 0.111 cm(0.0438 in.) whence r = 0.67 cm (0.264 in.).

Conclusion

The foregoing study has demonstrated the adequacy of Toan's assumptions regarding the modifications of the power law velocity when applied to the 90 deg corner boundary layer insofar as the estimation of the interference displacement thickness is concerned. This agreement is maintained as adverse pressure gradients are imposed on the corner flow. It must be emphasized that this agreement was obtained using experimental values of δ/ϵ_0. These results constitute the foundation for the extension to the case when $\alpha < 90$ deg, for α sufficiently small so that the main objection to the application of the momentum integral equation to the corner boundary layer may be lifted. The corner boundary layer parameters may thus be obtained analytically and the interference displacement thicknesses evaluated with some measure of credibility.

Finally, a qualitative study of the effect of introducing a fillet in the 90 deg corner was attempted, applying the results obtained for corner flows with $\alpha < 30$ deg to a polyhedral approximation of the fillet.

The necessity of defining an interference displacement area and thickness for this case in analogy with Gersten's definitions for a 90 deg corner without fillet, coupled with the desirability of obtaining a fully expanded flow for every corner used in the approximation, limits the minimum fillet radius to 2 δ_1. With values of the interference displacement thickness interpolated for $0 < r < 2\,\delta_1$, the plots of δ_3 versus r (Fig. 12) qualitatively illustrate the drastic reduction of separation probability in the corner when a fillet is provided.

Application of these results to a turbocompressor channel flow is seen to be straightforward, and it may be added that the inclusion of secondary flows generated on the endwall and blade surface could be easily included in the calculation of the interference thicknesses.

Since the calculation of δ_3/L as a function of r is based on the interference displacement area generated by the corner flow in a dihedral, the value of r necessary to prevent separation at X/L where δ_3/L is maximum should be maintained constant for a considerable distance upstream of this point. Downstream, r may be calculated locally according to the procedure described in the example so that an adequate fillet radius profile could be represented by Fig. 15(f).

In the case of a blade row, this requirement may be tempered by

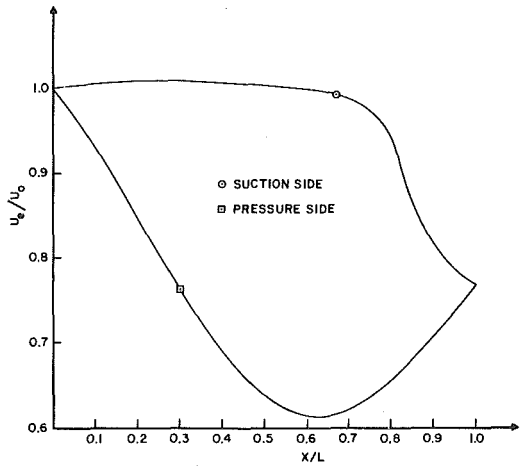

Fig. 15(*a*) Potential flow velocity in suction and pressure corners

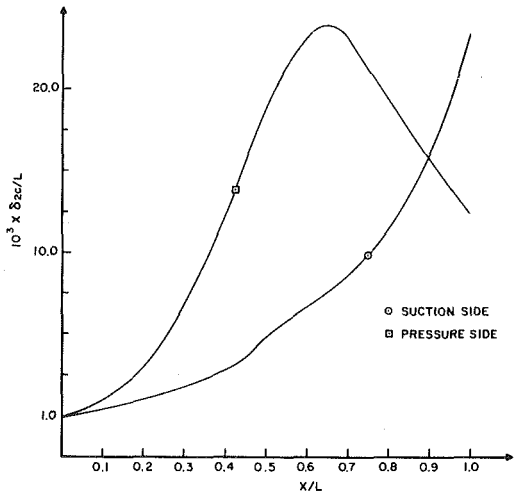

Fig. 15(*d*) Corner momentum displacement thickness on pressure and suction sides

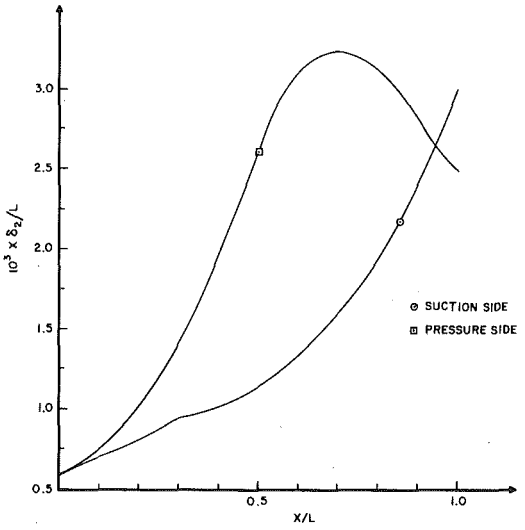

Fig. 15(*b*) Momentum displacement thickness on pressure and suction sides

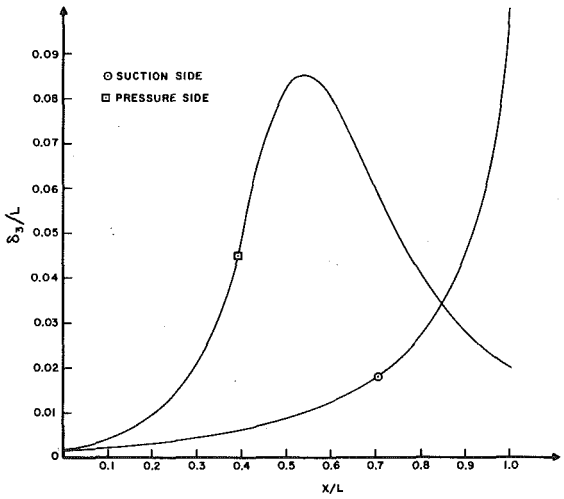

Fig. 15(*e*) Corner interference displacement thickness on pressure and suction sides

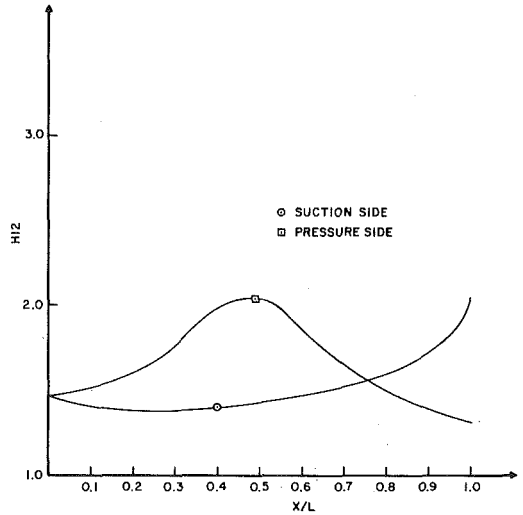

Fig. 15(*c*) Shape parameter *H*12 on pressure and suction sides

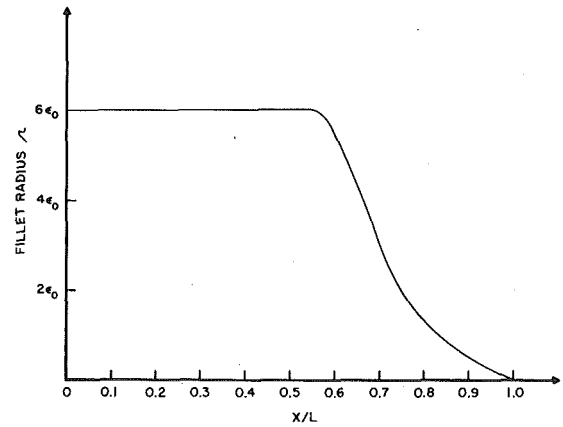

Fig. 15(*f*) Fillet radius profile versus dimensionless distance from leading edge

other considerations, such as the desirability of maintaining a lower profile drag and the necessity of taking into account the variation of the local angle between blade and hub along the corner. Some unpublished experiments have indicated that for low speed, moderately loaded airfoils, small fillets produce less loss than large ones if they are of constant radius around the full circumference of the airfoil. Because this is obviously contrary to boundary layer requirements, one might conclude that a small fillet near the leading edge is desirable, transitioning to a larger radius as one moves downstream. The optimum channel configuration design may result in the local angle between hub and blade varying from acute to obtuse values or vice versa. As α becomes smaller than 90 deg the foregoing study indicates that δ_3/L decreases and hence r. For α assuming values greater than 90 deg, the study of turbulent flow in triangular ducts given in reference [14] indicates a complete similarity of corner flow phenomena (wall shear stress, corner vortices) with square ducts and it may be safely surmized that the enhancement of corner vortices in this case will result in larger values of δ_3/L and hence of the fillet radius necessary to prevent corner separation.

Acknowledgments

I wish to express my gratitude to Dr. Arthur J. Wennerstrom for his guidance, advice, and support throughout this work.

References

1 Hoerner, S. F., "Fluid Dynamic Drag," 1965, Chapter 8, pp. 10–15.
2 Carrier, G. F., "The Boundary Layer in a Corner," *Quarterly Applied Mathematics,* Vol 4, 1946, pp. 367–370.
3 Cheng, Sin-I. and Levy, R. H., "The Boundary Layer in a Corner," Report 485, AFOSR TN 59-1165, 1959, Princeton University, Princeton, NJ.
4 Bertotti, B., "Teoria dello Strato Limite SU un diedro," Rendiconti Instituto Lombardo, A92, 1958, pp. 553–566.
5 Eichelbrenner, E. A., "La Couche Limite Turbulents a l'Interieur d'un Diedre," *La Recherche Aeronautique,* No. 83, Jul-Aug, 1961, pp. 1–8.
6 Gersten, K., "Corner Interference Effects," NATO, Advisory Group for Aerospace Research and Development, Report 299, Mar 1959.
7 Bragg, G. M., "The Turbulent Boundary Layer in a Corner," *Journal of Fluid Mechanics,* Vol. 36, 1969, pp. 485–503.
8 Paradis, M. A., "Couche Limite Turbulente a l'Interieur d'um Diedre," Master of Science Thesis, April 1963, Laval University, Quebec, Canada.
9 Eichelbrenner, E. A., and Toan, N. K., Comptes Rendus de l'Academie des Sciences, Vol. 269, Paris, Nov 3, 1969, pp. 869–872.
10 Zamir, M., "Boundary-Layer Theory and the Flow in a Streamwise Corner," *Aeronautical Journal of the Royal Aeronautical Society,* Vol. 74, April 1970, pp. 330–332.
11 Suter, P., "Theoretical Untersuchung Uber die Seitenwandgrenzschichten in Axialverdich tern," Miteilungen Aus dem Institut fur Thermische Turbomaschinen, Zurich, Switzerland, 1960, pp. 93–101.
12 Toan, N. K., "Application of Integral Methods to the Turbulent Corner Flow Problem," Trans ASME, 71-WA/FE-36.
13 Schlichting, H., "The Incompressible Turbulent Boundary Layer with Pressure Gradient," *Boundary Layer Theory,* 6th ed., McGraw-Hill, N.Y., 1968, pp. 627–643.
14 Aly, A. M. M., Trupp, A. C. and Gerrard, A. D., "Measurements and Prediction of Fully Developed Turbulent Flows in an Equilateral Triangular Duct," *Journal of Fluid Mechanics,* Vol 85, Part 1, 7 Mar. 1978, pp. 57–83.

Printed in U. S. A.

B. R. Hollworth

Assistant Professor,
Mechanical and Industrial Engineering Department,
Clarkson College of Technology,
Potsdam, NY
Mem. ASME

L. Dagan

Development Engineer,
Eastman Kodak Company,
Kodak Park,
Rochester, NY

Arrays of Impinging Jets with Spent Fluid Removal through Vent Holes on the Target Surface

Part 1: Average Heat Transfer

Measurements of average convective heat transfer are reported for square arrays of impinging air jets. The target plate on which the jets impinge is perforated so that spent air is withdrawn through the plate rather than at one or more edges of the array, as is usually the case in such investigations. Jet holes and vent holes had the same diameters, but the spacing of the jet holes was twice that of the vent holes. This information is especially relevent to the design of hybrid cooling configurations, in which a surface is cooled by the combined mechanisms of impingement and transpiration. Tests were conducted for both inline arrangements (with a vent hole opposite each jet orifice) and for staggered arrangements; and the latter always yielded higher average heat transfer. The degradation of performance of inline arrays was most pronounced when the clearance between the jet orifice plate and the target plate was small. Under these conditions, a significant portion of each jet flows directly out through the opposing vent without "scrubbing" the target surface. Arrays with staggered vent holes yield heat transfer rates consistently higher (sometimes by as much as 35 percent) than the same jet array with edge venting. The authors attribute the superior performance of the former geometry to high local heat transfer due to boundary layer suction in the vicinities of the vent holes.

Introduction

Impinging jets have found a large number of applications where high rates of convective heat (or mass) transfer are required. These include the heat treating of some metals, the tempering of glass, the drying of paper stock, and the cooling of electronics components and critical parts of the hot sections of high performance gas turbine engines. Such systems have also been given recent consideration as a means to improve heat transfer between solid surfaces and the working fluid in solar collectors. In the broader sense, all heat transfer "augmentation" techniques have gained importance owing to their potential for improving the efficiency of energy systems and thereby aiding in the energy conservation effort.

It is well known that the thermodynamic efficiency of a gas turbine engine is increased by raising the turbine inlet (i.e., combustor discharge) temperature. Temperatures approaching 3000°F (1650°C) are not uncommon in state-of-the-art engines. At such operating temperatures, it becomes necessary to cool the combustor and the first stages of the turbine using air bled from the engine's compressor. Of course, diverting air for cooling purposes has the effect of reducing engine efficiency—hence it is mandatory to develop schemes which provide maximum thermal protection while using a minimal flow of coolant. A "hybrid" cooling scheme (see Fig. 1) uses the combined mechanisms of impingement, transpiration, and film cooling to achieve this end. The spent impingement fluid is vented through passages in the target surface into the hot gas to achieve additional cooling benefit.

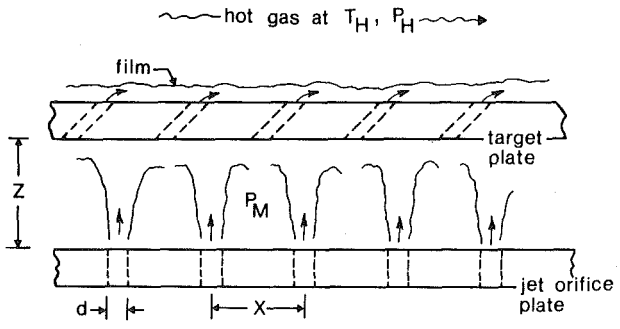

Fig. 1 Hybrid cooling system

Previous experiments [1–3] have shown the impingement-side convection coefficient to be very sensitive to the flow field adjacent to the impingement surface; and the nature of this flow is strongly influenced by the manner in which spent air is withdrawn after impingement. Most of these impingement studies have dealt with arrangements where the spent air was removed along one or more edges of the array rather than through vent holes on the target surface itself.

Contributed by the Gas Turbine Division and presented at the Gas Turbine Conference and Products Show, New Orleans, La., March 10–13, 1980 of THE AMERICAN SOCIETY OF MECHANICAL ENGINEERS. Manuscript received at ASME Headquarters December 10, 1979. Paper No. 80-GT-42.

Table 1 Test variables

jet orifice diameter[1]	d 5.0 mm and 2.5 mm
jet Reynolds number	Re 3000 to 35,000
jet Prandtl number	Pr 0.72 (air near room temperature)
nondimensional jet-to-jet spacing	$\overline{X}$ 5, 10, 15, 20
nondimensional spacing between jet orifice plate and target plate	$\overline{Z}$ 1 to $\overline{X}$

[1] Nominal diameters are 5.0 and 2.5 mm. Actual diameters are 5.08 and 2.54 mm.

Hence, it is apparent that data obtained from these investigations may not be applied to the design of a hybrid system, with its unique mode of spent air removal. In fact, the current study was initiated to generate impingement-side heat transfer information which could be applied specifically to such systems. More precisely, the objectives were:

1 to measure average convective heat transfer coefficients, and
2 to measure local heat transfer coefficients, and use flow visualization and integral techniques to relate the details of the heat transfer distribution to the fluid dynamics of such configurations.

This paper reports the results of the first phase of the study (average heat transfer measurements), and the results of the second portion of the work will be reported in a subsequent paper.

Average heat transfer coefficients were measured while varying the independent test variables over ranges generally appropriate to gas turbine cooling applications. The appropriate set of dimensionless variables which incorporate coolant flow rate, system geometry, and fluid properties for impingement situations is well known; the relationship between the average convection heat transfer coefficient and these variables is of the form

$$\overline{\mathrm{Nu}} = f\left(\mathrm{Re}, \mathrm{Pr}, \overline{X}, \overline{Z}, \begin{matrix}\text{vent hole size} \\ \text{and placement}\end{matrix}\right) \quad (1)$$

where the variables are defined in the Nomenclature section, and the term "vent hole size and placement" will be discussed in some detail in following paragraphs. The ranges over which test parameters were varied are summarized in Table 1, and the total test program contained in the neighborhood of 200 test points. Jets are formed by 4 × 4 square arrays of round orifices drilled into a flat surface which is oriented parallel to the target plate. The orifices are square-edged with length/diameter = 1.0; they were flow-calibrated and found to have a discharge coefficient of 0.80 over the range of flows used during the heat transfer tests.

The ranges given in Table 1 correspond generally to those used by Hollworth and Berry [4] in an earlier heat transfer study in which spent air was vented along all four edges of a 4 × 4 array of jets which impinged on a solid target surface. One exception is that the current study includes data at a jet spacing of $\overline{X} = 5$. This spacing is used in practical applications, but was not included in the first investigation which was restricted to measuring heat transfer for arrays having large jet-to-jet spacing ($\overline{X} \geq 10$). It was anticipated from the results of the earlier study that there is no appreciable jet diameter effect. Therefore, the bulk of the heat transfer measurements are made using d = 5.0 mm. The smaller holes (d = 2.5 mm) are used primarily to generate data at the lowest Reynolds number (Re = 3000). For the ranges of Re and d given in Table 1, jet exit velocities never exceed 150 m/s. Hence, it may be presumed that compressibility effects are small.

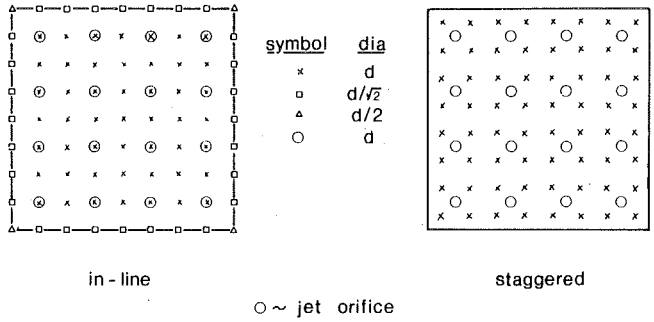

Fig. 2 Vent hole configurations

It remains to discuss the geometry of the matrix of vent holes. These correspond to the transpiration passages in the hybrid cooling system of Fig. 1. There are, of course, an unlimited number of choices for the diameters of these holes, their spacing, and their locations relative to the jet holes. In order to keep variations at a manageable level, it was established that a good representative vent geometry would be:

holes: round, with same nominal diameter as jet orifices
array: square
spacing: half that of jet orifices
placement: (*a*) directly in-line with jet orifices
(*b*) staggered relative to jet orifices

Fig. 2 shows the two basic (inline versus staggered) configurations which were tested. In all cases, there are 16 jets, therefore (nominally) 64 vent holes. The smaller vent holes around the perimeter of the inline array serve to produce the same flow pattern which would exist in an array of infinite extent.

It seems appropriate to offer some justification for this choice of vent geometry in terms of the performance of hybrid cooling configurations to which the heat transfer data will be applied. It is assumed that the vents are circular and laid out in square arrays, as such configurations are most easily machined. In most gas turbine cooling systems, jet orifices and transpiration passages are roughly the same size, both having diameters in the neighborhood 0.2 to 1.0 mm. The same techniques (laser, electron beam, electric discharge, etc.) are available for microdrilling both types of holes. Moreover, all three modes of cooling tend to perform better as hole size is decreased—neglecting possible plugging of smaller passages by particulate matter carried by the air. It is logical, therefore, to use vent holes having the same nominal diameter as the jet orifices for this study.

In hybrid cooling systems, the total available pressure differential ($[P_0–P_H]$ in Fig. 1) is usually 5–10 atmospheres. However, the largest part of the pressure drop must take place across the jet orifices. If the pressure difference across the transpiration plate ($[P_M–P_H]$ in Fig. 1) is much more than 1 atmosphere (depending on hot gas velocity and density, break-out angle of film cooling apertures, etc.), the film is virtually blown off the surface and thus provides little or no thermal protection. In order to induce the larger pressure drop across the jet orifice plate, this plate must be made less "porous" than the transpiration plate. If we restrict both plates to having round holes of the same diameter in square arrays, then the spacing of the jet holes must be greater than that of the vents.

The spacing between vent holes was chosen to optimize performance of the film cooling portion of the cooling system. The optimum

Nomenclature

A = area of target plate, m^2
d = nominal diameter of jet orifices, mm
E = voltage supplied to target plate heaters, volts
G = coolant flow per unit area of target surface, kg/s-m^2
$\bar{h}$ = average impingement heat transfer coefficient, W/m^2-°C
I = current supplied to target plate heaters, amps
K = thermal conductivity of test fluid, W/m-°C
$\dot{m}$ = total coolant flow rate, kg/s
$\overline{\mathrm{Nu}}$ = average Nusselt number, $\bar{h}$d/k
Pr = Prandtl number
q = rate of convective heat transfer, W
Δq = heat transfer correction, W
Re = jet Reynolds number
T_0 = jet plenum temperature
T_s = target surface temperature
X = center-to-center spacing of jet orifices
$\overline{X} = X/d$
Z = normal distance between jet orifice plate and target plate
$\overline{Z} = Z/d$
μ = test fluid dynamic viscosity, Pa·s
ρ = test fluid density, kg/m^3

value of (jet hole spacing)/(vent hole spacing) was taken to be that one which yields a coolant injection velocity equal roughly to 1/2 the velocity of the hot gas stream, which is a fairly acceptable rule of thumb for gas turbine film cooling calculations. The resultant value of this ratio varies somewhat from one application to the next, depending upon the pressures and temperatures of the hot gas and the coolant, and the hot gas velocity. It was determined by the authors (see [5]) that the ratio varies between 1.5 and 2.5 for most engine conditions likely to be encountered. Hence, it was logical to choose a value of (jet spacing/vent spacing) = 2.0 for this investigation.

Now that the diameter and spacing of the vent passages have been determined, it remains only to lay out the vent array relative to the jet array. The first, and most obvious, choice is to arrange them inline with one vent directly opposite each jet. It was expected that such an arrangement would not perform well at small $\overline{Z}$, as the jets would be discharged directly through the opposing vents without first scrubbing the target surface. Anticipating this problem, tests are conducted also on configurations having vents staggered relative to the jets (see Fig. 2) so that there is no vent opposite any jet orifice.

Finally, it should be reiterated that, while this sort of impingement scheme is used as part of a hybrid system, this study includes no measurements associated with transpiration or film cooling. The three mechanisms are sufficiently uncoupled so that the design/analysis of a hybrid system may be carried out by treating the three separately and patching together the results. In fact, there exist extensive bodies of literature on film and transpiration cooling considered independently.

Experimental Apparatus and Procedures

The test system is shown in Fig. 3. It consists of an air delivery loop, a plenum with interchangeable jet orifice plates, and an electrically heated target plates on which the jets impinge. In fact, it is essentially the same rig used by Hollworth and Berry in the earlier impingement study cited above. The only noteworthy modifications are the following:

1 Target plates with vent holes were fabricated to replace the solid plates used in the earlier study.
2 Side skirts were added between the jet plate and the target plate so that all spent air was constrained to exhaust through the vent holes.

The air supply loop consists of a reciprocating air compressor (which supplies filtered and dried air at a pressure of approximately 6 bars), along with equipment to control and measure air flow to the heat transfer rig. Air flow is modulated with hand-operated valves, and a pressure regulator maintains the pressure upstream of the test rig—and therefore the flow rate—constant during each test. Flow rate is measured with a bank of rotameters rated accurate to ±1 percent full scale. A safety valve in the supply line protects against overpressurizing the plenum.

The jet plenum is an airtight box fabricated from aluminum plate. There are, in fact, two such plenums—a large one to accommodate larger jet array plates, and a smaller box for the smaller arrays. Both contain a baffle and a screen to insure that air is evenly distributed among the several jet orifices. Total temperature is measured with two iron-constrantan thermocouples in the plenum, and total pressure is measured with U-tube manometers. Interchangeable orifice plates are used to provide the eight jet arrays (two values of d, four values of $\overline{X}$) indicated in Table 1. The standoff ($\overline{Z}$) between the jet plate and target plate is set and maintained with wooden dowels at the four corners; they are located as far as possible from the vents to minimize interference with the flow. Four side skirts (made from 13-mm thick plexiglas) are used to prevent spent air from exhausting at the edges of the target surface. These are clamped tightly between the jet plate and target plate and all mating surfaces are made airtight using rubber gaskets.

Jets impinge on a flat isothermal target consisting of a 6-mm thick copper plate heated by electrical heaters cemented to its back surface. There are two such target plates for each jet plate, one with an inline vent pattern and one with a staggered pattern, as shown in Fig. 2. The a-c power source is a Variac, and the rate of power delivered to the

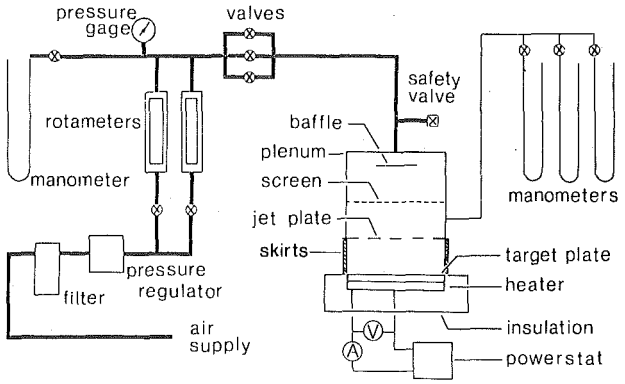

Fig. 3 Schematic of heat transfer rig

plate is determined by measuring the voltage (E) and the current (I) in the heater circuit. The voltage is measured with a precision (±1/2 percent) digital voltmeter, and the current is determined by measuring the voltage drop (using the same DVM) across a precision 0.01 ohm resistor connected in series with the bank of resistive heaters. Each heater/plate assembly is insulated with 50 mm of foam insulation glued to its back surface, to minimize heat loss to the surroundings. Holes, with the same diameter and locations as those in the target plate, are bored through the insulation to allow removal of spent air. Each copper plate is instrumented with at least five imbedded iron-constantan thermocouples to measure the surface temperature, T_s. Details concerning the installation and locations of the thermocouples are given in [4].

When designing the test rig, the original intention was to use jet and vent holes having exactly the same diameters and shapes. It was later determined that the convective heat transfer inside the vent holes (a potential source of error in this experiment) could be reduced by relieving the downstream end of the vent holes (see Fig. 4) to produce what was essentially a sharp-edged orifice. The original shape had a discharge coefficient (C_d) of 0.80, and subsequent flow calibrations indicated that the redesigned orifice had $C_d' = 0.62$ in the range of flows to be used in this program. In order that the test configuration with redesigned vents retain the same flow versus pressure drop characteristics as the original configuration, the vent diameters were increased slightly to compensate for the decrease in discharge coefficient. The adjusted vent hole diameters (d') were determined using

$$d' = \sqrt{\frac{C_d}{C_d'}}\, d \cong 1.14d, \tag{2}$$

where d is the jet orifice diameter. The vent spacing is kept at exactly 1/2 the jet spacing as originally proposed. For most target plates, the heaters were resistive elements laminated between two silicone rubber pads. However, for a few of the plates with small clearances between vents, narrow (approximately 3-mm wide) Nichrome strip heaters were used instead.

The procedure for running each test was straightforward. Four spacers of the appropriate length (Z) were installed between the jet plates and vent plate, the side skirts were attached, and the assembly was clamped tightly together. The cooling air was turned on and the flow rate adjusted to give the desired Re. At this point, the rig was checked for air leaks in the line between the flow meters and the plenum, past the skirts, etc. Electric power to the heaters was turned on and the Variac adjusted until the target plate temperature T_s was 50°C above the plenum temperature T_0—which was equal essentially to room temperature for these tests. In a few cases, the Nichrome elements tended to overheat; it was necessary to hold the plate temperature 20–30°C above room temperature in these instances. A sufficient time interval was allowed for the rig to reach steady-state, then the following data were taken:

- indicated air flow, along with pressure and temperature at rotameter discharge to correct for off-calibration conditions
- plenum pressure and total temperature

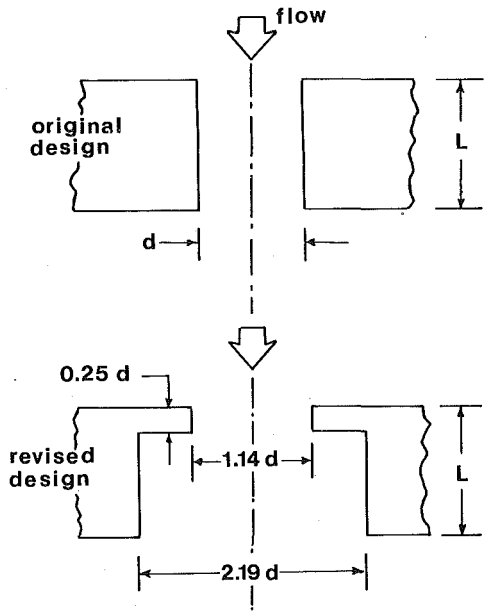

Fig. 4 Section through large vent passage (Note: d = 5.08 mm, L = 6.35 mm)

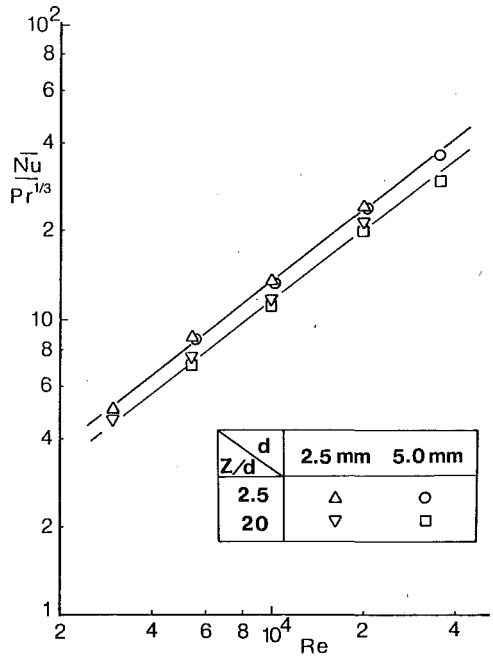

Fig. 5 Average heat transfer for staggered array with $\overline{X}$ = 20

- target plate temperature
- voltage and current to heaters
- room temperature and atmospheric pressure.

Results and Discussion

Space-averaged heat transfer coefficients were calculated from the test data using

$$\overline{h} = \frac{EI - \Delta q}{A(T_s - T_0)} \tag{3}$$

The area, A, was taken to be 16 X^2; no adjustment was made for the presence of the vent holes. The term Δq accounts for several types of heat loss from the target plate. These include:

- conduction losses through the insulation on the back side of the plate
- radiation from the impingement surface
- convection heat transfer *inside* the vent passages ($\overline{h}$ includes only the impingement effect)
- heat losses at the edges of the plate, due to the fin effect associated with the skirts.

The first three contributions were computed, and the last one was measured using heat flux sensors glued to the edges of the plates; details are given in [5]. The size of the correction Δq varied from 4 percent to 29 percent of EI, and the average was about 11 percent.

The surface temperature T_s was taken to be the arithmetic average of the readings from the several thermocouples imbedded in each plate. Based on these temperature measurements, the target plates were acceptably isothermal; individual readings seldom differed from the mean by more than 3°C. Because jet velocities were low and the overall ΔT ($\Delta T \equiv T_s - T_0$) was fairly large, it was decided that the plenum temperature T_0 was an adequate approximation for the recovery temperature—which is, in general, the effective fluid temperature to be used in equation (3). The average experimental uncertainty in $\overline{h}$ was calculated using the method given by Holman [6] and found to be about ±4 percent; the worst case value was ±9 percent.

In correlating results from these tests, the heat transfer coefficients and coolant flow rates are generally expressed nondimensionally as an average impingement Nusselt number and a jet Reynolds number, respectively, given by

$$\overline{\mathrm{Nu}} = \overline{h}d/K \tag{4}$$

and

$$\mathrm{Re} = \frac{\dot{m}}{16\frac{\pi}{4}d^2}\frac{d}{\mu} \tag{5}$$

All air properties (K, μ, Pr) are evaluated at a "film" temperature halfway between T_s and T_0, using property tables in [7].

Fig. 5 shows typical variation of average heat transfer (expressed as $\overline{\mathrm{Nu}}/\mathrm{Pr}^{1/3}$) with air flow (expressed as Re). As the test fluid was always near STP, Pr was taken as 0.72 throughout, and the traditional assumption $\overline{\mathrm{Nu}} \sim \mathrm{Pr}^{1/3}$ was employed. Fig. 5 is representative of data for all other geometries tested in that:

1 There is no hole size effect. Values of $\overline{\mathrm{Nu}}$ using d = 2.5 and 5.0 mm were (within experimental uncertainty) equal for the same values of the independent nondimensional parameters.
2 $\overline{\mathrm{Nu}}$ plotted against Re in log-log coordinates were virtually straight lines for all $\overline{X}$ and $\overline{Z}$.

Based on these two observations, then, it was concluded that data would fit a relation of the form

$$\overline{\mathrm{Nu}} = \mathrm{Re}^m \mathrm{Pr}^{1/3} f(\overline{X}, \overline{Z}, \text{staggered or inline}) \tag{6}$$

where the exponent m might vary with geometry. The least squares method was used to fit a best line to the four data points for each geometry, and m was found to vary generally between 0.73 and 0.87. The most apparent trend was a tendency for m to decrease as $\overline{X}$ was increased; this occurred consistently for both the inline and staggered arrays. The values of m which best fit *all* data were 0.799 for the staggered arrays and 0.816 for the inline arrays. Despite these variations in m with geometry, data were found to correlate well using:

$$\frac{\overline{\mathrm{Nu}}}{\mathrm{Re}^{0.80}\mathrm{Pr}^{1/3}} = f(\overline{X}, \overline{Z}, \text{staggered or inline}). \tag{7}$$

Fig. 6 shows average heat transfer data for staggered and inline arrays with $\overline{X}$ = 10 displayed using this format, which is especially convenient for showing the effects of geometry upon heat transfer. The general behavior is typical of that for all $\overline{X}$ tested. The most apparent conclusion is that the performance of inline arrays is decidedly inferior to that of staggered arrays, especially at small standoff (i.e., small $\overline{Z}$). Though this funding is significant, it was not unexpected. The authors presume that for inline arrays, a significant portion of each cooling jet flows directly out through the opposing vent without scrubbing the target surface, as shown in Fig. 7. At small $\overline{Z}$, the vent captures a larger fraction of the total jet flow and the degradation is most pronounced. Fig. 6 indicates also that optimum standoff for staggered

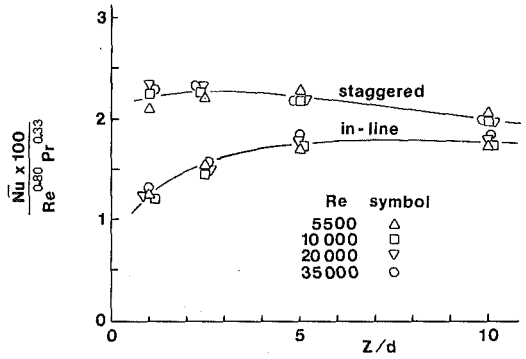

Fig. 6 Effects of standoff for $\overline{X} = 10$

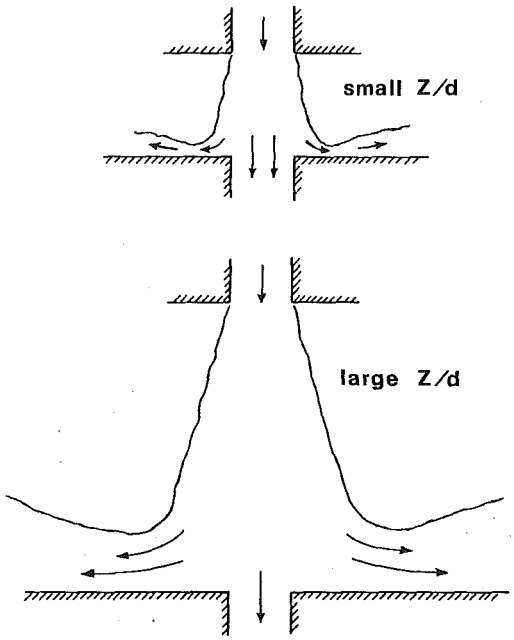

Fig. 7 Capture of jet by vent hole

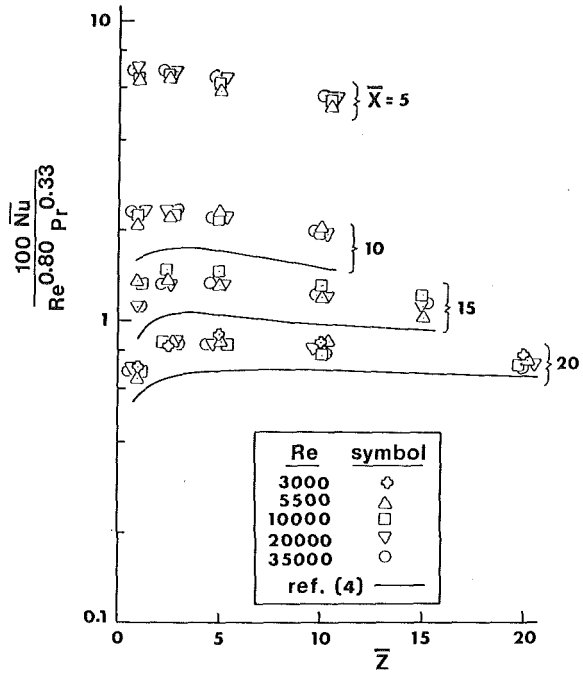

Fig. 8 Performance comparison: staggered arrays versus arrays with edge venting

Table 2 Comparison of inline and staggered arrays: typical data

	values of $\frac{\overline{Nu}\text{ (inline)}}{\overline{Nu}\text{ (staggered)}}$			
	$\overline{X} = 5$	$\overline{X} = 10$	$\overline{X} = 15$	$\overline{X} = 20$
$\overline{Z} = 1$	0.40	0.56	0.60	0.80
$\overline{Z} = 2.5$	0.51	0.66	0.61	0.76
$\overline{Z} = 5$	0.69	0.80	0.72	0.88
$\overline{Z} = 10$	0.84	0.89	0.83	0.88

arrays with ($\overline{X} = 10$) is $\overline{Z} \cong 2.5$; this was the case for $\overline{X} = 5$, 15, and 20 as well.

One can take the ratio $\eta \equiv \overline{Nu}(\text{inline})/\overline{Nu}(\text{staggered})$ as being indicative of the cooling effectiveness of the inline arrays relative to the staggered arrays. This ratio would, in general, vary with Re, $\overline{Z}$ and $\overline{X}$. Because both $\overline{Nu}$-values vary roughly with $Re^{0.80}$, η becomes virtually independent of Re, as Fig. 6 shows. Fig. 6 (for $\overline{X} = 10$) shows, also, a fairly representative variation of η with $\overline{Z}$. At small standoff ($\overline{Z} = 1$), $\overline{Nu}$ for the inline array may be less than 1/2 that of the corresponding staggered array. At larger $\overline{Z}$ (e.g., $\overline{Z} = 10$) the inline arrays yield average heat transfer varying (dependently upon $\overline{X}$) between 84 and 90 percent of the value for the staggered array. Based on data at $\overline{Z} =$ 15 and 20, it appears that η tends asymptotically toward 1.0 as $\overline{Z}$ is further increased. Based on data for all arrays, η tends to be larger at large $\overline{X}$; Table 2 gives values of η versus $\overline{X}$ for a few representative values of $\overline{Z}$ and shows this trend.

There is some scatter in the data (as Table 2 also indicates) which is most pronounced at small $\overline{Z}$. It is expected that the heat transfer for a jet impinging upon a surface, with an inline vent hole, is sensitive even to the slightest misalignment between the two holes. If the vent aperture of Fig. 7 were offset by, for example, 1/4 d relative to the jet orifice, the amount of jet air *not* directly captured by the vent would increase significantly—yielding a correspondingly higher convection heat transfer coefficient. It is apparent that this effect would be most severe at small $\overline{Z}$; as $\overline{Z}$ is increased, the jet spreading also increases and the capture effect, in general, diminishes in importance. Undoubtedly, there was some unintentional misalignment (in some cases more than others) introduced during:

- the machining of jet and vent plates,
- the aligning of plates when setting up or adjusting the rig for each test,
- the running of the tests if any asymmetries in the flow field deflected jets from straightline trajectories.

The authors feel that such incidental (and probably slight) misalignment is reflected in the behavior of the data in Table 2. The fact remains that the significantly better heat transfer offered by staggered arrays strongly suggests that these be used by the designer in favor of inline geometries. For this reason, the remainder of this paper focuses on data for staggered configurations.

Average heat transfer for staggered arrays correlates in much the same way (see equation (7)) as does the data from [4]. It is possible, therefore, to make a direct comparison between the cooling capabilities of jet arrays with spent air removal through vent holes and arrays with edge venting, as shown in Fig. 8. It is apparent, from inspection of this figure, that arrays with staggered vent holes offer consistently better performance for all $\overline{X}$ and $\overline{Z}$ where common data are available. The increment in heat transfer depends upon the geometry of the array. Arrays with staggered vents show the most pronounced performance advantage as the hole spacing $\overline{X}$ is decreased. At $\overline{X} = 10$, these arrays yield $\overline{Nu}$ about 35 percent higher than the same array with air removal along the edges; for $\overline{X} = 15$ and 20, these figures drop to 32 percent and 24 percent, respectively. There is some tendency, also, for the increment in heat transfer to increase as $\overline{Z}$ is made smaller. The percentages quoted above were averaged over $\overline{Z}$ for $1 \leq \overline{Z} \leq 10$, which is the range for most gas turbine cooling situations.

The authors suggest that the superior performance of the staggered arrays is due to boundary layer suction, which produces high local heat transfer coefficients in the vicinities of the vent holes. These holes are

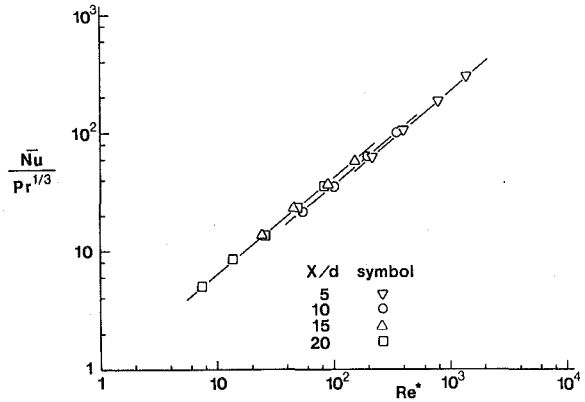

Fig. 9 Average heat transfer versus coolant flow per unit area of target surface for staggered arrays with $\overline{Z} = 2.5$

located at sites fairly far removed from the stagnation points of the impinging jets, where heat transfer coefficients would otherwise (i.e., if edge venting were employed) be quite low—especially for large $\overline{X}$. Thus, the addition of vent holes tends to increase the array-averaged h over that associated with a solid target plate with edge venting. It is anticipated that local heat transfer measurements to be undertaken as part of Phase II of this program will support this explanation.

A sensible way to compare the cooling power of various impingement geometries is to compare their respective heat transfer coefficients at the same coolant flow *per unit area of target surface,* as was done by Hollworth and Berry [4], and by Metzger, et al. [3] for jets in a crossflow. Fig. 9 shows $\overline{Nu}/Pr^{1/3}$ plotted against a modified Reynolds number (Re*) based on the coolant flow per unit area of target surface (G). This variable is defined as

$$Re^* = \frac{4}{\pi}\frac{Gd}{\mu} = \frac{Re}{(\overline{X})^2}, \tag{8}$$

so that constant Re* corresponds to constant G. Fig. 9 was plotted for staggered arrays at $\overline{Z} = 2.5$ (optimum standoff) and shows that arrays with widely-spaced jets (but high flow per jet) outperform arrays with more jets (per unit area) but less flow per jet. At the same G, arrays with $\overline{X} = 10$ give $\overline{h}$ about 5 percent higher than the array with $\overline{X} = 5$, while arrays with $\overline{X} = 15$ and 20 give $\overline{h}$ about 15 percent larger than does $\overline{X} = 5$. Heat transfer measurements made by Hollworth and Berry showed essentially the same behavior; average heat transfer coefficients increased consistently as $\overline{X}$ increased. Finally, two comments should be made regarding the application of this information to the design of hybrid cooling system:

1 *Cooling flow and available pressure difference may be essentially fixed for a given design situation.* These dictate the value of $\overline{X}$, and the designer may not be at liberty to select jet-to-jet spacing to maximize impingement heat transfer.
2 While large $\overline{X}$ yields best performance for the impingement portion of a hybrid system, it may not necessarily be the best choice (if a choice is even possible) with regard to total system performance. For example, transpiration cooling systems tend to be more effective when the mass flow rate per coolant passage is low, which (at fixed G) corresponds to small $\overline{X}$. The design of an optimum hybrid configuration must involve integrating impingement heat transfer information with transpiration and film cooling data.

Conclusions

Extensive measurements of average convective heat transfer are reported for square arrays of turbulent air jets impinging on a flat surface. Spent air is withdrawn via square arrays of vent holes (same nominal diameter as jet orifices) on the target surface. The resulting data should be valuable for the design of hybrid impingement/transpiration/film cooling configurations, which employ the same type of spent air removal. The most significant findings were the following:

1 Tests were conducted for vent arrays having vent-to-vent spacing = 1/2 (jet-to-jet spacing). Inline arrays (with a vent directly opposite each jet hole) showed poor heat transfer performance compared to staggered arrays (with no vent opposite any jet). This effect was most pronounced for small $\overline{Z}$, which is generally the range of interest for gas turbine applications. Staggered arrays are thus recommended.
2 Arrays with staggered vents consistently yield higher heat transfer rates (usually by 20–30 percent) than do the same arrays with edge venting.
3 At the same coolant flow per unit area of target surface, (staggered) arrays with large $\overline{X}$ produce higher $\overline{h}$ than those with small $\overline{X}$.

The results reported here point up general trends in heat transfer behavior for impingement heat transfer behavior for such geometries. All data presented are for jet-to-jet spacing = 2 (vent-to-vent spacing). The author cautions against attempting to extend these data to geometries where this ratio differs significantly from 2.0.

Acknowledgments

The authors wish to thank the National Science Foundation, who supported this study under Grant No. ENG77-14630.

References

1 Kercher, D. M., and Tabakoff, W., "Heat Transfer by a Square Array of Round Air Jets Impinging Perpendicular to a Flat Surface Including the Effect of Spent Air," ASME JOURNAL OF ENGINEERING FOR POWER, Vol. 92, No. 1, Jan. 1970, pp. 73–82.

2 Chance, J. L., "Experimental Investigation of Air Impingement Heat Transfer Under an Array of Round Jets," *Tappi,* Vol. 57, No. 6, 1974, pp. 108–112.

3 Metzger, D. E., "Heat Transfer Characteristics for Inline and Staggered Arrays of Circular Jets with Crossflow of Spent Air," ASME *Journal of Heat Transfer,* Vol. 101, No. 3, Aug. 1979, pp. 526–531.

4 Hollworth, B. R., and Berry, R. D., "Heat Transfer from Arrays of Impinging Jets with Large Jet-to-Jet Spacing," ASME *Journal of Heat Transfer,* Vol. 100, No. 2, May 1978, pp. 352–357.

5 Dagan, L. and Hollworth, B. R., "Arrays of Impinging Jets with Spent Fluid Removal through Vent Holes on the Target Surface, Part 2: Average Heat Transfer," Report No. MIE-046, Mech. and Ind. Engr. Dept., Clarkson College of Technology, 1979. Currently being written.

6 Holman, J. P., *Experimental Methods for Engineers,* 3rd ed., McGraw-Hill, pp. 44–51.

7 Holman, J. P., *Heat Transfer,* 4th ed., McGraw-Hill, p. 503.

M. E. Crawford
Department of Mechanical Engineering,
The University of Texas at Austin,
Austin, TX 78746
Assoc. Mem. ASME

W. M. Kays
Dean, School of Engineering,
Stanford University,
Stanford, CA 94305,
Fellow, ASME

R. J. Moffat
Director, Thermosciences Division,
Department of Mechanical Engineering,
Stanford University,
Stanford, CA 94305,
Mem. ASME

Full-Coverage Film Cooling

Part I: Comparison of Heat Transfer Data for Three Injection Angles

Wind tunnel experiments were carried out at Stanford between 1971 and 1977 to study the heat transfer characteristics of full-coverage film cooled surfaces with three geometries: normal-, 30 deg slant-, and 30 deg × 45 deg compound-angled injection. A flat full-coverage section and downstream recovery section comprised the heat transfer system. The experimental objectives were to determine, for each geometry, the effects on surface heat flux of injection blowing ratio (M), injection temperature ratio (θ), and upstream initial conditions. Spanwise-averaged Stanton numbers were measured for blowing ratios from 0 to 1.3, and for two values of injection temperature at each blowing ratio. The heat transfer coefficient was defined on the basis of a mainstream-to-wall temperature difference. Initial momentum and enthalpy thickness Reynolds numbers were varied from 500 to about 3000. This paper compares the experimental results for the three injection geometries. In addition, the effects of hole spacing and number of rows of holes were examined.

Introduction

Advanced technology for ground-based and aircraft gas turbines is oriented towards achieving higher cycle pressure and temperature ratios to improve cycle thermodynamic efficiency and fuel economy. An integral part of this new technology is development of cooling methods to protect turbine blades from the potentially blade-melting hot combustion gases. Use of these cooling methods will allow the blades to operate at a low enough temperature to insure long blade life while improving the cycle thermodynamic performance. Several potential methods for cooling ultra high-temperature turbines are currently being investigated. These include liquid cooling, use of ceramic-coated components, and gaseous film cooling. With the latter, compressor-bypassed air is ducted to convectively cool the interior of the blade and then is ejected through the blade surface.

Film cooling may be accomplished either by transpiration through a porous blade surface or by full-coverage film cooling through arrays of discrete spaced holes. Transpiration cooling offers the advantages of minimal aerodynamic effect on the potential core above the blade and of depositing the coolant into the sublayer region of the boundary layer, which, in the limit, reduces the surface heat flux to zero. Its chief drawbacks are blade structural problems and pore clogging due to contaminants in the coolant. Full-coverage film cooling (FCFC) is an alternative method of introducing coolant into the boundary layer without the drawbacks of transpiration cooling.

Research into FCFC was first reported by LeBrocq, et al. [1]. They studied the effects on velocity profile and adiabatic wall temperature of in-line and staggered hole patterns and hole axis angle. Two important conclusions were that a staggered hole array minimized adverse effects on the boundary layer velocity profile, and inclined injection was preferable over normal injection for behind-hole cooling. Metzger, et al. [2] conducted a FCFC heat transfer study using in-line and staggered hole patterns with normal injection. Their results indicated a significant increase in the adiabatic-wall heat transfer coefficient over flat plate values (no-blowing) traditionally used with single- and double-row film cooling. Mayle and Camarata [3] carried out a FCFC heat transfer study using a staggered-hole array with 30 deg × 45 deg compound-angled holes. They found that the adiabatic-wall heat transfer coefficient increased significantly when either the mass-flux ratio or hole density was increased. Sasaki, et al. [4] studied the effect on adiabatic wall temperature of nonsquare staggered hole spacing (i.e. spanwise hole spacing of three diameters and streamwise spacings of five and ten diameters). Their data were used to support development of an effectiveness prediction model.

A hydrodynamic and heat transfer study of FCFC is being carried out at Stanford University. The objective of the study is to amass sufficient data to support development of analytical methods for predicting momentum and heat transfer with FCFC. During the period 1971 to 1977, three test surfaces were investigated using normal-, 30 deg slant-, and 30 deg × 45 deg compound-angled injection, each with staggered arrays and hole spacings of five and ten diameters. The experimental heat transfer program focused on three parameters for each geometry tested: θ, coolant temperature parameter; M, mass flux ratio; and upstream boundary layer conditions. This paper presents a summary of the results and conclusions drawn from that phase of the Stanford investigation. Full documentation and tabular forms of the data can be found in [5–8]. Part II of this paper contains representative Stanton number graphs of the data.

Experimental Methodology and Procedures

Heat Transfer with Full-Coverage Film Cooling. A conventional means for describing convective heat transfer from a surface (on a flux basis) is via the rate equation

$$\dot{q}'' = h(T_\infty - T_w) \tag{1}$$

Contributed by the Gas Turbine Division and presented at the Gas Turbine Conference and Products Show, New Orleans, La., March 10–13, 1980 of THE AMERICAN SOCIETY OF MECHANICAL ENGINEERS. Manuscript received at ASME Headquarters December 10, 1979. Paper No. 80-GT-43.

where T_∞ is the mainstream temperature,[1] T_w is the wall temperature and h is the local heat transfer coefficient.

The bulk of two- and three-dimensional film-cooling research to date has used a modified form of equation (1) with T_∞ being replaced by T_{aw}, the temperature an adiabatic wall would attain in the presence of film cooling. The heat transfer coefficient is replaced by h_0, the coefficient that whould exist without injection. Much of the early experimental research involved obtaining distributions of T_{aw} for various geometries and injection conditions. When T_{aw} is properly nondimensionalized, an expression called "effectiveness" obtains. It ranges numerically from 0 to 1 and reflects the degree to which the downstream surface is protected by the upstream coolant injection (i.e., it will be 0 for no protection, and it will be 1 if the coolant causes the downstream surface heat flux to be reduced to zero, that is, T_{aw} equals the injectant temperature).

The conventional meaning of effectiveness as the sole indicator of surface protection from high heat flux is not valid in the region where the actual heat transfer coefficient, h, differs appreciably from h_0. This variation occurs in the region near a hole or a row of holes and is due to the effects of the coolant injection on the hydrodynamic boundary layer. Surface heat flux with film cooling is a two-parameter problem requiring information on both h and effectiveness.

The Stanford film-cooling research program has adopted equation (1) to describe heat transfer with full-coverage film cooling, without reference to "effectiveness." All effects of film cooling are carried in h. This approach was first described in [9] and seems to be first used by Metzger, et al. in [2]. Its focal point is the linearity of energy equation, which would govern the Stanford film-cooling experiments. A nondimensional temperature parameter is defined

$$\theta = \frac{T_\infty - T_j}{T_\infty - T_w} \tag{2}$$

where T_j is the coolant injection temperature. Using superposition theory on the linear thermal energy equation yields a calculation equation for h,

$$h(\theta) = h(\theta = 0) + \theta \cdot [h(\theta = 1) - h(\theta = 0)] \tag{3}$$

Calculation of h for a given injection temperature requires information on h for two values of the temperature parameter, for the same value of M.

Use of equation (1) for film cooling permits an easy comparison of the transfer coefficients with and without film cooling, because both coefficients have the same temperature-driving potential. Equation (1) can also be used to describe transpiration cooling heat transfer; hence it is simple to compare full-coverage film cooling with transpiration cooling (transpiration is a $\theta = 1$ condition), since the transpired coolant leaves the surface at the same temperature as the surface. The comparisons can easily be made on a Stanton number basis, where $St = h/(\rho c U)_\infty$. Correlations for St_0 (without film cooling) and St (with transpiration cooling) can be found in [10].

[1] For a flow Mach number greater than about 0.25, a mainstream recovery temperature or adiabatic wall temperature should be used.

With a given full-coverage film-cooling geometry, the film-cooling Stanton number depends on both the hydrodynamic and the thermal characteristics of the coolant and mainstream flow, and on the surface thermal boundary condition. Hydrodynamic characteristics are described by the coolant-to-mainstream mass flux ratio (blowing ratio), based on the flow area of one hole,

$$M = \frac{(\rho U)_j}{(\rho U)_\infty} \tag{4}$$

where (ρU) is the mass density-velocity product and the subscripts ∞ and j denote mainstream and coolant conditions. The thermal characteristics of the coolant, mainstream, and surface are defined by θ, the temperature parameter given in equation (2). The initial condition of the boundary layer, at the start of the film-cooling region, can be represented by its momentum thickness Reynolds number, $Re\delta_2 = U_\infty \delta_2/\nu$ and its enthalpy thickness Reynolds number, $Re_{\Delta_2} = U_\infty \Delta_2/\nu$.

Stanford Experimental Program. As mentioned in the introduction, the Stanford experimental program focused upon three parameters for each geometry tested: θ, M, and upstream boundary layer conditions. Three geometries were investigated, all using flat surfaces with eleven rows of holes in each surface. The hole angles corresponded to normal-angled injection (90 deg to the surface), slant-angled injection (30 deg to the surface in the downstream direction), and compound-angled injection (30 deg slant injection that was skewed 45 deg from the downstream direction). The holes were spaced five diameters apart in the spanwise and streamwise directions.

The θ parameter was controlled by using one constant temperature for the surface and another for the mainstream, while varying the secondary injection temperature. Values chosen were $T_j = T_\infty$ defining $\theta = 0$, and $T_j = T_w$ defining $\theta = 1$. The M parameter was controlled by varying the injection velocity using a constant mainstream velocity. The injection temperature was kept within 15 K of the surface temperature to eliminate density effect, and M varied from 0 (a baseline data point without blowing) to about 1.5. The upstream initial conditions were set by controlling the hydrodynamic and thermal boundary layer development over the preplate. The momentum thickness Reynolds number, Re_{δ_2}, varied from 500 to 3000, and Re_{Δ_2} varied from 500 to 2000. The ratio of hole diameter to momentum thickness varied from 10 at the low initial momentum Reynolds number down to 2 at the high values.

Experimental Facility. The experimental program was carried out in a closed-loop wind-tunnel facility. The tunnel floor consisted of a preplate, a test section, and an instrumented afterplate, with all plates capable of being heated to a temperature 15 K above that of the mainstream. A secondary air loop of the wind tunnel delivered air, heated or cooled, to the discrete-hole test section. Figure 1 shows a schematic of the wind tunnel.

The main air loop of the wind tunnel was driven by a blower which delivered air through a delivery duct, oblique header, heat exchanger, screen pack, and contraction nozzle, and into the tunnel duct. The duct was 51 cm wide, 20 cm high, and 2.5 m long. Flow left the tunnel

Nomenclature

A = area associated with one hole, P^2
c = specific heat at constant pressure
D = hole diameter (jet diameter)
h = local heat transfer coefficient
$h(\theta)$ = spanwise-averaged heat transfer coefficient with full-coverage film cooling, equation (3)
h_0 = heat transfer coefficient without film cooling
M = mass flux, or blowing, ratio, equation (4)
P = pitch, hole-to-hole spacing
Pr = Prandtl number
$\dot{q}''$ = wall heat flux
Re_{δ_2} = Reynolds number based on δ_2
Re_{Δ_2} = Reynolds number based on Δ_2
St = Stanton number based on h
St_0 = Stanton number based on h_0
T = temperature
U = velocity
α = hole injection angle, Fig. 2
Δ_2 = enthalpy thickness,

$$\Delta_2 = \int_0^\infty \frac{\rho U}{\rho_\infty U_\infty}\left(\frac{T - T_\infty}{T_w - T_\infty}\right)dy$$

δ_2 = momentum thickness,

$$\delta_2 = \int_0^\infty \frac{\rho U}{\rho_\infty U_\infty}\left(1 - \frac{U}{U_\infty}\right)dy$$

$\delta_{.99}$ = boundary layer thickness where $U = .99\ U_\infty$
θ = temperature parameter, equation (2)
ν = kinematic viscosity
ρ = density

Subscripts

aw = adiabatic wall
j = evaluated at injectant conditions
w = evaluated at wall.
∞ = evaluated at free stream conditions

duct through a plenum box that supplied both the secondary blower and the primary blower. Velocity could be varied in steps from 7 m/s to 35 m/s, and the velocity was held constant along the test section and afterplate by adjustment of the flexible top wall of the tunnel.

The secondary air loop of the wind tunnel provided heated, measured air to the injection holes. The flow was delivered via eleven individual ducts, one for each row of holes, each containing a hot-wire anemometer type of flow measurement device.

Special precautions were required to control vortex build-up associated with compound-angled injection. A vortex control system was designed to suck away the corner vortex build-up and reinject the fluid through the opposite wall, thus insuring that the flow remained uniformly vectored in the test section and recovery section. Flow visualization experiments were conducted to establish the proper flow through the vortex control system.

Copper plates, 0.5 cm deep by 45 cm wide by 6 cm long in the flow direction, formed the test surface, with the first plate blank (the upstream guard plate) and the eleven downstream plates containing alternate rows of nine holes and eight holes, each 1.02 cm in diameter. The holes were spaced on 5 diameter centers, in both the spanwise and flow directions, and formed a staggered array. Heater wires were glued into two grooves machined into the back side of each plate. The plates were supported by an aluminum frame across their ends, using phenolic standoffs along their spans to minimize conduction heat loss from the plates and to isolate the plates from each other. Four iron-constantan thermocouples were installed from the backside of each plate, with each thermocouple located midway between two adjacent holes. Low-conductivity air-delivery tubes extended back from the plate surface, and one tube in each row contained an iron-constantan thermocouple. The secondary air temperature was corrected for heat pick-up between the thermocouple station and the exit. The cavity was loosely packed with insulating material and closed with bottom plates. Both the frame and bottom plates were heated to minimize conduction loss from the plates. The test-plate power system delivered stabilized a-c power to each plate, metered by inserting a wattmeter into the circuit. The reading was corrected for calibration and wattmeter losses. Uncertainty in plate power measurement was about 0.3 w, or about 2 percent of the average power level for the experiments.

The preplate and afterplate of the test surface were identical in design, and each was formed of 48 copper plates, each 2.6 cm long in the flow direction. Twenty-four plates were supported by rectangular copper tubes which passed hot water for plate-temperature control. The plates were arranged such that the downstream half of the preplate and the upstream half of the afterplate were heated. Calibrated heat flux meters were located in the afterplate and were used to obtain Stanton number data for the flow as it recovered from the blowing region effect. Uncertainty in afterplate heat flux measurements was estimated at 3 percent.

Heat-Flux Data Acquisition. Heat-flux measurements were obtained in the film-cooling region using a steady-state energy-balance technique. The electrical power delivered to a plate containing a row of holes was measured, and all energy losses from the plate other than by convection from the working surface were accounted for as accurately as possible. Energy-loss modes were modeled in the data-reduction program as radiation from the plate top surface, conduction between the plate and frame, conduction between adjacent plates, and convection between the plate hole area and the injectant. The resulting average heat flux for the plate was then defined as $\dot{q}''_{s\text{-}a} = (E\text{-}L)/A_{\text{tot}}$, where E is the energy supplied to the plate, L is the sum of the energy-loss modes other than by forced convection, and A_{tot} is the total plate area. Since the plate has holes spaced P apart across the span and the injectant boundary condition was spanwise periodic, the area for heat flux can be interpreted as that associated with one hole. This is depicted in Fig. 2. Accuracy for the Stanton number data is estimated using a root-sum square uncertainty analysis to be ± 2.5 percent for the $\theta = 1$ data and ±5 percent for the $\theta = 0$ data. The larger uncertainty for the latter data reflects the uncertainty tied to the plate-injectant convective loss constant.

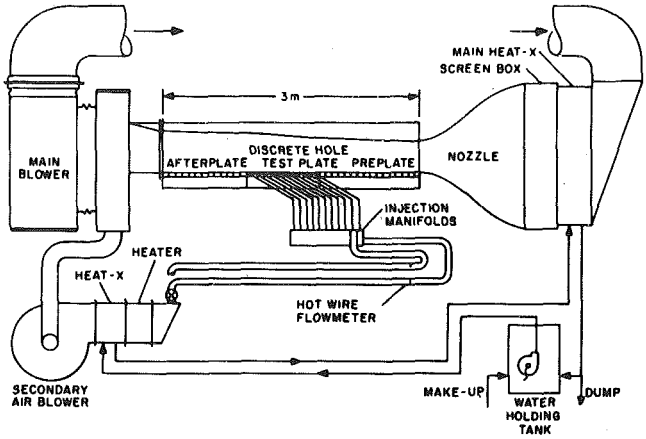

Fig. 1 Flow schematic of wind tunnel test facility, configured for slant-angled injection

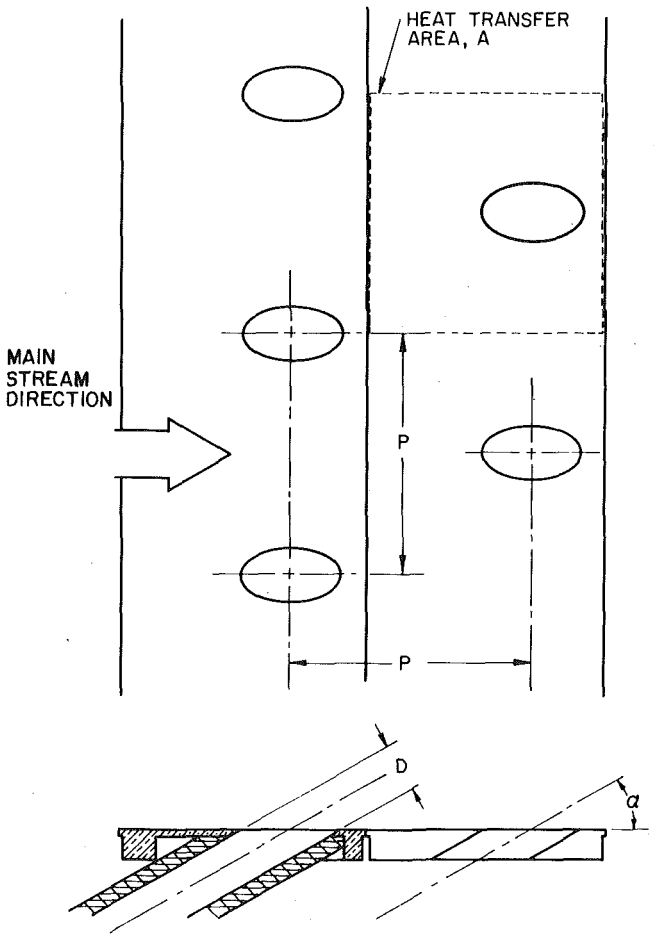

Fig. 2 Film cooling surface geometry, configured for slant-angled injection and $P/D = 5$

Heat Transfer Data

Comprehensive sets of experimental data were acquired for each of the three injection angles, and the data parameter maps were similar for each surface tested. This permits easy comparison of heat transfer coefficients for the three injection angles, and these comparisons are given in the following subsections. Plots of some of the experimental data for the three angles are given in Part II of this paper.

Temperature Parameter. For a given mass flux ratio and set of upstream initial conditions, the heat transfer coefficient is a linear function of the temperature parameter, θ. Equation (3) describes this dependence, and it will apply for all conditions in which the thermal

energy equation remains approximately linear. The reader is referred to [5, 6] which experimentally confirms the superposition approach for obtaining heat transfer coefficients with θ greater than unity. Superposition with film cooling and large temperature differences has been confirmed by Ville and Richards [11]. Metzger and his coworkers [2, 12] use superposition to obtain their film-cooling effectiveness data.

For the Stanford film-cooling studies, data were taken for $\theta \simeq 0$ and $\theta \simeq 1$. The data were then superposition-adjusted to $\theta = 0$ and $\theta = 1$ for presentation of the data. The $\theta = 0$ heat-transfer coefficient is the appropriate value for use with the adiabatic effectiveness approach to film cooling [9, 12], and the $\theta = 1$ data can be compared with transpiration data. For advanced gas-turbine application, the θ range for a given M is 1.25 to 1.75 [11].

The actual effect of θ on the Stanton number is described in the following subsections. The important point is that, with superposition, only two data bases are required, and the heat transfer coefficient for a given θ follows from equation (3). This is experimentally very convenient and simple, and it allows other data bases to be analytically produced for testing computer programs that model full-coverage film cooling.

Mass Flux Ratio. The effect of mass flux ratio on Stanton number for the three injection geometries can best be seen by plotting St versus M for different streamwise locations in the full-coverage region. Figure 3 presents these data for the third, sixth, and tenth film-cooling rows. In the figure the plotted data are $\theta = 0$ (open symbols) and $\theta = 1$ (shaded symbols), while the $\theta = 1.5$ line is obtained using equation (3). Initial momentum and enthalpy thickness Reynolds numbers were about 3000 and 2000, respectively.

From the figure four major points are evident: (1) normal-angled injection results in a higher St than either slant- or compound-angle injection geometries; (2) both angled data sets show a minimum in St around $M = 0.5$ to 0.5; (3) in the initial cooling region (row 3), high blowing can cause the St to exceed the unblown value even at $\theta = 1.0$; and (4) past the initial cooling region, compound-angled injection provides the lowest heat transfer coefficient. By row 10 the surface heat flux with compound-angled injection is essentially zero in the M range from 0.4 to 0.6.

In assessing the relative merits of injection geometries, the spanwise-averaged heat transfer performance should not be the only consideration. From an aerodynamic point of view it is advantageous to have the injectant enter the boundary layer with as much streamwise momentum as possible. Slant-and compound-angled injection have an advantage over normal-angled injection in this respect. A second point for consideration is the possibility of lateral and streamwise variations in local heat flux. The flow visualization data of Colladay and Russell [13] indicate that compound-angled injection might result in more uniform heat flux.

The FCFC data indicate a minimum in Stanton number around $M = 0.4$ to 0.5. This minimum is observable in both of the oblique data sets at high initial Reynolds numbers. (No high-M data were obtained with normal-angled injection). However, the minimum occurs with all three geometries at low initial Reynolds number—to be discussed in the next subsection). Above $M = 0.5$, for these constant-property experiments, the jets of coolant apparently cause a region of disturbed flow with high heat transfer coefficient behind the jets, and the average Stanton number increases. Note that St at $\theta = 0$ could easily be approximated as a power-law function of M.

A point to be raised concerns which injection parameter is appropriate to describe high-velocity, variable-property turbine blade flows.

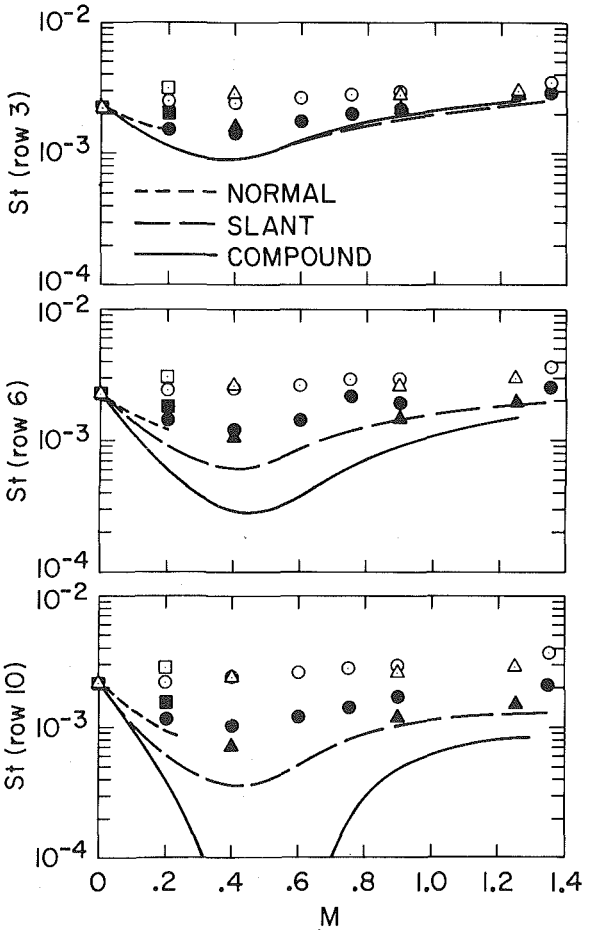

Fig. 3 Superposition-predicted Stanton numbers at $\theta = 1.5$, based on data at $\theta = 0$ (open symbols) and $\theta = 1$ (shaded symbols). $Re_{\delta_2} \simeq 3000$. Symbols: □, normal; ○, slant; △, compound angled injection

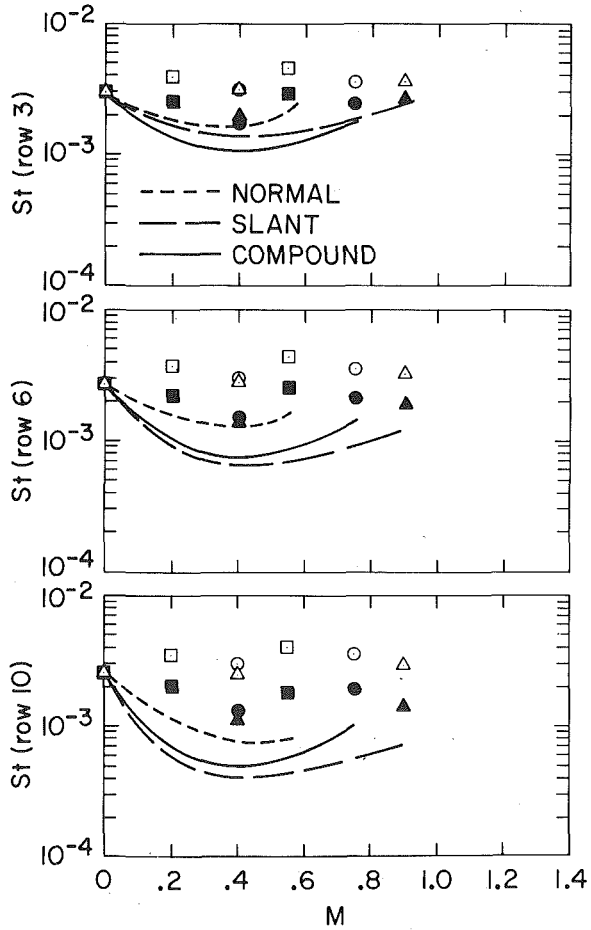

Fig. 4 Superposition-predicted Stanton numbers at $\theta = 1.5$, based on data at $\theta = 0$ (open symbols) and $\theta = 1$ (shaded symbols). $Re_{\delta_2} \simeq 550$. Symbols: □, normal; ○, slant; △, compound-angled injection

The present full-coverage film-cooling data show that a minimum Stanton number occurs but does not allow one to choose between associating it with a mass ratio of 0.40 or a momentum ratio of 0.16. Most slot-film-cooling studies use correlations based on M, and most transpiration cooling studies use an area-averaged M value to reflect the percentage of coolant added to the sublayer of the boundary layer. On the other hand, variable property studies for effectiveness downstream of film-cooling injection [14] indicate that a momentum ratio should be considered. That ratio is also used to correlate jet-in-crossflow trajectory data.

Initial Conditions. Full-coverage data sets have been taken for three injection geometries with heated starting lengths and with momentum thickness Reynolds numbers of about 550 and 3000 (also at 1800 for compound-angled injection). In addition, a number of unheated starting-length data runs were made. Only the heated starting-length data will be discussed here. The step-wall temperature data will probably be useful for numerical modeling of the data and can be found in [5–7].

Figure 4 contains Stanton number data from the third, sixth, and tenth film-cooling rows for the 550 momentum and enthalpy thickness Re. These plots are similar to those in Fig. 3 for high initial Re. The tenth row low Re data are seen to lie between the third and sixth high Re data (closer to the sixth). In the initial film-cooling region (row 3), the heat transfer coefficients for the low initial Re are larger than for the high initial Re data. The tenth row low-Re data are seen to lie between the third and sixth row high-Re data (closer to the sixth).

The higher Stanton number for a lower initial Re is also a characteristic of two-dimensional boundary layer flows [10]. This suggests that the ratio of the film-cooled Stanton number for $\theta = 1$ to the unblown Stanton number, St_0, might be independent of the initial conditions. The data in Figs. 3 and 4 were normalized by St_0 obtained at $M = 0$, and the ratios for both initial conditions were plotted in Fig. 5. In Fig. 5 most of the data ratios for a given geometry, for both initial conditions, are within 10 percent of each other at every value of M. The scatter is even less by the tenth row data. This suggests that for a hole spacing of five diameters, the full-coverage film cooling retains a boundary-layer-like character, and the major effect of the initial conditions is similar to that found in unblown boundary layers.

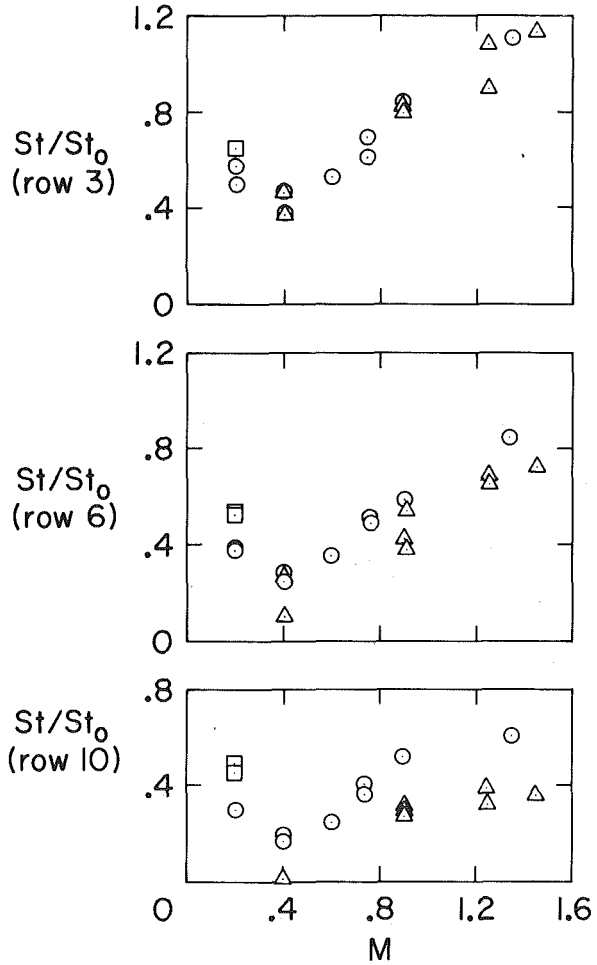

Fig. 5 Ratio of film cooled-to-unblown Stanton numbers at $\theta = 1$ and various initial conditions. Symbols: □, normal; ○, slant; △, compound-angled injection

Where the St ratio data for a given M exhibits scatter, the higher St ratio comes from the lower initial Re data. This suggests that a higher turbulence level may be associated with the jets of coolant emerging into the thinner boundary layer. This increased turbulence effect is counteracted to some degree by the emerging jets remaining closer to the wall in a low Re boundary layer, thus providing better cooling for the near-wall region. For the low initial Re, the ratio of initial $\delta_{.99}$ boundary layer thickness-to-jet diameter is about one, while for the high Re it is about five. The Stanton number ratio at a given M may be affected by the local boundary layer (or momentum) thickness. For these experiments the effect appears to be second order.

Number of Rows of Holes. The effect due to changing the number of rows of holes was studied for the slant-angled injection geometry. The data were taken for $P/D = 5$ and 6 and 11 rows of injection. The six-row geometry was obtained by shutting off the first five rows of injection. The two geometries had about the same initial Re_{δ_2} but different Re_{Δ_2}.

Two blowing ratios were used in the study: $M = 0.4$ and $M = 0.9$, but only the low-M data are shown plotted in Fig. 6 versus enthalpy thickness Reynolds number. The high-M data are given in [8], and the data trends are identical. Arrows on the figure indicate the first and last blowing rows. The six-row data are seen to be about 5 to 10 percent above the corresponding eleven-row data, but the trend is similar. Once blowing begins, the St data for $\theta = 1$ drop below the St_0 reference line, achieving a reduction in St of about 30 percent by the sixth row of holes. The downstream area past the last row of holes is called the recovery region. For the six-row geometry the recovery region St jumps up to within 10 percent of St_0, indicating minimal downstream protection. The last data point is about 60 hole diameters downstream. The eleven-row recovery region data show the benefit of additional rows of cooling, since the Stanton number remains low in the recovery region.

For $\theta = 0$ the Stanton number lies above St_0, but in the recovery region it quickly drops to within 4 or 10 percent of St_0.

The thermal boundary layer growth is a strong function of the temperature parameter, θ, of the injection. For $\theta = 1$ the thermal boundary layer grows about as rapidly as the momentum boundary layer. For $\theta = 0$ the periodic injection of fluid having the same enthalpy as the mainstream retards the thermal boundary layer growth. The momentum boundary layer is the same for the two cases. Past the last row of holes the increased turbulence production ceases (see Yavuzhurt, et al. [15]). Thus the mechanism for diffusing out the thick $\theta = 1$ thermal boundary layer for return to St_0 is reduced. The $\theta = 0$ thermal boundary layer has an enthalpy thickness much nearer the equilibrium value. Once the turbulent diffusivity drops, the boundary layer rapidly returns to near-equilibrium conditions.

Hole Spacing. Some data for each of the three injection geometries were taken at a pitch-to-diameter of 10 to provide additional data bases for modeling purposes. The $P/D = 5$ test sections were used, and $P/D = 10$ was obtained by plugging alternate holes and rows in the arrays with modeling clay. The normal- and slant-angled data were acquired with low initial Re, and the compound-angled data were acquired with high initial Re. The data may be obtained from [5–7]. The slant-angled data are presented in Part II of this paper.

Comparison of $P/D = 5$ with $P/D = 10$ data for a given injection angle showed the following: (1) the St decrease below St_0 for $\theta = 1$ was much less for the wider hole spacing; (2) the data indicated a minimum in St for $\theta = 1$ and M about 0.4, with higher St for higher M; and (3) in the recovery region downstream of the last row of holes, the St rapidly returned to St_0, indicating much less recovery-region pro-

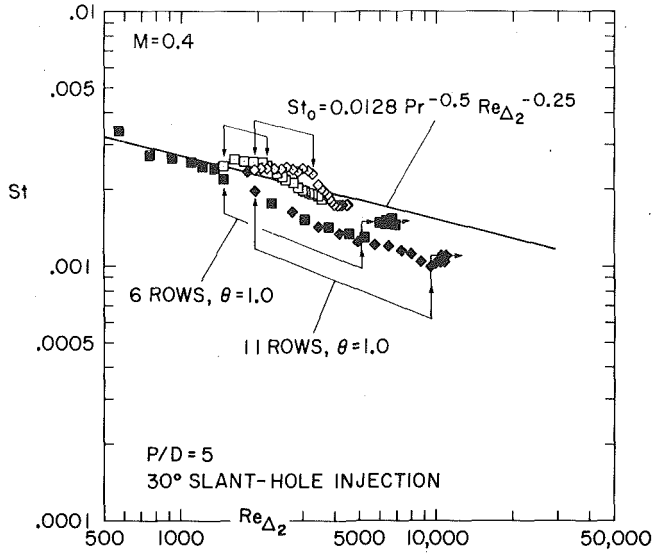

Fig. 6 Spanwise-averaged Stanton numbers for 6 and 11 rows of cooling with M ≃ 0.4 and $\theta = 0$ (open symbols) and $\theta = 1$ (shaded symbols). $Re_{\delta_2} \simeq 3000$. Symbols: ◇, 11 row; □, 6 row data

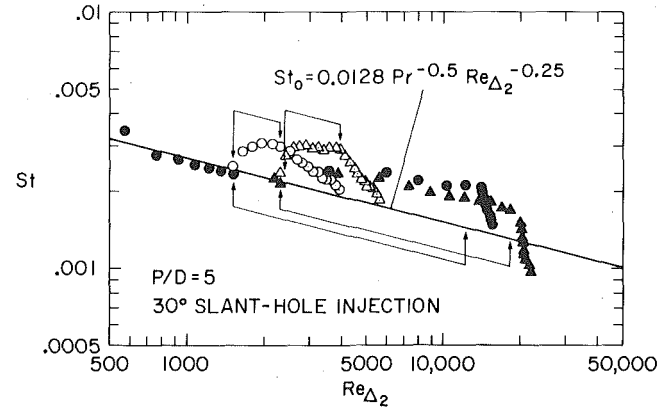

Fig. 7 Spanwise-averaged Stanton numbers for 6 and 11 rows of cooling with $M \simeq 0.9$ and $\theta = 0$ (open symbols) and $\theta = 1$ (shaded symbols). $Re_{\delta_2} \simeq 3000$. Symbols: △, 11 row; ○, 6 row data

tection than with the same M and smaller P/D. Points (1) and (2) reflect the fact that for a given M there is less coolant addition as P/D increases. Point (2) indicates that increasing M provides more coolant but does not result in a lower St. This is because M is related, in part, to the emerging jet trajectory, and larger M causes the fluid to travel further out into the boundary layer before being turned and diffused back into the near-wall region. This same data trend was observed by Mayle and Camarata [3].

Concluding Remarks

Experimental heat transfer studies have been carried out for three injection geometries. Injection of wall-temperature fluid into the boundary layer causes the Stanton number to drop in a manner analogous to transpiration cooling. Unlike transpiration however, full-coverage film cooling displays a minimum in Stanton number for a mass flux ratio, M, of about 0.4 to 0.5. Increasing M above 0.4 results in an increasing Stanton number. Past the initial cooling region the compound-angled injection geometry provides the lowest Stanton number for a given M. Variation in initial conditions upstream of the blowing section has a second-order effect on the Stanton number distribution. Studies of six and eleven rows of holes for slant-angled injection show that the latter gives much better surface protection downstream of the last row of holes. With six rows, the Stanton number rapidly returns to the unblown value in the recovery region, whereas with eleven rows, its remains suppressed longer. Studies of five and ten diameter hole-spacing geometries showed the latter to provide much less surface protection. Of the three injection geometries, compound-angled injection seems to be preferable to slant- and normal-angled injection.

Acknowledgments

The data contained herein were obtained as a part of the doctoral research of H. Choe and M. E. Crawford, and Engineer's degree research of H. K. Kim. The authors wish to thank NASA Lewis Research Center for the support through contract NAS3-14336. We are grateful to Drs. R. S. Colladay and R. E. Gaugler for their interest in the research.

References

1 LeBrocq, P. V., Launder, B. E., and Priddin, C. H., "Discrete Hole Injection as a Means of Transpiration Cooling—An Experimental Study," *Proceedings of the Institution of Mechanical Engineers*, Vol. 187, 1973, p. 149.

2 Metzger, D. E., Takeuchi, D. I., and Kuenstler, P. A., "Effectiveness and Heat Transfer with Full-Coverage Film Cooling," ASME JOURNAL OF ENGINEERING FOR POWER, Vol. 95, 1973, p. 180.

3 Mayle, R. E., and Camarata, F. J., "Multihole Cooling Film Effectiveness and Heat Transfer," ASME OF JOURNAL OF HEAT TRANSFER, Vol. 97, 1975, p. 534.

4 Sasaki, M. et al., "Film Cooling Effectiveness for Injection from Multirow Holes," ASME JOURNAL OF ENGINEERING FOR POWER, Vol. 101, 1979 p. 101.

5 Choe, H., Kays, W. M., and Moffat, R. J., "Turbulent Boundary Layer on a Full-Coverage, Film-Cooled Surface—An Experimental Heat Transfer Study with Normal Injection," NASA Rep. CR-2642, 1976, (Also Stanford Univ., Dept. of Mech. Engrg., Report HMT-22).

6 Crawford, M. E. Kays, W. M., and Moffat, R. J., "Heat Transfer to a Full-Coverage, Film-Cooled Surface with 30° Slant-Hole Injection," NASA Rep. CR-2786, 1976. (Also Stanford Univ., Dept. of Mech. Engrg.,) Report HMT-25).

7 Kim, H. K., Moffat, R. J., and Kays, W. M., "Heat Transfer to a Full-Coverage, Film-Cooled Surface with Compound-Angle (30° and 45°) Hole Injection," NASA Rep. CR-3103, 1979. (Also Stanford Univ., Dept. of Mech. Engrg., Report HMT-28).

8 Crawford, M. E., Kays, W. M., and Moffat, R. J., "Full Coverage Film Cooling on Flat, Isothermal Surfaces: A Summary Report on Data and Predictions," Stanford Univ., Dept. of Mech. Engrg., Report HMT-30, 1979.

9 Choe, H., Kays, W. M., and Moffat, R. J., "The Superposition Approach to Film Cooling," ASME Paper 74-WA/HT-27, New York, 1974.

10 Kays, W. M., and Moffat, R. J., "The Behavior of Transpired Turbulent Boundary Layers," in *Studies in Convection*, Vol. 1, Academic Press, London, 1975.

11 Ville, J. P., and Richards, B. E., "The Measurement of Film Cooling Effectiveness on Turbine Components in Short Duration Wind Tunnels," AGARD Symposium on high Temperature Problems in Gas Turbine Engines, Ankara, Turkey, Sept. 1977.

12 Metzger, E. E., Carper, H. J., and Swank, L. R., "Heat Transfer with Film Cooling Near Nontangential Injection Slots," ASME JOURNAL OF ENGINEERING FOR POWER, Vol. 90, 1968, p. 157.

13 Colladay, R. S., and Russell, L. M., "Streakline Flow Visualization of Discrete Hole Film Cooling for Gas Turbine Applications," ASME JOURNAL OF HEAT TRANSFER, Vol. 98, 1976, p. 245.

14 Pederson, D. R., Eckert, E. R. G., and Goldstein, R. J., "Film Cooling with Large Density Differences Between the Mainstream and the Secondary Fluid Measured by the Heat-Mass Transfer Analogy," ASME JOURNAL OF HEAT TRANSFER, Vol. 99, 1977, p. 620.

15 Yavuzkurt, S., Moffat, R. J., and Kays, W. M., "Full-Coverage Film Cooling: 3-Dimensional Measurements of Turbulence Structure and Prediction of Recovery Region Hydrodynamics," NASA Rep. CR-3104, 1979. (Also Stanford Univ., Dept. of Mech. Engrg., Report HMT-27).

M. E. Crawford
Department of Mechanical Engineering
The University of Texas at Austin,
Austin, TX 78746
Assoc. Mem. ASME

W. M. Kays
Dean, School of Engineering
Stanford University
Stanford, CA 94305
Fellow, ASME

R. J. Moffat
Director, Thermosciences Division
Department of Mechanical Engineering
Stanford University
Stanford, CA 94305
Mem. ASME

Full-Coverage Film Cooling

Part II: Heat Transfer Data and Numerical Simulation

Experimental research into heat transfer from full-coverage film-cooled surfaces with three injection geometries was described in Part I. This part has two objectives. The first is to present a simple numerical procedure for simulation of heat transfer with full-coverage film cooling. The second objective is to present some of the Stanton number data that was used in Part I of the paper. The data chosen for presentation are the low-Reynolds number, heated-starting-length data for the three injection geometries with five-diameter hole spacing. Sample data sets with high blowing ratio and with ten-diameter hole spacing are also presented. The numerical procedure has been successfully applied to the Stanton number data sets.

Introduction

In Part I of the paper, an overview of full-coverage film cooling (FCFC) was presented, followed by a discussion of the experimental methodology and procedures used in the Stanford FCFC study. The experimental heat transfer study was carried out using three test surfaces with normal-, 30 deg slant-, and 30 deg × 45 deg compound-angled injection. Three parameters were investigated: θ, coolant temperature parameter; M, mass flux ratio; and upstream boundary layer conditions. A summary of the effects of these parameters on heat transfer coefficient for the three injection angles and the effects of number of rows of cooling holes were then presented in Part I.

Part II of the paper has two objectives. The first is to present a simple numerical procedure for simulation of heat transfer with full-coverage film cooling. The second objective is to present some of the Stanton number data that was used in Part I of the paper. The data chosen for presentation are the low-Reynolds number, heated-starting-length data for the three injection geometries, with five-diameter hold spacing. Sample data sets with high blowing ratio and with ten-diameter hole spacing are also presented. The trends in the data sets presented in Part II are indicative of all the other data sets acquired with different initial conditions.

Background

The intent of the analysis part of the Stanford film-cooling research was to incorporate the Stanford experimental data base into a program that could predict heat transfer. Both integral and two-dimensional methods were studied in detail. The integral method showed promise for normal-angled injection at low to moderate M [1], but for slant-angled injection [2] the $\theta = 0$ data had a trend completely different from the normal injection data, and it was not amenable to simple correlation. Thus, the integral method was abandoned.

Choice of a two-dimensional finite-difference boundary layer method in preference to a three-dimensional method was based upon several factors. First, the general flow field is boundary layer in nature, and the departures from two-dimensional behavior are spanwise periodic. This permits defining spanwise-averaged velocity and temperature quantities which are continuous in the flow direction. This approach has been developed in detail by Choe [1] and Herring [3]. Second, the primary data used in development of the method were intended to be the data acquired in the experimental phase of this program. The construction of the apparatus is such that the data are inherently spanwise-averaged Stanton numbers representing the area-averaged effects of injection from a row of holes. The third criterion relates to the program's utility as a design tool, which requires short execution times and small computer-core requirements. Recently, Launder and his colleagues [4,5] have had success with a three-dimensional elliptic/parabolic boundary layer program coupled to a two-equation model of turbulence, but their success has been limited to low to moderate M. Patankar, et al. [6] also had success with simulating a jet-in-cross flow using an elliptic procedure and a two-equation model.

It is difficult to identify the physical criteria which should be used to assess the merits of a proposed simulation program. Candidates include: heat transfer and friction coefficients, temperature and velocity profiles, and profiles related to the turbulence within the flow field. Ideally one would like a numerical program capable of reproducing all attributes of the flow field for any prescribed geometry and initial and boundary conditions. For simple shear flows we are approaching this realization. However, when even the best programs are applied to complex flows (of which film-cooled boundary layers are a class), the predictions often deviate from the experimental data in one way or another and the programs must be doctored to yield satisfactory predictions. One should probably not use the word prediction in these cases, but instead call it simulation. And, one should not use a specialized program beyond the limits of the geometry and initial and boundary conditions of the data bases used to develop it.

The program reported here is a specialized program made by modifying a well-tested boundary layer program to include an injection model for introducing coolant, and by introducing a turbulence-augmentation model for simulating the shear layer interaction within the boundary layer. There is no claim that this program will predict the detailed attributes of the flow field. It was intended only

Contributed by the Gas Turbine Division and presented at the Gas Turbine Conference and Products Show, New Orleans, La., March 10–13, 1980 of THE AMERICAN SOCIETY OF MECHANICAL ENGINEERS. Manuscript received at ASME Headquarters December 10, 1979. Paper No. 80-GT-44.

to develop a program to replicate the spanwise-averaged Stanton number data bases available at Stanford. We would expect, however, that success in predicting these spanwise-averaged data would imply the possibility of at least limited success in modeling the gross aspects of the flow.

Simulation Program

The differential method that has been developed to simulate the data consists of a two-dimensional boundary layer program, STAN5 (whose nucleus is the original Spalding-Patankar program), with added routines to model coolant injection and turbulence augmentation. The resulting program is called STANCOOL, and it is documented in [7].

The program solves the boundary layer equations by a marching process in the streamwise direction. Fluid is injected into the calculational boundary layer by stopping the program when a row of holes is encountered and inserting the injectant into the stream tubes between the wall and a model-calculated "jet penetration point" within the boundary layer. The increased turbulence from jet-boundary layer interaction is modeled by augmenting the Prandtl mixing length. Two constants are required, in addition to the accepted constants for predicting flow over a flat, slightly rough plate.

The boundary layer equations being solved are those described in the STAN5 documentation report [8] for flow over a flat surface:

$$\frac{\partial}{\partial x}(\rho U) + \frac{\partial}{\partial y}(\rho V) = 0 \tag{1}$$

$$\rho U \frac{\partial U}{\partial x} + \rho V \frac{\partial U}{\partial y} = -g_c \frac{dP}{dx} + \frac{\partial}{\partial y}\left(\mu_{eff} \frac{\partial U}{\partial y}\right) \tag{2}$$

$$\rho U \frac{\partial I^*}{\partial x} + \rho V \frac{\partial I^*}{\partial y} = \frac{\partial}{\partial y}\left[\mu_{eff} \frac{\partial I^*}{\partial y} + \frac{\mu_{eff}}{g_c J}\left(1 - \frac{1}{\mathrm{Pr}_{\mathrm{eff}}}\right)\frac{\partial}{\partial y}\left(\frac{U^2}{2}\right)\right] \tag{3}$$

where $I^* = I + U^2/2g_cJ$. The effective viscosity and effective Prandtl number are defined in terms of an eddy viscosity, ϵ_m, and the turbulent Prandtl number, Pr_t.

$$\mu_{eff} = \rho(\nu + \epsilon_M) \tag{4}$$

$$\mathrm{Pr}_{\mathrm{eff}} = \frac{1 + (\epsilon_M/\nu)}{\frac{1}{\mathrm{Pr}} + \frac{\epsilon_M}{\nu}\cdot\frac{1}{\mathrm{Pr}_t}} \tag{5}$$

Eddy diffusivity for momentum is modeled by the Prandtl mixing length.

$$\epsilon_M = \ell^2 \left|\frac{\partial U}{\partial y}\right| \tag{6}$$

The mixing-length distribution used in the program is described in the subsection on turbulence augmentation. The turbulent Prandtl number is presumed to follow the flat-plate variation described in [8]: for air, it is 1.72 at the wall and drops to 0.86 in the outer region.

Boundary conditions for the two-dimensional flow equations are

$$U(x,0) = 0$$

$$V(x,0) = 0$$

$$\lim_{y\to\infty} U(x,y) = U_\infty \text{ (constant)}$$

$$I^*(x,0) = I^*_w \text{ (constant)}$$

$$\lim_{y\to\infty} I^*(x,y) = I^*_\infty \text{ (constant)}$$

Injection Model. The injection model is a calculational technique for inserting coolant into the boundary layer each time the marching process encounters a row of holes. Three candidate injection models were examined; transpiration at the wall, slot-type injection parallel to the wall, and distributed injection.

Testing of these models was carried out using the same turbulence model. The procedure was to find the injection and turbulence model constants that allowed prediction of the $\theta = 1$ Stanton number data for a given set of initial conditions, and then test the $\theta = 0$ case. The predictions were deemed successful when the same injection and turbulence model constants predicted both the $\theta = 0$ and $\theta = 1$ Stanton number data.

Nomenclature

A = area associated with one hole, P^2
A^+ = van Driest damping constant
C_D = drag coefficient, jet in crossflow
D = hole diameter (jet diameter) van Driest damping function, equation (19)
F = mixing length decay function, equation (21)
F_D = drag force, jet in crossflow
g_c = proportionality constant, Newton's Second Law
$h(\theta)$ = spanwise-averaged heat transfer coefficient with full-coverage film cooling
I = static enthalpy
I^* = stagnation enthalpy
J = conversion constant, mechanical to thermal energy
ℓ = mixing length
$\dot{m}$ = mass flow rate per unit depth in a stream tube
$\delta\dot{m}$ = incremental mass flow rate in a stream tube due to injection, equation (8)
$\dot{m}_j$ = mass flow rate of injectant, equation (16)
M = mass flux, or blowing, ratio $M = (\rho U)_j/(\delta U)_\infty$
P = pitch (hole-to-hole spacing), or pressure
Pr = Prandtl number
Pr_t = turbulent Prandtl number
$\mathrm{Pr}_{\mathrm{eff}}$ = effective Prandtl number, equation (5)
PD = penetration distance, Fig. 2
Re_x = Reynolds number based on distance x from virtual origin, turbulent boundary layer
Re_{Δ_2} = Reynolds number based on Δ_2
Re_{δ_2} = Reynolds number based on δ_2
St = Stanton number, $h(\theta)/(\rho c U)_\infty$
T = temperature
U = velocity component, x direction
V = velocity component, y direction
x = distance, streamwise direction
x' = local x distance, measured from point of injection
y = distance, cross-stream direction
y^+ = dimensionless y, $y^+ = y\sqrt{\tau_w/\rho}/\nu$
α = hole injection angle, Fig. 2
Δ_2 = enthalpy thickness

$$\Delta_2 = \int_0^\infty \frac{\rho U}{\rho_\infty U_\infty}\left(\frac{T - T_\infty}{T_w - T_\infty}\right)dy$$

δ_2 = momentum thickness

$$\delta_2 = \int_0^\infty \frac{\rho U}{\rho_\infty U_\infty}\left(1 - \frac{U}{U_\infty}\right)dy$$

δ = boundary layer thickness where $U = 0.99\,U_\infty$
ϵ_M = eddy diffusivity for momentum, equation (6)
κ = von Karman constant
λ = outer layer length scale constant
$\lambda_{\max,a}$ = augmented length scale constant
λ_{eff} = effective $\lambda_{\max,a}$, equation (22)
θ = temperature parameter, $\theta = (T_\infty - T_j)/(T_\infty - T_w)$
μ_{eff} = effective viscosity, equation (4)
ν = kinematic viscosity
ψ = stream function, Fig. 1
$\delta\psi$ = stream tube, Fig. 1
ρ = density
τ = shear stress

Superscripts

$(^-)$ = average value of quantity within stream tube

Subscripts

a = augmented turbulence quantity
j = evaluated at injectant conditions
max,a = maximum value, augmented turbulence quantity injection
new = average quantity within stream tube after injection
old = average quantity within stream tube before injection
w = evaluated at wall
2-D = two-dimensional turbulence quantity
∞ = evaluated at free stream conditions

The first injection model to be tested was the transpiration model developed by Choe [1]. This model uniformly distributes the injectant over the area around the injection holes. It was found to be a successful model for low M but failed for $M = 0.4$.

A slot-type model was then developed to more accurately simulate the way the coolant is injected into the boundary layer. This model extended the range of successful predictions to $M = 0.6$, but failed for still higher M. The empirical constant for this model was the slot height, or jet-penetration point, and the injectant was distributed equally between the wall and the slot height, or jet-penetration point, and the injectant was distributed equally between the wall and the slot height. Physically, as M increases, the slot height should increase to model the fact that the jets of coolant penetrate farther into the boundary layer. However, as the height was increased, the momentum effects that should have been associated with large M diminished due to the model requirement for uniform injectant distribution. An attempt was made to allow the slot of injectant to reside above the wall for high M, but this resulted in even poorer heat transfer predictions. Evidently, for moderate to high M, turbulent mixing and jet-boundary layer interaction combine to distribute some of the injectant in the near-wall region, even though the bulk of the coolant does arrive at or near the penetration point. These facts suggested examining a distributed injection model.

In constructing the distributed injection model, consideration was taken of the physical process occurring when the jets enter the boundary layer. The jet-in-crossflow discussion by Abramovich [9] and the film-cooling flow-visualization study of Colladay and Russell [10] were used as guides.

For low M the jets do not penetrate but are immediately "knocked over" by pressure and drag forces on the emerging jets, as a consequence of the boundary layer flow. For higher M, the jets leave the surface entirely and are turned in the downstream direction by pressure and shear forces which overcome the jet's resistance to change of direction. In either case, as a jet emerges into the boundary layer the shear layer at the injectant-boundary layer interface promotes entrainment of boundary layer fluid into the jet, and eventually the injectant becomes diffused into the existing boundary layer.

The injection process and entrainment-diffusion process are modeled together. As a jet passes through the stream tubes that comprise the boundary layer, drag forces are presumed to "tear off" some of the injectant. The injectant that is shed into a given stream tube is then accelerated by drag forces. Shedding commences at the wall and continues until the total amount shed equals the injectant mass flow rate per unit width of film-cooled surface. The point where shedding is complete is named the penetration distance.

Equations that describe the model are obtained from one-dimensional mass, momentum, and thermal energy balances on the element of injectant bounded between two stream surfaces. This element is shown in Fig. 1. For flow between these surfaces,

$$\dot{m}_{\text{new}} = \dot{m}_{\text{old}} + \delta\dot{m} \tag{7}$$

where $\dot{m}_{\text{old}}$ is the flow rate upstream and $\delta\dot{m}$ is the injectant that is shed into the stream tube (on a rate basis). From a momentum balance consideration,

$$(\dot{m}_{\text{old}} + \delta\dot{m})\overline{U}_{\text{new}} = \dot{m}_{\text{old}}\overline{U}_{\text{old}} + \delta\dot{m}U_j\cos\alpha \tag{8}$$

where $\overline{U}_{old}$ is the mass-averaged velocity of the upstream fluid and U_j is the velocity of the injectant. The U_j velocity is assumed not to vary with y. This is the simplest way to preserve overall momentum within the boundary layer (i.e., $\Sigma\delta\dot{m}U_j = \dot{m}_jU_j$, where $U_j = M\rho_\infty U_\infty/\rho_j$).

The drag forces that tear off the injectant are assumed to accelerate $\delta\dot{m}$ from its initial velocity up to the new stream-tube velocity,

$$F_D = \delta\dot{m}(\overline{U}_{\text{new}} - U_j\cos\alpha) \tag{9}$$

The drag forces can be defined in terms of a drag coefficient for convenience,

$$F_D = C_D\frac{1}{2}\rho A_j(\overline{U}_{\text{old}})^2 \tag{10}$$

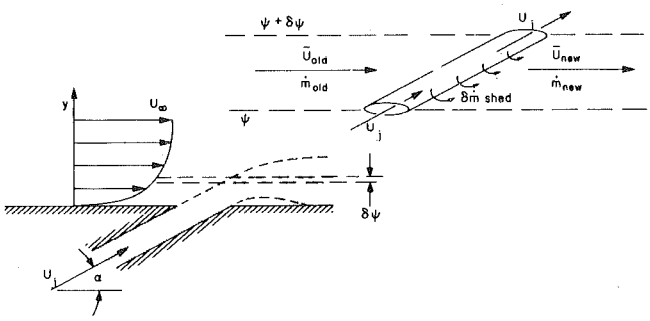

Fig. 1 Flow element for constructing injection model

where A_j is the cross-sectional area of the jet, $(D\cdot\delta y)/\sin\alpha$ for a stream tube that is δy in width (proportional to $\delta\psi$).

By introducing the definition $\dot{m}_{\text{old}} = \rho\overline{U}_{\text{old}}(\delta y\cdot P)$, where P is the distance between adjacent jets, and combining with the above equations, the ratio of the mass shed from the coolant jet to the existing mass between the stream tubes (on a rate basis) can be written as

$$\frac{\delta\dot{m}}{\dot{m}_{\text{old}}} = \left[\frac{2(P/D)}{C_D}\left(1 - \frac{U_j\cos\alpha}{\overline{U}_{\text{old}}}\right) - 1\right]^{-1} \tag{11}$$

A mass-averaged velocity ratio can be formed by rearranging equation (8):

$$\frac{\overline{U}_{\text{new}}}{\overline{U}_{\text{old}}} = \left[1 + \left(\frac{\delta\dot{m}}{\dot{m}_{\text{old}}}\right)\frac{U_j\cos\alpha}{\overline{U}_{\text{old}}}\right]\left(1 + \frac{\delta\dot{m}}{\dot{m}_{\text{old}}}\right)^{-1} \tag{12}$$

From energy balance consideration

$$\overline{I}^*_{\text{new}}(\dot{m}_{\text{old}} + \delta\dot{m}) = \dot{m}_{\text{old}}\overline{I}^*_{\text{old}} + \delta\dot{m}I^*_j \tag{13}$$

where $\overline{I}^*_{\text{old}}$ is the mass-averaged stagnation enthalpy of the upstream fluid and I_j^* is that of the injectant (assumed not to vary with y to satisfy overall energy conservation). A mass-averaged enthalpy ratio can be formed by rearranging equation (13):

$$\frac{\overline{I}^*_{\text{new}}}{\overline{I}^*_{\text{old}}} = \left[1 + \left(\frac{\delta\dot{m}}{\dot{m}_{\text{old}}}\right)\frac{I^*_j}{\overline{I}^*_{\text{old}}}\right]\left(1 + \frac{\delta\dot{m}}{\dot{m}_{\text{old}}}\right)^{-1} \tag{14}$$

In the prediction program, the injection model, based on the analysis given above, is contained in a subroutine, and it is invoked whenever a row of holes is encountered. The empirical input is the mass shed ratio, defined as

$$\frac{\delta\dot{m}}{\dot{m}_{\text{old}}} = \text{DELMR} = f(M,P/D,\alpha) \tag{15}$$

The DELMR expression is used in lieu of equation (11), for simplicity. With this as input, the routine processes each flow tube from the wall outward. The velocities are adjusted according to equation (12) to conserve momentum, and the stagnation enthalpies are adjusted according to equation (14). The injection process is terminated at the stream tube where

$$\dot{m}_j = \rho_jU_j\frac{\pi D^2}{4P} = \sum_i \text{DELMR}\cdot\delta\psi_i \tag{16}$$

Note the introduction of P to put the flow rate on a per-unit depth basis (consistent with the dimensions of ψ). The y location where flow injection is terminated is PD, the penetration distance.

Turbulence Augmentation Model. The turbulence model accounts for the effects of coolant injection on the turbulent transport terms by altering the eddy viscosity. Three turbulence models were studied: mixing-length augmentation tied to the transpiration injection model, to the distributed injection model, and to a turbulence kinetic energy (TKE) model.

Development and testing of the augmented mixing-length model for use with transpiration was carried out by Choe [1] for normal-angled injection. He made detailed pitot tube surveys of the spanwise distribution of the velocity field within the full-coverage region. From a set of ten profiles between $-P/2$ and $+P/2$ he constructed a spanwise-averaged profile. He then integrated the momentum equation,

using an analogy between wall friction and heat transfer, and obtained an average shear-stress distribution through the boundary layer. A mixing-length distribution was determined using the velocity profile derivatives and the shear stress distribution. The mixing-length distribution was found to be nearly identical to that of a two-dimensional boundary layer in the near-wall region and near the free stream, but in the central part of the boundary layer it was higher. The augmented mixing length was modeled by a one-parameter curve fit to the experimental distribution.

Crawford [2] carried out the same velocity profile study for the slant-angled injection and found the same augmented mixing-length profile as did Choe. The Crawford model is similar to Choe's, but the model parameter describing the peak in augmentation is directly tied to the distributed injection model.

A turbulence kinetic energy model was investigated in hopes of circumventing some of the recovery region problems encountered with the Crawford model. Yavuzkurt, et al. [11] carried out a detailed velocity and Reynolds stress study of the flow field over the slant-angled injection test section and in its recovery region. He developed a very successful TKE model for recovery region predictions, solving the TKE equation with a length-scale model developed from experimental data. Efforts were then made to develop a similar length-scale model for the full-coverage region, but with only marginal success. Rather than use different schemes in the full-coverage and recovery regions, the Choe-type model, as modified by Crawford was adopted.

The eddy diffusivity for momentum is modeled by algebraically augmenting the Prandtl mixing length using

$$\frac{\ell}{\delta} = \left(\frac{\ell}{\delta}\right)_{2\text{-D}} + \left(\frac{\ell}{\delta}\right)_a \tag{17}$$

where the subscript 2-D refers to the two-dimensional mixing length and the a denotes the departure due to the jet-boundary layer interaction. The two-dimensional mixing-length distribution is that used in STAN5:

$$\ell_{2\text{-D}} = \begin{cases} \kappa y D, & \kappa y < \lambda\delta \\ \lambda\delta, & \kappa y \geq \lambda\delta \end{cases} \tag{18}$$

where D is the van Driest damping function,

$$\text{D} = 1 - \exp(-y^+/A^+) \tag{19}$$

In the above equation, κ is the von Karman constant; λ is the outer layer length-scale constant; δ is the 99 percent boundary layer thickness, $y^+ = y\sqrt{\tau_w/\rho}/\nu$; and A^+ is the van Driest damping constant. A^+ was about 22 in the full-coverage region, and it was 25 in the recovery region. The smaller A^+ in the film-cooling region reflected the effect of surface roughness due to the holes. The A^+ transition was handled according to the first-order lag equation described by Crawford and Kays [8].

Augmentation of the two-dimensional mixing length is depicted in Fig. 2. The curve represents a departure from the two-dimensional distribution, with a maximum located at PD/δ. The augmented mixing-length distribution is a curve fit to Fig. 2, and it is superimposed on the two-dimensional distribution according to equation (17).

$$\ell_{\max,a} = \lambda_{\max,a} \cdot \delta \cdot F \tag{20}$$

where F is an exponential function that decays the $\lambda_{\max,a} \cdot \delta$ product on either side of PD/δ.

$$F = 2.718\left(\frac{y}{PD}\right)^2 \cdot \exp[-(y/PD)^2] \tag{21}$$

The mixing-length augmentation is a maximum in the vicinity of the injection site, and it decreases in the downstream direction. A model for this decay was developed by Yavuzkurt [11], based on his hydrodynamic studies of the recovery region, downstream of the last row of holes. He found that the augmented turbulence decayed with a time constant proportional to the boundary layer thickness. To model this decay the $(l/\delta)_{\max,a}$ in equation (20) is replaced by an effective value, $(l/\delta)_a$; and $\lambda_{\max,a}$ is replaced with

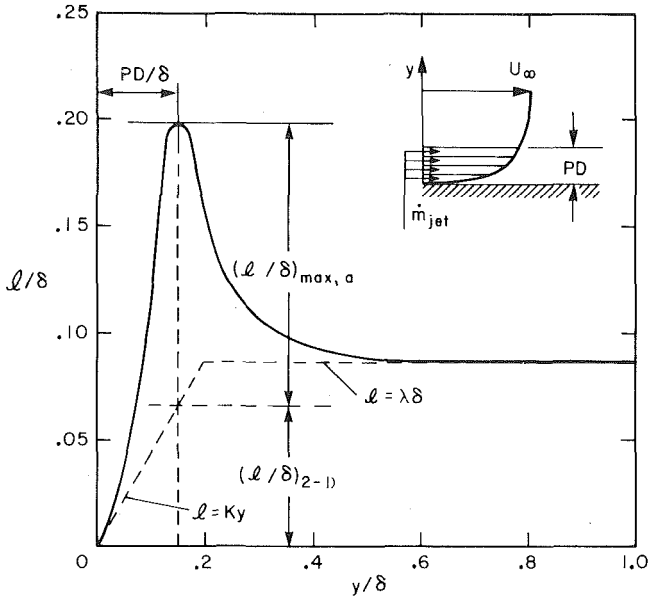

Fig. 2 Augmentation of the two-dimensional Prandtl mixing length, with the peak occurring at the penetration distance location

$$\lambda_{\text{eff}} = \lambda_{\max,a} \cdot \exp[-(x'/\delta)/2] \tag{22}$$

where x' is the streamwise distance, measured from the point of injection, and the time constant for decay is two boundary-layer thicknesses.

In the prediction program, the mixing length is computed using

$$\ell = \begin{Bmatrix} \kappa y \\ \lambda\delta \end{Bmatrix} + \lambda_{\text{eff}} \cdot F \cdot \delta \tag{23}$$

and in the near-wall region the mixing length is damped by multiplying it by equation (19). The empirical input to the turbulence-augmentation model is

$$\lambda_{\max,a} = \text{ALAM} = f(M,P/D,\alpha) \tag{24}$$

and λ_{eff} is computed using this input variable and equation (22). The x' is zero at each injection location and increases linearly in the downstream direction.

The success of this turbulence-augmentation model is due partly to its being directly tied to the injection model through PD, the penetration distrance. In the turbulence model, PD was arbitrarily assigned to coincide with the mixing-length maximum; in retrospect, perhaps it should have been the outermost edge of the mixing-length perturbation, because for large M, where PD/δ approaches unity, half the augmentation is located in the potential core. This problem was discovered only after the model had been used for most of the low to moderate M predictions. To overcome this problem for high M or for thin initial boundary layers, PD/δ was never allowed to exceed 0.8 (arbitrarily fixed).

Summary and Constants for the Model. The STANCOOL program is basically the STAN5 boundary layer program with an appended subroutine COOL that contains the injection model. The turbulence-augmentation model resides within the existing subroutine AUX. Boundary conditions for the program consist of specifying the wall temperature and free-stream velocity at various x locations (usually constants, independent of x).[1] The initial conditions are experimentally obtained velocity and temperature profiles upstream of the first row of cooling holes. A three-by-eleven array contains x locations and the M and θ parameter values for the eleven rows of film-cooling holes.

Program STANCOOL commences integration upstream of the first

[1] For low-velocity, constant-property flows the stagnation enthalpy and temperature variable are interchangeable.

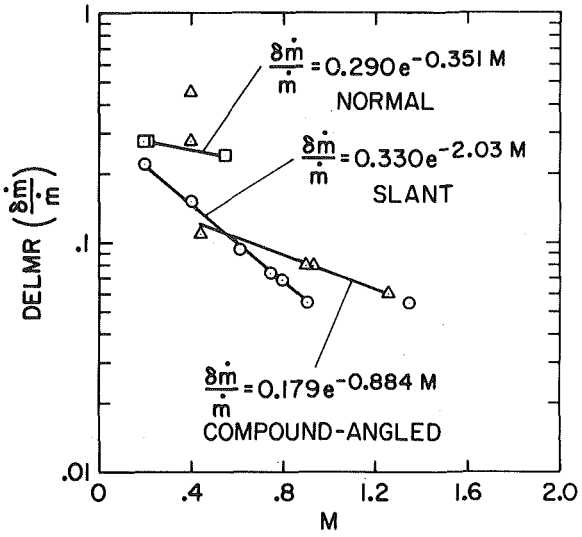

Fig. 3 Injection model constants. Symbols: □, normal; ○, slant; △, compound-angled injection

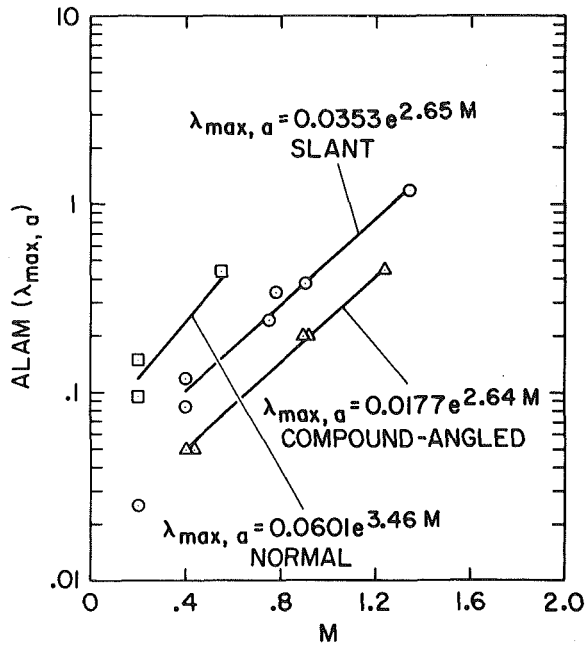

Fig. 4 Turbulence-augmentation constants. Symbols: □, normal; ○, slant; △, compound-angled injection

row of holes. When the program encounters a row of holes, it stops and the velocity and temperature profiles are augmented according to equations (12) and (14), with $(\delta\dot{m}/\dot{m}_{old})$ being replaced by DELMR, the input injection constant. Injection commences at the surface and proceeds outward, stream tube by stream tube, until $\Sigma\delta\dot{m} = \dot{m}_j/P$. The final stream tube y location is PD, the penetration distance. With PD determined, the exponential function F (equation (21)) is determined for the augmented mixing length. Integration is restarted, and at each integration point downstream, λ_{eff} is computed according to equation (22), with $\lambda_{max,a}$ being replaced by ALAM, the input turbulence constant. The total mixing length is determined using equation (23). For each row of holes this series of steps is repeated.

The input injection and turbulence augmentation constants were determined for each heated starting length, $P/D = 5$ data set contained in [1, 2, 7, 12]. Figures 3 and 4 show these constants and curvefits.

Data and Predictions

Initial success in development of the STANCOOL program was described in [2], and the results are summarized as follows. The injection model was tested at $M = 0.4$ and five initial conditions: unheated starting lengths with momentum Reynolds numbers of 1900, 2700, and 4800, and heated starting lengths with momentum/enthalpy Reynolds numbers of 2700, 1800 and 500, 500. The same value of DELMR successfully predicted all five data sets. In addition, all but the low Reynolds number case used the same ALAM. For low Re the value had to be increased about 20 percent. The prediction program was then used to simulate film cooling with 24 rows of holes and slant-angled injection at $P/D = 5$. The predicted Stanton number trend was identical to that for 11 rows (i.e., nearly constant St for $\theta = 0$ and a continued decreasing St for $\theta = 1$). Predicted velocity and temperature profiles with $M = 0.4$ were compared to pitot-tube and thermocouple experimental spanwise-averaged profiles. The predicted velocity profile was in qualitative agreement, and the $\theta = 0$ and $\theta = 1$ predicted temperature profiles were almost identical to the experimental profiles.

Due to space limitations, only a part of the data used in Part I can be presented. It was decided that graphs of Stanton number data with low initial Reynolds numbers would be presented. The approximate initial momentum and enthalpy thickness Reynolds numbers are: 550,600 normal; 500,500 slant; and 500,650 compound. One set of data at high initial Reynolds number with slant-angled injection is also presented.

Stanton number data for slant-angled injection and $P/D = 5$ are shown in Fig. 5–7. In the graphs film cooling commences with the second data point (the first is the upstream guard plate). The prediction for $M = 0$ in Fig. 5 shows the slight roughness effect that the hole array has on the sublayer. Smooth-walled boundary layer friction coefficients and Stanton numbers can be successfully predicted with $A^+ = 25$. In the full-coverage region, though, A^+ had to be decreased to 22 to simulate the roughness effect. The arrows denote the last row of holes and the start of the recovery region.

For $\theta = 0$ the predicted St spikes upward and for $\theta = 1$ there is a corresponding downward spike in response to the injectant. The predicted rate of recovery in the x direction after each spike is similar to that found in the recovery region after the last row of holes, and it reflects the effect of injectant on the thermal boundary layer. The recovery region predictions are satisfactory for low M, but deviate for high M and $\theta = 1$.

For $\theta = 0$ and slant-angled injection the experimental data immediately rises above the $M = 0$ baseline data and becomes almost constant and independent of x until the recovery region. In contrast the $\theta = 1$ injectant causes a continual decrease in St, similar to transpiration cooling.

There are two important points concerning the data in Fig. 5. The first is that in the initial film cooling region where the boundary layer is extremely thin relative to hole diameter (first few rows of holes), the high blowing ratio provides almost no heat transfer reduction. This feature becomes more pronounced as M is increased above unity. The second point, in favor of high blowing ratios, is the continued reduction in heat transfer coefficient past the last row of holes. This suggests that interrupted hole arrays may be viable (i.e., a set of ten rows, followed by a recovery region before the next set of rows).

Figure 6 shows slant-angled data for $P/D = 10$ and the same initial conditions as Fig. 5. For $M = 0$ the effect of every other row being plugged can be seen by the slight dip in Stanton number. The predictions with blowing are similar to those of Fig. 5. Again the recovery region $\theta = 1$ prediction at high blowing deviates from the data.

The effect of the damped mixing-length augmentation, equation (22), can be seen in the figure. The effect of hole spacing on Stanton number can be seen by comparing the data in Figs. 5 and 6. For $\theta = 1$ and the last row of holes on the film-cooled surface, $P/D = 10$ gives a 25–35 percent higher Stanton number, indicating less surface protection.

A high blowing ratio data set is shown in Fig. 7. Initial conditions are much larger than for the data in Figs. 5 and 6. The important point from the graph is that, even with a relatively thick initial boundary layer (five times that for low-initial Re data, see Part I), the heat

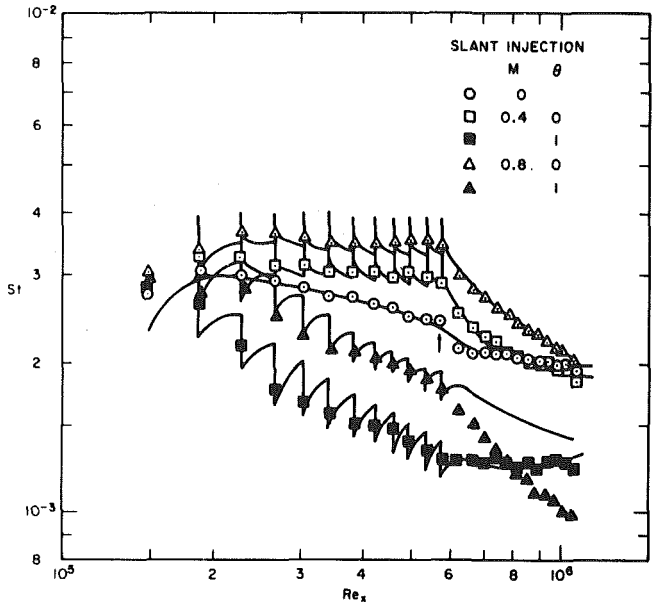

Fig. 5 Slant-angled injection with $P/D = 5$ and initial momentum and enthalpy Reynolds numbers of 500 and 500

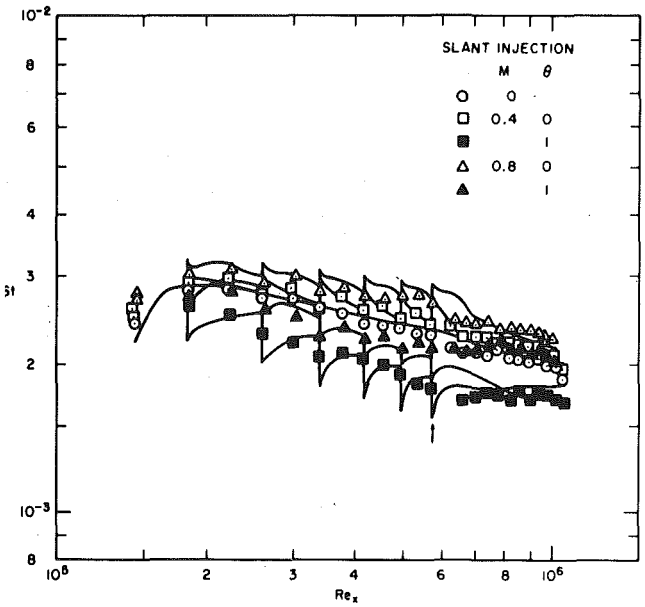

Fig. 6 Slant-angled injection with $P/D = 10$ and initial momentum and enthalpy Reynolds numbers of 500 and 500

transfer coefficient for $\theta = 1$ in the initial blowing region is 20 percent above the unblown value. This suggests that the jets of coolant greatly increase the turbulence production, and they have minimal cooling effect until the boundary sufficiently thickens. Blowing ratios greater than unity will probably have detrimental effects on the turbine blade aerodynamics.

Compound-angled injection data are shown in Fig. 8. The predictions are within about 10 percent of the data, but not nearly as good as the slant-angle predictions. The most significant feature of the data appears to be in the recovery region where, once the blowing ceases, the Stanton number with $\theta = 1$ begins to recover towards the $M = 0$ baseline. This is in marked contrast to the slant-angled injection data.

Normal-angled injection data are shown in Fig. 9. Note the difference in how the predictions rise to a maximum and then fall between each row of holes. The blowing ratios for normal injection are different from those for the oblique injection data sets, but the data trend is somewhat similar.

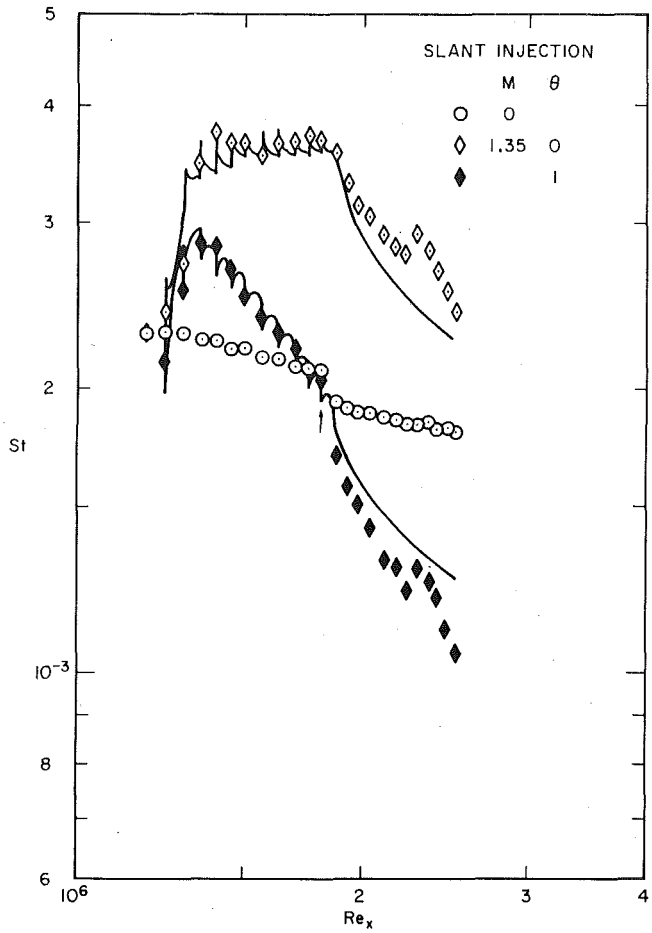

Fig. 7 Slant-angled injection with $P/D = 5$ and initial momentum and enthalpy Reynolds numbers of 3000 and 2100

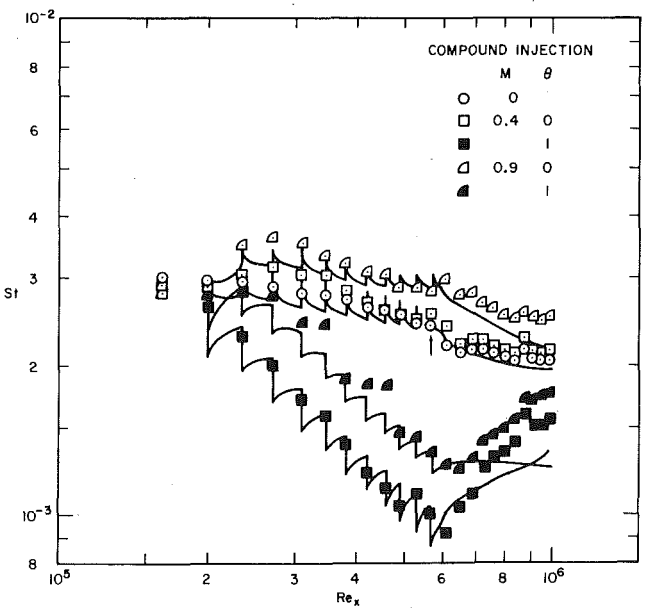

Fig. 8 Compound-angled injection with $P/D = 5$ and initial momentum and enthalpy. Reynolds numbers of 500 and 650

Discussion

There are four distinct flow fields on the film-cooled surface: (1) the initial film-cooling region; (2) the "asymptotic" film-cooling region (past the first few rows of holes); (3) the recovery region for low M; and (4) the recovery region for moderate to high M. It is not surprising that STANCOOL adequately models regions (2) and (3) and not (1) and (4). Region (2), the asymptotic film-cooling region, is represented

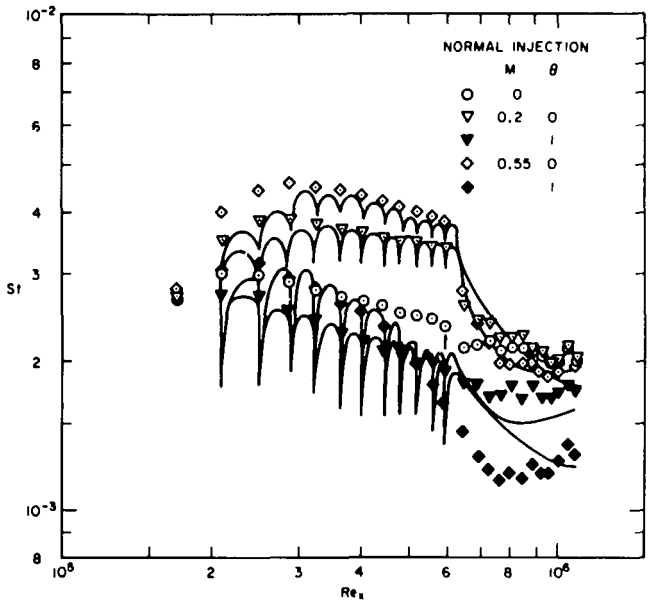

Fig. 9 Normal-angled injection with P/D = 5 and initial momentum and enthalpy Reynolds numbers of 550 and 600

by the injection and turbulence augmentation model. Region (3), the recovery region for low M, is indirectly modeled by the relatively fast decay of the augmented turbulence to its two-dimensional value and the fact that the recovery region profiles are not too different from the two-dimensional value.

For moderate to high M in the recovery region, the turbulence also quickly decays, but the velocity profiles are very flat and far from the two-dimensional value (Yavuzkurt, [11]). This causes turbulence production that is less than the two-dimensional value and seems to be the primary cause for the continual drop in Stanton number in the recovery region. The depression of the mixing-length below its two-dimensional value for moderate to high M is not modeled in STANCOOL.

The initial film-cooling region represents the transition from two-dimensional flow to three-dimensional spanwise-periodic flow. This region is not modeled in STANCOOL. The transition region is fairly short (several rows) for normal- and slant-angled injection and high initial Reynolds number. The region is longer (five to six rows) for low initial Reynolds number (a thin boundary layer compared to the jet diameter). For compound-angled injection the transition region occupies at least six rows of film cooling, and the flow field is distinctly different from normal- and slant-angled injection because of its strong streamwise vorticity.

Concluding Remarks

This paper describes a numerical procedure developed to simulate heat transfer with full-coverage film cooling. The procedure uses the STAN5 program, whose nucleus is the original Spalding-Patankar program. Routines have been added to the STAN5 program to model the injection process and turbulence augmentation. The turbulence level is modeled by algebraically augmenting the mixing length, with the augmentation keyed to a penetration distance for the injected fluid. Development of the injection and turbulence models was the outgrowth of detailed hydrodynamic and thermal boundary layer studies. Most of the Stanford data bases for normal-, slant-, and compound-angled injection have been successfully predicted using the same injection and turbulence model. Two model parameters are required, and they are a function of blowing ratio and geometry. Based on our experience with simple flows, including transpired turbulent boundary layers, we would expect the STANCOOL program to have at least limited success in extrapolating the predictions to the compressible, high velocity, pressure gradient conditions of a gas turbine engine. But, the effects of mainstream turbulence, rotation, and curvature would be missing. One point not yet answered is which should be used to describe the DELMR and ALAM prediction constant correlations for compressible, high-velocity flows: the ratio of coolant-to-mainstream velocity, the mass flux ratio, or the momentum ratio.

Acknowledgments

The data contained herein were obtained as a part of the doctoral research of H. Choe and M. E. Crawford, and Engineer's degree research of H. K. Kim. The authors wish to thank NASA Lewis Research Center for the support through contract NAS3-14336. We are grateful to Drs. R. S. Colladay and R. E. Gaugler for their interest in the research.

References

1 Choe, H., Kays, W. M., and Moffat, R. J., "Turbulent Boundary Layer on a Full-Coverage, Film-Cooled Surface—An Experimental Heat Transfer Study with Normal Injection," NASA Rep. CR-2642, 1976. (Also Stanford Univ., Dept. of Mech. Engrg., Report HMT-22).

2 Crawford, M. E., Kays, W. M., and Moffat, R. J., "Heat Transfer to a Full-Coverage, Film-Cooled Surface with 30° Slant-Hole Injection," NASA Rep. CR-2786, 1976. (Also Stanford Univ., Dept. of Mech. Engrg., Report HMT-25).

3 Herring, H. J., "A Method of Predicting the Behavior of a Turbulent Boundary Layer with Discrete Transpiration Jets," ASME JOURNAL OF ENGINEERING FOR POWER, Vol. 97, 1975, p. 214.

4 Bergeles, G., Gosman, A. D., and Launder, B. E, "The Prediction of Three- Dimensional Discrete-Hole Cooling Processes. Part 1—Laminar Flow," ASME *Journal of Heat Transfer*, Vol. 98, 1976, p. 379.

5 Bergeles, G., Gosman, A. D., and Launder, B. E., "The Turbulent Jet in a Cross Stream at Low Injection Rates: A Three-Dimensional Numerical Treatment," *Numerical Heat Transfer*, Vol. 1, 1978, p. 217.

6 Patankar, S. V., Basu, D. K., and Alpay, S. A., "Prediction of the Three-Dimensional Velocity Field of a Deflected Turbulent Jet," ASME *Journal of Fluids Engineering.*, Vol. 99, 1977, p. 758.

7 Crawford, M. E., Kays, W. M., and Moffat, R. J., "Full-Coverage Film Cooling on Flat, Isothermal Surfaces: A Summary Report on Data and Predictions," Stanford Univ., Dept. of Mech. Engrg., Report HMT-30, 1979.

8 Crawford, M. E., and Kays, W. M., "STAN5—A Program for Numerical Computation of Two-Dimensional Internal/External Boundary Layer Flows," NASA Rep. CR-2742, 1976. (Also Stanford Univ., Dept. of Mech. Engrg., Report HMT-23).

9 Abramovich, G. N., *The Theory of Turbulent Jets*, MIT Press, Cambridge, MA, 1963.

10 Colladay, R. S., and Russell, L. M., "Streakline Flow Visualization of Discrete Hole Film Cooling for Gas Turbine Applications," ASME *Journal of Heat Transfer*, Vol. 98, 1976, p. 245.

11 Yavuzkurt, S., Moffat, R. J., and Kays, W. M., "Full-Coverage Film Cooling: 3-Dimensional Measurements of Turbulence Structure and Prediction of Recovery Region Hydrodynamics," NASA Rep. CR-3104, 1979. (Also Stanford Univ., Dept. of Mech. Engrg., Report HMT-27).

12 Kim, H. K., Moffat, R. J., and Kays, W. M., "Heat Transfer to a Full-Coverage, Film-Cooled Surface with Compound-Angle (30° and 45°) Hole Injection," NASA Rep. CR-3103, 1979. (Also Stanford Univ., Dept. of Mech. Engrg., Report HMT-28).

13 Mayle, R. E., and Camarata, F. J., "Multihole Cooling film Effectiveness and Heat Transfer," ASME *Journal of Heat Transfer*, Vol. 97, 1975, p. 534.